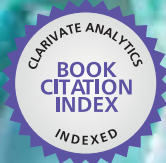# Advanced Topics in Crystallization

Edited by Yitzhak Mastai

ADVANCED TOPICS IN CRYSTALLIZATION

Edited by **Yitzhak Mastai**

Advanced Topics in Crystallization
http://dx.doi.org/10.5772/58651
Edited by Yitzhak Mastai

Contributors

Vadim Glebovsky, Nicole Stieger, Marique Aucamp, Wilna Liebenberg, Uziel Sandler, Nobuyuki Tanaka, Dong Nyung Lee, Min Gan, Xiaohui Fan, Xuling Chen, Humphrey Moynihan, Chika Nozaki Kato, Yousef Javadzadeh, Solmaz Maleki Dizaj, Zhila Vazifehasl, Masumeh Mokhtarpour, Nurit Taitel-Goldman, Ana Paula Badan Ribeiro, Lireny Aparecida Guaraldo Gonçalves, Renato Grimaldi, Luiz Antonio Gioielli, Lisandro Pavie Cardoso, Theo Guenter Kieckbusch, Maria Aliciane Fontenele Domingues, Renu Chadha, Dimpy Rani, Parnika Goyal, Gila Levi, Ortal Lidor-Shalev

Notice

Statements and opinions expressed in the chapters are these of the individual contributors and not necessarily those of the editors or publisher. No responsibility is accepted for the accuracy of information contained in the published chapters. The publisher assumes no responsibility for any damage or injury to persons or property arising out of the use of any materials, instructions, methods or ideas contained in the book.

We are IntechOpen,
the world's leading publisher of Open Access books
Built by scientists, for scientists

3,750+
Open access books available

115,000+
International authors and editors

119M+
Downloads

151
Countries delivered to

Our authors are among the
Top 1%
most cited scientists

12.2%
Contributors from top 500 universities

Interested in publishing with us?
Contact book.department@intechopen.com

Numbers displayed above are based on latest data collected.
For more information visit www.intechopen.com

Meet the editor

Prof. Yitzhak Mastai was born in 1966 in Tel Aviv, Israel. He obtained his B.Sc. in physical chemistry from Bar-Ilan University in 1989. He received his PhD from the Weizmann Institute of Science with Prof. Gary Hodes on nanomaterials synthesis (1999). He then went to the Max Planck Institute of Colloids and Interfaces for three years. During this time, he was a *postdoctoral* fellow alongside Prof. M. Antonietti and Prof. H Cölfen, working on biomimetic chemistry and chiral polymers. In 2003, he joined the staff of the Chemistry Department at Bar-Ilan University, where he is currently a Professor at the Institute of Nanotechnology. In this role, he leads the nano chirality laboratory. Prof. Mastai's earlier interests include nanomaterials synthesis and characterization. His current research focuses on the synthesis and analysis of chiral nanosurfaces, chiral self-assembled monolayers and polymeric chiral nanoparticles. Prof. Mastai has *published more than* 120 scientific articles and many book chapters and has edited two books on various aspects of nanomaterials and chirality at the nanoscale.

Contents

Preface

Crystallization is certainly among the most studied processes in science and is of great practical importance. This is because crystals are the pillars of modern technology. Without them, there would be no electronic or photonic industry and no fibre optic communications, solid state lasers, non-linear optics, piezo-electric, electro-optic or crystalline films for micro-electronics and computer industries. Crystallization is an elemental separation technique. It is one of the most simple self-assembly processes that is used to create order from the atomic to macroscopic scale. Finally, crystallization creates beautiful crystals of aesthetical value, which have fascinated humankind for centuries. Crystallization is an interdisciplinary subject that covers physics, chemistry, material science, chemical engineering, metallurgy, crystallography, mineralogy, etc.

It is not astonishing that crystallization processes have been studied for a long time, beginning in a systematic and scientific fashion at the end of the 18th century with alchemy. Over the past few decades, there has been a growing interest in crystal growth and crystallization processes, particularly in view of the increasing demand of materials for technological applications. Having been studied for over a century, one might think that a process of such scientific and technological importance is well known, right down to the finest details. However, this is not the case. The understanding of crystallization, beginning with the atomic level, is still rather restricted. The same can be said for the interface of a crystal with solvents and other dissolved compounds.

The overall purpose of this book is to provide timely and in-depth coverage of selected advanced topics of crystallization. This book goes into considerable detail about the many elements of knowledge that are needed to understand, both quantitatively and qualitatively, the advanced subjects of the crystallization process. The chapters in this book have been contributed by the most respected researchers in this area and cover the frontier areas of research and developments in crystallization processes. They incorporate the most recent developments and applications of crystallization technology. Divided into three sections, this book provides the latest research developments in many aspects of crystallization including the crystallization of biological macromolecules and pharmaceutical compounds, the crystallization of nanomaterials and the crystallization of amorphous and glassy materials. It is our hope that you, as readers, find this book useful for your work. If so, this will be the best reward for us.

I wish to thank all of the authors for their contributions to this book. Additionally, it is my pleasure to acknowledge the assistance of Ms Iva Lipović, who showed continued support during the write-up of this book and preparation of the final format.

Finally, I would like to acknowledge my family, who has supported me throughout all my years of studying science - to my wife, Dina von Schwarze, and to our children, Michael, Reut and Noa for their patience and support.

Yitzhak Mastai

Department of Chemistry and the Institute of Nanotechnology

Bar-Ilan University,

Ramat-Gan, Israel

Crystallization of Biological Macromolecules and Pharmaceutical Compounds

Solvent-Interactive Transformations of Pharmaceutical Compounds

Marique Elizabeth Aucamp, Wilna Liebenberg and Nicole Stieger

Additional information is available at the end of the chapter

1. Introduction

A major factor which determines the overall success of a pharmaceutical product is the solid-state form in which the active pharmaceutical compound exists. It is a well-known fact that most pharmaceuticals possess the ability to exist in different solid forms. The solid-state of a compound significantly influences the physical-, chemical and mechanical properties exhibited by the drug [1, 2]. Subsequently, these properties not only affect the processability and stability of a drug, but also the dissolution and bioavailability thereof [3]. Optimal drug performance depends to a large extent on the solid-state form used in the design and development of a pharmaceutical product. Considering the abovementioned facts it becomes quite evident why it is so important to select the best solid-state form of a given drug to be incorporated into a dosage form. Not only is it imperative that the appropriate solid-state form is chosen, but also to ensure that the specific form will remain unchanged during processing, manufacturing as well as during distribution and storage of the final product [4]. Knowledge of solid-state forms of drugs and the identification of possible transformations have developed from mere scientific interest to matters that must be addressed for every dosage form.

Usually, the most stable solid-state form of a given drug is preferred for incorporation into marketable formulations, because a metastable form may transform to its stable counterpart. Such a transformation may lead to precipitation from solution, physical instability of the dosage form and even changes, and resultant unpredictability, in the bioavailability thereof [5]. Whilst the most stable solid-state forms of drugs offer the best shelf-life for products, they are also always the least soluble forms. This is the reason why there is now a heightened interest in the use of metastable solid-state forms such as metastable polymorphs, amorphous drugs and amorphous solid dispersions, in pharmaceutical products. A decade ago the incorporation of metastable forms in dosage forms was almost unthinkable and a contradiction of pharmaceutical manufacturing guidelines, but it is steadily becoming more commonplace. The

challenge facing pharmaceutical researchers is understanding and preventing/managing the tendency of these metastable forms to invariably revert to their most thermodynamically stable solid-state form, either during processing, storage, distribution or patient administration [3].

Transformations often result from the interaction of a drug with a solvent. These transformations are usually classified as: solvent-mediated, solution-mediated or solvent-exchange processes. A review of current literature quickly shows that these terms, especially the first two, are often used interchangeably and that many authors have different views on which process is involved in a given transformation. It is evident that the different solvent-interactive processes need to be defined more clearly and, by reverting to fundamental principles, this chapter aims to do just that.

2. Overview of solid-state transformations

A solid-state transformation may be defined as any transition from one solid-state form of a compound to another solid-state form resulting in the same composition but different packing arrangement. The phenomena that govern solid-state transformations can be classified as thermodynamic, kinetic and molecular recognition. Competition or reinforcement between these processes is affected by mechanical, thermal and chemical stresses. Molecular recognition determines the number of possible solid-states for any given molecular entity. Thermodynamics control the relative stability and the conditions/direction in which a transformation can occur, but kinetics determines how long a transformation will take [6, 7, 8]. The transformations that may occur in drugs are classified in accordance to the general underlying process(es) of the transformation(s). The following are listed by Zhang *et al*. [4]: solid-solid, solvent-mediated and solution-mediated. All solid-state transformation types will not be discussed in this chapter but for the sake of completeness and to serve as a quick reference guide, Table 1 summarises solid-state transformations, as described in literature, in terms of the type of transformation, possible underlying process(es) as well as processing steps that might induce each transformation. The next few paragraphs will briefly discuss all solid-state transformations. Special attention will be paid to the transitions involving solvent-interactive transformations and these will be discussed in more detail throughout the chapter.

Solid-solid transformations occur as a direct conversion from one solid-state form to another without an intermediate solution or melt phase. Melt-induced transformation occurs when a solid-state form of a drug is melted and subsequently cooled. Parameters such as the cooling rate, nucleation rate and the presence of impurities or seed crystals determine the solid-state form that will be produced. In such a solid-melt-solid process, both the initial form and the resultant form can be either crystalline or amorphous [4]. Solution-mediated and solvent-mediated transformations are typically respectively described only as occurring in solution or in the presence of a solvent (or solvent vapour). Two important facts that should be highlighted here is that almost any environment or processing method can initiate a solid-state transformation and also that it can be extremely difficult to identify the causative agent or process.

The study and proper understanding of the types of solid-state transformations is currently seen as imperative within the pharmaceutical industry. Recently more and more attention is

being paid to the identification of solid-state transitions of drugs and excipients. As mentioned earlier, the physical state in which an active pharmaceutical ingredient (API) exists is determinant towards the stability, processability, solubility and bioavailability of the compound [2]. Transformation studies of pharmaceutical compounds will assist in the identification of the type of solid-state transformation that occurs, which in turn will help to identify the mechanism of the transformation process and most importantly the processing step responsible for the transformation. Information obtained through transformation studies will allow pharmaceutical scientists to make appropriate, cost-effective and time saving decisions throughout the manufacturing process of a pharmaceutical product.

Transformation type	Transformation result	Transformation process	Possible processing step involved
Solvation or hydration	• Transformation of an anhydrous crystalline form to a solvate or hydrate	• Solution-mediated • Solvent-mediated	• Crystallisation • Wet granulation • Pelletisation • Exposure to humidity/moisture during manufacturing or storage
Desolvation or dehydration	• Solvate/hydrate to amorphous form • Solvate/hydrate to anhydrous crystalline form	• Solid-solid	• Exposure to dry conditions during manufacturing or storage • Processing steps involving the drying of the drug i.e. spray-drying, freeze-drying or fluid-bed drying
Polymorphic transformation	• Polymorphic form X to polymorphic form Y of a drug	• Solid-solid • Solution-mediated • Solid-melt-solid	• Grinding/milling • Compression • Heating • Recrystallisation • Heating above melting point, followed by cooling • Dissolution or solubility testing of metastable forms
Vitrification	• Crystalline form to amorphous form • Solvate/hydrate to amorphous form	• Solid-solid • Solid-melt-solid	• Milling • Compression • Dehydration of solvates/hydrates • Spray-drying • Freeze-drying • Quench cooling of the melt
Crystallisation	• Amorphous form to crystalline form	• Solution-mediated • Solid-solid	• Heating • Grinding/milling • Humidity or plasticiser-induced crystallisation • Dissolution or solubility testing of amorphous drugs

Table 1. Summary of solid-state transformations of drugs [4, 9]

The unintentional transformation of a solid form to another is an unwanted occurrence within the pharmaceutical industry. If necessary preventative steps aren't put in place, a multitude of unplanned solid-state transitions can occur throughout the manufacturing and processing cycle of a pharmaceutical compound, leading to unexpected and unwanted product properties. One unintended transition can lead to an array of problems that detrimentally affect further processing and development steps. Solid-state transformations may also be advantageous, if they are utilised in a controlled and conscious manner to deliberately obtain alternate solid-state forms.

3. Solvent-interactive transformations

Within the context of solid-state transformations, we propose the use of *"solvent-interactive transformations"* as a collective term for all transformations that are caused or accelerated by the presence of solvent. One often sees the two terms, solvent- or solution-mediated transformations, used interchangeably by many authors when, in fact, they are very different processes. The synonymous use of these two terms can be attributed to a lack of proper understanding of the different pathways that the two transformations follow. This section aims to explain the subtle but extremely significant differences between solvent- and solution-mediated transformations, as well as to put forth a new concept namely *"solvent-catalysed transformation"*.

In an effort to obtain sufficient information to clarify the discrepancies that exist with the current use of the terms solvent- and solution-mediated, a literature study was undertaken. Table 2 provides a summary of some of the misconceptions and overly generalised statements found in literature.

Solvent-mediated transformation	Solution-mediated transformation
-	Always: Metastable form → Stable form
Driving force is the removal of solvent from the system	-
Transformation occurs during drying/removal of solvent	Transformation occurs when metastable form is in contact with the saturated solution of the drug
Transition occur out of solvent	Transition occurs in solvent

Table 2. Summary of some of the misconceptions and overly generalised statements regarding solvent- and solution-mediated transformations, as currently found in literature [4, 5, 9, 10, 11]

Our attempts to extract, from literature, concrete facts and unambiguous definitions that could be applied to explain the difference between solvent- and solution-mediated transformation, has met mostly with failure. To make sense of all the contradictory information that is available in current texts, we have opted for a fresh start in defining the relevant terms based on fundamentals. The first question that needs to be answered is: What does "*mediation*" mean in scientific context?

Mediate: "Exhibiting indirect causation, connection, or relation" [12] or "Connected indirectly through another person or thing" [13]. From these definitions it is clear that only those solvent-interactive transformations in which the initial solid form does not directly transform to a second solid form may be described as being either solvent- or solution-*mediated*.

Mediation may be further elaborated upon by employing, in its most simple form, the concept of a statistical mediation model (Figure 1) [14]. According to such a model, the initial solid form (Form X) is the independent variable, because it is the starting material and its existence is independent of both the transformation itself (B) and the product of transformation (Form Y). In a mediated process, there is no direct causal relationship (C) between the independent variable (starting material) and the dependent variable (product of the transformation). Instead, the relationship between the independent variable and the dependent variable is governed by a mediator variable, which in this case is either a solution or a solid-solvent association.

The product of a mediated transformation may be either more or less stable than the starting material. Dissolution testing of a metastable starting material may cause solution-mediated transformation to a more stable form, but recrystallisation techniques may also be used to produce metastable forms of a stable starting material *via* solution-mediated transformation. It is important to keep in mind that this chapter focusses on but one variable, the role of solvents, but in real-world applications the outcome of a mediated transformation will be dependent on numerous thermodynamic and kinetic variables [6].

Many solid-solid transformations are capable, given enough time, of converting one form to another without the aid of solvent interaction (F), but they occur much more rapidly in the presence of a solvent or solvent vapour (E). To occur without mediation, such transformations need to be thermodynamically favoured and therefore can only result in products that are more stable than the starting material. The fact that solvents can accelerate these transformations is evidence of solid-solvent interaction (solvent-interactive transformation), but direct conversion rules out mediation. In these instances the solvent or solvent vapour acts as a catalyst to transformation by reducing the energy barrier and increasing the rate at which the transformation occurs. This is a purely kinetic phenomenon. We therefore propose the use of the term "*solvent-catalysed transformation*" for cases where a solvent or solvent vapour increases the rate of a non-mediated transformation.

Some authors [4, 9, 10] have described solvent-mediated processes as requiring the removal of the solvent to obtain the transformation product. We believe that this may be ascribed to a failure to distinguish between multiple transformations. It is much more likely that solvent-mediated transformation will have resulted in a metastable form (Form Y) that subsequently transformed, *via* regular non solvent-interactive solid-solid transformation (G), to a more stable form (Form Z). Another possibility is that said metastable form (Form Y) could have undergone solvent-catalysed transformation to a more stable form (Form Z).

From the above discussion, the following definitions were distilled:

Solvent-interactive transformation: A solid-state transformation which is *caused or accelerated* by the presence of solvent in liquid or vapour form.
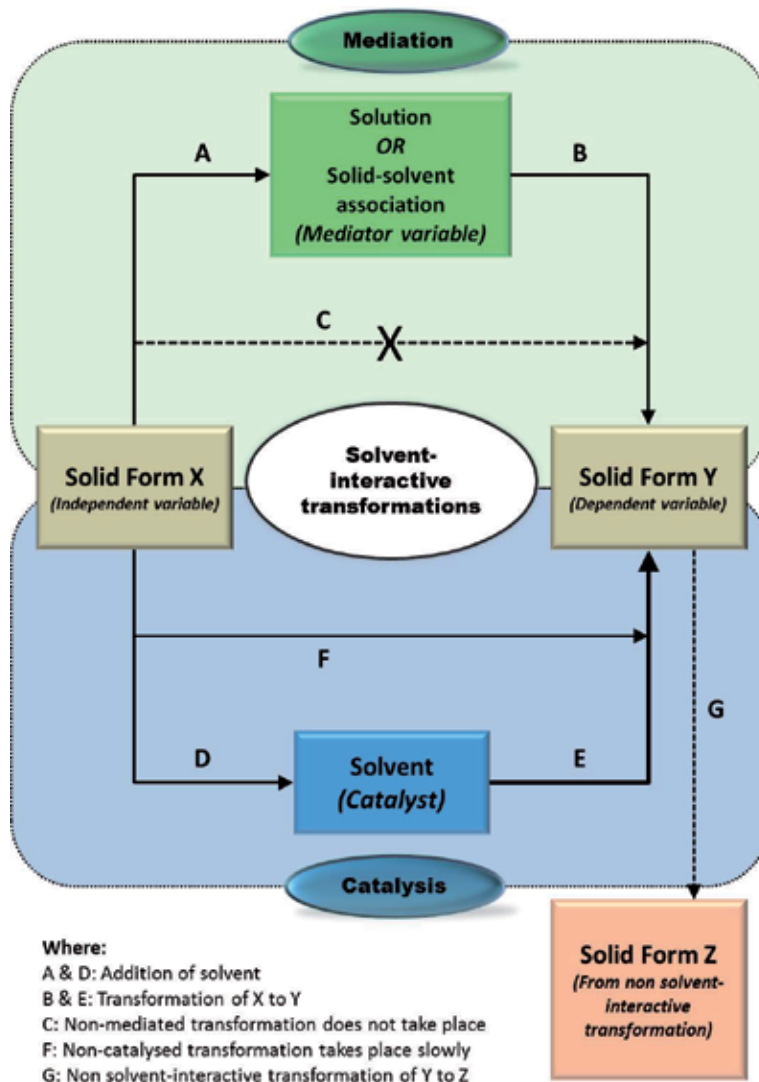
Figure 1. Solvent-interactive transformations.

Three types of solvent-interactive transformation exist:

- **Solution-mediated transformation:** A solid-solution-solid transformation of the solid-state in which *no direct* transformation of the starting material to the product takes place, but which is instead mediated by a *solution* of the starting material in a solvent that was introduced in liquid or vapour state.

  Examples:

  ○ Dissolution: metastable form transforms to stable form

- ◦ Recrystallisation to obtain polymorphs, hydrates and solvates

- ◦ Vapour sorption on the surface of the starting material resulting in deliquescence and subsequent transformation to a hydrate/solvate or more stable polymorph

- **Solvent-mediated transformation:** A solid-solid transformation of the solid-state in which *no direct* transformation of the starting material to the product takes place, but which is instead mediated by an interaction between the *undissolved* starting material and a solvent that was introduced in liquid or vapour state.

  Examples:

  - ◦ Anhydrous form converting to a hydrate or solvate

  - ◦ Solvent exchange resulting in a change of structure

  - ◦ Crystallisation of an amorphous form to a *solvate or hydrate*

- **Solvent-catalysed transformation:** A *direct*, *non-mediated*, solid-solid transformation of the solid-state which is accelerated by the *catalytic effect* of a solvent introduced in liquid or vapour state.

  Example:

  - ◦ Accelerated crystallisation of an amorphous form to an *anhydrous* crystalline form due to plasticisation

With fundamental definitions now having been set, Table 2 should be reconsidered. It is now obvious that the driving force for solvent-mediated transformation cannot be the removal of the solvent and that any transformation subsequently taking place outside of the solvent during drying has to be a non solvent-interactive solid-solid transformation. It is equally obvious that solution-mediated transformation is not limited to metastable forms that convert to more stable forms. The last two statements about solution-mediated transformation in Table 2 are perhaps not erroneous *per se*, but they are vague enough to warrant further discussion. A metastable form will convert to a more stable form *via* solution-mediated transformation if a saturated solution of the metastable form, supersaturated regarding the stable form, exists. Transformation will happen through nucleation and crystal growth of the stable form. This means that continued contact with the metastable form is only required to feed and maintain crystal growth of the stable form. As for the transformation taking place "in solvent", the presence of solvent is most definitely required for a solution of the starting material to be obtained, however the starting material needs not necessarily have been placed "in solvent". If solvent vapour were to adsorb onto the starting material, and said material is sufficiently soluble in that solvent, the solid may deliquesce to create a solution layer around it in which solution-mediated transformation could take place.

The processes and implications of solvent-interactive transformations will be discussed, with reference to practical examples, in the following section.
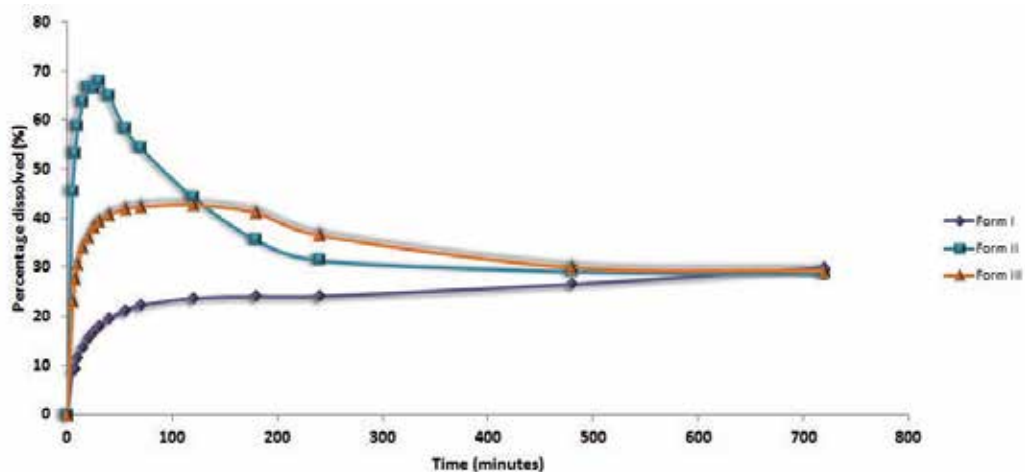
Figure 2. Dissolution profiles obtained from powder dissolution studies of different roxithromycin solid-state forms at 25°C and 100 rpm rotational speed. (Form I=roxithromycin monohydrate; Form II=amorphous roxithromycin; and Form III=roxithromycin anhydrate).

4. Implications of solvent-interactive transformations

Solid-state transformations can affect a significant number of solid dosage form attributes. Aspects like dissolution, bioavailability, stability, appearance, manufacturability, hardness, to name but a few, can be influenced by solid-state transformations [15]. The effect of solvent-interactive transformations on the dissolution and bioavailability of metastable drugs is of particular concern, especially with poorly soluble drugs where a further decrease in solubility or dissolution rate will negatively impact bioavailability and subsequent treatment outcomes [4]. In this section the macrolide antibiotic, roxithromycin, will be used as a model drug to illustrate the effects of solvent-interactive transformations on solid-state properties.

Studies on the physico-chemical properties of roxithromycin showed that solid-state transformations attributable to solvent interaction are possible. Solution-mediated transformation of roxithromycin metastable forms to the thermodynamically favoured form was identified during dissolution studies. Powder dissolution studies were done using three solid-state forms of roxithromycin [16]. During the dissolution studies of the roxithromycin solid-state forms, the solid-state transformation of the metastable forms to the stable monohydrate was demonstrated. Powder dissolution studies were done in distilled water at 25°C with a rotational speed of 100 rpm. No medium replacement was done, because doing so will mask or suppress the transformation. During the dissolution process a steady decline in the dissolved roxithromycin concentration was observed after about 120 minutes for roxithromycin Form III (anhydrate). In comparison, the transformation of the amorphous form of roxithromycin (Form II) to stable Form I resulted in a concentration decrease after approximately 40 minutes (Figure 2).

Further studies of the solution-mediated transformation process of roxithromycin solid-state forms were done utilising X-ray powder diffraction (XRPD) and subsequent principal

component analysis (PCA). During the XRPD experiments anhydrous and amorphous roxithromycin (Form III and II, respectively) were separately exposed to a sufficient amount of distilled water to allow dissolution, resulting in the nucleation and crystal growth of Form I. This experiment was performed at 25°C (± 2°C). From the experimental data of the transformation process of Form III to Form I it was possible to quantify the transformation process. This was done by following either the decrease or increase of a particular Bragg peak, characteristic to the solid-state forms under investigation. This method was investigated and established as an accepted technique to determine phase transformations by Klug and Alexander in 1974 [17].

The decrease of the anhydrous portion and subsequent increase of the monohydrate form of roxithromycin is plotted *versus* time in Figure 3. With the help of the phase proportion graph the investigators were able to determine the time required for Form III to completely disappear [16].

The XRPD cluster analysis of amorphous roxithromycin is depicted in Figure 4. The plot shows a 25% conversion from cluster 1 to cluster 23 and further cluster analysis eventually showed a 100% conversion of Form II to stable Form I as depicted in Figure 5.
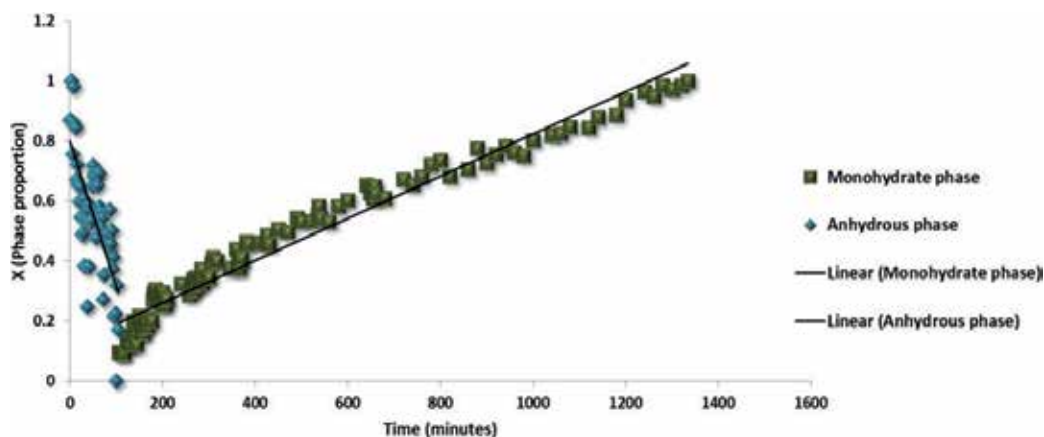
Figure 3. Phase conversion of anhydrous roxithromycin (Form III) to the stable monohydrate (Form I) at 25°C (± 2°C). Adapted, with permission from [16].

The pharmaceutical impact of such a solid-state transformation can be significant. Currently, the incorporation of metastable forms of drugs into solid dosage forms is at the order of the day due to their improved dissolution and solubility properties. When considering a solution-mediated transformation such as described above, one can see that it will lead to a decrease in the solubility and dissolution rate of a drug, which will ultimately influence the bioavailability negatively. At this time no reports could be found on solution-mediated transformations that have occurred *in vivo*, but we could also not find any mention of it yet having been investigated at all. In theory it could happen that the *in vivo* rate of dissolution of an orally administered solid metastable form might exceed the maximum possible rate of absorption for that specific
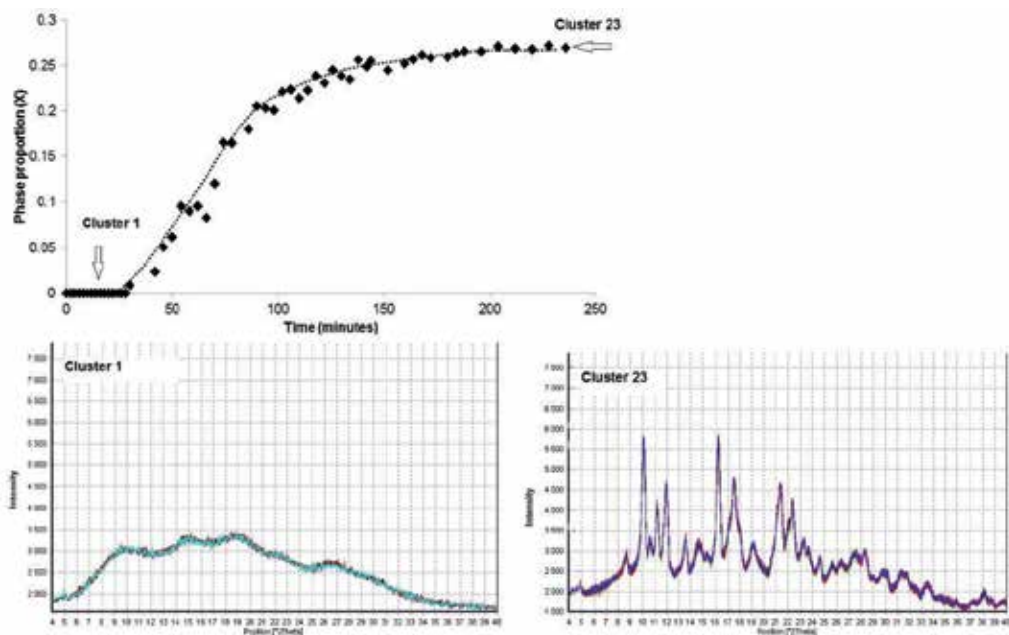
Figure 4. Phase conversion of amorphous roxithromycin at 25°C (± 2°C) determined with XRPD cluster analysis (PCA).
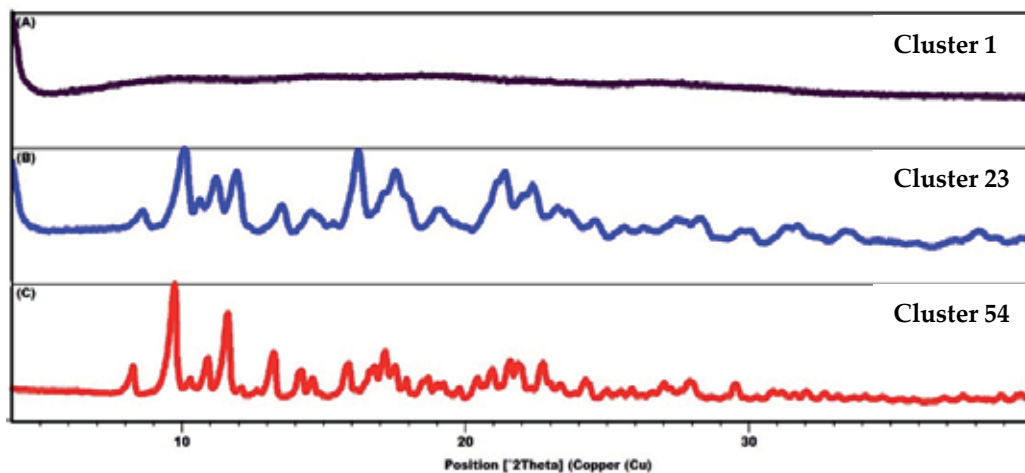
Figure 5. Representative XRPD patterns showing the solid-state transformation of amorphous roxithromycin (A). (B=PCA Cluster 23: partial conversion; C=PCA Cluster 54: complete conversion to Form I).

drug, resulting in a supersaturated solution that can lead to nucleation and crystal growth of the more stable, less soluble drug within the gastro-intestinal tract.

Another theoretical possibility is that, during dissolution testing, the undissolved portion of a metastable solid could undergo solvent-mediated and/or solvent-catalysed transformation

parallel to the solution-mediated process in which the dissolved portion is participating. To investigate the possibility of parallel solvent-interactive transformations occurring during the dissolution testing of metastable roxithromycin forms, vapour-sorption studies were performed. The vapour sorption isotherm given in Figure 6 shows no recrystallisation due to solvent-interactive transformation. Had solvent-interactive crystallisation taken place, it would have been evident from a step increase or-decrease in the weight of the sample [18] as opposed to the observed gradual increase and decrease corresponding to relative humidity. A step increase in the weight during crystallisation can be explained by the incorporation of solvent molecules in the new crystal structure to form a solvate/hydrate by solvent-mediated transformation. When a step increase is observed during sorption analysis, care should be taken to rule out the possibility of deliquescence however, this will likely manifest as a more drawn-out process of weight gain and the sample will become visibly wet. Deliquescence of a sample due to the exposure to vapour might lead to a solution-mediated transformation. A step decrease in sample weight associated with solvent-interactive transformation can be ascribed to the fact that a form results which has a denser crystal structure, more efficient molecular packing arrangement and fewer voids which may accommodate solvent molecules. The transformation to a denser form therefore leads to the displacement of solvent molecules from the solid and a resultant decrease in sample weight. A step decrease may be observed if an anhydrous crystalline form is obtained *via* solvent-catalysed transformation OR if the hydrate/solvate, produced *via* solvent-mediated transformation, incorporates less solvent than the starting material can accommodate at the same humidity level.

Evaporative recrystallisation (at 25°C ± 2°C) of roxithromycin monohydrate (Form I) from dichloromethane (DCM) results in a roxithromycin DCM solvate *via* solution-mediated transformation. Drying of the DCM solvate in an oven at 50°C for 24 hours, results in desolvation to roxithromycin anhydrate (Form III) by means of a non solvent-interactive solid-solid transformation. The XRPD patterns of Form I, Form III and the DCM solvate are given in Figure 7.

Roxithromycin is also capable of a solid-state transformation through a solvent-mediated process by means of solvent exchange. Mallet *et al.* [19] reported the transformation of a 1:1 roxithromycin acetonitrile (ACN) solvate to roxithromycin Form I *via* a solid-solid transformation in the presence of water vapour. During this study, well-defined single crystals of the roxithromycin ACN solvate were removed from the crystallisation medium and maintained at 100% relative humidity (RH) and ambient temperature. The investigators observed that the initially clear crystals became opaque after 48 hours however, the shape of the crystals remained unchanged. Subsequent analysis of the opaque crystals showed that the acetonitrile molecules had been replaced by water, resulting in a stoichiometry of 1:1 (roxithromycin : water). One might argue that the transition could also have been due to a solution-mediated process since an environment of 100% RH could have led to deliquescence of the crystals and resultant dissolution and recrystallisation. Further studies by Aucamp [20] however, showed that the same transformation will occur at ambient conditions. The study showed that, upon storage of the acetonitrile solvate crystals

at ambient conditions (25°C / 65% RH), the same transformation occurs, resulting in roxithromycin : water (1:1) stoichiometry.
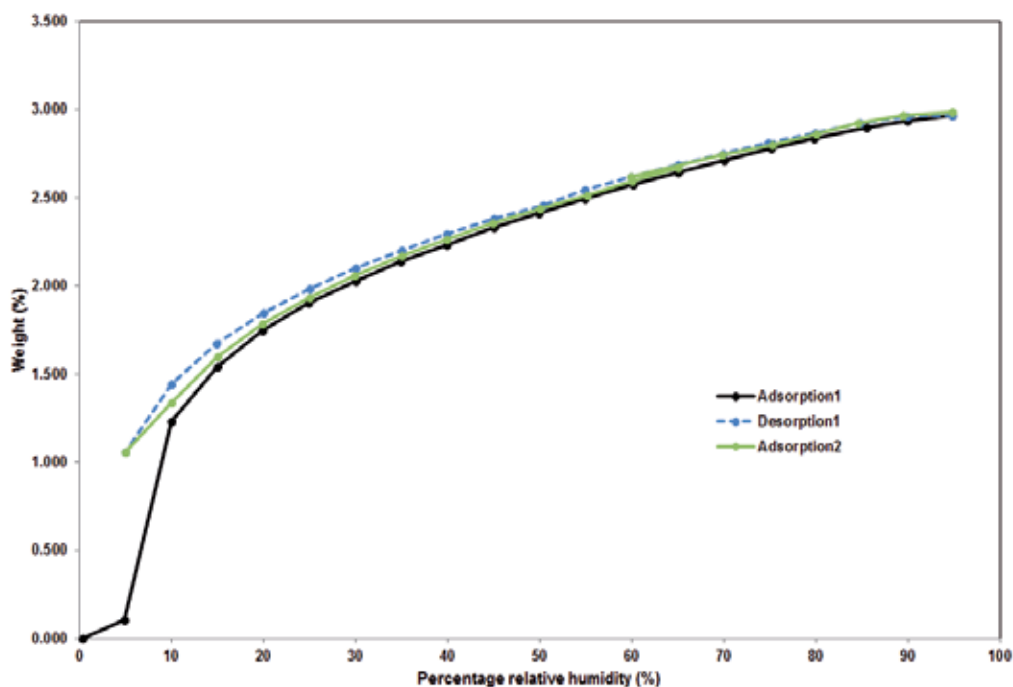
Figure 6. Moisture sorption isotherms of amorphous roxithromycin. Adapted, with permission, from [16].

Considering the fact that it can be challenging to determine whether any given solvent-interactive transformation is occurring in isolation, in parallel with others, or even as part of a number of transformation steps, care should be taken when interpreting experimental observations and, where possible, multiple techniques should be used to verify results.

5. Solid-state transformations and pharmaceutical manufacturing

The previous sections focused on neat APIs and transformations that occur during pre-formulation steps. However, it should be mentioned that the combination of drugs with excipients might also lead to significant phase changes. Tablets and capsules contain drugs and excipients and are formulated in such a manner that enhanced performance and physical appearance will be obtained. Even if the physico-chemical properties of the drug are taken into
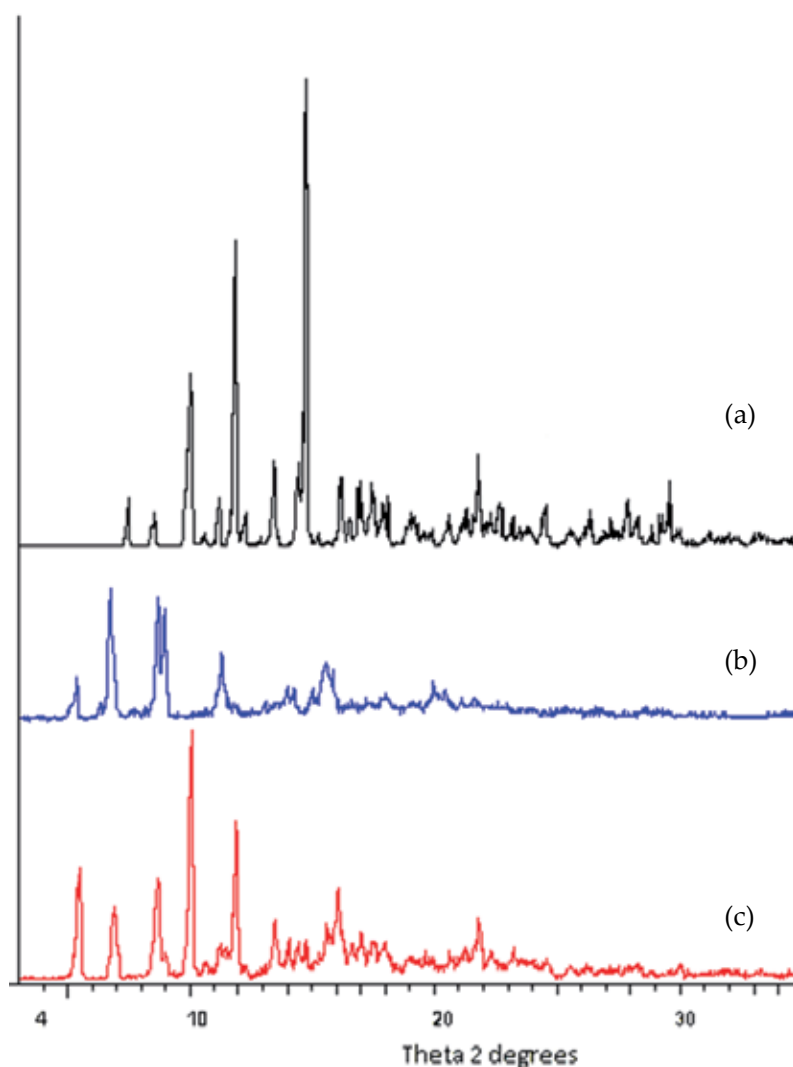
Figure 7. XRPD patterns of (a) roxithromycin monohydrate (Form I), (b) a roxithromycin DCM solvate and (c) roxithromycin anhydrate (Form III). Single crystal structural data of roxithromycin Form I (monohydrate) is available from the Cambridge Structural Database (reference code: FMPROA) [19].

account and compensated for, the excipients included in the formulation, as well as, the manufacturing steps taken, can still cause unforeseen solid-state transformations of the drug. It cannot be emphasised enough that, after an in-depth physico-chemical study of the drug, the next step should be to investigate the effects that excipients and processing of the drug in combination with excipients will have on the solid-state properties of the drug. Excipients may facilitate conversion of an amorphous form to a crystalline form or *vice versa*. Hydration or dehydration of a drug might be triggered by an excipient, which might lead to the formation of metastable or stable forms or mixtures of various crystalline forms of a given drug. All of

these solid-state changes can have detrimental effects on the product stability and ultimately the treatment of patients.

A multitude of processes are employed during the manufacturing of solid dosage forms (Figure 8). Although some of these methods do not involve the use of solvents, it should be realised that these methods can alter the solid-state of the drug and this altered state might be prone to solvent-interactive transformations at a later stage.

Generally, the first step during the manufacturing of a solid dosage form is size reduction of the drug particles. Size reduction is necessary to improve morphological characteristics, powder flow properties and uniformity. Size reduction is usually achieved through milling [4]. Milling or grinding imparts mechanical stress and often generates heat that might cause dehydration or complete/partial vitrification of the drug. If the intactness of the preferred solid-state is not confirmed at this stage, any undetected solid-state transformation will be problematic during ensuing stages of manufacturing or during after-production quality testing. Therefore, because milling can cause solid-solid transformations it is imperative to understand that incorporation of a drug, with an already altered state, into a product will most probably lead to solvent-interactive transformations during other stages of the production cycle.

Granulation is often the next processing step to which a drug is subjected. During this step, the combination of the drug with some or other excipients come into play. Granulation is a processing step that is employed to improve flowability, cohesiveness, compressibility and/or lubrication of the bulk material. There are very few APIs that do not need improvement in terms of flowability or compressibility and therefore a substantial percentage of drugs are granulated before further formulation steps towards tablet/capsule production. Two types of granulation are commonly used in industry, namely: wet granulation and dry granulation. Wet granulation is the most widely used due to its versatility and superior results in terms of bulk properties. Even though wet granulation is usually the preferred method for granulation it is also the most likely to induce solid-state transformations. The liquid used during the granulation process, drying parameters, drug loading, solubility of the drug in the granulation fluid and the procedure for including the drug into the granules are all factors that may affect the solid-state form of the drug. Wet granulation creates favourable conditions for solvent-interactive transformations to occur, often resulting in hydration/solvation, polymorphic conversions, vitrification or crystallisation [4].

In solid dosage form manufacturing, the use of dry granulation is reserved for drugs that are sensitive to moisture and/or elevated temperatures, because it requires neither solvents for granulation nor heat for drying. The mechanical stresses imparted on the drug through the dry granulation process can lead to solid-solid transformations that ultimately might lead to solvent-interactive transformation further along the manufacturing process. For both wet-and dry granulation, mixing with excipients might also induce solid-state transformations due to incompatibility reactions that might occur.

Spray-drying is a technique that produces homogenous particles of uniform shape and size. This process requires the complete or partial dissolution of the drug in a solvent and therefore increases the probability of solid-state changes due to solvent-interactive transformation.
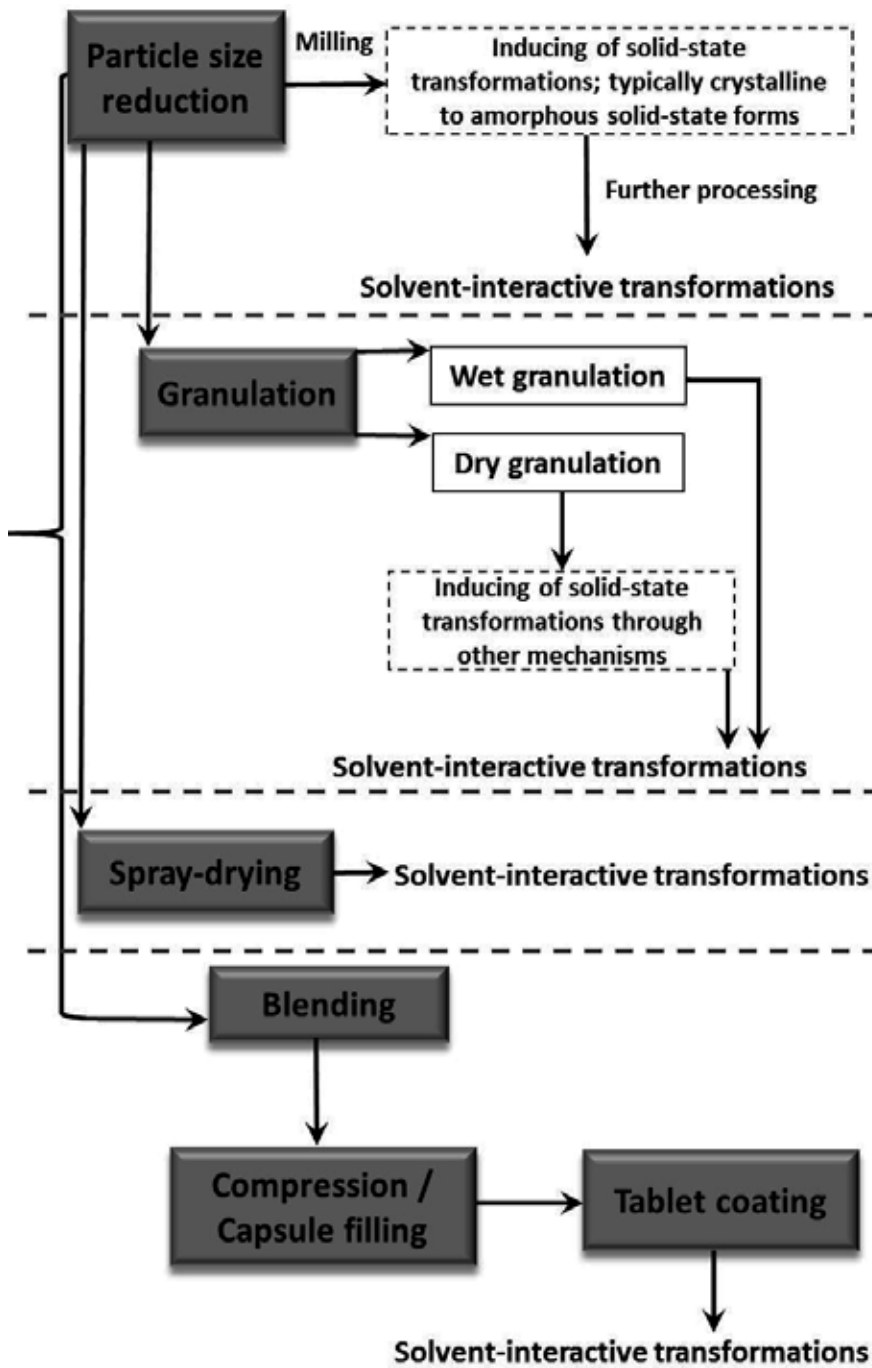
Figure 8. Flow diagram illustrating the processing steps for a pharmaceutical product, to obtain a solid dosage form, indicating where solvent-interactive transformations can occur.

Solvent removal from the spray of droplets is a rapid process that may lead to crystallisation of a metastable form or even another polymorphic form [4, 21].

After powder characteristics have been improved, a second granulation or blending step usually follows. This processing step is generally considered a low energy and- intensity step and is unlikely to induce solid-state changes, although it should not be completely excluded as a possibility. Also, the fact that the drug is now being mixed with lubricants, glidants and disintegrants makes the detection of phase changes more difficult. Tablet compression is another high energy process that can induce solid-solid transformations to metastable forms. Following compression of the drug-excipient blends, a coating process may be required or desired. In most cases it is unlikely that a solid-state change will occur during film-coating due to the fact that process parameters have been optimised to such an extent that the period of time for which the tablet is subjected to the coating solution is minimal. Drying of the coating by means of an efficient air exchange method also ensures a short exposure time of the tablet to the coating solution [4]. On the other hand, coating procedures used in the manufacture of modified release products may cause problems. Generally, in the case of modified release products, a portion of the total dose may be applied as a drug coating layer. This coat is essential in providing immediate release for fast onset of action. Typically, the drug layer is applied by spraying a drug-excipient solution or suspension onto the tablet surface. Dissolving or suspending the drug in a liquid significantly increases the probability of solvent-interactive transformations occurring. Furthermore, the rapid solvent removal after the coating process could lead to the precipitation of an altered solid-state form in the coating layer [4].

Considering all the pitfalls and challenges mentioned above, it becomes clear that solid-state transformations and the prevention thereof are of critical importance to the pharmaceutical industry. Not only must the pharmaceutical scientist keep a watchful eye out for solvent-interactive transformations occurring during the manufacturing of neat drugs, but attention must also be paid to solid-solid transformations arising during final product manufacturing.

6. Regulatory requirements: Solid-state characterisation and monitoring

According to the Food and Drug Administration's (FDA's) guideline on drug substances it is a regulatory requirement that the solid-state form of a drug be controlled throughout all processing and manufacturing steps. It is also required that the solid-state form of a drug must be known at any given time during the product manufacturing process, as well as during storage and distribution. Guidelines established by the International Conference for Harmonization (ICH) require a complete polymorphic study of a new drug prior to the product development stage [1, 4, 22].

Nearly a decade ago, a regulatory framework, namely Process Analytical Technology (PAT), was established. This FDA initiative encompasses the following:

1. To ensure product quality and performance through the design of effective and efficient manufacturing processes;

2. Specifications of products and processes are based on a mechanistic understanding of how processing steps and formulation can affect product performance;

3. Continuous and real-time quality assurance of the pharmaceutical compound;

4. Risk-based regulatory approaches to understand how formulation and manufacturing processes can affect the quality and performance of the end-product; and

5. The establishment of process control strategies to prevent or mitigate the risk of having a poor quality product at the end of a manufacturing process.

PAT was developed to ultimately build quality into pharmaceutical products. The guide highlights the necessity for understanding processes that could detrimentally affect pharmaceutical products [22, 23]. It is not only thorough initial characterisation (and the reporting of knowledge gained) that is essential, but also the continuous monitoring of pharmaceutical ingredients during the manufacturing of medicines. In essence, this guide states that the solid-state form used to produce a dosage form must be known, as well the effects of solid-state changes on the performance or stability of the drug product. The influence that solvent-interactive transformations can have on the solid-state properties of a drug was discussed in detail in the previous sections of this chapter.

Numerous analytical techniques are available for the rigorous characterisation and monitoring of solid-state forms of APIs. To avoid oversights and inconclusive results, it is always advisable to use multiple complimentary techniques. Advances made in the refinement of techniques, and the improvement of equipment sensitivity, allow for better characterisation of not only new chemical entities (NCEs), but also older ones for which comprehensive data was not previously available. The "re-discovery" of older drugs is important and opens up many opportunities for the development of optimised products with improved patient treatment outcomes.

7. Characterisation techniques

Many analytical techniques are used to study and characterise the solid-state forms of APIs. The following paragraphs will elaborate on the techniques and the valuable information that can be obtained from the resulting data. Rather than defining the techniques or explaining in detail the underlying principles on which they are based – information that is widely available – we will focus on their application within the context of solid-state transformations.

7.1. X-Ray Powder Diffraction (XRPD)

XRPD is used to generate X-ray diffraction patterns that are unique to a specific crystalline arrangement of a particular drug. This may serve as an identification method for specific polymorphs. Any change in crystal structure will result in changes in the peak positions of the diffraction pattern. XRPD may also be used to quantify the relative proportions of two forms during a transformation process by monitoring changes in relative peak intensity, of peaks unique to each of the two forms, over time. If an X-ray diffractometer is equipped with a

controlled temperature-and humidity-chamber, transformations due to temperature or moisture changes can be studied [24].

An amorphous material gives a diffraction "pattern" that lacks peaks, but instead features broad humps, referred to as an amorphous halo [23]. Crystallisation of an amorphous material can be confirmed if peaks appear on the diffraction pattern. The amorphous halo is not meaningless or devoid of information, but is the result of the short-range order within the material. If an amorphous halo is recorded with a high-energy X-ray source, and pair-distribution-function analyses are performed, the extent of short-range order can be determined and sometimes even "matched" to the most similar crystalline polymorph [25].

7.2. Differential Scanning Calorimetry (DSC)

This thermal method measures the amount of energy taken up or released by a sample during a heating and/or cooling program. Thermal events such as melting, glass transition, desolvation and crystallisation are recorded on a thermogram showing heat flow against temperature or time. Any given solid-state form of a drug will have thermal events that are characteristic for that particular form. Changes in the number or nature of thermal events are indicative of changes in the solid-state, as are changes in the temperature at which melting of crystalline materials occur. Integration of the area under the heat flow curve yields the enthalpy change associated with that particular thermal event. Although DSC analysis is not a direct method for quantifying solid-state changes due to solvent-interactive transformations, it is still a helpful tool to identify whether changes did occur and to what extent solid-state characteristics were affected [4, 23].

7.3. Thermogravimetric Analysis (TGA)

TGA is a thermal technique that measures sample mass change under either isothermal conditions or ramped heating at a set rate [26, 27]. Weight loss at temperatures lower than the melting point of the drug is usually due to the loss of solvent. Adsorbed/absorbed moisture or solvent vapour is usually lost gradually, whilst solvent included in the crystal structure is typically lost in a characteristic step-wise manner. Weight loss profiles can be analysed to determine the amount or percentage of weight lost at any given temperature [26]. By factoring in the respective molecular weights of the drug and the lost solvent, one can also determine the stoichiometric relationship.

7.4. Hot Stage Microscopy (HSM)

This is one of the simplest and oldest thermal analysis methods. It is used to study solid-state transformations by observing a sample as it is heated and cooled. HSM is used to visually confirm DSC findings and to identify thermal events that cannot be conclusively identified from DSC thermograms. Possible observations include morphology, birefringence (polarising filter required), solid-solid transformations, interaction between different compounds, dissolution of one compound in another, sublimation and/or evaporation, vapour deposition, melting/liquefaction, crystallisation/solidification, charring/decomposition, crystal growth

and rate thereof. Gas evolution during desolvation can be observed if a sample is covered in a drop of mineral oil [28].

7.5. Vibrational spectroscopy and microscopy

The most prominent vibrational spectroscopic methods for solid-state form identification are infrared-(IR) and Raman spectroscopy. These two techniques can be used as qualitative and quantitative analytical methods. Although these techniques are generally used as complimentary methods they are still important, especially for investigating differences in hydrogen-bonding patterns that often differ with solid-state forms [8, 29]. An IR or Raman spectrum consists of several absorption bands, each band is related to a specific vibrational or rotational frequency. These frequencies are dependent on the intermolecular interactions and bond strength. Therefore, the obtained 'pattern' due to the vibrational frequencies is highly characteristic of a given drug. Any changes in the spectra due to solid-state transformations will be identifiable through changes in the relative intensities, frequencies, number and contours of the absorbance bands [24]. Confocal Raman microscopy can be used for the identification of a particular solid-state form of a drug in solid dosage forms. Not only is this a useful application for determining drug homogeneity in the dosage form, but the identification of solid-state transformations is also possible. Raman microscopy furthermore allows the investigation of amorphous-to-crystalline transformation at the dissolving interface of a solid dosage form [30].

7.6. Dissolution studies

In vitro dissolution studies are extremely useful for the identification and even quantification of solvent-interactive transformations. As mentioned earlier, the incorporation of metastable solid-state forms in solid dosage forms, especially amorphous forms, has become increasingly prevalent over the last decade. However, it has been demonstrated that general methods for testing dissolution and equilibrium solubility are not optimised for determining the true solubility advantage that these metastable forms offer [31].

Solution-mediated transformation, occurring during dissolution, involves three stages: (1) a pre-transformation stage, during which the metastable phase dissolves at a constant rate; (2) the transformation stage that begins after the solution has become supersaturated with respect to the stable form. During this stage the nucleation and crystal growth of the stable form, as well as dissolution of both forms occur. The relative amount of the stable form increases and as a result thereof the overall dissolution rate decreases until no metastable form is left. After the transformation stage, a steady-state stage (3) is reached (Figure 9) [32]. Aaltonen *et al.* [32] reported a Raman spectroscopy method that is ideal for accurately determining drug concentration in solution as well as the concomitant analysis of the solid phase within the dissolution environment.

7.7. Microcalorimetry

Microcalorimetry is a technique that has a variety of applications in the pharmaceutical research environment. This technique involves the real-time monitoring of chemical and
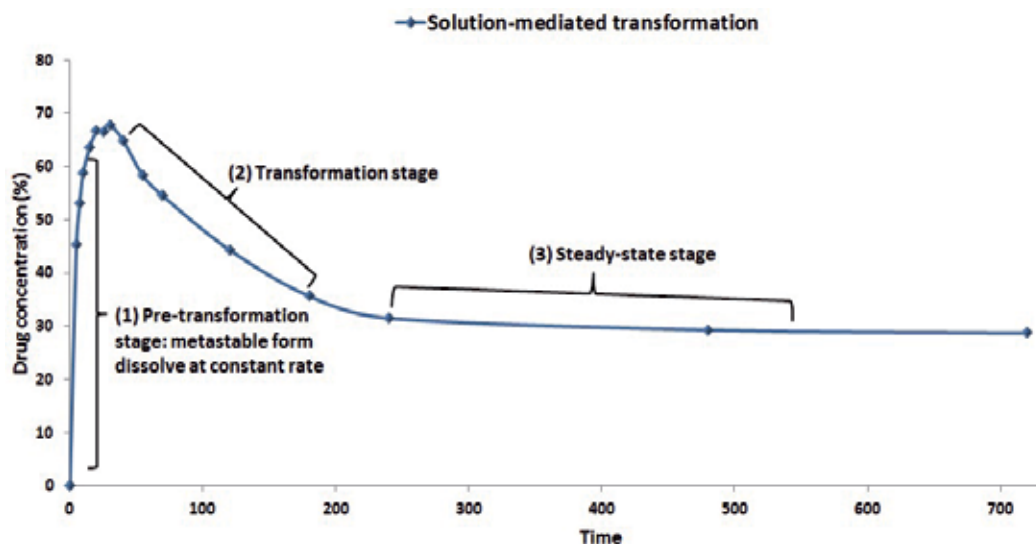
Figure 9. Typical dissolution graph showing the effect on concentration of solution-mediated solid-state transformation of a metastable drug to a stable form of the drug.

physical processes occurring when a compound is subjected to certain conditions (temperature, humidity, solvent vapour or in combination with another compound). The monitoring process can extend over a period of hours or days and it measures the onset, rate, extent and energetics of reactions or transformations. During microcalorimetric analysis, the heat flow of a sample is measured and recorded *versus* elapsed time. This analytical tool was developed around the basic principle that all chemical and physical processes are either exothermic or endothermic. Microcalorimetry is such a sensitive method that it can detect very slow processes. It will also detect physical or chemical reactions that generate minuscule amounts of heat. To study solid-state transformations due to solvent vapour exposure, a small amount of drug will be added to an inert ampoule and a micro hygrostat filled with the solvent will be inserted into the ampoule [33]. A specific humidity environment can also be created within the sealed ampoule by using a micro hygrostat containing saturated salt solutions and maintaining the calorimeter at a specific temperature. Any solid-state transformation will be seen as either an increase or decrease in the measured heat flow. The heat flow data can be applied to calculate the kinetics of a transformation process.

7.8. Vapour sorption analysis

Vapour sorption analysis, also known as dynamic vapour sorption (DVS), is a gravimetric technique that measures the amount and rate of solvent absorption/adsorption by a sample. Typically, water sorption-desorption isotherms are obtained by exposing a sample to a relative humidity (RH) cycle ranging from 0 – 98% and plotting the corresponding weight change. During typical vapour sorption studies the temperature is kept constant at 25°C ± 0.5°C, however some sorption analysers have the ability to apply a temperature ramp as well.

Sorption analyses usually involves 3 steps, namely a first up-ramping of the RH (0 to 98%), secondly a downwards ramp of the RH (98 to 0%) and thirdly and finally another upward ramping (0 to 98%). These RH ramping steps are usually applied when one wants to study the effect that water has on a drug during high % RH conditions. The resulting moisture sorption and desorption isotherms will indicate any change in the sample weight during the humidity ramps. Differences in the adsorption and desorption isotherms is referred to as hysteresis.

The solid-state change of an amorphous drug can be detected through sorption analysis. The glass transition is the point where an amorphous material becomes less stable and rearrangement to the more stable crystalline structure occurs. Typically the glass transition is affected by temperature and humidity. Hence, it can be determined using either ramped temperature experiments at constant humidity or using ramped humidity experiments at constant temperature. The amorphous material gains weight until the glass transition is reached. Then, as the amorphous drug rearranges to the crystalline form, there is a step increase or decrease in weight [18]. Another occurrence that can easily be identified from vapour sorption studies is that of deliquescence. Drugs that are susceptible to deliquescence will absorb very little moisture during a humidity ramp until the % RH reaches a "critical" level. At that point the drug will absorb any available moisture. This will result in a rapid increase of the monitored sample weight [34]. It should be noted that, if possible, vapour sorption studies should be performed in conjunction with XRPD, DSC and/or TG analyses. This will assist in the definitive identification of solid-state changes due to exposure of the drug to vapour.

8. Conclusion

Pharmaceutical compounds have the ability to exist in different solid-state forms. The rearrangement of molecules, that allows a single drug to present itself in various solid-state forms, presents an array of challenges to scientists working in the pharmaceutical industry. Different solid-state forms of the same API differ in terms of physical, chemical and mechanical properties. The understanding of the solid-state properties of APIs is imperative and even more so the factors that can induce changes in the solid-state of a given drug.

This chapter focussed on the solid-state form changes that may occur due to solvent-interactive transformations. There is much confusion and contradiction in current literature when it comes to differentiating the types of solvent-interactive transformations. We have concluded that solvent-interactive transformations may be either indirect and mediated or direct and non-mediated. The latter is a solvent-catalysed solid-solid transformation, whilst the former can be either a solvent-mediated solid-solid transformation or a solution-mediated solid-solution-solid transformation.

Solvent-interactive transformations can affect not only drugs but also excipients used in the formulation of a drug into a dosage form. It is essential to identify possible pitfalls, caused by solvent-interactive transformations, during the complete drug processing and dosage form manufacturing cycle. It is important to know that solvent-interactive transformations can change the solid-state form of a drug at any point between the very start of manufacturing

right up to the time when the drug is absorbed *in vivo* after having been administered to a patient.

Author details

Marique Elizabeth Aucamp, Wilna Liebenberg and Nicole Stieger*

*Address all correspondence to: Nicole.Stieger@nwu.ac.za

Centre of Excellence for Pharmaceutical Sciences, North-West University, Potchefstroom, South Africa

References

[1] Yu, L.X., Furness, M.S., Raw, A., Woodland Outlaw, K.P., Nashed, N.E., Ramos, E., Miller, S.P.F., Adams, R.C., Fang, F., Patel, R.M. Holcombe, F.O., Chiu, Y-Y. and Hussain, A.S. Scientific Considerations of Pharmaceutical Solid Polymorphism in Abbreviated New Drug Applications. Pharmaceutical Research 2003; 20(4):531-536.

[2] Blagden, N., De Matas, M., Gavan, P.T. and York, P. Crystal Engineering of Active Pharmaceutical Ingredients to Improve Solubility and Dissolution Rates. Advanced Drug Delivery Reviews 2007; 59:617-630.

[3] Savolainen, M., Kogermann, K., Heinz, A., Aaltonen, J., Peltonen, L., Strachan, C. and Yliruusi, J. Better Understanding of Dissolution Behaviour of Amorphous Drugs by *In-situ* Solid-state Analysis using Raman Spectroscopy. European Journal of Pharmaceutics and Biopharmaceutics 2009; 71:71-79.

[4] Zhang, G.G.Z., Law, D., Schmitt, E.A. and Qiu, Y. Phase Transformation Considerations During Process Development and Manufacture of Solid Dosage Forms. Advanced Drug Delivery Reviews 2004; 56:371-390.

[5] Gu, C-H., Young, V. Jr. and Grant, D.J.W. Polymorphs Screening: Influence of Solvents on the Rate of Solvent-mediated Polymorphic Transformation. Journal of Pharmaceutical Sciences 2001; 90(11):1878-18.

[6] Stieger, N. and Liebenberg, W. Chapter 7: Recrystallization of Active Pharmaceutical Ingredients. In: Andreeta, M.R.B. (ed.) Crystallization – Science and Technology. Rijeka: InTech. 2012. p. 183-204.

[7] Rodríguez-Homedo, N., Kelly, R.C., Sinclair, B.D. and Miller, J.M.. Crystallization: General Principles and Significance on Product Development. In: Swarbrick, J. (ed.) Encyclopedia of Pharmaceutical Technology. 3rd edition. New York: Informa Healthcare. 2006. p. 834-857.

[8] Rodríguez-Spong, B., Price, C.P., Jayasankar, A., Matzger, A.J. and Rodríguez-Horne-do, N. General Principles of Pharmaceutical Solid Polymorphism: A Supramolecular Perspective. Advanced Drug Delivery Reviews 2004; 56:24-274.

[9] Morris, K.R., Griesser, U.J., Eckhardt, C.J. and Stowell, J.G. Theoretical Approaches to Physical Transformations of Active Pharmaceutical Ingredients during Manufacturing Processes. Advanced Drug Delivery Reviews 2001; 48:91-114.

[10] Rodriguez-Hornedo, N. and Murphy, D. Significance of Controlling Crystallization Mechanisms and Kinetics in Pharmaceutical Systems. Journal of Pharmaceutical Sciences 1999; 88(7):651-660.

[11] Murphy, D., Rodríguez-Cintrón, F., Langevin, B., Kelly, R.C. and Rodríguez-Horne-do, N. Solution-mediated Phase Transformation of Anhydrous to Dihydrate Carbamazepine and the Effect of Lattice Disorder. International Journal of Pharmaceutics 2002; 246:121-134.

[12] Merriam-Webster English Dictionary. 2014. Mediate. http://www.merriam-webster.com/dictionary/mediate. (Accessed 2 September 2014).

[13] Oxford English Dictionary. 2014. Mediate. http://www.oxforddictionaries.com/definition/english/mediate. (Accessed: 2 September 2014).

[14] MacKinnon, D.P. Introduction to Statistical Mediation Analysis. New York: Taylor & Francis; 2008. 477p.

[15] Vippagunta, S.R., Brittain, H.G. and Grant, D.J.W. Crystalline Solids. Advanced Drug Delivery Reviews 2001; 48:3-26.

[16] Aucamp, M.E., Stieger, N., Barnard, N. and Liebenberg, W. Solution-mediated Phase Transformation of Different Roxithromycin Solid-state Forms: Implication on Dissolution and Solubility. International Journal of Pharmaceutics 2013; 449:18-27.

[17] Klug, H.P and Alexander, L.E. Diffraction Procedures for Polycrystalline and Amorphous Materials, 1974. Second edition. Wiley, New York. 992p.

[18] Burnett, D.J., Thielmann, F. and Booth, J. Determining the Critical Relative Humidity for Moisture Induced Phase Transformations. International Journal of Pharmaceutics 2004; 287:123-133.

[19] Mallet, F., Petit, S., Lafont, S., Lemarchand, D. and Coquerel, G. Solvent Exchanges among Molecular Compounds: Two Extreme Cases of Pharmaceutical Interest. Journal of Thermal Analysis and Calorimetry 2003; 73:459-471.

[20] Aucamp, M.E. Physico-chemical Properties and Polymorphism of Roxithromycin. PhD Thesis. North-West University, Potchefstroom, 2010. 148p.

[21] Shekunov, B.Y. and York, P. Crystallisation Processes in Pharmaceutical Technology and Drug Delivery Design. Journal of Crystal Growth 2000; 211:122-136.

[22] The Food and Drug Administration of the United States of America. Guidance for Industry: PAT – A Framework for Innovative Pharmaceutical Development, Manufacturing, and Quality Assurance. http://www.fda.gov/cvm/guidance/published.html. (Accessed 26 August 2014.)

[23] Newman, A.W. and Byrn, S.R. Solid-state Analysis of the Active Pharmaceutical Ingredient in Drug Products. Drug Discovery Today 2003; 8(19):898-905.

[24] Brittain, H.G. Characterisation of Pharmaceutical Compounds in the Solid State. In: Ahuja, S. and Scypinski, S. (eds). 2nd edition. Handbook of Modern Pharmaceutical Analysis. Burlington: Academic Press. 2011. p. 11-58.

[25] Chieng, N., Trnka, H., Boetker, J., Pikal, M., Rantanen, J. and Grohganz, H. Detecting Phase Separation of Freeze-dried Binary Amorphous Systems Using Pair-wise Distribution Function and Multivariate Data Analysis. International Journal of Pharmaceutics 2013; 454:167-173.

[26] Brown, M.E. Introduction to Thermal Analysis: Technique and Applications. London: University Press, 1998. 265p.

[27] Wendlandt, W.W. Thermal Analysis. New York: John Wiley, 1986. 652p.

[28] Stieger, N., Aucamp, M.E., Zhang, S.-W. and De Villiers, M.M. Hot-stage Optical Microscopy as an Analytical Tool to Understand Solid-state Changes in Pharmaceutical Materials. American Pharmaceutical Review 2012;15(2).

[29] Heinz, A., Strachan, C.J., Gordon, K.C and Rades, T. Analysis of Solid-state Transformations of Pharmaceutical Compounds Using Vibrational Spectroscopy. Journal of Pharmacy and Pharmacology 2009; 61:971-988.

[30] Vogt, F.G. and Williams, G.R. Advanced Approaches to Effective Solid-state Analysis: X-Ray Diffraction, Vibrational Spectroscopy and Solid-state NMR. American Pharmaceutical Review 2010; 13(7).

[31] Hancock, B.C. and Parks, M. What is the True Solubility Advantage for Amorphous Pharmaceuticals? Pharmaceutical Research 2000; 17(4):397-404.

[32] Aaltonen, J., Heinänen., P., Peltonen, L., Kortejärvi, H., Tanninen, V.P., Christiansen, L., Hirvonen, J., Yliruusi, J. and Rantanen, J. *In Situ* Measurement of Solvent-mediated Phase Transformations during Dissolution Testing. Journal of Pharmaceutical Sciences 2006; 95(12):2730-2737.

[33] Giron, D. Investigations of Polymorphism and Pseudo-polymorphism in Pharmaceuticals by Combined Thermoanalytical Techniques. Journal of Thermal Analysis and Calorimetry 2001; 64:37-60.

[34] Hassel, R.L. Moisture Sorption Analysis of Pharmaceuticals. TA Instruments Technical Note. TA329a. http://www.tainstruments.com/main.aspx?n=2&id=181&main_id=599&siteid=11 (Accessed: 5 September 2014).

Crystallization of the Long Biological Macro-Molecules

Uziel Sandler

Additional information is available at the end of the chapter

1. Introduction

Phase transition in molecular crystals and molecular liquids is a complicated phenomenon. The energy of intra-molecular interaction is higher than the characteristic temperatures of the transitions, so the structural transformations are determined by a competition between the inter-molecular interactions that try to put the molecules in some ordered state and tendency of the entropy to break of this order. Since the small molecules interact with small number of the neighbors, mean-field-approximation is inadequate and calculating of the free energy requires non-trivial higher approximations. Besides, the relevant parameters of the inter-molecular interactions depend on details of the molecular structure and correct estimation of them requires a complex quantum-mechanical calculation, so huge numerical calculations should be done in the real cases.

In this chapter we will consider the system that consists of the long semi-flexible macromolecules[1] or molecular aggregates (LM). We will assume also that the energy of the relevant intra-units interactions is of the same order as a characteristic temperature of the phase transformations. In such a case above mentioned complications could be avoided by using the concepts of "quasi-monomers" or "blobs" (see [13, 16] and references therein). Because of the macroscopic nature of these units, an effective inter-unit interaction are defined by their geometrical properties, while most details of the internal structure and internal interactions of the units become irrelevant. Moreover, since for the relevant densities each macro-unit interacts with large number of the neighbors, so the mean-field-approximation could be quite adequate for calculation of the most the thermodynamic characteristics and these calculations can be done analytically.

---

[1] A molecule will be called "long" if it length L is much more than it thickness a and "semi-flexible" if it persistent length l_p is much more than it thickness and much less than the molecule's length: $L \gg l_p \gg a$.

---

2. Experimental study of phase transitions in the biological materials

2.1. The collagenous materials

A novel material was developed by exerting high pressure and temperature on natural leather material[2] in an oxygen poor environment. This material, which was called pleather, is thermoplastic [2]. The leather itself may be inexpensive scrap which is commutated into fine particles (∼2 mm). By using common plastic forming techniques it is possible to mould this material into various shapes. Pleather, having a warmer feel than polymers, could replace polymers in furniture parts and prestigious packaging, where the price of genuine leather makes it use prohibitive.

Figure 1. SEM micrograph of internal structure of *leather*. Adapted with permission from Ref. [14]. Ĭ [1995] American Physical Society.

The structure and properties of leather and their building unit, the collagen molecule, at atmospheric pressure and moderate temperatures have been extensively studied (see e.g. [8] and the bibliography there). The collagen molecule in helix form, has a length of $3000A$ and a diameter of $15A$. The three folded spirals are bonded by relatively weak, mainly hydrogen, bonds. The spiral consists of about 300 segments and each one contains approximately 3 amino-acid residues with $20 - 30$ Carbon and Nitrogen atoms [8]. It was shown that at temperatures $310^o - 330^oK$ the collagen molecules are reversibly denatured ("melted" [9]). The structure of collagenous material that emerges after compression at pressures between $5 - 30MPa$ and at temperatures $310^o - 390^oK$ have been investigated. Scanning Electron Micrographs (SEM) taken after treatment [2], at room temperature, show how the fibrous open leather structure transforms into a composite matrix, where left over fibers are

---

[2] The term leather pertains to hides from cow and sheep that are chemically treated to make it stronger and to give more resistance to heat.
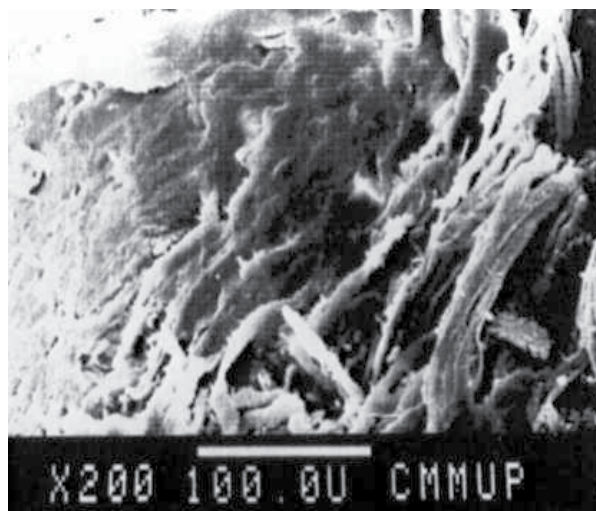
Figure 2. SEM micrograph of *compressed leather* at room temperature. Pressure: $750atm$ Adapted with permission from Ref. [14]. ľ [1995] American Physical Society.

embedded in a continuous material (see Fig.1, Fig.2 and article [12]). By chromatography and electrophoresis methods it was shown that harsher processing conditions (higher temperature and pressure) produce an extensive degradation of the collagen superstructure, without degradation of the amino acid chains of the collagen molecule.

The biochemical [12] and mechanical properties of the material, compression strength, Young's modulus and bulk density have been studied at various processing parameters [4]. The effect of pressure on the sol-gel transition in an aqueous solution of collagen (gelatin) has been investigated in [11]. It was found, that high pressure shifts the temperature interval of collagen denaturation to higher temperatures.If the temperature is low ($T \ll T_{d1}$, where $T_{d1} \approx 310^o K$) the helix form is stable. At higher temperature, hydrogen and other weak bonds, which stabilize the helix form, become unstable and the helix breaks down to random coils [8]. This transition, however, is not sharp, but spreads over a temperature interval of $30^o - 40^o K$. This indicates that a cooperative process takes place and not a real phase transition [9]. For higher temperature ($T \geq T_{d2}$, $T_{d2} \approx 350^o K$) collagen molecules are "melted" completely. This process of the breakdown of the ordered helix structure, held together by non-covalent bonds, to a randomly coiled phase is called denaturation. The organized fibers are stable for $T \ll T_{d1}$ and break down for $T \geq T_{d2}$.

2.2. Crystallization of bacterial DNA

Bacterial DNA is an important example of a closed circular macromolecule. Although the tightly packed crystalline state is generally considered as incompatible with life, simple living systems use crystallization for different purposes. In viruses and bacteriophages DNA crystallization is used for accommodating large amounts of DNA in a very small volume. Bacteria use crystallization for protection against varied environmental assaults, thus promoting their endurance and virulence [17, 18, 29]. DNA condensation was

extensively studied during the last decade. This phenomenon has been found to be complicated, strictly depending on the DNA's topology and the cytoplasm's composition [17, 19] and involving the influence of different forces [20, 21]. DNA crystallization includes many processes and could lead to different condensed states: liquid crystals, DNA-protein co-crystals, DNA toroid [17, 18, 22].

DNA crystallization was studied in wild-type Escherichia coli AB1157 (recA1,lexA1) as well as various recA mutants, which were grown to midlogarithmic phasein LB medium without NaCl. Cultures then were exposed to DNA-damaging agents like UV irradiation (20 Jym2, 254 nm) or 100 mg of nalidixic acid. The cells were incubated at 37řC for different times from 15 to 120 min, afterwards the E.coli cells were fixed by ultrafast freezing in liquid ethane. For each time point 3 independent experiments were conducted and about 10^3 cell slices were screened. After a wash with the blocking solution, the grids were incubated with gold-conjugated goat antirabbit IgG for 1 h, dried, and stained with uranyl acetate. Images of the intracellular crystals were digitized with an Imacon Flextight scanner [18].

In the SEM micrographs bacterial chromatin of the active cells is demarcated as amorphous spaces, which are irregularly spread over the cytoplasm. After exposing to DNA-damaging agents, the cells show the SOS response, where the DNA breaks by stalling its activity. Continuous addition of nalidixic acid leads to an expansion of the assembly, whose average length increases up to 4 times after 60 min. Further incubation does not affect an expansion but results in a higher lateral order. The crystalline morphology of bacteria that have sustained prolonged exposure to DNA-damaging agents is clear seen in Fig.3.
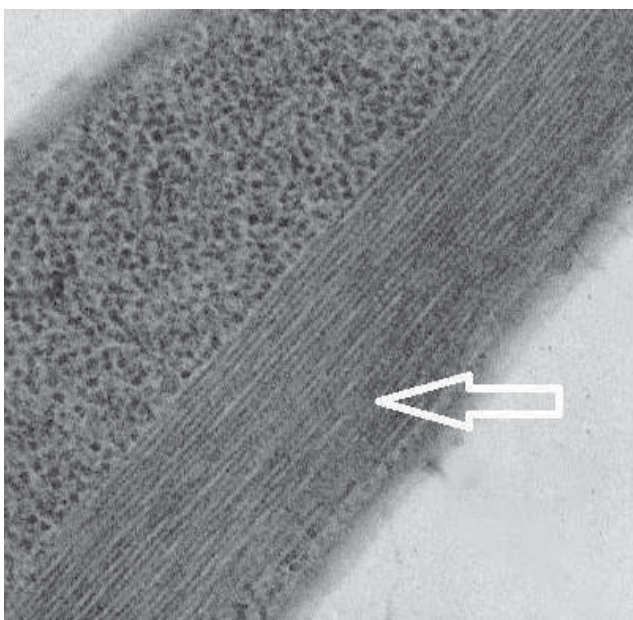
Figure 3. SEM micrograph of E. coli has been exposed to DNA-damaging agents. The array shows crystallized DNA. Adapted with permission of the author from Ref.[18].

3. Qualitative consideration of the theoretical approach

It is well known [6] that properties of phase transition in the polymer and liquid crystal systems are determined by general characteristics of the molecule's geometry and analytical behavior of the intermolecular forces, while particular details of these features are less relevant. So, we can assume that near the phase transition the major factors that determine the process of the LM crystallization are the topology of the LM molecule and the behavior of the effective LM's segment-segment interactions.

The liquid-crystal ordering of a LM is determined by the angular-dependence of interactions between LM segments. At low density, the LM pieces interact only at a small number of points, but when the solvent approaches the crossover point the number of collision points increases. When typical length between the collision points become approximately the same as the persistent length, the rigidity of a long molecule becomes important and there is a tendency to align quasi-straight pieces with quasi-parallel structure. This means that in the high density state of LM the phase transition from disordered to liquid-crystal-like ordered phase [5], should take place.

Let us estimate critical volume fraction of the molecules near crystallization point. The average number of binary collisions between LM quasi-straight pieces can be estimated as:

$$k_L \sim N \left(\frac{L}{l_p} \right)^2 v,$$ (1)

where N is number of the molecules in the volume V and v is an interaction volume. So, we have

$$k_L \sim L \frac{cv}{a^2 l_p^2},$$ (2)

where - c is the volume fraction of LM segments. On the other hand, the average distance between collision points is on the order of:

$$\bar{l}_k \sim \frac{L}{k_L} \sim \frac{a^2 l_p^2}{cv}.$$ (3)

Critical volume fraction - c_*, where structural phase transition could take place, can be estimated from $\bar{l}_k \sim l_p$

$$c_* \sim \frac{a^2 l_p}{v}$$

Since part of the LM shorter than l_p can be considered as an almost rigid rod, for v we can use an excluded volume approximation $v \sim l_p^2 a$, which leads to

$$c_* \sim \frac{a}{l_p}.$$ (4)

This "naive" estimation is consistent with more rigorous calculations for the liquid-crystal ordering of long semi-flexible molecules under pressure (see Sec.4.1).

4. Crystallization of the collagenous materials

4.1. A phase transition under pressure at low temperatures

Although the main assumptions of our theory are general enough to apply to a whole class of compressed materials made from various natural or artificial fibers, we will discuss here a concrete case of collagen made material - natural leather, which is made up of fibers of the collagen molecules (see Section 2.1). At low temperature the fibers are stable and can be considered as basic units. If the volume fraction of fibers - c, is relatively small which occurs at low pressure, the fibers intermingle in a disordered way and interact only at a relatively small number of points (see Fig.1). When the pressure is increased the number of fibers per volume fraction increases and the interaction between the fibers becomes important.

If we designate a typical coefficient of elasticity per unit of length of fiber as γ, the persistence length (quasi-straight pieces) l_p, will be of order γ/T where T is the temperature. The condition, that l_p is much longer than the diameter a of the fibers, can be expressed as $aT/\gamma \ll 1$. It can also be seen from the SEM micrographs Fig.1, that the typical length of fiber L is much longer than l_p. So $LT/\gamma \gg 1$. The energy of a fiber consists of its elastic energy and the energy of interaction with other fibers. It follows from experimental data [12],[2] that an ordered phase appears for quite a large value the of fiber's volume fraction. In this case repulsive short-range forces between fibers are dominant. It is obvious also that the interaction between two quasi-straight pieces depends on the angle between them.

In the mean field approximation (MFA) the angular dependent part of the energy of interaction between one fiber and the others can then be represented in the form:

$$\Delta U_i = \int_0^L dl\ U[\boldsymbol{s}_i(l)]$$

where

$$U(\boldsymbol{s}) = \frac{Tc}{a} \int_{\boldsymbol{n}^2=1} d\boldsymbol{n}\ S(\boldsymbol{n}) u\left(\boldsymbol{s}; \boldsymbol{n}\right)) \tag{5}$$

Here $\boldsymbol{s}_i(l)$ is the unit tangent vector of the fiber (i) at a distance l from the beginning of the fiber, $S(\boldsymbol{n})$ is the average fraction of the quasi-straight pieces of the fibers that are directed in the direction $\boldsymbol{n}$ and $Tcu(\boldsymbol{s}, \boldsymbol{n})/a$ is the angular dependent interaction between two pieces of fibers.

If we assume the simplest form for the elastic energy of the fibers (isotropic approximation), than in the lowest order on a/l_p part of the energy, which depends on the local orientation of the fiber pieces will be:

$$\Delta \mathcal{E}_{MFA} = \frac{1}{2} \sum_i^N \int_0^L dl \left\{ \gamma \left(\frac{\partial \boldsymbol{s}_i}{\partial l}\right)^2 + U[\boldsymbol{s}_i(l)] \right\} \tag{6}$$

where N is the total number of fibers. The free energy of the system can be expressed as path integral over all the possible shapes of the fibers:

$$\mathcal{F} = \mathcal{F}_0 - T \ln \left[\int \prod_i \mathcal{D}\{s_i(l)\} \exp \left(-\frac{\Delta \mathcal{E}_{MFA}}{T} \right) \right] \tag{7}$$

where $\mathcal{F}_0$ is the part of free energy which does not depend on the elasticity and shapes of the fibers.

In the usual way[3] the path integral (7) may be written in the form:

$$\mathcal{F} = \mathcal{F}_0 - N \ln \left(\sum_n \exp - E_n L \right) \tag{8}$$

where E_n is the eigne-value of the Schrodinger-like equation associated with this path integral

$$\frac{\partial \psi}{\partial l} = \frac{T}{2\gamma} \nabla_s^2 \psi - \frac{U(s)}{2T} \psi \tag{9}$$

here s is a unit vector and $\nabla_s^2 = \partial^2/\partial\theta^2 + \tan^{-1}\theta\partial\theta + \sin^{-2}\theta\partial^2/\partial\varphi^2$ is the angular part of the Laplacian operator.

In the ordered phase the "depth of the potential well - $(U_{max} - U_{min})/2T$" is large compared to the "kinetic energy -$T/2\gamma$", because, the phase transition to the ordered phase occurs for $c \sim 1$ [2] and

$$max \left(\frac{\gamma}{T^2} U \right) \sim \frac{c\gamma}{aT} \sim c\frac{l_p}{a} \gg 1.$$

while $min(U) \approx 0$. On the other hand, in a disordered phase $S(n) \equiv 1/4\pi$ and $U(s) = const$. In both cases the energy spectrum will be discrete and the gap between the ground state and the 1st exited state will be about

$$E_1 - E_0 \sim \frac{T}{\gamma}.$$

As $LT/\gamma \sim L/l_p \gg 1$, the ground state is dominant, and we obtain for the free energy per unit volume

$$F = F_0 + \frac{Tc}{a^2} E_0 \tag{10}$$

and for $S(n)$

$$S(n) = |\psi_0(n)|^2 = \Psi^2(n) \tag{11}$$

---

[3] See more precise consideration in Sec.5

E_0 can be obtained by using the variation principle from which we find that

$$F = F_0 + \frac{Tc}{2a^2} \int d\boldsymbol{s} \left[\frac{T}{\gamma} \left(\frac{\partial \Psi}{\partial \boldsymbol{s}} \right)^2 + \frac{c}{a} \int d\boldsymbol{n} \Psi^2(\boldsymbol{s}) u(\boldsymbol{s}; \boldsymbol{n}) \Psi^2(\boldsymbol{n}) \right] \tag{12}$$

This is a well known Ψ^4 field Hamiltonian. The function $\Psi(\boldsymbol{s})$ must be found by minimizing F under the restriction

$$\int d\boldsymbol{s} \Psi^2 = 1 \tag{13}$$

It can be done in many ways. Here we will use the simple approximation, which Onsager used in his treatment of liquid crystals [5]. In this approximation it is assumed that $\Psi(\boldsymbol{s})$ is a narrow peaked function in an ordered phase

$$\Psi(\boldsymbol{s}) = \phi\left(\lambda(\boldsymbol{s} \cdot \boldsymbol{s}_0)\right) \quad (\lambda \gg 1) \tag{14}$$

where $\boldsymbol{s}_0$ is the direction of an average orientation of the quasi-straight pieces, while in a disordered phase $\Psi(\boldsymbol{s}) \equiv \sqrt{1/4\pi}$ (this means that in a disordered phase $\lambda = 0$) [4]. The parameter λ should be found by minimizing F.

The difference between the free energy in the ordered and disordered phases is

$$\Delta F \simeq \frac{Tc^2}{2a^3} \left\{ g\left(\frac{Ta}{\gamma c} \right) - 1 \right\} \tag{15}$$

where the specific form of the function $g(x)$ depends on the behavior of $u(\boldsymbol{s}, \boldsymbol{n})$ near $\boldsymbol{s} \approx \boldsymbol{n}$. If it is assumed that near $\boldsymbol{s} \approx \boldsymbol{n}$ the behavior of $u(\boldsymbol{s}, \boldsymbol{n})$ is of the form

$$f \propto \eta [\boldsymbol{s} \times \boldsymbol{n}]^{2\nu} \tag{16}$$

(η is a constant $O(1)$), then in the Onsager approximation one finds[5]

$$g(x) \approx (\mu x)^{\frac{\nu}{1+\nu}} \tag{17}$$

with

$$\mu \approx (4\kappa\nu\eta)^{\frac{1}{\nu}} \tag{18}$$

---

[4] Onsager used the function ϕ in the form $\phi(x) = A \cosh(\lambda x)$, but the final results are weakly sensitive to the concrete form of $\phi(x)$.

[5] The parameter λ here is

$$\lambda = \begin{cases} \left(4\nu ac \frac{T_*}{T}\right)^{1/1+\nu} \gg 1 & \text{if } T < T_* c \\ 0 & \text{if } T > T_* c \end{cases}$$

which justifies the use of the approximation (14)

The numerical coefficient κ is $O(1)$ and depend on the explicit form of the test function (14). It is obvious from (15), that for fixed T and a specific value of the fiber fraction

$$c_* = \frac{T}{T_*} \tag{19}$$

where

$$T_* = \frac{\gamma}{\mu a}$$

the material undergoes a first order phase transition from the disordered to the ordered phase. The ordered phase is stable for $T < T_*$ and it is called *compressed leather* (see Fig.2).

The order parameter $\mathcal{Q}$, that describes the ordering in the orientation of the fibers, can be defined as

$$\mathcal{Q} \approx \frac{1}{2} \left(3 \int dn S(n)(n \cdot s_0)^2 - 1 \right) \tag{20}$$

In the ordered phase using (11) with $\Psi(n)$ from (14) one obtains

$$\mathcal{Q} \approx 1 - \frac{3}{\lambda} \approx 1 - 3(4va)^{-1/1+\nu} \left(\frac{T}{T_* c} \right)^{\frac{1}{1+\nu}} \tag{21}$$

(in the disordered phase $\mathcal{Q} = 0$). The difference between thermodynamic parameters of the ordered and disordered phase can be obtained as follows

$$q \sim \frac{T_*}{a^3} \frac{\nu}{1+\nu} \left(\frac{T}{T_*} \right)^3 \tag{22}$$

$$\Delta C \sim \frac{1}{a^3} \frac{\nu(1+2\nu)}{(1+\nu)^2} \left(\frac{T}{T_*} \right)^{\frac{\nu}{1+\nu}} c^{\frac{2+\nu}{1+\nu}} \tag{23}$$

$$\Delta K_B \sim \frac{Tc^2}{a^3} \left(1 - \frac{2+\nu}{2(1+\nu)^2} \left(\frac{T}{T_* c} \right)^{\frac{\nu}{1+\nu}} \right) \tag{24}$$

where q is the latent heat, C is the specific heat, K_B is the bulk modules, and Δ indicates the difference between ordered and disordered phase. In general, the ordered phase consists of domains with different fiber orientation (see Fig.2) but the energy of the domain boundaries gives a small contribution to ΔF.

It should be noted, that for large volume fraction of the collagen fibers the form of their cross sections changes, and therefore so do the effective diameter and elasticity. Furthermore, the elasticity of the fiber bundles and coefficient ρ in the expression (12) depend on temperature,

so that we must consider $T_* = T_*(T, c)$. If T is less than T_{d1} (T_{d1} is the lowest temperature of collagen denaturation: $T_{d1} \sim 350^0 K$) the inner structure of the fibers almost doesn't change and the dependence $T_* = T_*(T, c)$ is quite weak. In general such dependence does not change the expressions for the free energy and order parameter, but additional terms appear in the other thermodynamic quantities. However, as most of the expressions contains T_* in a low power they are relatively insensitive to its variations. It is not anticipated that a change from the isotropic approximation for the elastic energy to a more realistic approximation would produce changes of any significance.

4.2. A phase transition under increasing temperature at high pressure

If we increase the temperature of *compressed leather* with fixed c, to a temperature higher than $T_0 = cT_*$ a first order phase transition from the ordered to the disordered phase takes place. If $T_0 \ll T_{d1}$ this phase will be *leather*. A more complex situation occurs for $T_0 > T_{d1}$. If the temperature is higher than T_{d1} the helix form of the collagen molecule becomes unstable, the molecules melt and the fibers are destroyed. The approach of the previous Section fails, because the variation in the internal free energy of the fibers plays a major role [10]. The structure of the material for $T \geq T_{d1}$ is determined by the competition between the melting and ordering of the collagen molecules. We will describe the behavior of the material by using the following model.

In a first approximation the leading term of the free energy can be represented as

$$F = F_0 + c f_{mol} + T c e_{orien} + F_{int} \tag{25}$$

where f_{mol} is the free energy of a single collagen molecule, e_{orien} is the orientation dependent part of the entropy and F_{int} is the energy of intermolecular interaction. In order to calculate f_{mol} we use an approximation which is close to the well-known Zimm-Bragg model. The latter is in good agreement with the real behavior of the collagen molecules (see, for example [9]).

Consider a collagen molecule that contains sN segments in helix form and pN boundaries between "helix" and "coil" parts of the molecule (in the literature s is called spirality), where N is the number of segments in the molecule. N is large. Let us call the free energy of a segment in helix form - ε_h, in coil form - ε_c and the energy of segments on the boundary between helix and coil parts as ε_s ($\varepsilon_h - \varepsilon_c = \Delta U - T \Delta S \equiv \Delta S (T_m - T)$, where ΔU and ΔS are the differences between the internal energy and entropy of a spiral and a melted segment). As the collagen molecule can be considered as a one-dimensional system, we can calculate the free energy f_{mol} in an analogous way as for the 1D-Ising model. The result is [9]:

$$f_{mol} = - (\varepsilon_c - \varepsilon_h) s + \varepsilon_s p - T \{ s \ln s + (1 - s) \ln (1 - s) - \tag{26}$$

$$-2p \ln p - (s - p) \ln (s - p) - (1 - s - p) \ln (1 - s - p) \} \tag{27}$$

The last two terms in (25) can be obtained in the MFA approximation (see Sec.4.1)

$$e_{orien} = s \int_{\boldsymbol{n}^2=1} d\boldsymbol{n}\, g(\boldsymbol{n}) \ln\left(4\pi g(\boldsymbol{n})\right); \tag{28}$$

$$F_{int} = \frac{c^2}{2} \left\{ s^2 \int_{\boldsymbol{n}^2=1} d\boldsymbol{k} d\boldsymbol{n}\, g(\boldsymbol{k}) g(\boldsymbol{n}) U(\boldsymbol{k}; \boldsymbol{n}) + 2T\chi_{sh} s\left(1-s\right) + T\chi_{ss}\left(1-s\right)^2 \right\} \tag{29}$$

where $g(\boldsymbol{n})$ is the average fraction of the segments in helix form that are directed in the direction $\boldsymbol{n}$. The first term in (29) corresponds to the interaction between helix-helix segments, while the others describe the interaction between helix-coil and coil-coil segments resp.

The energy of interaction between spiral segments we write in the form

$$U(\boldsymbol{k}; \boldsymbol{n}) \simeq T\chi_{hh} u(\boldsymbol{k}; \boldsymbol{n}), \tag{30}$$

We assume as above, that near $\boldsymbol{k} \approx \boldsymbol{n}$

$$u \propto |\boldsymbol{k} \times \boldsymbol{n}|^{2\omega}, \tag{31}$$

which corresponds to a repulsive interaction in an excluded-volume approximation[6]. In this approximation, $\omega = 0$ corresponds to the bundles made from hard spheres, $\omega = 0.5$ to the bundles made from hard bars, $\omega = 1$ corresponds to MaierŰSaupe approximation and larger ω may be used for arch-like "hemstitch" units. We will also assume that in a first approximation the coefficients $\chi_{hh} \approx \chi_{hs} \approx \chi_{ss} \approx n_s\chi$ are of the same order. n_s is the number of atoms in the segments.

Using Onsager approximation for $g(\boldsymbol{k})$ [5] and integrating (29) over $\boldsymbol{n}$ and $\boldsymbol{k}$, we obtain for $\lambda \gg 1$:

$$Tce_{orien} + F_{int} \simeq Tc \left\{ s\left(\ln\lambda - 1\right) + s^2 \frac{cn_s\chi}{2} \zeta\left(\omega\right)\lambda^{-\omega} - s^2 \frac{cn_s\chi}{2} \right\} + \frac{Tc^2 n_s\chi}{2} \tag{32}$$

where coefficient $\zeta\left(\omega\right)$ is (see Appendix 1)

$$\zeta\left(\omega\right) = 2^{2\omega+1}\pi^{-1/2}\Gamma\left(\frac{3}{2} + \omega\right).$$

---

[6] In fact, $U(\boldsymbol{k}; \boldsymbol{n})$ must includes the term that corresponds to an attractive interaction. This term has the form:

$$\delta U \sim -\frac{p}{s}\mu u_{attr}(\boldsymbol{k}; \boldsymbol{n}).$$

In our theory, however, δU can be neglected for the following reasons: for $s \leq 1$ and $\varepsilon_s \gg \varepsilon_c - \varepsilon_h$, δU is small because $p \ll s$. On the other hand, if $s \ll 1$ and $p \sim s$ the whole term $s^2 \int_{\boldsymbol{n}^2=1} d\boldsymbol{k} d\boldsymbol{n}\, g(\boldsymbol{k}) g(\boldsymbol{n}) U(\boldsymbol{k}; \boldsymbol{n})$ in (29) is small and can be neglected.

In the disordered phase $g(\mathbf{k}) \equiv 1/4\pi$ and the interaction term in this approximation does not depend on spirality:

$$F'_{int} = \frac{Tc^2}{2} \left\{ \chi_{hh}s^2 + 2\chi_{sh}s\left(1-s\right) + \chi_{ss}\left(1-s\right)^2 \right\} \approx \frac{Tc^2 n_s \chi}{2}. \tag{33}$$

In the ordered phase the quantities s, p and λ have to be found by minimizing (25). This gives

$$\lambda = \left(\frac{c}{c_0}\right)^{1/\omega} s^{1/\omega}, \tag{34}$$

$$\frac{(1-s-p)s}{(s-p)(1-s)} = \frac{\lambda}{\tau} \exp \frac{2}{\omega} \left(-\frac{c}{\zeta c_0}s + 1 - \frac{\omega}{2} \right), \tag{35}$$

$$\frac{p^2}{(s-p)(1-s-p)} = \sigma, \tag{36}$$

where

$$\tau = \exp \frac{\varepsilon_c - \varepsilon_h}{T} \equiv \exp \Delta S \frac{T_m - T}{T},$$

$$\sigma = \exp -\frac{\varepsilon_s}{T}, \tag{37}$$

$$c_0 = \frac{2}{\chi n_s \omega \zeta}. \tag{38}$$

(for collagen $\varepsilon_s \gg T_m$, $\omega \approx 0.5$, $n_s \sim 2 \cdot 10^1$ and $\Delta S \sim 10$). If $cs \ll c_0$, λ is small and the above used approach fails. For such c and s however, the angle-dependent interaction between molecules becomes irrelevant, and the system will be in the disordered phase. In this phase $\lambda = 0$ and the free energy F' can be calculated in an explicit form. The result is [9]

$$F' \approx F_0 - cT \ln \frac{\tau + 1 + \sqrt{(\tau-1)^2 + 4\sigma\tau}}{2} + \frac{Tc^2 n_s \chi}{2}. \tag{39}$$

The order parameter in the ordered phase is

$$Q \approx 1 - \frac{3}{\lambda} + o\left(\frac{1}{\lambda^2}\right) \simeq 1 - 3\left(\frac{c_0}{c}\right)^{1/\omega} s^{-1/\omega}. \tag{40}$$

Note, that we have here

$$\frac{\partial \ln{(1-\mathcal{Q})}}{\partial \ln c} = \frac{\partial \ln{(1-\mathcal{Q})}}{\partial \ln s} \approx -\frac{1}{\omega}, \tag{41}$$

while for the phase transition under pressure at low temperatures it is obtained in Sec.4.1 that:

$$\frac{\partial \ln{(1-\mathcal{Q})}}{\partial \ln c} \approx -\frac{1}{1+\nu}, \tag{42}$$

So in (41) the dependence of $\mathcal{Q}$ on ω is much stronger for small ω, than the dependence of $\mathcal{Q}$ on small ν in (21). These derivations depend only on ω or ν and thus measurement of $\mathcal{Q}$ gives important information on the type of inter-fiber interaction.

The solution of the system (34)-(36) that corresponds to large λ, is

$$1 - s \approx \frac{1}{\tau}\left(\left(\frac{c}{c_0}\right)\exp\left(-\frac{2c}{\zeta c_0}+2-\omega\right)\right)^{\frac{1}{\omega}} \ll 1$$

$$\mathcal{Q} \approx 1 - 3\left(\frac{c}{c_0}\right)^{-\frac{1}{\omega}}. \tag{43}$$

The phase transition temperature - T_c is found from the condition $F_{order}\left(T_c\right) = F'_{disorder}\left(T_c\right)$. So we obtain:

$$\Delta S\frac{T_c - T_m}{T}_c \simeq \xi\left(\omega, \frac{c}{c_t}\right) - \ln\left(1 + \frac{\sigma e^{-2\xi}}{1 - e^{-\xi}}\right), \tag{44}$$

$$\xi \approx \frac{\rho\left(\omega\right)\left(c/c_t - 1\right) - \ln\left(c/c_t\right)}{\omega},$$

$$\rho = \ln\rho + \ln\zeta\left(\omega\right)e^{1-\omega}, \tag{45}$$

$$c_t = \zeta\rho c_0. \tag{46}$$

The ordered phase can be stable only if $c > c_t = \zeta\rho c_0$. Thus $\lambda > \left(\zeta\rho\right)^{1/\omega}$ and the above used approximation (32) is valid, because $\zeta\rho > 1$.

The derivative of the transition temperature to the pressure

$$\frac{\partial T_c}{\partial P} \propto \frac{\partial T_c}{\partial c} \sim \frac{T_c^3}{q\omega T_m}\left(1 + \sigma\frac{\left(2 - e^{-\xi}\right)e^{-2\xi}}{\left(1 - e^{-\xi}\right)^2}\right)\left(\frac{c_t}{c}\right)\left(\rho\frac{c}{c_t} - 1\right) > 0 \tag{47}$$

is positive. The latent heat and the jump in compressibility for this case are

$$q \sim c_t T_c \Delta S \tag{48}$$

$$\Delta \kappa \propto \frac{c_t T_c}{\omega} \left(1 - 2\rho \frac{c}{c_t} \right) < 0. \tag{49}$$

For the jumps in the orientation order parameter and in the spirality we have

$$\Delta \mathcal{Q} \simeq 1 - 3 \left(\frac{c_t}{\zeta \rho c} \right)^{\frac{1}{\omega}}, $$

$$\Delta s \simeq 1 - \exp \frac{1}{\omega} \left(1 - \rho \frac{c}{c_t} \right), \tag{50}$$

so the phase transition is of first order. Note, that in our approximation these jumps strongly depend on the exponent of the small-angle interaction between the molecules segments.

The restriction $c_t \leq 1$ leads to

$$n_s \geq n_{s0}(\omega) = \frac{2\rho}{\chi \omega} \tag{51}$$

and for $n_s < n_{s0}(\omega)$ the phase transition does not exist.

The numerical solution of the system (34)-(36) is shown in Fig.4. On the left hand side ($c < c_t$) cooperative "melting" takes place, while on the right hand side ($c > c_t$) a first order phase transition can clearly be seen. The inter-molecular interaction transforms the cooperative "melting" to the phase transition of the first order.

5. Crystallization of a Closed Long Macromolecule

In the previous Section we have discussed crystallization of the long open macromolecules, even though closed long macromolecules (CLM) are also widespread components of living systems. Major efforts in these and many other works were put forth to understand the peculiarities, structures and thermodynamics of condensed states of CLM. In contrast, the present paper focuses on the phase transition to a crystalline state and on the behavior of its general characteristics, like jumps of the CLM local density, the liquid crystal order parameter and transition entropy, which are biologically significant, because DNA packaging capacity and sharpness of the transition directly influence bacteria protection efficiency [17].

It is well known [6] that properties of phase transition in the polymer and crystal systems are determined by general characteristics of the molecule's geometry and analytical behavior of the intermolecular forces, while particular details of these features are less relevant. So, we can assume that near the phase transition the major factors that determine the process of the CLM crystallization are the topology of the CLM molecule and the behavior of the effective
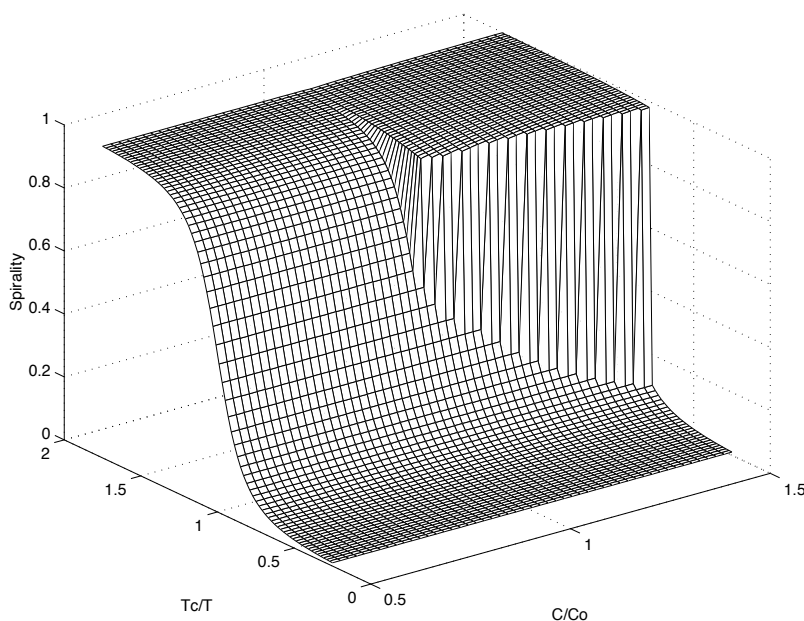
Figure 4. Spirality as a function of the normalized inverse temperature and volume fraction of the molecules. Adapted with permission from Ref. [14]. ľ [2000] American Physical Society.

CLM's segment-segment interactions. The condensation process of a long macromolecule includes two phenomena: collapse of the molecule's chain and structural ordering of the long semi-flexible molecule's segments. Separately, each of these phenomena has been discussed in literature [6, 13, 16, 27], but, as we will see later, these processes influence each other, so their combined consideration leads to considerable change in the theoretical approach.

Consider a long closed macromolecule with a hard-core diameter a, persistent lengths l_p and total length L. (For bacterial DNA: $l_p/L \sim 10^{-4}$, $a/l_p \sim 10^{-2}$). Above the crossover point between good and poor solvent, an effective repulsion between CLM segments dominates over effective attraction and CLM remains in a low density "coil" state. Near the crossover point, segment-solvent interactions compensate contribution of binary segment-segment repulsion, so that below the crossover the effective attraction becomes dominant and the molecule undergoes transition into a compact globular form. Since segment-solvent interactions are independent of the segments' orientations, such compensation takes place only for angular-independent contributions to binary collisions.

In contrast, the liquid-crystal ordering of a CLM is determined by the angular-dependence of interactions between CLM segments. At low density, the CLM pieces interact only at a small number of points, but when the solvent approaches the crossover point the number of collision points increases. When typical length between the collision points become approximately the same as the persistent length, the rigidity of a CLM molecule becomes important and there is a tendency to align quasi-straight pieces with quasi-parallel structure. This means that in the high density state of CLM the phase transition from disordered to liquid-crystal-like ordered phase [5], should take place. However, "naive" estimation (4) is even qualitatively incorrect in the case of the condensation of a long macromolecule. In the liquid-crystal ordering that is accompanied by molecular collapse in a poor solvent,

non-binary interactions should be taken into account and the critical volume fraction is given by (see below):

$$\rho_c \sim \left(\frac{a}{l_p} \right)^{\frac{\omega}{1+2\omega}} \gg \rho_*, \tag{52}$$

where quantity ω is determined by a small-angle-limit of angular-dependent interactions between two CLM segments [15].

The Hamiltonian of a DNA molecule in bacteria is very complicated and includes many variables describing a DNA molecule, solvent components and DNA associated proteins. It can be simplified, however, by integrating the microscopic Hamiltonian over the solvent and the protein's degrees of freedom. Of course, the resulting Hamiltonian will still be sophisticated and will include nonlinear terms with derivatives and terms with nonlocal segment-segment interaction. Near the transition point, however, where the CLM density ρ is of the order of $o(a/l_p, \bar{K}l_p)$ (where $\bar{K}$ is an average local curvature of the molecule, see later), the nonlinear derivative terms can be omitted for the lowest approximation on a/l_p, $\bar{K}l_p$, while nonlocal contribution to the segment-segment interactions can be treated by using self-consisting-field approximation, which is, apparently, valid in the transition region (see below and corresponding discussion in [14]).

We will assume that the molecule's core is twisted around its centerline, so in a mechanical equilibrium state the molecule is super-coiled [23, 25] (Fig. 5). Since for bacterial DNA: $\bar{K}l_p \lesssim 10^{-1}$ [23], we will consider a case: $a/l_p \ll 1$, $l_p/L \ll 1$ and $\bar{K}l_p \ll 1$.
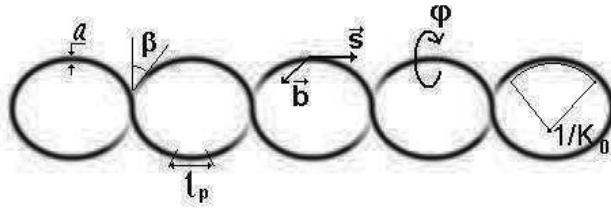
Figure 5. Super-coiled macromolecule. l_p is the effective bending persistent lengths, s is a unit tangent vector and b is a unit bi-normal vector. β is the opening angle of the super-helix, a is the hard-core diameter, φ is the twist angle and K_0 is a local curvature. Reproduced with permission from Ref.[15].

For the lowest order on a/l_p and $K_0 l_p$ energy of deformation of the super-coiled CLM can be approximated as [15]:

$$\frac{\mathcal{H}_S}{T} = \int_0^L \left\{ \frac{l_p}{2} \left(\frac{ds}{dl} - K_0(l)[s \times b] \right)^2 + \frac{l_t}{2} \left(\frac{d\varphi}{dl} - \Omega_0(l) \right)^2 \right\} dl,$$

where the molecule is considered as a semi-flexible chain, with the contour parameter l and the contour length L. l_p and l_t are the effective bending and torsion persistent lengths ($l_p \sim l_t$). $s(l)$ is a unit tangent vector at the point l and $b(l)$ is a corresponding unit bi-normal vector. $\varphi(l)$ is the twist angle. Note that b, s and φ are related as $db/d\varphi = [s \times b]$. The terms are proportional to K_0 and Ω_0 ensure minimum of $\mathcal{H}_S$ at an initial super-coiled state with local curvature $K_0(l)$ and local twist per unit length $\Omega_0(l)$.

The effective energy of interactions between the molecule pieces and the molecule and solvent components can be taken into account by adding an effective field U, induced by the renormalized segment-segment interactions:

$$\mathcal{H}_{PT} = \mathcal{H}_S + \frac{1}{a} \int_0^L U(\boldsymbol{x}(l), \boldsymbol{s}(l), \varphi(l)) dl,$$

where $\boldsymbol{x}(l)$ is a coordinate vector at the point l. It follows from Eqs. (1) and (4) that near the transition point each quasi-straight piece interacts with a large number of neighbors $[k_{neigh} \sim \rho_c v/a^2 l_p \sim (l_p/a)^{1+\omega/1+2\omega} \gg 1]$. Therefore, the term $U(\boldsymbol{x}, \boldsymbol{s}, \varphi)$ can be obtained by using a self-consisting-field approach [14]. In this region the repulsive and attractive contributions to binary collisions between the molecule's pieces compensate each other and high order collisions become significant [6]. Such compensation, however, takes place only for angular independent contributions, so we should keep higher order terms only for angular independent contributions, while for angular-dependent interactions we could take into account only collisions of the lowest order. Thus, the interaction energy can be approximated as:

$$U \simeq T\varrho(\boldsymbol{x}) \left(\oint d\boldsymbol{s}' \, d\varphi' \, \gamma(\boldsymbol{s} - \boldsymbol{s}'; \varphi - \varphi') g(\boldsymbol{x}, \boldsymbol{s}', \varphi') + \Phi(\varrho(\boldsymbol{x})) \right),$$ (53)

where function $g(\boldsymbol{x}, \boldsymbol{s}', \varphi')$ describes local fraction of quasi-straight segments with twist φ', which are oriented along the direction $\boldsymbol{s}'$. $\varrho(\boldsymbol{x})$ is the local density of the CLM segments near point $\boldsymbol{x}$. $\gamma(\boldsymbol{s} - \boldsymbol{s}'; \varphi - \varphi')$ describes the angular-dependent part of energy of interactions, while angle-independent contributions are included in the term $\Phi(\varrho)$. It is assumed that the first term (53) is vanished for $g(\boldsymbol{x}, \boldsymbol{s}, \varphi) = const$. Using the same arguments as in [6, 16], we can consider $\Phi(\varrho)$ as an analytical function and expand it over ϱ:

$$\Phi \simeq \tau + \kappa\varrho.$$ (54)

Note, that for the main approximation, higher order terms in (54) should be omitted, because they lead to higher order contributions to the free energy $\sim o\left((a/l_p)^{4\omega/(1+2\omega)}\right)$. $\tau > 0$ corresponds to a good solvent and $\tau < 0$ to a poor solvent and it depends on the chemical composition of the solvent.

It should be noted that because $g(\boldsymbol{x})$ and $\varrho(\boldsymbol{x})$ are slowly changed within the interaction scales, we can use local approximation for the functions γ and Φ. Corresponding contribution to the free energy per unit volume can be found from [26]:

$$\mathcal{F} = -\frac{T\rho}{a^2 L} \ln \int d^3\boldsymbol{x} \oint d\boldsymbol{s} \, d\varphi \, \mathcal{G}(\boldsymbol{s}, \varphi, \boldsymbol{x}|\boldsymbol{s}, \varphi + 2\pi m, \boldsymbol{x}; L),$$ (55)

where $\mathcal{G}(\boldsymbol{s}_0, \varphi_0, \boldsymbol{x}_0|\boldsymbol{s}_1, \varphi_1, \boldsymbol{x}_1; L)$ is a Green function of Hamiltonian $\mathcal{H}_{PT}$ and $\oint$ designates integration over φ and directions of $\boldsymbol{s}$ and ρ is the average volume fraction of the molecule

(m is an integer number). It can be shown in a standard way [6] (see Appendix 2) that for the first approximation on (a/l_p) and $K_0 l_p$, $\mathcal{G}$ is:

$$\frac{\partial \mathcal{G}}{\partial L} - \widehat{H}\mathcal{G} = \delta(L)\delta(s_1 - s_0)\delta(x_1 - x_0)\delta(\varphi_1 - \varphi_2), \tag{56}$$

with

$$\widehat{H} = -(s \cdot \nabla) - K_0\left(A \cdot \frac{\partial}{\partial s}\right) - \Omega_0\frac{\partial}{\partial \varphi} + \frac{1}{2l_p}\frac{\partial^2}{\partial s^2} \tag{57}$$

$$+ \frac{1}{2l_t}\frac{\partial^2}{\partial \varphi^2} - \frac{K_0}{2}\frac{\partial A}{\partial s} - \frac{U}{aT};$$

$$A = [s \times b] = \frac{(e - s(e \cdot s))\cos\varphi + [e \times s]\sin\varphi}{\sqrt{1 - (e \cdot s)^2}},$$

where $\partial/\partial s$ and $\partial^2/\partial s^2$ - are gradient and Laplacian over the angular variable s, while ∇ is gradient over the space variable x, (e is a constant unit vector, which reflects initial orientation of the super-helix. The free energy, of cause, is invariant under arbitrary rotation of e).

If $K_0(l), \Omega_0(l)$ are changed slowly on scale l_p, where $\mathcal{G}$ significantly changes (this is typical for bacterial DNA [25]), we can use adiabatic approximation for Green function [26] and write:

$$\mathcal{G} \simeq \sum_i w_i^+(s_1, \varphi_1, x_1)w_i^-(s_0, \varphi_0, x_0)\exp - \int_0^L E_i(K_0(l), \Omega_0(l))dl, \tag{58}$$

where l is considered as an imaginary time and $\{E_i\}$ is the energy spectrum of the equation

$$\widehat{H}w_i \simeq -E_i w_i. \tag{59}$$

$w_i^-(s, \varphi, x) = w_i^+(-s, -\varphi, x)$ and they are normalized as $\int w_i^+ w_i^-\, d^3x\, ds\, d\varphi = 1$.

The main contribution to the sum in Eq. (58) is given by the lowest part of the energy spectrum. The structure of this part depends on the ratio of l_p^{-1}, l_t^{-1} to the depth of the "potential well": $\sim (U_{max} - U_{min})/T$. If this ratio is small, the lowest part of the spectrum will be discrete, otherwise it will be continuous. In the high density phase this ratio can be estimated as $Tl_p^{-1}/(U_{max} - U_{min}) \sim a/\rho l_p \sim \rho_*/\rho_c$, so, for $\rho_c \gg \rho_*$ the lowest part of the spectrum is discrete. (In the low density phase $\nabla w = 0$ and $U \simeq const.$, and the spectrum is obviously discrete, because s and φ are changed in the finite regions.) Since a gap between the ground and the first exited state is about $E_1 - E_0 \sim l_p^{-1}$, so $[\exp -L(E_1 - E_0)] \sim \exp -L/l_p \ll 1$, we can keep in (58) only the term with the lowest E_0 [15].

Then, free energy is expressed as:

$$\mathcal{F} \simeq \frac{T\rho}{a^2 L} \int_0^L E_0(K_0(l), \Omega_0(l)) dl + o(a/L).$$

Rewriting w in the pseudo-polar form:,

$$w(\boldsymbol{s}, \boldsymbol{x}, \varphi) = u(\boldsymbol{s}, \boldsymbol{x}, \varphi) \exp[K_0 l_p f(\boldsymbol{s}, \boldsymbol{x}, \varphi)], \tag{60}$$

where

$$u(\boldsymbol{s}, \varphi, \boldsymbol{x}) = \sqrt{w(\boldsymbol{s}, \varphi, \boldsymbol{x}) w(-\boldsymbol{s}, -\varphi, \boldsymbol{x})}$$

$$K_0 l_p f(\boldsymbol{s}, \boldsymbol{x}, \varphi) = \ln\left(\sqrt{w(\boldsymbol{s}, \varphi, \boldsymbol{x})/w(-\boldsymbol{s}, -\varphi, \boldsymbol{x})}\right), \tag{61}$$

one obtains (see Appendix 3):

$$\mathcal{F} = \frac{T}{a^3} \int d^3\boldsymbol{x} \oint d\boldsymbol{s}\, d\varphi \left\{ \frac{a}{2l_p}\left(\frac{\partial u}{\partial \boldsymbol{s}}\right)^2 + \frac{a}{2l_t}\left(\frac{\partial u}{\partial \varphi}\right)^2 + \right.$$

$$\left. + \left[\frac{U(\boldsymbol{s}, \boldsymbol{x}, \varphi)}{T} + h\left(\left(\frac{\partial f}{\partial \boldsymbol{s}}\right)^2 + \frac{l_p}{l_t}\left(\frac{\partial f}{\partial \varphi}\right)^2\right)\right] u^2 \right\}, \tag{62}$$

where $h = a l_p \overline{K^2} = a l_p L^{-1} \int_0^L K_0^2 dl$. For DNA molecule h can be estimated as $h \simeq (l_p/2a)\sigma^2 \cos^4 \beta$ [25], where σ is super-helical density and β is an opening angle of the super-helix.

Expression (62) should be minimized over $u(\boldsymbol{s}, \boldsymbol{x}, \varphi)$ under restriction (see Appendix 3):

$$\left(\frac{\partial}{\partial \boldsymbol{s}} \cdot \left(u^2 \frac{\partial f}{\partial \boldsymbol{s}}\right)\right) + \frac{l_p}{l_t}\frac{\partial}{\partial \varphi}\left(u^2 \frac{\partial f}{\partial \varphi}\right) = \tag{63}$$

$$= \left(\frac{\partial}{\partial \boldsymbol{s}} \cdot (u^2 \boldsymbol{A})\right) + \frac{\Omega_0}{K_0}\frac{\partial u^2}{\partial \varphi} + \frac{1}{K_0}\left(\nabla \cdot \boldsymbol{s} u^2\right),$$

$$\int d^3\boldsymbol{x} \oint d\boldsymbol{s}\, d\varphi\, u^2(\boldsymbol{s}, \boldsymbol{x}, \varphi) = 1$$

In order to find the minimum of (62) we will use the Onzager approach [5], where it is assumed that $u = \exp \lambda \psi(\boldsymbol{s}, \boldsymbol{x})$ and the function $\psi(\boldsymbol{s}, \boldsymbol{x})$ has a maximum in the direction of the local average orientation of quasi-straight segments. The parameter λ is found by minimizing $\mathcal{F}$ and it is assumed that $\lambda > 0$ in the ordered phase and $\lambda = 0$ in the disordered one.

To define factor $\gamma(s - s'; \varphi - \varphi')$, note that for $\lambda \gg 1$ (which is correct near the phase transition in our case), the function $u(s, x)$ has a narrow maximum in the direction of the local average orientation of quasi-straight segments. Because in the used approximation $g = u^2$, the small-angle collisions give the main contribution to the angular-dependent term in (53). This means that the behavior of γ near $|\theta| \ll 1$, where θ is the angle between s and s', is relevant and we will approximate γ as

$$\gamma \simeq \varsigma + \eta |\theta|^{\omega},$$

The constant $\varsigma < 0$ ensures that the average of $\gamma(s - s'; \varphi - \varphi')$ is vanished (we will assume later that ς is included in τ). Generally speaking, η is an analytical function of $(\varphi - \varphi')$, but for $\Omega_0 l_t \ll K_0 l_p$ dependence γ on φ can be neglected. For the excluded volume contribution and for the forces that were considered in [21] $\omega = 1$ should be chosen.

The final result depends weakly on the specific form of the prob function u (see Appendix 5) and can be obtained explicitly for $\lambda \gg 1$. Somewhat exhausting but straightforward calculations show that $\lambda \sim [\eta \Gamma(2 + \omega) \rho l_p / a]^{1/1+\omega}$, so $\lambda \gg 1$ for $\rho \gg a/l_p$. (Here Γ is Gamma function). Finally one obtains

$$\mathcal{F} \simeq T a^{-3} \left[(\tilde{a}/l_p)^{\alpha} \rho^{2-\alpha} + \tau \rho^2 + \kappa \rho^3 + h\rho \right],\qquad(64)$$

with $\alpha = \omega/1 + \omega$ and $\tilde{a} \sim [\eta \Gamma(2 + \omega)]^{1/\omega} a$.

It is easy to show (see Appendix 4) that near point:

$$\tau_c \simeq -2\kappa \rho_c \left\{ 1 + (1 - \alpha) \left(\frac{\alpha \sigma}{\kappa \sigma_c} \Lambda \right)^{-1/1+\alpha} \right\},\qquad(65)$$

where $\sigma_c \simeq [(\eta \Gamma(2 + \omega))^{-1/2\omega} \alpha^{(3+\alpha)/2(1+\alpha)} \cos^{-2} \beta] \kappa^{(\alpha-1)/2(1+\alpha)} (\tilde{a}/l_p)^{(1+3\alpha)/2(1+\alpha)}$, the system undergoes the first order liquid-crystal phase transition with critical volume fraction of the molecule:

$$\rho_c \simeq c_o \left(\frac{\tilde{a}}{l_p} \right)^{\alpha/1+\alpha} \frac{\sigma}{\sigma_c} \Lambda \left(\frac{\sigma}{\sigma_c} \right),\qquad(66)$$

where $c_o \simeq (\alpha/\kappa)^{1/1+\alpha}$ and function Λ satisfies to

$$(\sigma_c/\sigma)^{1+\alpha} \Lambda^{1-\alpha} - \Lambda^2 + 1 = 0.\qquad(67)$$

It has an asymptotic:

$$\Lambda\left(\frac{\sigma}{\sigma_c}\right) \simeq \begin{cases} \sigma_c/\sigma \text{ for } \sigma \ll \sigma_c \\ 1 \quad \text{ for } \sigma \gtrsim \sigma_c \end{cases}$$

The jump of entropy near the transition point is:

$$\Delta S_c = q/T \sim (\tilde{a}/l_p)^{2\alpha - 1/1 + \alpha} \rho_c^{2-\alpha}, \tag{68}$$

where q is latent heat and it is relatively small, while a jump of the liquid-crystal order parameter

$$\mathcal{Q}_c \simeq 1 - \frac{3}{\lambda(\rho_c)} \sim 1$$

is large.

It is clearly seen that there is a well defined critical value of the super-helical density - σ_c, that alters the transition properties. For $\sigma \ll \sigma_c$ the transition's parameters are independent of the super-helical density:

$$\tau_c \sim -\kappa \left(\frac{\tilde{a}}{l_p}\right)^{\alpha/1+\alpha},$$

$$\rho_c \sim \left(\frac{\tilde{a}}{l_p}\right)^{\alpha/1+\alpha},$$

and the phase transitions in the closed and the open macromolecule are the same. However, in the opposite case $\sigma_c \lesssim \sigma$ the situation is cardinally changed:

$$\tau_c \sim -\kappa \left(\frac{\tilde{a}}{l_p}\right)^{\alpha/1+\alpha} \frac{\sigma}{\sigma_c}\left[1 + o\left((\sigma_c/\sigma)^{1/1+\alpha}\right)\right],$$

$$\rho_c \sim \left(\frac{\tilde{a}}{l_p}\right)^{\alpha/1+\alpha} \frac{\sigma}{\sigma_c},$$

so, super-helical density becomes one of the major factors that influence the crystallization process. This case corresponds to bacterial DNA, where the crossover value $\sigma_c \sim 5 \cdot 10^{-3}$ is very small, while typical values of the super-helical density are $\sigma \sim 5 \cdot 10^{-2} \gg \sigma_c$. It can be seen that super-helicity doesn't prevent phase transition to the crystalline state but decreases the transition point and increases sharpness of the phase transition. Qualitative behavior of $\rho(\tau), \rho_c(\sigma), \tau_c(\sigma)$ and $Q_c(\sigma)$ is shown in Fig. 6. It should be noted that free energy (64) contains only bulk contribution, because the surface contribution is proportional to $(\rho a/L)^{1/3}$ and should be neglected in the used approximation.
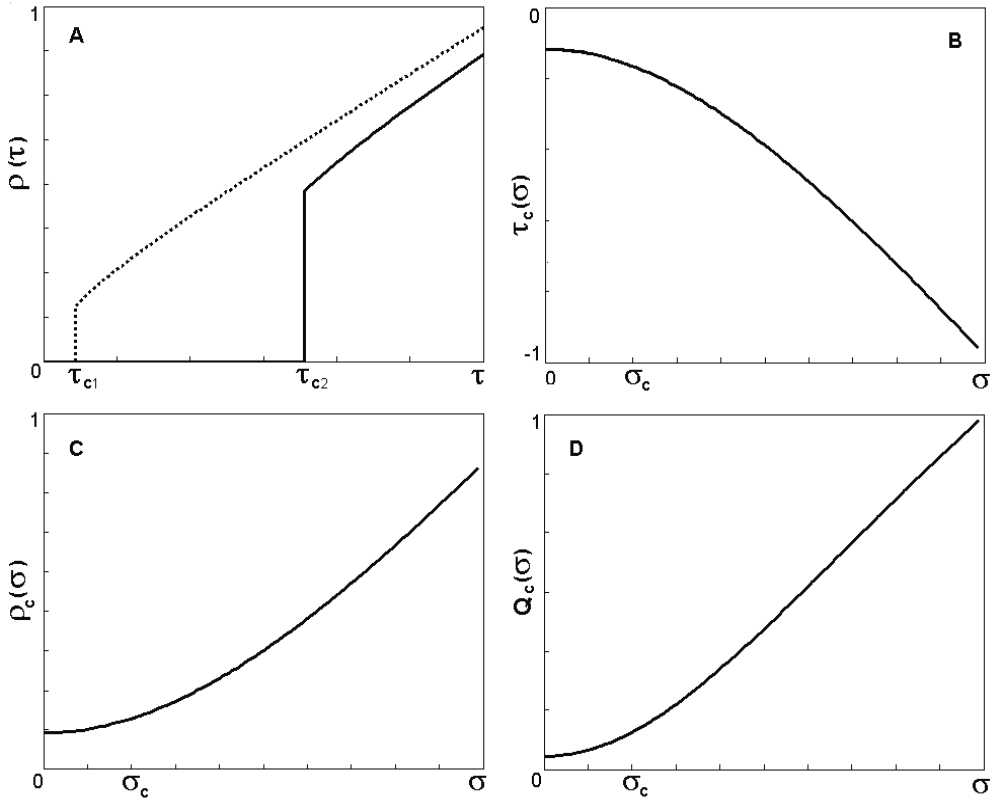
Figure 6. Behavior of the transition's parameters. **A** - behavior of $\rho(\tau)$ for different σ. Dashed line $\sigma = 0$, solid line $\sigma \gg \sigma_c$. **B** behavior of $\tau_c(\sigma)$, **C** - behavior of $\rho_c(\sigma)$, **D** - behavior of $Q_c(\sigma)$. Reproduced with permission from Ref.[15].

It should be emphasized that condition $a/l_p \ll 1$ is essential for liquid-crystal ordering. Although our approach is not quantitatively validated for $a/l_p \sim 1$, one can hope that it qualitatively correctly predicts the behavior of the system characteristics in this limit. Since for $a \sim l_p$ it should take $\lambda = 0$, the liquid crystal ordering should not take place in this case.

6. Discussion

The MFA is the most crucial approximation in our theory but it is a reasonable one. At low temperatures each quasi-straight piece of a fiber or collagen molecule interacts with a large number of neighbors and, therefore, fluctuations of the concentration are irrelevant. On the other hand, the phase transitions are of the first order and fluctuations of the order parameter are therefore small. Note, that main assumptions, which have been used in the Sec.4, are general enough to apply the theory to a class of compressed materials made from various fibers. It could be used, for example, for implant materials made from actin myofibrils or for artificial wood made from natural cellulose fibrils.

It has been shown in [12], [2], that a novel material can be developed by exerting high pressure and temperature on natural leather material. The production is done in an oxygen poor environment in order to prevent burning of the leather. The resulting material, which was called *pleather*, is thermoplastic.

For low pressure, heating leads to destruction of the leather, but for high pressure it leads to the appearance of an amorphous material. This transformation corresponds to the transition described here. For this transition the jump of Young's modulus is strongly correlated with the jump in the compressibility. The theory predicts the stabilization of the spiral form of the collagen molecules at high pressure and the sensitivity of the transition to an uniaxial stress [10]. The spiral form stabilization has been found already in an aqueous solution of collagen [11], while the sensitivity to an uniaxial stress should be tested by experiment. Other predictions of the theory like positive shift of the transition temperature with pressure and small latent heat of the transitions are in good agreement with the experimental observations [12], [2] as well.

It should be noted, that in the real material the phase transition under heating is not reversible and after cooling the system does not return to the initial low-temperature phase. This effect is connected with the cross-links between collagen molecules in the coil form. These cross-links are not important for the behavior under heating, because until the phase transition the spirality of collagen is large. However, if we cool the material after phase transition the cross-links prevents spiralization and, therefor, stabilize the disordered phase.

Considering the bacterial DNA crystallization, one can say [28] that the cellular conditions that determine super-helical parameters regulate the packaging of DNA as well and, therefore, regulate bacterial endurance and virulence. The theory predicts crucial role of super-helicity in DNA condensation, which has been found experimentally [19, 24, 28]. It was found also that the condensation conditions of closed (with $\sigma \simeq 3 \cdot 10^{-2}$) and of open DNA are different [19]. For $\omega = 1$, which looks reasonable in the considered situation, $\rho_c \sim 0.4$ and $Q_c \sim 0.75$ are in qualitative agreement with the experimental observation.

Apparently, the situation $a/l_p \sim 1$ is realized in eucaryote cells, where the initial phase of DNA packing is presented by fiber that comprises a string of repeating units: the nucleosomes, where DNA molecules wind around histone cores. The nucleosomes are connected by pieces of free DNA, so the flexibility of the fiber is close to the flexibility of the DNA chain, while the fiber's effective diameter is approximately of nucleosome size: $a_{nucl} \sim l_p$, so there is no liquid crystal crystallization. In fact, in this situation, the "beads on string" model [16] seems more appropriate. It is shown [16] that in this case an ordinary collapse of the chain to a friable, non-crystalline state must occur. This supports the hypothesis [29] that nucleosomes were formed to counteract spontaneous transition of the eucaryotic DNA into crystalline state.

Acknowledgment

Appendix 1

We have for $\lambda \gg 1$:

$$F \simeq F_0 + \frac{\chi T c^2}{2D^3} \int_0^1 dx \left(\frac{TD}{\chi \gamma c} \left(1 - x^2\right) A\lambda^2 \left(\phi'(x)\right)^2 \exp\left(\lambda \phi(x)\right) + \right.$$

$$\left. +2^\omega \kappa A^2 \exp\left(\lambda \phi(x)\right) \int_0^1 dy \exp\left(\lambda \phi(y)\right) |x - y|^\omega P_\omega \left(\left| \frac{2 - x - y}{x - y} \right| \right) \right).$$

where

$$\kappa = \lim_{\vec{n} \to k} \frac{u(\boldsymbol{n}, \boldsymbol{k})}{|\boldsymbol{n} \times \boldsymbol{k}|^{2\omega}},$$

$$\omega = \lim_{n \to k} \frac{1}{2} \frac{\partial \ln u(\boldsymbol{n}, \boldsymbol{k})}{\partial \ln |\boldsymbol{n} \times \boldsymbol{k}|}.$$

and P_ω is a Legendre function. Since the main contribution to these integrals gives $x \sim y \sim 1$ we can put: $\phi(y) \simeq \phi(1) - \phi'(1)(1 - y) + o\left((1 - y)^2\right) \simeq \phi(1) - u + o(u^2)$ and obtain for the coefficient $\zeta(\omega)$

$$\zeta = 2^\omega \kappa \int_0^\infty du\, dz\, e^{-u-z} |u - z|^\omega P_\omega \left(\left| \frac{u + z}{u - z} \right| \right) + o\left(e^{-\lambda}\right) \simeq$$

$$\simeq 2^{\omega+2} \kappa \int_0^\infty du'\, dz' (uz)\, e^{-u'^2 - z'^2} \left| u'^2 - z'^2 \right|^\omega P_\omega \left(\left| \frac{u'^2 + z'^2}{u'^2 - z'^2} \right| \right) =$$

$$= 2^{\omega+2} \kappa \int_0^{2\pi} d\varphi\, \sin\varphi \cos\varphi \left| \sin^2\varphi - \cos^2\varphi \right|^\omega P_\omega \left(\left| \frac{1}{\sin^2\varphi - \cos^2\varphi} \right| \right) \times$$

$$\times \int_0^\infty dr\, r^{2(1+\omega)+1} \exp\left(-r^2\right)$$

$$= 2^{\omega-1} \kappa \int_0^\infty dx\, x^{1+\omega} e^{-x} \int_0^\pi d\phi\, \sin\phi\, |\cos\phi|^\omega P_\omega \left(\left| \frac{1}{\cos\phi} \right| \right) =$$

$$\simeq 2^\omega \kappa \Gamma(2 + \omega) \int_1^\infty dz\, z^{-2-\omega} P_\omega(z).$$

where $\Gamma(x)$ is Gamma function. So

$$\zeta(\omega) = 2^{2\omega} \Gamma(1 + \omega) \kappa.$$

If the term $|\boldsymbol{n} \times \boldsymbol{k}|^{2\omega}$ gives the main contribution to $u(\boldsymbol{n}, \boldsymbol{k})$, we obtain

$$\kappa \approx \frac{2\Gamma\left(\frac{3}{2} + \omega\right)}{\sqrt{\pi}\Gamma(1 + \omega)},$$

and for $\omega \leq 1$

$$\zeta(\omega) \approx 2^{2\omega}(1 - 0.02\omega).$$

Appendix 2

Green function $\mathcal{G}(\boldsymbol{s}_0, \varphi_0, \boldsymbol{x}_0 | \boldsymbol{s}_1, \varphi_1, \boldsymbol{x}_1; L)$ is defined as:

$$\mathcal{G}(\boldsymbol{s}_0, \varphi_0, \boldsymbol{x}_0 | \boldsymbol{s}_1, \varphi_1, \boldsymbol{x}_1; L) = \underbrace{\int\int \mathfrak{D}\boldsymbol{x}(l)\boldsymbol{s}(l)\varphi(l)} \exp - \frac{H_{PT}(L)}{T},$$

with: $\boldsymbol{x}(0) = \boldsymbol{x}_0$; $\boldsymbol{s}(0) = \boldsymbol{s}_0$; $\varphi(0) = \varphi_0$; $\quad \boldsymbol{x}(L) = \boldsymbol{x}_1$; $\boldsymbol{s}(L) = \boldsymbol{s}_1$; $\varphi(L) = \varphi_1$,

where $\underbrace{\int\int \mathfrak{D}\boldsymbol{x}(l)\boldsymbol{s}(l)\varphi(l)}$ is a path integral over all possible shapes of a molecule chain. This Green function satisfies the equation [6] (see Fig. 7):

$$\mathcal{G}(\boldsymbol{s}_0, \varphi_0, \boldsymbol{x}_0 | \boldsymbol{s}, \varphi, \boldsymbol{x}; L) = \int \oint d^3\boldsymbol{x}' \, d\boldsymbol{s}' \, d\varphi' \, \mathcal{G}(\boldsymbol{s}_0, \varphi_0, \boldsymbol{x}_0 | \boldsymbol{s}', \varphi', \boldsymbol{x}'; L - dL)$$
$$\mathcal{G}(\boldsymbol{s}', \varphi', \boldsymbol{x}' | \boldsymbol{s}, \varphi, \boldsymbol{x}; dL). \tag{69}$$
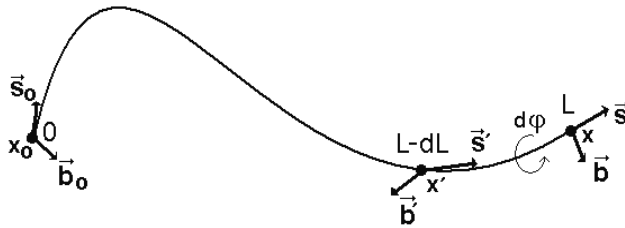
Figure 7. To equation (69). L is a macromolecule's contour length, persistent lengths, $\boldsymbol{s}_0, \boldsymbol{s}', \boldsymbol{s}$ are unit tangent vectors, $\boldsymbol{b}_0, \boldsymbol{b}', \boldsymbol{b}$ are unit bi-normal vectors, φ is the twist angle and $\boldsymbol{x}_0, \boldsymbol{x}$ are coordinate vectors at initial and end points of the molecule. Reproduced with permission from Ref.[15].

If dL is small the function $\mathcal{G}(\boldsymbol{s}', \varphi', \boldsymbol{x}' | \boldsymbol{s}, \varphi, \boldsymbol{x}; dL)$ can be presented as:

$$\mathcal{G}(\boldsymbol{s}',\varphi',\boldsymbol{x}'|\boldsymbol{s},\varphi,\boldsymbol{x};dL) \simeq \frac{1}{Z}\exp-\left\{\frac{l_p}{2}\left[\frac{\boldsymbol{s}-\boldsymbol{s}'}{dL}-\boldsymbol{K}\left(\frac{\boldsymbol{s}+\boldsymbol{s}'}{2},\frac{\varphi+\varphi'}{2},L-\frac{dL}{2}\right)\right]^2\right.$$

$$+\frac{l_t}{2}\left[\frac{\varphi-\varphi'}{dL}-\Omega_0\left(L-\frac{dL}{2}\right)\right]^2+$$

$$\left.+\frac{1}{aT}U\left(\frac{\boldsymbol{s}+\boldsymbol{s}'}{2},\frac{\varphi+\varphi'}{2},\frac{\boldsymbol{x}+\boldsymbol{x}'}{2}\right)\right\}dL, \tag{70}$$

where Z is a proper normalization multiplier. Observing that $\boldsymbol{x}' = \boldsymbol{x} - \boldsymbol{s}dL$ and symbolling:

$$\sqrt{dL}\boldsymbol{p} = \boldsymbol{s} - \boldsymbol{s}' - \boldsymbol{K}dL,$$
$$\sqrt{dL}t = \varphi - \varphi' - \Omega dL,$$

and keeping in (70) the lowest on dL terms one obtains:

$$\mathcal{G}(\boldsymbol{s}',\varphi',\boldsymbol{x}'|\boldsymbol{s},\varphi,\boldsymbol{x};dL) \simeq \frac{1}{Z}\left[1-\frac{l_p}{2}\left(\boldsymbol{p}\cdot\left(\boldsymbol{p}\cdot\frac{\partial}{\partial\boldsymbol{s}}\right)\boldsymbol{K}\right)dL-\frac{l_p}{2}t\left(\boldsymbol{p}\cdot\frac{\partial\boldsymbol{K}}{\partial\varphi}\right)dL-\right.$$

$$\left.-\frac{l_t}{2}\left(t^2\frac{\partial\Omega_0}{\partial L}\right)dL+\frac{U(\boldsymbol{s},\varphi,\boldsymbol{x})}{aT}dL\right]\exp-\left(\frac{l_p\boldsymbol{p}^2}{2}+\frac{l_pt^2}{2}\right). \tag{71}$$

Correspondingly, for $\mathcal{G}(\boldsymbol{s}_0,\varphi_0,\boldsymbol{x}_0|\boldsymbol{s}',\varphi',\boldsymbol{x}';L-dL) = \mathcal{G}(\boldsymbol{s}_0,\varphi_0,\boldsymbol{x}_0|\boldsymbol{s}-\sqrt{dL}\boldsymbol{p}-\boldsymbol{K}dL,\varphi-\sqrt{dL}t-\Omega_0 dL,\boldsymbol{x}-\boldsymbol{s}dL;L-dL)$ one has

$$\mathcal{G}(\boldsymbol{s}_0,\varphi_0,\boldsymbol{x}_0|\boldsymbol{s}',\varphi',\boldsymbol{x}';L-dL) \simeq \mathcal{G}(\boldsymbol{s}_0,\varphi_0,\boldsymbol{x}_0|\boldsymbol{s},\varphi,\boldsymbol{x};L) +$$

$$+\left[\frac{\boldsymbol{p}^2}{2}\frac{\partial^2\mathcal{G}}{\partial\boldsymbol{s}^2} = \frac{t^2}{2}\frac{\partial^2\mathcal{G}}{\partial\varphi^2} - \frac{\partial\mathcal{G}}{\partial L}-\right.$$

$$-\left([\boldsymbol{K}+dL^{-1/2}\boldsymbol{p}]\cdot\frac{\partial\mathcal{G}}{\partial\boldsymbol{s}}\right)-[\Omega_0+dL^{-1/2}t]\frac{\partial\mathcal{G}}{\partial\varphi}-(\boldsymbol{s}\cdot\nabla\mathcal{G})-$$

$$\left.-\frac{1}{2}t\left(\boldsymbol{p}\cdot\frac{\partial^2\mathcal{G}}{\partial\boldsymbol{s}\partial\varphi}\right)\right]dL. \tag{72}$$

Substituting (71),(72) to (69) and integrating over $(\boldsymbol{p},t)$ one obtains (56),(57).

Appendix 3

Using (60) in (59) and taking into account that $u(-\boldsymbol{s},-\varphi,\boldsymbol{x}) = u(\boldsymbol{s},\varphi,\boldsymbol{x})$; $f(-\boldsymbol{s},-\varphi,\boldsymbol{x}) = -f(\boldsymbol{s},\varphi,\boldsymbol{x})$, one obtains:

$$- Eu(\pm \boldsymbol{s}, \pm \varphi, \boldsymbol{x}) = \frac{1}{l_p} \left(\frac{\partial^2 u}{\partial \boldsymbol{s}^2} \right) + \frac{1}{l_t} \left(\frac{\partial^2 u}{\partial \varphi^2} \right) + K_0 l_p \left[\Omega_0 \frac{\partial f}{\partial \varphi} + \left(\boldsymbol{K} \cdot \frac{\partial f}{\partial \boldsymbol{s}} \right) + (\boldsymbol{s} \cdot \nabla f) \right] u$$

$$+ \left[K_0^2 l_p^2 \left(\frac{1}{l_p} \left(\frac{\partial f}{\partial \boldsymbol{s}} \right)^2 + \frac{1}{l_t} \left(\frac{\partial f}{\partial \varphi} \right)^2 \right) + \frac{1}{2} \frac{\partial \Omega_0}{\partial l} - \frac{U}{aT} \right] u +$$

$$\pm \left\{ -\Omega_0 \frac{\partial u}{\partial \varphi} - \frac{1}{2} \frac{\partial \boldsymbol{K}}{\partial \boldsymbol{s}} u - (\boldsymbol{s} \cdot \nabla u) - \left(\boldsymbol{K} \cdot \frac{\partial u}{\partial \boldsymbol{s}} \right) + \right.$$

$$+ K_0 l_p \left[\frac{1}{l_p} \left(\frac{\partial u}{\partial \boldsymbol{s}} \cdot \frac{\partial f}{\partial \boldsymbol{s}} \right) + \frac{1}{l_t} \left(\frac{\partial u}{\partial \varphi} \frac{\partial f}{\partial \varphi} \right) + \right. \tag{73}$$

$$\left. \left. + \frac{1}{2 l_p} \left(\frac{\partial^2 f}{\partial \boldsymbol{s}^2} \right) u + \frac{1}{2 l_t} \left(\frac{\partial^2 f}{\partial \varphi^2} \right) u \right] \right\}.$$

Subtracting the expressions with different signs one obtains (63). Summing the expressions with different signs, multiplying both sides by $u(\boldsymbol{s}, \varphi, \boldsymbol{x})$ and integrating over $\boldsymbol{s}, \varphi, \boldsymbol{x}$ and dl/L one obtains (62).

Actually, restriction (63) ensures that w_0^+ and w_0^- have the same eigenvalue E_0. Indeed, it follows from (73) and (63) that $w_0^+ \hat{H} w_0^- = w_0^- \hat{H} w_0^+$. Let us assume that:

$$-E_0^+ w_0^+ = \hat{H} w_0^+,$$
$$-E_0^- w_0^- = \hat{H} w_0^-.$$

Multiplying the first equation by w_0^- and the second by w_0^+ one obtains:

$$(E_0^+ - E_0^-) w_0^- w_0^+ = w_0^+ \hat{H} w_0^- - w_0^- \hat{H} w_0^+ = 0.$$

So, $E_0^+ = E_0^- = E_0$.

Appendix 4

Since $\mathcal{F}(\rho)$ in Eq (64) is not singular for any positive ρ, phase transition to the crystalline state can be only of a first order. The transition point τ_c and jump of volume fraction of the molecule ρ_c should be found from the conditions:

$$\mathcal{F}(\rho_c) = \mathcal{F}(0),$$
$$\frac{\partial \mathcal{F}}{\partial \rho_c} = 0,$$

or

$$\left(\tilde{a}/l_p\right)^\alpha \rho_c^{1-\alpha} + \tau_c\rho_c + \kappa\rho_c^2 + h = 0,$$
$$(2-\alpha)\left(\tilde{a}/l_p\right)^\alpha \rho_c^{1-\alpha} + 2\tau_c\rho_c + 3\kappa\rho_c^2 + h = 0,$$

which after simple algebraic transformations lead to Eqs. (65)-(67).

Appendix 5

Various forms of $\psi(\boldsymbol{s}, \boldsymbol{x})$, corresponding to different structures of condensed phases, have been checked. For laminar-like ordering this function can be chosen in the form of:

$$\psi \sim -[\boldsymbol{s} \times \boldsymbol{e}]^2,$$

for toroid-like ordering it is:

$$\psi \sim -(\boldsymbol{s} \cdot \boldsymbol{e})^2 - ([\boldsymbol{s} \times \boldsymbol{e}] \cdot [\boldsymbol{e} \times \boldsymbol{x}])^2 / [\boldsymbol{e} \times \boldsymbol{x}]^2,$$

while for cholesteric ordering it is :

$$\psi \sim -\left([\boldsymbol{s} \times \boldsymbol{k}] \cos(2\pi q(\boldsymbol{e} \cdot \boldsymbol{x})) + [\boldsymbol{s} \times \boldsymbol{p}] \sin(2\pi q(\boldsymbol{e} \cdot \boldsymbol{x}))\right)^2,$$

where $1/q \gg 1$ is a cholesteric repeat, $|\boldsymbol{k}| = |\boldsymbol{p}| = 1$, $\boldsymbol{e} = [\boldsymbol{k} \times \boldsymbol{p}]$ and $(\boldsymbol{k} \cdot \boldsymbol{p}) = 0$. With accuracy to slight variance in the numerical coefficients, all forms of $\psi(\boldsymbol{s}, \boldsymbol{x})$ lead to the same expression for the free energy. This means that the Onzager approach is unreliable concerning information about the specific structure of the crystalline state. On the other hand, this approach gives a reasonable approximation the for thermodynamic properties of the phase transition.

Author details

Uziel Sandler

Jerusalem College of Technology, Jerusalem, Israel

References

[1] B. de Castro, M.Ferreira , R.T.Markus and A.Wyler, Influence of Prossesing Temperature and Pressure on Stability of the Structure of Hot Pressed Ground Leather, J.Macromol. Sci. ,1997, A34(1), 109-112.

[2] A.Wyler, R.T.Markus and B.de Castro B. , A Model for the Internal Structure of Hot Pressed Leather, J. Soc. Leather Technol. and Chem., 75, (1991), 52-55.

[3] K. Gekko and M. Fukamizu, Int.J.Biol.Macromol, 1991, 13, 295-300.

[4] P. Fratzl *et. al.*, Fibrillar Structure and Mechanical Properties of Collagen, J. of Structeral Biol., 1997, 122, 119Ű122.

[5] P.G.de Gennes ,The Physics of Liquid Crystals. Oxford: Clarendon Press; 1974.

[6] P.G.de Gennes, Scaling Concepts in Polymer Physics, Ithaca and London: Cornell Univ.Press; 1979.

[7] A. Khohlov, Concept of Quasimonomers and Its Application to Some Problems of Polymer Statistics. Polymer, 1978, 9, 1387.

[8] P. Kronick, Fundamentals of Leather Manufacturing, ed.E.Heideman, Ch.4, Darmstadt, Germany: Edward Roether KG. Publ.; 1993.

[9] A.A. Vedenov, The Physics of Solutions, Contemporary Problems in Physics, Science, Moscow; 1984; D. Poland, H.A. Scherada, Theory of Helix-Coil Transitions in Biopolymers, New York: Academic Press; 1970.

[10] P.G.de Gennes, (private communication).

[11] K. Gekko and M. Fukamizu, Int.J.Biol.Macromol, , 1991, 13,299.

[12] B. de Castro, M.Ferreira , R.T.Markus and A.Wyler, J.Macromol. Sci., 1997, A34(1), 109.

[13] A.R. Khokhlov, A.N. Semenov, Liquid-Crystalline Ordering in the Solution of. Partially Flexible Macromolecules, Physica A 112, 1982, 605-614; A.R. Khokhlov, A.N. Semenov, On the Theory of Liquid-Crystalline Ordering of Polymer Chains with limited flexibility, J.Stat.Phys., 1985, 38, 161-182; Zheng Yu Chen, Nematic Ordering in Semiflexible Polymer Chains, Macromolecules, 1993, 12, 3419-3423; H. Noguchi, K. Yoshikawa, Folding path in a semiflexible homopolymer chain: A Brownian dynamics simulation, J.Chem.Phys, , 2000, 113, 854-862 (and references there).

[14] U. Sandler, A. Wyler, Phase Transitions under Pressure in Collagenous Material, Phys.Rev.Lett., 1995, 74, 3073-3076; Phase transitions in fiber materials, Phys.Rev.B, 2000, 61, 16-19.

[15] U. Sandler U, Theory of Crystallization of a Closed Macromolecule, Inter. J. of Biological Macromolecules (IJBIOMAC), 2010, 47, 439-444.

[16] I.M. Lifshitz, A.Yu. Grosberg, A.R. Khokhlov, Some problems of the statistical physics of polymer chains with volume interaction, Rev.Mod.Phys, 1978, 50, 684-713.

[17] A. Minsky, E. Shimoni, D. Frenkiel-Krispin, Stress, order and survival, Nature Rev. Mol. Cell Biol,2002, 3, 50-60.

[18] S. Levin-Zaidman, D. Frenkiel-Krispin, E. Shimoni, I. Sabanay, S. G. Wolf and A. Minsky, Ordered intracellular RecAŰDNA assemblies: A potential site of in vivo RecA-mediated activities, PNAS,2000, 97, 6791 - 6796.

[19] C.L. Ma,V.A. Bloomfield, Condensation of supercoiled DNA induced by *MnCl$_2$*, Biophys.J., 1994,67, 1678-1681.

[20] V.A. Bloomfield, DNA condensation, Curr.Opin.Struct.Biol., 1996, 6, 334-341.

[21] A.A. Kornyshev, S. Leikin, Electrostatic interaction between long, rigid helical macromolecules at all interaxial angles, Phys.Rev.E, 2000, 62, 2576-2596.

[22] F. Livolante, A. Leforestier, Condensed phases of DNA: structures and phase transitions, Prog.Polym.Sci., 1996, 21, 1115-1164.

[23] N.R. Cozzarelli, T.C. Boles, and White, J.H., Primer on the Topology and Geometry of DNA Supercoiling, in: N.R. Cozzarelli, J.C. Wang, (Eds.), DNA Topology and Its Biological Effects, NY: Cold Spring Harbor Laboratory Press, Cold Spring Harbor, 1990, 139-184.

[24] J. Torbet and E. DiCapua, Supercoiled DNA is interwound in liquid crystalline solutions, The EMBO Journal, 1989, 8, 4351-4356.

[25] T.C. Boles, J.H. White and N.R. Cozzarelli, Structure of plectonemically supercoiled DNA, J. Mol. Biol. 1990, 213 931-951.

[26] A.A. Abrikosov, A.P. Gor'kov, M.E. Dzyaloshinskii, Quantum field theoretical methods in statistical physics, 2ed., Pergamon; 1965.

[27] M. Takahashi, K. Yoshikawa, V.V. Vasilevskaya, and A.R. Khokhlov, Collapse of single DNA molecule in poly(ethylene glycol) solutions. J. Chem. Phys. 1995, 102, 6595-6602; S. Kidoaki, K. Yoshikava, Folding and unfolding of a giant duplex-DNA in a mixed solution with polycations, polyanions and crowding neutral polymers, Biophys.Chem., 1999, 76, 133-143.

[28] Z. Reich, E.J. Wachtel, and A. Minsky, Liquid-crystalline mesophases of plasmid DNA in bacteria, Science, 1994, 264, 1460-1463; S.S. Zacharova *et al.*, Liquid Crystal Formation in Supercoiled DNA Solutions, Biophys.J., 2002, 83,1119-1129.

[29] A. Minsky, R. Ghirlando, Z. Reich, Nucleosomes a Solution to a Crowded Intracellular Environment, J.Theor.Biol., 1997, 188, 268-274.

Impurity Exclusion and Retention during Crystallisation and Recrystallisation — The Phenacetin by Ethylation of Paracetamol Process

Danielle E. Horgan, Lorraine M. Crowley,
Stephen P. Stokes, Simon E. Lawrence and
Humphrey A. Moynihan

Additional information is available at the end of the chapter

http://dx.doi.org/10.5772/59715

1. Introduction

A key issue facing the pharmaceutical and fine chemical industries is the generation of impurities during process chemistry and the retention, or otherwise, of these during crystallisation and subsequent processing. FDA guidelines [1] recognise organics, inorganics and residual solvents as possible impurities, and that organic impurities can arise during manufacturing or storage from starting materials, by-products, intermediates, degradation products, reagents, ligands and catalysts. Actual or potential impurities which can arise during synthesis, purification and storage must be noted and listed in the specification for any new drug substance. As crystallisation is the most important method of product isolation and purification in pharmaceutical manufacturing, the presence of impurities in the crystallisation medium or in the crystal product is clearly a significant issue. The presence of impurities in the crystalline product may affect the specification compliance of the batch. Any impurities present must be known, quantified and below specified limits. Impurities in the crystallisation medium can affect nucleation and growth rates, crystal form, including polymorphism or solvate formation, and morphology, including habit and crystal size distribution.

An example of the inter-relationship between process chemistry, impurities and crystallisation outcome is given by (*R,R*)-formoterol tartrate (1) [2]. The final step in the formation of this compound was salt formation which also resulted in the precipitation of a crystalline product. Compounds (2), (3), (4) and (5) in Figure 1 were identified as impurities in this material. Impurity (2) is a degradation product arising from hydrolysis of the formamide group of (1).

Compounds (3), (4) and (5) arise as side-products of hydrogenation steps in the synthesis of (1). Three crystal forms of (*R,R*)-formoterol tartrate were identified, polymorphic forms A and B and a hydrate (form C). The initially precipitated material was form B and contained all four impurities in quantities of 0.04% to 0.64%, above the specified levels. Recrystallisation of the precipitated material gave crystals of form A, the thermodynamically preferred form, in which impurities (4) and (5) were no longer detectible, impurity (3) was reduced by 50%, but the levels of impurity (2) were increased due to further formamide degradation. Alternatively, warming the initially slurry of compound (1) resulted in significant redissolution of all four impurities, and formation of hydrate form C. Combination of re-slurrying and recrystallisation also gave low levels of all four impurities and solid material as the preferred crystal form A.
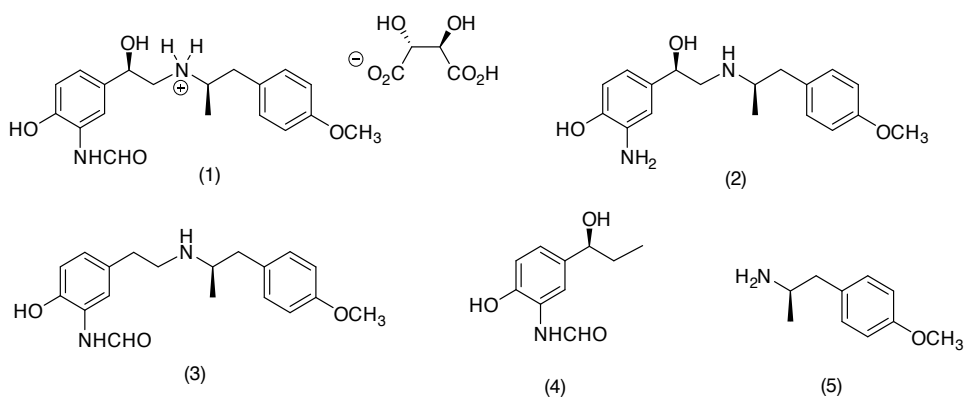

Figure 1. Molecular structure of (*R,R*)-formoterol tartrate (1) and impurity compounds (2), (3), (4) and (5) [2].

There are several examples in the literature of process impurities affecting polymorphic outcome. An excellent example concerns sulfathiazole (compound 7 in Figure 2), which is prepared by a process in which the final step is the hydrolysis of the acetamido precursor (6) [3]. Residual starting material (6) has a major impact on the polymorphic form of the resulting sulfathiazole solid, favouring form II. Crystallisation of pure sulfathiazole under identical conditions results in forms III or IV being obtained. This outcome was well rationalised on the basis of the hydrogen bonding networks present in the polymorphs and the capacity of the amide impurity (6) to interact with these. Another example concerns 5-haloaspirin derivatives (compounds 8 in Figure 3). These compounds are usually prepared by acetylation of the corresponding salicyclic acid derivatives. Anhydrides (9) are process intermediates and impurities in such reactions. Two polymorphs of compounds (8) have been noted, designated forms I and II. Impurity anhydrides (9) promote the formation of the form II polymorphs over forms I [4]. An example which has been studied in detail concerns an unidentified 'API X' (compound 10 in Figure 4) [5]. Three polymorphs of this compound are known, designated forms A, B and C. The crystal structures and supramolecular packing motifs of these forms have been fully characterised. A dimer involving H•••F hydrogen bonds (Figure 4) was one of the motifs found in forms A and B. A number of process impurities were found (Figure 5) and the impact of these on crystallisation of 'API X' investigated. For example, it was found

that impurities (11) and (12) (Figure 5) inhibited the transformation of form A to form B at 30 °C in IPA. Under these conditions, form B is the thermodynamically preferred form and batches of pure form A, or form A in the presence of impurities (13) or (14), transform to form B. It was noted that impurities (11) and (12) possess the molecular groups necessary for formation of a dimer motif of the type shown in Figure 4, whereas impurities (13) and (14) lack such groups. Impurities (11) and (12) can therefore mimic dimers of 'API X' and affect the polymorphic transformation.
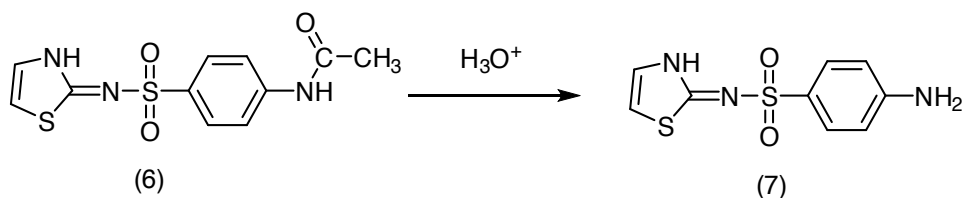

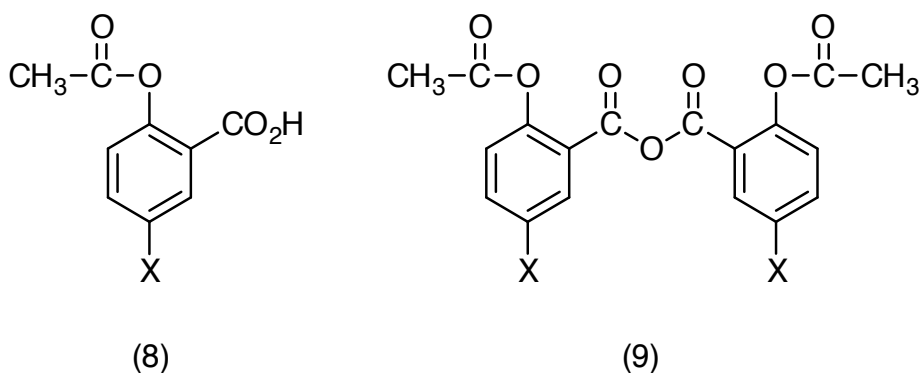**Figure 2.** Final step in the preparation of sulfathiazole (7).

Figure 3. Structures of 5-haloaspirins (8) and corresponding anhydride impurities (9); X = Cl or Br.
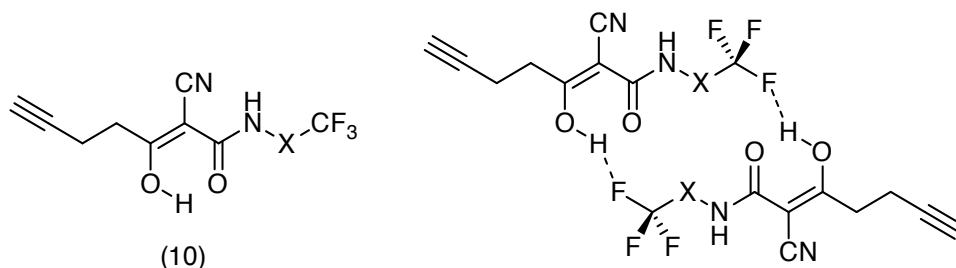

Figure 4. Structure of 'API X' (10). Group X, which is not a halogen, is unidentified in the publication [5]. On the right is a dimer motif of compound (10) present in polymorphs A and B involving H•••F hydrogen bonds.
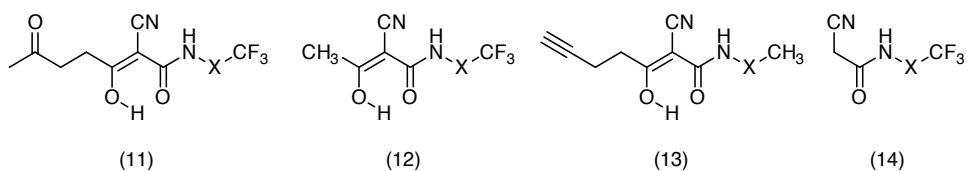
Figure 5. Process impurities present in the crystallisation of 'API X' [5].

Impurities can also have an effect on crystal morphology. For example, crystallisation of stavudine (compound 15 in Figure 6) from IPA gave needle-like crystals with sub-optimal filtration properties. Thymine (16), which can be present as a process impurity in quantities up to 1%, resulted in crystallisation of less acicular crystals with improved filtration properties [6]. The impact of impurities on crystal habits has been studied in detail in the case of benzamide (17). The most stable polymorph of benzamide crystallises from ethanol as plates which display the most growth in the *b* crystallographic direction; this direction also coincides with an 'amide ladder' motif (Figure 7). Impurities or additives which can engage with the amide ladder motif can affect the observed crystal habit. Benzoic acid (18) was found to reduce growth in the *b* crystallographic direction while 2-toluamide (19) was found to reduce growth in the *a* direction, giving smaller prisms elongated in the *a* and *b* directions respectively [7]. The presence of 2'-aminoacetophenone (20) was found to result in growth of polycrystalline benzamide aggregates as a consequence of compound (20) 'end-capping' the amide ladder motif, but also allowing for growth of a new benzamide crystallite [8]. Another example concerns phenyl salicylate (21). In this case, the concept of site-specific adsorption on crystal surfaces has been used to simulate adsorption with molecular modelling methods, to allow prediction of crystal morphology in the presence of impurities, giving good prediction of variation in habit due to phenyl benzoate (22), benzophenone (23) or benzhydrol (24) impurities [9].
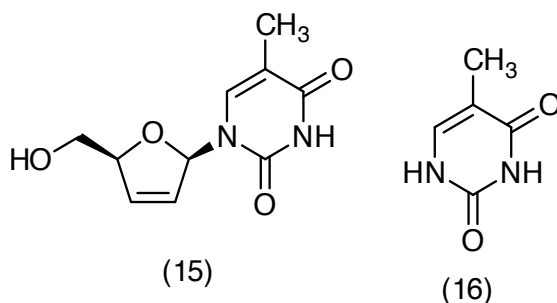
Figure 6. Molecular structures of stavudine (15) and thymine (16).
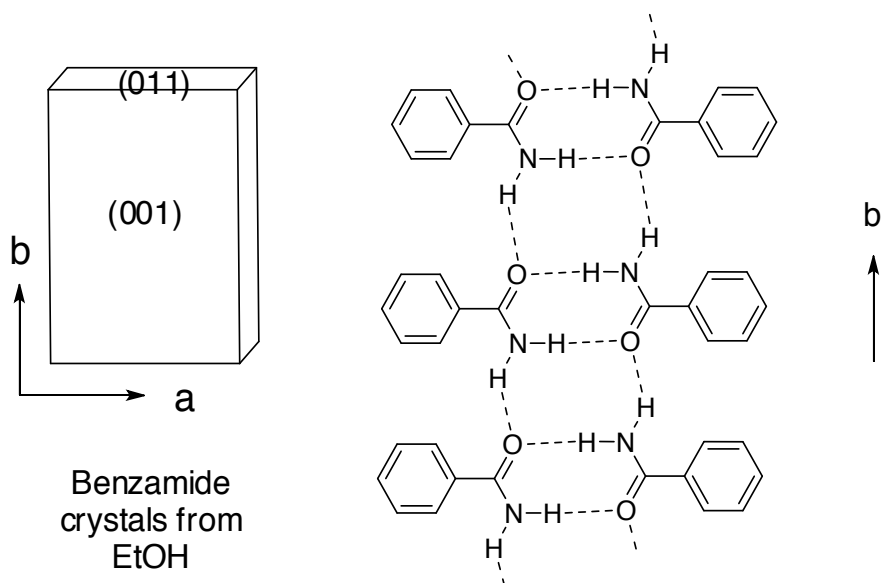
Figure 7. (Left) Typical habit of benzamide crystals grown from ethanol. (Right) 'Amide ladder' motif found in the crystal structure of benzamide.
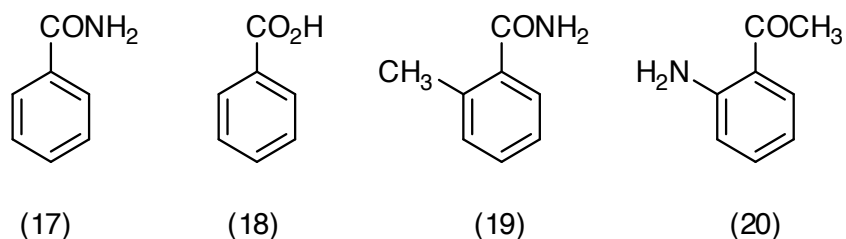
Figure 8. Molecular structure of benzamide (17) and impurities (18), (19) and (20).
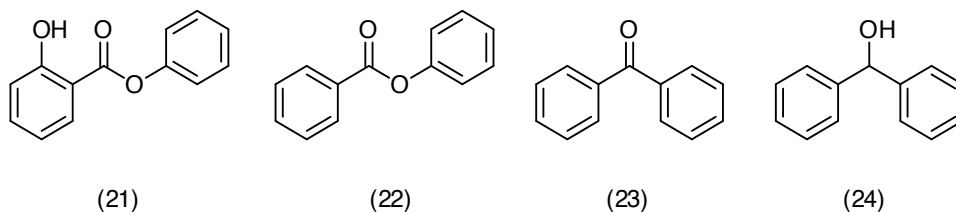
Figure 9. Molecular structures of phenyl salicylate (21), phenyl benzoate (22), benzophenone (23) and benzhydrol (24).

A challenging issue with regard to impurities in crystalline materials is the location of impurities within crystals, both with respect to the distribution of the impurities and the mode

of binding of the impurity 'guests' within the crystal 'host'. In manufacturing scale crystalli-sation, impurities are often adsorbed on crystal surfaces and can be removed by efficient washing. For example, a process for the crystallization of bisphenol A gave product which was 99.5% pure. It was found that the main source of impurities was from mother liquor adhering on crystal surfaces. The temperature stages of the crystallization protocol were changed to decrease the amount of fine crystals and increase the average crystal size. This allowed for improved separation of crystal product from the mother liquor, giving material of 99.8% purity. As the remaining impurities were likely to be trapped within the crystals, recrystalli-zation was found to improve the quality of the bisphenol A product up to 99.99% [10]. Impurities which are not removable by washing may be located within the crystal and may be interacting with some aspect of the crystal lattice. X-Ray diffraction methods average over the diffracting domains and so do not detect the presence of impurity molecules routinely. Relatively few studies have investigated the location and supramolecular binding of exoge-nous molecules within molecular crystals. One such example concerns the crystallisation of L-asparagine monohydrate from water. Other amino acids present as impurities in solution can be incorporated into L-asparagine monohydrate crystals but to differing extents and distribu-tions. Careful sequential dissolution and analysis studies on individual L-asparagine mono-hydrate crystals showed that most amino acid impurities were largely located on the outer or surface layers of the crystals. However, L-aspartic acid was found to be incorporated into L-asparagine monohydrate crystals in significant quantities (> 10%) and to be distributed relatively uniformly throughout the crystal, indicating a possible systematic substitution of L-aspartic acid molecules for L-asparagine molecules within the L-asparagine monohydrate crystals [11]. This possibility was confirmed by neutron diffraction studies of deuterated L-asparagine monohydrate crystals grown in the presence of deuterated aspartic acid, which showed a reduction in symmetry from $P2_12_12_1$ for L-asparagine monohydrate crystals to $P2_1$ for crystals grown with aspartic acid impurity, due to systematic substitution of aspartic acids molecules for aspargine molecules at specific sites in the crystal lattice [12].

In the course of studies on the crystallisation and morphology of phenacetin (26) [13], we observed a significant impurity arising with one of the main routes for preparing this com-pound, involving many of the issues encountered in the literature examples outlined above. Further investigation of this involved aspects such as the origin of impurities in the process chemistry, retention or rejection of specific impurities, the removal of impurities by washing and/or recrystallisation, and the supramolecular interactions between host crystals and retained impurities. These issues are described in the following section. Phenacetin has proved to be a useful compound for the study of crystallisation issues, as it is a relatively simple molecule but, as a former drug substance, of sufficient pharmaceutical relevance to be a worthwhile model.

2. Results and discussion

Phenacetin (4-ethyloxyacetanilide) (26) is a close analogue of paracetamol (acetaminophen or 4-hydroxyacetanilide) (27). Phenacetin was used as an analgesic and anti-pyretic drug before

being withdrawn due to nephrotoxicity [14]. Processes for the large scale manufacture for phenacetin have been described, in particular by the acetylation of *para*-phenetidine (4-ethyloxyaniline) (25) [15]. An essential part of these processes is the isolation of the phenacetin product as a crystalline precipitate of sufficient purity and crystal size distribution to meet pharmacopoeial requirements. For example, carrying out of the acetylation at temperatures over 100 °C in high boiling aromatic hydrocarbons, followed by cooling to under 10 °C with seeding, gives large scale batches of phenacetin of pharmacopoeial quality [16]. Alternative routes to phenacetin include the *O*-ethylation of paracetamol (27) which can be a more convenient process on a laboratory scale [17]. Both of these routes are summarised in Figure 10. Both routes give phenacetin as a crystalline product which, if required, can be further recrystallised to improve purity or particle properties.
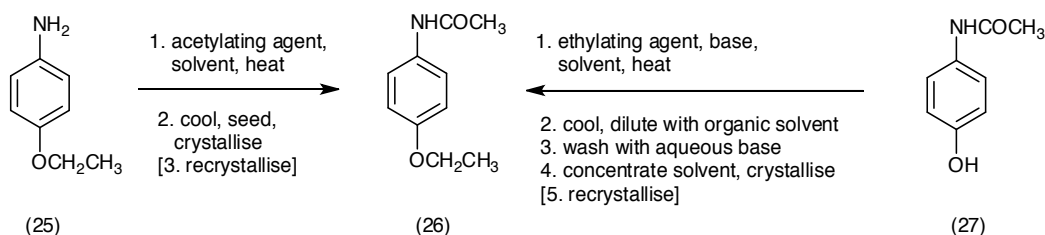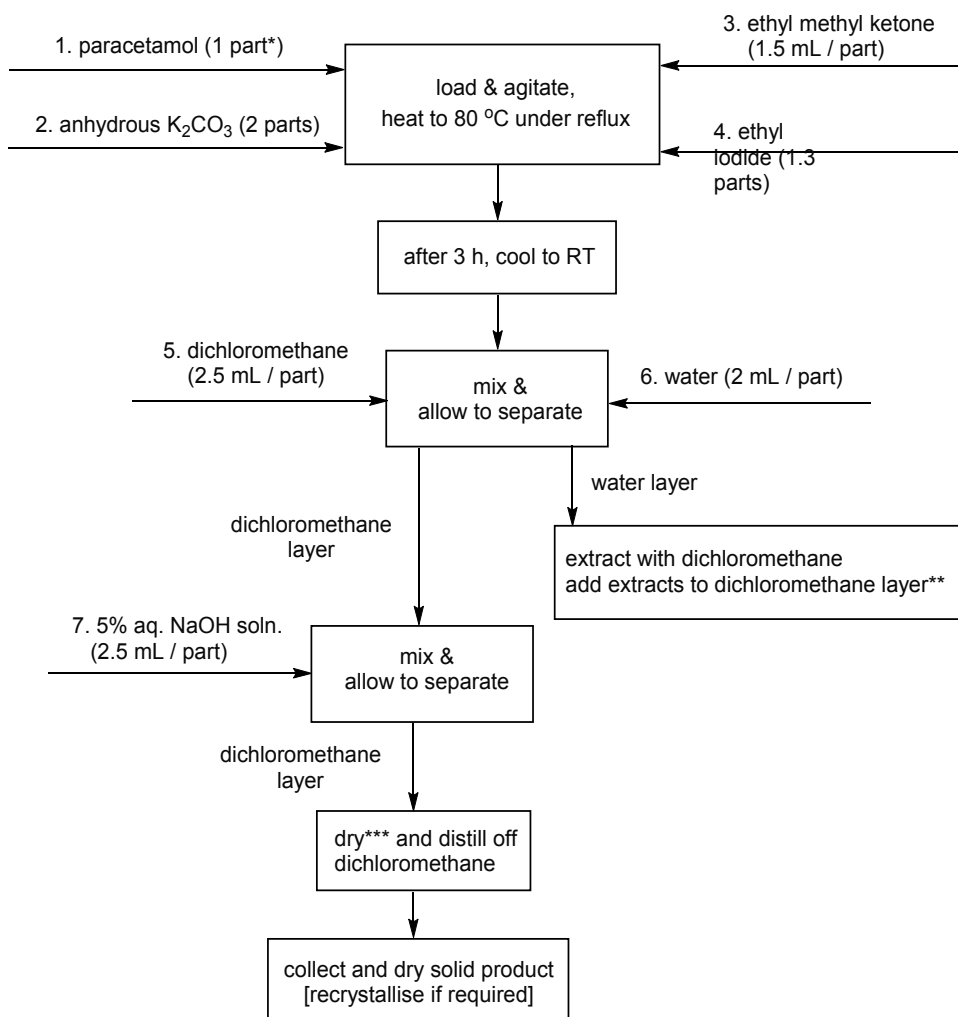

Figure 10. Summary of processes for the preparation of phenacetin (26) from *para*-phenetidine (25) or paracetamol (27).

Both routes summarised in Figure 10 were studied by us as part of an investigation into the phase, morphology, size distribution and purity of phenacetin batches obtained by various routes and using various crystallisation regimes [13]. For the reasons discussed in the Introduction, impurities, their origin in the process chemistry and their persistence in crystallised and recrystallised material, was a subject of particular importance in this investigation. Impurity issues were not found to be particularly significant in the acetylation route to phenacetin. However, we did find significant impurities arising from the ethylation route, which were subject to further investigation.

Figure 11 shows a block flow diagram for the ethylation process. This is an adaptation of the procedure described by Volker *et al* [17]. The reagents were charged to the reaction vessel in the order given and the mixture heated to the boiling point of ethyl methyl ketone with agitation. After three hours, the solution was allowed to cool, diluted with dichloromethane and washed with water to remove potassium iodide by-product. The final product yield could be improved marginally by extraction of the aqueous wash with dichloromethane and addition of the extracts to the main dichloromethane solution. This was washed with aqueous sodium hydroxide to remove unreacted paracetamol. The dichloromethane solution was dried to remove water dissolved in the dichloromethane, either by washing with brine or using a solid drying agent. Finally, the dichloromethane solvent was removed by distillation and the solid phenacetin product isolated and dried. Yields of product at this stage were typically 70-90%. The material can be subsequently recrystallised to improve purity or control particle properties.

Figure 11. Block flow diagram for the synthesis of phenacetin (26) using the ethylation of paracetamol (27) process.

*Relative quantities of reagents and solvent (parts) are based on molar equivalents.

**Extraction of the water washing to improve yield is optional.

***Final dichloromethane solution can be dried prior to removal of solvent by washing (with brine) or using a solid drying agent ($MgSO_4$) followed by filtration.

The phenacetin product was confirmed by ^{1}H NMR and IR spectroscopy (see the Experimental Methods section for details). DSC analysis of samples showed a single thermal event corresponding to melting with an on-set at 133 °C, agreeing with the literature value of 133.5 to 135.5 °C [18]. PXRD analysis (Figure 12) showed excellent correspondence with the theoretical pattern generated from the CIF file for the phenacetin structure recorded by Hansen et al [19] (CSD refcode PYRAZB21), which is a more recently determined structure than that reported

by Patel et al [20]; essentially showing that the phenacetin product is the expected crystal form, namely a monoclinic $P2_1/c$ structure with $Z = 4$. The initially obtained phenacetin solid could be recrystallised from a variety of solvents. Dichloromethane, ethanol, water and acetonitrile were found to be the most useful, giving yields of 70-90% of recrystallised phenacetin. PXRD and DSC analysis of the recrystallised material gave data which were essentially identical to those obtained from the initially obtained solid. Figure 13 shows examples of the DSC data, showing melting points lying within the range 134-139 °C. Micrographs showing typical morphologies of phenacetin crystals obtained from these solvents are shown in Figure 14. Those obtained from dichloromethane were typically block-like prisms, needles from ethanol, flaky plates from water and elongated prisms from acetonitrile.
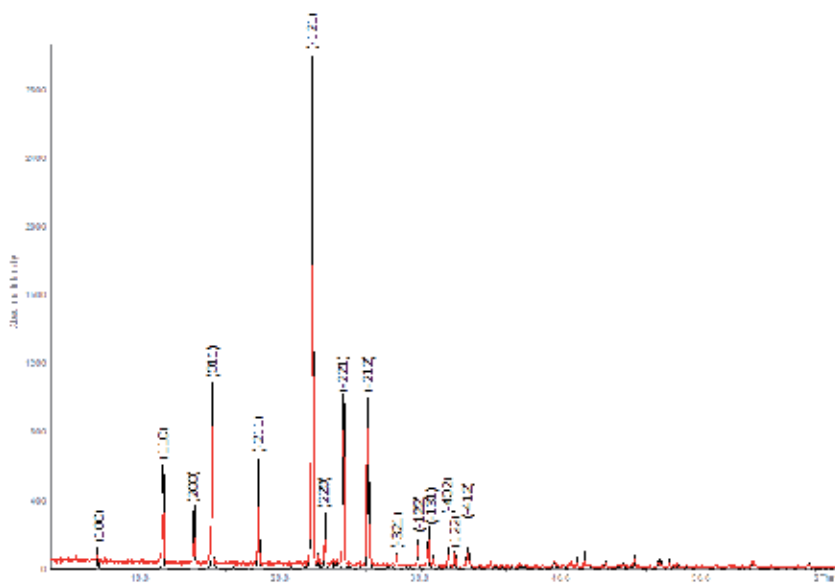
Figure 12. PXRD pattern of (in red) phenacetin (26) product and (in black) the theoretical pattern generated from PYR-AZB21 [19] including indices of the diffraction peaks.

The purity of the phenacetin batches was determined by HPLC. No residual paracetamol starting material was detected. However, an unknown impurity was observed, eluting after paracetamol and before phenacetin. The intensity of the impurity peak suggested its presence in approximately 1% quantity, assuming a structural similarity to phenacetin. Likely candidates for this impurity were compounds (28) or (29) in Figure 15, arising from competing *N*- or *O*-ethylation at the amide groups, or di-ethylated analogues (30) or (31). To confirm or reject these compounds as the unknown impurity, it was necessary to independently synthesise both the amide-ethylated (28 or 29) and di-ethylated (30 or 31) derivatives. These were prepared *via* the route shown in Figure 16, which involved an initial protective *O*-benzylation of paracetamol, followed by ethylation of the amide group. Under the ethylation conditions (potassium *tert*-butoxide base in dry THF, ethyl iodide and sodium iodide), the *O*-benzyl group was also

Figure 13. DSC data of phenacetin recrystallised from water (magenta curve), dichloromethane (blue curve), ethanol (black curve) and acetonitrile (green curve).

Figure 14. Optical micrograph of phenacetin recrystallised from (top left) dichloromethane, (top right) ethanol, (bottom left) water and (bottom right) acetonitrile.
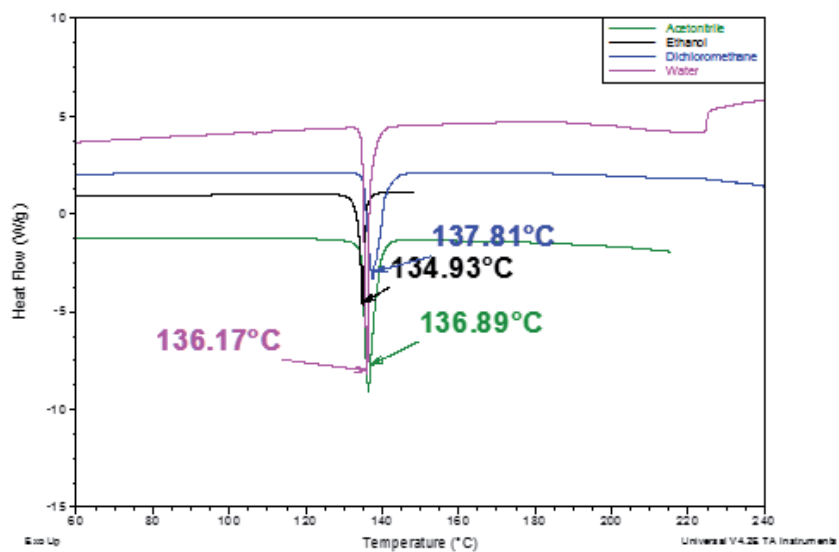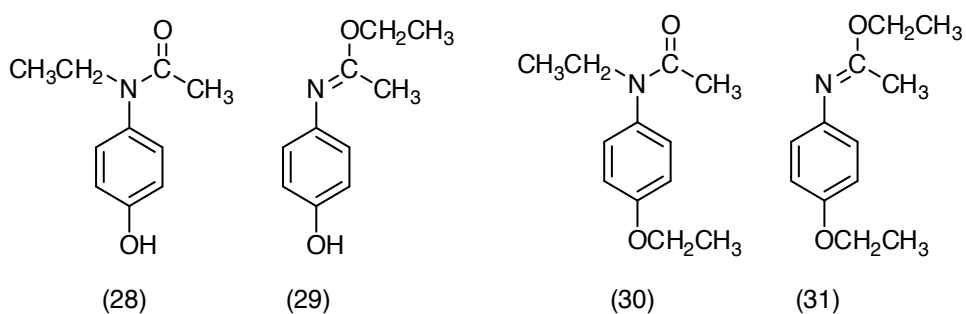
Figure 15. Possible impurity products arising from the preparation of phenacetin by ethylation of paracetamol.
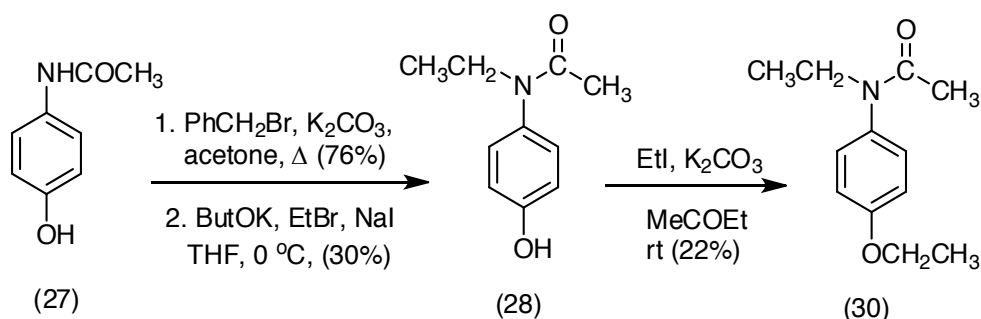
Figure 16. Preparation of *N*-ethyl derivative (28) and *N,O*-diethylated derivative (30).

removed, giving the amide-ethylated derivative (28) without need for a specific debenzylation step. This is likely to be a consequence of iodide induced cleavage of the benzylic C-O bond. A further *O*-ethylation step gave the diethylated derivative (30). In both derivatives, ethylation at the amide group was found to occur on nitrogen rather than oxygen, i.e. compounds (29) and (31) were not observed.

HPLC of samples of phenacetin containing the unknown impurity, of samples of *N*-ethyl derivative (28), and of samples of phenacetin containing the unknown impurity also spiked with *N*-ethyl derivative (28) (Figure 17), provide strong evidence that the unknown impurity was *N*-ethyl derivative (28), i.e. *N*-ethylparacetamol. This is a perfectly reasonable finding in terms of the process chemistry, i.e. in reaction of paracetamol (27) with ethyl iodide and potassium carbonate in ethyl methyl ketone, *O*-ethylation to give phenacetin (26) is the major process while approximately 1% of the batch undergoes competing amide *N*-ethylation to give impurity (28). Impurity (28) was not detected in recrystallised samples of phenacetin, i.e. a single recrystallization step was sufficient to remove the impurity.

Of particular interest was to examine the impact of *N*-ethyl impurity (28) on the crystallisation of phenacetin (26) in terms of the crystallisation process, the resulting crystal form and the resulting crystal morphology. These studies were carried out on samples on phenacetin which

Figure 17. HPLC of a phenacetin sample containing the unknown process impurity spiked with *N*-ethylparacetamol (28). Phenacetin elutes at 5.312 min, while the unknown impurity and *N*-ethylparacetamol (28) co-elute at 4.130 min.

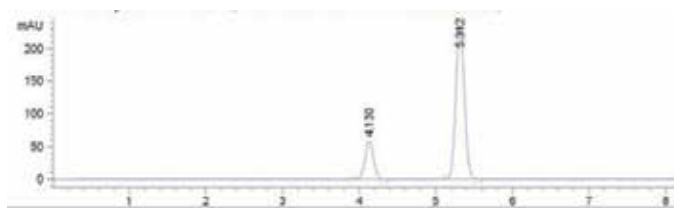were shown to be pure by HPLC. In addition to investigating the impact of impurity (28), the effect of the paracetamol starting material was also examined.

Addition of either paracetamol (27) or *N*-ethylparacetamol (28) as a 1% impurity was found to have no detectible effect on the metastable zone width (MSZW) of crystallisation of phenacetin from ethanol. i.e. the equilibrium solubility and metastable solubility curves were not significantly changed (Figure 18). Addition of paracetamol at levels as high as 10% impurity likewise gave rise to no discernible change in the MSZW. Likewise, PXRD data of samples of phenacetin recrystallised in the presence of 1% of either paracetamol (27) or *N*-ethylparacetamol (28) were all identical to those previously obtained for phenacetin (e.g. as in Figure 12) implying that no change was observed in the phenacetin crystal form due to the presence of the impurities, at least that would be detectible by PXRD. The same finding was observed from crystals grown in the presence of 10% paracetamol impurity. Inclusion of paracetamol (27) or *N*-ethylparacetamol (28) impurities in phenacetin (27) crystallisations from ethanol had a significant impact on the morphologies of the resulting phenacetin crystals. Crystallisation of pure phenacetin from ethanol give acicular needles (Figure 19). Inclusion of the impurities resulted in smaller and less elongated crystals, as shown in Figure 20 for 1% and 10% paracetamol impurity. While the phenacetin crystals grown in the presence of 1% impurity retained their essential morphology with a more prismatic, rather than acicular, habit, the crystals obtained in the presence of 10% impurity were agglomerated particles which lacked well developed faces.
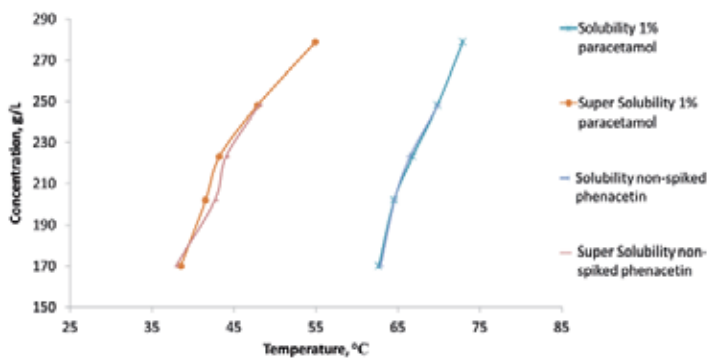
Figure 18. MSZW of pure phenacetin compared with samples of paracetamol-spiked phenacetin.
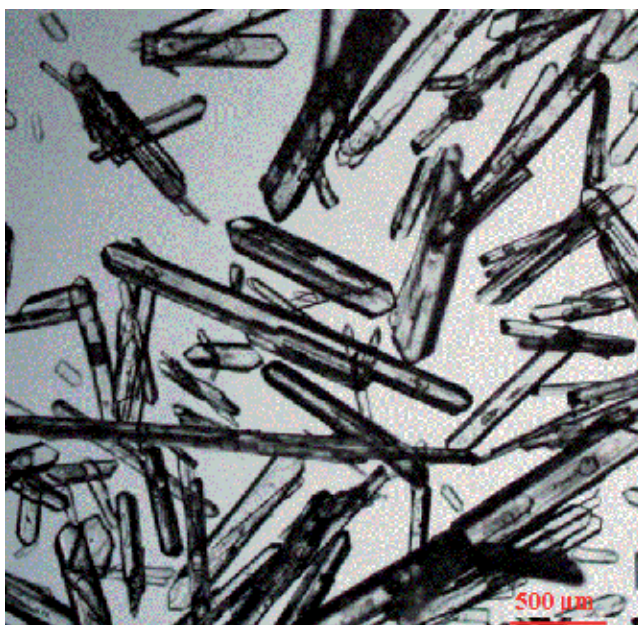
Figure 19. Acicular crystals of pure phenacetin grown from ethanol.
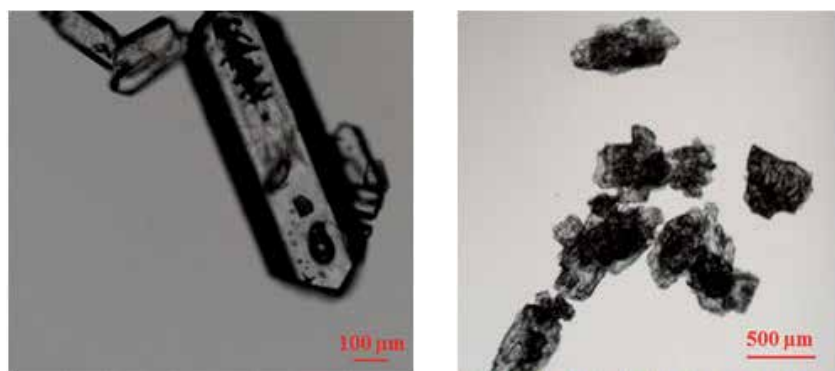
Figure 20. Phenacetin crystals grown from ethanol in the presence of (left) 1% w/w paracetamol and (right) 10% w/w paracetamol impurity.

Pure phenacetin crystallised from ethanol grows as acicular prisms as shown in Figure 19. Figure 21 shows one of these crystals mounted on the goniometer of an X-ray diffractometer; sufficient diffraction data has been collected to allow the crystallographic directions to be determined. This shows that the needles are elongated along the *a* crystallographic direction. Figure 22 shows the crystal structure of phenacetin [19] viewed both along the *b* and *c* axes. These images show that the ethyloxy and acetyl groups of the phenacetin molecules are oriented along the *a* crystallographic direction. The most important supramolecular motif

present in the structure is a so-called amide C(4) chain, i.e. a repeated hydrogen bond between secondary amide hydrogens and carbonyl oxygen atoms (N-H•••O=C-N-H•••O=C). As the motif is a hydrogen bonding chain with four atoms in the repeat unit, it is designated C(4) according to Etter's notation [21]. The C(4) chain is lying in the *bc* plane. In crystallisation of phenacetin from ethanol, hydrogen bonding by the hydroxyl group of ethanol to surface carbonyls or N-H groups are likely to reduce the rate of growth in the *b* and *c* crystallographic directions, giving rise to the needles elongated along *a*, as seen in Figure 19. Figure 23 shows a phenacetin crystal grown from ethanol containing 1% paracetamol. The crystal is typical of those grown in the presence of 1% paracetamol impurity, i.e. it is a reasonably well formed elongated prism, but not a needle. The direction of elongation is still the *a* crystallographic direction, i.e. the paracetamol impurity has had the greatest effect in the direction of most crystal growth for the pure crystals.
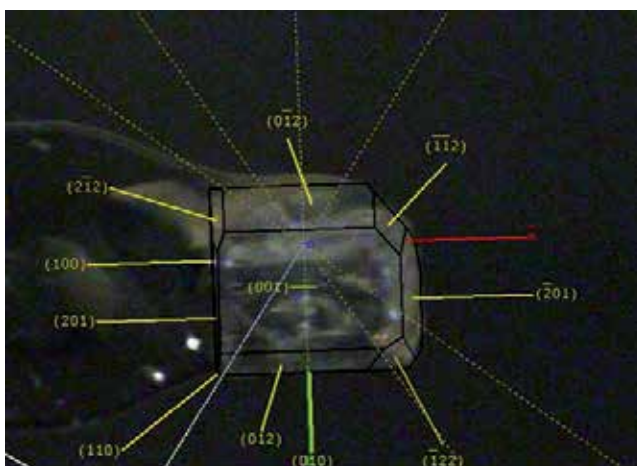
Figure 21. A crystal of pure phenacetin grown from ethanol mounted on the goniometer of an X-ray diffractometer and the directions of the crystallographic axes and indices of the main faces determined. Note that the crystal is a needle, similar to those shown in Figure 19, which has been cut to allow mounting onto the diffractometer. The cut is perpendicular to the *a* axis direction and has exposed a fresh (100) face.

As mentioned above, the initially formed phenacetin material found to have 1% of *N*-ethylparacetamol (28) present as an impurity, was not detected in recrystallised batches of phenacetin, i.e. it was removed by recrystallization. The staring material for a chemical process is always a candidate impurity, however, no residual paracetamol (27) starting material was detected in the initially crystallised phenacetin material. Part of the phenacetin by ethylation of paracetamol process involves an aqueous base extraction intended to remove unreacted paracetamol (addition 7 in Figure 11). While this step would be expected to minimise the amount of paracetamol starting material present, some residual paracetamol impurity could still be a possibility requiring investigation. As a phenol, *N*-ethylparacetamol (28) should also be to some extent extractible with an aqueous base wash, although less so than paracetamol, which is more hydrophilic. Nonetheless, *N*-ethylparacemol (28) was found to be present as an
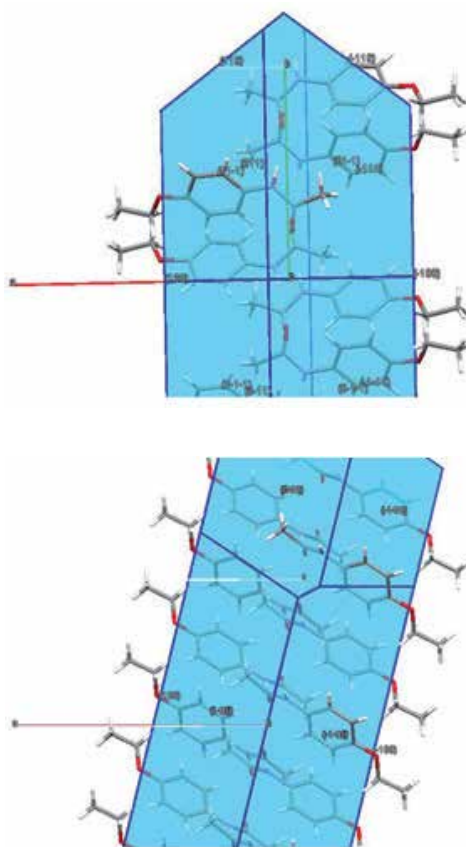
Figure 22. Images of the crystal structure of phenacetin generated from the structure reported by Hansen et al [19], viewed (top) in the *ab* plane along *c* (which corresponds to the orientation shown in Figure 21) and (bottom) in *ac* plane along *b*.

impurity. However while impurity (28) could be removed by recrystallization, spiking experiments with paracetamol found that this was a more persistent impurity. Recrystallisation of phenacetin from ethanol in the presence of 1% or 10% w/w of added paracetamol gave phenacetin crystals containing, respectively 0.16% and 6.0% paracetamol impurity by HPLC. Growing phenacetin crystals therefore appear to have differing affinity for *N*-ethylparacetamol and paracetamol as impurities for inclusion, with the former being generally excluded while the latter is incorporated to a considerable extent. A second recrystallisation was often necessary to fully remove paracetamol impurity.

The relative preferential exclusion of *N*-ethylparacetamol and inclusion of paracetamol can be rationalised by consideration of the crystal structure of phenacetin. As mentioned above, the most significant supramolecular motif present in the structure is an amide C(4) chain. Only primary or secondary amides, such as phenacetin, can participate in amide C(4) chains. Tertiary amides, such as *N*-ethylparacetamol, can 'end-cap' such chains by accepting a hydrogen bond at the amide carbonyl oxygen; however they cannot continue the chain. Hence,
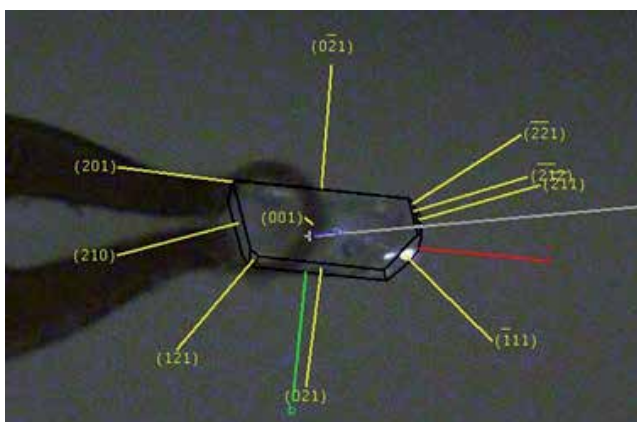
Figure 23. A crystal of phenacetin grown from ethanol containing 1% paracetamol, mounted on the goniometer of an X-ray diffractometer and the directions of the crystallographic axes and indices of the main faces determined. Note that the crystal is intact as grown and has not been cut.

inclusion of *N*-ethylparacetamol molecules results in discontinuation of the phenacetin C(4) chain and is incompatible with the bulk crystal structure. By comparison, paracetamol, as a secondary amide, can participate in an amide C(4) motif. The key point of difference in the molecular structures of phenacetin and paracetamol is the replacement of the ethyloxy group of phenacetin by a hydroxyl group in paracetamol. In the crystal structure of phenacetin, the ethyloxy groups occupy hydrophobic regions as shown in Figure 24. The replacement of a small number of ethyl groups by hydrogen atoms in these regions seems reasonable. Therefore, it is feasible that a small number of paracetamol molecules could take the place of phenacetin molecules in phenacetin crystals, while *N*-ethylparacetamol molecules could not easily be accommodated within continuous phenacetin crystallites. These proposed supramolecular interactions are shown schematically in Figure 25.
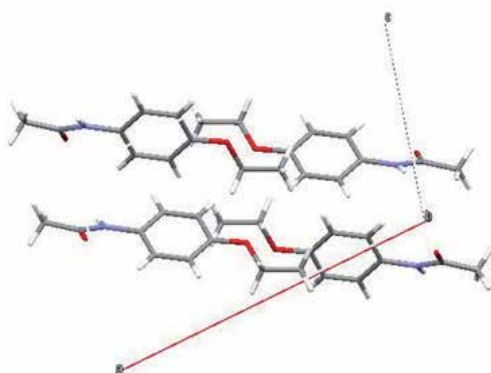
Figure 24. View of the crystal structure of phenacetin [19] along the *b* crystallographic axis, showing the packing of the phenacetin ethyloxy groups.
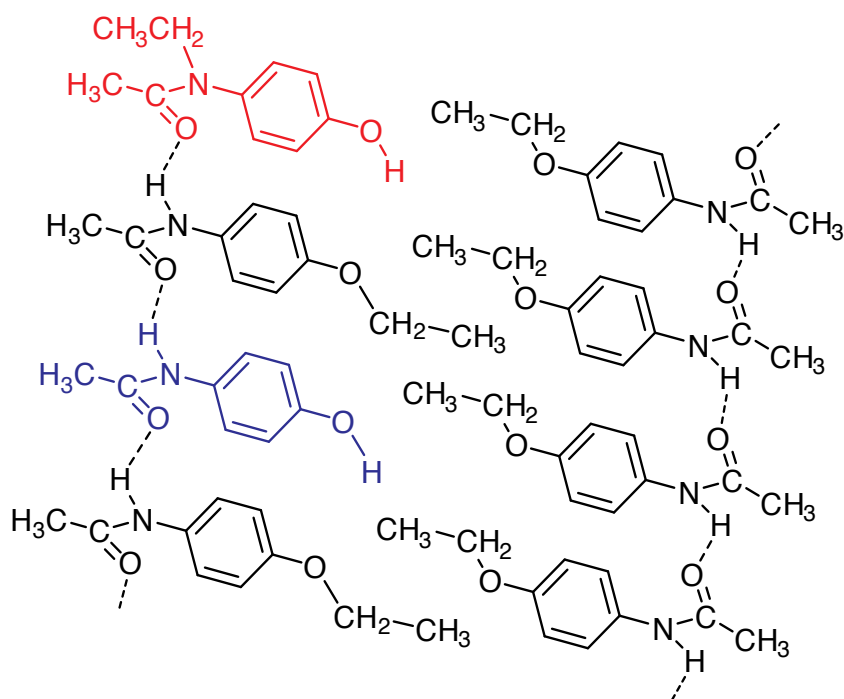
Figure 25. Schematic representation of the molecular packing in the crystal structure of phenacetin incorporating *N*-ethylparacetamol (red) and paracetamol (blue) molecules. The phenacetin molecules are linked by an amide C(4) hydrogen bonding chain [21] shown using dashed lines. The ethyloxy groups of the phenacetin molecules occupy a hydrophobic region of the structure. The *N*-ethylphenacetin molecule (red) can 'end-cap', but not continue the C(4) chain, while the paracetamol molecules (blue) can fully participate in the C(4) chain. The hydroxyl groups of both paracetamol or *N*-ethylparacetamol could feasibly sit within the hydrophobic region containing the ethyloxy groups.

The proposal discussed above and illustrated in Figure 25 suggests the possibility of substantial and possibly systematic inclusion of paracetamol molecules in phenacetin crystals. To investigate this possibility, a series of successive dissolution experiments were carried out on individual phenacetin crystals, in a similar manner to those described by Addadi et al in the investigation of L-asparagine monohydrate / L-aspartic acid host / guest systems [11, 12]. The crystals for this study were grown from ethanol solutions of phenacetin containing either 5%, 10% or 15% (w/w phenacetin) of added paracetamol. Examples of these crystals are shown in Figure 26. These crystals were then dissolved in methanol-water (40:60) in three successive dissolutions, i.e. approximately one third of the crystal dissolved in the first dissolution step, another third in the second and the remainder of the crystal dissolved in the final step. After each dissolution, the resulting solution was analysed by HPLC for phenacetin and paracetamol content. The data obtained are given in Table 1. These data show that the paracetamol content of the crystals is considerably greater in the outermost portions of the crystals which are dissolved in the first dissolution step. This may include paracetamol which has deposited on crystal surfaces as well as paracetamol which has been included within the crystals. Importantly, paracetamol is still present in the second and innermost portions of the crystals.

Therefore, the paracetamol impurity is being incorporated into the phenacetin crystals at all stages of crystal growth, and especially in the later stages of growth. Possibly, increased up-take of paracetamol impurity is connected to a significant reduction and termination of crystal growth.
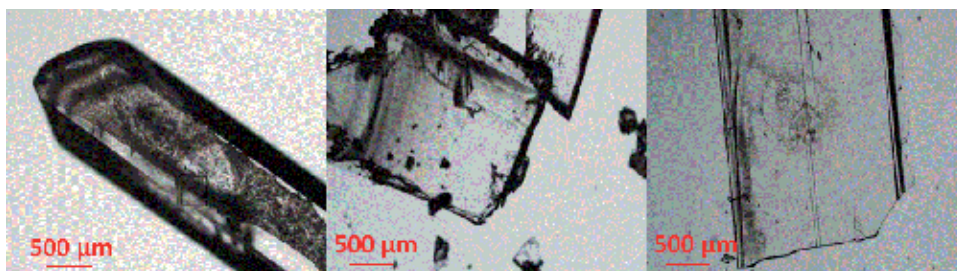
Figure 26. Examples of phenacetin crystals grown from ethanol containing (left to right) 5%, 10% and 15% (w/w phenacetin) added paracetamol.

Dissolution Step	% Impurity added	% Paracetamol	% Phenactin
1st	5	14.16	85.47
2nd	5	1.57	98.32
3rd	5	0.71	99.14
1st	10	7.88	91.59
2nd	10	0.40	99.38
3rd	10	0.00	99.53
1st	15	5.42	94.48
2nd	15	2.83	97.06
3rd	15	1.87	98.09

Table 1. Three stage dissolution of individual phenacetin crystals grown from ethanol containing paracetamol; HPLC analysis of solution from each dissolution step.

The above finding raises the possibility that phenacetin molecules may be systematically replaceable by paracetamol molecules to some extent in the crystal structure of phenacetin. If this was to be the case, it should be possible to obtain phenacetin / paracetamol co-crystals. This possibility was investigated by attempting co-crystallisation of 1:1 and 2:1 phenacetin : paracetamol mixtures, both from solution and by neat grinding. PXRD of the resulting solids (Figure 27) were all very similar to those for phenacetin with some additional peaks, for example at $2\theta = 12.0°$ and $23.2°$. This does not confirm formation of a co-crystal.
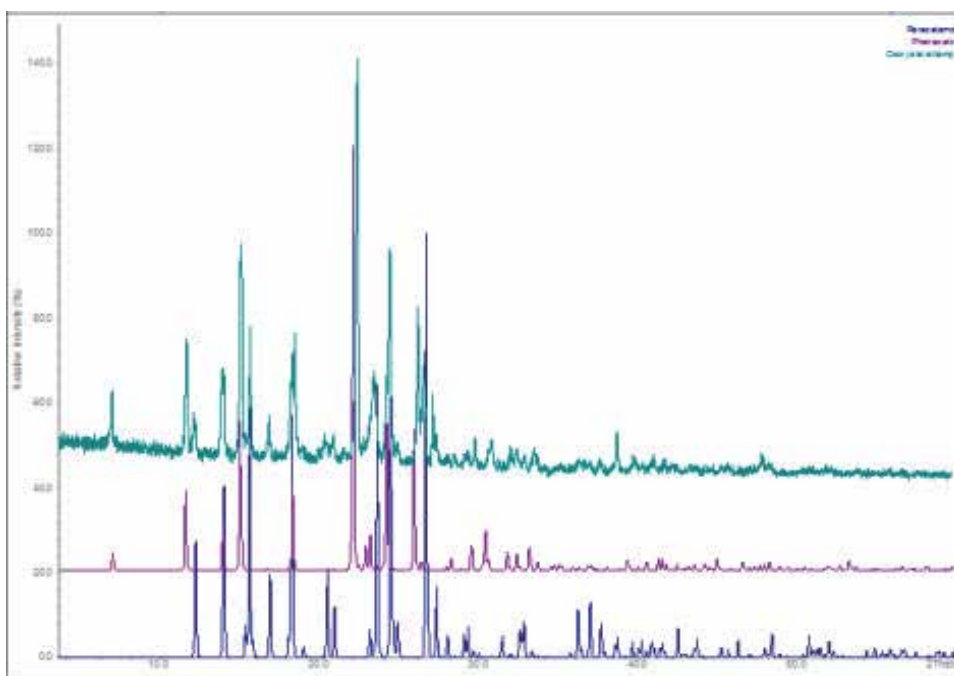
Figure 27. PXRD patterns for (top), material obtained by attempted cocrystallisation of phenacetin and paracetamol (1:1 neat grinding); (middle) theoretical pattern for phenacetin generated from PYRAZB21 [19]; (bottom) theoretical pattern for monoclinic paracetamol [22].

3. Conclusions

The preparation of phenacetin (26) by *O*-ethylation of paracetamol (27) has been investigated as a study into the generation of process impurities and their impact on crystallisation and recrystallisation of crystalline solid products. In the *O*-ethylation of paracetamol, paracetamol is reacted with ethyl iodide in the presence of potassium carbonate base in ethyl methyl ketone solvent heated to 80 °C. After cooling to room temperature, the reaction mixture is dissolved in dichloromethane and washed with water, aqueous sodium hydroxide, dried and the solvents removed to give a crystalline solid. This can be recrystallised from solvents including ethanol, acetonitrile, water or dichloromethane, giving rise to crystals as, respectively, needles, prisms, plates or thin plates. Yields from this process were in the range of 70-90%, providing material consistent with the structure of phenacetin by ^{1}H NMR and IR spectroscopy. The crystal form of all phenacetin batches obtained was consistent with the structure reported by Hansen et al [19] and previously by Patel et al [20] even when analysed by both PXRD and DSC.

HPLC analysis of the initially obtained phenacetin solid showed the presence of a compound not corresponding to phenacetin or the starting material. Likely candidates for this impurity

were compound (28), formed by competing ethylation at the amide rather than the phenolic site of phenacetin, or compound (30) formed by diethylation. Independent synthesis of both compounds followed by HPLC comparison of these with the impurity confirmed that the impurity was compound (28), i.e. *N*-ethylparacetamol, present in, typically, 0.9% quantities in initially obtained phenacetin solid. Impurity (28) was not detected in any samples of recrystallised phenacetin, i.e. the impurity was removed by recrystallisation.

Both *N*-ethylparacetamol (28) and the starting material in the process, paracetamol (27), were investigated in spiking experiments at a 1% level for their impact on the generation of supersaturation and on crystal form and morphology in crystallisations of phenacetin from ethanol. Paracetamol (27) was also investigated at a 10% impurity level. Neither impurity was found to have any effect on MSZW, or on crystal form. However, significant changes were observed on crystal morphology, which transforms from needles for pure phenacetin, to smaller elongated prisms with 1% impurities and to polycrystalline agglomerates with 10% paracetamol. Orientation of crystals on an X-ray diffractometer show that the needles were elongated along the *a* crystallographic axis and that the shorter prisms were also elongated in the *a* direction. The ethyloxy and acetamido groups of phenacetin are directed along the *a* direction, while an amide C(4) chain lies in the *bc* plane. In crystallisations of phenacetin from ethanol, growth in the *bc* directions is hence impeded by hydrogen bonding of the solvent, leaving the *a* direction as the fastest growing direction. As would be expected, the impurities have the most impact in the fastest growing direction, reducing the extent of growth in that direction to change the crystal habit from needles, to small elongated prisms, to polycrystalline agglomerates.

HPLC analysis of samples of phenacetin crystallised in the presence of quantities of paracetamol (27) or *N*-ethylparacetamol (28) and then recrystallised showed that whereas *N*-ethylparacetamol (28) can be effectively removed by recrystallisation, paracetamol (27) when present as an impurity is incorporated into phenacetin crystals by a greater extent and is also retained within the crystals to a significant extent even after recrystallisation. Phenacetin and paracetamol are both secondary amides and so can participate in amide hydrogen bonded C(4) chains. *N*-Ethylparacetamol (28), as a tertiary amide, cannot participate in an amide C(4) chain, but can terminate such a chain. Hence it is feasible that a paracetamol impurity molecule can substitute for a phenacetin molecule in the bulk of the crystal lattice in a manner not possible with *N*-ethylparacetamol. *N*-Ethylparacetamol impurity can add to phenacetin crystals at the ends of amide chains, or by other supramolecular interactions, but cannot be easily accommodated within the crystal lattice and so is incorporated to a lesser extent and is easily removed by recrystallisation. This proposal offers a rationale for the respective retention and rejection of paracetamol and *N*-ethylparacetamol by phenacetin crystals, which is summarised schematically in Figure 25. This model requires the phenolic hydrogen of paracetamol (or *N*-ethylparacetamol) to reside within a region dominated by phenacetin ethyl groups, which is not unreasonable.

The above proposal raises the possibility that paracetamol molecules could systematically substitute for phenacetin molecules in phenacetin crystals, in a manner best exemplified by the case of L-aspartic acid in L-aspargine monohydrate described by Addadi et al [11, 12]. To

examine this possibility, we carried out a series of sequential dissolution experiments on single crystals of phenacetin grown in the presence of 5 to 15% paracetamol impurity and analysed the resulting solution for phenacetin and paracetamol. The results, given in Table 1, show that the majority of the incorporated impurity resides in the outer layers or surface of the crystals, although detectible quantities of impurity can be found throughout the crystal. This suggests that paracetamol incorporation into phenacetin crystals is occurring at all stages of crystal growth, but becomes most prevalent in the later stage of growth and may be associated with the termination of crystal growth. This implies that systematic substitution of paracetamol for phenacetin molecules in the crystal lattice is probably not occurring, but that solid solutions of paracetamol in phenacetin may be occurring. The possibility of phenacetin / paracetamol cocrystallisation was examined but conclusive formation of cocrystals was not obtained.

The phenacetin by ethylation of paracetamol system has produced some instances of impurity behaviour which is highly characteristic of the synthesis and crystallisation of molecular organic compounds as pharmaceuticals or fine chemicals. A process impurity, *N*-ethylpara-cetamol, does form and is present in the initially precipitated crystals, but is easily removed by recrystallisation as a likely consequence of its limited ability to engage with the supramo-lecular packing of the phenacetin crystal structure. By contrast, the starting material, parace-tamol, is well incorporated and retained within phenacetin crystals, quite likely as a consequence of its compatibility with the crystal structure of phenacetin. The paracetamol impurity in phenacetin crystal system is therefore a good model on which to investigate methods for removing recalcitrant structurally-related impurities. Selective co-crystallisation is one method which has received recent attention [23, 24] and which could be vary amenable to this system. Many co-crystals of paracetamol have been prepared. What is required in this case is paracetamol co-crystals in which the phenolic hydroxyl group of paracetamol is engaged in a specific supramolecular motif. This allows a key point of differentiation from phenacetin, in which the phenolic hydroxyl group is replaced by an ethyloxy group. *N*-Methylmorpholine, pyrimidine [25] and trimethylglycine [26] form such co-crystals with paracetamol. In further studies on this system, these compounds will be investigated as putative selective paracetamol impurity removers.

4. Experimental methods

All chemicals were purchased from Sigma-Aldrich. ^{1}H NMR spectra were recorded on either a Bruker AVANCE 300 MHz spectrometer or a Bruker AVANCE 400 MHz spectrometer. Chemical shift values are expressed as parts per million (ppm). High resolution mass spectra were recorded on a Waters LCT Premier LC-MS instrument in electrospray ionisation (ESI) positive mode using 50 % acetonitrile / water containing 0.1 % formic acid as eluent; samples were made up in acetonitrile.

Preparation of phenacetin (26) by ethylation of paracetamol (27), typical procedure. A mixture of 1.51 g (10 mmol) of paracetamol (27), 2.76 g (20 mmol) of anhydrous potassium carbonate, 15 mL of methyl ethyl ketone and 2.0 g (13 mmol) of ethyl iodide was heated to reflux for 3 hours

with magnetic or mechanical stiring. The solution was allowed to cool to room temperature before addition of 25 mL of dichloromethane and washing with 20 mL of deionised water. The aqueous layer was extracted with 2 x 25 mL portions of dichloromethane which were combined with the dichloromethane layer, washed with 25 mL of 5% aq. sodium hydroxide solution before drying over $MgSO_4$ and concentration on the rotary evaporator. The material was further dried in air to give a white solid: 1.66 g, 93% yield; mp: 133-136 °C (lit. mp 133.5-135.4 °C [18]) IR (KBr disc) 3286 (N-H), 1660 (C=O), 1510, 1481 and 1245 (C-O) cm^{-1}. ^1H NMR (300MHz; CDCl$_3$) 1.40 (3H, t, J_{H-H} = 6.9 Hz, CH$_2$CH$_3$), 2.15 (3H, s, COCH$_3$), 4.00 (2H, q J_{H-H} = 6.9 Hz, CH$_2$CH$_3$), 6.81-6.88 (2H, m, -ArH x 2), 7.09 (1H, br s, NH), 7.34-7.40 (2H, m, ArH x 2).

Differential Scanning Calorimetry (DSC) was carried out on a TGA Q1000 DSC with an RCS 40 cooling system using crimped aluminium pans at a variety of cooling rates between 2 to 10 °C/min.

Powder X-Ray Diffraction (PXRD) data was recorded on a Stoe Stadi MP diffractometer operating in transmission mode, with a tube voltage of 40 kV and current of 40 mA, using Cu $K\alpha_1$ monochromated radiation (1.5406 Å) and a gas-filled PSD detector. Diffraction was recorded over 5 to 60 °2θ in steps of 2 °/min. Samples were held between acetate foils and were not ground. Calculated patterns were generated from crystallographic information files using the THEO function on Stoe WinX^{POW} software with a pseudo-Voight profile shape and a gauss component of 0.8. Tables 2 and 3 give the calculated °2θ, *hkl* and intensity values for the calculated diffraction patterns for phenacetin and monoclinic paracetamol, calculated from PYRAZB21 [19] and HXACAN01 [22] respectively.

°2θ	*hkl*	I/I_{max} (%)
6.832	100	4.677
11.459	110	20.171
13.688	200	12.701
14.964	011	36.491
18.283	-211	21.346
22.119	-121	100
23.035	220	5.758
24.354	-221	0.012
26.088	-212	34.429
28.184	-321	3.304
29.647	-122	5.813
30.432	-131	8.592
31.852	-402	4.655
32.282	122	3.794
33.219	-412	2.392s

Table 2. Powder X-ray diffraction peaks (°2θ), diffracting plane indices (*hkl*) and relative intensities (I/I_{max}) for the calculated pattern for phenacetin based on the crystal structure reported by Hansen et al [19], CSD refcode PYRAZB21, calculated for X-rays of wavelength 1.5406 Å.

º2θ	hkl	I/I$_{max}$ (%)
12.096	110	28.197
13.854	001	41.197
15.478	-201	59.166
16.769	011	20.322
18.140	-211	57.475
18.866	020	2.711
20.363	120	21.266
20.812	111	12.428
23.016	-311	6.563
23.482	021	64.893
24.330	220	83.339
24.821	310	0.292
26.561	121	100
27.209	-112	17.247
27.916	002	5.282
29.917	-411	7.444
31.330	221	5.179
32.702	-412	8.321
36.103	-511	11.289
36.853	330	13.205
37.559	202	6.217
38.565	-132	4.862
40.048	-431	0.275
42.373	430	0.662
43.553	013	4.524
46.130	241	4.354
48.245	-233	5.479
50.569	051	0.001

Table 3. Powder X-ray diffraction peaks (°2θ), diffracting plane indices (*hkl*) and relative intensities (*I/I*$_{max}$) for the calculated pattern for monoclinic paracetamol based on the crystal structure reported by Haisa et al [22], CSD refcode HXACAN01, calculated for X-rays of wavelength 1.5406 Å.

Recrystallisations: Samples of phenacetin (2) were dissolved in the minimum amount of boiling solvent required for dissolution. The solutions were allowed to cool to room temperature and

held isothermally with evaporation of solvent until solid material had formed. Crystals were isolated by filtration and dried under vacuum for 24 h.

Optical microscopy: Crystals were viewed using a Nikon Eclipse 50i POL Polarizing Microscope equipped with a Nikon DS-Fi1 CCD camera.

HPLC was carried out using an Agilent 1100 series HPLC, equipped with quaternary pump and degasser, and a YMC-Pack ODSA column (250 x 4.6 mm, 5ɥm). The column was eluted with a phosphate buffer at a flow rate of 1 mL/min and injection volume of 5 μL. The oven temperature was maintained at 20°C. The detector was initially set at 350 nm. The elution was isocratic, using methanol-water (60:40 v/v). Under these conditions, paracetamol eluted at 3.0 min and phenacetin at 5.3 min. Calibration curves were constructed by injection of different volumes of a stock solution (1 mg/mL) of compound (phenacetin or paracetamol) and plotting the ratios of the peak heights against the quantities injected. Calibration curves for phenacetin and paracetamol had R^2 values of 0.9993 and 0.9985 respectively.

Synthesis of candidate impurity compounds (28) and (30)

Paracetamol (27) (1.00 g, 6.6 mmol) and potassium carbonate (1.82 g, 13.2 mmol) were dissolved in 40 mL of acetone. Benzyl bromide (0.66 mL, 6.6 mmol) was added, and the solution was heated under reflux for 72 h. After this time, one further equivalent of potassium carbonate (1.82 g, 13.2 mmol) and 0.5 equivalents of benzyl bromide (0.32 mL, 3.3 mmol) were added and the reaction was heated under reflux for a further 24 h. Upon cooling, 50 mL of dichloromethane were added and the solution was washed with 2 x 40 mL of deionised water, dried over $MgSO_4$ and concentrated on a rotary evaporator to give a white solid (*O*-benzylparacetamol): 1.20 g, 75.5% yield; mp 140 °C (lit. mp 140 °C.) [18, 27] IR (KBr) 3282 (N-H), 1659 (-NHCO-), 1603, 1527 and 1243 cm^{-1}; ^{1}H NMR (400MHz, CDCl$_3$) 2.15 (3H, s, -COC**H**$_3$), 5.04 (2H, s, -OC**H**$_2$-), 6.90-6.95 (2H, m, -Ar**H** x 2), 7.04 (1H, br s, -N**H**-), 7.27-7.34 (1H, m, -Ar**H**), 7.34-7.44 (6H, m, -Ar**H** x 6). *O*-Benzylparacetamol (1.00 g, 4.15 mmol), NaI (0.62 g, 4.15 mmol) and EtBr (0.59 g, 5.39 mmol) were stirred together in 15 mL anhydrous THF with potassium *t*-butoxide (1.40 g, 12.45 mmol). The reaction was carried out at 0 °C under a N$_2$ atmosphere for 96 h, before quenching *via* the addition of 37% aq. HCl solution. The solution was concentrated to a syrup under reduced pressure and the syrup dissolved in methanol (30 mL). A spatula tip of an amberlyst ion exchange resin (15 hydrogen form) was added in order to neutralise excess potassium *t*-butoxide. Following a 6 h stir, the amberlyst resin was removed by filtration. Deionised water (25 mL) and 25 mL of dichloromethane were added. The aqueous layer was washed a further two times with 25 mL portions of dichloromethane. The organic layers were combined and dried over $MgSO_4$, before concentration under reduced pressure to give a yellow solid which upon analysis was determined to be *N-ethyl-N-(4-hydroxyphenyl)acetamide (28)*: 0.22 g, 30% yield; mp 173-175 °C (lit. mp 187-188 °C.) MS (ESI-TOF) m/z: [M + Na]+ Calcd for C$_{10}$H$_{13}$NO$_2$; Found 180.1020.. IR (KBr disc) 3200 (O-H stretch), 3109 (Ar C-H stretch), 3024 (Ar C-H stretch), 1668 (amide C=O stretch) and 1514 cm^{-1} (Ar C=C bend). ^{1}H NMR (400MHz, CDCl$_3$) 1.10 (3H, t, J_{H-H} = 7.1 Hz, -CH$_2$C**H**$_3$), 1.82 (3H, s, C**H**$_3$CO-), 3.67-3.74 (2H, m, -C**H**$_2$CH$_3$), 6.86-6.91 (2H, m, -Ar**H** x 2), 6.98-7.03 (2H, m, -Ar**H** x 2).

N-Ethyl-*N*-(4-hydroxyphenyl)acetamide (28) (0.09 g, 0.49 mmol), ethyl iodide (0.075 g, 0.485 mmol) and K_2CO_3 (0.13 g, 0.97 mmol) were stirred in 2 mL of methyl ethyl ketone at r.t. for 14 h, after which one further equivalent of ethyl iodide (0.075 g, 0.485 mmol) was added and the solution was heated at reflux for 2 h. Upon cooling, 5 mL of deionised water was added and the aqueous solution was extracted with 3 x 5 mL portions of diethyl ether. The organic layers were combined, washed with 20 mL of brine and dried over $MgSO_4$, before concentrating under reduced pressure and drying under vacuum for 24 h. *N-Ethylphenacetin (30)* was obtained as thick yellow syrup: 40 mg, 40% yield; HRMS (ESI-TOF) m/z: [M + Na]+ Calcd for $C_{12}H_{17}NO_2Na$ 208.1329; Found 208.1338. ^{1}H NMR (300MHz, $CDCl_3$) 1.02 (3H, t, J_{H-H} = 7 Hz, -NCH_2CH_3), 1.36 (3H, t, J_{H-H} = 7 Hz, -OCH_2CH_3), 1.73 (3H, s, CH_3CO-), 3.63 (2H, q J_{H-H} = 7 Hz, -OCH_2CH_3), 3.97 (2H, q, J_{H-H} = 7 Hz, -NCH_2CH_3), 6.80-6.86 (2H, m, -Ar**H** x 2), 6.90-7.02 (2H, m, -Ar**H** x 2).

Metastable Zone Width (MSZW) determinations were carried out in a 1L HEL Autolab jacketed glass reaction vessel with Huber P20 silicone thermofluid controlled by a Huber unistat 815 thermoregulator. Agitation was *via* a four blade pitched impeller agitator held at 180 rpm with an overhead motor. Vessel contents temperature was measured by a PTFE PT100 thermocouple. Anti-solvent was added using a ProMinent gamma/L pump. Heating and cooling, agitation and addition of solvent was programmed using HEL WinISO software. Nucleation and particle counts were monitored using a HEL Lasertrack *in situ* laser probe. Ethanol was selected as the crystallising solvent for the MSZW investigation. These involved phenacetin spiked with *N*-ethylparacetamol *(28)* or paracetamol (27) in ratios of 0% (i.e. for determination of the MSZW of pure phenacetin in ethanol) or 1% quantities, and paracetamol in 10% w/w impurity. (It was not feasible to synthesise sufficient quantities of compound (28) for using as an impurity in 10% w/w quantities.) Using the solubility curve for ethanol [13] a saturated solution of phenacetin at 60 °C was prepared. The solution was heated to 70 °C to ensure complete dissolution. The solution was then cooled to 20 °C, at which point 80 g of solvent was added in order to change the concentration. The step was repeated multiple times in order to obtain the MSZW diagrams for spiked phenacetin in ethanol.

Single crystal X-ray goniometer measurements were carried out on a Bruker APEX II DUO diffractometer using the APEX2 v2009.3-0 software [28]. Crystal structure images were prepared using Mercury [29] using the data reported by Hansen et al [19], CSD refcode PYRAZB21.

Serial dissolution study: Growth of large single crystals of phenacetin spiked with paracetamol was accomplished by allowing a spiked solution to concentrate over a period of one week. 50 mg of phenacetin was dissolved in 1.5 mL of ethanol along with 2, 4 and 6 mg of paracetamol in order to obtain 5, 10 and 15% spikes respectively. Gentle heating was required to aid dissolution. Large single crystals were collected and were washed carefully with cold ethanol. Serial dissolution of the spiked phenacetin crystals was accomplished by placing each individual crystal within a glass sample vial and partially dissolving the crystal in methanol-water (40:60). The crystals were firstly weighed (each was typically 4-5 mg) and 1 mL/mg of solvent was used. The crystals were physically removed from the solution upon visual estimation of approximately one third dissolution (typically 1-2 mins.). The crystals were then

transferred to a second and subsequently third vial for further dissolution. The residual solutions were analysed by HPLC as described above.

Co-crystallisation was attempted using physical mixtures of phenacetin and paracetamol in 1:1 and 1:2 ratios. Mixtures recrystallised from ethanol or were ground in a Retsch MM400 ball mill [30].

Acknowledgements

Author details

Danielle E. Horgan, Lorraine M. Crowley, Stephen P. Stokes, Simon E. Lawrence and Humphrey A. Moynihan[*]

*Address all correspondence to: h.moynihan@ucc.ie

Department of Chemistry / Analytical and Biological Chemistry Research Facility / Synthesis and Solid-State Pharmaceutical Centre, University College Cork, Cork, Ireland

References

[1] U.S. Department of Health and Human Services Food and Drug Administration. ICH Guidance for Industry: Q3A Impurities in New Drug Substances, June 2008. http://www.fda.gov/cder/guidelines.htm

[2] Tanoury GJ, Hett R, Kessler DW, Wald SA, Sennayake CH. Taking Advantage of Polymorphism To Effect an Impurity Removal: Development of a Thermodynamic Crystal Form of (*R,R*)-Formoterol Tartrate. Organic Process Research and Development 2002; 6: 855-862.

[3] Blagden N. Crystal engineering of polymorph appearance: the case of sulphathiazole. Power Technology 2001; 121:46-52.

[4] Solanko, KA, Bond AD. Influence of impurities on the crystallisation of 5-X-aspirin and 5-X-aspirin anhydride polymorphs (X = Cl, Br, Me). CrystEngComm 2011; 13: 6991-6996.

[5] Mukuta T, Lee AY, Kawakami T, Myerson AS. Influence of Impurities on the Solution-Mediated Phase Transformation of an Active Pharmaceutical Ingredient. Crystal Growth and Design 2005; 5: 1429-1436.

[6] Mirmehrabi M, Rohani S, Murthy KSK, Radatus B. Polymorphic Behaviour and Crystal Habit of an Anti-Viral/HIV Drug: Stavudine. Crystal Growth and Design 2006; 6: 141-149.

[7] Berkovitch-Yellin Z, Addadi L, Idelson M, Lahav M, Leiserowitz L. Controlled Modification of Crystal Habit via "Tailor-Made" Impurities. Application to Benzamide. Angewandte Chemie Supplementary 1982; 1336-1345.

[8] Blagden N, Song M, Davey RJ, Seton L, Seaton CC. Ordered Aggregation of Benzamide Crystals Induced Using a "Motif Capper" Additive. Crystal Growth and Design 2005; 5: 467-471.

[9] Fiebig A, Jones MJ, Ulrich J. Predicting the Effect of Impurity Adsorption on Crystal Morphology. Crystal Growth and Design. 2007; 7: 1623-1627.

[10] Moyers CG. Chemical Engineering Progress 1986; 82: 42-46.

[11] Addadi L, Weinstein S, Gati E, Weissbuch I, Lahav M. Resolution of conglomerates with the assistance of tailor-made impurities. Generality and mechanistic aspects of the "rule of reversal". A new method for the assignment of absolute configuration. Journal of the American Chemical Society. 1982; 104:4610-4617.

[12] Weisinger-Lewin Y, Frolow F, McMullan RK, Koetzle TF, Lahav M, Leiserowitz, L. Reduction in crystal symmetry of a solid solution:a neutron diffraction study at 15 K of the host/guest system asparagine/aspartic acid. Journal of the American Chemical Society. 1989; 111:1035-1040.

[13] Moynihan HA, Kelly DM. Phenacetin Crystallization: Cooling Regimes and Crystal Morphology. In: Marcello Rubens Barsi Andreeta (ed.) Crystallization - Science and Technology. Rijeka: InTech; 2012. p329-348.

[14] Clissold SP. Paracetamol and Phenacetin. Drugs 1986; 32(Suppl. 4): 46-59.

[15] Adams R, Johnson RJ, Wilcox CF. Laboratory Experiments in Organic Chemistry, 7th Edition. New York: Macmillan Publishing Co.; 1979.

[16] Eaker CM, Campbell JR. Acetophenetidine. US Patent 2,887,513. May 19, 1959.

[17] Volker EJ, Pride E, Hough C. Drugs in the Chemistry Laboratory. Journal of Chemical Education. 1979; 56(12): 831.

[18] Neubert ME, Norton P, Fishel DL. Molecular Crystals and Liquid Crystals. 1975, 31: 253-257.

[19] Hansen LK, Perlovich GL, Bauer-Brandl A. Redetermination of p-ethoxyacetanilide (phenacetin). Acta Crystallographica E. 2006; E62: o2712-o2713.

[20] Patel U, Patel TC, Singh TP. Structure of phenacetin. Acta Crystallographica C. 1983; C39: 1445-1447.

[21] Etter MC. Encoding and decoding hydrogen-bond patterns of organic compounds. Accounts of Chemical Research. 1990; 23: 120-126.

[22] Haisa M, Kashino S, Kawai R, Maeda H. The Monoclinic Form of *p*-Hydroxyacetamilide. Acta Crystallographica. 1976; B32:1283-1285.

[23] His KH, Kenny M, Simi A, Myerson AS. Purification of Structurally Similar Compounds by the Formation of Impurity C-Former Complexes in Solution. Crystal Growth and Design. 2013; 13: 1577-1582.

[24] Weber CC, Wood GPF. Kunov-Kruse AJ, Nmagu DE, Trout BL, Myerson AS. Quantitative Solution Measurement for the Selection of Complexing Agents to Enable Purification by Impurity Complexation, Crystal Growth and Design. 2014; 14: 3649-3657.

[25] Oswald IDH, Allan DR, McGregor PA, Motherwell WDS, Parsons S, Pulham CR. The formation of paracetamol (acetaminophen) adducts with hydrogen-bond acceptors. Acta Crystallographica Section B 2002; 58: 1057-1066.

[26] Maeno Y, Fukami T, Kawahata M, Yamaguchi K, Tagami T, Ozeki T, Suzuki T, Tomono K. Novel pharmaceutical cocrystals consisting of paracetamol and trimethylglycine, a new promising cocrystals former. International Journal of Pharmaceutics 2014; 473: 179-186.

[27] Rastogi N, Kant P, Sethi R, Shukla S, Harrison DA. Synthesis of a series of aminomethylated 5-nitro-1H-benzo[d]imidazoles, 6-nitrobenzo[d]oxazol-2(3H)-ones and 4-nitroisoindoline-1,3-diones as antileishmanial and antimicrobial agents. Indian Journal of Heterocyclic Chemistry 2010; 2092): 149-152.

[28] APEX2 v2009.3-0. Bruker AXS: Madison, WI, 2009.

[29] Macrae CF, Bruno IJ, Chisholm JA, Edginton PR, McCabe P, Pidcock E, Rodriguez-Monge L, Taylor R, van de Streek J, Wood PA, Journal of Applied Crystallography. 2008, 41: 466-470.

[30] Eccles KS, Morrison RE, Stokes SP, O'Mahony GE, Hayes JA, Kelly DM, O'Boyle NM, Fabian L, Moynihan HA, Maguire AR, Lawrence SE. Utilizing Sulfoxide...Iodine Halogen Bonding for Cocrystallization. Crystal Growth and Design. 2012; 12: 2969-2977.

Spherical Crystallization of Drugs

Yousef Javadzadeh, Zhila Vazifehasl,
Solmaz Maleki Dizaj and Masumeh Mokhtarpour

Additional information is available at the end of the chapter

http://dx.doi.org/10.5772/59627

1. Introduction

Oral way is the most important route of drug administration for obtaining systemic pharma‐
cological effects. In this route, the solid dosage form specially tablets, are the first choice of
patient because of their some special advantages like easy administration by the patient, unit
dosage form with greatest dose precision and least content variability, lower cost and temper
proof nature [1]. Due to unfavourable physical and mechanical properties and poor aqueous
solubility of some drugs, their formulation process becomes problematic. Crystallization is the
main process in the pharmaceutical industry for particle formation and may be defined as the
process in which a solid compound precipitates from a saturated solution in the form of crystals
[2, 3].Most active pharmaceutical ingredients are manufactured in a crystalline shape for their
chemical stability during transportation, packaging and storage. Many factors including
thermodynamic (*e.g.*, solubility, solid-liquid interfacial tension, solvent activity, temperature,
etc.), kinetic (*e.g.*, supersaturation, molecular mobility, meta-stable zone width) and molecular
recognition (hydrogen bonds, non-covalent bonds, molecular networks) influence the rate and
mechanisms by which crystals are formed from liquid solutions [3, 4]. The driving force for
crystallization is supersaturation. Supersaturation can be generated by increasing the solute
concentration (solvent evaporation) or decreasing the solute solubility (*e.g.*, temperature
change, anti-solvent addition, pH change, salting-out) [5]. The next step is the formation of
macroscopic crystals from stable nuclei, called crystal growth. This step is controlled by
internal (crystal structure) and external factors (temperature, impurities, supersaturation,
solvent type) and determines the particle morphology [6].

The size and shape are very important parameters that influence the separation process which
will in turn have an effect on the yield and quality of the resulting fractions during the
crystallization process [7]. Particle orientation was influenced by crystal habit, therefore can
modify the flowability, packing, compatibility, syringability, physical stability and dissolution

profile of a drug molecule. For example, it has been showed that symmetrically shaped crystals of ibuprofen have better compaction and flow properties than needle shaped crystals [8, 9]. It seems that optimization of crystal properties is an alternative method for modifying the dissolution properties of drugs and therefore their bioavailability [10, 11].

Poor physical and mechanical properties of drug particles have been traditionally covered by various granulation methods. Enlargement of particle size is an important procedure during manufacturing of tablets [12]. There are different techniques for enlargement of particle size such as wet granulation, dry granulation, extrusion spheronization and spherical crystallization methods [13]. These techniques have important role in modifying primary and secondary properties of pharmaceutical substances. Kawahima and Capes (during the 1970 decade) suggested enlargement of particles size during the crystallization process. According to their report, controlling the crystal's agglomeration leads to spherical agglomerates with accorded properties [14].

In 1986, Kawashima applied the spherical crystallization method for size enlargement of drugs in the pharmaceutical field. Spherical crystallization defined by him as "An agglomeration process that transforms crystalline drugs directly into a compacted spherical form for improving the flowability, solubility and compactability" [14, 15]. Spherical agglomeration (SA) and emulsion solvent diffusion (ESD) are two major techniques for spherical crystallization. In fact the ammonia diffusion systems (ADS) and crystallo-co-agglomeration (CCA) are extended forms of these methods [16]. Spherical agglomeration consists of precipitating fine crystals of the drug substance and then aggregating them using a wetting agent (should be a non-miscible liquid).In the emulsion solvent diffusion technique, the continuous phase is a non-miscible iquid with drug. Indeed in this method, a quasi-emulsion is formed by droplets of solvent containing the drug and then crystallization occurs inside the droplets because of the counter diffusion of the solvents through the droplets [15]. Under controlled conditions, such as solvent composition, temperature regulation, supersaturation generation, or mixing speed, crystallized particles are able to agglomerate into the spherical dense agglomerates simultaneously.

2. Spherical crystallization

Good flowability, mechanical strength and compressibility are the main requirements for commercial production of a particulate solid into the tablet dosage form [14]. Nowadays, great advancements are accessible by powder technology, and various studies are made to produce primary and secondary particles of pharmaceutical substances for different applications. The spherical crystallization is a particle size enlargement method that applies crystallization and agglomeration using bridging liquid [17]. Indeed, this method is a particle design technique that crystallization and agglomeration can be performed simultaneously in one step for transforming crystals directly into the compacted spherical forms [18, 19]. By using this method, direct tabletting of drug instead of further processing like mixing, granulation, sieving and drying is possible [15, 16, 19].This technique is capable of subsequent processes such as separation, filtration and drying more efficiently and is able to have an effect on the secondary properties of the crystals such as flowability, compressibility and wettability. Using this technique, the precipitated crystals can be agglomerated during the final synthesis step into

more or less spherical particles with sizes between 300 and 500 mm without any binders. Spherical crystallization has been considered as a very effective method in improving the dissolution profile of some poorly water soluble drugs [13, 14, 19].

Mechanical properties of the spherical agglomerates like packability, flowability, compressibility, mechanical strength and elastic recovery are very important for the handling and bioavailability of the particles [20]. Stronger bonding occurs during compression of agglomerated crystals compared to single crystals and greater tensile strength is obtained from agglomerated crystals compared to single crystals. It was demonstrated that the spherical agglomerates are more compressible and suitable for preparing compressed dosage forms than conventional crystals. The stronger bond forces formed from agglomerated crystals lead to greater plastic deformation and higher tensile strength compared to those created from single crystals [21]. Jbilou et al. reported that the improvement of compression ability of the agglomerated crystals of ibuprofen compared to marketed single crystals (in spite of high crystallinity) is related to the isotropic texture of the agglomerate [22].

2.1. Principle of spherical crystallization

The saturated solution of the drug in a good solvent is poured into a poor solvent. A third solvent known the bridging liquid is added in small amounts to wet the crystal surface and promote the formation of liquid bridges between the drug crystals for forming spherical agglomerates [23]. In this process the poor and good solvents should be freely miscible and the affinity between the solvents must be stronger than the affinity between drug and the good solvent. Furthermore, the bridging liquid should not be miscible with the poor solvent and should preferentially wet the precipitated crystals [15]. Advantages and disadvantages of spherical crystallization method are summarized in Table 1.

Advantages	Disadvantages
Physicochemical properties of pharmaceutical crystals are mainly improved for pharmaceutical process i.e. milling, mixing and tabletting by using this technique [24].	Selection of suitable solvents is a tedious process [2].
Use of this technique leads to conversion of crystalline forms of a drug into polymorphic form that may have better bioavailability [23].	Optimization of processing parameters (temperature, agitation) is difficult [16].
This technique could enable subsequent processes such as separation, filtration, drying, etc. to be carried out more efficiently [15].	
Preparation of microsponges, microspheres and nanospheres, microballoons, nanoparticles and micro pellets as novel particulate drug delivery system is possible by it [25].	
It can be used for masking of the bitter taste of drug [15].	

Table 1. Advantages and disadvantages of spherical crystallization

2.2. Main steps involved in the growth of agglomeration

Bermer and Zuider Wag classified the growth of agglomeration in four steps: Flocculation zone, zero growth zone, fast growth zone and constant size zone [26].

2.2.1. Flocculation zone

The bridging liquid is adsorbed on the surface of crystals and links the particles by forming bridge between them [15, 26].

2.2.2. Zero growth zone

In this zone, loose floccules are converted into the tightly packed pellets. The entrapped fluid is squeezed out onto the surface of the small floccules. The driving force for these conversions is governed by the agitation of the slurry, pellet-pellet and pellet-stirrer collision [27].

The rate limiting step in agglomeration growth process occurs in zero growth zones when bridging liquid is squeezed out of the pores as the initial floccules are transformed into small agglomerates.

2.2.3. Fast growth zone

When sufficient bridging liquid has squeezed out of the surface of the small agglomerates, the fast growth zone is observed. Coalescence is the process in which the large size particle is formed following random collision of well-formed nucleus. For successful collision process, slightly excess surface moisture of nucleus is required [27, 28].

2.2.4. Constant size zone

This zone involves stopping of agglomeration growth. In this zone, even a slight decrease in size of agglomerates may be observed probably due to attrition, breakage and shatter. Four zones for agglomeration growth are illustrated in Figure 1 [26-28].
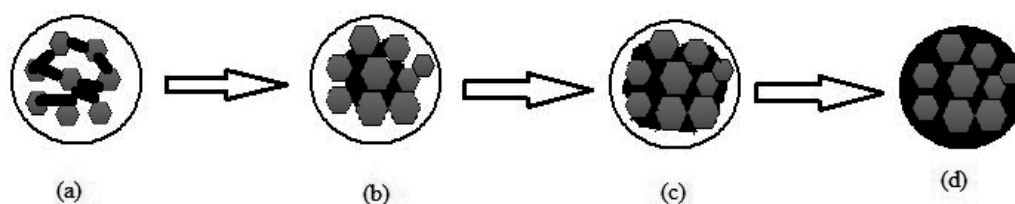

Figure 1. Four steps for agglomeration growth: a) flocculation zone, b) zero growth zone, c) fast growth zone, d) constant size zone

3. Spherical agglomeration technique

There are three main stages for spherical agglomeration method. The first stage is the choice of the crystallization method to precipitate crystals from solution. The thermal, physico-

chemical or chemical methods may be used in this stage. The second step is the selection of the wetting agent that should be immiscible with the solvent of the crystallization process. At the end stage, the hardening of the agglomerates is performed. Agglomeration may occur as a consequence of the coalescence of agglomerates with the liberated bridging liquid [29].

Spherical crystallization has been employed for several high dose drugs with poor compressibility and poor water solubility [24].

Spherical agglomeration is a valuable technique in the formulation of microspheres, microsponges, nanospheres, microballoons and nanoparticles as novel drug delivery systems [30]. Spherical agglomeration is also employed in processes such as granulation, balling, pelletization, tabletting, compaction, flocking and sintering in order to produce, *e.g.*, nuclear fuel pellets, ceramic powders, carbon blacks, catalysts, commercial fertilizers, pesticides and pharmaceutical products [31]. The main parameters in spherical agglomeration are the choice of the solvent system, amount and type of the bridging liquid, the presence of additives, initial particle size, solubility, the agitation rate and temperature. These parameters influence not only the productivity but also the micrometrics properties such as particle size distribution, morphology and strength of the product [17]. Figure 2 shows the principle of spherical agglomeration.
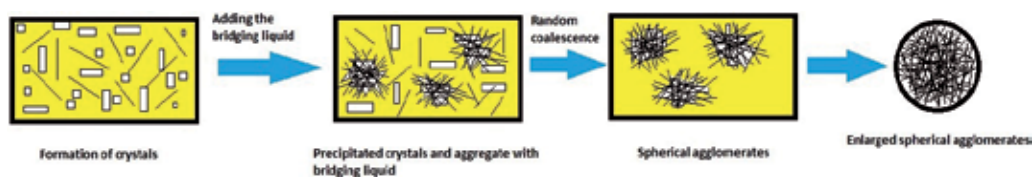
Figure 2. Principle of spherical agglomeration

3.1. Solvent system

Polarity of the solvent and its interactions with hydrophobic phases of the growing crystals have an influence on shape, surface irregularity and roundness of the crystals agglomerate [32]. Commonly three types of solvents are used in spherical agglomeration [27]: a) A perfect solvent for the drug, b) anti-solvent and c) bridging liquid that should be added for promoting the formation of agglomerates. Bridging liquid not only has wetting property but also acts as an interparticle binder promoting agglomeration. The bridging liquid should not be miscible with the anti-solvent. Meanwhile, anti-solvent and solvent systems should not be miscible and the affinity between them must be stronger than those between drug and solvent [15, 17, 25]. The solvent system and its composition are usually selected by trial and error. Examples of solvent systems in preparing spherical agglomeration of some drugs are given in Table 2. Also the common solvent system in spherical crystallization method is shown in Figure 3.

Drug	Solvent system			Technique	References
	Good solvent	Poor solvent	Bridging liquid		
Flubiprofen	Acetone	Water	Hexane	SA	[33]
Salicylic acid	Ethanol	Water	Chloroform	SA	[34]
Aspirin	Acid buffer,	Methanol,	Chloroform	SA	[35]
Fenbufen	THF	Water	Isopropyl acetate	SA	[36]
Nabumetone	Ethanol	Water	Cyclohexane	SA	[37]
Naproxen	Acetone-ethanol	Water	Chloroform	SA	[38]
Roxythromycin	Methanol	Water	Choroform	SA	[39]
Mebendazole	Acetone	Water	Hexan,Octanol, Dichloromethane	SA	[40]
Valsartan	Acetone	Water	Choroform	SA	[41]
Celocoxib	Acetone	Water	Chloroform	SA	[42]
Ascorbic acid	Water	Ethyl acetate	Ethyl acetate	SA,ESD	[43]
Aspartic acid	Methanol	Water	-	SA	[44]
Ibuprofen	Ethanol	Water	Ethanol	SA	[22]
Ibuprofen-Paracetamol	Dichloromethane	Water	Dichloromethane	CCA	[45]
Benzoic acid	Ethanol	Water	Chloroform	SA	[46]
Aceclofenac	Acetone	Water	Dichloromethane	SA	[47]
Indomethacin	Dimethyl formamide	Water	Chloroform	SA	[48]
Indomethacin Mepirizole	Ethyl acetate	Water	Ethyl acetate	CCA	[49]
Ibuprofen-Talc	Dichloromethane	Water	Dichloromethane	CCA	[50]
Glibenclamide	Dichloromethane	Water	Chloroform	SA	[51]
Tranilast	Acetone	Water	Dichloromethane	SA	[52]
Aminophylline	Ethanol	Water	Chloroform	SA	[53]
Bromohexin Hcl	Dichloromethane	Water	Dichloromethane	CCA	[54]
Ketoprofen	Isopropyl acetate	Water	Choroform	SA	[55]
Propiphenazone	Ethyl alcohol	Water	Isopropyl acetate	SA	[14]
Acetylsalicyclic acid	Ethanol	Water	Carbon tetrachloride	SA	[56]
Ketoprofen-talc	Dichloromethane	Water	Dichloromethane	CCA	[57]

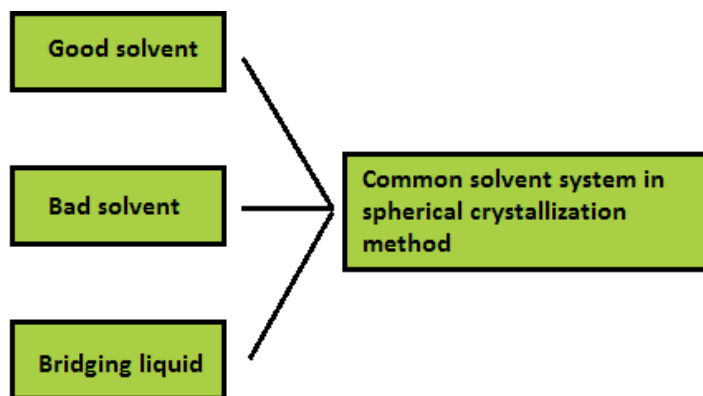**Table 2.** Solvent systemsin preparing spherical agglomeration of drugs

Figure 3. Common solvent system in spherical crystallization method

3.2. Bridging liquid

The amount of bridging liquid is a critical factor in the spherical crystallization method. There are some studies about the enlargement of agglomerates by increasing the amount of bridging liquid [58]. Generally, increasing amount of the bridging liquid leads to an increase in agglomerate size [59]. According to a research, addition of a smaller amount of bridging liquid produced larger particles of acebutolol (up to 1,000mm) and vice versa a greater amount of bridging liquid formed smaller particles (around 600mm) [25, 60]. The rate of addition of bridging liquid in the system also influences the spherical nature of the crystals [32, 61]. The strength of the bridges not only depends on the interfacial tension between the bridging liquid and the medium but also depends on the rheology of the bridging liquid [32].

There are very limited reports on the systematic selection of the solvent system and bridging liquid for spherical crystallization. Most articles do not address the reasoning behind their solvent selection. Chow and Leung proposed some rules for selection of solvent system and bridging liquid [26]: For water soluble compounds, an organic solvent that is miscible with water is employed as the poor solvent and salt solutions in high concentration without common ions can be applied as the bridging liquid. In the case of compounds that are soluble in one or more organic solvents, water is used as the poor solvent and a water-immiscible organic solvent as the bridging liquid. For compounds that are only soluble in water-miscible organic solvents, a saturated aqueous solution of the compound and an organic solvent could be used as poor and bridging solvents respectively. Finally for materials with insufficient solubility in water or any organic solvent, a water-immiscible organic solvent employ as the poor solvent and salt solutions in high concentration without common ions as the bridging liquid. In the latter case because of insufficient solubility of drug powder in bridging liquids, presence of a binding agent such as PVP 40000 or PEG 10000 is necessary for agglomeration [25].

Chloroform has been employed as a bridging liquid in the preparation of some spherical crystal drugs such as: salicylic acid, Aspirin, Roxithromycin, Trimethoprim, Tranilast anhydrate and

Tranilast monohydrate. Isopropyl acetate has been used in the spherical crystal preparation of Propyphenazone, Acebutolol hydrochloride, Tolbutamide and Fenbufen for this mean. Because the strength of liquid bridges is proportional to the interfacial tension between the bridging liquid and the solid, surfactants are not usually used as bridging liquid [31]. Figure 4 shows the mechanism of liquid bridge formation in spherical agglomeration.
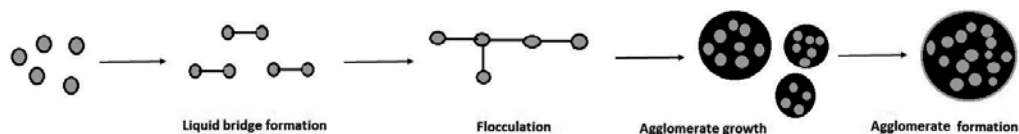

Figure 4. The mechanism of liquid bridge formation in spherical agglomeration

3.3. The presence of additives

The presence of additives such as polymeric material and surface active agents are able to influence molecular aggregation during the crystallization process [40]. The viscosity of the medium and surface tension are reduced by surfactants that in which affect the nucleation process. The existence of these additives in the spherical agglomeration process may also reduce the processing time and improves the bioavailability and micrometric properties of the drug.

Crystallization is inhibited by some of the polymers such as methylcellulose, hydroxypropyl methyl cellulose (HPMC) andpolyvinyl pyrrolidone (PVP). Among these, PVP has been found to be the most effective crystallization inhibitor. These anti-nucleant polymers are incompatible with the host molecules of the growing crystals surface. Then their incorporation into the lattice alters growth characteristics of the host molecules [62].

3.4. Particle size

Particle size distributions of the drugs and their excipients can exert major effects on the mixing process and therefore on possible segregation in the mixed materials. The particle size distribution in powder material can also influence the flowability and bioavailability of certain active drugs. When the concentration of the organic phase is close to the saturation of the liquid phase, the particles have soft (gel like) and sticky structure. These sticky structures during the process lead to particles sticking to the impeller and crystallizer wall. Indeed, the gel like structure is achieved when the mass transfer from the organic phase to aqueous phase is too slow. Then the life-time of the emulsion is much higher leading to an enhancement in coalescence frequency of the droplets [61].

3.5. Solubility of drug

As mentioned earlier, the solvent system for spherical crystallization includes a poor solvent, a good solvent for the drug and bridging liquid. Venkadari Rammohan Gupta described a method for the selection of solvents that is dictated by the solubility characteristic of the drug

[42].Physical state of a drug product (whether microagglomerate or irregular macro-agglomerates or a paste of drug substance) may be controlled by selecting of proper solvent proportions. The solvent proportions is determined by performing solubility tests and then constructing triangular phase diagram for defining the region of mutual immiscibility using ternary diagram [63].

3.6. Mode and intensity of agitation

Similar to the consolidation in granulation process, in the spherical agglomeration process, the spherical shape particles are formed due to mechanical forces of the agitation over a long period of time. In several reports, effects of the agitation rate were reported, and it is one of the main parameters to determine average diameter of the agglomerated crystals [64]. Mode and intensity of agitation in conjugation with the amount of bridging liquid determines the rate of agglomerate formation and their ultimate size. High speed agitation is required for the dispersion of the bridging liquid throughout the system. Altering of the agitation pattern leads to change in force acting on the agglomerate and therefore has an effect on the shape of the agglomerate.

Some drugs require low agitation rate for crystallization, whereas some need elevated rate. Blandin et al. stated that a higher stirring rate leads to obtaining less porous and more resistant agglomerates [24].

The rate of crystallization in the system determines nature of the agitation speed. If the rate of drug crystallization was high, then the elevated agitation speed is required for agglomeration. The used blade for agitation has important role on the shape of agglomerates. Commonly screw-type agitator with four flat blades is used for maintaining the shape. The sharper blades will cut the agglomerates and irregular agglomerates will be formed [65]. By increasing agitation rate, the shear force of the system increases and the outcome is more consolidated agglomerates. By applying a rate above the optimum stirring rate, and due to an increase in disruptive forces, the agglomeration process becomes less efficient [66, 67].

Maghsoodi et al. showed that increase of the agitation time before adding the bridging liquid leads to bigger and more elongated crystals. According to their report, needle-like particles are more difficult to pack than isotropic particles in this situation. They also changed the stirring time after the addition of bridging liquid. Their results showed that the spherical shape of the agglomerates does not appear immediately but develops gradually [68].

3.7. Temperature of the system

Temperature has a major influence on the shape, size and texture of the agglomerates. The effect of temperature on spherical crystallization is maybe due to its effect on the drug solubility [69].Kawashima et al. [1984] tested the temperature influence on the spherical agglomeration of salicylic acid in a tertiary system (water-ethanol-chloroform). By increasing the temperature, the solubility of drugs is increased and then a decrease in the recovery of the crystals is observed. At lower temperature, recovery of the crystals increases and the constituent crystal size and the solubility of chloroform in the solvent mixture diminishes [70]. Furthermore,

temperature has an effect on the crystallization stages such as nucleation, crystallization and agglomeration of crystals. According to Kawashima and Capes [1984], spherical agglomeration follows first order kinetics with respect to increasing number of agglomerates with time. The bulk density of the agglomerates also decreases by increasing the crystallization temperature [70].

3.8. Residence time

The residence time that agglomerates remain suspended in reaction mixture influences the size, shape and strength of agglomerates. During long residence time because of the solubilization of the agglomerates by the bridging liquid, the agglomerates break down into smaller crystals and the size of agglomerated particles decreases [32]. Then the optimization of residence time for the agglomeration of recrystallized crystals is necessary. Below the optimized residence time, incomplete effusion of good solvent and bridging liquid from the formed droplets in the dispersion medium leads to the incomplete agglomeration [32].

4. Quasi-emulsion solvent diffusion

In this process, the quasi-emulsion of drug solution in good solvent with a poor solvent (non-solvent) is formed. Due to counter diffusion of good solvent and poor solvent, crystallization of the drug occurs. Stabilization of emulsion by proper polymer is required in this method. In fact, the drug and polymer are co-precipitated in order to form drug crystals according to the polymer properties. Residual good solvent in droplets acts as a bridging liquid to agglomerate the generated crystals [8, 27].
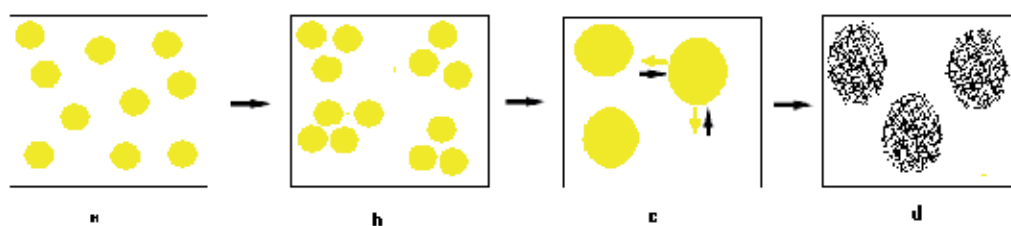
Figure 5. The mechanism of emulsion solvent diffusion method: a) emulsion formation, b) coalescence of emulsion droplet,c) diffusion of good solvent to outer phase and poor solvent into of the droplet, d) growth of crystal shell and final agglomerates

Patil and Sahoo prepared the spherical agglomerates of glibenclamide by emulsion solvent diffusion method. They used methanol, chloroform and water as good solvent, bridging liquid and poor solvent respectively. According to their results, particle size, flowability, compactibility and packability of plane and agglomerates with additives except with polyvinyl pyrrolidone were preferably improved for direct tabletting compared with raw crystals of glibenclamide. Their results also showed significant improvement in solubility and dissolution

rate of plane and agglomerates with additives except with polyvinyl pyrrolidone, compared with the raw crystals of the drug. The authors believe that improved properties of spherically agglomerated crystals is due to their large and spherical shape and enhanced fragmentation during compaction that is supported by increased tensile strength and less elastic recovery of its compact [28]. The mechanism of emulsion solvent diffusion method is shown in Figure 5.

5. Ammonia diffusion method

Ammonia diffusion components consist of ammonia water as a good solvent and also bridging solvent, poor solvent and hydrocarbon or halogenated hydrocarbon (acetone). The hydrocarbon is miscible with the system, and it should reduce the miscibility of the ammonia water with poor solvent. The diffusion process across the droplet consists of moving poor solvent inside and ammonia out of the droplet. Then the drug crystals precipitatein ammonia water slowly and agglomerates are grown [8, 27].Figure 6 shows this process.
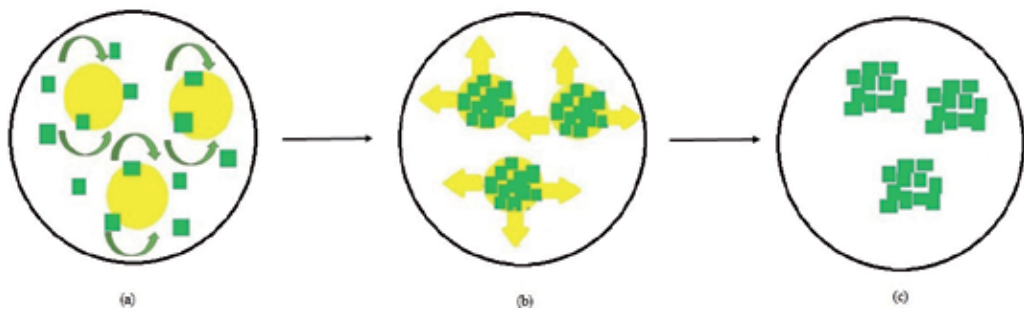

Figure 6. Ammonia diffusion method for preparation of spherical crystallization: a) movement of poor solvent into the droplet, b) movement of ammonia out of the droplet, c) the drug crystals precipitate in ammonia water slowly and agglomerates are grown

6. Crystallo-Co-Agglomeration (CCA) technique

Due to the hydrophobic nature of most excipients, incorporation of them in the formed agglomerates using organic bridging liquid is complicated [71, 72]. Then spherical agglomeration could not be employed for low-dose or poorly compressible materials. Crystallo-co-agglomeration technique is one of the novel particles designing technique (developed by Kadam et al) that could be able to overcome the mentioned limitation of spherical crystallization [30].This process includes continuous stirring of drug and excipients in liquid medium. The continuous stirring is necessary for loading of the drug consistently in the agglomerates. In expansion concept, crystallo-co-agglomeration technique involves simultaneous crystallization and agglomeration of drug substance with or without excipients from good solvent and/ or bridging liquid by the addition of a poor solvent. The formed crystal of drug has minuscular

form and therefore the drug dissolution and bioavailability are improved by using this method [73, 74]. Sometimes bridging liquid also serves as a good solvent. To overcome drug loss due to co-solvency, the good solvent should be volatile and immiscible with poor solvent [74].

Bridging liquid can affect on the rate of agglomeration and also on the strength of the agglomerates. Smaller amount of the bridging liquid leads to fine particles whereas larger amount produces coarse particles. When the stirring rate is increased, the agglomeration will be reduced (because of increasing disruptive forces). Porosity diminishes by increasing concentration of the solid [66].

Commonly the crystallo-co-agglomeration method can be performed in two ways: solvent change method and alternate method [75]. In solvent change method, crystallo-co-agglomerates can be obtained by the crystallization as well as the agglomeration. One or more drugs simultaneously crystallize and agglomerate from the system containing good solvent and bridging liquid by the addition of a poor solvent. In the alternate method, the crystallization of drug is performed from a system containing good solvent and bridging liquid and then its simultaneous agglomeration is done with an insoluble diluent or a drug by the addition of a poor solvent. Figure 7 shows the steps involved in crystallo-co-agglomeration technique [76].
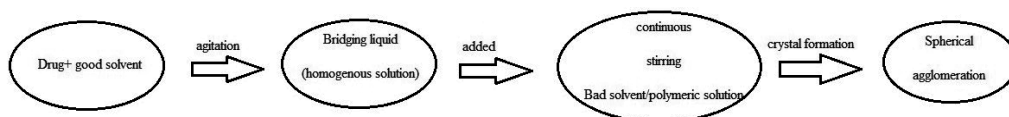

Figure 7. Steps involved in crystallo-co-agglomeration technique

6.1. The effect of various factors on crystallo-co-agglomeration process

Crystallo-co-agglomeration technique depends on numerous factors such as the formulation and process variables which have an effect on the processes of crystallization and agglomeration. The selection of diluent, solvent system, internal phase, amount and type of polymers will have an influence on the final agglomerates [75].

Excipients and polymers play a key role in the preparation of crystallo-co-agglomerates, an excellent alternative to wet granulation process to prepare particles for direct compression [77].The difference in the physicochemical properties of the drug molecules and the excipient is the main factor in the selection of a solvent system for the crystallo-co-agglomeration technique. Various polymers like hydroxy propyl methylcellulose (HPMC), poly ethylene glycol (PEG), ethyl cellulose (EC) and poly vinyl pyrrolidone (PVP) may be used to improve poor compressibility and handling qualities of pure drugs by crystallo-co-agglomeration technique [75]. The micromeritic and drug release properties of the agglomerates are improved as well. About low dose drugs, diluents are applied for the enlargement of size in the crystal-co-agglomeration technique. Diluents should be inert and inexpensive. They should also be insoluble in aqueous phase so that the drug loss through the continuous or external phase be avoided [74].

In preparation of directly compressible agglomerates, excipients should have affinity toward the bridging liquid. Talc is a hydrophobic excipient and has preferential wetting with bridging liquid therefore is a suitable excipients for incorporation in the crystallo-co-agglomeration process [30, 71, 74].

6.2. Advantages of crystallo-co-agglomerates

Agglomerates which are prepared using crystallo-co-agglomeration technique have numerous advantages compared to other spherical agglomeration methods. Excellent flow properties, large surface area and less chances of dose dumping from final crystals are some of these advantages. Large surface area leads to uniform distribution of the drug through gastro-intestinal tract and therefore better absorption and bioavailability is achieved and the toxicity is also reduced.

Unlike SA, CCA is utilizable for size enlargement of all, low dose, high dose, single, two, or more drugs in combination with or without diluent [78].

Furthermore, the single step generation of agglomerate, less processing cost, less number of unit operations and simplicity of the process adapted it to an economic method. In fact, simplicity and capability to generate spherical agglomerates in a single step are the reasons for the unique place of crystallo-co-agglomerates technique in the oral drug delivery route. By crystallo-co-agglomerates technique and proper selection of suitable excipients and polymers, modified release of drug substances from drug-loaded agglomerates is achievable [30, 71, 74]. It is also possible to create placebo drugs by producing agglomerates of plain excipients (talc agglomerates) [74].

7. Conclusion

Spherical crystallization is the novel particle design technique, in that crystallization and agglomeration may be carried out simultaneously in one step and could be able to transform the fine crystals into a spherical shape directly. In consequence of these modifications, certain micrometric properties may also be modified. Then this technique is an efficient method in the optimization of crystal properties for modifying the required micrometric and dissolution properties of the drugs. In this method, agglomerates with higher bulk density, better flowa-bility and compactibility will be obtained. Then the spherical crystallization can be applied for manufacturing spherical crystals of poorly soluble drugs in order to improve their flowability and compactibility properties. This technique also is helpful in improving wettability, bioavailability and dissolution rate of these types of drugs. An optimized spherical crystalli-zation process, concerning the form of the agglomerates and reproducibility of the product, can be applied as an attractive approach for direct tabletting. The final tablet dosage form prepared using spherical crystallization technique exhibits improvements in strength, hardness, friability, disintegration profile and dissolution rate compared to those prepared using granulation method. As a noticeable point, proper selection of solvent, bridging liquid and diluents has an influence on the release, dissolution, absorption and bioavailability of the

drug substance and reduce toxicity as well. Agglomerates prepared by crystallo-co-agglomeration technique have numerous advantages over the spherical agglomerates. Spherical agglomeration could not be employed for low-dose or poorly compressible materials due to hydrophobic nature of the most excipients. In crystallo-co-agglomeration process, designing of agglomerates containing two drugs or a low-dose or poorly compressible drug in combination with diluents is possible. On the whole, spherical crystallization technique seems to be promising technique in which the drug crystals are changed by applying different solvents for obtaining direct compressible spherical agglomerates. This leads to save money and time in tablet making processes. If it is able to scale up, the direct compression of poorly compressible drugs will be feasible. Other agglomeration techniques are still less economical than direct compression tabletting. As an important point, in this process the residues of organic solvent after the formation of agglomerates should be monitored.

Author details

Yousef Javadzadeh[*], Zhila Vazifehasl, Solmaz Maleki Dizaj and Masumeh Mokhtarpour

*Address all correspondence to: javadzadehy@yahoo.com

Drug Applied Research Center and Faculty of Pharmacy, Tabriz University of Medical Sciences, Iran

References

[1]   Wening K, Breitkreutz J. Oral drug delivery in personalized medicine: unmet needs and novel approaches. International journal of pharmaceutics. 2011;404(1):1-9.

[2]   Shekunov BY, York P. Crystallization processes in pharmaceutical technology and drug delivery design. Journal of crystal growth. 2000;211(1):122-36.

[3]   Mullin JW. Crystallization: Butterworth-Heinemann; 2001 ,Technology & Engineering - 600 pages.

[4]   Rodríguez-hornedo N, Murphy D. Significance of controlling crystallization mechanisms and kinetics in pharmaceutical systems. Journal of pharmaceutical sciences. 1999;88(7):651-60.

[5]   Chaudhary A, Nagaich U, Gulati N, Sharma V, Khosa R. Enhancement of solubilization and bioavailability of poorly soluble drugs by physical and chemical modifications: a recent review. J Adv Pharm Educ Res. 2012;2(1):32-67.

[6]   Vedantam S, Ranade VV. Crystallization: Key thermodynamic, kinetic and hydrodynamic aspects. Sadhana. 2013;38(6):1287-337.

[7] Normah I, Cheow C, Chong C. Crystal habit during crystallization of palm oil: effect of time and temperature. International Food Research Journal. 2013;20(1):417-22.

[8] Prathipati S, Ganesan V. Spherical crystallization: a method to improve physico-chemical properties. Int J Pharm Sci Review and Res. 2011;6(1):60-3.

[9] Javadzadeh Y, Hamedeyazdan S, Asnaashari S. Recrystallization of Drugs: Significance on Pharmaceutical Processing. In: Sztwiertnia K, editor.2012

[10] Hammouda Y, El-Khordagui L, Darwish I, El-Kamel A. Manipulation of powder characteristics by interactions at the solid–liquid interface: 1-sulphadiazine. European journal of pharmaceutical sciences. 1999;8(4):283-90.

[11] Javadzadeh Y, Mohammadi A, Khoei NS, Nokhodchi A. Improvement of physicomechanical properties of carbamazepine by recrystallization at different pH values. Acta pharmaceutica. 2009;59(2):187-97.

[12] Adibkia K, Bozorgmehr Z, Dastmalchi S, Shokri K, Shahlavie P, Javadzadeh Y. Evaluating retardation and physicochemical properties of co-ground mixture of Na-diclofenac with Magnesium stearate. Research in Pharmaceutical Sciences. 2012;7(5):S657.

[13] Nokhodchi A, Maghsoodi M. Preparation of spherical crystal agglomerates of naproxen containing disintegrant for direct tablet making by spherical crystallization technique. AAPS PharmSciTech. 2008;9(1):54-9.

[14] Di Martino P, Di Cristofaro R, Barthelemy C, Joiris E, Palmieri Filippo G, Sante M. Improved compression properties of propyphenazone spherical crystals. International journal of pharmaceutics. 2000;197(1):95-106.

[15] Bharti N, Bhandari N, Sharma P, Singh K, Kumar A. Spherical Crystallization: A Novel Drug Delivery Approach. Asian journal of biomedical and pharmaceutical sciences. 2013;3(18):10-6.

[16] Mahanty S, Sruti J, Patra CN, Rao MB. Particle design of drugs by spherical crystallization techniques. Int J Pharm Sci Nanotech. 2010;3:912-8.

[17] Gupta M, Srivastava B, Sharma M, Arya V. Spherical crystallization: A tool of particle engineering for making drug powder suitable for direct compression. Int J Pharm Res Devt. 2010;1:1-10.

[18] Parida R. Evaluation parameters for spherical agglomerates formed by spherical crystallization technique. Int J Pharm Biol Sci. 2010;1:1-10.

[19] Paradkar A, Pawar A, Chordiya J, Patil V, Ketkar A. Spherical crystallization of celecoxib. Drug development and industrial pharmacy. 2002;28(10):1213-20.

[20] Nokhodchi A, Maghsoodi M, Hassan-Zadeh D, Barzegar-Jalali M. Preparation of agglomerated crystals for improving flowability and compactibility of poorly flowable and compactible drugs and excipients. Powder technology. 2007;175(2):73-81.

[21] Maghsoodi M. How spherical crystallization improves direct tableting properties: a review. Advanced pharmaceutical bulletin. 2012;2(2):253.

[22] Jbilou M, Ettabia A, Guyot-Hermann A-M, Guyot J-C. Ibuprofen agglomerates preparation by phase separation. Drug development and industrial pharmacy. 1999;25(3): 297-305.

[23] Kawashima Y. New processes—application of spherical crystallization to particulate design of pharmaceuticals for direct tabletting and coating and new drug delivery systems. Powder technology and pharmaceutical processes handbook of powder technology. 1994;9:493-512.

[24] Krishna E, Gupta DVRM, Jyothi S. Sherical cristallization- a modern technique for direct compression of pharmaceutical substances. Asian journal of pharmaceutical and Clinical Research. 2012;5(4):114-7.

[25] Kovačič B, Vrečer F, Planinšek O. Spherical crystallization of drugs. Acta pharmaceutica. 2012;62(1):1-14.

[26] Patil S, Sahoo S. Pharmaceutical overview of spherical crystallization. Der Pharmacia Lettre. 2010;2(1):421-6.

[27] Patil S, Sahoo S. Spherical Crystallization: a method to improve tabletability. Research Journal of Pharmacy and Technology. 2009;2(2):234-7.

[28] Patil S, Sahoo S. Improvment in compressibility, flowability and release of glibenclamide by spherical crystallization with additives. Digest journal of nanomaterials & biostructures (DJNB). 2011;6(4).

[29] Ikegami K, Kawashima Y, Takeuchi H, Yamamoto H, Isshiki N, Momose D-i, et al. Primary crystal growth during spherical agglomeration in liquid: designing an ideal dry powder inhalation system. Powder technology. 2002;126(3):266-74.

[30] Ribardiere A, Tchoreloff P, Couarraze G, Puisieux F. Modification of ketoprofen bead structure produced by the spherical crystallization technique with a two-solvent system. International journal of pharmaceutics. 1996;144(2):195-207.

[31] Huang AY, Berg JC. Gelation of liquid bridges in spherical agglomeration. Colloids and surfaces :A physicochemical and engineering aspects. 2003;215(1):241-52.

[32] Yadav A, Bhagat N, Mastud P, Khutale R. An Overview of Optimization of Spherical Crystallisation Process.

[33] Chourasia M, Jain NK, Jain S, Jain N, Jain S. Preparation and characterization of agglomerates of flurbiprofen by spherical crystallization technique. Indian journal of pharmaceutical sciences. 2003;65(3):287-91.

[34] Kawashima Y, Okumura M, Takenaka H. The effects of temperature on the spherical crystallization of salicylic acid. Powder technology. 1984;39(1):41-7.

[35] Deshpande M, Mahadik K, Pawar A, Paradkar A. Evaluation of spherical crystalliza-
tion as a particle size enlargement technique for aspirin. Indian journal of pharma-
ceutical sciences. 1997;59(1):32.

[36] Martino PD, Barthelemy C, Piva F, Joiris E, Palmieri G, Martelli S. Improved dissolu-
tion behavior of fenbufen by spherical crystallization. Drug development and indus-
trial pharmacy. 1999;25(10):1073-81.

[37] Viswanathan CL, Kulkarni SK, Kolwankar DR. Spherical agglomeration of mefenam-
ic acid and nabumetone to improve micromeritics and solubility: A technical note.
AAPS PharmSciTech. 2006;7(2):E122-E5.

[38] Maghsoodi M, Hassan-Zadeh D, Barzegar-Jalali M, Nokhodchi A, Martin G. Im-
proved compaction and packing properties of naproxen agglomerated crystals ob-
tained by spherical crystallization technique. Drug development and industrial
pharmacy. 2007;33(11):1216-24.

[39] Chourasia M, Vijaya R, Jain N, Jain S, Jain S, Jain N. Preparation and characterization
of spherical crystal agglomerates for direct tableting by the spherical crystallization
technique. Indian drugs-Bombay. 2004;41(4):214-20.

[40] Kumar S, Chawla G, Bansal AK. Spherical crystallization of mebendazole to improve
processability. Pharmaceutical development and technology. 2008;13(6):559-68.

[41] Tapas AR, Kawtikwar PS, Sakarkar DM. Spherically agglomerated solid dispersions
of valsartan to improve solubility, dissolution rate and micromeritic properties. Inter-
national journal of drug delivery. 2011;2(4).

[42] Gupta V, Mutalik S, Patel M, Jani G. Spherical crystals of celecoxib to improve solu-
bility, dissolution rate and micromeritic properties. Acta pharmaceutica. 2007;57(2):
173-84.

[43] Kawashima Y, Imai M, Takeuchi H, Yamamoto H, Kamiya K, Hino T. Improved
flowability and compactibility of spherically agglomerated crystals of ascorbic acid
for direct tableting designed by spherical crystallization process. Powder technology.
2003;130(1):283-9.

[44] Szabó-Révész P, Göczõ H, Pintye-Hódi K, Erõs I, Hasznos-Nezdei M, Farkas B. De-
velopment of spherical crystal agglomerates of an aspartic acid salt for direct tablet
making. Powder technology. 2001;114(1):118-24.

[45] Pawar AP, Paradkar AR, Kadam SS, Mahadik KR. Crystallo-co-agglomeration: A
novel technique to obtain ibuprofen-paracetamol agglomerates. AAPS PharmSci-
Tech. 2004;5(3):57-64.

[46] Katta J, Rasmuson ÅC. Spherical crystallization of benzoic acid. International journal
of pharmaceutics. 2008;348(1):61-9.

[47]   Usha AN, Mutalik S, Reddy MS, Ranjith AK, Kushtagi P, Udupa N. Preparation and, in vitro, preclinical and clinical studies of aceclofenac spherical agglomerates. European journal of pharmaceutics and biopharmaceutics. 2008;70(2):674-83.

[48]   Dixit M, Kulkarni P, Subhash P, Reddy R. Spherical agglomeration of indomethacin by solvent change method. International journal of pharma research and development online. 2010;2(9).

[49]   Kawashima Y. Development of spherical crystallization technique and its application to pharmaceutical systems. Archives of pharmacal research. 1984;7(2):145-51.

[50]   Pawar A, Paradkar A, Kadam S, Mahadik K. Agglomeration of ibuprofen with talc by novel crystallo-co-agglomeration technique. AAPS PharmSciTech. 2004;5(4):30-5.

[51]   Mishra VK, Dwivedi S, Sakalle P, Jain G, Gupta D, Gupta D. Method development for spherical crystallization of glibenclamide and evaluation of micromeritic properties. Drug invention today. 2010;2(2):119-22.

[52]   Kawashima Y, Niwa T, Takeuchi H, Hino T, Itoh Y, Furuyama S. Characterization of polymorphs of tranilast anhydrate and tranilast monohydrate when crystallized by two solvent change spherical crystallization techniques. Journal of pharmaceutical sciences. 1991;80(5):472-8.

[53]   Kawashima Y, Aoki S, Takenaka H, Miyake Y. Preparation of spherically agglomerated crystals of aminophylline. Journal of pharmaceutical sciences. 1984;73(10): 1407-10.

[54]   Jadhav N, Pawar A, Paradkar A. Design and evaluation of deformable talc agglomerates prepared by crystallo-co-agglomeration technique for generating heterogenous matrix. AAPS PharmSciTech. 2007;8(3):E61-E7.

[55]   Dixit M, Kulkarni P, Kini AG. Spherical agglomeration of ketoprofen by solvent change method. International journal of pharmaceutical sciences review & research. 2010;4(3).

[56]   Goczo H, et al. Development of spherical crystals of acetylsalicylic acid for direct tablet-making. Chemical and pharmaceutical bulletin. 2000;48(12):1877-81.

[57]   Chavda V, Maheshwari RK. Tailoring of ketoprofen particle morphology via novel crystallocoagglomeration technique to obtain a directly compressible material. Asian journal of pharmaceutics. 2008;2(1):61.

[58]   Thati J, Rasmuson ÅC. On the mechanisms of formation of spherical agglomerates. European journal of pharmaceutical sciences. 2011;42(4):365-79.

[59]   Kawashima Y, Furukawa K, Takenaka H. The physicochemical parameters determining the size of agglomerate prepared by the wet spherical agglomeration technique. Powder technology. 1981;30(2):211-6.

[60]   Kawashima Y, Cui F, Takeuchi H, Niwa T, Hino T, Kiuchi K. Parameters determining the agglomeration behaviour and the micromeritic properties of spherically ag-

glomerated crystals prepared by the spherical crystallization technique with miscible solvent systems. International journal of pharmaceutics. 1995;119(2):139-47.

[61] Teychené S, Sicre N, Biscans B. Is spherical crystallization without additives possible? Chemical Engineering Research and Design. 2010;88(12):1631-8.

[62] Raghavan S, Trividic A, Davis A, Hadgraft J. Crystallization of hydrocortisone acetate: influence of polymers. International journal of pharmaceutics. 2001;212(2): 213-21.

[63] Wypych G. Handbook of solvents: ChemTec Publishing; 2001, New York.

[64] Adibkia K, Hamedeyazdan S, Javadzadeh Y. Drug release kinetics and physicochemical characteristics of floating drug delivery systems. Expert opinion on drug delivery. 2011;8(7):891-903.

[65] Kawashima Y, Naito M, Lin S, Takenaka H. An experimental study of the kinetics of the spherical crystallization of aylline sodium theophylline monohydrate. Powder technology. 1983;34(2):255-60.

[66] Bos A, ZUIDERWEGI F. Size of agglomerates in batchwise suspension agglomeration. Chemical engineering research & design. 1987;65(2):187-94.

[67] Tambo N, Watanabe Y. Physical aspect of flocculation process—I: Fundamental treatise. Water Research. 1979;13(5):429-39.

[68] Maghsoodi M, Derakhshandeh K, Yari Z. On the mechanism of agglomeration in suspension. Advanced pharmaceutical bulletin. 2012;2(1):25.

[69] Kulkarni P, Nagavi B. Review article-spherical crystallization. Indian journal of pharmaceutical education. 2002;36(2):66-73.

[70] Thati J. Particle engineering by spherical crystallization: Mechanisms and influence of process conditions (Doctoral thesis). 2011.

[71] Garala K, Patel J, Patel A, Raval M, Dharamsi A. Influence of excipients and processing conditions on the development of agglomerates of racecadotril by crystallo-co-agglomeration. International journal of pharmaceutical investigation. 2012;2(4):189.

[72] Gohel M, Jogani PD. A review of co-processed directly compressible excipients. J Pharm Pharm Sci. 2005;8(1):76-93.

[73] Alsaidan SM, Alsughayer AA, Eshra AG. Improved dissolution rate of indomethacin by adsorbents. Drug development and industrial pharmacy. 1998;24(4):389-94.

[74] Paradkar AR, Pawar AP, Jadhav NR. Crystallo-co-agglomeration: A novel particle engineering technique. Asian journal of pharmaceutics. 2010;4(1):4.

[75] Jolly CM, Lekshmi P, Constantine I, Bijin E, Valsalakumari J, Pramod K. Crystallo-co-Agglomeration: An innovative technique for size enlargement and improved flow

properties of Powders. Research & reviews: Journal of material sciences. 2013;1(2): 1-14.

[76] Shoyele SA, Cawthorne S. Particle engineering techniques for inhaled biopharmaceuticals. Advanced drug delivery reviews. 2006;58(9):1009-29.

[77] Raval MK, Sorathiya KR, Chauhan NP, Patel JM, Parikh RK, Sheth NR. Influence of polymers/excipients on development of agglomerated crystals of secnidazole by crystallo-co-agglomeration technique to improve processability. Drug development and industrial pharmacy. 2013;39(3):437-46.

[78] Kadam S, Mahadik K, Paradkar A. A process for making agglomerates for use as or in a drug delivery system. Indian patent(NO. 183036), 14 Feb 1997.

Advances in Lipids Crystallization Technology

Maria Aliciane Fontenele Domingues, Ana Paula Badan Ribeiro,
Theo Guenter Kieckbusch, Luiz Antonio Gioielli, Renato Grimaldi,
Lisandro Pavie Cardoso and Lireny Aparecida Guaraldo Gonçalves

Additional information is available at the end of the chapter

http://dx.doi.org/10.5772/59767

1. Introduction

In recent years, the industrial sector of oils and fats has become an important area of research and technological development. The number of studies related to the physical properties of oils and fats has been increasing; these properties are broadly the melting and crystallization behavior and the crystalline and oxidative stability of oils and fats.

The crystallization behavior of lipids has important implications in the industrial processing of food products whose physical characteristics depend largely on fat crystals. Such products include chocolates, margarines, spreads, fats for confectionery and bakery, dairy products, and commonly used shortenings [1]. Meanwhile, crystallization is the most important physical problem of oils and fats [2], particularly problems such as unwanted polymorphic transitions, oil exudation, the development of fat bloom, formation of crystalline agglomerates, and fatty bases with a maximum solid fat content or incompatibility of induction periods with certain industrial applications. Thus, recent research has focused on understanding the phenomena involved in the crystallization of lipids in an attempt to achieve effective solutions to stabilize or modify this process, depending on the nature of the raw material and its industrial application. To that effect, the use of emulsifying agents as crystallization modifiers has marked the trend of research in the oils and fats field. In the past, studies were based on the effect of emulsifiers on the crystallization of pure triglycerides or model systems [3, 4, 5], while recent research has focused on the effect of emulsifiers on the crystallization properties of different types of fats such as milk fat [6, 7, 8], low-trans fats [9, 10], palm oil and its fractions [11, 12], cocoa butter [13], in the crystallization of emulsions [14, 15], and production of organogels, which constitute the structuring oils of emulsifiers [16]. While studying the effects of emulsifiers in fatty systems is of great interest for the improvement of industrial bases, particularly

with respect to fat for use in chocolate, confectionery, and baking, there is limited research on the role of these compounds as crystallization modifiers of natural and commercial fats [17].

Crystallization of lipids is a serious problem in the food industry with respect to actual industrial processes and post-crystallization events. The crystallization issue presents additional aggravating considerations related to climatic differences between countries and the transport and storage conditions imposed by long distances between producing regions and final distribution regions. Thus, there is a need for appropriate solutions for processes involving crystallization and stabilization of raw materials of significant industrial relevance, such as palm oil and fractionated and interesterified fats, which are now replacing partially hydrogenated fats (or trans fats) in most industrial applications. Therefore, the topic discussed in this chapter is highly relevant to the oils and fats production sector.

2. Oils and fats

Edible oils and fats are essential nutrients of the human diet, playing a vital role in providing essential fatty acids and energy. Chemically, natural oils and fats consist of multi-component mixtures of triacylglycerols (TAGs), which are glycerol esters and fatty acids. Additionally, polar lipids (minority lipids) such as diacylglycerols (DAGs),monoacylglycerols (MAGs), free fatty acids, phospholipids, glycolipids and sterols are found solubilized in the triacylglycerol matrix. The triacylglycerol composition determines the physical properties of oils and fats, affecting the structure, stability, flavor, aroma, storage quality, and sensory and visual characteristics of foods [18].

The physical properties of an oil or fat are of fundamental importance to determine its use. This is particularly true for a large quantity and variety of oils and fats used in various forms, including foods. The difference between the words "oil" and "fat" refers to a fundamental physical property, the fluidity or consistency at room temperature. The components of fat characterize it as a material composed of an intimate mixture in the liquid and solid phases, and its physical state can vary from a viscous fluid to a solid or brittle plastic [19].

3. Physical properties of oils and fats

3.1. Crystallization behavior

Plastic fats consist of a lattice network in a continuous oil matrix. The crystallization process is a spontaneous ordering of the system, characterized by the total or partial restriction of movement caused by physical or chemical links between the triacylglycerol molecules. Differences in crystal shapes result from different molecular packings. A crystal, therefore, consists of molecules arranged in a fixed pattern known as a lattice. Its high degree of molecular complexity allows the same set of TAGs be packaged into several different and relatively stable structures [20].

Crystallization of fats determines important properties of foods, including: (i) the consistency and plasticity of fat-rich products such as butter, margarine and chocolate during the stages of production and storage; (ii) sensory properties such as the melting sensation in the mouth; (iii) physical stability with respect to the formation and settling of crystals, oil exudation and coalescence of particles and emulsions; and (iv) visual appearance, for example the shininess of chocolates and toppings [21]. In most foods, isolated crystallization of TAGs is considered the event of greatest importance, although the crystallization of minority lipids such as DAGs, MAGs and phospholipids plays a fundamental role in the quality of various products [22].

3.1.1. Crystallization mechanism of the lipids

Crystallization is generally divided into four distinct phases. Initially, in order to obtain the formation of crystals from the liquid state, the system must reach the supersaturation zone, in which there is a driving force for crystallization. Once the appropriate driving force to overcome the energy barrier for crystallization is reached, nucleation occurs and molecules in the liquid state join together to create a stable nucleus. After the formation of stable nuclei, a rapid transition to the next stage of crystallization occurs, crystal growth, i.e., during which additional molecules (or growth units) are incorporated into the crystal lattice, decreasing the driving force of supersaturation. Unless restricted by a kinetic constraint, growth continues until the system reaches equilibrium, at which the driving force for crystallization approaches zero and the maximum volume of the crystal phase is obtained [23].

3.1.2. Nucleation

According to Boistelle [24], nucleation involves the formation of molecule aggregates that exceed a critical size, and are therefore stable. Once a crystal nucleus has formed, it begins to grow due to the incorporation of other molecules from the adjacent liquid layer that is continuously filled by the supersaturated liquid surrounding the crystal [24].

A crystal nucleus is the smallest crystal that can exist in solution at a given temperature and concentration. The formation of a nucleus from the liquid phase, i.e., the nucleation process, requires the organization of molecules in a crystalline lattice of critical size after overcoming an energy barrier. The mechanisms of nucleation are generally classified as primary nucleation, which can be homogeneous or heterogeneous, and secondary nucleation. It is currently suggested that nucleation occurs via a two-step process. Molecular oscillations in the liquid phase lead to local organization of molecules into amorphous clusters (instead of crystal embryos, as postulated by classical nucleation theory – Gibbs, 1800), which then aggregate to form an amorphous cluster of critical size. This formation of amorphous aggregates is the first step in nucleation. At some point the molecules in the cluster are transformed into a crystalline structure, which is the second step for the formation of a stable nucleus. The combination of these two events characterizes the induction time before the onset of visual nucleation. This type of nucleation, however, rarely occurs under the conditions of industrial processes. In practice, nucleation is usually dominated by the heterogeneous mechanism in the majority of systems, where external surfaces or catalytic sites, such as molecules of different composition, are used to reduce the energy barrier. Although the exact mechanism of heterogeneous

nucleation is not yet fully elucidated, the phenomenon can be described as the result of interactions between the solid particle and the supersaturated fluid, causing the local ordering of molecules for formation of the nucleus. Secondary nucleation is the formation of a new nucleus in the presence of existing crystals, which may occur if microscopic crystalline elements are separate from an already formed surface, thus resulting in crystal fracture into small stable nuclei [22, 23, 25, 26].

When the nuclei formed achieve favorable dimensions, these elements become crystallites whose growth depends not only on external factors (supersaturation, solvents, temperature, impurities), but also internal factors (structure, connections, defects). Consequently, the crystal growth rate can vary by several orders of magnitude. Growth occurs by binding of molecules to a crystalline surface. At the same time, molecules are also detached. There is a continuous movement of molecules on the crystal surface, and the result of these processes determines the rate of growth, which is directly proportional to subcooling and varies inversely with the viscosity of the system [21]. Although nucleation and crystal growth are often considered separate events, they are not mutually exclusive. Nucleation also occurs as crystals grow from existing nuclei [27].

3.1.3. Recrystallization

Recrystallization was defined by Fennema [28] as any change in the number, size, shape, orientation or perfection of the crystals after completion of initial solidification.

The basic mechanism of the recrystallization process is size-dependent equilibrium (melting temperature or solubility) documented by the Gibbs-Thomson effect. Small crystals, due to the small radius of curvature of the surface, are slightly more soluble or have a slightly lower melting point than larger crystals. Over time, these differences promote the disappearance of small crystals and growth of larger crystals. These changes generally occur without a change in volume of the crystalline phase, and are driven by the difference in thermodynamic equilibrium based on the size of the crystals. These crystals occur slowly at a constant temperature, but their presence increases with temperature swings as the phenomenon referred to as Melting-Recrystallization becomes dominant. When the temperature rises during a temperature cycle, the crystals melt or dissolve to maintain phase equilibrium. The small crystals, which are less stable, disappear first. When the temperature starts to decrease during the temperature cycle, the volume of the crystal phase increases, but only by growing and without the formation of new nuclei. The mass of small crystals that melted is redispersed among the larger crystals. As the average size of the crystals increases, the number of crystals decreases as a result of these thermodynamic effects. Thus, a dispersion of many small crystals tends to minimize the surface energy (and surface area) by recrystallization [23, 29].

The final stage of crystallization in foods occurs during storage, and a population of crystals undergoes a recrystallization step, reaching a more broad equilibrium state. This phenomenon is of primary concern during storage of foods, and is responsible for changes to the texture of ice cream, fat bloom in chocolates and toppings and exudation of oil in products rich in fat. In lipid systems, the recrystallization process involves changes to the internal arrangement of the crystalline structure via polymorphic transformation [30].

3.1.4. Crystallization kinetics

Crystallization kinetics intensively influences the final structure of fats and shows to be closely related to their rheological and plasticity properties. When monitoring the formation of the solid crystalline material with respect to time it is possible to verify the nature of the crystallization process. Characterization of crystallization kinetics can be performed according to the induction time (τ_{SFC}) or the nucleation period (relative to the beginning of crystal formation) and the maximum solid fat content-SFC_{max}. The induction time reflects the time required for formation of a stable nucleus of critical size in the liquid phase [31]. As a definition, the τ_{SFC} is the time required for obtaining one crystalline nucleus per unit volume. The τ_{SFC} generally increases with increasing isothermal crystallization temperature and decrease of the sample melting point. Another useful parameter for evaluating isothermal crystallization is the crystallization stability time (t_{cs}), defined as the total time for stabilization of the solid fat content at a given temperature. This parameter consists of the sum of the time characteristics for nucleation and crystal growth [32].

The model most widely used to describe the kinetics of isothermal phase transformation is the Avrami model, developed in 1940, which relates the kinetics determined experimentally with the form of growth and final structure of the crystal lattice [33]. The Avrami equation gives an indication of the nature of the crystal growth process and is given by

$$\frac{SFC\,(t)}{SFC\,(\infty)} = 1 - e^{-kt^n} \,, \tag{1}$$

where *SFC(t)* describes the solid fat content (%) as a function of time, *SFC(∞)* is the limit of the solid fat content when time tends to infinity, k is the Avrami constant (min^{-n}), which takes into account both nucleation and growth rate of the crystals and n is the Avrami exponent, which indicates the mechanism of crystal growth [27]. The crystallization half-life ($t_{1/2}$) reflects the magnitude k and n according to the relationship

$$t_{1/2} = \left(\frac{0.693}{k}\right)^{1/n} \,. \tag{2}$$

Currently, the most common analytical technique for the investigation of crystallization kinetics of fats is nuclear magnetic resonance (NMR). However, various analytical techniques such as differential scanning calorimetry (DSC), polarized light microscopy (PLM), as well as rheological and turbidimetric techniques can be successfully employed. Understanding of the phenomena involved in crystallization kinetics is improved when considering combined use of various instrumental methods [34].

3.1.5. Polymorphism

Long-chain compounds, such as fatty acids and their esters, may exist in different crystal forms. Solids of the same composition which may exist in more than one crystal form are called polymorphs. Polymorphism can be defined in terms of the manifestation ability of different cellular structures, resulting from different molecular packings. The crystal habit is defined as

the crystal shape. From a crystallographic perspective, the habit reflects the growth direction within the crystal, while morphology outlines the set of faces determined by the symmetrical components of the crystal. This distinction allows crystals of the same morphology to present different crystal habits [26].In fat, crystals are solids with atoms arranged in a regular three-dimensional pattern. A cell is the repeating unit that makes up the complete structure of a given crystal. A sub-cell, in turn, is the smallest structure in the real unit of the cell, defined as the mode of transverse packing of aliphatic chains in the TAGs. The polymorphic forms of a fat are identified based on their sub-cell structure [24]. In lipids three specific sub-cell types predominate, referring to the polymorphsα, β′ and β, according to current polymorphic nomenclature (Figure 1). The α form is metastable with hexagonal chain packing. The β′ form has intermediate stability and orthorhombic perpendicular packing, while the β form has greater stability and triclinic parallel packing. The melting point increases with increasing stability ($\alpha \rightarrow$ β′ $\rightarrow$β), as a result of differences in the molecular packing density [35].

The polymorphic nature of the TAGs is well established. It is also well-known that the mixing of different fatty acid fractions in a TAG produces a more complex polymorphic behavior. Thus, saturated monoacid TAGs present simple polymorphism, followed by TAGs with mixed saturated fatty acids. The mixed saturated/unsaturated fatty acids exhibit more complex polymorphisms [36]. TAGs typically crystallize in the α and β′ forms first, although the β form is most stable. This phenomenon is related to the fact that the β form has a higher free energy of activation for nucleation. Polymorphic transformation is an irreversible transformation process of the less stable form to the more stable form (transformation of the monotrophic stage), depending on the temperature and time involved. At constant temperature, the α and β′ forms can transform, as a function of time, to the β form via the liquid-solid or solid-solid mechanisms [37]. The transformation velocity is dependent on the degree of homogeneity of the TAGs. Fats with low variability of TAGs quickly transform into the stable β form. Fats which consist of a random distribution of TAGs can present the β′ form indefinitely. Additionally, factors such as formulation, cooling rate, heat of crystallization and degree of agitation affect the number and type of crystals formed. However, because fats are complex mixtures of TAGs, at a given temperature the different polymorphic forms and liquid oil can coexist [1].

Fats with a tendency to crystalize in the β′ form include soybean, peanut, canola, corn and olive oil, as well as lard. In contrast, cotton and palm oils, milk fat and suet tend to produce β′ crystals that commonly persist for long periods [21]. In particular, for cocoa butter six polymorphic forms are verified as a result of its unique triacylglycerol composition, wherein symmetrical monounsaturated TAGs predominate. The characteristic nomenclature of cocoa butter polymorphs are based on the roman numeral system (I to VI), where the I form is the least stable and the V form is associated with the desirable crystalline habit in chocolates, which may transform during storage into the VI form, which presents improved stability. However, combinations of this nomenclature with Greek nomenclature are typically encountered, where the forms V and VI are recognized as βV and βVI [38, 39].

The crystal structure of fats is important for the formulation of shortenings, margarines and fat products in general, since each crystal shape has unique properties with respect to plasticity, texture, solubility, and aeration. Fat with crystals in the β′ form present greater functionality,
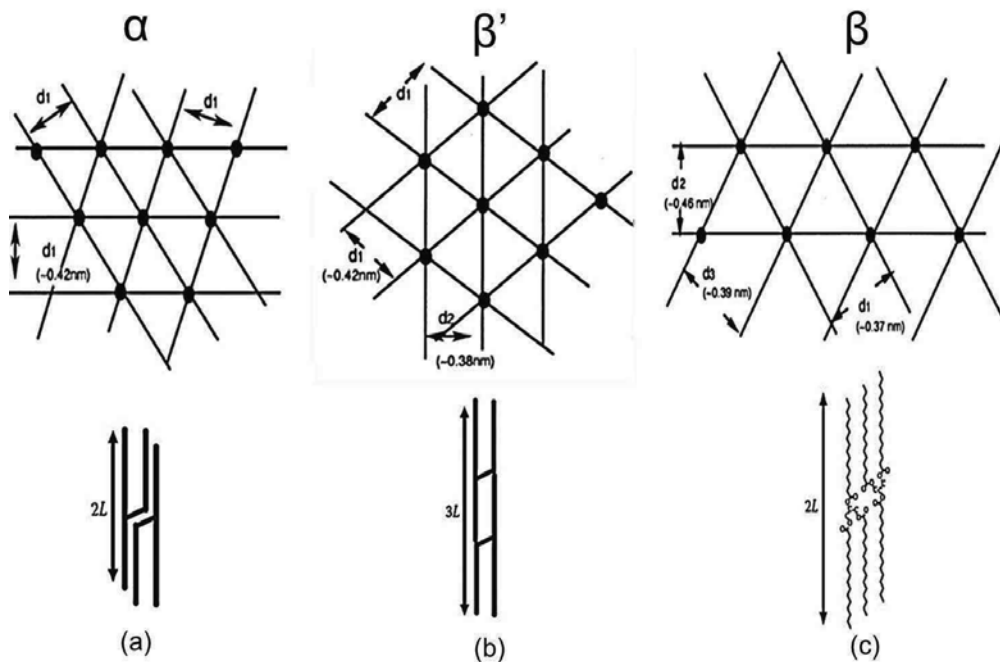
Figure 1. Spatial projections of the crystalline forms α, β 'and β. Packings: (a) H: hexagonal; (b): orthorhombic; (c) T: triclinic [40].

because they are softer and provide good aeration and creaminess properties. Therefore, the β' form is the polymorph of interest for the production of fat-rich foods such as margarine and confectionary and baking products. For the production of chocolates with good physical and sensory characteristics the βV form is the desirable polymorph, since it is associated with properties such as brightness, uniformity, snap characteristic and improved shelf life [18].

X-ray diffraction is an analytical technique used to identify the polymorphism of crystals by determining the dimensions of the crystalline unit and sub-cells. Due to different geometrical configurations, polymorphs diffract x-rays at different angles. In fats, high diffraction angles correspond to short spacings (distances between parallel acyl groups in the TAG) of sub-cells and allow for verifying the different polymorphs [41].

3.1.6. Microstructure

The lipid composition and crystallization conditions influence the crystal habit, i.e., different crystal morphologies are possible. Crystals aggregate into larger structures forming a lattice, which characterizes the microstructural level of a fat. The microstructure concept includes information regarding the state, quantity, shape, size, and spatial and interaction relationship between all components of the crystal lattice and has tremendous influence on the macroscopic properties of fats [42].

According in [43], the microstructural structure or meso-scale of a crystalline lattice for a fat may be defined as the set of structures with dimensions between 0.5μm and 200μm. Its quantification is achieved primarily by visualization of its geometry. Structural levels in a typical crystal lattice are defined when the fat crystallizes after its complete fusion. Like nanostructural elements (0.4-250nm), TAGs crystallize in specific polymorphic states. Most tags crystallize as spherulites, which implies that crystal growth occurs radially. The formed crystals grow to dimensions of 1 to 4 μm and then combine to form agglomerates (larger than 100μm) in a process governed by mass and heat transfer. The aggregation process continues until a continuous three-dimensional network is formed from the combination of these microstructures, trapped in the liquid fat phase [44]. This structural hierarchy has been recognized by several researchers. However, the arrangement of molecules in the crystalline state also depends on factors such as the cooling rate, crystallization temperature and stirring speed, if necessary [45].

Crystal growth can occur in one, two or three dimensions, characterizing the formation of needle, disk, or spherulite-shaped crystals, respectively [46], and these shapes can be predicted from the results shown by the value of the Avrami exponent (n) (Table 1). According in [47], the application of fats in food products requires that the average diameter of the crystals is less than 30μm to avoid a sensation of grittiness in the mouth.

Avrami exponent (n)	Type of crystal growth	Expected nucleation
3+1 = 4	growth of spherulites	sporadic nucleation
3+0 = 3	growth of spherulites	instantaneous nucleation
2+1 = 3	growth of disks	sporadic nucleation
2+0 = 2	growth of disks	instantaneous nucleation
1+1 = 2	growth of rods	sporadic nucleation
1+0 = 1	growth of rods	instantaneous nucleation

(SHARPLES, 1966) [48]

Table 1. Values of the Avrami exponent (n) for different types of crystal nucleation and growth.

Another factor that characterizes the formation of the microstructural network of fats is the fractal dimension. The fractal dimension is a parameter that describes the spatial distribution of the mass within the crystal lattice [44]. Fractal geometry was proposed by Benoit Mandelbrot (1982) as a method for quantifying natural objects with a complex geometrical structure which challenged quantification by regular geometric methods (Euclidean geometry). In classical Euclidean geometry, objects have integer dimensions: the reader would be familiar with the reasoning that a line is one-dimensional, a plain a two-dimensional object and the volume of an object is three-dimensional. Thus, Euclidean geometry is suitable for measuring objects that are ideal, or regular. One can imagine that if enough twists are placed on a line or a plane, the resulting object can be classified as an intermediate between a line and a plane. The dimension

of such an object is fractional (i.e., between 1 and 2 or between 2 and 3) and such an object can be classified as a fractal object, based on the fact that instead of presenting a Euclidean dimension (integer), it has a fractional dimension [49]. One of the most important characteristics of fractal objects is their similarity, in other words, fractals objects look the same in different magnitudes, at least in a certain range of scales.

Most scientific research on crystallization of fats has been directed towards establishing relationships between lipid composition or polymorphism and macroscopic properties of fats, without in-depth consideration of the microstructure of the crystal lattice, which can lead to failures in predicting the macroscopic properties [50]. In Marangoni and Rousseau [51] investigated the possibility that the solid fat content and/or polymorphic shape of the crystals is not determinant for the mechanical properties of mixtures containing milk fat with canola oil, but instead the macroscopic structure of the crystal lattice in the liquid oil matrix. From the study of fractal dimensions and the application of this theory to the rheological study of milk fat with canola oil moistures, it was observed that the fractal dimension (D_b) was the only "indicator" in accordance with the associated changes to the rheology of the product resulting from interesterification. Traditional physical indicators, such as polymorphism and solid fat content, failed to demonstrate the expected changes. Thus, the study confirmed the importance of the fractal dimension, a fundamental indicator of the crystal lattice capable of explaining changes in rheology of fats not attributed to other measurable properties of the network [49]. According in [27], systems with higher fractal dimension values demonstrate higher packing orders of the microstructural elements.

One of the methods most used for calculating the fractal dimension is the box counting method, where grids with length l_i are placed on the micrographs of the crystalline lattice of a fat obtained by the polarized light microscopy technique. Any lattice containing particles above a threshold value is considered an occupied lattice (solid). The number of occupied grids N_i of side length l_i is counted. This process is repeated for grids with different lateral lengths. The fractal dimension of box counting, D_b, is calculated as the opposite slope of the linear regression curve for the log-log graph of the number of occupied grids N_b versus the lateral length l_b, given by

$$D_b = -\frac{\Delta \ln N_b}{\Delta \ln l_b}.$$ (3)

To reduce errors, the grids with extreme sizes should be exempted from the calculation [52]. Polarized light microscopy (PLM) is the most widely used technique for visualization of microstructural network of fats and has been applied so as to explain the differences in texture of fat mixtures, showing crystalline types and morphological alterations in crystal growth [53].

4. Control of crystallization

Control of crystallization to prevent crystal growth or to achieve the desired crystalline attributes is crucial for obtaining high-quality products with long useful life. Understanding

the principles that underlie the crystallization phenomena is necessary to achieve this control [23]. Figure 2 presents a schematic of the crystallization process, storage of fats and associated mechanisms.

The behavior of crystallization, polymorphic transformation and microstructure of a fat is due to a combination of individual physical properties of each TAG and phase behavior of different TAG mixtures. In general, the specific composition of a fat is one of the most important factors for final development of the crystal structure [54].
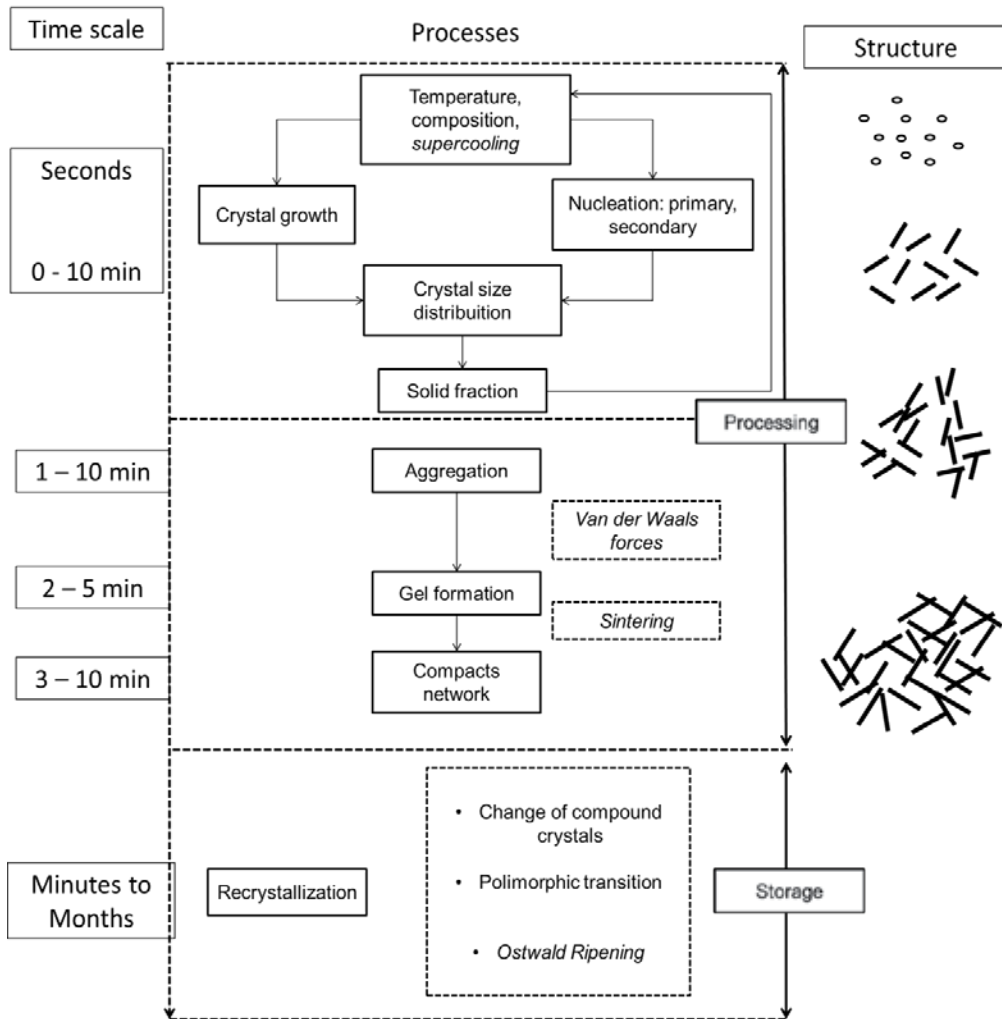

Figure 2. Process schematic of the process involving crystallization and storage of fats. Adapted from [55].

Crystallization of fats is a critical factor associated with the structure and properties of most foods. The stability of many processed food products is influenced by changes in the physical

state of the fats and changes in the crystallization processes, since the events of nucleation and crystal growth occur simultaneously at different rates as they are affected by conditions such as degree and rate of super-cooling, viscosity and agitation [13].

In the initial stages of food processing, the relative rates of nucleation and crystal growth determine the distribution, shape and size of the crystals, parameters that are directly related to the characteristics of consistency and texture. However, during the storage phase, several post-crystallization phenomena may occur, significantly affecting the properties and stability of foods. These include polymorphic transitions to thermodynamically more stable phases, formation of new crystals and crystal growth, and migration of oil or small crystals. It should be noted, however, that such events are not chronological; polymorphic transitions can occur even in the early stages of processing [31].

Additionally, in post-crystallization processes the phenomena known as sintering or bonding of adjacent surfaces can be verified, as well as spontaneous dissolution, also known as Ostwald ripening. The term sintering is described as the formation of solid bridges between fat crystals, with formation of a cohesive network associated with the undesirable increase in the hardness of the fat phase. Ostwald ripening, in turn, is associated with dissolution of previously existing small crystals in the fat phase and development of crystals with undesirable dimensions and weak crystal lattices, which causes loss of consistency of the products [56].

Furthermore, in some specific products the control of crystallization means, above all, avoiding this process, even if it is thermodynamically favored or due to storage or processing conditions [8]. Thus, control of crystallization and polymorphic transitions in fats is a factor of fundamental importance for the food industry.

5. Fats for industrial use

5.1. Interesterified fats

Interesterification is a technological alternative to the partial hydrogenation process, since it enables the production of oils and fats with specific functionalities. Due to the growing concern of the nutritional impact of *trans* fatty acids on health, interesterification has been indicated as the main method for obtaining plastic fats with low levels of *trans* isomers or absence of these compounds. In contrast to hydrogenation, this process does not promote the isomerization of double bonds of fatty acids and does not affect the their degree of saturation [57].

In the interesterification process the fatty acids are rearranged in the glycerol molecule. Interesterification is promoted by an alkaline catalyst (chemical interesterification) or by lipases (enzymatic interesterification). The alkaline catalysts most frequently used are sodium methoxide and sodium ethylate [58]. In chemical interesterification the fatty acids are randomly distributed in the glycerol molecule along the three available positions within each molecule. When specific lipases are used to catalyze the interesterification reaction, rearrangement can occur in the *sn1* and *sn3* positions of the glycerol molecule, maintaining the *sn2* position [59].

Chemical interesterification is currently the process most utilized by industry. The random distribution of fatty acids along the glycerol molecules leads to changes in the triacylglycerol composition, which alters the overall solids profile of the fat. In interesterified fats, the random distribution of fatty acids results in great variability of TAGs, with intermediate melting points (S_2U and U_2S). Such variability in TAGs, associated with the formation of partial acylglycerols, promotes slower crystallization and indefinite maintenance of the polymorphic form β' [58, 60, 61]. Other observations, such as decreased size of the crystals as well as distribution in the crystal lattice, were also observed in some studies [62].

5.2. Palm oil

Palm oil is obtained from the mesocarp of the fruit *Elaesis guineensis*. It is semi-solid at room temperature, consisting primarily of TAGs of palmitic and oleic acids. Palm oil is the vegetable oil most used worldwide in the food industry. In June 2013, world production of palm oil reached 58 million tons, surpassing the production of soybean oil [63]. As a result of increased production, many studies are focused on palm oil, especially regarding its crystallization behavior and nutritional aspects. Compared to other vegetable oils, palm oil presents a unique and differentiated fatty acid composition, containing similar percentages of saturated and unsaturated fatty acids. It also presents a significant content of saturated fatty acids (10 to 16%) in the *sn-2* position of the TAGs, as well as significant levels of palmitic acid (44%). In addition to these features, palm oil contains small percentages of MAGs and DAGs as minor components, which are produced during maturation of palm fruits and oil processing. The DAGs, specifically, correspond to 4-8% of the composition of palm oil, with variations according to origin and processing conditions. The removal of these compounds, however, is difficult even under optimal refining conditions [18, 64, 65].

The crystallization behavior of palm oil is extremely important from a commercial point of view, because it is characterized by the crystal habit β', a fact that, combined with its characteristics of plasticity, ensures its application in margarines, spreads, bakery and confectionery fats, as well as general purpose shortenings. The functional properties of palm oil and its fractions appear to be strongly related to its composition and the quantity and type of crystals formed at the temperature of application. However, the crystals of palm oil require a long time for $\alpha \rightarrow \beta'$ transition, a factor considered inadequate from an industrial process standpoint. Resistance to transformation into β' is mainly attributed to the DAGs. Recent studies on the interactions between TAGs and DAGs in palm oil during crystallization show that the latter have a deleterious effect on the characteristics of crystallization, with intensity proportional to the concentration of these minority lipids in palm oil and its fractions [66, 67]. According in [68], the negative effect of DAGs on the crystallization of palm oil may be related to the low nucleation rate of TAGs in the presence of these compounds.

In addition to the slow crystallization of palm oil, another factor of great concern in industry is its post-processing stability. Palm oil is often associated with hardening problems during storage. In some products based on this raw material, undesired crystal growth occurs which results in gritty texture and poor spreadability [69]. These crystalline shapes may reach dimensions greater than 50 μm after a few weeks of storage, leading to non-uniformity of the

processed products [68]. In margarines, specifically, the formation of crystal agglomerates with mean diameter between 0.1 and 3mm is observed, which can easily be observed with the naked eye [70]. In [71] found that the main TAGs of palm oil, 1-palmityl-2-oleoyl-palmitine (POP) and 1-palmityl-diolein (POO), have limited miscibility with each other, which results in formation of large POP crystals surrounded by POO. When these agglomerates are formed, there occurs the joining of other saturated TAGs in a process that promotes β′ →β transition. Therefore, to ensure the stability of the β′ polymorph in palm oil-based products this is a question of great industrial interest, given the great economic importance associated with the use of this raw material.

5.3. Palm Mid Fraction (PMF)

The product of the first fractionation stage of palm olein is termed the soft palm mid fraction (soft PMF), which presents high levels of monounsaturated triacylglycerols, rapid melting and tendency to crystallize in β′, making it an excellent raw material for the production of margarines and shortenings in general [72, 73].

Classically, two methods are proposed for the production of soft PMF: the olein route (most common in Asia) and the stearin route, which is preferentially used in South America because of the need for olein with high iodine index in the first fractionation stage. The best CBE's are obtained via the olein route, where the second fractionation stage of the triacylglycerols SSU-SUS focuses selectively on soft PMF. In dry fractionation, soft PMF concentrates more than 73% of SSU-SUS triacylglycerols, and the content of SSS triacylglycerols is low. Thus, refractionation of soft PMF produces an excellent hard PMF, particularly enriched in SSU-SUS triglycerides (85%-90%) with low content of SSS triglycerides, and the DAG content can be kept low enough to avoid any adverse effect on the crystallization properties of the fraction [74].

Due to the closely related structural properties, TAGs can produce co-crystals by intersolubility, which frequently present solid solutions, monotectic interactions, eutectic systems and formation of molecular compounds [1]. As a result, the efficiency of fractionation depends not only on the separation efficiency, but is limited by the phase behavior of TAGs in the solid state. Thus, intersolubility of TAGs is a challenge in the dry fractionation process, including the route: olein → soft PMF → hard PMF.

6. Crystallization problems in raw materials of great industrial importance

Most natural oils and fats have limited application in their unaltered forms, imposed by their particular composition of fatty acids and TAGs. Thus, oils and fats for various industrial applications are chemically modified by hydrogenation or interesterification, or physically by fractionation or mixture [75]. Although used for a long time, partial hydrogenation results in significant formation of *trans* fatty acids, associated with negative health effects [76].

In Brazil, controversial issues surrounding the role of *trans* fatty acids in the diet have led to progressive changes in legislation, aiming to include more information for consumers.

Resolution RDC No. 360, of December 23, 2003, approved by the MERCOSUR, obligated the declaration of *trans* fatty acids on the nutritional label of foods. Companies had until July 31, 2006 to meet regulations, so that the *trans* fat content is declared in relation to the standard portion of a certain food, together with statements of total and saturated fats [77]. In response, Brazilian industries opted for the progressive substitution of *trans* fat in many products through the development of base fats with functionality and economic viability equivalent to partially hydrogenated fats, but without substantial increase in the content of saturated fatty acids in foods.

In this sense, interesterification was found to be the main alternative for obtaining plastic fats with low levels of *trans* isomers or lack thereof. In particular, chemical interesterification of liquid oils with fully hydrogenated oils (hardfats) is currently the alternative of greatest versatility to produce zero *trans* fats, producing base fats favorable for the preparation of commonly used shortenings [61]. The use of blends, i.e., mixtures of fats with different physical properties, and fractionation also represent additional alternatives to obtain base fats with appropriate physical and plasticity properties to be used in various products, although with potential limited by the chemical composition of the raw materials [21].

Although the interesterification, fractionation and mixing processes are very functional from a technological point of view, the substitution of partially hydrogenated fats in food products, especially in shortenings and confectionery products, is currently a challenge since appropriate crystallization and texture properties are difficult to obtain in the absence of *trans* fatty acids [78].

In particular, adequacy of crystallization kinetics of these base fats is of utmost importance so that their use may be adjusted to the limitations of industrial processes and to improve control of processing steps that involve recrystallization of the fat fraction, ensuring quality of the final product [79]. Contrarily, previously standardized processing times and equipment must be altered according to the characteristics of the fat used. This fact becomes particularly important as new fat fractions began to replace partially hydrogenated fats in most industrial applications, mainly in the production of biscuits and bakery products, where it is noted that fats with the same apparent solids profile present very different crystallization properties [80]. In the specific case of interesterified fats, the formation of partial acylglycerols, such as MAGs and DAGs as a result of chemical interesterification, can influence the crystallization kinetics via alterations to the crystal nucleation process [81]. According in [82], 0.1% of the catalyst sodium methoxide, used for randomization, can produce between 1.2 and 2.4% of MAGs+DAGs. Because the typical catalyst content used industrially ranges from 0.1 to 0.4%, concentrations of these minority lipids may be greater than 9%. Although minority lipids present influence on the crystallization properties of these fats, their complete removal is still difficult and expensive, especially on a large scale [22].

Considering that in the Brazilian industry this substitution process is relatively recent, the problems of crystallization behavior due to the unsuitability of new fat fractions are numerous and aggravated, mainly due to regional differences in climate and conditions of transport and storage. In this context, highlighted problems include unwanted polymorphic transitions, oil exudation, development of fat bloom, formation of crystalline agglomerates, and base fats with

a maximum solid fat content or induction periods incompatible with certain industrial applications. Studies on modification, stabilization and control of crystallization of these base fats are therefore of crucial importance for development of the edible oils industry.

7. General characteristics of emulsifiers

In a classic definition, an emulsifier is an expression applied to molecules which migrate to interfaces between two physical phases, and are therefore more concentrated in the interfacial region than in the solution phase [83]. The main molecular characteristic of an emulsifier is its amphiphilic nature, characterized by an ionic group (polar region) and a hydrocarbon chain (nonpolar region). According to their polar and nonpolar regions, emulsifiers are designated as hydrophilic or lipophilic, which affects their solubility in water or oil [84]. Thus, the term hydrophilic-lipophilic balance (HLB) was suggested, which measures the affinity of an emulsifier for oil or water. Regarding emulsifiers in foods, lipophilic properties are generally the most important, but the hydrophilic-lipophilic balance (HLB) may vary considerably according to the chemical composition of the emulsifier. The dual affinity of emulsifiers results in the formation of a single phase between initially immiscible substances (emulsion). Furthermore, these compounds perform functions that in some products are not related to emulsification, including modification of the crystal habit during crystallization of oils and fats [83].

The concept of HLB makes it possible to characterize the various emulsifiers or mixtures of emulsifiers. In general, the following guidelines are used for applying an emulsifier based on its HLB:

- HLB of 3-6: a good water/oil emulsifier;

- HLB of 7-9: a good wetting agent;

- HLB of 10-18: a good oil/water emulsifier.

Nevertheless, the HLB value is limited because it provides a one-dimensional description of the emulsifier properties, and omits information such as the molecular weight and temperature dependence. It is also difficult to calculate useful HLB values for various important emulsifiers in food applications (eg: phospholipids). Additionally, HLB values do not include the important crystallization properties of emulsifiers [85].

Regarding the crystallization properties, in the crystal structure of emulsifiers, the predominant factor is the hydrophilic portion which is the relatively larger portion of the molecule. The size of the hydrophilic group, along with the extension and spatial distribution of hydrogen bonding between adjacent groups, has a much larger influence on the molecular packing of the crystal than the nature of the fatty acid chain. A simple emulsifier, such as a monoacylglycerol, generally crystallizes in the double chain length (DCL), while those with larger hydrophilic groups more frequently crystallize in the SCL configuration (Figure 3) [83].
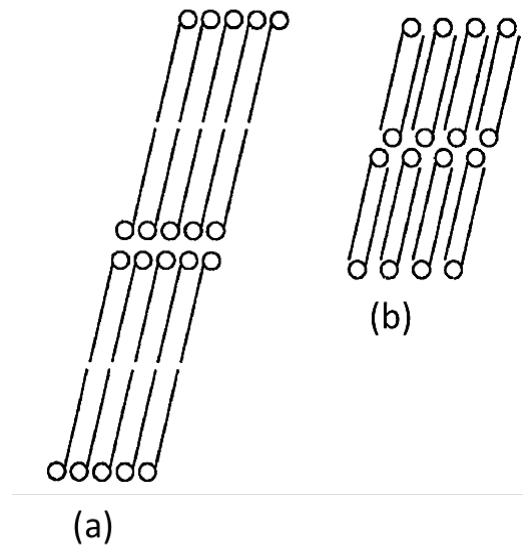
Figure 3. Configurations in (a) DCL (*double chain length*) and (b) SCL (*single chain length*) (STAUFFER, 1999)

Among crystallization properties, an important feature of emulsifiers is their ability to create mesophases. Mixtures of emulsifiers with water form different physical structures, depending on the emulsifier/water ratio and temperature. These mixtures are opalescent dispersions, often called "liquid crystals", but are better known as mesophases. This term (which means "between stages") reflects the nature of the mixture. On a micromolecular level, the emulsifier agent and water are separated phases, but at the macro level the mixture becomes uniform and is stable (that is, the phases do not separate) [86]. Liquid crystals are thermodynamic mesophases of the condensed material with a certain degree of ordering between the crystalline solid and liquid states [87]. There are two main families of liquid crystals: thermotropic and lyotropic. Thermotropic liquid crystals are composed of molecules, or mixture of molecules, which exhibit shape anisotropy (also known as anisometry). These molecules may have the shape of rods (most common), disks and arcs, among others. The structural and ordering differences of these individual molecules occur as a function of temperature, and therefore are called thermotropic. On the other hand, lyotropic liquid crystals are mixtures of amphiphilic molecules and polar solvents, which under determined conditions of temperature, pressure and relative concentrations of different components, present the formation of aggregated molecular superstructures, which are organized in space, showing some degree of order [88]. The amphiphilic molecules such as emulsifiers may present both behaviors (thermotropic and lyotropic) in this case, called amphotropic liquid crystals [88, 89]. A simplified schematic of the formation of some thermotropic and lyotropic mesophase structures is shown in Figure 4.
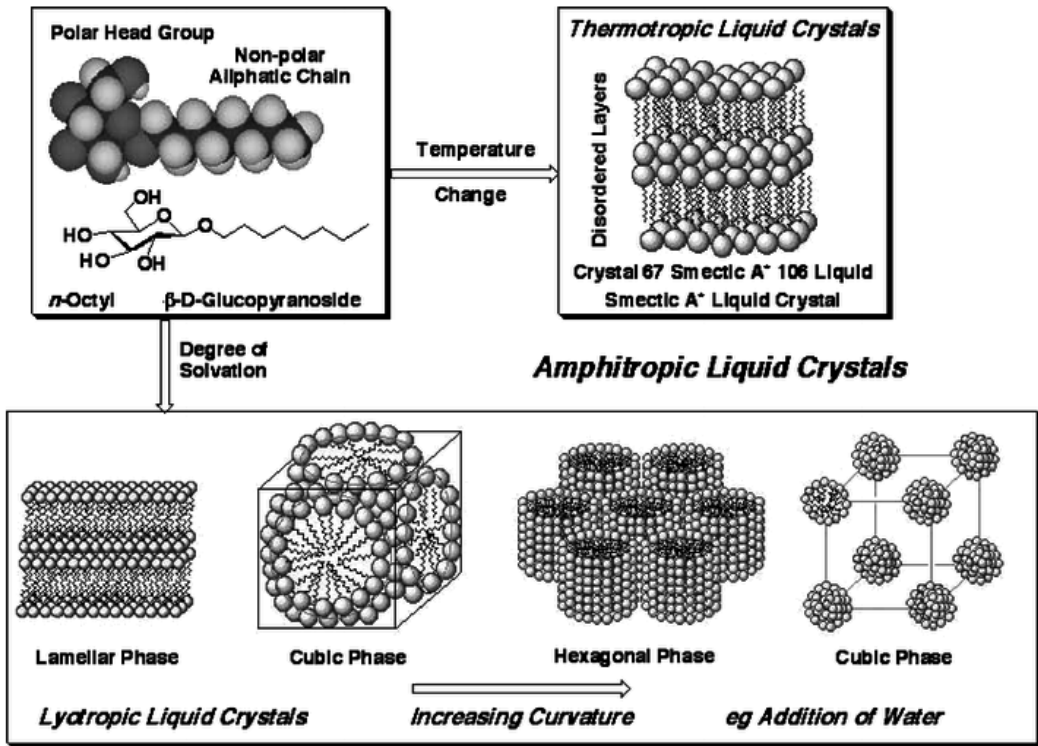
Figure 4. Structural schematic of the thermotropic and lyotropic mesophases formed by n-octyl β-D-glucopyranoside. Adapted from [89].

7.1. Use of emulsifiers as crystallization modifiers

In addition to their known functions of emulsification and stabilization of emulsions, emulsi-fiers can modify the behavior of the continuous phase of a food product, giving it specific benefits. In fat-rich products, emulsifiers may be used to control or modify the crystallization properties of the fat phase. Study of the effects of emulsifiers in fat systems is of great interest to improve industrial products, particularly with respect to fat for use in chocolate, confec-tionery and baking. However, the role of these compounds as modifiers of crystallization in natural and commercial fats is little exploited in technical literature [17]. To date, the vast majority of studies on the use of emulsifiers as modifiers of the crystallization process in fats were carried out with fully hydrogenated oils, model systems or pure TAGs, and therefore do not reflect the need to control crystallization in fats for industrial application [9, 90].

In general, the effect of emulsifiers appears to be related to different crystalline organizations and the creation of imperfections. Some of them can slow transformations via steric hindrance, while others promote these transformations by favoring molecular displacements [3]. Two different mechanisms have been reported in literature to interpret the effect of emulsifiers on crystallization of fats. The first refers to the action of these additives as hetero-nuclei, acceler-

ating crystallization by direct catalytic action as impurities. During crystal growth, emulsifiers would be adsorbed at the surface of the crystals and would therefore modify the incorporation rate of TAGs and crystal morphology. The second mechanism, of greater consensus among various authors, considers that the TAGs and emulsifiers would be amenable to co-crystallize due to the similarity between their chemical structures. Thus, the structural dissimilarity also entails delays in nucleation and potential inhibition of crystal growth [7, 86].

According to this second mechanism, emulsifiers are associated with triacylglycerol molecules by their hydrophobic groups, especially through acyl-acyl interactions. The acyl group of emulsifiers determines its functionality with respect to the TAGs. The main effects of these additives on the crystallization of fats occur during the stages of nucleation, polymorphic transition and crystal growth, altering physical properties such as crystal size, solid fat content and microstructure. The question of promoting or inhibiting crystallization, however, is still debatable. In general, studies indicate that emulsifiers with acyl groups similar to the fat to be crystallized accelerate this process [12].

Currently, it is known that the behavior of emulsifiers during the crystallization of fats can be divided into three cases: (1) limited miscibility between emulsifier molecules and TAGs: in this situation the emulsifier acts as an impurity and the interaction results in imperfect crystals, which may promote or retard crystal growth and polymorphic transitions, depending on the compatibility of hydrophobic ends in their structures; (2) high degree of miscibility between emulsifiers and TAGs that promotes the formation of molecular compounds; (3) total immiscibility between emulsifiers and TAGs, where emulsifiers can act as crystallization germs and microstructure modifiers [11, 86].

Emulsifiers with high potential for controlling crystallization of base fats include sorbitan esters of fatty acids, fatty esters and polyesters of sucrose, commercial standard lecithin and chemically modified lecithin, and the polyglycerol polyricinoleate [30]. Many studies have confirmed that emulsifier affect the crystallization induction times, the composition of nucleation germs, rates of crystal growth and polymorphic transitions [91]. However, the results are still very incipient, and require greater explanation.

7.2. Sugar-based emulsifiers

While the derivatization of oils and fats to produce a variety of emulsifiers with a wide range of application has shown to be well established for many years [92], the industrial production of emulsifiers based on oils, fats and carbohydrates is relatively new. Such emulsifiers result from a product concept based on the exclusive use of renewable resources, where sucrose, glucose and sorbitol are the most used raw materials in industry. The sugar-based emulsifiers most used in the food industry are sorbitan and sucrose esters.

7.2.1. Sorbitan esters

Sorbitol is a hexameric alcohol, obtained by the hydrogenation of glucose. Its free hydroxyl groups can react with fatty acids to form sorbitan esters (SE). In SE production, a reaction mixture containing a specific fatty acid, sorbitol and the catalyst (sodium or zinc stearate) is

heated in an inert atmosphere to promote simultaneous esterification and cyclization reactions. The fatty acid/sorbitol mole ratio determines the formation of monoesters and triesters. The SE most well-known and used industrially include lauric, palmitic, stearic and oleic acids [17]. Figure 5 shows the chemical structure of a sorbitan tristearate.

Sorbitan tristearate (STS or *Span* 65) and sorbitan monostearate (SMS) are recognized for their ability to efficiently modify crystal morphology and consistency of fats, such as anti-bloom agents in confectionery products containing cocoa butter and in substitutes of cocoa butter, indicated as potential controllers of crystallization. It is assumed that these compounds can delay or inhibit the transition of fat crystals to a more stable form. Moreover, the SE showed to be particularly effective in stabilizing the polymorph β′ in margarines and modification of the solid fat content of fats in general, promoting fusion profiles adequate for the body temperature [18]. They can also be selective as dynamic controllers of polymorphic transitions in fat, due to their ability to create hydrogen bonds with neighboring TAGs, in a process known as The Button Syndrome, whereby the presence of a specific emulsifier does not form a preferred polymorph, but rather controls the degree of mobility of the molecules and their potential to undergo configurational changes. In this process, emulsifiers can modulate the polymorphic transformations in the solid state or via the liquid state, and the temperature regime used to control the physical state of crystals during the polymorphic transition and extension of the mobility of the molecules, thereby regulating the rate of polymorphic transformation [4].
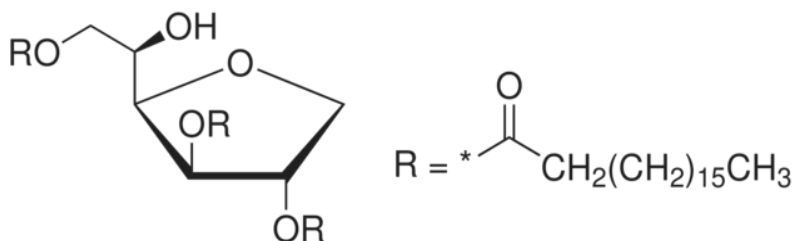

Figure 5. Chemical structure of Sorbitan Tristearate (STS).

According in [91], STS is the additive with greatest potential for modification of crystallization in cocoa butter, particularly in inhibiting the βV →β VI transition and fat bloom due to its high melting point (55°C) and chemical structure similar to the TAGs present in the oils and fats, permitting facilitated co-crystallization by this emulsifier and formation of solid solutions with these TAGs. In [93], the addition of 0.5% (w/w) of STS to base fats for margin had a stabilizing effect on the polymorph β′. According in [11] observed the formation of small crystal aggregates in mixtures of palm oil/palm kernel olein when adding 0.09% (w/w) of STS, in addition to increasing the rate of crystallization of these mixtures. In a review article, in [16] emphasized the use of STS and/or combinations thereof with other emulsifiers such as soy lecithin, the current alternative of greatest interest for the control of polymorphic transitions and structuring of the crystal lattice in fats, since the TAGs-STS interaction promotes the formation of

regular crystals that melt at 40°C, the melting point characteristic of most base fats for industrial applications.

7.2.2. Sucrose esters

Sucrose fatty esters can be used in a wide range of food applications and are mainly utilized in the bakery, confectionery, desserts and special emulsion industries [94]. Sucrose esters, particularly mono-and di-esters, are extremely functional emulsifiers, since they provide a number of unique advantages for the food industry. They are non-toxic compounds, without taste or odor, easily digested sucrose and fatty acids, as well as biodegradable under aerobic and anaerobic conditions. They are produced by interesterification of sucrose and fatty acids by various reaction types and conditions. Their structure is typically composed of polar and nonpolar groups in the same molecule as other emulsifiers, but the eight possible positions for esterification with fatty acids allow for these molecules to obtain different lipophilic/hydrophilic properties. Partially esterified sucrose esters, especially the mono-, di-and tri-esters, are more versatile for use in food applications, where the degree of esterification is controlled by the fatty acids/sucrose ratio in the reaction mixture. Monoesters (~70% of monoesters) are hydrophilic, while the di-, tri-, and polyesters are increasingly hydrophobic [95]. The degree of saturation and size of fatty acid chains used also significantly influences the properties of these compounds [17, 86]. Figure 6 shows the chemical structure of a sucrose ester of stearic acid and that of behenicacid.
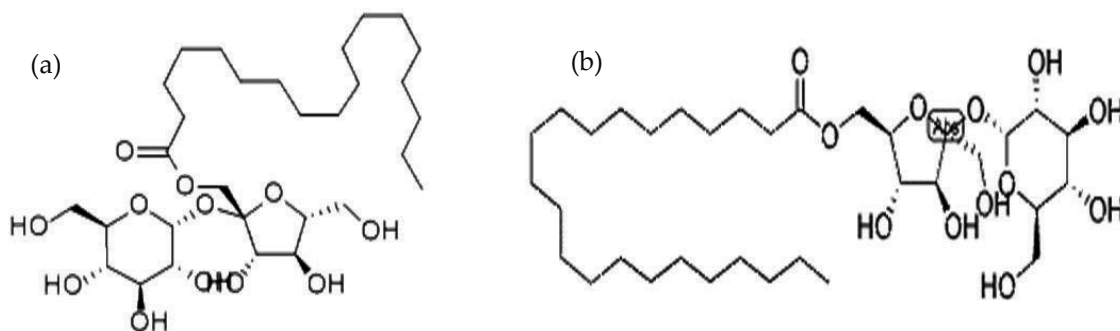

Figure 6. Chemical structures of: (a) sucrose stearate and (b) sucrose behenate.

The fatty acids most commonly used in sucrose esters are the lauric (C12), myristic (C14), palmitic (C16), stearic (C18), oleic (C18) and behenic acids (C22). By changing the nature or number of fatty acid groups, a wide range of HLB values can be obtained. Commercial sucrose esters are mixtures with various degrees of esterification, due to their complexity, and exhibit diverse behaviors, like lipids. Consequently, they are used in studies on the crystallization of fats. The sucrose esters most studied to date are esters of stearic acid and palmitic acid, especially in the studies of [9, 96, 97]. However, according to [9], few studies explore the effect of these emulsifiers on the induction period, and the rate of crystallization and development of polymorphic forms in fatty systems.

Acknowledgements

Author details

Maria Aliciane Fontenele Domingues[1*], Ana Paula Badan Ribeiro[1], Theo Guenter Kieckbusch[2], Luiz Antonio Gioielli[3], Renato Grimaldi[1], Lisandro Pavie Cardoso[4] and
Lireny Aparecida Guaraldo Gonçalves[1]

*Address all correspondence to: aliciane@fea.unicamp.br

1 School of Food Engineering, University of Campinas, Campinas, Brazil

2 School of Chemical Engineering, University of Campinas, Campinas, Brazil

3 Faculty of Pharmaceutical Sciences, University of São Paulo, São Paulo, Brazil

4 Institute of Physics "Gleb Wataghin", University of Campinas, Campinas, Brazil

References

[1] Sato, K. Crystallization behavior of fats and lipids: a review. Chemical Engineering Science 2001; 56(7) 2255-2265.

[2] Lidefelt, J.O. Handbook: vegetable oils and fats. AarhusKarlshamn; 2007.

[3] Aronhime, J.S.; Sarig, S.; Garti, N. Mechanistic considerations of polymorphic transformations of tristearin in the presence of emulsifiers. Journal of American Oil Chemists' Society 1987; 64(4) 529-533.

[4] Aronhime, J.S.; Sarig, S.; Garti, N. Dynamic control of polymorphic transformation in triglycerides by surfactants: the Button Syndrome. Journal of American Oil Chemists' Society 1988; 65(7) 1144-1150.

[5] Aronhime, J., S. Sarig, and N. Garti. Emulsifiers as additives in fats: effect on polymorphic transformations and crystal properties of faty acids and triglycerides. Food structure 1990; 9(4) 337-352.

[6] Puppo, M. C., Martini, S., Hartel, R. W., & Herrera, M. L. Effects of Sucrose Esters on Isothermal Crystallization and Rheological Behavior of Blends of Milk-fat Fraction Sunflower Oil. Journal of food science 2002; 67(9) 3419-3426.

[7]   Cerdeira, M., Martini, S., Hartel, R.W., Herrera, M.L. Effect of sucrose ester addition on nucleation and growth behavior of milk fat-sunflower oil blends. Journal of Agricultural and Food Chemistry. Columbus, v.51, p. 6550-6557, 2003.

[8]   Cerdeira, M., Pastore, V., Vera, L.V., Martini, S., Candal, R.J., Herrera, M.L. Nucleation behavior of blended high-melting fractions of milk fat as affected by emulsifiers. European Journal of Lipid Science and Technology. Weinheim, v.107, p. 877-885, 2005.

[9]   Cerdeira, M., Martini, S., Candal, R.J., & Herrera, M.L. Polymorphism and growth behavior of low-*trans* fat blends formulated with and without emulsifiers. Journal of American Oil Chemists' Society 2006; 83(6) 489-496.

[10] Martini, S.; Herrera, M.L. Physical properties of shortenings with low-trans fatty acids as affected by emulsifiers and storage conditions. European Journal of Lipid Science and Technology 2008; 110(2) 172-182.

[11] Miskandar, M.S. *et al*. Effects of emulsifiers on crystallization properties of low-melting blends of palm oil and olein. Journal of Food Lipids 2006; 13(1) 57-72.

[12] Miskandar, M.S. *et al*. Effects of emulsifiers on crystal behavior of palm oil blends on slow crystallization. Journal of Food Lipids 2007; 14(1) 1-18.

[13] Toro-Vazquez, J.F., Rangel-Vargas, E., Dibildox-Alvarado, E., Charó-Alonso, M.A. Crystallization of cocoa butter with and without polar lipids evaluated by rheometry, calorimetry and polarized light microscopy. European Journal of Lipid Science and Technology 2005; 107(9) 641-655.

[14] Awad, Tarek, and Kiyotaka Sato. Effects of hydrophobic emulsifier additives on crystallization behavior of palm mid fraction in oil-in-water emulsion. Journal of the American Oil Chemists' Society 2001; 78(8) 837-842.

[15] Sonoda, T., Takata, Y., Ueno, S., Sato, K. Effects of emulsifiers on crystallization behavior of lipid crystals in nanometer-size oil-in-water emulsion droplets. Crystal growth & design 2006; 6(1) 306-312.

[16] Pernetti, M., van Malssen, K.F., Flöter, E., Bot, A. Structuring of edible oils by alternatives to crystalline fat. Current Opinion in Colloid & Interface Science 2007; 12(4) 221-231.

[17] Hasenhuettl, G.L. Overview of Food Emulsifiers. In: Food Emulsifiers and Their Applications. Ed. Hasenhuettl, G.L., Hartel, R.W. springer:New York, 1-7, 2008.

[18] O'brien, R.D. Fats and Oils Analysis. In: Fats and Oils – Formulating and Processing for Applications. Ed. O'brien, R.D. 2nd ed.CRC Press:New York, 2004.

[19] Timms, R. E. Phase behaviour of fats and their mixtures. Progress in Lipid Research 1984; 23(1) 1-38.

[20] Kawamura, K. The DSC thermal analysis of crystallization behavior in palm oil. Journal of American Oil Chemists' Society 1979; 56(8) 48-52.

[21] Foubert, I., Dewettinck, K., Van de Walle, D., Dijkstra, A., Quinn, P. (Physical properties: structural and physical characteristics. In: The Lipid Handbook. 3th ed. Ed. Gunstone, F.D.; Harwood, J.L.; Dijkstra, A.J. CRC Press:Boca Raton, 471-508, 2007.

[22] Metin, S.; Hartel, R.W. Crystallization of fats and oils. In: Bailey´s Industrial Oil and Fat Products. Ed. Shahidi, F. Wiley Interscience:New York, 45-76, 2005.

[23] Hartel, R.W. Advances in Crystallization in Foods. Annual Review of Food Science and Technology 2013; 4(1) 277-292.

[24] Boistelle, R. Fundamentals of nucleation and crystal growth. In: Crystallization and Polymorphism of Fats and Fatty Acids. Ed. Garti, N.; Sato, K. Marcel Dekker:New York, 189-226, 1988.

[25] Erdemir, Deniz, Alfred Y. Lee, and Allan S. Myerson. Nucleation of crystals from solution: classical and two-step models. Accounts of chemical research 2009; 42(5) 621-629.

[26] Lawler, P.J.; Dimick, P.S. Crystallization and polymorphism of fats. In: Food lipids: chemistry, nutrition, and biotechnology. Ed. Akoh, C.C. CRC Press:Boca Raton, 275-300, 2002.

[27] Wright, A.J.; Narine, S.S.; Marangoni, A.G. Comparison of experimental techniques used in lipid crystallization studies. Journal of American Oil Chemists' Societ 2000, 77(12) 1239-1242.

[28] Fennema, Owen R., William D. Powrie, and Elmer H. Marth. Low temperature preservation of foods and living matter. Marcel Dekker, Inc., 1973.

[29] Hartel Rw. Mechanisms and kinetics of recrystallization in ice cream. In The Properties of Water in Foods: ISOPOW 6, ed. DS Reid, London: Blackie, 287-319, 1998.

[30] Lonchampt, P.; Hartel, R.W. Fat bloom in chocolate and compound coatings. European Journal of Lipid Science and Technology 2004; 106(4) 241-274

[31] Himawan, C., V. M. Starov, and A. G. F. Stapley. Thermodynamic and kinetic aspects of fat crystallization. Advances in colloid and interface science 2006; 122(1) 3-33.

[32] Hachiya, I.; Koyano, T.; Sato, K. Seeding effects on solidification behavior of cocoa butter and dark chocolate. I. Kinetics of solidification. Journal of American Oil Chemists' Society 1989; 66(12) 1757-1762.

[33] Narine, S.S.; Humphrey, K.L.; Bouzidi, L. Modification of the Avrami model for application to the kinetics of the melt crystallization of lipids. Journal of American Oil Chemists' Society 2006;.83(11) 913-921.

[34] Cerdeira, M.; Candal, R.J.; Herrera, M.L. Analytical techniques for nucleation studies in lipids: advantages and disadvantages. Journal of Food Science 2004; 69(9) 185-191.

[35] Martini, S.; Awad, T.; Marangoni, A.G. Structure and properties of fat crystal networks. In: Modifying Lipids for Use in Food. Ed. Gunstone, F. Woodhead Publishing:Cambridge, 142-169, 2006.

[36] Sato, K.; Ueno, S. Polymorphism in fats and oils. In: Bailey´s Industrial Oil and Fat Products. Ed. Shahidi, F. Wiley Interscience:New York, 77-120, 2005.

[37] Herrera, M.L.; Marquez Rocha, F.J. Effects of sucrose ester on the kinetics of polymorphic transition in hydrogenated sunflower oil. Journal of American Oil Chemists' Society 1996; 73(3) 321-326.

[38] Loisel, C., Keller, G., Lecq, G., Bourgaux, C., Ollivon, M. Phase transitions and polymorphism of cocoa butter. Journal of American Oil Chemists' Society 1998; 75(4) 425-439.

[39] Schenck, H.; Peschar, R. Understanding the structure of chocolate. Radiation Physics and Chemistry 2004; 71(3) 829-835.

[40] Marangoni, Alejandro G., and Leendert H. Wesdorp. Structure and properties of fat crystal networks. CRC Press, 2012.

[41] Campos, R. Experimental Methodology. In: Fat Crystal Networks. Ed. Marangoni, A.J. Marcel Dekker:New York, 267-349, 2005.

[42] Shi, Y.; Liang, B.; Hartel, R.W. Crystal morphology, microstructure, and textural properties of model lipid system. Journal of American Oil Chemists' Society 2005;.82(6) 399-408.

[43] Narine,S.S.; Marangoni, A.G. Microstructure. In: Fat Crystal Networks. Ed. Marangoni, A.J. Marcel Dekker:New York, p.179-255, 2005.

[44] Marangoni, A.G.; Narine, S.S. Identifying key structural indicators of mechanical strengh in networks of fat crystals. Food Research International 2002; 35(10) 957-969.

[45] Tang, D.; Marangoni, A.G. Modeling the rheological properties and structure of colloidal fat crystal networks. Trends in Food Science & Technology 2007; 18(9) 474-483.

[46] Mcgauley, S.E., Marangoni, A.G. Static crystallization behavior of cocoa butter and its relationship to network microstructure. In: Physical Properties of Lipids. Ed. Marangoni, A.G.; Narine, S.S. C.C. CRC Press:Boca Raton, 85-123, 2002.

[47] Herrera, M.L., Falabella, C., Melgarejo, M., Añón, M. C. Isothermal crystallization of hydrogenated sunflower oil: I – nucleation. Journal of American Oil Chemists' Society 1998; 75(10) 1273-1280.

[48] Sharples, A. Introduction to Polymer Crystallization. *St. Martin's Press:New York, 1966.*

[49] Narine, Suresh S., Marangoni, A.G."Fractal nature of fat crystal networks. Physical Review E 1999; 59(2) 1908.

[50] Marangoni, A.G., Hartel, R.W. Visualization and structural analysis of fat crystal networks. Food technology (USA) (1998).

[51] Marangoni, A.G.; Rousseau, D. Is plastic fat rheology governed by the fractal nature of the fat crystal network? Journal of the American Oil Chemists' Society 1996; 73(8) 991-994.

[52] Awad, T. Marangoni, A.G. Comparison Between Image Analysis Methods for the Determination of the Fractal Dimensions of Fat Crystal Networks. Fat Crystal Networks 2005; 391-399.

[53] Gioielli, L.A.; Simões, I.S.; Rodrigues, J.N. Crystal morphology and interactions of binary and ternary mixtures of hydrogenated fats. Journal of Food Engineering 2003; 57(4) 347-355.

[54] Vereecken, j., Foubert, I., Smith, K. W., Dewettinck, K. Effect of SatSatSat and SatOSat on crystallization of model fat blends. European Journal of Lipid Science and Technology 2009; 111(3) 243-258.

[55] Walstra, P., Kloek, W., Vliet, T.V. Crystallization processes in fats and lipid systems. Sato, K., Garti, N. (Eds.), Marcel DekkerNew York, 289, 2001.

[56] Johansson, D.; Bergensthal, B. Sintering of fat crystal networks in oil during post-crystallization processes. Journal of American Oil Chemists' Society 1995; 72(8) 911-920.

[57] Norizzah, A. R., Chong, C. L., Cheow, C. S., & Zaliha, O. Effects of chemical interesterification on physicochemical properties of palm stearin and palm kernel olein blends. Food chemistry 2004; 86(2) 229-235.

[58] Van Duijn, Gerrit. Technical aspects of trans reduction in modified fats. Oléagineux, Corps Gras, Lipides 2005; 12(5) 422-426.

[59] RozendaaI, A., Macrae, A.R. Interesterification of oils and fats. Lipid technologies and applications, 223, 1997.

[60] Rousseau, D., Marangoni, A.G. The Effects of Interesterification on the Physical Properties of Fats. Physical properties of lipids, 2002.

[61] Ribeiro, A.P.B., Grimaldi, R., Gioielli, L. A., Gonçalves, L. A. Zero *trans* fats from soybean oil and fully hydrogenated soybean oil: Physico-chemical properties and food applications. Food Research International 2009; 42(3) 401-410.

[62] Meng, Z., Liu, Y. F., Jin, Q. Z., Huang, J. H., Song, Z. H., Wang, F. Y., Wang, X. G. Characterization of graininess formed in all beef tallow-based shortening. Journal of agricultural and food chemistry 2010; 58(21) 11463-11470.

[63] USDA. Oilseeds: world market s and trade. http://apps.fas.usda.gov/psdonline/circulars/oilseeds.pdf (accessed 20 January 2013).

[64] Smith, P.R. The effects of phospholipids on crystallisation and crystal habit in triglycerides. European Journal of Lipid Science and Technology 2000; 1 122-127.

[65] Okawachi, T.; Sagi, N. Confectionery fats from palm oil. Journal of American Oil Chemists' Society. 1985; 62 421-425.

[66] Che Man, Y.B., Shamsi, K., Yusoff, M. S. A., Jinap, S. A study on the crystal structure of palm oil-based whipping cream. Journal of American Oil Chemists' Society 2003;.80 409-415.

[67] Chong, C.L., Kamarudin, Z., Lesieur, P., Marangoni, A., Bourgaux, C., Ollivon, M. Thermal and structural behavior of crude palm oil: crystallization at very slow cooling rate. European Journal of Lipid Science and Technology, 2007; 109 410-421.

[68] Watanabe, A., Tashima, I., Matsuzaki, N., Kurashige, J., Sato, K. On the formation of granular crystals in fat blends containing palm oil. Journal of American Oil Chemists' Society 1992;.69 1077-1080.

[69] Omar, Z., Let, C. C., Seng, C. C., Rashid, N. A. Crystallization and rheological properties of hydrogenated palm oil and palm oil blends in relation to crystal network. European Journal of Lipid Science and Technology 2005; 107 634-640.

[70] Garbolino, C.; Bartoccini, M.; Floter, E. The influence of emulsifiers on the crystallization behaviour of a palm oil-based blend. European Journal of Lipid Science and Technology 2005; 107 616-626.

[71] Tanaka, L.; Miura, S.; Yoshioka, T. Formation of granular crystals in margarine with excess amount of palm oil. Journal of American Oil Chemists' Society. 2007; 84 421-426.

[72] Braipson-Danthine, Sabine, and Veronique Gibon. Comparative analysis of triacylglycerol composition, melting properties and polymorphic behavior of palm oil and fractions. European journal of lipid science and technology 2007; 109(4) 359-372.

[73] Gibon, V., Ayala, J.V., Dijckmans, P., Maes, J., Greyt, W. Future prospects for palm oil refining and modifications. Oléagineux, Corps Gras, Lipides 2009; 16(4) 193-200.

[74] Gibon, V. Fractionation of lipids for use in food. F.D. Gunstone (Ed.), Modifying Lipids for Use in Food, CRC Press, Boca Raton, FL, pp. 201–233, 2006.

[75] Erickson, D.R. Practical Handbook of Soybean Processing and Utilization. Ed. ERICKSON, D.R. American Soybean Association, St. Louis, Missouri and American Oil Chemists'Society, Champaign, Illinois, p.227-296, 1995.

[76] Hunter, J.E. Dietary levels of *trans*-fatty acids: basis for health concerns and industry efforts to limit use. Nutrition Research 2005; 25 499-513.

[77] ANVISA. Visa Legis: Legislação em Vigilância Sanitária. Disponível em:<www.e-legis.bvs.br/leisref>. Acesso em: 19abril 2009.

[78] Reyes-Hernández, J., Dibildox-Alvarado, E., Charó-Alonso, M. A., & Toro-Vazquez, J. F. Physicochemical and rheological properties of crystallized blends containing *trans*-free and partially hydrogenated soybean oil. Journal of American Oil Chemists' Society. 2007; 84 1081-1093.

[79] Foubert, I., Dewettinck, K., Janssen, G., & Vanrolleghem, P. A. Modelling two-step isothermal fat crystallization. Journal of Food Engineering 2006; 75 551-559.

[80] Bell, A., Gordon, M. H., Jirasubkunakorn, W., & Smith, K. W. Effects of composition on fat rheology and crystallisation. Food Chemistry 2007; 101 799-805.

[81] Herrera, M.L.; Gatti, M.L.; Hartel, R.W. A kinetic analysis of crystallization of a milk fat model system. Food Research International 1999; 32 289-298.

[82] Minal, J. An introduction to random interesterification of palm oil. Palm Oil Developments. Kuala Lumpur, v.39, p.1-6, 2003.

[83] Stauffer, C. E. Emulsifiers for the Food Industry. In: Bailey's Industrial Oil and Fat Products, 2005.

[84] Garti, N. Food emulsifiers and stabilizers. Food shelf life stability, chemical, biochemical and microbiological changes. CRC Press, Boca Raton, p. 211-263, 2001.

[85] Bergenståhl, Björn. "Physicochemical aspects of an emulsifier functionality." *Food emulsifiers and their applications*. Springer New York, 2008. 173-194.

[86] Garti, N. Food Emulsifiers: Structure-Reactivity. Relationships, Design, and Applications In: Physical Properties of Lipids. Ed. Marangoni, A.G.; Narine, S.S. C.C. CRC Press, Boca Raton, p.265-386, 2002.

[87] Sastry, S. S., Mallika, K., Rao, B. G. S., Tiong, H. S., Lakshminarayana, S. Identification of phase transition temperatures by statistical image analysis. Liquid Crystals 2012; 39(6) 695-700.

[88] Neto, A.F., Salinas, S.R.A. The Physics of Lyotropic Liquid Crystals: Phase Transitions and Structural Properties. OUP Oxford, 2005.

[89] Goodby, J.W., Görtz, V., Cowling, S. J., Mackenzie, G., Martin, P., Plusquellec, D., Fitremann, J. Thermotropic liquid crystalline glycolipids. Chemical Society Reviews 2007; 36(12) 1971-2032.

[90] Rousseau, D. *et al*. Regulating the $\beta' \to \beta$ polymorphic transition in food fats. Journal of American Oil Chemists' Society 2005; 82, 7-12.

[91] Weyland, M.; Hartel, R. Emulsifiers in Confectionery. In: Food Emulsifiers and their Applications. Ed. Hasenhuettl, G.L., Hartel, R.W. springer, New York, p. 285-304, 2008.

[92] Hill, K., Ferrenbach, C. Sugar-based surfactants for consumer products and technical applications. Fett-Lipid 1999; 101(1) 25-33.

[93] Young, N.; Wassell, P. Margarines and Spreads. In: Food Emulsifiers and their Applications. Ed. Hasenhuettl, G.L., Hartel, R.W. springer, New York, p. 307-325, 2008.

[94] Van Ingen, B. Sucrose esters, not a "sweet" solution. Disponível em: http://www.flavours.asia/uploads/7/9/8/9/7989988/white_paper_sucrose_esters_not_a_sweet_solution.pdf. (accessed 20 January 2013).

[95] Garti, N.; Yano, J. The Roles of Emulsifiers in Fat Crystallization. In: Crystallization Processes in Fat and Lipid systems Ed. Garti; N.; Sato, K., Marcel Dekker, Suíça p. 211-250, 2001.

[96] Elisabettini, P.; Desmedt, A.; Durant, F. Polymorphism of stabilized and nonstabilized tristearin, pure and in the presence of food emulsifiers. Journal of American Oil Chemists' Society 1996; 73, 187-192.

[97] Martini, S.; Cerdeira, M.; Herrera, M.L. Effect of sucrose esters on the crystallization behavior of bulk oil systems. Journal of American Oil Chemists' Society 2004;.81, 209-211.

Role of Crystallization in Genesis of Diverse Crystal Forms of Antidiabetic Agents

Renu Chadha, Dimpy Rani and Parnika Goyal

Additional information is available at the end of the chapter

1. Introduction

Crystallization is a crucial step in the manufacturing and processing of active pharmaceutical ingredients (API's) in pharmaceutical industry [1]. As crystallization is coupled with molecular recognition, a slight alteration in crystallization conditions can affect crystal and powder properties accompanied with thermodynamic and mechanical properties [2]. So, the selection of an appropriate solid form of an active pharmaceutical ingredient (API) in the early stages of drug development is very important as it can be pure crystalline form or its non covalent modification such as polymorph, amorphate, hydrate, solvate, salt or co-crystals exhibiting unique physicochemical properties (solubility, dissolution rates, stability and bioavailability) and other performances characteristics of drug [3].

Existence of a crystalline solid into many crystalline forms leads to polymorphism which is a phenomenon, hard to predict. It may be of two types either conformational (due to existence of various conformers of molecule) or packing polymorphism (due to difference in crystal packing). On thermodynamic consideration, there are also two types of polymorphism i.e., monotropic system (when the transition of one form to another is irreversible) and enantiotropic system (reversible forms) [4]. In general, least stable crystal form crystallizes out first, not the most stable form. Metastable crystal form (unstable) tend to change to more stable from under particular conditions [5]. Crystal forms are the entities which are similar at molecular level but dissimilar in supramolecular aspect [6].

The various conditions used in the process of crystallization is the chief cause of generation of different crystal forms of a molecule and the difference in the properties of various crystal forms is due to different crystal packing and lattice energy [4]. Advancement in synthesis has gained control on the synthesis and purity of drugs but still lag behind in controlling the

crystallinity and physical crystal forms. Different forms of a crystalline solid can be controlled by controlling the crystallization process.

The best method used for obtaining the variety of crystal forms is crystallization as it is traditional, easy and unbeatable process. Crystallization techniques may be solvent or non-solvent based and varied methods give rise to different forms. Solvent crystallization techniques include solvent evaporation, slow cooling of the solution, diffusion, vapour diffusion while non solvent techniques include sublimation, thermal treatment, desolvation of solvates, grinding and crystallization from melt etc. The choice of appropriate technique may be decided depending on the amount of sample and physical stability or solubility of drug [7-8].

Different crystal forms due to different crystal lattice have different physicochemical properties and thus therapeutic effects. Thus, Pharmaceutical companies usually search for a crystal form or polymorph with the best properties for therapeutic use and manufacturability. Selection of an optimized crystal form is of more relevance as regulatory bodies are showing their interest in physico-chemical characterization of APIs. Polymorphism is also important to be considered because this phenomenon is not exhibited by only drug molecule but also by other solid forms prepared by drug using crystal engineering approaches like salts, solvates, co-crystals etc. However, the discovery and genesis of various crystal forms is quite tiresome and expensive [9-12].

This chapter has focused on the various crystal forms of anti-diabetic agents and techniques employed in their preparation.

Diabetes mellitus is an unceasing disease in the society that requires life-long pharmacological and non-pharmacological management. Among this, type 2 diabetes mellitus is more prevalent. For the management of type 2 diabetes mellitus, various oral agents have been approved. The main problem of these agents is their dissolution limited bioavailability. To overcome this issue various attempts like CD complexes, solid dispersion, crystal engineering approaches and exploring the more soluble polymorphic form have been made.

2. Case studies of crystal forms of antidiabetics

Several crystalline forms of anti-diabetics have been described in the past. A general account of different crystal forms, their method of preparation along with transition / melting temperature are detailed in table 1.

3. Sulfonyluraeas

3.1. Acetohexamide

Potentiality of polymorphism in acetohexamide was first observed by Girgis-Takla and Chroneos in 1977. They reported two polymorphic forms (polymorphs A and B), distinguished

by IR spectra and further characterized by Mueller and Lagas. However, forms showed no notable differenceon drying at 60°C in vaccum [13-14]. Graf *et al.* proposed keto-enoltautomerism for their stability, confirmed by IR spectra. Polymorph A (enol form) forms six membered ring via bonding of an O—H and S=O group intramolecularly while polymorph B (keto form) shows intermolecular bonding of C=O of urea to a sulphonamide N—H [15-16].

Kuroda *et al*. collected three crystal forms (Form I, Form II and $CHCl_3$ – II) out of which one was found to be chloroform solvate. Form II was found to be 1.2 times more soluble than Form I [17].Yokoyama *et al.* estimated the thermodynamic values (transition temperature - 154°C & heat of transition - 230°C) of crystal forms (Form I and Form II) from solubility studies. Both forms were found equally bioavailable inbeagle dogs [18].Another forms Form IV by Graf *et al* and Form II and III by Al-Saieq and Rileywere investigated [19-20]. Later Graf et al. found that Form II was mixture of I and IV, while Form III (by Al-Saieq and Riley) on heating, converted to a new polymorph V [15].

Another crystal form of acetohexamide (Form VI) by Aldawsari*et al.* was reportedand was more soluble in water, and more bio-available in rats as compared to other already reported crystal forms [21].

3.2. Chlorpropamide

Various publications on the crystal forms (about 16) of chlorpropamide were reported (by Simmons *et al.*, Burger *et al*., and Saieq *et al.*)[22-24], but the provided data could not distinguish existing crystal forms in actual [1-3]. Ueda *et al.* depicted convex shaped dissolution curve for Form C (by simmons *et al.*) and Form II (by saieq *et al.)*that indicates crystallization along with anhydrate to hydrate phase transformation [25].

After that, Debrushchak*et al*. adopted a new methodology for nomenclature (α, β, γ, δ, ε) on the basis of the order of their crystal structure established. Form α, β, γ and δ correspond to previously reported Form III, II, IV and VI respectively and was found that all forms transformed to ε (Form I) crystal form.On cooling up to 200 K, crystal form ε, converted to another new form (ε′). This new form resembled to α form in aspect of cell parameters and molecular conformation while to ε form in case of packing (Z shaped ribbons). Form α, β, γ has same intermolecular hydrogen bonding but differ in packing and number of molecules in unit cell [26-30].

Bifurcated intermolecular hydrogen bonding pattern of carbonyl group has been seen with the two amine hydrogen atoms, and SO_2 oxygen atom acquires hydrogen from the nitrogen attached to alkyl tail.With regard to enthalpy of transition, conversion of α, β, γ and δ to ε should be in order of β > γ > δ > α but β polymorph infracts it because of structural difference [31].

All these polymorphs are conformational polymorphs as they showed difference in torsion angles. (as shown in figure 1) [32]
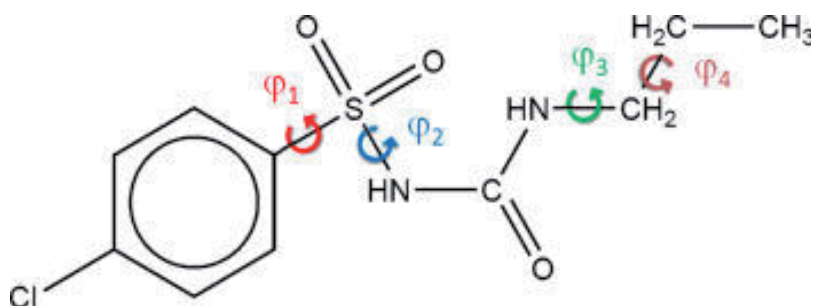
Figure 1. Chlorpropamide with possible torsion angles [32]

Process of crystallization was also found to be affected by the presence or absence of 2-hydroxybutyl-β-cyclodextrin as chlorpropamide crystallized to metastable Form II and III in presence, whereasto Form A in the absence at 4°C. Even the appearance of crystal form was dependent on the concentration and temperature [33].

3.3. Tolbutamide

Several Tolbutamide polymorphs are reported by several groups of workers. [34-42]. Two forms reported by Simmons *et al*[34] (Forms A and B) are identical with the Burger's Form I and III [35], respectively, and have been well characterized. However, Burger's Forms II and IV have been not fully characterized.

3.4. Glimepiride

Two polymorphs (Form I and II) are reported in literature. New crystalline form (Form II) was prepared by recrystallization from an ethanol/water system was found to have different dissolution profile and solubility [43] and it transformed to Form I over 140°C.

3.5. Glibenclamide

Crystallisation of glibenclamide from different solvents and quick cooling of melt gave three polymorphic forms and pseudopolymorphs (solvates), which were significantly different with regard to solubility and melting properties. [44-45] A new crystalline form of glibenclamide,with higher melting point (218°C) and lower solubility, was formed during an attempt to elucidate transitional phases by melting, cooling and reheating by A. Panagopoulou-Kaplani, *et al*[46].

4. Meglitinides

4.1. Nateglinide

Various solvates/ hydrates (about 26) of nateglinide have been patented which eventually converts to either Form B or Form H. [47] The S polymorph was crystallized from the melt or

by isothermal treatment of B or H forms at temperatures higher than their melting points which is the only stable form, while the polymorphs B and H are metastable forms. The anhydrous polymorph, if stored at room temperature and humidity, gradually changes to H polymorph while, if stored in water vapour saturated atmosphere, it gets back water and reverts to the hemihydrate form. On the contrary, both an isothermal treatment at 80 ∘C and melt cooling bring to the B polymorph [48].

4.2. Repaglinide

S enantiomer of repaglinide was found active hypoglycemic agent andthree crystalline forms (Form I, II and III) were crystallized from various solvents by solvent/antisolvent and slow evaporation method. Form II (low melting crystal form) on further heating showed second melting endotherm at 127-130°C and converted to Form I if crystallized in ethanol/water mixture [49].

5. Biguanides

5.1. Metformin hydrochloride

Two polymorphs (form A and B) has been identified out of which form A is more thermodynamically more stable while highly metastable structure, which correlates with the difficulty in handling this polymorph [50]. These two polymorphs and their mixture has been evaluated by Scott L. Childs, *et al* using capillary crystallization and thermal microscopy techniques. Crystal structure of these forms arereported [51]. Both structures are monoclinic (P21/c) with one complete metformin cation and one chloride anion in the asymmetric unit as shown in figure 2.
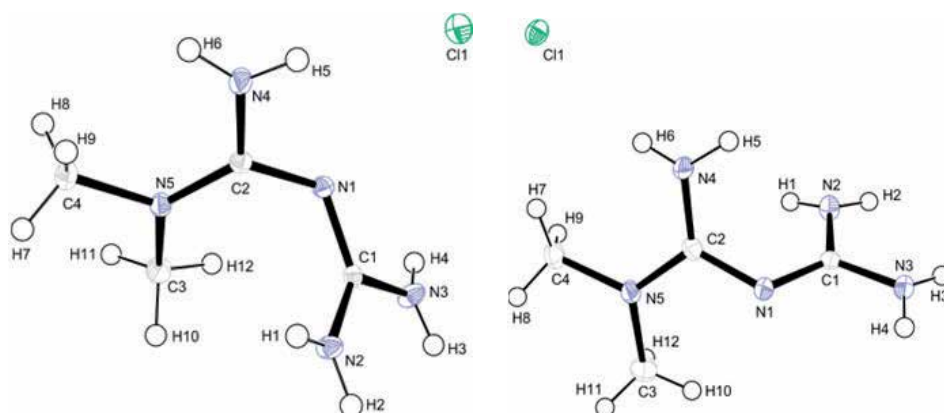

Figure 2. Metformin hydrochloride Form A and B shown, respectively at 50% probability ellipsoids. [50]

6. Thiazolididiones

6.1. Rosiglitazone

Various crystalline forms of maleate salt of rosiglitazone are reported in literature. Choudary *et al.* and Blackler *et al.* put illumination on crystalline hydrates of salt [52-54]. Chebiyyam *et al.* described four crystalline forms (Form I, II, III and IN) while Birari *et al.* described two forms (Form A and B). Form A was detected more stable than B and all the other crystal forms, amorphous form, hydrate and anhydrate converted to Form A [55-56]. Kansal*et al.* depicted three crystal forms (Form I, III and IV) for hydrobromide salt of rosiglitazone and formulated Form III in compacted dosage form, while Greil *et al.* elaborated two hydrates (Form A and C), one solvate (Form D) and three anhydrate (Form B, B1 and E). 1:1 hydrates were recovered which may lose their water content at different temperature. Form B and B1 have shown same melting endotherm temperature but they were distinguished by PXRD [57-58].

6.2. Pioglitazone hydrochloride

Only two polymorphic form I and II has been evaluated which are patented [59].

6.3. Troglitazone

Various crystalline forms of troglitazone are patented. Polymorphs 1,2,3 and 6 are obtained by different modes of recrystallization while form 4 and 5 are derived by heating any one of the form 1, 2, 3 or 6 [60].

7. Dipeptidyl peptidase-4 inhibitor

7.1. Alogliptin

In literature, six crystal forms of tartrate (Form A, B, C, D, E and F) and one crystalline form of benzoate salt of alogliptin (Form A) were reported. Among the crystal forms of alogliptin tartrate, Form A was found to be more stable and all forms during stability studies converted to Form A. The most stable form were analyzed for solubility and alsoestablished thermally stable up to 200°C and a variable hydrate.

Form A of benzoate salt was found to be much stable and amorphous form converted to stable Form A during heating [61-62].
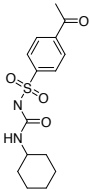
7.2. Linagliptin benzoate

Crystalline forms of linagliptin benzoate have been patented. Form II is less hygroscopic then Form I. Thus, can be easily handled in standard pharmaceutical processing conditions and no special packing is required during its storage [63].
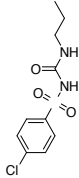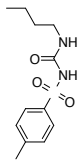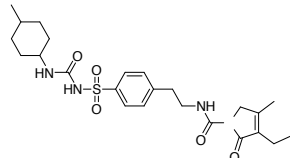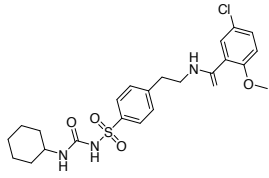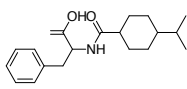
7.3. Sitagliptin

Numerous solvates and crystal forms of sitagliptin phosphate have been patented. All the reported crystalline solvates converted to Form II on desolvation and on heating metastable Form II converted to Form I (at 45°C) and to Form III at 110°C. Form I (stable at higher temperature) and Form III (stable at lower temperature) have enantiotropic relation [64]. Form IV, also a metastable form, slowly converted to crystalline sitagliptin phosphate monohydrate [65]. Huang *et al.* prepared Form V and processed them to pharmaceutical formulation [66].
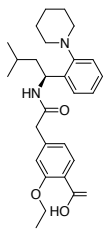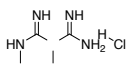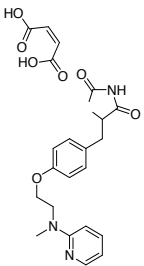
7.4. Saxagliptin

Monohydrate, hemihydrates and mixture of thereof of saxagliptin had been prepared and patented [67].Nine polymorphic forms of saxagliptin hydrochloride (Form K, T, Z, N, S, O, B, C and D) had been evaluated either from its amorphous form or dihyrate form and being patented. Forms K, S, N and Z are polymorphically pure, Form D is a hydrate, Form T is in a mixture with ammonium chloride, Form O is in a mixture with form K and saxagliptinmono-chydrochloridemonohydtare while Form B is in a mixture with saxagliptinmonochydrochlor-idedihyrate [68]
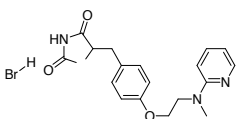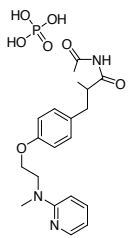
Drug	Crystal form	Solvent used	Method of preparation	Transition (T)/ Melting endotherms(M)	References
ACETOHEXAMIDE	Polymorph A	Glacial acetic acid	Slow evaporation	180-183°C	[13]
	Polymorph B	Chloroform	Slow evaporation	183-185°C	
	Form I (triclinic)	Ethanol/ methanol/ acetone	Slow evaporation	187°C	[17]
	Form II (monoclinic)	Ethanol: water (1:1)	Heating, slow evaporation	157°C (T), 186°C (M)	
	$CHCl_3 - II$	Hot chloroform	Slow evaporation	164–169°C (T), 182°C (M)	
	Form IV	Hot benzene	Slow evaporation	184-186°C	[19]
	Form II (mixture of I and IV)	Hot Isobutanol	Slow evaporation	176-178°C	[20]
	Form III	Chloroform	Rapid cooling of saturated solution at 55°C	-	
	Form V	-	Heating Form III at 160°C	-	[19]
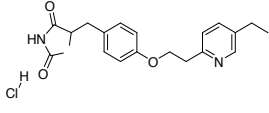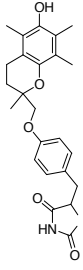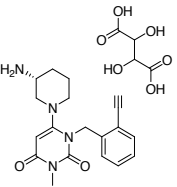
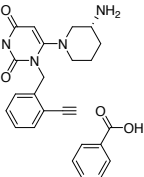| Drug	Crystal form	Solvent used	Method of preparation	Transition (T)/ Melting endotherms(M)	References
	Form VI	HP-β-CD in sodium phosphate buffer of pH 8.0	Titration to 0.5 M HCl, filteration, cooling	-	[21]
	Form A/ III/ /IV	Ethanol-water mixture	Slow evaporation	121-122°C	
	Form B /II /V	-	Recystallization from melt of Form A	124-127°C	[22-24]
	Form C /I	-	Heat Form A at 120°C	128-130°C	
	Form IV	Carbon tetrachloride	Slow evaporation	122-123°C	[23]
	Form V	Benzene	Desolvation of benzene solvate	< 118°C	
	Form II	Chloroform	Rapid evaporation	-	[24]
CHLORPROPAMIDE	Form III	Hexanol	Rapid cooling	-	
	Form α (orthorhombic)	Ethanol	Slow evaporation	124°C (T), 127-128°C (M)	[26]
	Form β (orthorhombic)	Heptane-ethyl acetate	Solvent-antisolvent addition	125-127°C	
	Form γ (monoclinic)	Heptanes: ethyl acetate (1:2)	Freezing at -20°C	120°C (T), 128°C (M)	[27]
	Form δ (orthorhombic)	Heptanes: ethyl acetate (2:1)	Slow evaporation	124°C (T), 128°C (M)	
	Form ε (orthorhombic)	-	Solid transformation of Form α	128°C	
TOLBUTAMIDE	Form I	Benzene: hexane (2:1)	Solvent-antisolvent addition, slow evaporation	127°C	[38]
	Form II	-	Form IV stored at 60°C, 75% RH, 10min.	100°C (T), 127°C (M)	

Drug	Crystal form	Solvent used	Method of preparation	Transition (T)/ Melting endotherms(M)	References
	Form III	Ethanol: water (2:1)	Solvent-antisolvent addition, slow evaporation	113°C (T), 127°C (M)	
	Form IV	Ethanol: DCM (1.2:1)	Spray drying	80°C, 100°C (T), 127°C (M)	
	Form V	Conc. HNO$_3$, methanol	Cocrystallisation with p-nitrophenol, p-phenylenediboronic Acid in ethanol	-	[69]
GLIMEPIRIDE	Form I	Ethanol and chloroform	Slow evaporation	207°C	[43]
	Form II	Ethanol: water (1:1)	Heating, slow evaporation	140°C (T), 207°C (M)	[70]
GLIBENCLAMIDE	Form I	-	Slow evaporation	174°C	[45]
	Form III	-	Slow evaporation	153°C	
	Solvate	pentanol/ toulene	Slow evaporation	109°C	[44]
	New Form	-	Sublimation of glassy state at 130-160 °C	218 °C	[46]
	Glassy form	-	Quench cooling of melt	42- 56°C (T), 90-135°C (exotherm), 198°C (M)	
NATEGLINIDE	Form B	Methanol: water (7:3)	Cooling at 10°C	128-130°C	[71]
	Form H	Acetone: water (2:3)	Cooling at 10°C	138-141°C	
	Form S	-	Melting/ isothermal treatment of Form B/H	172 °C	[48]
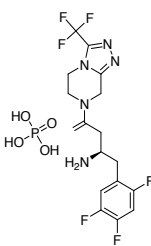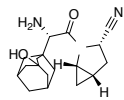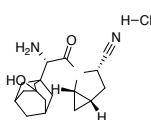
Drug	Crystal form	Solvent used	Method of preparation	Transition (T)/ Melting endotherms(M)	References
S-REPAGLINIDE	Form I	Ethanol/water (2:1), acetone/pet ether, methanol/ water, THF/ MTBE, ethyl acetate/pet ether, n-propanol/ water, ACN/ water, MIBK/ MTB, diethyl ketone/MTB, t-butanol/water, methyl ethyl ketone/n-heptane, diglyme/n-heptane, methyl ethyl ketone/ MTBE, 1,4-dioxane/n-heptane, n-butanol/MTBE, chloroform/n-hexane	Solvent-antisolvent, slow evaporation	130-131°C	[49]
	Form II	Pet ether: toluene (5:3)	Rapid cooling	99-101°C	
		Toluene	Heating followed by cooling		
	Form III (from Form I, II and amorphous form)	Dichloromethane and pet ether	Cooling and stirring	80-84°C	
METFORMIN HYDROCHLORIDE	Form A	Methanol: water (2:1)	slow evaporation	-	[50]
	Form B	Acetone: water (3:1)	slow evaporation	-	
ROSIGLITAZONE MALEATE	Hydrate	Acetonitrile: water (30:1)/ THF: water	Heating followed by cooling	-	[52]

Drug	Crystal form	Solvent used	Method of preparation	Transition (T)/ Melting endotherms(M)	References
		(30:1)/ methyl ethyl ketone: water (30:1)/ ethyl acetate: water (100:1)/ isopropanol: water (33:1)			
	Hydrate	Ethanol and water (2.1%v/v)	Heating followed by cooling	-	[53-54]
		Methanol-water/ acetonitrile-water/ ethanol-water	Heating followed by cooling		
		Methanol-water	Heating followed by cooling		
		Water	Heating followed by cooling		
		Ethyl acetate-water	Heating followed by cooling		
	Form I	Ethanol	Heating followed by cooling	100.53°C	[55]
	Form II	Acetone	Heating followed by cooling	127.67°C	
	Form III	Methanol	Heating followed by cooling	126.41°C	
	Form IN	1,4-dioxane	Heating followed by cooling	125.39°C	
	Form A	Methanol-ethyl acetate	Heating solution in methanol followed by addition of ethyl acetate		[56]
		Acetonitrile	Heating the solution followed by reflux and cooled		
	Form B	Isopropyl alcohol	Heating followed by cooling	-	

Drug	Crystal form	Solvent used	Method of preparation	Transition (T)/ Melting endotherms(M)	References
		Methanol	Addition of methanol to acetone solution of salt		
		Isopropyl alcohol / THF	Heating of Suspension of Form A followed by cooling		
		-	Heating followed by cooling		
ROSIGLITAZONE HYDROBROMIDE	Form I	Acetone	Reflux, cooling	-	[57]
	Form III	Demineralised water	Reflux, cooling	-	
	Form IV	Acetone	Heating Form I in acetone	-	
ROSIGLITAZONE PHOSPHATE	Form A	Acetone and water	Stirring of suspension	171-177°C	[58]
		Ethanol and water	Stirring of suspension		
	Form B	Acetone and water	Stirring of suspension	175-176°C	
	Form B1	-	Stirring of suspension	175-176°C	
	Form C	Acetone: water (1:1)	Phosphoric acid added to solution of Form B	-	
			Stirring of suspension of Form A		
	Form D	Methanol	Heating of suspension of Form A	-	
	Form E	Ethanol	Heating followed by cooling	167-172°C	
PIOGLITAZONE HYDROCHLORIDE	Form I	DMF/ Methanol/ acetic acid	Heating followed by cooling	198°C	[59]

Drug	Crystal form	Solvent used	Method of preparation	Transition (T)/ Melting endotherms(M)	References
	Form II	Acetic acid, water	Heating followed by cooling	183°C	
TROGLITAZONE	Form 1	Benzene: acetone (100: 1)	Slow evaporation	179°C	[60]
	Form 2	Benzene extraction, DCM added	Fast evaporation at -10°C	110°C (T), 175°C (M)	
	Form 3	Acetone: benzene (1:2)	Cooling at 5°C	185°C	
	Form 4	-	Form I heated to melt	56°C (T), 110 °C (exotherm), 177°C (M)	
	Form 5	-	Heating of Form IV at 130 °C	157°C (exotherm), 180°C (M)	
	Form 6	Acetone: benzene (1:4)	Cooling of solution of Form I at 5 °C	105°C	
ALOGLIPTIN TARTRATE	Form A	Acetone: water (2:3) or methanol	Filtration, slow evaporation	172.5°C	[61]
		Hot methanol and acetone/ methanol and toluene	Cold acetone/ toluene was added in filtered solution of hot methanol and alogliptin tartrate, slow evaporation		
		water	Heating, slow evaporation		
	Form B	Tetrahydrofuran: water (2:1)/ dioxane: water (2:1) / acetonitrile: water (4:3)	Filtration, slow evaporation	124.4°C	

Drug	Crystal form	Solvent used	Method of preparation	Transition (T)/ Melting endotherms(M)	References
	Form C	Ethanol: water (1:1) / isopropanol: water (1:1)	Filtration, slow evaporation	122.4°C	
	Form D	water	Heating at 80°C, filtered and cooling	173.3°C	
		methanol	Placed amorphous form with methanol in sealed chamber for several weeks		
	Form E	Water: acetonitrile (4:21) / water: dioxane (2:1)	Heating at 50°C, filtered, slow evaporation	121.9°C	
	Form F	-	Placed amorphous form with saturated salt solution at 84% RH in sealed chamber	-	
ALOGLIPTIN BENZOATE	Form A	Acetone / Methanol	Filtration, fast evaporation	186°C	[62]
		Acetonitrile	Heating slurry at 60°C, filtration, slow evaporation		
		Ethanol: isopropyl acetate (99:1)	Reflux, cooling		
LINAGLIPTIN BENZOATE	Form I	Isopropanol	Slow evaporation	-	[63]
	Form II	Acetonitrile	Slow evaporation	193°C	

Drug	Crystal form	Solvent used	Method of preparation	Transition (T)/ Melting endotherms(M)	References
SITAGLIPTIN PHOSPHATE	Solvate	Methanol/ ethanol/ 1-propanol/ 2-propanol/ acetone/ acedtonitrile	By contacting with solvent for 5 minutes	213.61°C	[64]
	Form I	Isoamyl alcohol/ water	Slow evaporation	215.37°C (T), 217.27°C (M)	
	Form II	-	Desolvation of ethanol solvate	114.6°C (T), 213.80°C (M)	
	Form III	Isoamyl alcohol/ water	Slow evaporation	80.90°C (T), 215.94°C (M)	
	Form IV	-	Heating monohydrate form above 58°C	213.3°C	[65]
	Form V	Methanol-water/ acetone-water	Heating followed by cooling	214.88°C	[66]
		Methanol, n-butanone, THF, ACN, DMC and water	Distillation at 55°C		
SAXAGLIPTIN	Form H-1 (monohydrate)	Ethanol	Kept in desiccator in atmosphere of respective solvents	-	[67]
		Dibutylether			
		Water, 80% RH			
SAXAGLIPTIN HYDROCHLORIDE	Form K	Ethyl acetate, Conc. HCl	Reflux, cooling	-	[68]
	Form T	Saturated ammonium chloride pH 4.53	Precipitation	-	
	Form Z (Dihydrate)	Ethyl alcohol, Methylisopropyl ketone	Precipitation	-	
	Form N	2- butanol	Reflux, cooling	-	
	Form S	Wet ethyl acetate, Conc. HCl	Heating followed by cooling	-	

Drug	Crystal form	Solvent used	Method of preparation	Transition (T)/ Melting endotherms(M)	References
	Form O	0.8 M HCl/ Ethyl alcohol	Heating followed by cooling	-	
	Form B	Ethyl alcohol, Methylethylketone	stirring	-	
	Form C	Propyl alcohol	Heating followed by cooling	-	
	Form D (hydrate)	1-butanol	Heating, stirring	-	

Table 1. Crystalline Forms of Antidiabetics

8. Conclusion

The crystallization process has profound impact on crystal forms, which further affect biopharmaceutical properties of pharmaceutical solids. Various crystal forms of antidiabetics have been reported in literature and some have even gained the status of a patent. The existence of these different crystal forms are possible due to presence of sulphoxamide, carboxamide, thiazolidendione, etc. groups in these agents. For the optimized pharmaceutical acceptable solid form, one must be cognizant of the potentiality of an API to exist in various crystal forms by altering the crystallization conditions. Because of this, screening of new crystal forms of API's has become a vital part of drug discovery and development in past decade.

Acknowledgements

Author details

Renu Chadha[*], Dimpy Rani and Parnika Goyal

*Address all correspondence to: renukchadha@rediffmail.com

University Institute of Pharmaceutical Sciences, Panjab University, Chandigarh, India

References

[1] Chen J, Sarma B, Evans JMB, Myerson AS. Pharmaceutical Crystallization. Crystal Growth & Design 2011;11:887-895. http://pubs.acs.org/doi/abs/10.1021/cg101556s

[2] Doherty R. The Application of Computational Chemistry to The Study of Molecular Materials. In: Myerson AS, Green D, Meenan P. (ed.) Crystal Growth of Organic Materials. Washington DC: American Chemical Society; 1996. p2–14.

[3] Byrn SR, Pfeiffer RR, Stowell JG. Solid-State Chemistry of Drugs. West Lafayette: SSCI; 1999.

[4] Grant DWJ. Theory and Origin of Polymorphism. In: Brittain HG. (ed.) Polymorphism In Pharmaceutical Solids. New York: Marcel Dekker, Inc. p1-34.

[5] Ostwald W. StudienÜber Die Bildnung Und Umwandlung Fester Körper.Zeitschrift-FürPhysicalischeChemie 1896;22 289–330.

[6] Desiraju GR. Polymorphism: The Same and Not Quite the Same. Crystal Growth & Design 2008;8(1):3-5. http://pubs.acs.org/doi/abs/10.1021/cg701000q

[7] Guillory JK. Generation of Polymorphs Hydrates Solvates and Amorphous Solids. In: Brittain HG. (ed.) Polymorphism in Pharmaceutical Solids. New York: Marcel Dekker, Inc. p183–226.

[8] Morissette SL, Almarsson O, Peterson ML, Remenar JF, Read MJ, Lemmo AV, Ellis S, CimaMJ,Gardner CR. High-Throughput Crystallization: Polymorphs, Salts, Co-Crystals and Solvates of Pharmaceutical Solids. Advance Drug Delivery Review 2004;56:275–300. http://www.sciencedirect.com/science/article/pii/S0169409X03002187

[9] FDA Pharmaceutical cGMPs for the 21st Century – A Risk Based Approach.U.S. Food andDrug Administration; 2004a.

[10] FDA Process Analytical Technology (PAT) – A Framework For Innovative PharmaceuticalDevelopment Manufacturing And Quality Assurance.U.S. Food and Drug Administration; 2004b.

[11] ICH Q8 Pharmaceutical Development.International Conference on Harmonization; 2005a.

[12] ICH Q9 Quality Risk Management.International Conference on Harmonization; 2005b.

[13] Girgis-Takala P, Chroneos I. The Polymorphism of Acetohexamide. Journal of Pharmacy and Pharmacology 1977;29(10):640-642 http://www.readcube.com/articles/10.1111/j.2042-7158.1977.tb11424.x

[14] Müller B, Lagas M. Some aspects of the polymorphism and stability of acetohexamide.PharmaceutischWeekblad 1979;1(1):449-56.

[15] Graf E, Bayer C, Abdallah O. On The Polymorphism of Acetohexamide. Pharm Ind 1984;46:955-959.

[16] Takla P, Dakas CJ. An infrared study of tautomerism in acetohexamide polymorphs. Journal of pharmacy and pharmacology 1989;41(4):227-30.

[17] Kuroda K, Yokoyama T, Umeda T, Takagishi Y. Studies on Drug Nonequivalence. VI. Physicochemical Studies on Polymorphism of Acetohexamide. Chemical and Pharmaceutical Bulletin 1978;26(8):2565-2568. http://ci.nii.ac.jp/naid/110003623330

[18] Yokoyama T, Umeda K, Kuroda K. Sato K, Takagishi Y. Studies on Drug Nonequivalence. VII. Bioavailability of Acetohexamide Polymorphs. Chemical and Pharmaceutical Bulletin 1979;27(6):1476-1478. http://www.ncbi.nlm.nih.gov/pubmed/544059

[19] Graf E, Beyer C, Abdallah O. PolymorphiebeiAcetohexamid. ActaPharmaceutica Technology 1979;25:9-20.

[20] Al-Saieq, S.S., Riley, G.S.Polymorphism in sulfonylurea hypoglycemic agents. III. Acetohexamide. PharmaceuticaActa Helvetiae1982;57:43–46.

[21] Aldawsari H, Altaf A, Banzar ZM, Lohara D, Nakabayashi M, Anraku M. Crystallization of A New Polymorph of Acetohexamide from 2-Hydroxybutyl-β-cyclodextrin Solution: Form VI with A High Aqueous Solubility. International Journal of Pharmaceutics 2013;453(2):315-321. http://www.ncbi.nlm.nih.gov/pubmed/23796835

[22] Simmons DL, Ranz RJ, Gyanchandani ND. Polymorphism in pharmaceuticals. II. Chlorpropamide. Canadian Journal of Pharmaceutical Sciences 1973;8(4):125-127.

[23] Burger A. ZurPolymorphieoralerAntidiabetika.ScientiaPharmaceutica 1975;43:152-161

[24] Aal-Saieq SS, Riley GS. Polymorphism in sulfonylurea hypoglycemic agents, II: chlorpropamide. PharmaceuticaActaHelvetiae 1982;57(1):8-11.

[25] H. Ueda, N. Nambu and T. Nagai, Dissolution behavior of chlorpropamide polymorphs. Chemical & pharmaceutical bulletin 1984;32(1):244-50. http://ci.nii.ac.jp/naid/110003624610/

[26] Koo CH, Cho SI, Yeon YH. The crystal and molecular structure of chlorpropamide. Archives of Pharmacal Research 1980;3(1):37-49. http://link.springer.com/article/10.1007/BF02884759#page-1

[27] Drebushchak TN, Chukanov NV, Boldyreva EV. A new polymorph of chlorpropamide: 4-chloro-N-(propylaminocarbonyl) benzenesulfonamide. ActaCrystallographica Section E: Structure Reports Online 2006;62(10):o4393-o4395. http://scripts.iucr.org/cgi-bin/paper?SJ2115

[28] Drebushchak TN, Chukanov NV, Boldyreva EV. A new-polymorph of chlorpropamide: 4-chloro-N-(propylaminocarbonyl) benzenesulfonamide. ActaCrystallographica Section C: Crystal Structure Communications 2007;63(6):o355-o357. http://scripts.iucr.org/cgi-bin/paper?ln3052

[29] Drebushchak V, Drebushchak TN, Chukanov N, Boldyreva EV. Transitions among five polymorphs of chlorpropamide near the melting point. Journal of Thermal Analysis and Calorimetry 2008;93(2):343-351. http://www.akademiai.com/content/190801rwku80k735/

[30] Drebushchak TN, Chukanov NV, Boldyreva EV. Two polymorphs of chlorpropamide: the-form and the high-temperature-form. ActaCrystallographica Section C: Crystal Structure Communications 2008;64(12):o623-o625. http://scripts.iucr.org/cgi-bin/paper?S0108270108034550

[31] Drebushchak TN, Chesalov YA, Boldyreva EV. A conformational polymorphic transition in the high-temperature-form of chlorpropamide on cooling: a new'-form. ActaCrystallographica Section B: Structural Science 2009;65(6):770-781. http://scripts.iucr.org/cgi-bin/paper?gp5033

[32] Ayala A, Caetano M, Honorato S, Mendes Filho J, Siesler H, Faudone S, et al. Conformational polymorphism of the antidiabetic drug chlorpropamide. Journal of Raman Spectroscopy 2012;43(2):263-272. http://onlinelibrary.wiley.com/doi/10.1002/jrs.3012/full

[33] Ishiguro T, Hirayama F, Iohara D, Arima H, Uekama K. Crystallization and polymorphic transitions of chlorpropamide in aqueous 2-hydroxybutyl-β-cyclodextrin solution. European Journal of Pharmaceutical Sciences 2010;39(4):248-55. http://www.sciencedirect.com/science/article/pii/S0928098709003649

[34] Simmons DL, Ranz RJ, Gyanchandani ND, Picotte P. Polymorphism in pharmaceuticals II (tolbutamide). Canadian Journal of Pharmaceutical Sciences 1972;7:121-123.

[35] Burger A. Zurpolymorphieoralerantidiabetika.ScientiaPharmaceutica 1975;43:161-168.

[36] Burger A, Ramberger R. On the polymorphism of pharmaceuticals and other molecular crystals. II. Applicability of thermodynamic rules. MikrochimicaActa 1979:273-316.

[37] Al-Saieq SS, Riley GS. Polymorphism in sulphonylurea hypoglycaemic agents: I. Tolbutamide. PharmaceuticaActaHelvetiae 1981;56:125-129.

[38] Leary JR, Ross SD, Thomas MJK. On characterization of the polymorphs of tolbutamide. Pharmaceutisch Weekblad, Scientific Edition 1981;3:62-66.

[39] Umeda T, Ohnishi N, Yokoyama T, Kuroda T, Kita Y, Kuroda K, Tatsumi E, Matsuda Y. A kinetic study on the isothermal transition of polymorphic forms of tolbutamide

and mefenamic acid in the solid state at high temperatures. Chemical and Pharmaceutical Bulletin 1985;33:2073-2078.

[40] Traue J, Kala H, Ko°hler M, Wenzel U, Wiegeleben A, Fo°rster B, Pollandt P, Pintye-Ho´di K, Szabo´-Re´ve´sz P, Selmeczi B. Untersuchungenzurpolymorphie von arzneistoffen in pulvern und tabletten. Pharmazie 1987;42:240-241.

[41] Georgarakis M. Untersuchungenzurpolymorphie von tolbutamid.Pharmazie 1989;44:209-210.

[42] Olives AI, Martin MA, del Castillo B, Barba C. Influence of the presence of trace amounts of metals on the polymorphism of tolbutamide. International Journal of Pharmaceutics 1996;14:1069- 1076.

[43] Endo T, Iwata M, Nagase H, Shiro M, Ueda H. Polymorphism of glimepiride: Crystallographic study, thermal transitions behavior and dissolution study. STP Pharma Sciences 2003;13(4):281–286.

[44] Suleiman MS, Najib NM. Isolation and physicochemical characterization of solid forms of glibenclamide International Journal of Pharmaceutics 01/1989; DOI: 10.1016/0378-5173(89)90134-8.

[45] Hassan MA, Salem MS, Sallam E, Al-Hindawi M.K. Preparation and characterization of a new polymorphic form and a solvate of glibenclamide. ActaPharmaceuticaHungarica 1997;7:81–88.

[46] Panagopoulou-Kaplani A, Malamataris S. Preparation and characterisation of a new insoluble polymorphic form of glibenclamide. International Journal of Pharmaceutics 2000;195:239–246.   http://www.sciencedirect.com/science/article/pii/ S0378517399004019.

[47] Wizel S, Frenkel G, Gome B. Polymorphic forms of Nateglinide. US patent 2006/0004102 A1, 2006.

[48] Brunia G, Berbennia V, Milanesea C, Girellaa A, Cardinib A, Lanfranconib S, Marinia A.New solid modifications of nateglinide Journal of Pharmaceutical and Biomedical Analysis2010;51:1054–1059.

[49] Reddy MS, Eswaraiah S, Trippapnchar MV, Shanmugam G, Madhavi M, Kumar KN.Polymorphic forms of (S)-Repaglinide and the processes for preparation thereof. US Patent20,040,102,477; 2004.

[50] Scott LC, Leonard JC, Jeanette TD, David AC, Barbara CS, Patrick Stahly G. A Metastable Polymorph of Metformin Hydrochloride: Isolation and Characterization Using Capillary Crystallization and Thermal Microscopy Techniques Crystal Growth & Design 2004; 4(3):441-449. http://pubs.acs.org/doi/abs/10.1021/cg034243p.

[51] Hariharan M, Rajan SS, Srinivasan R. ActaCrystallographica Section C: Crystal Structure Communication 1989;45:911-913. http://scripts.iucr.org/cgi-bin/paper?fe0015.

[52] Choudary BM, Lynch IR, Sasse MJ, Plc SB. Substituted thiazolidinedione derivative, process for its preparation and its pharmaceutical use. PCT/EP1998/008153(Date: 1999-06-24)

[53] Blackler PD, Lee DC, Sasse MJ, Plc SB.Hydrate of 5-[4-[2- (n-methyl-n- (2-pyridil)ami-no) ethoxy]benzyl] thiazolidine-2, 4-dione maleic acid salt. PCT/EP1998/008154(Date: 1999-06-24)

[54] Blackler PD, Lee DC, Sasse MJ, Plc SB 5-[4-[2- (n-methyl-n- (2-pyridyl)amino) ethoxy]benzyl] thiazolidine-2, 4-dione, maleic acid salt, hydrate as pharmaceutical. PCT/EP1998/008155(Date:1999-06-24)

[55] Chebiyyam P, Gaddam OR, Krishnamurthi V, Mamillapalli RS, Seella VR. Novel polymorphic forms of 5-[4-[2-[n-methyl-n-(2-pyridyl)amino]ethoxy]benzyl] thiazolidine-2,4-dione maleate and process for their preparation.US PatentApplication No. PCT/US2001/029896(Date: 2002-04-4)

[56] Birari DR, Kankan RN, Phull MS, Rao DR. Process for the production of polymorphs of rosiglitazone maleate. US Patent Application No. PCT/GB2004/003519(Date: 2005-03-10)

[57] Kansal VK, Nayal S, Rafilovich M, Ranjan H. Polymorphic forms of rosiglitazone hydrobromide and processes for their preparation. Google Patents; Patent Application No. 12/583,509, (Date:2009-03-25).

[58] Greil J, Ludescher J, Wolf S. Rosiglitazone Phosphate and Polymorphic Forms. Google Patents Application No. PCT/EP2005/001378(Date:2005-2-11).

[59] Shlomit Wizel, Serguei Finogueev, Jean Hildesheim Pioglitazone Hydrochloride. US patent 2003/0139603 A1, 2003.

[60] Krishnamurthi Vyas; Chebiyyam Pmbhakar; Smelling Dhamaraja Rao; Mamillapalli Ramabadhra,Sarina; Om Gaddam Reddy; Rajagopalan Ramanujam; Chakrabarti, Polymorphic Forms of Troglitazone Having Enhanced anti-Diabetic Activity and a Process for their Preparation. US patent 005700820A, 1997.

[61] Leonard J. Chyall, Lafayete, Keith Lorimer, Linda J, Mcclausland. Polymorphs of Tartrate Salt of 2-[2-(3-(R)-Amino-Piperidin-1-Yl)-5-Fluoro-6-Oxo-6h-Pyrimidin-1yl-methyl]-Benzonitrile and Methods of Use Therefore (US 2007/0066636). Application No.: 11/531,638. (Date: 2007-03- 22).

[62] Marom E, Rubnov S. Polymorphs of Alogliptin benzoate. Google Patents;US Patent Application. 13/697,455. (Date:2012-11-12).

[63] Sandoz AG Hotter, Andreas, Pichler, Arthur Polymorph of Linagliptin Benzoate International Publication No. WO/2012/152837, (Date: 15.11.2012).

[64] Robert MW, Joseph DA, Chen AM, Cypes S, Russell R. Ferlita, KH, Christopher L, Evangelia S. Novel Crystalline Forms Of A Phosphoric Acid Salt Of A Dipeptidyl Peptidase-Iv Inhibitor. PCT/US04/27983(Date:2006-12-21)

[65] Chen AM, Wenslow RM. Novel Crystalline Form of a Phosphoric Acid Salt of a Dipeptidyl Peptidase-IV Inhibitor. PCT/US2004/030434(Date: 2004-09-17)

[66] Huang CG, Huang MH. Crystalline Polymorph of Sitagliptin Phosphate and Its Preparation.US Patent. US 2009/0247532 A1(Date: 2009-10-01).

[67] Marina Ratkaj, TomislavBilj an, Marina Marinkovic, Saxagliptin Intermediates,Saxagliptin Polymorphs andProcesses for Preparation Thereof US Patent No. 8,501,960 B2, 2013.

[68] Marina Marinkovic,Marina Ratkaj, Oliver Frankovic, Tina Mundorfer. Polymorphs of Saxagliptin Hydrochloride And Processes for Preparing Them. US Patent No. 2013/0158091 A1, 2013.

[69] Naba KN, Ashwini N. Novel form V of tolbutamide and a high Z' crystal structure of form III Crystal Engineering Communication 2011;13:47. http://pubs.rsc.org/en/content/articlelanding/2011/ce/c0ce00073f.

[70] Rudy B, Sumaia AP, Leonardo MBF, Ade´Lia E. De Almeida Antoˆ Nio C. Doriguetto MB, De Arau´ Jo, He´Rida RNS. A Discriminating Dissolution Method for Glimepiride Polymorphs Journal Of Pharmaceutical Sciences 2012;101(2):794-804. http://onlinelibrary.wiley.com/doi/10.1002/jps.22799/pdf.

[71] Michito S, Yoshihito K, Takao O, Yasuo I, Satoji Takahashi, Yottukaichi, Methods For Producing Nateglinide B-Type Crystals. US Patent No. 7,544,834 B2, 2009.

Crystallization of Nano and Amorphous Materials

Photonic Contribution to the Glass Transition of Polymers

Nobuyuki Tanaka

Additional information is available at the end of the chapter

1. Introduction

The glass transition for polymers has been investigated for a long time as the mysterious physical phenomena of solid or liquid phases from the initial studies on the equation of state in pressure (P), volume (V), and temperature (T) to the recent thermal analyses with the temperature modulated differential scanning calorimeter (TMDSC) [1 – 9]. Polystyrene (PS) is one of polymers taking a leading part in the studies on the glass transition of polymers, so far showing the heat capacity jump of 28 ~ 31 J/(K mol) at the glass transition. The temperature modulation of TMDSC emerged the latent heat capacity jump at the glass transition temperature (T_g), confirming the heat capacity jump data on the basis of PVT relations for PS. Also for poly(ethylene terephthalate) (PET), the abrupt heat capacity jump at T_g was observed on TMDSC curves, being not found with the standard DSC [8]. Recently, in the advances of the studies on the photonic contribution to the glass transition of polymers, the mysterious glass transition has been reasonably understood as the quantum phenomena [10 – 16]. For frozen polymer glasses, the heat capacity jump at T_g should start from the first order hole phase transition and then the glass parts should be unfrozen accompanying with the enthalpy and entropy jumps [10]. The holes are generally neighboring with the ordered parts, which are formed as pairs during the enthalpy relaxation at temperatures below T_g. First in this chapter, for isotactic PS (iPS) and PET, the heat capacity jump at the glass transition was discussed as the discontinuous change of energy in quantum state of the photon holes, followed by unfreezing of the glass parts. IPS and PET have the benzene rings being able to cause the resonance by neighboring in the side groups or the skeletal chains, respectively. Further, the details on the heat capacity jump found for iPS were also investigated for isotactic polypropylene (iPP) with methyl groups of the same 3/1 helix structure [16]. The resonance suggests the presence of remarkable photons in holes. The dimension of them is characterized by the

geometric molecular structure, e.g., the distance between reflectors such as benzene rings, affecting to the amplitude as a wave. While for the photon holes, the constant volume heat capacity could be defined as the differential coefficient of the internal energy of holes [10 – 16]. So for iPS, PET, and iPP, in order to confirm the identity in two heat capacities of ordered parts and holes in pairs, the heat capacity jump data per molar structural unit at the glass transition were compared with that per molar photon for the holes in ordered part / hole pairs. Here it should be noted that in the ordered part / hole pairs, the molar photon used for photon holes is equivalent to the molar structural unit for ordered parts numerically.

For iPS, PET, and iPP, surely the heat capacity jump at the glass transition was due to the discontinuous change of energy in quantum state of the resonant photon holes between neighboring benzene rings, but methyl groups for iPP, followed by unfreezing of the glass parts [14 – 16]. For iPS, the substance of the helix–coil transition with the enthalpy of 16.1 kJ/mol, but being smaller than the glass transition enthalpy of 18.9 kJ/mol, was shown as the ordered part / hole pairs. For PET, the ordered part / hole pairs were like the mesophase crystals with the glassy conformational disorder of ethylene glycol parts. For iPP, the helical sequences with the enthalpy of 7.4 kJ/mol or the nodules of mesophase with the enthalpy of 12.1 kJ/mol, interchanging between ordered parts and crystals automatically, were shown as the ordered part / hole pairs, depending on the presence of the crystallization upon cooling from the melt. According to above results, it could be understood that the glass transition of polymers investigated for a long time was only the collateral unfreezing phenomena of the glass parts starting by the disappearance of ordered part / hole pairs formed during the enthalpy relaxation at temperatures below T_g.

On the other hand, for iPS and iPP, from the quantum demand of hole energy at regular temperature intervals of 120 K for iPS and 90 K for iPP, the homogeneous glasses free from ordered part / hole pairs with T_g= 240 K and 180 K have been predicted, respectively [15, 16]. T_g of them could be understood as the first order glass phase transition temperature of the homogeneous glass [17, 18]. But, as one of other quantum possibilities for these polymers, the liquids with T_g= 0 K have also been predicted. In this connection, the equilibrium melting temperature, T_m^∞= 450 K, for α form crystals of iPP was corresponding to 5 times the interval of 90 K. The sift of melting from α to γ form crystals between two peaks of a DSC double melting peak curve observed upon heating was discussed, relating to the formation and then disappearance of crystal / hole pairs.

2. Theoretical treatments and discussion

When the hole energy in the ordered part / hole pairs excited at the glass transition, being in equilibrium with the flow parts, is given by h^h (= $3C_v^{ph}T$), the heat capacity per molar photon for holes, C_p^{h*} (= C_p^{flow}), is given by [10 – 16] (see section **4**):

$$C_p^{h\,*}\left(= C_p^{flow}\right)=3C_p^{ph}\left(1 + TdlnJ_h \big/ dT\right) \tag{1}$$

where C_p^{flow} is the heat capacity per molar structural unit for the flow parts, being equal to C_p^x of the heat capacity per molar structural unit for the excited ordered parts [19], C_v^{ph} (= 2.701R) is the constant volume molar heat capacity for photons [20], R is the gas constant, J_h is the number of holes lost by T, and 3 is the degree of freedom for photons. When $dJ_h/dT = 0$ at T_g and the end temperature, T_l, of the glass transition, C_p^{h*} at those temperatures is given by $3C_v^{ph}$. Thus, the heat capacity jump per molar photon, ΔC_p, at the glass transition is given by:

$$\Delta C_p \left(= C_p^{h\,*} - C_v^{ph}\right) = 2C_v^{ph} \left(= 44.9 \; J \left/ \left(K \; mol^*\right)\right.\right) \tag{2}$$

In Eq. (2), ΔC_p should be due to the discontinuous energy change from a quantum ground level for photons in the holes, that is, $(1/2)h\nu$ (= h_0^h/N_A) to $(3/2)h\nu$ (= $3h_0^h/N_A$), where h is Planck constant, ν (= c/λ) is the frequency per second, c is the velocity of light, λ is the wavelength, N_A is Avogadro constant, and h_0^h is the zero– point energy per molar photon, which also is used as the energy unit bellow. The holes in the excited ordered part / hole pairs should be in dynamical equilibrium with the spatial tubes between a chain and neighboring chains in the flow parts [21]. At the glass transition, the sigmoidal mean heat capacity curve of C_p as shown in Fig. 1 is observed generally. Even in this case, the C_p for ordered parts should be equal to the C_p^h of the mean heat capacity for the holes in ordered part / hole pairs at the glass transition:

$$C_p = C_p^h = \alpha C_v^{ph} + (1 - \alpha) C_p^{ph} \tag{3}$$

where α and $1 - \alpha$ are the fractions of ordered part / hole pairs with the respective holes of C_v^{ph} and C_p^{ph} (= $3C_v^{ph}$), and C_p^{ph} is the adiabatic molar heat capacity for photons. On the other hand, the C_p for ordered parts in pairs could be divided into two components [22]:

$$C_p = \Delta C_p^x + C_p^r \tag{4}$$

under $\int_{T_g}^{T_l} C_p dT = \int_{T_g}^{T_l} \Delta C_p^x dT$ and $\int_{T_g}^{T_l} C_p^r dT = 0$,

where ΔC_p^x (= $C_p^{h*} - 3C_v^{ph}$) is the relative component heat capacity per molar structural unit for the excited ordered parts and C_p^r is the heat capacity change per molar structural unit due to the crystallization followed by the melting. At the glass transition, ΔC_p^x shows a peak against T, reflecting the size distribution of ordered parts. Fig. 1 shows the representative C_p curve composed of ΔC_p^x and C_p^r at the glass transition for polymers.

Thus, for iPS, PET, and iPP, ΔC_p (= $2C_v^{ph}$) per molar photon (mol*) was compared with the reference value of heat capacity jump, ΔC_p^{exp}, per molar structural unit (mol) [8]. The results deviated from $\Delta C_p/\Delta C_p^{exp} = 1$. Table 1 shows the comparison of ΔC_p (= $2C_v^{ph}$) with ΔC_p^{exp} for these polymers, together with h^h/h_x at T_g, where h_x is the enthalpy per molar structural unit for ordered parts [14 – 16].
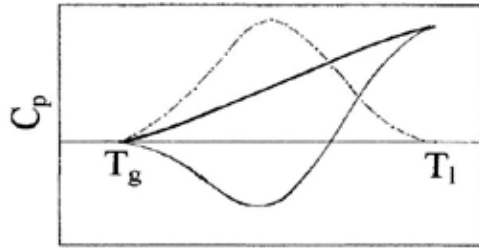
Figure 1. The components of the C_p curve (the thick line) at the glass transition for polymers. The dash – dotted line is the relative component ΔC_p^x curve for the excited ordered parts with a size distribution and the thin line is the component C_p^r curve due to the crystallization and then melting.

Polymer	T_g K	ΔC_p^{exp} J/(K mol)	ΔC_p J/(K mol*)	$\Delta C_p/\Delta C_p^{exp}$	h^h/h_x
iPS	359*1	30.8	44.9	1.5	1.5 or 1.0
PET	342	77.8 (80.4, 46.5*2)	44.9	0.6 (0.6)	1.0
iPP	270	19.2	44.9	2.3	1.5 or 2.5

The values in ( ): our data of Fig. 6. *1: see Table 2. *2: ΔC_p^{exp} at T_m^∞= 535 K.

Table 1. The values of T_g, ΔC_p^{exp}, ΔC_p (= $2C_v^{ph}$), $\Delta C_p/\Delta C_p^{exp}$, and h^h/h_x for iPS, PET, and iPP.

However, the values of $\Delta C_p/\Delta C_p^{exp}$ were correlated to h^h/h_x of the number of structural units holding one photon potentially (described below). h_x at T_g is given by [10, 23]:

$$h_x = h_g + \Delta h \tag{5}$$

where h_g {$= RT_g^2(\partial lnv_f/\partial T)_p$} is the glass transition enthalpy per molar structural unit due to the discontinuous free volume change of v^* from $v_f = v_0$ to $v_0 + v^*$ at T_g, v_f and v_0 are the free volume and the core free volume per molar structural unit. h_g is given approximately by three expressions; (1) RT_g^2/c_2 or $\varphi_g E_a$ (in WLF equation [24], φ_g {$= 1/(2.303c_1)$} is the fraction of the core free volume in glasses, c_1 and c_2 are constant, and E_a is the activation energy), (2) the molar enthalpy difference between the super – cooled liquid and the crystal at T_g; $H_g^a – H_g^c$, and (3) the sum of the conformational and cohesive enthalpies per molar structural unit at T_g; $h_g^{conf} + h_g^{int}$. For PET and iPP, the additional heat per molar structural unit, Δh, needed to melt all ordered parts by T_l in Fig. 1 is given by [10, 23]:

$$\Delta h = \Delta H - Q \tag{6}$$

where $\Delta H = H_m^a – H_c^a$, H_m^a is the enthalpy per molar structural unit for the liquid at T_m^∞, H_c^a is the enthalpy per molar structural unit for the super– cooled liquid at the onset temperature, T_c, of a DSC crystallization peak upon cooling, and Q is the heat per molar structural unit

corresponding to the total area of the DSC endothermic peak upon heating. While, in the case of $h_x^{conf} \neq h_g^{conf} = 0$ at T_g, Δh is derived as [10]:

$$\Delta h = T_g \{s_g^{conf} - (RlnZ_0)/x\} \tag{7}$$

with $s_g^{conf} = (RlnZ + RT_g dlnZ/dT)$

where h_x^{conf} is the conformational enthalpy per molar structural unit for ordered parts, s_g^{conf} is the conformational entropy per molar structural unit at T_g, Z is the conformational partition function for a chain, Z_0 (= Z/Z_t) and Z_t are the component conformational partition function for a chain regardless of temperature and depending on the temperature, respectively, and x is the degree of polymerization. For PET and iPP, the values of Δh from Eq. (7) were a little smaller than those from Eq. (6), respectively. In the case of $h_x^{conf} = h_g^{conf}$, $\Delta h = (RT_g lnZ_t)/x$ was derived, applying to nylon 6 [10].

2.1. Isotactic polystyrene

From $h^h = (3/2)N_A h\nu$ and h^h (= $3C_v T_g$)= 24.2 kJ/mol* at T_g= 359 K, the wavenumber of $1/\lambda$= 1350 cm^{-1} was derived for a photon in holes [10]. This agreed nearly with the conformation sensitive band of 1365 cm^{-1} assigned to benzene rings [25, 26]. Further from the assigned relation of one photon to one structural unit numerically, the unity of $h^h/h_x = \Delta C_p/\Delta C_p^{exp}$= 1 at the glass transition was expected [10], applying to the ordered sequences of– *TTTT*– (see Fig. 2), where *T* is the trans isomer. However, $\Delta C_p/\Delta C_p^{exp}$ was 1.5 (see Table 1), where T_1 in ΔC_p^{exp} is ~381 K [8]. Accordingly, the number of structural units holding one photon potentially in holes, n (= h^h/h_x), is defined here necessarily. Fig. 2 shows the sequence models of– *TTTT*– (n= 1) and unstable– *TCTC*– (n = 2) for iPS, where *C* is the cis isomer.
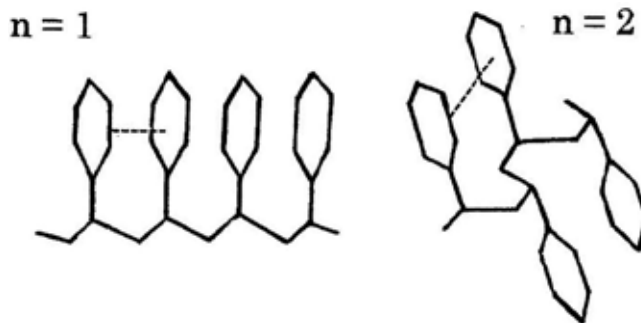
Figure 2. The sequence models of– *TTTT*– (n = 1) (Left) and unstable– *TCTC*– (n = 2) (Right) for iPS. The dashed line shows one of the photon sites between benzene rings.

According to h^h/h_x= 1.5, h_x (= $2h_0^h$) = 16.1 kJ/mol was derived. This corresponded to $\Delta C_p T_g$= 16.1 kJ/mol* of the C_p jump energy for holes at T_g. While h_x can be also derived from the δ solubility parameter, δ {= $(h_0/V)^{1/2}$}, where h_0 is the latent cohesive energy per molar structural unit,

corresponding to the heat of vaporization or sublimation and V is the molar volume of structural units. The relations among h_0, h_u, h_x, and h_g at temperatures before and after T_g are given by [19, 27]:

$$h_0 = h_g + h_x \text{ or } h_g + h_x + h_u \text{ at } T \leq T_g \tag{8}$$

$$h_0 = h_x \text{ or } h_x + h_u \text{ at } T > T_g \tag{9}$$

where h_u is the heat of fusion per molar structural unit. For crystalline polymers, h_u is contained in Eqs. (8) and (9). For iPS, $h_0 = 35.0$ kJ/mol was derived from $\delta = 9.16$ (cal/cm^3)$^{1/2}$ of the mean of 12 experimental values (≥ 9.0 (cal/cm^3)$^{1/2}$) [28], and the value of h_x from Eq. (8), 16.1 kJ/mol, agreed with that from $h^h/h_x = 1.5$ perfectly. However it was smaller than h_g (= RT_g^2/c_2) = 18.9 kJ/mol. The difference in h_g and h_x, 2.8 kJ/mol, agreed with the cohesive energy of methylene residues of $h_m^{int} = 2.8$ kJ/mol [29], suggesting that the ordered part / hole pairs might fill softly the parts in glassy bulks.

T_g K	h_0 kJ/mol	h_g kJ/mol	Δh kJ/mol	h_x kJ/mol	h^h kJ/mol*	h^h/h_x
359*1 (360)	43.1*2	18.9	5.3	24.2*4	24.2	1
359*1 (360)	35.0*2,*3	18.9	−2.8	16.1	24.2	1.5
240	1.7*2	1.7*5	−1.7	0	0 (16.1)	---

*1: experimental value [30]. *2: from Eq. (8). *3: from $\delta = 9.16$ (cal/cm^3)$^{1/2}$. *4: h_x for the excited ordered parts or $- TTTT-$ sequences. *5: $h_g = h_g^{int} + h_g^{conf}$ from $h_g^{int} = - f_g^{conf}$ at $T_g = 240$ K (see Fig. 4, described below). The value in ( ) of h^h column is h^h (= $3C_v^{ph}T$) at 240 K.

Table 2. The values of T_g, h_0, h_g, Δh, h_x, h^h, and h^h/h_x for iPS.

Table 2 shows the values of T_g, h_0, h_g, Δh, h_x, and h^h at $h^h/h_x = 1$ and 1.5 for iPS. In the 4th line, $h^h = h_x = 0$ and $h_g = 1.7$ kJ/mol at 240 K are shown (discussed below). The relation of $h^h = h_x = 0$ is brought by the energy radiation of $2h_0^h$ (= 16.1 kJ/mol*) at T_g and the energy loss of h_0^h (= 8.1 kJ/mol*) upon cooling from T_g obeying:

$$h^h = h_0^h - 3C_v^{ph}(T_g - T) \tag{10}$$

In Eq. (10), the specific temperature of 240 K at $h^h = 0$ agreed with the hole temperature at h^h (= $3C_v^{ph}T$)= 16.1 kJ/mol*. In the glasses upon heating from 0 K, the generation of ordered part / hole pairs at 240 K and succeedingly, the instant radiation of the hole energy of 16.1 kJ/mol* should bring the same state as that of $h^h = 0$ at 240 K upon cooling, suggesting $T_g = 240$ K for the homogeneous glass free from the ordered part / hole pairs. Altering $3C_v^{ph}$ (= C_p^{ph}) in Eq. (10) to C_v^{ph}, the temperature at $h^h = 0$ was $T_g = 0$ K. While for the glasses including the ordered part /

hole pairs, T_g= 360 K (see Table 2) was expected from the quantum demand of hole energy at regular temperature intervals of 120 K.

For iPS, the rotational isomeric 2–state (RIS) model of T (trans) and G (gauche) or G' (gauche') is known well [31]. Fig. 3 depicts the helix structure of – $TGTGTG$ – (n = 3) for iPS. From h^h/h_x (= n) = 1.5, the intermediate sequences (n = 1.5) between the right or left handed helical sequence (n = 3) and the aperiodic sequence (n = 0), displaying the helix–coil transition, were predicted as the sequences of ordered parts [14, 15]. The frequency of occurrence, Γ, of the helix–coil transition should be given approximately by h^h/h_0^h in Eq. (10) with h^h/h_0^h= 0 at T = 240 K. The ΔC_p (= $3C_v^{ph}$) at T_g= 240 K in a glassy state of Γ = 0 was 67.4 J/(K mol*) [15].
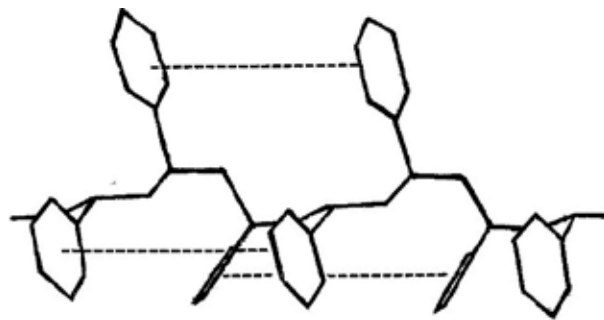
Figure 3. The 3/1 helix structure of – $TGTGTG$– (n = 3) and the photon sites (dashed line parts) between benzene rings for iPS.
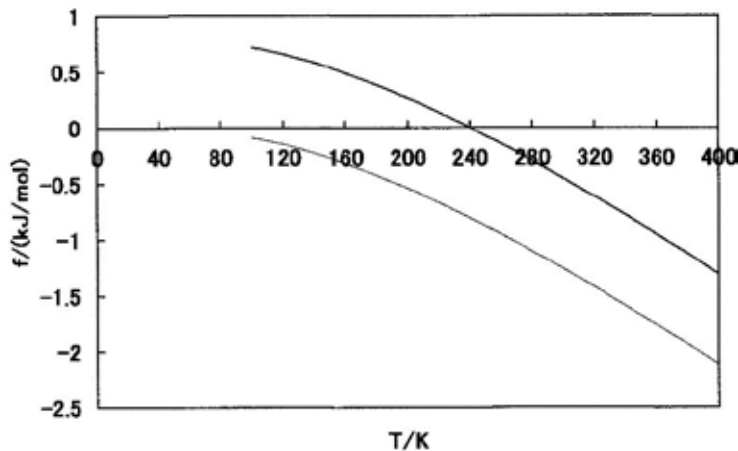
Figure 4. The relation between f and T calculated for the RIS model chains (x = 100) of iPS. The thin line is f = f^{conf} and the thick line is f = f^{conf}+ 0.81 kJ/mol.

Fig. 4 shows the relation between f (= f^{conf} or f^{conf}+ 0.81 kJ/mol) and T calculated for the RIS model chains (x = 100) with the normalized statistical weight of η = 1 applied to TG isomer of

iPS, where f^{conf} is the conformational free energy per molar structural unit, being minus and decreasing with an increase in temperature. Adding the value of $-f^{conf}$ (= 0.81 kJ/mol) at 240 K to all values of the original thin line, the thick line of f^{conf}+ 0.81 kJ/mol is depicted. In the case of $-f^{conf}$= h^{int}, i.e., $(h^{conf}+ h^{int}) - Ts^{conf}$= 0 at 240 K, the sum of $-f^{conf}$ (= 0.81 kJ/mol) and h^{conf} (= 0.89 kJ/mol), 1.70 kJ/mol, should be the ultimate h_g at the first order glass phase transition for the homogeneous glass free from the ordered part / hole pairs (see Table 2), where h^{int} is the cohesive enthalpy per molar structural unit, and h^{conf} and s^{conf} are the conformational enthalpy and entropy per molar structural unit.

Fig. 5 shows the schematic chart of the instantaneous state changes at T_g (= 360 K) upon cooling and heating as a working hyposesis. The ordered part / hole pairs formed instantaneously at T_g upon cooling have h^h= $h_0{}^h$ and h_x= $2h_0{}^h$. At T_g upon heating, the ordered part / hole pairs are excited by absorbing the photon energy of $2h_0{}^h$ for the holes and adding the energy of $h_0{}^h$ for the ordered parts, followed by the absorption of h_g for the glass parts. The equilibrium relation at the melting transition among the ordered parts, the holes, and the flow parts is shown by the dashed lines in Fig. 5. In order to melt the excited ordered part / hole pairs perfectly, further the latent heat of $h_0{}^h$ is needed at T_g.
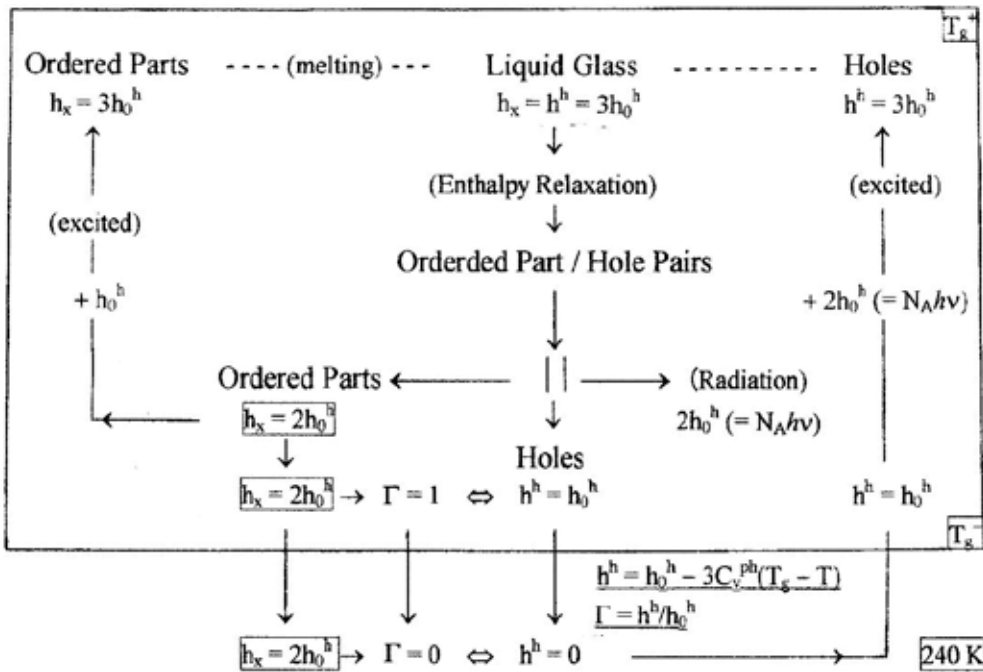
Figure 5. The schematic chart of the instantaneous state changes at T_g for iPS. The arrow marks of ↓ and ↑ show the cooling and heating directions, respectively. $T_g{}^+$ and $T_g{}^-$ are the glass transition temperatures upon cooling and heating, respectively. The h_x= $2h_0{}^h$ shows the substance of helix–coil transition between the helical sequence (n = 3) and the aperiodic sequence (n = 0). The arrow marks of ⇔ show the interaction between the ordered parts and the holes in the pairs. The Γ is the frequency of occurrence of the helix–coil transition. The dashed lines show the equilibrium relation of melting among ordered parts, flow parts, and holes in the excited state.

2.2. Poly(ethylene terephthalate)

For PET, h_x (= h_g+ Δh) = 24.1 kJ/mol was obtained from Eq. (5), being almost equal to h^h (= $3C_v^{ph}T_g$) = 23.0 kJ/mol* at T_g (= 342 K) [10, 23]. Thus, h^h/h_x (= n) = 0.95 was shown experimentally. However as shown in Table 1, $\Delta C_p/\Delta C_p^{exp}$ was 0.6. Table 3 shows the values of T_g, h_0, h_u, h_g, Δh, h_x, h^h, and h^h/h_x for PET. The two values of h_u, 23.0 and 28.5 kJ/mol, are assigned to the crystals with the conformational disorder of ethylene glycol parts and the smectic–c crystals with the stretched sequences, respectively [23, 32]. $\Delta C_p/\Delta C_p^{exp}$= 0.6 at the glass transition meant that one photon was situated in the neighboring phenylene residues comprising ~60 % of the structural unit length and 40 % of ΔC_p^{exp} was brought by unfreezing of the ethylene glycol parts in a glass state [14]. This was predicted also from the data by TMDSC [8]. From h^h= (3/2) $N_A h\nu$ and h^h (= $3C_v^{ph}T_g$) = 23.0 kJ/mol* at T_g= 342 K, $1/\lambda$ = 1290 cm^{-1} was derived, agreeing with 1288 cm^{-1} observed for the un–oriented samples [33].

T_g K	h_0 kJ/mol	h_u kJ/mol	h_g kJ/mol	Δh kJ/mol	h_x kJ/mol	h^h kJ/mol*	h^h/h_x
342	64.7*1	23.0 (535 K)	17.6*3	6.5	24.1	23.0	0.95
342	70.2*1, 68.2*2	28.5 (549 K)	17.6*3	6.5	24.1	23.0	0.95

*1: from Eq. (8). *2: from δ = 10.7 (cal/cm^3)$^{1/2}$ [19]. *3: h_g= RT_g^2/c_2^2. The values in () are T_m^∞ of the respective crystals [23].

Table 3. The values of T_g, h_0, h_u, h_g, Δh, h_x, h^h, and h^h/h_x for PET.
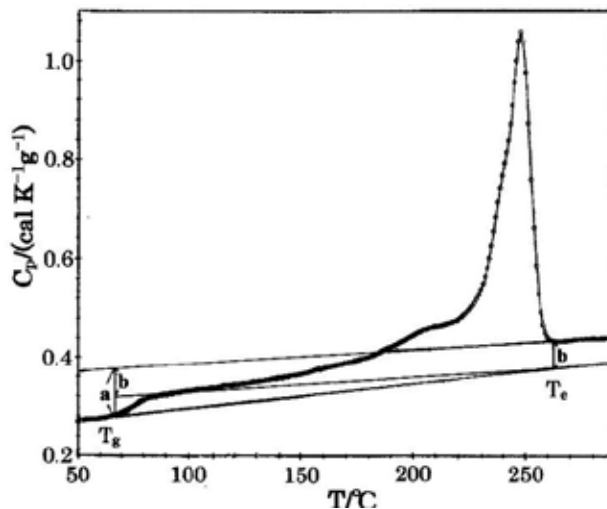
Figure 6. The C_p curve for the non–annealed PET film. The parts of a and b show the C_p jump to the liquid line at T_g and T_e.

Fig. 6 shows the C_p curve converted from DSC curve data for the non–annealed PET film cooled to 323 K (50 °C) at 5 K/min from 573 K (300 °C). T_g agreed almost with 342 K of [8]. T_e of the

end temperature of melting is 535 K (262 °C). The parts of a, b, and a – b of C_p jump to the liquid line at T_g and T_e were correlated to the structural unit length, the lengths of phenylene and glassy ethylene glycol residues, respectively. Fig. 7 shows the parts in the structural unit related to a, b, and a – b.
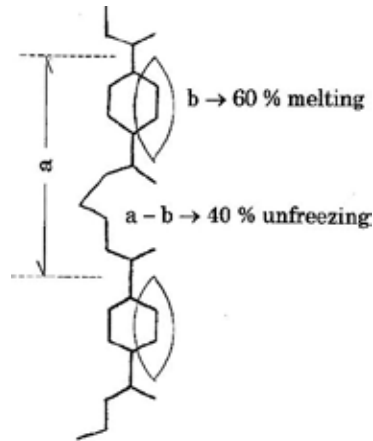

Figure 7. The parts in the structural unit related to the C_p jumps of a, b, and a – b shown in Fig. 6 for PET. The part attached to the spindle mark shows the phenylene residue holding one photon together with the neighboring same residue (omitted here).

2.3. Isotactic polypropylene

According to the scheme of the formation of ordered part / hole pairs at T_g upon cooling (see Fig. 5), for iPP with T_g= 270 K, h_x (= $2h_0^h$) = 12.1 kJ/mol was derived, much larger than $h_g \approx H_g^a - H_g^c$= 6.2 kJ/mol [34] and h_x (= $h_g+ \Delta h$) = 7.4 kJ/mol, where $\Delta h = \Delta H - Q$, $\Delta H = H_m^a - H_c^a$ (see Eqs. (5) and (6)). The used data are as follows: T_c= 403.6 K, T_m^∞= 450 K for α form crystals, ΔH = 4.89 kJ/mol [34], and Q = 3.76 kJ/mol for the sample annealed at 461.0 K for 1 hour [10, 35]. However, h_0 (= $h_g+ h_x$) = 18.3 kJ/mol from Eq. (8) was almost equal to h^h (= $3h_0^h$) = 18.2 kJ/mol*, meaning the appearance of frozen glasses with h_g= h_0^h+ 0.1 kJ/mol. For holes with C_p^{ph} even upon cooling from T_g, Eq. (10) showed the specific temperature of 180 K, at which all ordered part / hole pairs should be disappeared because of h^h= 0, corresponding to 240 K for iPS [15]. At temperatures below 180 K, all should be in a state of the homogeneous glass with T_g= 180 K. The ΔC_p (= $3C_v^{ph}$) = 67.4 J/(K mol*) at T_g= 180 K was the same as that of iPS with T_g=240 K. Fig. 8 shows the relation between f (= f^{conf} or f^{conf}+ 0.1 kJ/mol) and T calculated for RIS model chains (x = 100) with the normalized statistical weight of σ = 1 applied to *TT* isomer of iPP [36, 37]. The f^{conf} at temperatures below and above 180 K is minus and decreases with an increase in temperature. The absolute value of f^{conf}= – 0.102 kJ/mol at 180 K equaled to $h_g - h_0^h$= 0.1 kJ/mol at 270 K. Adding the cohesive enthalpy of h^{int}= 0.102 kJ/mol to f^{conf} (= – 0.102 kJ/mol), from f = f^{conf}+ h^{int}= 0 and h^{conf}= 0.18 kJ/mol at T_g= 180 K, h_g (= h^{conf}+ h^{int}) = 0.28 kJ/mol is derived as the first order glass phase transition enthalpy for the homogeneous glass composed

of isolated chains, but with the cohesive energy of h^{int} and free from ordered part / hole pairs (see Table 5).
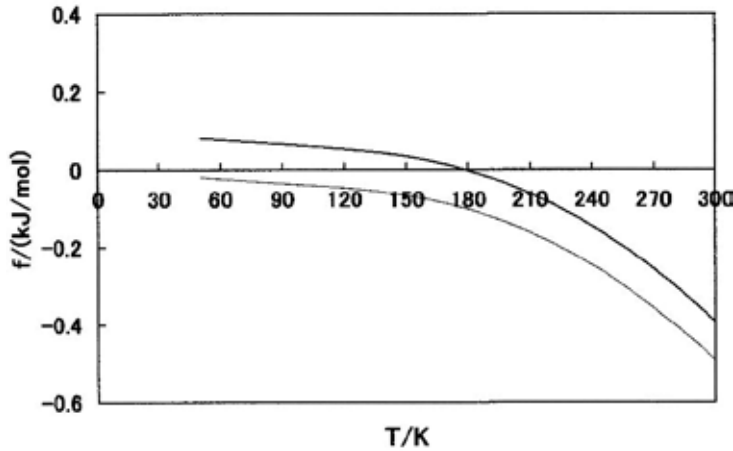

Figure 8. The relation between f and T calculated for RIS model chains (x = 100) of iPP. The thin line is f = f^{conf} and the thick line is f = f^{conf}+ 0.1 kJ/mol.

On the other hand, altering $3C_v^{ph}$ (= C_p^{ph}) in Eq. (10) to C_v^{ph}, the temperature at h^h= 0 was T_g= 0 K as well as iPS. From s^{conf}=0.38 J/(K mol) of constant at temperatures below 70 K, the sequence model of $-TGTGTG\textbf{TT}G'TG'TG'T-$ in a liquid state was predicted, where T is trans, G is gauche, G' is gauche' isomer, and TT is the trans–trans isomer shifting always to the left or right direction on a sequence [38]. From h_x= 12.1 kJ/mol, the nodules of mesophase interchanging between crystals and ordered parts automatically were predicted in the glasses. According to the equilibrium relation in crystals and ordered parts of this class (D in Table 4) given by f_x= $2f_u$ [10, 39], $2h_u - h_x$= 2.9 kJ/mol was derived using h_u= 7.5 kJ/mol for α form crystals, corresponding to $2T_m(s_u - s_x/2)$, which was almost equal to h_m^{int}= 2.8 kJ/mol of the cohesive energy of methylene residues in the sequences, where f_x and s_x are the free energy and entropy per molar structural unit for ordered parts, and f_u and s_u are those for crystals.

According to Flory's theory [40] on the melting of the fringe–type crystals with a finite crystal length of ζ, the end surface free energy of crystals per unit area, σ_e, at $(df_u/d\zeta)_\phi$= 0 is given by:

$$\sigma_e = \mu(RT\zeta/2)[1/(x - \zeta +1) + (1/\zeta)ln\{(x - \xi +1)/x\}] \tag{11}$$

where ϕ is the amorphous fraction and μ is the conversion coefficient of mol/m^3. In this context:

$$2\sigma_e/\zeta = \mu(f_x - f_u) \tag{12}$$

$$f_x' = RT[(1/\zeta)ln\{(x - \zeta +1)/x\} - lnP_c] \tag{13}$$

where P_c, given by $\{(x - \zeta + 1)/x\}^{1/\zeta}$ for fringe–type crystals, is the probability that a sequence occupies the lattice sites of a crystalline sequence. Moreover:

$$f_u - (f_x - f_x') = 0 \tag{14}$$

Eq. (11) is obtained when $\ln P_c = -1/(x - \zeta + 1)$. From Eq. (14), the relations are derived based on f_u and f_x at $f_x' \geq 0$, and those can be grouped into four equilibrium classes (A ~ D) and one non–equilibrium class (X) as shown in Table 4. Class A of $f_x = f_u$ at $f_x' = 0$ shows the dynamic equilibrium relation between the ordered parts and the crystal parts of same fringe–type, leading to $\sigma_e = 0$, and that, $\zeta = 0/0$ in Eq. (16) (described below). For class B, $f_u = -f_x'$ from Eq. (14) with $f_x = 0$ refers to the anti–crystal holes and $f_x = 0$ is assigned to the ordered parts of $\zeta = \infty$. The interface between the anti–crystal holes and the ordered parts should work as the reflector of photons. In this case, the even interface made of the folded chain segments should be avoided through the random reflection. According to Eq. (12) with $h_x - h_u = \sigma_e/(\mu\zeta)$, the respective interface energies of the hole and the ordered part are compensated each other at the common interface, thus leading to $f_x = 0$ [10]. For class C, $f_x = f_x'$ from Eq. (14) with $f_u = 0$ is assigned to the ordered parts of $\zeta \neq \infty$ (i.e., a kebab structure) and $f_u = 0$ to the crystals of $\zeta = \infty$ (i.e., a shish structure). Class D of $f_u (= f_x') = f_x/2$ is related to the equilibrium in crystal and ordered parts. For those with folded chains, the reversible change from crystal or ordered parts to other parts is expected to take place automatically. The relations in class X do not satisfy Eq. (14), suggesting that the holes of class B cannot be replaced by the crystals with $\zeta \neq \infty$. Fig. 9 shows the schematic structure models of bulk polymers conformable to A ~ X classes in Table 4.

f_x'	f_x	f_u	Class
$f_x' = 0$	$f_x = f_u$	$f_u = f_x$	A
$f_x' > 0$	$f_x = 0$	$f_u = -f_x'$	B
	$f_x = f_x'$	$f_u = 0$	C
	$f_x = 2f_u$	$f_u = f_x/2 = f_x'$	D
$f_x' > 0$	$f_x = 0$	$f_u = f_x'$	X

Table 4. Relations of equilibrium (A ~ D) and non–equilibrium (X) in f_x and f_u at $f_x' \geq 0$ for crystalline polymers [10, 39].

At the rapid glass transition absorbing the photon energy of $2h_0^h$ at T_g upon heating, the ordered part / hole pairs should be excited immediately and then melted, followed by unfreezing of the glass parts. At the slow glass transition, the disappearance and then crystallization of ordered part / hole pairs should occur upon heating, bringing the new crystal parts [16]. In the closed system that the both heats of crystallization and melting should be cancelled out according to Eq. (4), those should be melted by T_l in Fig. 1. While in the open system that the heat irradiated by crystallization was escaped out of the system, T_l corresponded to T_m^∞ (450 K for α form crystals) and $h_0 (= h_g + h_x + h_u) = 21.0$ kJ/mol in Eq. (8) agreed
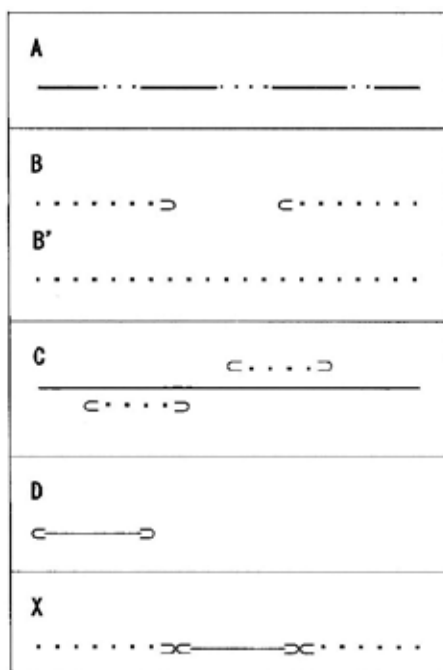
Figure 9. Schematic structure models of bulk polymers. A ~ X correspond to the classes in Table 4, respectively. •••: ordered parts, ¾¾ : crystals, ⊃ and ⊂: folded segments, the space between ⊃ and ⊂ of B: anti–crystal hole. B is equivalent to B'.

perfectly with the value of h^h (= $3h_0^h$)+ h_m^{int}, where h_x (= h_g+ Δh) is 7.4 kJ/mol, being larger than h_0^h (= h^h/3)= 6.1 kJ/mol*. In this context, $h_g - h_0^h$= 0.1 kJ/mol, $h_x - h_0^h$= 1.3 kJ/mol, and $h_u - h_0^h$= 1.4 kJ/mol. The sum of them was equal to h_m^{int}= 2.8 kJ/mol. Thus, n (= h^h/h_x) = 2.5 was shown, almost corresponding to $\Delta C_p/\Delta C_p^{exp}$= 2.3. Table 5 shows the values of T_g, h_0, h_u, h_g, h_x, h^h, and h^h/h_x for iPP. From h^h (= $3h_0^h$) = 18.2 kJ/mol* at T_g (= 270 K), the wavenumber of $1/\lambda$ = 1022 cm^{-1} was derived for a photon in holes [10]. This agreed nearly with 1045 cm^{-1} relating to the crystallinity [41]. Accordingly, one photon should be situated between the neighboring methyl groups in the helical sequence.

Tg K	h_0 kJ/mol	h_u kJ/mol	h_g kJ/mol	h_x kJ/mol	h^h kJ/mol*	h^h/h_x
270	18.3*1	---	6.2*3	12.1	18.2	1.5
270	21.1*1	7.5*2	6.2*3	7.4	18.2	2.5
180	0.28*1	---	0.28*4	0	0	---

*1: from Eq. (8). *2: h_u for α form crystals. *3: h_g= H_g^a – H_g^c, *4: h_g= h_g^{int}+ h_g^{conf} from h_g^{int}= – f_g^{conf} at T_g= 180 K.

Table 5. The values of T_g, h_0, h_u, h_g, h_x, h^h, and h^h/h_x for iPP.

2.3.1. Equilibrium melting temperature, T_m^∞

For PET discussed in the previous section **2.2**, T_l in Fig. 1 corresponded to T_m^∞= 535 K for the crystals with conformational disorder of ethylene glycol parts, but with a chain axis parallel to c-axis of a cell. This finding in PET was also discussed in iPP with T_m^∞= 435 K, 450 K, and 462 K for β, α, and γ form crystals, respectively, which were found by DSC measurements [35]. Above all, T_m^∞= 450 K for α form crystals could be T_l (in Fig.1) of the temperature expected from the quantum demand of hole energy at regular temperature intervals of 90 K. Experimentally, T_m^∞ is determined as the intersection temperature between an extrapolation line of $T_m = T_e$ in the melting peaks without superheating and a $T_m = T_a$ line, where T_m is the melting temperature from T_a to T_e, T_a is the annealing (crystallization) temperature, and T_e is the end temperature of melting peak. While at T_m^∞, the processes of melting and crystallization should occur reversibly, so that T_m^∞ equals to both temperatures of T_e and T_b of the onset temperature of melting, and that, there are two points of T_m^∞ at T_a (= T_e) and T_b (= T_e) on a $T_m = T_e$ line. The line through two points of T_m^∞ should be parallel to the abscissa of T_a, because T_m^∞ is only one [23]. For the bulk contained α form crystals with h_u= 7.46 kJ/mol, the sum of $h_g - h_0^h$= 0.1 kJ/mol, $h_x - h_0^h$= 1.3 kJ/mol, and $h_u - h_0^h$= 1.4 kJ/mol was equal to h_m^{int}= 2.8 kJ/mol (see section **2.3**). While for the bulk contained only γ form crystals with h_u= 8.70 kJ/mol, the difference in h_m^{int} and ($h_u - h_0^h$) was 0.2 kJ/mol, suggesting $h_g = h_x = h_0^h$+ 0.1 kJ/mol. Figs. 10 and 11 show the DSC single and double melting peak curves for the iPP films annealed at T_a= 461.0 K and 441.5 K for 1 hour, respectively. Here the single melting peak curve in Fig. 10 is divided into α and β peaks, and the double melting peak curve in Fig. 11 is divided into γ, α, and β peaks. In both Figures, T_b is the temperature that the extrapolation line from the line segment with a highest slope in the lower temperature side of the melting peak intersects the base line. The onset temperature of the extrapolation line, T*, is also the end temperature of the residual peak appeared by subtracting the area of single or double peak with T_b from the total endothermic peak area. The β peak is considered to be due to the melting of small crystals attached around the crystal lamellae of α form. The mean of end temperatures in β peaks found for some annealing samples agreed closely with T_e= 435 K of β form crystals [42].

Table 6 shows the values of T_b, T*, Q_m, ΔQ_m, Δh^h, and $\Delta h^h / \Delta Q_m$ in α and γ peak curves for the iPP films annealed at 461.0 K and 441.5 K for 1 hour. Where Q_m is the heat per molar structural unit corresponding to the area of α or γ peak from T_b and ΔQ_m is the heat per molar structural unit corresponding to the area from T_b to T* of α or γ peak and relating to the melting of crystals recrystallized newly from β to α form or α to γ form. For the holes of crystal / hole pairs formed newly by recrystallization from T_b to T* of β or α peak, the hole energy per molar photon, Δh^h, is given by [10]:

$$\Delta h^h = 3 C_v^{ph} \left(T^* - T_b \right) \tag{15}$$

As shown in Table 6, the small difference in ΔQ_m and Δh^h could be regarded as significant for the formation and then disappearance of crystal / hole pairs from T_b to T*. For the shift from

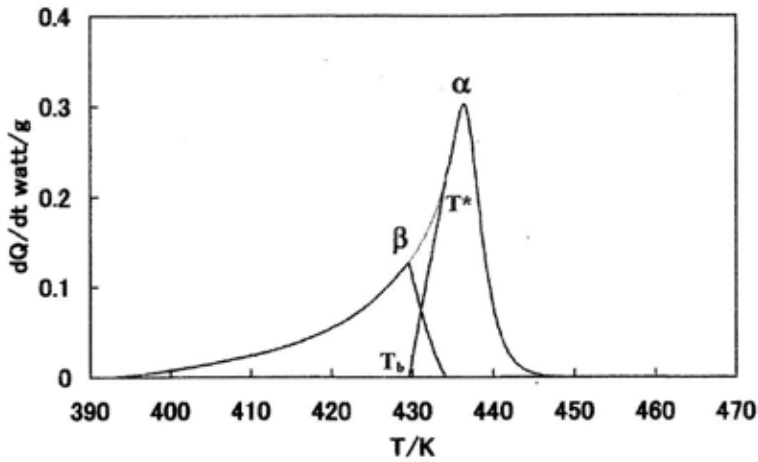**Figure 10.** DSC single melting peak curve composed of α and β peaks for the iPP film annealed at 461.0 K for 1 hour. The thin line is the part of an original DSC curve. T_b is the onset temperature of α peak and T* is the end temperature of β peak.
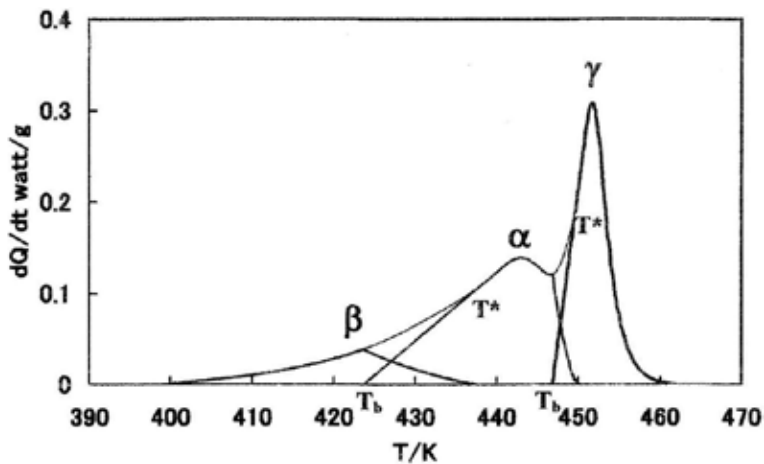

Figure 11. DSC double melting peak curve composed of α, β, and γ peaks for the iPP film annealed at 441.5 K for 1 hour. The thin lines are the parts of an original DSC curve. T_b is the onset temperature of γ or α peak and T* is the end temperature of α or β peak.

β to α peak in Fig. 11, $\Delta h^h / \Delta Q_m$ was 1.21 contrary to our expectation, but at T*= 435 K of the mean of T* (T_m^∞ for β form crystals), $\Delta h^h / \Delta Q_m = 0.98$ was derived. For the shift from α to γ peak, it was 0.61, meaning the melting of original γ form crystals with 39 % of ΔQ_m; 0.13 kJ/mol. The relay of melting from α to γ form crystals between two peaks of a DSC double melting peak curve should be done through the mediation of the formation and then disappearance of the crystal / hole pairs with 61 % of ΔQ_m; 0.20 kJ/mol (= Δh^h), which agreed with the difference in h_m^{int} and ($h_u - h_0^h$) perfectly, corresponding to ($h_g + h_x$) − $2h_0^h = 0.2$ kJ/mol suggested above.

T_a K	Form	T_b K	T^* K	Q_m kJ/mol	ΔQ_m kJ/mol	Δh^h kJ/mol	$\Delta h^h/\Delta Q_m$
461.0	α	429.6	434.2	2.05	0.38	0.24	0.63
441.5	α	423.7	437.7 (435)	2.16	0.78	0.94 (0.76)	1.21 (0.98)
	γ	446.9	449.9	1.64	0.33	0.20	0.61

The values in ( ) show T_m^∞, Δh^h, and $\Delta h^h/\Delta Q_m$ at T_m^∞ for β form crystals.

Table 6. The values of T_b, T^*, Q_m, ΔQ_m, Δh^h, $\Delta h^h/\Delta Q_m$ of α and γ peak curves for the iPP films annealed at 461.0 K and 441.5 K for 1 hour.

2.3.2. ζ distribution function, F (ζ)

Next, the α peak curve in Fig. 10 and the two divided peak curves of α and γ in Fig. 11 starting to melt at T_b were converted into the crystal length (ζ) distribution function, F(ζ). The ζ is according to Gibbs–Thomson given by:

$$\zeta = \left\{ T_m^\infty / \left(T_m^\infty - T_m \right) \right\} \left\{ 2\sigma_e / \left(\mu h_u \right) \right\} \tag{16}$$

where T_m is the corrected melting temperature. In the calculation of ζ, the values of T_m^∞, h_u, h_x, σ_e, and the corrected T_m are needed previously. For h_u, the reference value was used (see Table 8). The value of σ_e was evaluated by [43, 44]:

$$\sigma_e = \mu h_u c^* \left[\left\{ R T_m^2 + \left(H_x - h_x \right) \left(T_m^\infty - T_m \right) \right\} / \left\{ 2 \left(H_x - h_x \right) T_m^\infty \right\} \right] \tag{17}$$

with $H_x = 2h_u - Q_m$

where c^* is the cell length of c–axis. The term of square blanket in Eq. (17) is dimensionless. h_u refers to the heat of fusion of crystals with a crystal form liking to evaluate σ_e. h_x could be calculated from Eqs.(5) and (6), but in Fig. 11, using H_m^a at T_m^∞ of the other α or γ form crystals (sub–crystals). Table 7 shows the values of h_x for the iPP films annealed at 461.0 K and 441.5 K for 1 hour, together with the values of T_c, T_b, T_e, Q, ΔH, Δh, and h_g used in the calculation of h_x. Q and ΔH are defined in Eq. (6). The value of h_x for the iPP sample of T_a= 441.5 K was smaller than h_u of the sub–crystals (see Table 8). Further, the value of h_x in the row of γ form, 6.85 kJ/ mol, was ~0.7 kJ/mol larger than h_g (= 6.22 kJ/mol). Also the value of h_x in the line of α form, 8.07 kJ/mol, was ~0.7 kJ/mol larger than h_x (= 7.35 kJ/mol) for the sample of T_a= 461.0 K. Therefore, the value of h_0 (= h_g+ h_x+ h_u) in Eq. (8) for the iPP sample annealed at 441.5 K was 0.7 kJ/mol larger than that for the iPP sample of T_a= 461.0 K. The cause could be attributed to Δh affected by F(ζ) (see Eq. 18) of α form crystals, leading the characteristic R–L image (see Fig. 15).

Form[*1] (T_a/K)	T_c K	T_b K	T_e K	Q kJ/mol	ΔH kJ/mol	Δh kJ/mol	h_g kJ/mol	h_x kJ/mol
α (461.0)	403.6	429.6	449.2	3.76	4.89	1.13	6.22	7.35
α (441.5)	403.6	423.7	449.5	4.41	6.26 (γ)[*2]	1.85	6.22	8.07
γ (441.5)	403.6	446.9	461.9	4.41	5.04 (α)[*2]	0.63	6.22	6.85

*1: The form of main crystals liking to evaluate σ_e. *2: ΔH calculated using $H_m{}^a$ at $T_m{}^\infty$ of the sub–crystals with the form of α or γ shown in ( ).

Table 7. The values of h_x, T_c, T_b, T_e, Q, ΔH, Δh, and h_g for the iPP films annealed at 461.0 K and 441.5 K for 1 hour.

T_a K	Form	T_p K	h_u kJ/mol	h_x kJ/mol	h_0 kJ/mol	Q_m kJ/mol	σ_e J/m²
461.0	α	435.9	7.46	7.35	14.8	2.05	36.0×10^{-3} (26.7×10^{-3})
441.5	α	442.8	7.46	8.07	15.5	2.16	45.2×10^{-3} (30.8×10^{-3})
	γ	450.9	8.70	6.85	15.6	1.64	26.5×10^{-3} (22.2×10^{-3})

The values in ( ) are σ_e at $T_m{}^\infty$ ($Q_m = 0$).

Table 8. The values of σ_e, T_p, h_u, h_x, h_0 (= $h_x + h_u$), and Q_m for the iPP films annealed at 461.0 K and 441.5 K for 1 hour.

Table 8 shows the values of σ_e at T_p for α and γ form crystals contained in the iPP films annealed at 461.0 K and 441.5 K for 1 hour, together with the values of T_p, h_u, h_x, h_0, and Q_m used in the calculation of σ_e, where T_p is the melting peak temperature. The σ_e of α form was larger than that of γ form, because according to Eq. (17), the σ_e was mainly dependent on h_x. For α and γ forms in the sample of T_a= 441.5 K, h_0 (= $h_u + h_x$) at T (> T_g) of Eq. (9) was ~15.5 kJ/mol, nevertheless the values of h_u were different. T_p is corrected by 0.6 K (436.5 K → 435.9 K) for the sample of T_a= 461.0 K and 0.2 K (443.0 K → 442.8 K) for α form and 0.8 K (451.7 K → 450.9 K) for γ form in the sample of T_a= 441.5 K to the lower temperature side, according to our concept [45].

$F(\zeta)$ is defined as [23]:

$$F(\zeta) = (\delta Q_m / Q_m) / \zeta = n_\zeta / \{N_c(T_e - T_b)\} \tag{18}$$

where δQ_m (= $\zeta n_\zeta Q_m / \{N_c(T_e - T_b)\}$) is the heat change per molar structural unit per K, n_ζ is the number of crystal sequences with ζ, N_c is the number of structural units of crystals melted in the temperature range from T_b to T_e. $\delta Q_m / Q_m$ is given by:

$$\delta Q_m \big/ Q_m = \left(dQ \big/ dt \right) \Big/ \int_{T_b}^{T_c} (dQ / dt) dT \qquad\qquad (19)$$

where dQ/dt is the heat flow rate of DSC melting curve and t is time (see Figs. 10 and 11). Figs. 12 and 13 show F(ζ) of α and γ peak curves converted from the DSC single and double melting peak curves for the iPP films annealed at 461.0 K and 441.5 K for 1 hour.
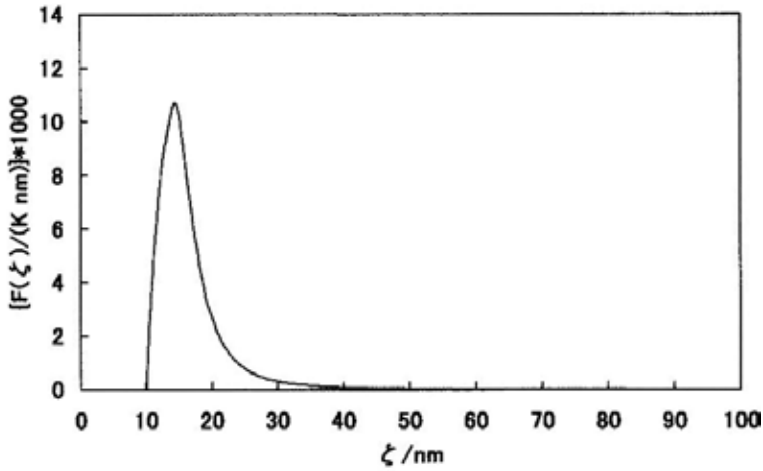
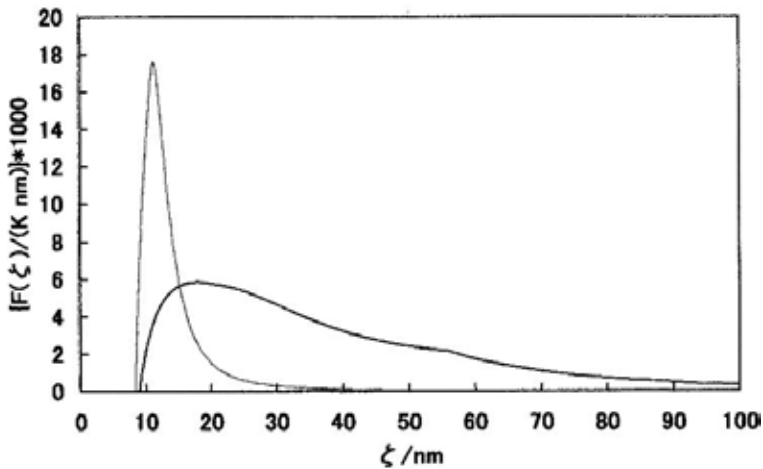**Figure 12.** F(ζ) of α peak curve for the iPP film annealed at 461.0 K for 1 hour.

Figure 13. f(ζ) of α (thick line) and γ (thin line) peak curves for the iPP film annealed at 441.5 K for 1 hour.

Table 9 shows the ζ range and ζ_p in F(ζ) of α and γ peak curves obtained for the samples of T_a= 461.0 K and 441.5 K, where ζ_p is ζ at the maximum of F(ζ). For α peak, F(ζ) in Fig. 12 showed a sharp peak with the ζ range of 10 nm ~ 3870 nm and ζ_p= 14.6 nm, and in Fig 13, F(ζ) showed the roundish curve with the ζ range of 10 nm ~ 250 nm and ζ_p= 19.5 nm, whereas for γ peak, F(ζ) showed the sharp peak with the ζ range of 8 nm ~ 840 nm and ζ_p= 11.2 nm. The maximum of ζ was calculated using T_e ($\sim T_m^\infty$) observed actually for each sample. At T_e= T_m^∞, the maximum of ζ should be infinite at $\sigma_e \neq 0$, because the melt at T_e could be interchanged in equilibrium to the imaginary crystals of $\zeta = \infty$. In the σ_e= 0 of the class A in Table 4, ζ = 0/0 of indetermination at T_m^∞ is derived from Eq. (16). The refraction point at ζ = 55 nm on the thick line of α peak in Fig. 13 is that of dQ/dt at T_b (= 446.9 K) in Fig. 11. For the sample of T_a= 441.5 K, the ζ range of α peak was narrower than that of γ peak, because upon cooling, α form crystals should be formed around γ form crystals. As the result, the value of h_x at the interfaces between α and γ form crystals increased only ~0.7 kJ/mol (derived above). The ζ range of α peak calculated for the sample of T_a= 461.0 K was much larger than those of α and γ form crystals for the sample of T_a= 441.5 K.

T_a K	Form	ζ range nm	ζ_p nm
461.0	α	10 - 3870	14.6
441.5	α	10 - 250	19.5
	γ	8 - 840	11.2

Table 9. The ζ range and ζ_p in F(ζ) of α and γ peaks for the iPP films annealed at 461.0 K and 441.5 K for 1 hour.

In the last stage, the ζ distribution of a single–crystal like image was drawn from F(ζ). The number of crystal sequences in a radius direction, R_n, is given by [10]:

$$R_n = \left(\Delta N / \pi \right)^{1/2} \tag{20}$$

with $\Delta N = N_c \left(T_e - T_b \right) \left(\int_{\zeta_n}^{\zeta_x} F(\zeta) d\zeta - \int_{\zeta_n}^{\zeta} F(\zeta) d\zeta \right)$

where ζ_x and ζ_n are the maximum and the minimum of ζ, respectively. Figs. 14 and 15 show the representation of R (= ±R_n) and L (= ±ζ/2) for α and γ form crystals in the iPP films (per 1g) annealed at 461.0 K and 441.5 K for 1 hour.

From the comparison of both figures, the change of image in α form crystal lamellae by annealing, and further in Fig. 15, the difference in packing states of α and γ form crystals in same ζ range can be seen at the view of 2D disk image.
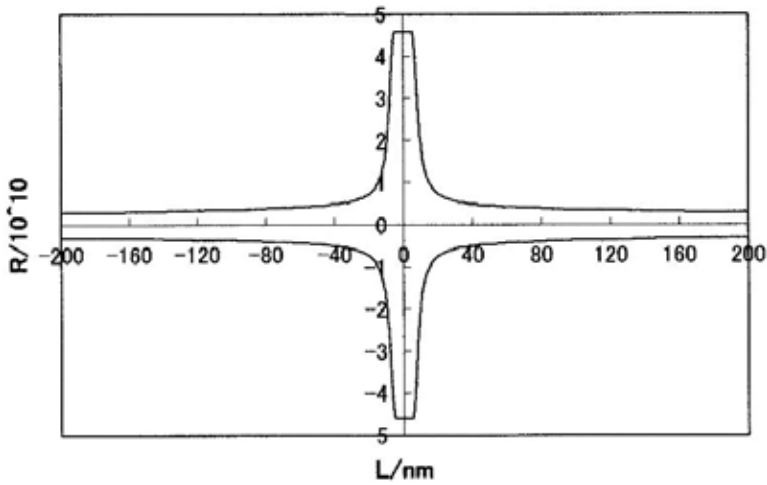
Figure 14. Representation of R (= ±R_n) and L (= ±ζ/2) for α form crystals in the iPP film (per 1g) annealed at 461.0 K for 1 hour. The horizontal lines show R of the imaginary crystals melting from ζ_n to ζ= 0.
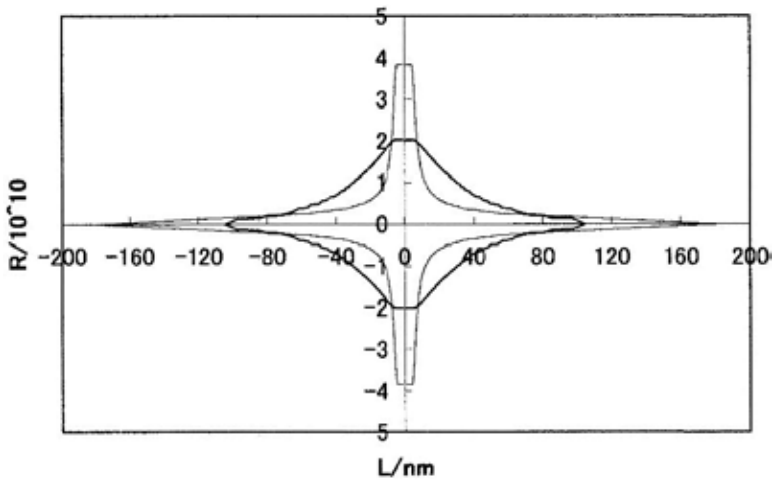
Figure 15. Representation of R (= ±R_n) and L (= ±ζ/2) for α (thick line) and γ (thin line) form crystals in the iPP film (per 1g) annealed at 441.5 K for 1 hour. The horizontal lines show R of the imaginary crystals melting from ζ_n to ζ = 0.

3. Conclusion

For iPS, PET, and iPP, the heat capacity jump at the glass transition was due to the discontinuous change of energy in quantum state of the photon holes between neighboring benzene rings, but methyl groups for iPP, followed by unfreezing of glass parts. For iPS and iPP, the homogeneous glasses free from ordered part / hole pairs with T_g= 240 K and 180 K were predicted, respectively. For iPP, the cohesive energy of methylene residues was subdivided into the transition enthalpies of glasses, ordered parts, and crystals, whereas for iPS, it agreed

with the difference between the transition enthalpies of glasses and ordered parts, but the transition enthalpy of glasses was larger than that of ordered parts. The photonic contribution of 60 % to the heat capacity jump at the glass transition found for PET meant that one photon was situated in the neighboring phenylene residues comprising ~60 % of the structural unit length and the residual jump of 40 % was brought by unfreezing of the ethylene glycol parts in a glass state. $T_m^{\infty} = 450$ K for α form crystals of iPP could be the temperature of the quantum demand of hole energy at regular temperature intervals of 90 K. The shift of melting from α to γ form crystals by DSC measurements was done through the mediation of the formation and then disappearance of crystal / hole pairs. The interface parts formed in α and γ form crystals by annealing brought the excess energy of ~0.7 kJ/mol to the enthalpy of the ordered parts. This result was reflected clearly to the single crystal like image depicted on the basis of the crystal length distribution function.

4. A list of abbreviations (italic in Eqs.)

α : fraction of ordered part / hole pairs with C_v^{ph}

$1 - \alpha$: fraction of ordered part / hole pairs with C_p^{ph}

C_p : mean heat capacity per molar structural unit for ordered parts in ordered part / hole pairs

C_p^h : mean heat capacity per molar photon for holes in ordered part / hole pairs

C_p^{h*}: heat capacity per molar photon for holes in excited ordered part /hole pairs

C_p^{ph} : adiabatic molar heat capacity for photons

C_v^{ph} : constant volume molar heat capacity for photons

C_p^{flow} : heat capacity per molar structural unit for flow parts

C_p^r : heat capacity change per molar structural unit due to crystallization followed by melting

C_p^x: heat capacity per molar structural unit for ordered parts in excited ordered part /hole pairs

c : velocity of light

c* : cell length of c–axis

c_1 and c_2 : constants in WLF equation

dQ/dT : heat flow rate of DSC melting curves

δQ_m : heat change per molar structural unit per K

ΔC_p : heat capacity jump per molar photon at the glass transition

ΔC_p^{exp} : experimental heat capacity jump per molar structural unit at the glass transition

ΔC_p^x : relative component heat capacity per molar structural unit for excited ordered parts

Δh : additional heat per molar structural unit needed to melt all ordered parts

Δh^h : hole energy of crystal / hole pairs formed newly by recrystallization

δ : solubility parameter

E_a : activation energy

$F(\zeta)$: crystal length (ζ) distribution function

f : free energy per molar structural unit

f^{conf} : conformational free energy per molar structural unit

f_g^{conf} : conformational free energy per molar structural unit at T_g

f_x : free energy per molar structural unit for ordered parts

f_u : free energy per molar structural unit for crystals

ϕ : amorphous fraction

Γ : frequency of occurrence of the helix–coil transition

H_m^a : enthalpy per molar structural unit for the liquid at T_m^∞

H_c^a : enthalpy per molar structural unit for the super–cooled liquid at T_c

H_g^a : enthalpy per molar structural unit for the super–cooled liquid at T_g

H_g^c : enthalpy per molar structural unit for the crystal at T_g

h^h : hole energy per molar photon for holes in ordered part / hole pairs

h_0 : latent cohesive energy per molar structural unit

h_0^h : zero–point energy per molar photon, or energy unit per molar photon

h_u : heat of fusion per molar structural unit

h_x : enthalpy per molar structural unit for ordered parts

h_g : glass transition enthalpy per molar structural unit

h^{conf} : conformational enthalpy per molar structural unit

h_g^{conf} : conformational enthalpy per molar structural unit at T_g

h_x^{conf} : conformational enthalpy per molar structural unit for ordered parts

h^{int} : cohesive enthalpy per molar structural unit

h_g^{int} : cohesive enthalpy per molar structural unit at T_g

h_m^{int} : cohesive energy per molar structural unit for methylene residues

h : Plank constant

η : statistical weight

J_h : number of holes lost by T at the glass transition

φ_g : fraction of core free volume in glasses

λ and $1/\lambda$: wavelength and wave number

mol : molar structural unit

mol* : molar photon

μ : conversion coefficient of mol/m^3

N_A : Avogadro constant

N_c : number of structural units of crystals melted in the temperature range from T_b to T_e

n : number of structural units holding one photon potentially

n_ζ : number of crystal sequences with ζ

ν : frequency per second

P : pressure

P_c : probability that a sequence occupies the lattice sites of a crystalline sequence

Q : heat per molar structural unit corresponding to the total area of DSC endothermic curve

Q_m : heat per molar structural unit corresponding to the area of a DSC melting curve from T_b

R : gas constant

R_n : number of crystal sequences at the radius direction of an imaginary single crystal lamella depicted on the basis of $F(\zeta)$

s_u : entropy of fusion per molar structural unit

s_x : entropy per molar structural unit for ordered parts

s^{conf} : conformational entropy per molar structural unit

s_g^{conf} : conformational entropy per molar structural unit at T_g

σ_e : end surface free energy of a crystal per unit area

σ : statistical weight

T : temperature

T_g : glass transition temperature

T_m : melting temperature

T_m^∞ : equilibrium melting temperature

T_e and T^* : end temperature of DSC melting peak curve

T_l : end temperature of the glass transition

T_c : onset temperature of DSC crystallization peak curve upon cooling

T_b : onset temperature of DSC melting peak curve upon heating

T_a : annealing temperature

T_p : DSC melting peak temperature

V : volume per molar structural unit

v_f : free volume per molar structural unit

v_0 : core free volume per molar structural unit

x : degree of polymerization

Z : conformational partition function for a chain

Z_0 : component conformational partition function for a chain regardless of temperature

Z_t : component conformational partition function for a chain depending on temperature

ζ : crystal length

ζ_p : crystal length at the maximum of $F(\zeta)$

ζ_n : crystal length at the minimum of ζ

ζ_x : crystal length at the maximum of ζ

Acknowledgements

Author details

Nobuyuki Tanaka[*]

Address all correspondence to: thermodyna_nt@kki.biglobe.ne.jp

Gunma University, Gunma, Japan

References

[1]   T. G. Fox, P. J. Flory, J. Polym. Sci., 14, 315(1954).

[2]   G. Natta, P. Corradini, D. Sianesi, D. Morero, J. Polym. Sci., 51, 527(1961).

[3]   G. Gee, Polymer, 7, 177(1966).

[4]   A. L. Renninger, D. R. Uhlmann, J. Polym. Sci., Phys., 16, 2237(1978).

[5]   R. J. Roe, A. E. Tonelli, Macromolecules, 12, 878(1979).

[6]   L. H. Judovits, R. C. Bopp, U. Gaur, B. Wunderlich, J. Polym. Sci., 24, 2725(1986).

[7]   G. Brinke, L. Oudhuis, T. S. Ellis, Thermochimica Acta, 238, 75(1994).

[8]   B. Wunderlich, "Thermal Analysis of Polymeric Materials", Springer, (2005).

[9]   B. Wunderlich, J. Appl. Polym. Sci., 105, 49(2007).

[10] N. Tanaka, Y. Mastai Ed: "Advances in Crystallization Processes", InTech, p163(2012).

[11] N. Tanaka, Preprints of 45th Japanese Conference on Calorimetry and Thermal Analysis (Hachioji), p20(2009).

[12] N. Tanaka, Preprints of 46th Japanese Conference on Calorimetry and Thermal Analysis (Tsu), p27(2010).

[13] N. Tanaka, Preprints of 47th Japanese Conference on Calorimetry and Thermal Analysis (Kiryu), p27(2011).

[14] N. Tanaka, 62nd SPSJ Annual Meeting, Polymer Preprints (CD), Kyoto, 62, (2013).

[15] N. Tanaka, Preprints of 49th Japanese Conference on Calorimetry and Thermal Analysis (Narashino), p137(2013).

[16] N. Tanaka, 63th SPSJ Annual Meeting, Polymer Preprints (CD), Nagoya, 63, (2014).

[17] F. Zamponi, Nature Phys., 7, 99(2011).

[18] G. Biroli, Nature Phys., 10, 555(2014).

[19] N. Tanaka, Polymer, 33, 623(1992).

[20] L. H. Hill, "Introduction to Statistical Thermodynamics", Addison–Wisley, Massachusetts, p456(1960).

[21] T. McLeish, Physics Today, 61, No. 8, (2008).

[22] N. Tanaka, Thermochimica Acta, 374, 1(2001).

[23] N. Tanaka, Polymer, 49, 5353(2008).

[24] J. D. Ferry, "Viscoelastic Properties of Polymers", Reinhold, New York, (1961).

[25] M. Kobayashi, S. Hanafusa, T. Yoshioka, S. Koizumi, Japanese J. Polym. Sci. and Tech., 53, 575(1996).

[26] Spectroscopic Soc. of Japan, "Infrared and Raman Spectroscopy", Kodansha Sci., Tokyo, (2011).

[27] N. Tanaka, G. Wypych Ed: "Handbook of Solvents", ChemTech Publishing, Toronto, p253(2001).

[28] H. Burell, J. Brandrup, E. H. Immergut, "Polymer Handbook", Interscience, New York, (1966).

[29] C. W. Bunn, J. Polym. Sci., 16, 323(1955).

[30] H. Yoshida, Netsusokutei, 13(4), 191(1986).

[31] D. Y. Yoon, P. R. Sundararajan, P. J. Flory, Macromolecules, 8, 776(1975).

[32] G. Allegra Ed: "Interfaces and mesophases in polymer crystallization 2", Berlin, Springer, p288(2005).

[33] J. Stokr, B. Schneider, D. Doskocilova, J. Lovy, P. Sedlacek, Polymer, 23, 714(1982).

[34] B. Wunderlich, ATHAS databank (1992 Recommended Data).

[35] N. Tanaka, 56th SPSJ Annual Meeting, Polymer Preprints (CD), Nagoya, 56, (2006).

[36] P. J. Flory, J. E. Mark, A. Abe, J. Am. Chem. Soc., 88, 639(1966).

[37] A. Nakajima, M. Hosono, "Molecular Properties of Polymers", Kagakudojin, (1969).

[38] N. Tanaka, Polymer, 34, 4941(1993).

[39] N. Tanaka, 58th SPSJ Annual Meeting, Polymer Preprints (CD), Kobe, 58, (2009).

[40] P. J. Flory, J. Chem. Phys., 17, 223(1949).

[41] J. P. Luongo, J. Appl. Polym. Sci., 3, 302(1960).

[42] J. X. Li, W. L. Cheung, D. Jia, Polymer, 40, 1219(1999).

[43] N. Tanaka, Proceedings of the 5th Italian Conference on Chemical and Process Engineering, Florence, 949(2001).

[44] N. Tanaka, H. Fujii, J. Macromol. Sci., B42, 621(2003).

[45] N. Tanaka, Gunma University, Japanese Patent 4228080.

Controlled Crystallization of Gold Nanocrystals

Ortal Lidor-Shalev and Zion Elani

Additional information is available at the end of the chapter

http://dx.doi.org/10.5772/60020

1. Introduction

Nanoscience enables the design and synthesis of nanomaterials with tailored shapes and sizes. Novel metal NCs with controllable shapes are attractive due to their size and shape-dependent properties, and reveal higher surface-to-volume ratios, which make their electrical properties extremely sensitive to surface-adsorbed species and changes in the electronic structure, which cause variations in conductivity and resistance.

Great efforts have been devoted to the chemical synthesis of noble-metal NPs with controlled shapes. Of all the synthetic methods reported, it has been found that the most productive route for the formation of NPs with well-defined and controllable shapes is the chemical reduction of a metal salt.

Syntheses of NPs based on the bottom-up approach have two main processes: nucleation and crystal growth. The mechanism for the formation of NCs and NPs was first explained by the *LaMer* model [1, 2]. The *LaMer* mechanism proposes that at the beginning of the reaction, the nucleation starts by precursor reduction into elemental atoms that form small clusters. Once the concentration of the small clusters has reached a point of supersaturation, the small clusters start to aggregate into seeds.

The continuous growth of the seeds results in the formation of metal NCs. Presence of steric or electrostatic stabilizers may be required to prevent agglomeration of the nanoclusters by providing a barrier between the particles.

Despite the simplicity of this one-pot synthetic path for NCs, a common problem is that further nuclei and seeds may be formed throughout the synthesis, leading to broad distributions in size and shape for the resultant NCs.

The one-pot route must therefore be divided into two separate steps of nucleation and growth in order to improve controllability of the synthesis and uniformity of the NCs. This idea was

fundamental to the development of *seeded-growth* synthesis (also called *seed-mediated growth*) for the preparation of Au NRs.

This book chapter provides a review on Au NRs syntheses and properties and extends the discussion on the following issues:

- The s*eeded-growth synthesis* for obtaining Au NRs.

- The plausible mechanisms of *Ag(I)-assisted* and *stepwise additive syntheses.*

- Thermodynamics and kinetics control of nanostructures, particularly Au NCs.

Following this, we present the results of Au NRs that were synthesized in our study using the discussed procedures and the results for ability of those Au NRs to polarize light.

2. Au NRs and anisotropic structures

Anisotropic metal NPs show different physical and chemical properties along different axes, which are especially important in particles with aspect ratios (length/width) larger than 1. These anisotropic shapes have unique optical, electronic and catalytic properties, and are therefore commonly used as building blocks for a variety of applications in the areas of energy, biology and spectroscopy.

Au NRs have attracted the most attention of all anisotropic metallic NPs. Au is a highly unreactive metal and non-toxic, and Au NRs can therefore be used in drug delivery, disease therapy and biosensing applications [3-5]. In this chapter, we focus our discussion mainly on 2D NRs with anisotropic structure, particularly Au NRs. We present the Au NRs' properties, syntheses and possible structures, and our own results on the syntheses of Au NRs and their use as orientation sensors.

2.1. Synthetic approaches for Au NRs

Over the past few decades, anisotropic metal NRs have been prepared through a variety of synthetic approaches. The first synthesis of metal and metal oxide nanowires ("whiskers") was demonstrated in the 1960s, and used a *vapour–liquid–solid (VLS)* approach [6]. In the mid-1990s, a straightforward chemical synthesis was developed for colloidal metal NRs, using *electro-chemical* methods [7]. Since then, most colloidal synthetic methods for obtaining Au NPs use the strategy of reduction of Au salt by a reducing agent [8]. Most of the reactions occur in the presence of surface-capping ligands which prevent aggregation of the particles.

The first viable method that provided a simple wet chemistry route for obtaining Au NRs was developed in 2001, and was named s*eeded-growth synthesis* or *seed-mediated growth* [9]. The main limitation of this method was the low Au NR yield and the difficulty of separating the different shapes. In 2002, a second method for preparing Au NRs was developed, using the seed-mediated growth method in the presence of silver ions, which showed a substantial improvement in the NR yield [10]. These two methods are considered the basis for the synthesis of Au NRs and are described in Section 4.

In 2005, synthesis with a high yield of Au NRs in aqueous solution was described [11], as well as the modification of the different Au NR shapes [12]. In 2005, a review on Au NRs extensively described the Au NRs' optical properties, syntheses, characterization methods, mechanisms and applications [13].

A significant improvement in the synthesis of monodispersed Au NRs was reported in 2012 [14, 15]. Seed-mediated growth of a wide range of long Au NRs was reported in the same year [16], and a new technique for seedless growth of small Au NRs was also published [17].

Recent modifications have improved control over the aspect ratio of Au NRs and enabled control over the dimensions of NRs. In 2014, a further development in the one-step seed-mediated method for producing shape-controlled NRs was reported [18].

2.2. Seeded-growth synthesis of Au NRs

Seeded-growth synthesis provides a general method for synthesizing Au NRs and other anisotropic nanostructures with controlled shapes and sizes.

The synthetic path is based on two main steps:

1. *Seeding:* the first step is the formation of small seeds (1-5 nm). The seeds are generated under conditions of high supersaturation, which allow rapid growth of all crystal surfaces, but no shape control. This step typically involves reduction of $AuCl_4^-$ aqueous solution by a strong reducing agent (sodium borohydride) where Au(III) ions are reduced to Au(0) atoms which subsequently aggregate to form nuclei. Once the nuclei have grown past a critical size, sub-nanometre clusters are formed into uniform and spherical seeds with stable crystallinity and well-defined facets. The seeds thus obtained have extremely high surface energy, hence appropriate capping agents may be used to cap the surfaces of the particles and thereby decrease their surface energy.

2. *Crystal growth:* the second step is the growth of isotropic seeds into anisotropic nano-structures. Shape control is achieved by the direction surfactants that enable symmetry-breaking in the crystallization. These surfactants are structure-guiding agents which promote the formation of non-spherical and anisotropic shapes in the growth step. In this step, a mild reducing agent (ascorbic acid) reduces Au(III) ions to Au(I). The addition of seeds into the growth solution catalyses the reduction and enables the extra reduction from Au(I) into Au(0).

The aspect ratio of the Au NRs can be adjusted by variation of the concentration of seeds added to the growth solution. For example, addition of a smaller amount of seeds produces a higher aspect ratio and can potentially provide better control over the shape and size of the NCs.

Different reaction components have a strong influence on the product and have been widely investigated [19-26]. The significant parameters that affect the yield are concluded below:

1. Different surfactants with different chain lengths, head group structures and counter-ions.

2. The presence of Ag(I) ions in the growth solution.

3. The amount of seed added to the growth solution.

4. The reaction temperature and pH.

5. The concentration of reagents.

6. The ionic strength of the growth solution.

3. Mechanism

3.1. Reduction mechanism

The driving force of a redox reaction is defined as the difference between the redox potentials of two half cells (ΔE); accordingly, the value of ΔE has a great influence on the reduction kinetics. Higher ΔE causes a more spontaneous and rapid reaction. For instance, the use of a strong reducing agent (sodium borohydride in the seed solution) produces small seeds due to a rapid reaction and a high ΔE, whereas a mild reducing agent (ascorbic acid in the growth solution) enables the production of larger particles due to relatively slow reaction rate and a low ΔE.

3.2. Au NR seeded-growth mechanisms

In this section, we summarize the key procedures for shape-controlled Au NRs and review the commonly known mechanisms. Different mechanisms have been proposed for the synthesis of Au NRs; nevertheless, this process is still not fully understood [27, 28].

It is commonly suggested that preferential interactions of the surfactants or additives with crystallographic facets along Au NCs provide the shape-directing mechanism for NRs.

Overall, two different methods for seeded-growth synthesis of Au NRs are mostly used: (i) Ag(I)-assisted synthesis and (ii) stepwise additive synthesis. Both methods are based on the same principle: small seeds of Au NPs (1-5 nm) are first prepared by fast reduction through a strong reducing agent and, subsequently, the seeds are used to initiate further NC growth.

At present, centrifugation is necessary to separate the Au NRs from the mixture of other Au nanostructures in the solution.

In Ag(I)-assisted synthesis, there are only two solutions: the seed and the growth, while the stepwise additive synthesis uses a total of four solutions: the seed solution and three different growth solutions. The first growth solution (A) is used as the seed solution for the next growth solution (B), and this growth solution (B) is subsequently used as the seed solution for the last growth solution (C).

The differences in the reagents and conditions between the two methods are summarized in the following table:

Seed solution	Growth solution	Au NR structure
✔ CTAB (surfactant)* ✔ HAuCl₄ ✔ NaBH₄ (strong reducing agent) ✔ 1.5 nm CTAB-Au NCs with single-crystal motif	✔ CTAB (surfactant)* ✔ HAuCl₄ ✔ Ascorbic acid (mild reducing agent) Silver nitrate	Ag(I)-assisted synthesis Product: single-crystal NR • High rod yield • Aspect ratio of 4.5
✔ Citrate (surfactant)* ✔ HAuCl₄ ✔ NaBH₄ (strong reducing agent) 3.5 nm citrate-Au NCs with twinning faults motif	✔ CTAB (surfactant)* ✔ HAuCl₄ ✔ Ascorbic acid (mild reducing agent) ✗ No silver nitrate	Stepwise additive synthesis Product: penta-twinned NR • Low yield of NRs with further morphologies • Aspect ratio of 6-20

The two synthetic approaches produce different NR structures (Figure 1):

1. Penta-twinned-like rods obtained in the absence of silver ions.

2. Single crystal rods obtained in the presence of silver ions.
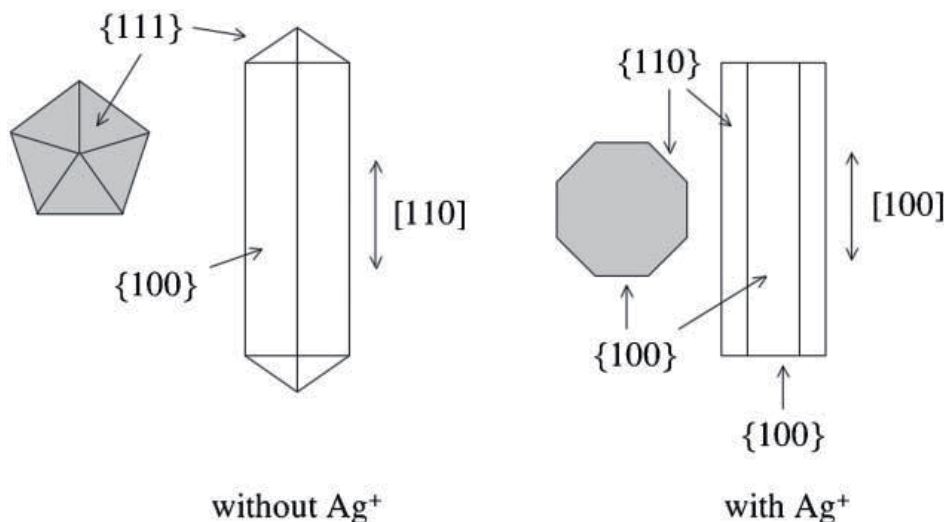
Figure 1. The structures for Au NR: penta-twinned with a [110] growth direction (left), and single crystal with a [100] growth direction (right) [29].

As mentioned above, the growth mechanism has not yet been fully proven for either process, but we describe here the most reasonable mechanisms for both Ag(I)-assisted and stepwise additive syntheses.

3.2.1. Ag(I)-assisted synthesis

The presence of small amounts of silver nitrate ($AgNO_3$) during the synthesis has a dramatic effect on the final shape and crystalline structure. Silver nitrate is used as a source for Ag(I) ions which are essential for producing high yields of NRs with low aspect ratio (less than 5). The concentration of the silver ions has excessive influence on NR dimensions [10]. Higher concentration produces a larger aspect ratio in the NRs.

The commonly accepted explanations of the possible mechanism are:

1. Adsorption of silver ions at the NR surface: during growth, Ag(I) ions (in the form of Ag$^+$Br$^-$) adsorb on the Au-CTAB interface and stabilize it. The Ag(I) ions adsorption onto the NR surface restricts growth by binding to specific facets and therefore promotes growth on the less covered facets. For example, an Ag monolayer on the Au{110} surface acts as a strong binding agent, and therefore the total growth rate in this direction is significantly decelerated.

2. Underpotential deposition (UPD): the silver ions cause underpotential deposition, which is the deposition of the first and sometimes second monolayer of a metal at potentials more positive than the *Nernst potential* of the metal being deposited. The UPD arises during addition of metal ions (e.g., Ag ions) onto a metallic substrate (e.g., Au NRs), therefore causing the symmetry-breaking.

The growth of Au NRs is directed by silver UPD on the longitudinal faces. Slower growth of {110} side faces and faster growth of {100} end facets results in a breaking of the growth symmetry and adjustment of the final anisotropic shape [30]. The growth rate between the Au{110} and Au{100} facets of the *f.c.c* (face-centred close-packed) Au structure can be simply attuned by varying the Ag ion concentration.

3.2.2. Stepwise additive synthesis

The shape and size control of the Au NRs is achieved by the preferential adsorption of CTAB onto the different NR facets [26, 31]. The widely accepted explanations of the mechanism are summarized below:

1. The CTAB acts as a stabilizer and is selectively adsorbed on certain growing faces of the NC, causing anisotropic growth in the NR structures. Selective binding of bromide to the {110} or {111} surfaces stabilizes those surfaces; therefore, the Au deposition at those sites is decelerated.

2. Formation of CTA-Au-Br complexes that template NR formation and slow the rate of Au deposition.

3. The CTAB is used as a surfactant and serves as a cationic micelles template for directing the growth. The CTAB micelles bilayer is composed of a first layer of quaternary ammonium head groups (facing the Au surface) and a second layer of surfactant head groups (facing the aqueous media). There are three interfaces of the CTAB bilayer:

4. The Au nanorod-CTAB interface, where the surfactant layer is bound to the Au surface by electrostatic interactions between the cationic head group of the quaternary ammonium and the anionic sites of the Au surface.

5. The CTAB bilayer itself, where the bilayer assembly is energetically favoured owing to hydrophobic interactions between the surfactants' tails and hydrophilic interactions of the charged head group with the aqueous media.

6. The outer CTAB exposed to the water media.

4. Adjustment of NC morphologies

4.1. Kinetics and thermodynamics in NCs

Syntheses of metallic NCs with a variety of shapes, including polyhedra, plates, wires, rods, bars and tripods have been previously reported [32, 33]. The rate of crystallization, types of product, morphology, size distribution and the particular properties are dependent on a large number of parameters. Those parameters include the crystallization conditions (for instance, temperature, stirring, seed structure and volume), and the composition-dependent parameters (for instance, pH, solvent, reagents, ratio between the elements and ionic strength).

The control over the yield of NCs can be divided into thermodynamics and kinetics control:

• *Thermodynamic control* is effective when the reduction rate is relatively fast. Commonly, seed formation is favoured by thermodynamics and represents the lowest surface energy of the NC shapes. The attempt to minimize the total surface energy of the system produces thermodynamically favoured shapes.

For the face-centred cubic (FCC) Au structure, the surface energies of the crystallographic facets are in the order of {111} < {100} < {110}, which implies that a single-crystal seed should take an octahedral or tetrahedral shape in order to maximize the expression of {111} facets, and therefore minimize the total surface energy of the solvent-exposed faces.

• *Kinetic control* is dominant when the reaction rate is significantly slowed down, which enables the formation of crystals with higher surface energy. As a result of the slower reaction rate, the concentration of reduced Au atoms is very low; therefore, the atoms aggregate into small clusters and produce shapes with higher surface energy.

4.2. Control over Au NC shape

As with other metallic NCs, Au NC shapes are adjusted by varying the reaction conditions. The parameters which have the strongest influence on NC structures and the exposed facets

are the seed structure and the ions added to the growth solution. As described in previous sections, silver ions (in the case of Ag(I)-assisted synthesis) and halides (in the case of step additive synthesis) are commonly used to adjust seed growth into different morphologies. The different Au NP morphologies are regulated by silver UPD (in the presence of silver ions) or by kinetics (in the absence of silver ions). The concentration of Ag ions in the growth solution and their interactions with the NP surface adjust the product to yield Au nanostructures such as bipyramids {110} or rhombic dodecahedra {110}. Kinetic control arises in the absence of silver ions, when the rate of the reaction affects the final product to yield Au nanostructures such as truncated bitetrahedra {111}, octahedra {111} or cubes {100}.

The formation of anisotropic or isotropic Au NCs can be explained by the *Gibbs free energy* formula (where ΔG* is the minimum energy necessary to form a nucleus). The activation energy (Ea) for anisotropic structures is much higher than the activation energy for isotropic structures and, as Figure 2 demonstrates, the change in the *Gibbs free energy* of anisotropic Au NPs is lower than the change in that of isotropic Au NPs. Consequently, isotropic structures are thermodynamically favoured and have a lower and more stable energy profile [25].
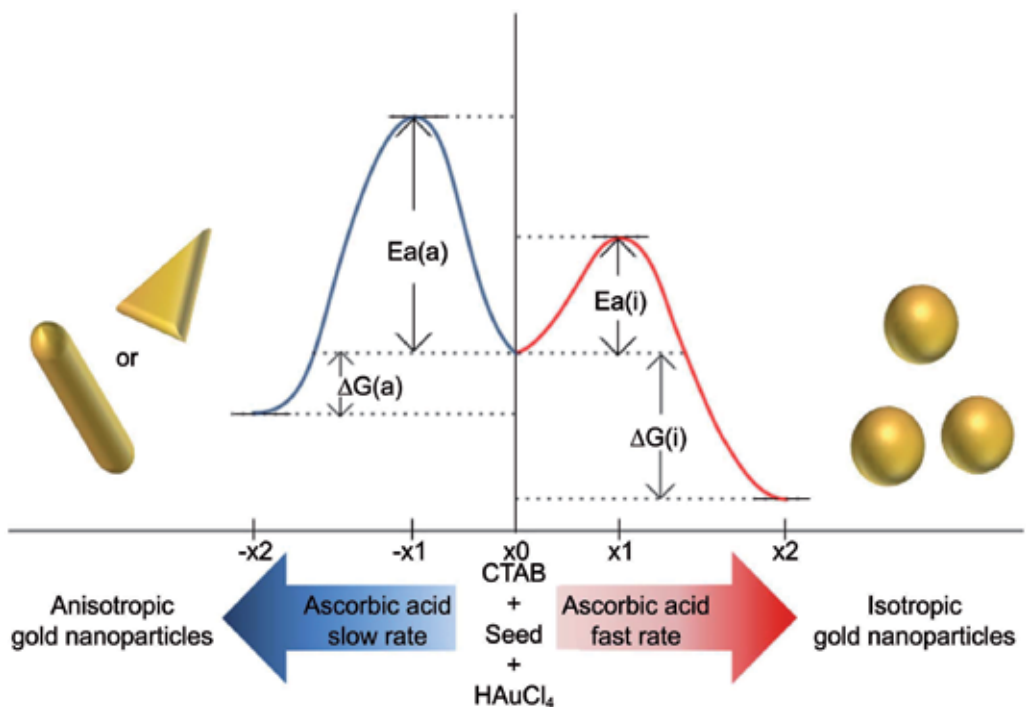
Figure 2. Proposed schematic diagram of the reaction pathway during thermodynamically and kinetically controlled synthesis [25].

Control of the addition rate of ascorbic acid into the growth solution changes the reaction rate and adjusts the product because, when ascorbic acid is added, the solution is supersaturated and has high Gibbs free energy. The fastest addition rate gave the highest initial concentration

of ascorbic acid, which led to small homogenous gold nanospheres obtained from the large number of small nuclei during the nucleation process. In this case, the supersaturated solution reduces the overall *Gibbs free energy* back to equilibrium by forming the thermodynamically favoured Au nanospheres. In order to increase the probability of Au anisotropic shape formation, the nucleation process has to stop while the growth process continues. In this case, the concentration of the growth species must be less than the minimum concentration of nucleation, and this is achieved by a slow addition rate of ascorbic acid.

A summary of the role played by the kinetics and thermodynamics in the case of Au NCs is presented in Figure 3. After the first chemical reduction of Au ions into atoms, the seeds' nucleation, taking the thermodynamically controlled path, produced morphologies of single-crystal, single-twinned or multiple-twinned seeds. Further growth of the seeds into NCs and anisotropic structures, in the presence of additives, obtains rod shapes (the pathways for anisotropic NRs are highlighted in blue and red). In the case of the kinetically controlled path, seeds with plate shapes are grown into hexagonal and triangular plates.
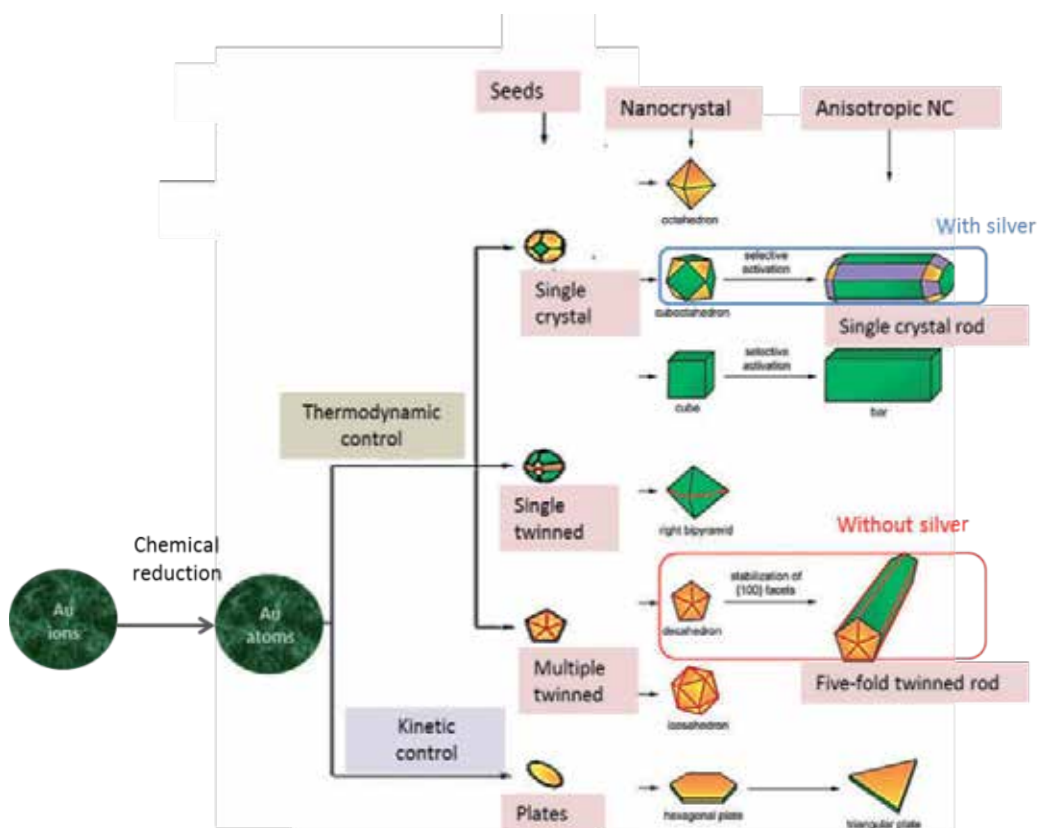
Figure 3. Scheme presenting the growth mechanism into different NCs and NRs. The scheme is based on reference [30] with additional explanations.

5. Results of Au NRs in our study

In our study, we used three well-established methods in order to synthesize Au NRs and additional shapes. The main aim was to obtain Au NRs in the absence of silver ions in order to investigate the ability of Au NRs to polarize light (see Section 7.2).

Below, we present environmental scanning electron microscope (E-SEM) images of Au NRs and other shapes that were synthesized in our work, based on the three established protocols.

5.1. Au NRs with aspect ratio of up to 4.7

The Au NRs were synthesized using the Ag(I)-assisted procedure based on reference [10]. The E-SEM images of the Au NR solutions showed an average aspect ratio of 4.5 and a regular length of 40 nm (Figure 4A).

- *Seed preparation:* CTAB solution (5 mL, 0.20 M) was mixed with 5.0 mL of 0.5 mM $HAuCl_4$. To the stirred solution, 0.60 mL of ice-cold 0.010 M $NaBH_4$ was added, which resulted in the formation of a brownish-yellow solution. Vigorous stirring of the seed solution was continued for 2 minutes and it was kept at 25 °C.

- *Preparation of Au NRs:* CTAB solution (5 mL, 0.20 M) was added to 0.2 mL of 4 mM $AgNO_3$ solution at 25 °C. To this solution, 5.0 mL of 1 mM $HAuCl_4$ was added, and after gentle mixing of the solution 70 µL of 0.0788 M ascorbic acid was added. Ascorbic acid as a mild reducing agent changes the growth solution from dark yellow to colourless. The final step was the addition of 12 µL of the seed solution to the growth solution at 27-30 °C. The colour of the solution gradually changed within 10-20 minutes.

5.2. Au NRs with aspect ratio of up to 20

The Au NRs were synthesized using the three-step seeding method (stepwise additive) with no presence of silver ions based on reference [26]. The produced Au NRs had a typical length of 280 nm and an average aspect ratio of 15 (Figure 4B).

- *Seed preparation:* A 20 mL aqueous solution containing $2.5*10^{-4}$ M $HAuCl_4$ and $2.5*10^{-4}$ M tri-sodium citrate was prepared in a flask. Next, 0.6 mL of ice cold 0.1 M $NaBH_4$ solution was added to the solution all at once, while stirring. The solution turned pink immediately after adding $NaBH_4$, indicating particle formation. The particles in this solution were used as seeds within 2-5 hours after preparation.

- *Preparation of Au NRs:* Three test tubes (labelled A, B and C), each containing 9 mL growth solution, consisting of $2.5*10^{-4}$ M $HAuCl_4$ and 0.1 M CTAB, were mixed with 0.05 mL of 0.1 M ascorbic acid. Next, 1.0 mL of the 3.5 nm seed solution was mixed with solution A after 15 seconds. After 30 minutes, 1 mL of B was mixed with C.
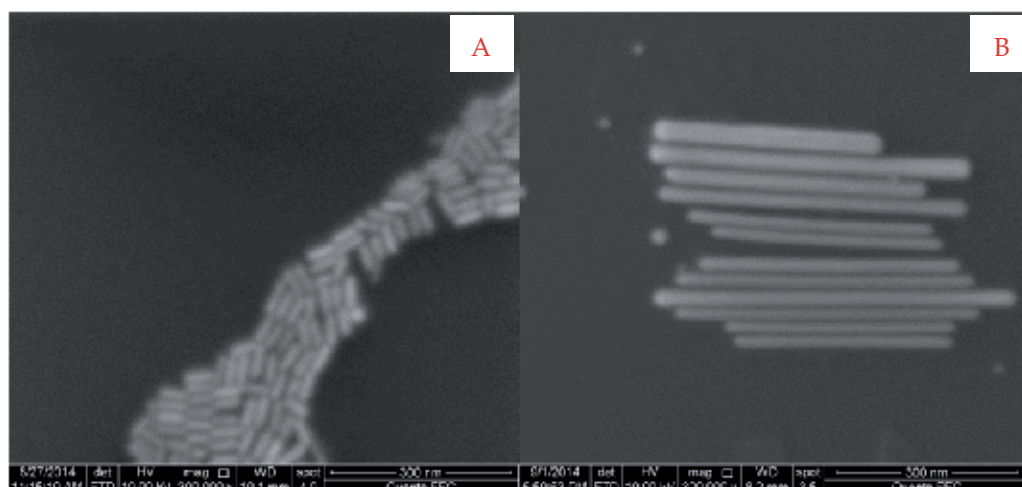
Figure 4. E-SEM image of Au NRs obtained in our study using (A) Ag(I)-assisted synthesis and (B) stepwise additive synthesis. The scale bar= 300 nm.

5.3. Au NRs and additional morphologies

The Au NRs were obtained by using one-step growth in the absence of silver ions, based on reference [26]. This sample formed different aspect ratio rods and bars, spheres, hexagonal plates, triangular plates, decahedrons and cuboctahedrons (Figures 5A and 5B). Separation of the different nanostructures using centrifugation was not successful.

• *The seed solution* was prepared using the same previously described seed preparation.

• *Preparation of Au NCs*: In a clean test tube, 10 mL of growth solution, containing 2.5 $*10^{-4}$ M $HAuCl_4$ and 0.1 M CTAB, was mixed with 0.05 mL of 0.1 M freshly prepared ascorbic acid solution. Next, 0.025 mL of the seed solution was added. No further stirring or agitation was done. Within 5-10 minutes, the solution colour changed to reddish-brown.

We used the same preparation method in all of the three procedures:

• *Procedure for shape separation:* Au NRs were concentrated and separated from spheres and surfactant by centrifugation. Next, 10 mL of the particle solution was centrifuged at 2000 rpm for 6 minutes. The supernatant, containing mostly spheres, was removed and the solid part containing rods and some plates was redispersed in 0.1 mL water.

• *E-SEM images* were acquired by environmental scanning electron microscope (E-SEM) with *Quanta* FEG, FEI instrument at acceleration voltages of 10 kV. The samples were prepared by placing 100 μL of the particle solution on 1 mm X 1 mm silicon wafers. The silicon wafers were previously washed with ethanol and water and dried under nitrogen stream.
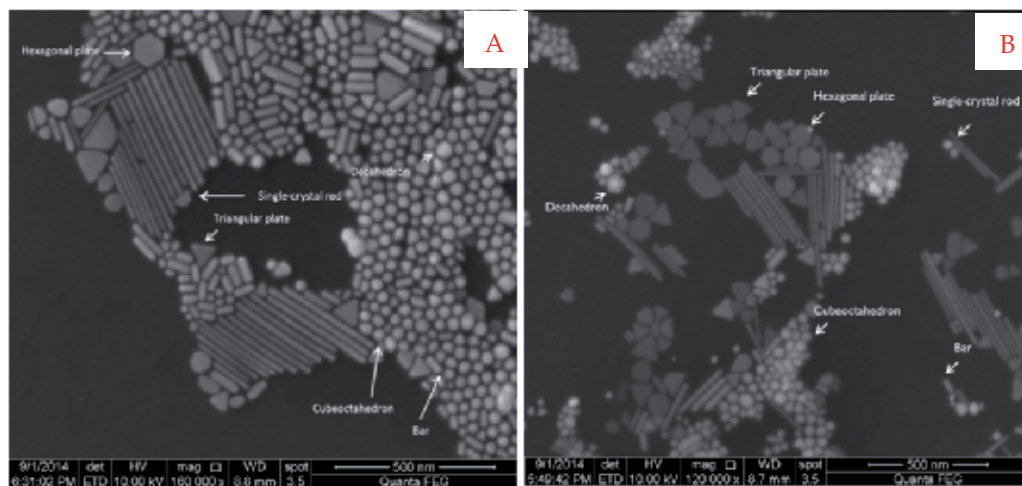
Figure 5. Different Au NC morphologies using silver-free seed-mediated growth. A and B are two different areas of the sample.

6. Applications of Au NRs

Au NRs are commonly used in industrial applications, including chemical sensing and plasmon-enhanced spectroscopies, in addition to innovative biosensors, optoelectronic devices, bioimaging, drug delivery and photothermal therapy [34].

6.1. Plasmon resonance of Au NRs

Plasmon resonance is an optical phenomenon that occurs when a metallic NP of an appropriate size interacts with incident photons and induces an oscillation of the conduction band electrons at the particle surface [35]. The electromagnetic field is enhanced when there is a plasmonic interaction between the wave and the metal.

There are two kinds of plasmon resonance:

1. *Surface plasmon resonance (SPR):* coherent oscillation of the surface conduction electrons excited by electromagnetic radiation.

2. *Localized surface plasmon resonance (LSPR):* small spherical metallic NPs are irradiated by light. The incident light causes the electrons of the NPs to delocalize, forming an electric field opposite to that of the wave. At specific frequencies, the electron oscillation is in resonance with the light wave.

The enhancement of the frequency in the local field is determined by the dielectric function of the metal, the dielectric constant of the surrounding medium, and the size and shape of the nanostructure. The effect of plasmonic NPs' size and shape on the SPR has been widely explored [14, 36, 37]. The plasmon resonance leads to a strong extinction of light at the plasmon resonance frequency and can be used for the development of innovative applications [38, 39].

The surface plasmon oscillations in Au NRs are different from those in spherical Au NPs, as they have longitudinal direction and transverse direction. The anisotropic shape displays two separate SPRs for their width and their length. Therefore, Au NRs have complex SPR owing to their high degree of polarizability.

The broad plasmon resonance of Au NRs provides a way of manipulating electromagnetic fields at the nanoscale and enables the investigation of different shape-dependent plasmonic behaviour [40]. The adjustment of plasmon resonance peaks has been extensively reported [41, 41, 43], as well as highly sensitive SPR detection methods using functionalized anisotropic Au NPs [42, 43]. The SPR peaks can be altered by variation of the Au NR aspect ratios, for example changing the CTAB concentration [44].

6.2. The use of Au NRs as orientation sensors by polarized light

Local orientation sensors are extremely important tools in the study of the properties of single molecules. The usage of these sensors is widely reported in a variety of fields including: liquid crystal orientation [45], molecular motors [46, 47], the structure of glasses and polymers [48], and the study of liquids in confined spaces [49].

The combination of the lightning rod effect together with the suppression of interband damping make them ideal materials for light scattering. Light scattered off Au NRs is intensely polarized along the long axis [50], making Au NRs perfect orientation sensors in principle.

In order to examine their polarization, Au NRs prepared by the seeded-growth method described in Section 6.2 (without silver nitrate). Ideally, in order to obtain a high yield of Au NRs, silver nitrate should be used in this method as a source for Ag(I), but the presence of silver on or within the Au NRs causes unwanted effects on their optical properties. On the other hand, the production of high-yield Au NRs in the absence of silver ions is very challenging. We wanted to overcome the disadvantages of both methods by producing Au NRs with high yield but in the absence of silver ions [26]. After we obtained the desired Au NRs, we tested their suitability for use as orientation sensors using images from a dark-field microscopy setup; dark-field microscopy uses a unique illumination technique that enhances the contrast in specimens that are not imaged well under normal bright-field illumination conditions. It works by illuminating the sample with light that will not be collected by the objective lens, and thus will not form part of the image. The detector will probe only the light that is scattered by objects in the field of view, while direct reflection will not be measured. Our equipment was based on an Olympus illumination platform with a dark-field objective lens MPlan FL-N 50X, NA=0.8 and an Andor iXON+DU-855 FM-CCD camera. The polarizations are images through a SAVART plate calcite and demonstrate the separation between P and S polarization.

The obtained Au NRs were loaded on a glass slide using the following procedure:

- Firstly, we cleaned the glass slide in a solution of 10 % weight alconox using sonication for 15 minutes.

- Cleaning in a DDW solution using additional sonication for 5 minutes.

- Cleaning in an acetone solution using a sonication for 15 minutes.

- Cleaning in ethanol using a sonication for 20 minutes.

- Finally, 20 μl from the solution was dried at the glass slide for 24 hours.
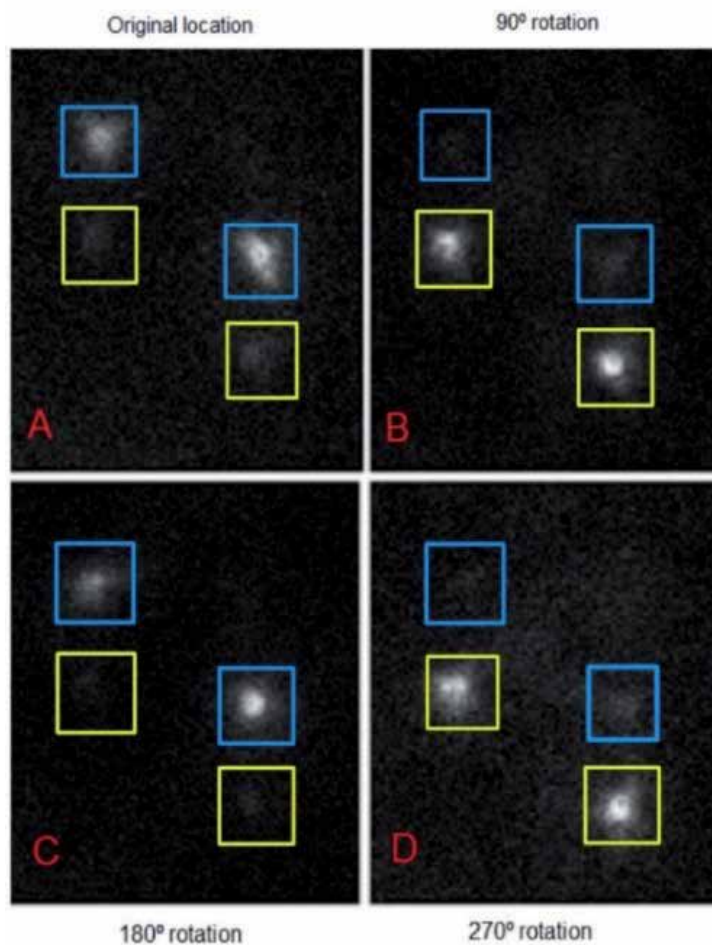
Figure 6. Images from a dark-field setup showing the polarization behaviour of two Au NRs through rotation of a polarizer by 90° rotations: (A) original location, (B) 90° rotation, (C) 180° rotation and (D) 270° rotation. Illumination is through a dark-field, so only scattered light is collected by an air objective, while a bifringent calcite crystal splits the light into orthogonal polarization directions. For ease of reference, the top dot of each Au NR is highlighted in blue and the bottom dot in yellow.

The sample of the dry solution of Au NRs was examined using dark-field microscopy. The Au NRs appeared as two separate dots (separated by a few pixels). This splitting is caused by the birefringent calcite crystal which displaces one polarization direction a few micrometres from the other. The scattering intensity of Au NR in one particular polarization direction is directly

related to the square of the cosine of the angle between the rod and the polarization direction (assuming a uniform illumination). Therefore, it is possible to calculate the orientation angle between the light source and the NR by measuring the intensity and using the cosine function of the arc. We concentrated on dots showing fluctuations, and therefore varying light intensity, between the two orientations. This fluctuation indicates that the light passing through the NR is polarized.

In order to verify the polarization obtained, we inserted a linear polarizer on top of the microscope. This polarizer caused a change in the intensity of the two dots directly related to the rotation of the polarizer (see Figure 6).

The rotation of the polarizer by 90° changed the bright dot into a dark one, and the dark dot into bright (Figures 6A and 6B, respectively). As expected, rotation of the polarizer by a further 90° (total 180°) returned the image to its original state (Figure 6C), while rotating the polarizer by a further 90° (total 270°) showed the same configuration as the 90° rotation (Figure 6D).

These results demonstrate the ability of Au NRs produced by this method to function as monitor orientation sensors at the nanoscale. Many possible applications can be developed from these new results; for example, binding Au NRs with an organic molecule would provide a method for imaging and sensing the positions of this molecule under different conditions in vitro or even in vivo.

7. Future inspiration

We would like to present some of the future challenges and inspirations we consider interesting for advancing innovations in the area of Au NRs.

A significant difficulty arises from the mixture of morphologies in Au NCs obtained using all synthetic methods. Separation approaches involve NR shape separation using surfactant-assisted self-assembly or centrifugation technique. However, the commonly used traditional purification methods, whereby NPs with different masses are separated using centrifugation, are not effective enough. Recently, an accurate purification method has been reported and targeted to overcome previous difficulties by separating NPs with different masses and shapes based on their surface area difference [51, 52]. A big challenge is to develop a highly effective separation technique for collecting Au NRs with different aspect ratios and to purify the rods from a mixture of additional shapes.

Furthermore, functionalization of Au NRs has been recently examined [53, 54]. Previous investigations have reported the formation of useful functional materials, devices and systems, and described their physical, chemical and biological properties. The main challenge will be to overcome the strong bond between the surfactants used in the synthesis and the Au NRs. In contrast to Au NPs, which are usually coated directly with thiols or a weakly-bound anion, Au NRs are synthesized in the presence of a strongly-bound surfactant, and the attempts to functionalize the NRs may lead to their aggregation [55, 59].

Moving forward, a challenging target ahead will be the discovery of new chemical and physical methods for functionalizing Au NRs with compounds that promote efficient binding, clearance and biocompatibility. Additionally, the development of newer characterization methods and facilities to produce further shape control of Au NRs is essential for further extensive modifications. Further advanced seed-mediated syntheses of Au NRs could produce additional control over the resulting shapes and improve reaction efficiency. We believe that the key challenge in the investigation of Au NRs is to understand and prove the seeded-growth mechanism; therefore, further investigations of the reaction kinetics and thermodynamics are still desired.

8. Conclusions

In this chapter, we gave an extensive report on the synthetic approaches for obtaining Au NCs, primarily NRs. We reviewed the history of Au NRs syntheses and described the improvements of the product in terms of size and shape control. We focused our discussion on the s*eeded-growth synthesis* as the common method for obtaining Au NRs and additional anisotropic morphologies. We defined the two main steps of the s*eeded-growth synthesis*, seeding and crystal growth, and extended the explanation of the role of different synthesis components. We specifically presented two different approaches for producing Au NRs, defined as (i) Ag(I)-assisted and (ii) stepwise additive syntheses. We broadly described the difference between the approaches in terms of the conditions, components and the resulting Au NRs' morphology and shape.

Although the mechanism for the syntheses of Au NRs is not fully understood, we presented the most plausible mechanisms. The most reasonable mechanisms for formation of anisotropic Au NCs were explained, as well as the role played by the kinetics and thermodynamics. We found it useful to continue our discussion on the overall adjustment of NCs' structures (which are divided into thermodynamics and kinetics control), and summarized the parameters which have the strongest influence on NC morphologies and shapes.

To illustrate and demonstrate the theory, we presented results of Au NRs obtained in our study based on well-established protocols. We described the experimental conditions for obtaining Au NRs with aspect ratios of up to 4.7 using the Ag(I)-assisted procedure and aspect ratios of up to 20 using the stepwise additive procedure (three-step seeding method). We presented E-SEM images of the Au NRs obtained in both of the cases, and also different Au NC morphologies using uncontrolled silver-free synthesis.

As described in the chapter, Au NRs reveal unique properties that are commonly used in nanotechnology applications. We elected to expand our discussion on two phenomenon: Au NRs' surface plasmon resonance, and the ability of silver-free Au NRs to polarize light. We offered a brief explanation of plasmon resonance and referenced some of the innovative applications. Furthermore, we examined the ability of silver-free Au NRs to polarize light. The intense of polarization along the long axis of Au NRs may lead to their extensive use as orientation sensors at the nanoscale.

Acknowledgements

Author details

Ortal Lidor-Shalev[*] and Zion Elani

*Address all correspondence to: ortalidor@gmail.com

Department of Chemistry, Bar Ilan Institute of Nanotechnology and Advanced Materials (BINA), Bar Ilan University, Ramat Gan, Israel

References

[1] LaMer K, Dinegar H. Theory, production and mechanism of formation of monodispersed hydrosols. J Am Chem Soc. 1950;72(8):4847–54.

[2] Thanh NTK, Maclean N, Mahiddine S. Mechanisms of nucleation and growth of nanoparticles in solution. Chem Rev. 2014 Aug 13;114(15):7610–30.

[3] Mieszawska AJ, Mulder WJM, Fayad ZA, Cormode DP. Multifunctional gold nanoparticles for diagnosis and therapy of disease. Mol Pharm. 2013 Mar 4;10(3):831–47.

[4] Gagner JE, Shrivastava S, Qian X, Dordick JS, Siegel RW. Engineering nanomaterials for biomedical applications requires understanding the nano-bio interface: A perspective. J Phys Chem Lett. 2012;3149–58.

[5] Shaw CF. Gold-based therapeutic agents. Chem Rev. 1999;99(1):2589–600.

[6] Wagner RS, Ellis WC. Vapor-liquid-solid mechanism of single crystal growth. Appl Phys Lett. 1964;4(5):89–90.

[7] Zande BMI Van Der, Fokkink LGJ, Henny M, Schmid C, Bachtold A, Huber R, et al. Template synthesis of nanowires in porous polycarbonate membranes: Electrochemistry and morphology. J Phys Chem B. 1997;5647(96):5497–505.

[8] Sardar R, Funston AM, Mulvaney P, Murray RW. Gold nanoparticles: Past, present, and future. Langmuir. 2009 Dec 15;25(24):13840–51.

[9] Jana NR, Gearheart L, Murphy CJ. Seed-mediated growth approach for shape-controlled synthesis of spheroidal and rod-like gold nanoparticles using a surfactant template. Adv Mater. 2001 Sep;13(18):1389–93.

[10] Nikoobakht B, El-Sayed MA. Preparation and growth mechanism of gold nanorods (NRs) using seed-mediated growth method. Chem Mater. 2003;(16):1957–62.

[11] Sau TK, Murphy CJ. Seeded high yield synthesis of short Au nanorods in aqueous solution. Langmuir. 2004 Jul 20;20(15):6414–20.

[12] Gou L, Murphy CJ, March RV, Re V, Recei M, May V. Fine-tuning the shape of gold nanorods. Chem Mater. 2005;(26):3668–72.

[13] Perezjuste J, Pastorizasantos I, Liz-Marzán LM, Mulvaney P. Gold nanorods: Synthesis, characterization and applications. Coord Chem Rev. 2005 Sep;249(17-18):1870–901.

[14] Jiang G, Hore MJ, Gam S, Composto RJ. Gold nanorods dispersed in homopolymer films: optical properties controlled by self-assembly and percolation of nanorods. ACS nano. 2012 Feb 28;6(2):1578–88.

[15] Ye X, Jin L, Caglayan H, Chen J, Xing G, Zheng C, et al. Improved size-tunable synthesis of monodisperse gold nanorods through the use of aromatic additives. ACS nano. 2012 Mar 27;6(3):2804–17.

[16] Wang Y-N, Wei W-T, Yang C-W, Huang MH. Seed-mediated growth of ultralong gold nanorods and nanowires with a wide range of length tunability. Langmuir. 2013 Aug 20;29(33):10491–7.

[17] Ali MRK, Snyder B, El-Sayed MA. Synthesis and optical properties of small Au nanorods using a seedless growth technique. Langmuir. 2012 Jun 26;28(25):9807–15.

[18] da Silva MGA, Meneghetti MR, Denicourt-Nowicki A, Roucoux A. Tunable hydroxylated surfactants: An efficient toolbox towards anisotropic gold nanoparticles. RSC Adv. 2014;4(49):25875–9.

[19] Murphy CJ, Thompson LB, Alkilany AM, Sisco PN, Boulos SP, Sivapalan ST, et al. The many faces of gold nanorods. J Phys Chem Lett. 2010 Oct 7;1(19):2867–75.

[20] Ortiz N, Skrabalak SE. On the dual roles of ligands in the synthesis of colloidal metal nanostructures. Langmuir. 2014 Jun 17;30(23):6649–59.

[21] Xia Y, Xiong Y, Lim B, Skrabalak SE. Shape-controlled synthesis of metal nanocrystals: Simple chemistry meets complex physics? Angew Chem Int Ed. 2009 Jan;48(1):60–103.

[22] Zhang HUI, Jin M, Xiong Y, Lim B, Xia Y. Shape-controlled synthesis of Pd nanocrystals and their catalytic applications. Accounts Chem Res. 2013;46(8):1783–94.

[23] Zhang J, Langille MR, Personick ML, Zhang K, Li S, Mirkin CA. Concave cubic gold nanocrystals with high-index facets. J Am Chem Soc. 2010 Oct 13;132(40):14012–4.

[24] DeSantis CJ, Peverly AA, Peters DG, Skrabalak SE. Octopods versus concave nanocrystals: Control of morphology by manipulating the kinetics of seeded growth via co-reduction. Nano Lett. 2011 May 11;11(5):2164–8.

[25] Hong S, Acapulco JAI, Jang H-J, Kulkarni AS, Park S. Kinetically controlled growth of gold nanoplates and nanorods via a one-step seed-mediated method. Bull Korean Chem Soc. 2014 Jun 20;35(6):1737–42.

[26] Jana NR, Gearheart L, Murphy CJ. Wet chemical synthesis of high aspect ratio cylindrical gold nanorods. J Phys Chem B. 2001 May;105(19):4065–7.

[27] Grzelczak M, Pérez-Juste J, Mulvaney P, Liz-Marzán LM. Shape control in gold nanoparticle synthesis. Chem Soc Rev. 2008 Sept;37(9):1783–91.

[28] Park K, Drummy LF, Wadams RC, Koerner H, Nepal D, Fabris L, et al. Growth mechanism of gold nanorods. Chem Mater. 2013 Feb 26;25(4):555–63.

[29] Petrova H, Perez-Juste J, Zhang Z, Zhang J, Kosel T, Hartland GV. Crystal structure dependence of the elastic constants of gold nanorods. J Mater Chem. 2006;16(40):3957–63.

[30] Lohse SE, Burrows ND, Scarabelli L, Liz-Marzán LM, Murphy CJ. Anisotropic noble metal nanocrystal growth: The role of halides. Chem Mater. 2014;34–43.

[31] Langille MR, Personick ML, Zhang J, Mirkin CA. Defining rules for the shape evolution of gold nanoparticles. J Am Chem Soc. 2012 Sep 5;134(35):14542–54.

[32] Tao AR, Habas S, Yang P. Shape control of colloidal metal nanocrystals. Small. 2008 Mar 3;4(3):310–25.

[33] Kumar S, Nann T. Shape control of II-VI semiconductor nanomaterials. Small. 2006 Mar;2(3):316–29.

[34] Kennedy LC, Bickford LR, Lewinski NA, Coughlin AJ, Hu Y, Day ES, et al. A new era for cancer treatment: Gold-nanoparticle-mediated thermal therapies. Small. 2011 Jan 17;7(2):169–83.

[35] Eustis S, El-Sayed MA. Why gold nanoparticles are more precious than pretty gold: noble metal surface plasmon resonance and its enhancement of the radiative and nonradiative properties of nanocrystals of different shapes. Chem Soc Rev. 2006 Mar;35(3):209–17.

[36] Desantis CJ, Weiner RG, Radmilovic A, Bower MM, Skrabalak SE. Seeding bimetallic nanostructures as a new class of plasmonic colloids. J Phys Chem Lett. 2013;4:3072–82.

[37] Mahmoud MA, El-Sayed MA. Different plasmon sensing behavior of silver and gold nanorods. J Phys Chem Lett. 2013;(4):1541–5.

[38] Tokel O, Inci F, Demirci U. Advances in plasmonic technologies for point of care applications. Chem Rev. 2014;(114):5728–52.

[39] Scaiano JC, Stamplecoskie K. Can surface plasmon fields provide a new way to photosensitize organic photoreactions? From designer nanoparticles to custom applications. J Phys Chem Letts. 2013 Apr 4;4(7):1177–87.

[40] Nehl CL, Hafner JH. Shape-dependent plasmon resonances of gold nanoparticles. J Mater Chem. 2008;18(21):2415–9.

[41] Vigderman L, Zubarev ER. High-yield synthesis of gold nanorods with longitudinal SPR peak greater than 1200 nm using hydroquinone as a reducing agent. Chem Mater. 2013;(25):1450–7.

[42] Shiohara A, Langer J, Liz-Marzán LM. Solution processed polydimethylsiloxane/gold nanostar flexible substrates for plasmonic sensing. Nanoscale. 2014;(6):9817–23.

[43] Sim HR, Wark AW, Lee HJ. Attomolar detection of protein biomarkers using biofunctionalized gold nanorods with surface plasmon resonance. Analyst. 2010 Oct; 135(10):2528–32.

[44] Abadeer NS, Brennan MR, Wilson WL, Murphy CJ. Distance and plasmon wavelength dependent fluorescence of molecules bound to silica-coated gold nanorods. ACS nano. 2014 Aug 26;8(8):8392–406.

[45] Higgins DA, Luther BJ. Watching molecules reorient in liquid crystal droplets with multiphoton-excited fluorescence microscopy. J Chem Phys. 2003;119(7):3935–42.

[46] Yasuda R, Noji H, Yoshida M, Kinosita K, Itoh H. Resolution of distinct rotational substeps by submillisecond kinetic analysis of F1-ATPase. Nature. 2001 Apr 19;410(6831):898–904.

[47] Noji H, Yasuda R, Yoshida M, Kinosita K. Direct observation of the rotation of F1-ATPase. Nature. 1997;299–302.

[48] Vanden Bout DA, Kerimo J, Higgins DA, Barbara PF. Spatially resolved spectral inhomogeneities in small molecular crystals studied by near-field scanning optical microscopy. J Phys Chem. 1996;3654(96):11843–9.

[49] Bryant Z, Stone MD, Gore J, Smith SB, Cozzarelli NR, Bustamante C. Structural transitions and elasticity from torque measurements on DNA. Nature. 2003 Jul 17;424(6946):338–41.

[50] Sönnichsen C, Franzl T, Wilk T, von Plessen G, Feldmann J. Drastic reduction of plasmon damping in gold nanorods. Phys Rev Lett. 2002 Jan;88(7):077402.

[51] Ahmad I, Zandvliet HJW, Kooij ES. Shape-induced separation of nanospheres and aligned nanorods. Langmuir. 2014 Jul 15;30(27):7953–79561.

[52] Jana NR, Rammohun R, Mahavidyalaya R. Nanorod shape separation using surfactant assisted self-assembly. Chem Commun. 2003;(March):1950–1.

[53] Hore MJA, Composto RJ. Functional polymer nanocomposites enhanced by nanorods. Macromolecules. 2014;875–87.

[54] Vigderman L, Khanal BP, Zubarev ER. Functional gold nanorods: Synthesis, self-assembly, and sensing applications. Adv Mater [Internet]. 2012 Sep 18 [cited 2014 Jul 12];24(36):4811–41, 5014. Available from: http://www.ncbi.nlm.nih.gov/pubmed/22740090

[55] Umar A, Choi S. Aggregation behavior of oppositely charged gold nanorods in aqueous solution. J Phys Chem C. 2013;11738–43.

Solid-Phase Crystallization of Amorphous Silicon Films

Dong Nyung Lee and Sung Bo Lee

Additional information is available at the end of the chapter

http://dx.doi.org/10.5772/59723

1. Introduction

Polycrystalline silicon thin-film transistors (poly-Si TFTs) have recently attracted considerable attention for their high field-effect mobility and response velocity [1,2]. For low fabrication cost, poly-Si TFTs should be made on inexpensive glass substrates. In order to lower the crystallization temperature of amorphous silicon (*a*-Si) below the intrinsic crystallization temperature (~600 ºC), effects of metal impurities on crystallization have been investigated using Au [3], Al [4], and Sb [5] forming eutectics with Si, and Pd [6] and Ni [7] forming silicides with Si. This process is referred to as metal-induced crystallization (MIC). Following the MIC, its variants, such as the metal-induced lateral crystallization (MILC) [8] and the field-aided lateral crystallization (FALC) [9–12], have been introduced as attempts to lower crystallization temperature and to reduce the contamination by a metal catalyst. For the MILC process, the flux of the diffusing species is governed only by the concentration gradient, but for the FALC process, the flux can be affected by not only the concentration gradient but also the applied electric potential gradient. In the FALC process, the crystallization front typically migrates from the negative electrode side to the positive electrode side. In the FALC, the application of a DC electric field increases the crystallization rate, as compared with the MILC (without any electric field) and MIC. In the FALC process, Ni and Cu, both of which are silicide forming metals, have been reported to produce high crystallization rates [12]. The mechanism of the crystallization induced by Ni was examined in detail by Hayzelden and his coworkers [13, 14] using *in situ* transmission electron microscopy (TEM) and high-resolution TEM.

The *a*-Si films are generally deposited on glass by physical or chemical vapor deposition. When annealed, they undergo crystallization by nucleation and growth. For the solid-phase crystallization of *a*-Si films on glass by heating, the directed crystallization, in which crystallization is favored in special crystallographic directions of crystallites, is not easily expected because both *a*-Si and glass are physically isotropic. However, the directed crystallization is rather general in the solid-phase crystallization of *a*-Si on glass at low temperatures [8,15–19]. Lee et

al. [8] advanced a model for the directed crystallization and later the model was further refined [20,21]. The model is introduced and is applied to the solid-phase epitaxial growth rate of *c*-Si in self-implanted Si(100) wafer, the solid-phase epitaxial growth rate of *c*-Si in self-implanted Si(100) wafer [22,23], the metal-induced crystallization of *a*-Si film on glass, and the silicide mediated crystallization.

2. Directed crystallization theory

The solid-phase transformation of a metastable amorphous material into a crystal, or the solid-phase crystallization of an amorphous material, needs the activation energy. The energy is usually supplied in the form of thermal energy by increasing the temperature of the material. When the nucleation occurs, the strain energy develops in the amorphous matrix as well as in the crystallites. The strain energy may be referred to as the accommodation strain energy. The strain energy is likely to give rise to inhomogeneous growth rates of crystallites due to their elastic anisotropy, if any. We discuss the evolution of the strain energy qualitatively [20,21].

The stress state of thin film deposits can be approximated by plane stress because the principal stress normal to the film surface is negligibly small compared with those along the surface. We consider a circular disk cut from a large, elastically isotropic metastable-phase sheet. When the disk is transformed into its stable phase, its dimension is likely to differ from the original diameter of the metastable phase due to a difference in density between the two phases. If the stable phase is elastically isotropic, the stable disk will be circular. When the density of the stable phase is higher than that of the metastable phase, the diameter of the stable-phase disk is smaller than that of the metastable phase, and vice versa. When the ends of the two phases are pulled toward each other and joined together, the strain and stress fields develop in the both phases.

In order to obtain the stress distribution of this system, we first adopt the solution of the stress distribution in a hollow cylinder subjected to uniform pressure on the inner and outer surfaces (Figure 1). The solution of this problem is due to Lamé and expressed as follows [22]:

$$\sigma_r = \frac{a^2 b^2 (p_o - p_i)}{(b^2 - a^2) r^2} + \frac{p_i a^2 - p_o b^2}{b^2 - a^2} \tag{1}$$

$$\sigma_\theta = -\frac{a^2 b^2 (p_o - p_i)}{(b^2 - a^2) r^2} + \frac{p_i a^2 - p_o b^2}{b^2 - a^2} \tag{2}$$

where σ_r and σ_θ denote the normal stress components in the radial and circumferential directions, and p_i and p_o the uniform internal and external pressures. Other symbols are defined in Figure 1. This solution is useful because it gives the stress distribution in the region

of $a < r < b$, which may be equivalent to the metastable region in the present case. When the cylinder is subjected to internal pressure only, $p_o = 0$, with $b \gg a$, Eqs. 1 and 2 give

$$\sigma_r = \frac{a^2 p_i}{b^2}\left(1 - \frac{b^2}{r^2}\right) \tag{3}$$

$$\sigma_\theta = \frac{a^2 p_i}{b^2}\left(1 + \frac{b^2}{r^2}\right) \tag{4}$$

These equations show that σ_r is always a compressive stress and σ_θ a tensile stress. If the cylinder is subjected to uniform internal tensile stress only, $p_i < 0$, σ_r is always a tensile stress and σ_θ a compressive stress. This is relevant to the case when the density of the stable phase is higher than that of the metastable phase, as in crystallization of a-Si. The magnitude of σ_r and σ_θ are maxima at $r = a$, decreasing with increasing r regardless of internal pressure or internal tensile stress.

When the stable phase is elastically anisotropic, the pulling displacement of the circumference of the stable phase depends on its stiffness, the stiffer the smaller displacement at a given force. The smaller displacement of the stable phase requires the larger pulling displacement of the metastable phase, which induces the higher strain energy in the metastable phase.
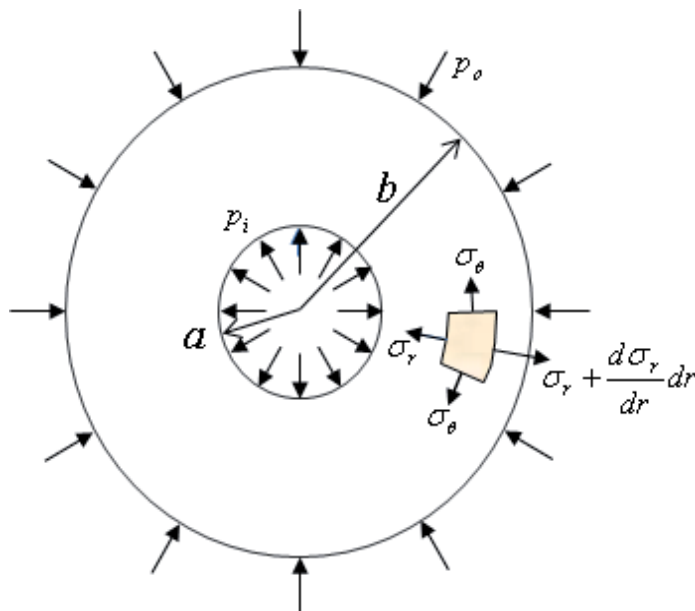
Figure 1. Hollow cylinder subjected to uniform pressure.

A qualitative account of this can be made using rectangular elements shown in Figure 2(a). The elements may be approximated by uniaxial specimens with fixed ends as shown in Figure 2(b). Let the metastable phase be elastically isotropic and its stiffness be C_m. If the stable phase is an elastically anisotropic single crystal, its stiffness is likely to vary with its crystallographic direction. C_h and C_l denote the stiffnesses of elements along different crystallographic directions of the stable phase, with $C_h > C_l$. The force F_1 for joining the specimen of C_l to that of C_m can differ from the force F_2 for joining the specimen of C_h to that of C_m.
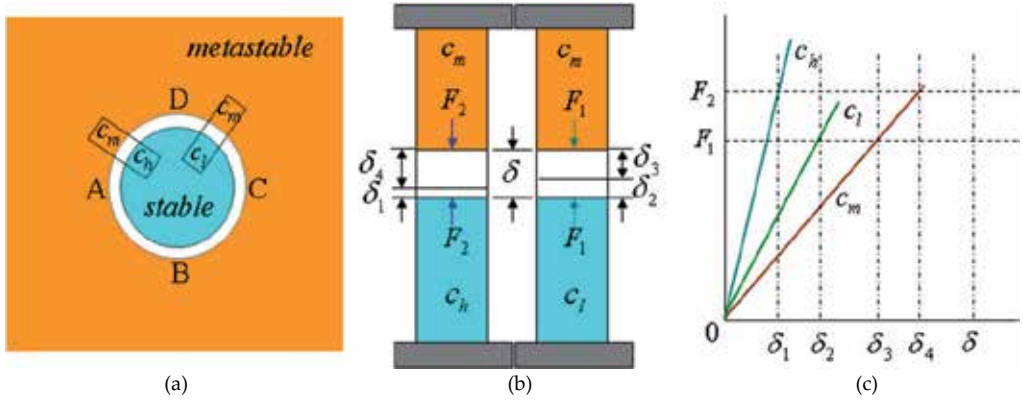
Figure 2. (a) Gap generated after circular metastable-phase ABCD is transformed into stable phase without generating stresses, when density of stable phase is higher than that of metastable phase, and hypothetical rectangular elements with different stiffness values. C_m is stiffness of metastable phase, and C_h and C_l are stiffnesses of stable phase with $C_h > C_l$. (b) Elements in (a) acting as tensile specimens with fixed ends. (c) Forces F_i and displacements δ_j necessary to join ends of metastable-phase and stable-phase specimens [21].

From Figure 2(c), we can obtain the following relations.

$$C_l = F_1 / \delta_2 \tag{5}$$

$$C_h = F_2 / \delta_1 \tag{6}$$

$$C_m = F_1 / \delta_3 = F_2 / \delta_4 \tag{7}$$

$$\delta = \delta_1 + \delta_4 = \delta_2 + \delta_3 \tag{8}$$

It follows from the above relations that

$$\left(C_m / C_h + 1 \right)\delta_4 = \left(C_m / C_l + 1 \right)\delta_3 \tag{9}$$

Since $C_h > C_l$, Eq. 9 gives $\delta_4 > \delta_3$ and hence we obtain $F_2 > F_1$ from Eq. 7.

The strain energy of the metastable phase adjacent to the stable phase with C_h is given by

$$W_2 = F_2 \delta_4 / 2 \tag{10}$$

Similarly, that of the metastable phase adjacent to the stable phase with C_l is given by

$$W_1 = F_1 \delta_3 / 2 \tag{11}$$

Since $\delta_4 > \delta_3$ and $F_2 > F_1$, we obtain $W_2 > W_1$. In other words, the metastable phase is subjected to the higher strain energy in the higher stiffness direction of the stable phase.

The stiffness C is related to Young's modulus E as $C = EA/L$ with A and L being the cross-sectional area and the length of the stable-phase element, respectively. Therefore, it can be stated that the highest strain-energy density region in the metastable phase containing a stable phase crystallite is the stable/metastable interface region in the highest Young's modulus directions of the stable phase. As the heating temperature increases, the strain energy contribution to the activation energy for continuing crystallization will decrease [21].

For a thin amorphous deposit, another form of strain energy can develop due to a difference in thermal expansion coefficient between the deposit and the substrate in addition to the accommodation strain energy. The strain energy is termed the thermal strain energy. The thermal stress developed in the thin deposit, which is associated with the thermal strain energy, is equivalent to an external stress along the surface. If the stress is planar isotropic, the directed crystallization is unlikely to occur along the deposit surface in the absence of the accommodation strain energy. However, the stress can influence the crystal growth rate.

3. Solid-phase epitaxial growth rate of crystalline Si in self-implanted Si(100) wafer

3.1. Uniaxial stress ranged from — 0.55 to 0.55 GPa

The a-Si/c-Si interface region is under the tensile stress because the density of c-Si is higher than that of a-Si (Section 4). According to Section 2, if the tensile stress in specimen is increased by external tensile forces, the strain energy in the interface region will increase, which in turn will increase the crystallization rate, and vice versa.

Aziz et al. [23] studied the solid-phase epitaxial growth rate of c-Si from a-Si by bending bar-shaped Si(001) wafers with a three-point bending system at about 540 °C. The Si wafers (p type, 1 ohm cm, 0.84 mm thickness) were implanted on both sides at 77 K with ^{30}Si$^+$ (60 keV, 1×10^{15} cm^{-2}; 180 keV, 2×10^{15} cm^{-2}) to create 280-nm-thick amorphous surface layers. The wafers were diced into bars >20 mm in length in the [110] direction by 5 mm in width.

One side of the elastically bent specimen is approximately under a uniaxial tensile stress state and the other side under a uniaxial compressive stress state, in which the stress ranged from –0.55 GPa (compressive) to 0.55 GPa (tensile). Their measured crystallization rate as a function of applied stress showed that the rate in the tension side was higher than that in the compression side. Aziz et al. claimed that the stress existed in the crystal at the crystalline-amorphous interface because there is no stress in the bulk of the a-Si due to stress relief by viscous flow [24]. Even though the initial stress in the a-Si could be completely relieved during the stress measurement, the stress developed in the a-Si at the c-Si/a-Si interface during crystallization might not be removed immediately.

Even if we cannot distinguish the initial stress from the stress developed during crystallization, it is apparent that the a-Si film on the tension side of the sample could be more stressed in tension than that on the compression side. Therefore, we can expect that the grain growth rate in the film on the tension side will be higher than that in the film on the compression side in agreement with the measured data.

3.2. Effect of hydrostatic pressure up to 3.2 GPa

Lu et al. [25] measured the hydrostatic pressure dependence of the solid-phase epitaxial growth rate of self-implanted Si(100) by using the in situ time-resolved interferometric technique and high-pressure diamond anvil cell. With fluid argon as the pressure transmission medium, a hydrostatic pressure environment was achieved around the sample. The external heating geometry employed provided a uniform temperature across the sample. At temperatures of 530–550 °C and pressures up to 3.2 GPa, the growth rate was enhanced by up to a factor of 5 over that at 1 atmosphere pressure (≈ 0.1 MPa).

This result appears to contradict the non-hydrostatic stress effect explained in Section 3.1. The crystallization of a-Si results in a decrease in volume. Therefore, a hydrostatic compression is expected to accelerate crystallization. We roughly estimate a hydrostatic pressure for the crystallization of a-Si without taking the thermal activation into account.

Let P and Δ denote the hydrostatic pressure and the volumetric dilatation for crystallization of a-Si, respectively. The pressure is related to the dilatation as follows:

$$P = -B\Delta \tag{12}$$

where B is the bulk modulus of a-Si and the volumetric dilatation Δ is defined as

$$\Delta = \frac{V - V_0}{V_0} \tag{13}$$

Here V_0 is the volume before crystallization, and V is the volume after crystallization. The density of c-Si at room temperature is 2320 to 2340 kg m^{-3} [26]. If the density of c-Si is set to be

2330 kg m^{-3}, the specific volume of c-Si is calculated to be $4.29{\times}10^{-4}$ m^3 kg^{-1}. Ion-implanted amorphous silicon is 1.8% less dense than c-Si at room temperature [27]. Therefore, the density of a-Si at room temperature is calculated to be 2288 m^3 kg^{-1} and its specific volume is calculated to be $4.37{\times}10^{-4}$ m^3 kg^{-1}. Since the volumes of a-Si and c-Si vary with temperature, we calculate those at 540 °C. The linear thermal expansion coefficients of a-Si and c-Si are almost the same, about $3{\times}10^{-6}$ K^{-1} [24, 28]. Therefore, the specific volume of a-Si at 540 °C is $4.39{\times}10^{-4}$ m^3 kg^{-1} {= $4.37{\times}10^{-4}{\times}[1+3{\times}3{\times}10^{-6}{\times}(540{-}25)]$}, and that of c-Si at 540 °C is $4.31{\times}10^{-4}$ m^3 kg^{-1} {= $4.29{\times}10^{-4}{\times}[1+3{\times}3{\times}10^{-6}{\times}(540{-}25)]$}. The volumetric dilatation at 540 °C is

$$\Delta = \left(4.31 - 4.39\right)/4.39 = -0.0182. \tag{14}$$

For lack of the bulk modulus of a-Si at 540 °C, it has been calculated using the biaxial modulus of ion-beam-sputtered a-Si at 110 °C, M_σ (110) = 140 GPa [24], the temperature dependence of M for Si(100) [24], and Poisson's ratio ν of a-Si film deposited by rf sputtering onto Si substrate in an atmosphere of $P_{H_2}/(P_{H_2}+P_{Ar})$ = 0.001 [29]. The bulk modulus B and the biaxial modulus M_σ can be expressed as

$$B = \frac{E}{3(1 - 2v)} \tag{15}$$

$$M_\sigma = \frac{E}{(1 - v)} \tag{16}$$

where E is Young's modulus. The temperature dependence of M_σ(T) for Si(100) is given by

$$\frac{d\ln M_\sigma(T)}{dT} = -62 \times 10^{-6}\text{K}^{-1}$$

From this we obtain M_σ (540) = 136 GPa. According to Jiang et al. [29], ν = 0.32. Substitution of M_σ (540) = 136 GPa and ν = 0.32 into Eq. 16 gives E (540) = 92.5 GPa. In this calculation, Poisson's ratio was assumed to be independent of temperature. From these elastic constants, the bulk modulus of a-Si at 540 °C, B (540) = 85.6 GPa, is obtained. Therefore, the hydrostatic pressure for crystallization at 540 °C is calculated as P (540) = 1.56 GPa. From this estimation we can see that hydrostatic pressures of the order of GPa will accelerate the crystal growth rate.

Stresses of the order of 0.1 GPa in Section 3.1 are too low to be effective in the grain growth of c-Si. On the other hand, its contribution to the local tensile stress developed in the a-Si/c-Si interface could be much higher. Therefore, the compressive stresses of the order of 0.1 GPa reduced the growth rate, and the tensile stresses increased the growth rate.

4. Crystallization of amorphous Si on glasses

According to the directed-growth theory described in Section 2, the highest crystallization rate would be along the maximum Young's modulus direction (MxYMD). In order to understand crystallization anisotropy of *a*-Si, we need to calculate Young's modulus of crystalline Si (*c*-Si). Young's modulus E for crystals of cubic system is given by Eq. 17 [30,31].,

$$1 / E = S_{11} + [S_{44} - 2(S_{11} - S_{12})](a_{11}^2 a_{12}^2 + a_{12}^2 a_{13}^2 + a_{13}^2 a_{11}^2) \tag{17}$$

where S_{11}, S_{44}, and S_{12} are the compliances referred to the symmetric axes and a_{1i} are the direction cosines of the uniaxial stress direction 1 referred to the symmetric axes *i*. For the [*hkl*] direction,

$$\alpha_{11} = h / \sqrt{h^2 + k^2 + l^2}, \alpha_{12} = k / \sqrt{h^2 + k^2 + l^2}, \alpha_{13} = l / \sqrt{h^2 + k^2 + l^2} \tag{18}$$

For silicon at 293 K, $S_{11} = 0.007685$, $S_{12} = -0.002139$, and $S_{44} = 0.01256$ GPa^{-1} [32], and [$S_{44} - 2 (S_{11} - S_{12})$] = $-0.00708 < 0$. Therefore, the maximum and minimum values of ($a_{11}^2 a_{12}^2 + a_{12}^2 a_{13}^2 + a_{13}^2 a_{11}^2$) in Eq. 17 are 1/3 for the <111> directions and 0 for the <100> directions, respectively. Therefore, the growth rate of *c*-Si is likely to be the highest in the <111> directions.

For *a*-Si film/SiO$_2$ glass-substrate structure, the thermal strain-energy is the highest near the interface between the film and the substrate, or in the deepest place of the *a*-Si film, which is under the highest compressive stress because the thermal expansion coefficient of Si is higher than that of the SiO$_2$ layer. At low temperatures, crystallization of *a*-Si is likely to be dominated by the accommodation strain-energy along with the thermal strain energy. In this case, crystallization is likely to start near the film/substrate interface and the highest growth directions (the <111> directions) tend to be parallel to the surface because the film stress is the highest along the film/substrate interface or the surface.

Because the thickness of the Si film including *a*-Si and *c*-Si is much smaller than the dimensions along the film surface, the stress in the thickness direction is negligible, and the film is approximately under the plane stress state. That is, the film stress is the highest along the interface or the film surface. Therefore, when the <111> directions are placed along the film surface, the growth rate of crystallites will be the highest.

Let two of four <111> directions, for example, the [111] and [–1 1 1] directions be placed along the surface, then the thickness direction becomes the [0–1 1] direction (110 projection in Figure 3). Thus, the texture of crystallites is approximated by the <110>//ND (ND: the surface normal direction) orientation with the <111> branches. When three of the <111> directions are at 19.4°to the film/substrate interface and one of the <111> directions is parallel to the thickness direction [(111) projection in Figure 3], the <111>//ND texture can be obtained. This possibility is based on the relatively small angle of 19.4°. The directed crystallization can give rise to the dendritic

growth of crystallites. As the annealing temperature increases, the strain energy contribution decreases and the thermal energy becomes dominant. In this case, the directed crystallization will be suppressed, resulting in equiaxed crystallization and random orientation.
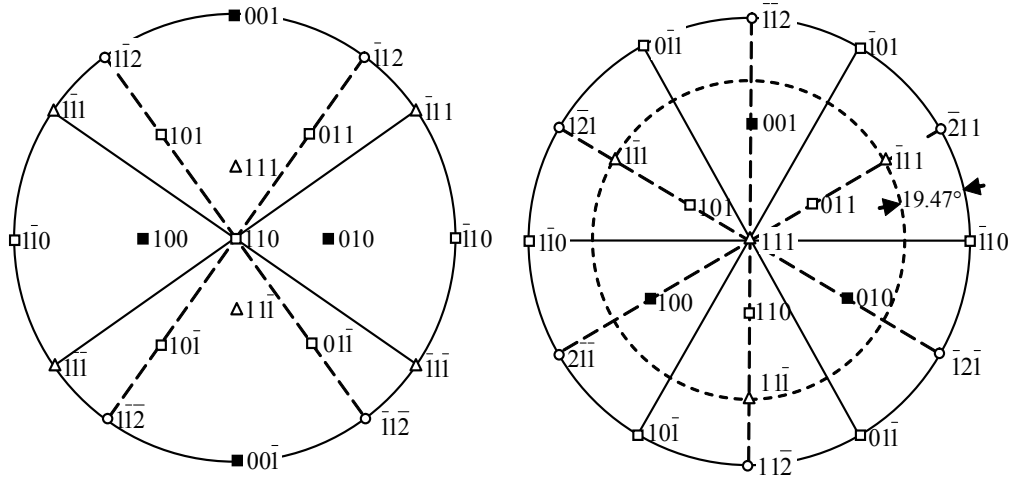
Figure 3. Cubic (110) and (111) stereographic projections [21].
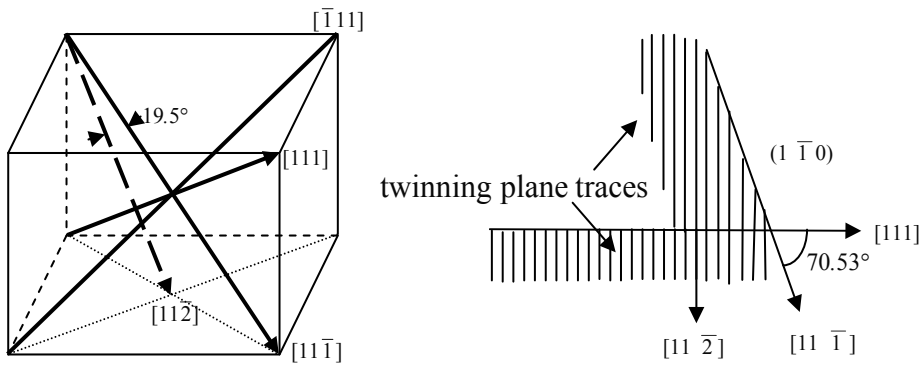
Figure 4. Twinning plane traces in [1–1 0]//ND oriented dendritic crystal whose branches are directed along [111] and [1 1–1] directions [20].

When the annealing temperature is high enough to activate the volume diffusion, the random orientation will change to the <111> texture because the {111} planes have the minimum surface energy density, to reduce the surface energy which is the major energy source in thin films. The <110> or <111> to random transition temperature or the random to <111> transition temperature is likely to decrease with increasing purity of Si films.

Silicon has a stacking-fault energy of about 50 mJ/m^2. This relatively small energy generates many twins during crystallization. The twinning planes and directions of *c*-Si are {111} and

<112>. Figure 4 shows the [1 1–2] twinning direction and twinning-plane traces in the [1–1 0]// ND oriented dendritic crystal whose branches are directed along the [111] and [1 1–1] directions. The angle between the [1 1–2] and [1 1–1] directions can appear smaller than 19.5°, when the specimen is slightly rotated about the [1 1–2] axis. This may make crystallites appear to grow along the <112> directions.

4.1. Evaporation-deposited *a*-Si films

Table 1 summarizes deposition conditions of a few *a*-Si films and their annealing textures. When heated at 650 °C for 1 h in flowing nitrogen in an open tube furnace, Si dendrites were observed. The selected area diffraction pattern of a dendrite indicated that dendrite arms were parallel to the <111> directions (Figure 5). The [1 1–1] was erroneously indexed as the [0 1–1] in [15]. When the heat-treatment temperature was raised to 850 °C, the film fully crystallized with equiaxed grains of 640 nm in normal mean size and dendrite remnants. The texture of the film was random. After heating at 1040 °C, the film had a microstructure consisting solely of equiaxed grains without dendrite remnants. The normal mean grain size for this film was 205 nm, and the texture of the film was random. The result is compatible with the prediction of the directed crystallization theory because the strain energy contribution to the activation energy decreases with increasing annealing temperature and in turn the anisotropic crystallization rate decreases [20].

film-thickness; deposition method	substrate	evapor. press. [Torr]	substr. temp. [°C]	deposit. rate [nm /min]	anneal. ambient	anneal. time. [h]	anneal. temp. [°C]	anneal. texture	Ref.
900 nm; evapor.	370 nm SiO$_2$ on <100> p-type Si	10^{-6}	300	300	Flowing N$_2$	1	650 850 1040	<110> random random	15
500 nm; evapor.	fused silica	base press. 10^{-10}	380	6	UHV or flowing N$_2$		600 700	random <111>	16
~100 nm; LPCVD 70 nm; Dose	glass		550		CF RTP RTP RTP CF	3 3 min 1 min 1 min 64	610 650 750 850 600	<110> <110> <110> <110> <111>	18

deposit.: deposition; evapor.: evaporation; substr.: substrate; temp.: temperature; anneal.: annealing;

CF: conventional furnace; RTP: rapid thermal process; Dose: implanted by a dose of 5×10^{15} cm^{-2} Si$^+$

at 30 keV; UHV: ultrahigh vacuum.

Table 1. Deposition conditions of *a*-Si films and their annealing textures

Whenever contamination is avoided prior to annealing under ultrahigh vacuum, crystalliza‐ tion occurred at 600 °C regardless of the substrate temperature in evaporation and the crystallized films had no texture [16]. They attributed the random orientation to the existence of voids in the amorphous films. However, the amorphous phase itself can give rise to the randomness at the absence of strain energies. The voids can reduce the strain energy of films, which in turn may enhance the random orientation. After annealing at 700 °C, the <111>//ND texture was obtained. In Anderson's work [15], the random orientation was obtained at 850 °C or 1040 °C and the <111>//ND texture was not observed within the experimental range. The differences are caused by differences in purity of the samples. Films obtained at lower pressures are likely to have higher purity. It is well known that the higher purity gives rise to the lower crystallization temperature.
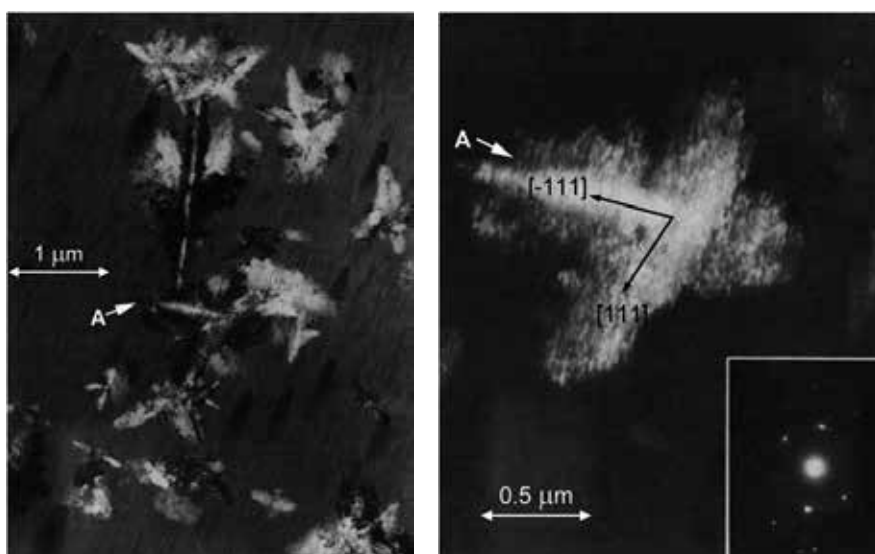
Figure 5. Dendritic c-Si nucleating in evaporated a-Si film and dark-field image of dendrite at A (Experimental results [15]).

4.2. Amorphous $Si_{1-x}Ge_x$ films on SiO_2

Hwang et al. [19] deposited a-$Si_{1-x}Ge_x$ films with x = 0–0.53 on thermally oxidized Si<100> wafers by molecular beam epitaxy. The nominal thickness of the film was 100 nm and the deposition temperature was 300 °C. The base pressure and the deposition pressure were 10^{-10} Torr and 10^{-9} Torr, respectively, and the deposition rate was about 3 nm/min. When annealed at 600 °C, a-Si film (x = 0) crystallized into dendritic forms similar to Figure 5 with a strong <111>//ND texture. As the Ge concentration, or x, increased, the relative intensity of the (111) peak decreased. Figure 6 shows TEM micrographs of $Si_{0.47}Ge_{0.53}$ films annealed at 550 °C. From x-ray diffraction results, the texture of the film could be approximated by random orientation, when thickness factors were not taken into account.

When thickness factors are taken into account, its texture could be approximated by <110> +<311>//ND. Even though the accurate texture of the films cannot be obtained by this method, the texture of the films could be approximated by random orientation with weak <110>//ND and <311>//ND components. The near-spherical crystallites and the near-random texture seem be related to an increased contribution of the thermal energy. The solidus temperature of $Si_{0.47}Ge_{0.53}$ is 1095 °C, which is lower than the melting point of Si, 1414 °C (Figure 7). Therefore, at an annealing temperature of 600 °C, crystallization of $Si_{0.47}Ge_{0.53}$ was dominated by the thermal energy. The aspect ratio of crystallites decreased with increasing content of Ge [19]. This also reflects an increase in thermal energy contribution with increasing Ge content. The grain size in fully crystallized Si-Ge films decreased with increasing Ge content. The crystal structures, lattice parameters, intrinsic stacking-fault energy, and elastic anisotropies of Ge and Si are similar, and so the characteristics of the Ge-Si alloys are likely to be similar to those of Ge and Si. Therefore, for a given annealing temperature T, the decrease in the solidus temperature is equivalent to an increase in T/T_m, with T_m being the absolute melting point of a reference material (*eg*. Ge or Si) in the Ge–Si system.
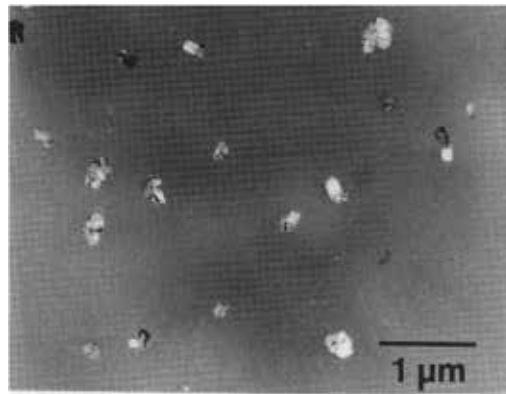
Figure 6. TEM of a-$Si_{0.47}Ge_{0.53}$ film after annealing at 550°C for 10 min [19].

The grain size G is likely to be reciprocally proportional to the nucleation rate dN/dt. Since the nucleation is a thermally activated process, the grain size and the nucleation rate can be expresses as

$$A/G = dN/dt = B\exp(-\frac{Q}{RT}) \tag{19}$$

where A and B are constants, and Q is the activation energy for nucleation. Therefore, we obtain

$$G = C\exp(\frac{Q}{RT}) \text{ or } \ln G = C_0 + \frac{Q}{RT} \text{ or } \ln G = C_0 + \frac{Q/T_m}{RT/T_m} \tag{20}$$
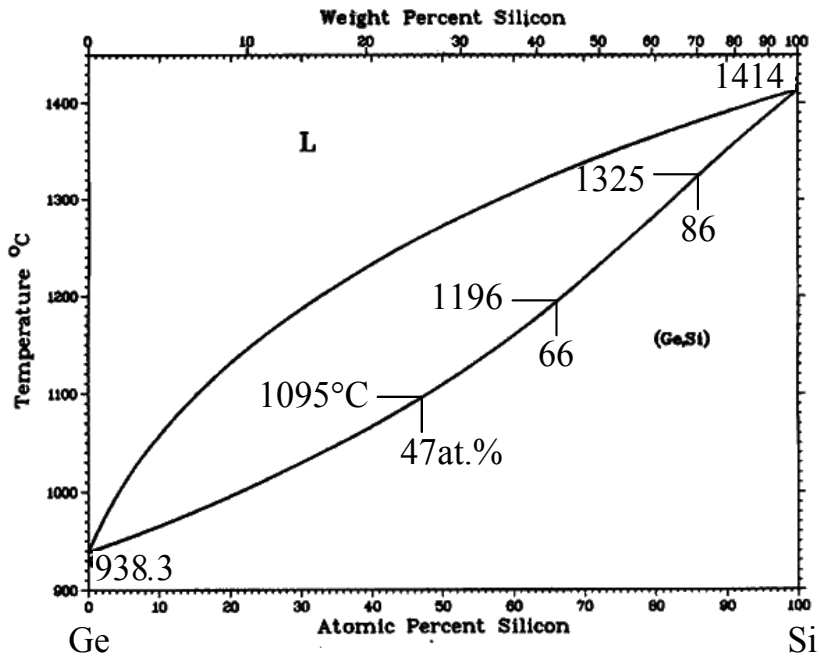
Figure 7. Ge–Si phase diagram [20]
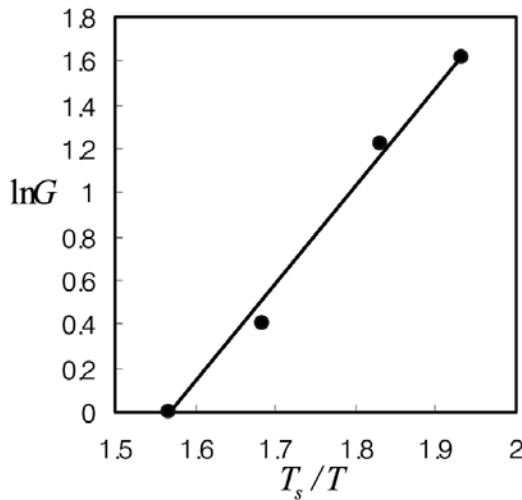
Figure 8. Relationship between ln G and T_s/T [20].

where C (= A/B) and C_0 (=ln C) are constants. As discussed above, T/T_m can be assumed to be proportional to T/T_s, with T_s being the solidus temperatures of the Ge–Si system. Then Eq. (20) can be expressed as

$$\ln G = C_0 + \frac{Q}{RT} = C_0 + \frac{Q_0 T_s}{RT} \tag{21}$$

Here Q_0 (= Q/T_m) is a constant. The relationship between ln G and T_s/T is plotted in Figure 8. The good linear relationship in the figure supports the above assumption.

5. Metal-induced crystallization

5.1. Copper-induced crystallization

Lee et al. [8] deposited an 80 nm a-Si on Corning 1737 glass by plasma-enhanced chemical vapor deposition (PECVD) at 280°C using Si_2H_6 and H_2 as source gases. The wafer was cut into 3×3 cm^2 square specimens for the subsequent process. To deposit copper on the a-Si film, the photoresist (PR) was spin-coated and patterned by a photolithographic process using rectangular mask patterns of 60×30 μm^2. A copper layer of 2 nm in thickness was deposited in a DC sputtering system. Copper on the PR patterns was removed by the lift-off method and only that deposited on the a-Si was left. The crystallization annealing was done at 500°C for 1 h in N_2 ambience. During the crystallization annealing an electric field of 1.80 kV/m was applied to the above metal-deposited specimen by the DC power supply.

From the crystallized specimen, 3 mm disks were cut using an ultrasonic cutter for TEM specimen preparation. For the plan-view studies of the a-Si film, the disks were mechanically back-thinned to a thickness of about 10 μm, and then ion milled on the glass substrate side at an accelerating voltage of 5 kV using a PIPS. The crystallization microstructure was characterized by TEM. High-resolution TEM (HRTEM) was performed at 400 kV in a JEM4010 (point-to-point resolution: 0.15 nm, JEOL Co., Ltd.). Energy dispersive X-ray spectroscopy (EDXS) was applied for composition analysis of a-Si and c-Si regions.

An enlarged view of the patterns between the electrodes is shown in Figure 9. The crystallization front migrates from the negative electrode side to the positive electrode side. A needlelike morphology of c-Si was clearly observed at the interface between the fully crystallized and amorphous regions indicated by 'O' in Figure 9 as shown in Figure 10 (a). As revealed in Figures 10 (b), almost all the c-Si needles exhibit the <011>//ND orientations with respect to the a-Si film surface normal and grew the <111> and <211> directions, forming an angle of 90° between the needles. The [011] diffraction pattern taken from the needle 'A' in Figure 10 (b) showed streaks along the [111] direction, indicating that there are many stacking faults or twins normal to that direction. The a-Si region was measured to contain (2.99 ± 0.97) at.% Cu on average by EDXS measurement of five areas. In fully crystallized regions many needles were interwoven, as shown in Figure 11. The regions contained (1.63 ± 0.15) at.% Cu on average by XEDS measurements of four areas. The solubility of Cu in c-Si is negligible, and therefore, the detected Cu is believed to arise from trapped Cu solutes in the interfaces between the interwoven c-Si needles. Figure 12 (a) shows an HRTEM image also revealing the growth directions of <111> and <211> with the <011>//ND orientation, which means the {011} planes

being parallel to the surface plane. At a higher magnification (Figure 12 (b)), three {111} twins and a stacking fault can be seen. In order to consider the role of any Cu silicides on the nucleation and growth of the *c*-Si needles, the edges of the *c*-Si needles were examined. Figure 13 displays the typical edge, where Cu silicides are not observed, and instead, Si lattice image is seen. Furthermore, Cu silicides are observed even in the *a*-Si and the crystallized region within the limited field of view. The *c*-Si region at the edge contains many {111} twins and stacking faults indicated by white triangles and arrows, respectively. There seems to be also some lattice distortion in some areas, due to defects (twins or stacking faults) which are not clearly visible. As in the NiSi$_2$-mediated crystallization (Section 5.2) Cu-induced crystallization proceeds in the <111> directions with a shape of needles as shown in Figure 10(b) and Figure 12 (a). The *c*-Si needles have the <011>//ND orientations.
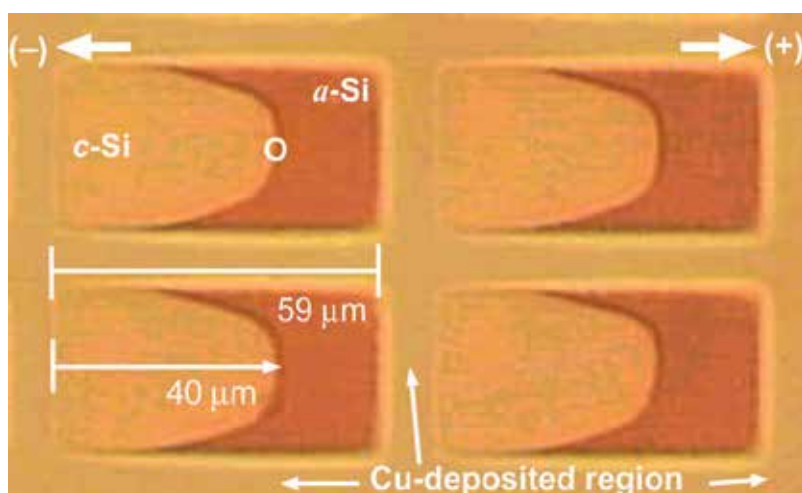
Figure 9. Optical image of patterns between electrodes [8].

Additionally, as shown in Figure 10 (b) and 12 (a), the growth occurs also in the <211> directions. At variance with the NiSi$_2$-mediated crystallization, however, as shown in Figure 13, Cu silicides are not observed at the leading edges of the *c*-Si needles, indicating that the crystallization of the Cu/*a*-Si system in this study is not mediated by any Cu silicides. Radnoczi et al. [4] suggested that Au, Sb, In and Al, which form eutectic with Si, dissolved in the a-Si film may loosen the covalent bonds in Si and make the *a*-Si even unstable, enhancing crystallization. Even though Cu is a silicide-forming metal, Cu atoms appear to enhance crystallization in a similar way to the eutectic-forming metals. Since Cu has a negligible solubility in crystalline Si [33], the Cu solute atoms are repelled by the *c*-Si. The Cu atoms will diffuse into the *a*-Si matrix, making the *a*-Si unstable, and the Si atoms will migrate into the *c*-Si side from the *a*-Si, resulting in crystallization. Diffusion of Cu atoms in *a*-Si seems to be rate-controlling. Without the application of any electric field during annealing at 500 °C (i.e., in the MILC process), the crystallization rate is reported to be 1.5–2 μm h^{-1} [12]. Copper is reported to diffuse in *a*-Si with $D > 10^{-12}$ cm^2 s^{-1} in a temperature range between 400 and 600 °C [34]. From the
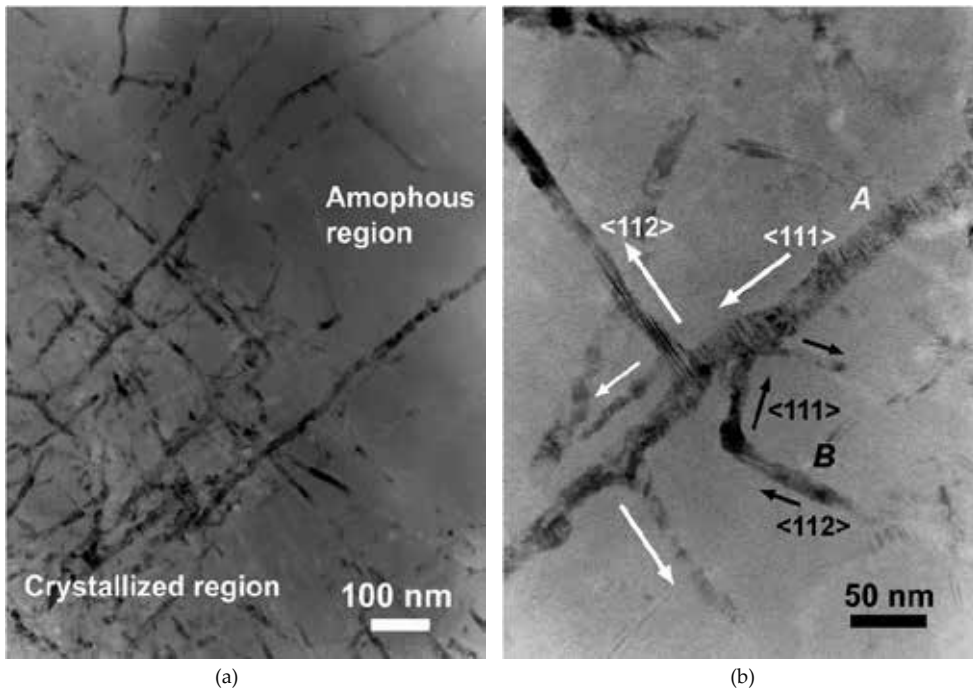
Figure 10. (a) Low magnification TEM image of partially crystallized *a*-Si revealing needlelike morphology of *c*-Si and (b) typical TEM image showing the *c*-Si needles grow in directions of <111> and <112> directions with <110>//ND orientations [8].

diffusivity value of 10^{-12} cm^2 s^{-1}, the minimum diffusion length ($\sqrt{Dt}$) is calculated to be 0.6 μm for 1 h at 500 °C. This diffusion length is in qualitative agreement with the crystallization rate obtained without any electric field in the MILC process (1.5–2 μm h^{-1}). Lee et al. [12] showed the increase in crystallization rate with an electric field of 210 V m^{-1} to 35 μm h^{-1}. Although some crystallization parameters such as pattern size, shape, and the applied electric field intensity are different, a high crystallization rate of ~40 μm h^{-1} was obtained. The crystallized pattern images in Figure 9 reveal that the macroscopic crystallization direction under an applied bias corresponds to that of electric field in the pattern.

It is suggested that the electric field in the FALC process can cause a kind of the electron wind effect (electromigration) via current flow in the pattern at the elevated temperature [35]. Choi et al. [35] propose that the electron wind effect explains the NiSi$_2$-mediated crystallization [13,14] and is limited to the diffusion of Ni in NiSi$_2$. When the current density is high enough, the momentum exchange induces the Ni atoms in NiSi$_2$ to migrate from the negative electrode side to the positive one (along the electron flow direction). In the Cu-mediated crystallization study [8], because no Cu silicides are observed at the leading edges of the *c*-Si needles, the application of the above-mentioned suggestion is not plausible. However, the electron wind effect is likely to hold for the diffusion of Cu in *a*-Si at the high temperature of 500 °C, because the resistivity of *a*-Si decreases with increasing temperature because of the exponential increase

in intrinsic carrier concentration, and at such high temperature, the electron flow in *a*-Si can cause the electron wind effect. The effect will accelerate the diffusion of Ni along the electron flow direction, and concomitantly, the crystallization rate.

(a)   (b)
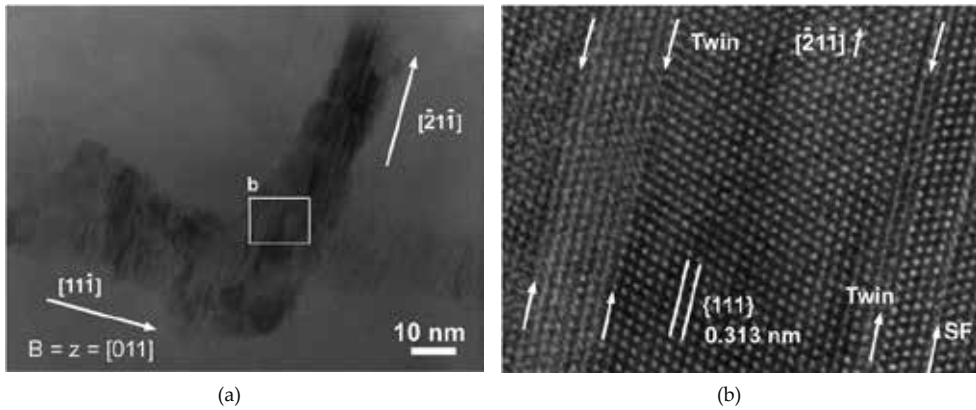
Figure 11. (a) High-resolution TEM image showing growth directions of <111> and <112> with <110>//ND orientation of *c*-Si needle. Beam direction (zone axis) is parallel to [011]. At higher magnification (b) of area indicated by white-lined box in (a), three {111} twin boundaries and one stacking fault (SF) are visible [8].
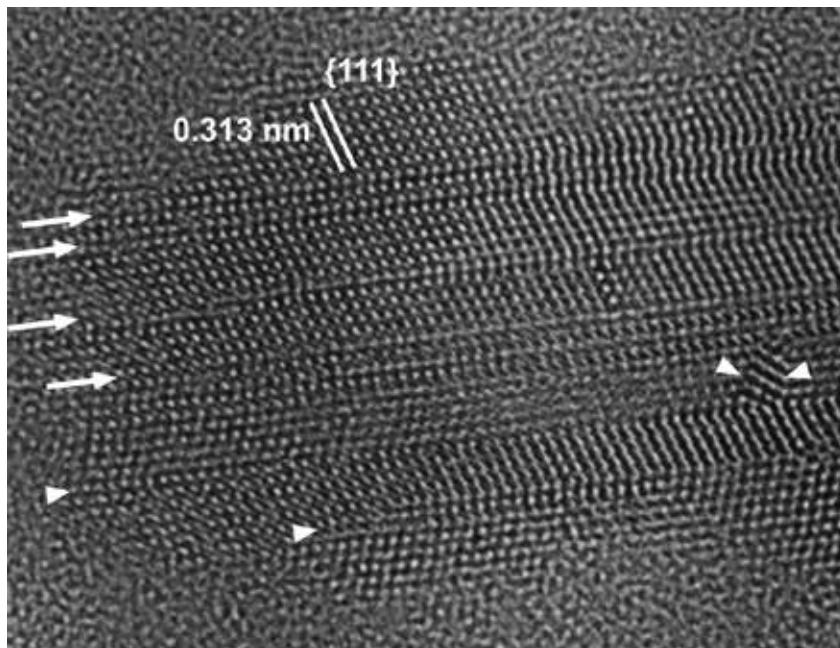
Figure 12. High-resolution image of typical edge without Cu silicides, where Si lattice image is shown. {111} twins and stacking faults are indicated by white triangles and arrows, respectively [8].

Crystallization behavior of a-Si in the Cu/a-Si bilayer (without any electric field in this case) was studied by Russell et al. [36]. They found that on heating to 175 °C, Cu$_3$Si phase appeared and subsequent heating to 485 °C resulted in the crystallization of the a-Si in the form of dendrites in the Cu$_3$Si matrix. At variance with the results of Russell et al., the matrix was observed to be still a-Si and discernible Cu silicides including Cu$_3$Si phase were not observed in the study by Lee et al. [8]. In the study by Russell et al., the thickness ratio of Cu to a-Si was determined to obtain an average composition of Cu$_{3-\delta}$Si, where δ is from 0.5 to 1. In this case the matrix (continuous phase) could become Cu$_3$Si phase. In the study by Lee et al. [8], however, the deposited Cu film (2 nm thick) is very thin with the thickness ratio to the a-Si underlying layer (80 nm) of 1:40. Therefore, as already mentioned, they could not be easily observed. They may act as heterogeneous nucleation sites for crystallization. However, the difficulty in observing the phases indicates that their nucleation density was too low and their size was too small to explain the observed, overall crystallization behavior, strongly implying that the presence of Cu solutes, not Cu silicides, enhances crystallization.

The <111> growth directions and the <011>//ND orientations observed by Lee et al. [8] are caused by anisotropic elastic properties of c-Si, although a-Si is isotropic because the strain energy can influence the crystallization rate as discussed in Sections 2 and 4. The higher strain energy will give rise to the higher crystallization rate. One of the major strain energy sources may be the thermal strain energy due to differences in thermal expansion coefficient between a-Si and the substrate glass. The thermal strain energy can influence the crystallization rate, but is not related to the directional crystallization. Since the thermal expansion coefficients of a-Si and c-Si are expected to be almost the same, the thermal strain energy between a-Si and c-Si can be negligible.

Another strain-energy may arise from the accommodation strain between a-Si and c-Si due to different structures and densities (The densities of a-Si and c-Si are measured to be 2.1 to 2.3 [37] and 2.32 to 2.34 [26], respectively). This strain energy can be anisotropic because of anisotropic elastic properties of c-Si, even though a-Si is isotropic. Since the thickness of the Si film including a-Si and c-Si is much smaller than the dimensions along the film surface, the stress in the plane normal direction (ND) is negligible, and the film is under the plane stress state. Initial Si crystallites will form in the surface layer, where the Cu concentration is highest, and they could be of a disk-shape. The surface orientation of c-Si disks is presumably random because they form from a- Si. However, their growth rates will vary with their orientations because different orientations give rise to different strain energies. According to the directed growth theory (Section 2), c-Si grows in its MxYMD <111>, resulting in the needlelike shape. If c-Si grows along the [1 1–1] direction, the growth front will be subjected to tensile stresses, which will increase with growth. When the stresses reach a point where the distance between atoms in c-Si/a-Si interface is too far to be shuffled, another <111> growth, $e.g.$, the [–1 1–1] growth, will be activated. When the <111> direction are parallel to the film surface, the c-Si needles can grow extensively and occupy large areas within the a-Si films, resulting in <110>// ND orientation (Figure 4). This may be expressed as the {110}<111> orientation.

The additional growth in the <211> directions may occur with the help of many {111} twins and stacking faults observed in the c-Si (Figure 12 (b) and Figure 13) which are certainly due

to the low stacking fault energy of Si (~50 mJ m^{-2}), even though the <211> growth directions are not favored in terms of the strain energy consideration. These {111} twins and stacking fault planes can generate steps for growth at the interface between the *c*-Si and *a*-Si, enhancing the growth in directions parallel to the twin and stacking fault planes. Because the angle between the <111> and <211> growth directions is 19.4°, we can make some errors in measurements. Even though there is some change in growth direction into <211>, the <011>//ND orientations will remain unchanged, as revealed in Figures 10 (b) and 12 (a).

5.2. Nickel-silicide mediated crystallization

Hayzelden et al. [13,14] studied the formation of buried precipitates of NiSi$_2$ in Ni-ion implanted *a*-Si and the subsequent NiSi$_2$-mediated crystallization of *a*-Si using *in situ* transmission electron microscopy (TEM) and high resolution TEM. *a*-Si thin films of 95 nm in thickness was deposited by low-pressure chemical-vapor deposition on Si substrates capped with 100 nm of thermally grown SiO$_2$. The *a*-Si could not crystallize from the *c*-Si substrate directly. Ion implantation of Ni into the *a*-Si was performed at an energy of 55 keV with doses of 1 and 5×10^{15} ions cm^{-2} to give a peak Ni concentration of 4×10^{20} and 2×10^{21} ions cm^{-3}, respectively, at a depth of approximately half the *a*-Si film thickness.

They observed that the NiSi$_2$ precipitates with CaF$_2$ structure formed in *a*-Si at about 400 °C, which were octahedra bounded by eight {111} faces. On the other hand, Yeh et al. [38] made a stacked structure of *a*-Si/Ni/SiO$_2$/Si(100) as follows: the <100>//ND oriented *p*-type Si wafers were chemically cleaned, followed by a dry oxidation in an atmospheric pressure chemical vapor deposition furnace to form a 3-nm-thick tunnel oxide. Subsequently, a 3.5-nm-thick Ni layer was deposited onto the tunnel oxide by electron beam evaporation. The Ni layer was capped by a 12.5-nm-thick *a*-Si layer deposited by sputtering. The stacked structure was, afterwards, dry oxidized at 900 °C to form a layer with control oxide on the top and NiSi$_2$ nanocrystals precipitated and embedded between tunnel oxide and control oxide. After dry oxidation, the well-separated and spherical NiSi$_2$ nanocrystals embedded in the SiO$_2$ layer are observed. The whole *a*-Si layer was oxidized to serve as the control oxide. The distance between NiSi$_2$ nanocrystals and the oxide/Si interface is about 10 nm indicating that about 3-nm-thick Si substrate was oxidized to contribute to about 6.5-nm-thick SiO$_2$ in addition to the 3-nm-thick tunnel oxide. The mean size and areal density of the NiSi$_2$ nanocrystals were measured to be ~ 7.6 nm and 3.3×10^{11} cm^{-2}, respectively. The nanocrystals were identified to be NiSi$_2$ phase. This indicates that the initial NiSi$_2$ crystals are spherical.

Figures 1 and 3 in [14] show that NiSi$_2$ precipitates embedded in Ni-implanted *a*-Si thin films appear partly rectangular and partly spherical and spherical precipitates look a little smaller than rectangular precipitates. Therefore, the initial shape of the precipitate may be spherical and the octahedral shape of NiSi$_2$ precipitates may not be intrinsic. MIC of *a*-Si in Section 5.1 showed that *c*-Si grew in its <111> directions without NiSi$_2$-mediation. This is associated with contribution of strain energy to activation energy for crystal growth at low crystallization temperatures (Section 2) or low transformation temperatures [39].

Eight {111} faces of a spherical NiSi$_2$ precipitate are likely to be the best spots for the nucleation of *c*-Si because the growth rate of *c*-Si is the highest in the <111> directions and the extremely

good lattice match between the {111} faces of $NiSi_2$ and c-Si [the lattice parameter of $NiSi_2$ (0.5406 nm) is nearly equal to that of c-Si (0.5430 nm)], resulting in the better stability of the {111} faces of $NiSi_2$ precipitate than other faces. The eight spots are shown in Figure 14. Therefore, the {111} faces are likely to grow and bound the precipitate, forming the octahedral shape during annealing. The gradual transition from spherical $NiSi_2$ to octahedral $NiSi_2$ is represented in Figure 15. In this way, a structure of a-Si/c-Si/$NiSi_2$/c-Si/a-Si may be formed in a-Si thin film. The c-Si precipitates on the left and right of $NiSi_2$ can differ in thickness. Let the left c-Si be thicker than the right c-Si. In order to distinguish the right c-Si from the left c-Si, the right c-Si is denoted by c-Si(I) and the left c-Si by c-Si(II), then the structure is expressed as a-Si/c-Si(II)/$NiSi_2$/c-Si(I)/a-Si.
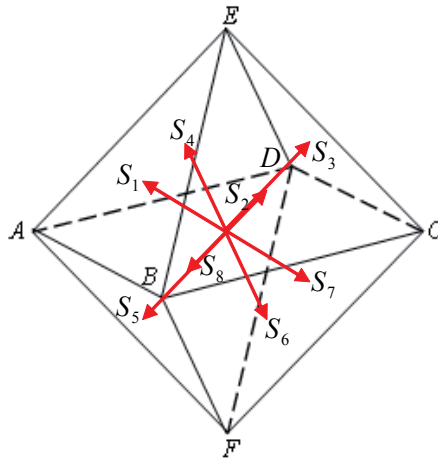
Figure 13. Octahedron bounded by {111} planes. S_1: center (c) of $\triangle ABE$, S_2: c of $\triangle BCE$, S_3: c of $\triangle CDE$, S_4: c of $\triangle ADE$, S_5: c of $\triangle ABF$, S_6: c of $\triangle BCF$, S_7: c of $\triangle CDF$, S_8: c of $\triangle ADF$. Triangles ($\triangle$) are {111} planes and edges are <110> directions. Arrows indicate <111> directions. S_1 to S_8 are on surface of one sphere.
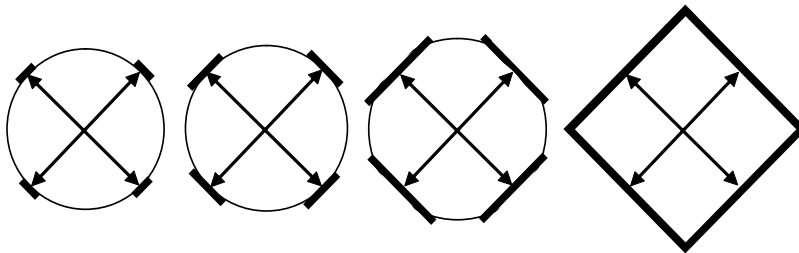
Figure 14. Schematic diagram showing gradual shape change from spherical $NiSi_2$ to octahedral $NiSi_2$. Arrows indicate <111> directions of $NiSi_2$ precipitate projected on a plane parallel to (001) plane. Black deposits indicate c-Si nucleated on {111} planes of $NiSi_2$ precipitate. Far left circle is made of S_1, S_2, S_3, S_4 or S_5, S_6, S_7, S_8 in Figure 13.

At about 500 °C, the epitaxial c-Si was nucleated on one or more of the $NiSi_2$ {111} surfaces and the c-Si needles grew in the <111> directions in the amorphous matrix with the <011>//ND

orientations (ND indicates the film surface normal). This may be expressed as {011}<111>. The NiSi$_2$ precipitates were observed to be always present at the leading edges of c-Si needles [13, 14].

The extremely good lattice match between c-Si and NiSi$_2$ and a mismatch between c-Si and a-Si give rise to stresses in c-Si near the c-Si/a-Si interface, as shown in Figure 15. Therefore, the average stress of c-Si layer in the structure of NiSi$_2$/c-Si/a-Si increases with decreasing thickness of the layer, and the molar free energy of c-Si is likely to increase with decreasing thickness. In the structure of a-Si/c-Si(II)/NiSi$_2$/c-Si(I)/a-Si, the molar free energy of c-Si(I) is likely to be higher than that of c-Si(II) and lower than that of a-Si, as shown in Figure 16. It can be seen from Figure 16 that tie lines drawn from both c-Si(I) and c-Si(II) to the NiSi$_2$ show that in equilibrium, NiSi$_2$ in contact with c-Si(I) is expected to be Si rich in comparison to NiSi$_2$ in contact with c-Si(II) [Si(I) > Si(II)].
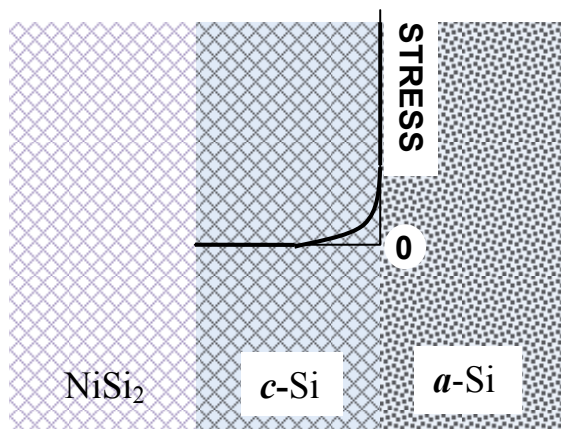
Figure 15. Schematic stress profile along thickness of c-Si

The driving force behind the NiSi$_2$ precipitate migration and Si crystallization, although not an equilibrium process, can be discussed by reference to an equilibrium free-energy diagram of the type shown in Figure 16. The driving force for the phase transformation is the reduction in free energy associated with the transformation of metastable a-Si to stable c-Si. Tie lines drawn from both a-Si and c-Si to the NiSi$_2$ show that in equilibrium, NiSi$_2$ in contact with a-Si is expected to be Si rich in comparison to NiSi$_2$ in contact with c-Si(I) and c-Si(II) [Si(a) > c-Si(I) > c-Si(II) in Figure 16].

The curvature of the NiSi$_2$ phase may be quite significant. For example, laser quenching has shown that the CaF$_2$ structure of NiSi$_2$ is capable of accommodating Si deficits of ~35 at.% [40]. The intersections of the tie lines with the energy axes yield the chemical potentials for Ni and Si at the c-Si/NiSi$_2$ (= NiSi$_2$/c-Si) and NiSi$_2$/a-Si interfaces. The chemical potential of the Ni atoms is lower at the NiSi$_2$/a-Si interface, whereas the chemical potential of the Si atoms is lower at the c-Si/NiSi$_2$ interface. A migrating NiSi$_2$ precipitate consuming a-Si at the leading interface and forming a trail of epitaxial c-Si [= c-Si(II)] is shown schematically in Figure 17. There is a

driving force for the forward diffusion of Ni atoms through the NiSi$_2$ and a driving force for the diffusion of Si atoms in the reverse direction through the NiSi$_2$. The consumption of a-Si at the leading edge and rejection of Si to the epitaxial c-Si trail [c-Si(II) in Figure 17] leads to the needlelike c-Si morphology. Note that the c-Si/NiSi$_2$ epitaxial interface is formed behind the migrating NiSi$_2$ precipitate.
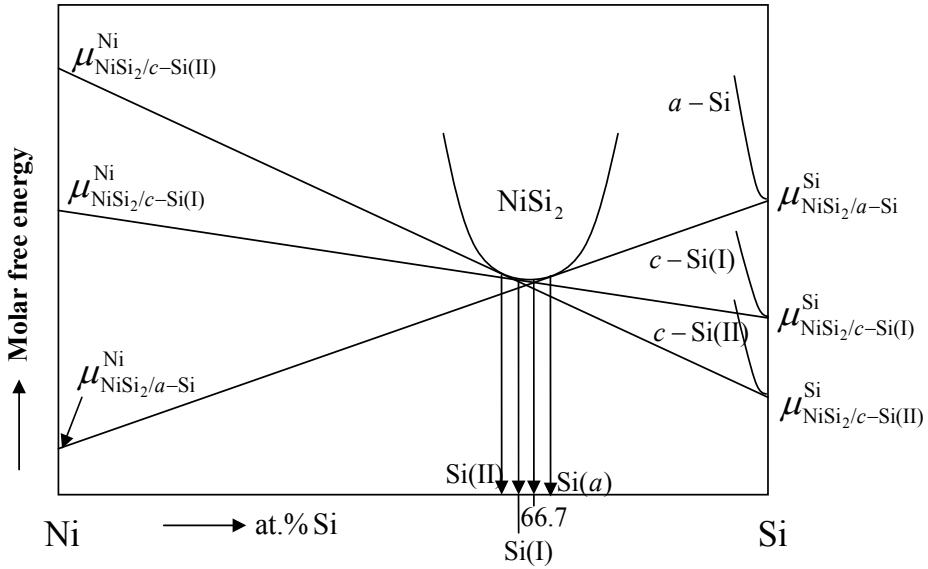
Figure 16. Schematic equilibrium molar free-energy diagram for NiSi$_2$ in contact with a-Si, c-Si(I), and c-Si(II). Si(a), Si(I), and Si(II) are Si contents in NiSi$_2$ in contact with a-Si, c-Si(I), and c-Si(II), respectively.
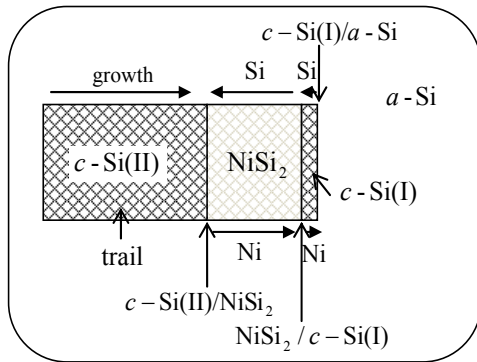
Figure 17. Schematic representation of diffusion direction of Si and Ni atoms in c-Si(II)/NiSi$_2$/c-Si(I)/a-Si system. Without c-Si(I), NiSi$_2$/c-Si(I) interface becomes NiSi$_2$/a-Si interface.

There are two limiting cases that describe the diffusional process of NiSi$_2$-mediated crystallization of a-Si. These can be the dissociative and nondissociative diffusion models. In the

dissociative model, the $NiSi_2$ layer dissociates to provide free Si for epitaxial growth at the *c*-Si/$NiSi_2$ interface, with new $NiSi_2$ formed at the leading $NiSi_2$/*a*-Si interface. In this case all the Si atoms that were originally in the $NiSi_2$ layer would be incorporated in the epitaxially grown *c*-Si and replaced by Si atoms from the *a*-Si. The diffusing species in the dissociative mechanism would be Ni atoms and the measured effective diffusivity would apply to Ni atoms. In the nondissociative model, Si atoms would simply diffuse through the $NiSi_2$ layer from the *a*-Si and bond to the epitaxial *c*-Si. The effective diffusivity would then apply to Si moving through the $NiSi_2$. In the sequential formation of Ni_2Si, NiSi, and $NiSi_2$ formed from thin-film diffusion couples of around 100 nm of Ni on Si, Ni is known to be the fast-diffusing species [41-43].

Figure 16 also shows that the chemical potential of the Ni atoms, μ^{Ni}, is higher at the $NiSi_2$/*c*-Si(II) interface, or the c-Si(II)/$NiSi_2$ interface, than at the $NiSi_2$/*c*-Si(I) interface, whereas the chemical potential of the Si atoms, μ^{Si}, is lower at the $NiSi_2$/*c*-Si(II) interface than at the $NiSi_2$/*c*-Si(I) interface. Therefore, the $NiSi_2$ layer dissociates to provide free Si for epitaxial growth at the *c*-Si(II)/$NiSi_2$ interface, with excess Ni at the *c*-Si(II)/$NiSi_2$ interface diffusing through $NiSi_2$ into the $NiSi_2$/*c*-Si(I) interface, interacting with *c*-Si(I) to form $NiSi_2$, resulting in depletion of Si in *c*-Si(I). The depleted Si is replaced by Si from *a*-Si because the molar free energy of *c*-Si(I) is lower than that of *a*-Si. In this way, the Ni atoms diffuses from the *c*-Si(II)/$NiSi_2$ interface through $NiSi_2$ and *c*-Si(I) into the *c*-Si(I)/*a*-Si interface, whereas the Si atoms effectively diffuse from the *c*-Si(I)/a-Si interface through the Si(I) and NiSi2 layers into the *c*-Si(II)/$NiSi_2$ interface. This process eventually makes the $NiSi_2$ precipitate migrate rightward consuming *a*-Si at the leading interface [*c*-Si(I)/*a*-Si] to form a trail of epitaxial *c*-Si(II) as shown in Figure 17. As this process proceeds, the *c*-Si(II) layer gradually thicken and the *c*-Si(I) layer gradually thin to a few layers, which is stable enough to survive because of the extremely good lattice match between $NiSi_2$ and *c*-Si. Consequently, the consumption of *a*-Si at the leading edge and rejection of Si to the epitaxial *c*-Si(II) trail take place and leads to the needlelike *c*-Si forming behind the migrating $NiSi_2$ precipitate.

The reason why during crystallization, the shape of the $NiSi_2$ precipitates at the leading edges of the *c*-Si needles assume the thin plate shape, whereas the leading edges of the *c*-Si needles are not flat (Figure 9) can be attributed to the extent of elastic anisotropy between $NiSi_2$ and *c*-Si. Zener's anisotropy factor, $A = 2(S_{11}-S_{12})/S_{44}$, is used to denote the extent of elastic anisotropy of cubic materials. When the ratio A is unity, the elastic properties are isotropic, but they can deviate from isotropy in two ways, by A being either greater than or less than unity. A = 1.83 for $NiSi_2$ ($S_{11} = 0.01219$, $S_{12} = -0.00505$, $S_{44} = 0.01887$ GPa^{-1} [44]) and A = 1.56 for *c*-Si (Section 4). Thus, the extent of elastic anisotropy of $NiSi_2$ is higher than that of c-Si, implying that the {111} planes of $NiSi_2$ have higher potential of existence than the {111} planes of *c*-Si. The higher Young's modulus reflects the higher bonding strength. Therefore, the region surrounding the interface edge is strained, which in turn gives rise to crystallization along the interface plane as well as along the needle axis. In this way, the *c*-Si needles fan out during its growth (Figure 18), and simultaneously, the $NiSi_2$ precipitates become thinner. As the interface area increases, the accommodation strain increases to a point such that coherency between the two crystals cannot be maintained, resulting in dissociation of the $NiSi_2$ crystal into a few smaller crystallites. These smaller precipitates continue to mediate the growth [14]. Because the growth is

mediated by the NiSi$_2$ whose {111} planes have higher potential of existance than that of c-Si, the {011}<111>-oriented growth for the NiSi$_2$-mediated crystallization remains without growth in other directions (e.g., <211> for the Cu-enhanced crystallization).

Diffusion of Ni through c-Si to reach the a-Si in Figure 18 is consistent with previous experiments on Ni-assisted Si epitaxy. Erokhin et al. [45] deposited a film of Ni on a c-Si/a-Si structure and observed Ni diffusion to the c-Si/a-Si interface to form NiSi$_2$ after annealing for 43 h at 350 °C. Decomposition of NiSi$_2$ at the NiSi$_2$/c-Si interface with Ni diffusion into the a-Si was suggested as a mechanism for Si crystallization. This is in good agreement with the model of dissociative diffusion of Ni from the NiSi$_2$/c-Si interface to leave an abrupt planar interface. Low-temperature crystallization has also been reported following Ni deposition on hydrogenated a-Si (a-Si:H) [43]. The silicidation process of Ni/a-Si:H on a fused silica substrate was investigated by in situ electrical resistance measurements and x-ray diffraction and Rutherford backscattering spectroscopy [7]. It was reported that NiSi formed first at 330 °C followed by NiSi$_2$ at 420 °C. Crystallization of the a-Si:H occurred at approximately 480 °C and it was suggested that such crystallization resulted from heterogeneous nucleation of c-Si on the NiSi$_2$ phase.
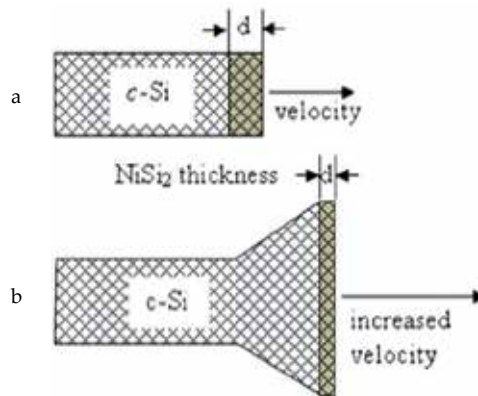
Figure 18. Schematic representation of diffusion-controlled growth of silicide-mediated crystallization of Si [14].

In Summary, the NiSi$_2$-mediated crystallization of a-Si can occur through the following processes. The initial shape of the NiSi$_2$ precipitated in the a-Si thin film is likely to be spherical and transforms into the octahedral shape during annealing because of the extremely good lattice match between c-Si and NiSi$_2$ and preferential growth of c-Si along its <111> directions. Crystalline silicon layers nucleated on the {111} faces of NiSi$_2$ precipitates can differ in thickness. This brings about a structure of a-Si/c-Si(II)/NiSi$_2$/c-Si(I)/a-Si with c-Si(II) layer being thicker than c-Si(I) layer. The c-Si(I) layer is more stressed than the c-Si(II) layer, and so the molar free energy of c-Si(I) is higher than that of c-Si(II), but lower than that of metastable a-Si. Therefore, in this system, the Ni atoms diffuse from the c-Si(II)/NiSi$_2$ interface through NiSi$_2$ into the c-Si(I)/a-Si interface, whereas the Si atoms diffuse from the c-Si(I)/a-Si interface

through NiSi$_2$ into the c-Si(II)/NiSi$_2$ interface, and the depleted Si atoms in the c-Si(I) layer are replaced by a-Si. This process eventually makes the NiSi$_2$ precipitate migrate consuming a-Si at the leading interface [c-Si(I)/a-Si interface] and forming the needlelike trail of epitaxial c-Si(II). Consequently, the c-Si(II)/NiSi$_2$ epitaxial interface is formed behind the migrating NiSi$_2$ precipitate. Migrating NiSi$_2$ precipitates resulted in crystallization of Si at temperatures as low as 484 °C, which is ~200 °C lower than the intrinsic temperature required for crystallization of pure a-Si. The NiSi$_2$-mediated crystallization rate is controlled by diffusion through the migrating NiSi$_2$ precipitates.

6. Conclusions

1. The solid-phase crystallization of an amorphous material needs the activation energy. The energy is usually supplied in the form of thermal energy by increasing the temperature of the material. When the nucleation occurs, the strain energy develops in the amorphous matrix as well as in the crystalline nuclei, or crystallites. The strain energy is the highest in the stable/metastable interface region in the highest Young's modulus directions of the stable phase. Therefore, the growth rate of the crystallites is the highest in the metastable phase along the maximum Young's modulus directions of the crystallites because the activation barrier can be surmounted by the strain energy when the thermal energy is not high enough to surmount the barrier. The strain energy is likely to give rise to inhomogeneous growth rates of crystallites due to their elastic anisotropy, if any. This directed crystallization theory can explain the following results.

2. The solid-phase epitaxial growth rate of c-Si from a-Si by bending the bar-shaped Si(001) wafers (p type, 1 ohm cm, 0.84 mm thickness) whose both sides were implanted to create 280–nm-thick amorphous surface layers, were elastically bent using a three-point bending system at about 540 °C. One side of the elastically bent specimen is approximately under a uniaxial tensile stress state and the other side under a uniaxial compressive stress state, in which the stress ranged from –0.55 GPa (compressive) to 0.55 GPa (tensile). The measured crystallization rate as a function of applied stress showed that the rate in the tension side was higher than that in the compression side. The result is understood because the a-Si film on the tension side of the sample could be more stressed than that on the compression side. On the other hand, at temperatures of 530–550 °C and hydrostatic pressures up to 3.2 GPa, the solid-phase epitaxial growth rate of self-implanted Si(100) was enhanced by up to a factor of 5 over that at 1 atmosphere pressure (≈ 0.1 MPa). This result appears to contradict the non-hydrostatic stress effect of the bent specimen. The crystallization of a-Si results in a decrease in volume. Therefore, a hydrostatic compression is expected to accelerate crystallization. However, the stress of -0.55 GPa is too low to yield effective densification.

3. Evaporated a-Si film crystallizes into dendrite forms with dendrite arms in the <111> directions at low annealing temperatures. As the annealing temperature increases the a-Si film crystallized with increasingly equiaxed grains and random textures. The results

are compatible with the directed crystallization theory because the strain energy contribution to the activation energy decreases with increasing annealing temperature and in turn the isotropic crystallization rate increases. The crystallization temperature decreases with increasing purity of a-Si films.

4. The solidus temperature of $Si_{0.47}Ge_{0.53}$ is 1095 °C, which is lower than the melting point of Si, 1414 °C. Therefore, at an annealing temperature of 600 °C, crystallization of a-$Si_{0.47}Ge_{0.53}$ was dominated by the thermal energy unlike Si. The aspect ratio of crystallites decreased with increasing content of Ge. This also reflects an increase in thermal energy contribution with increasing Ge content.

5. The crystallization behavior of a Cu-deposited a-Si/glass sample annealed at 500°C for 1 h with an electric field of 180V/cm has shown that the Si crystallites grow in the <111> and <112> directions with the <110>//ND orientation, assuming a needlelike shape. No Cu silicides are observed, and it seems that the Cu atoms in the a-Si film make the a-Si unstable, resulting in crystallization at the relatively low temperature. The growth directions of <111> and the <110>//ND orientations are compatible with the directed crystallization theory. The <112> directions can be possible with the help of many {111} twins and stacking faults in c-Si.

6. The $NiSi_2$-mediated crystallization of a-Si can occur through the following processes. The initial shape of the $NiSi_2$ precipitated in the a-Si thin film is likely to be spherical and transforms into the octahedral shape during annealing because of the extremely good lattice match between c-Si and $NiSi_2$ and preferential growth of c-Si along its <111> directions. Crystalline silicon layers nucleated on the {111} faces of $NiSi_2$ precipitates can differ in thickness. This brings about a structure of a-Si/c-Si(II)/$NiSi_2$/c-Si(I)/a-Si with c-Si(II) layer being thicker than c-Si(I) layer. The c-Si(I) layer is more stressed than the c-Si(II) layer, and so the molar free energy of c-Si(I) is higher than that of c-Si(II), but lower than that of metastable a-Si. Therefore, in this system, the Ni atoms diffuse from the c-Si(II)/$NiSi_2$ interface through $NiSi_2$ into the c-Si(I)/a-Si interface, whereas the Si atoms diffuse from the c-Si(I)/a-Si interface through $NiSi_2$ into the c-Si(II)/$NiSi_2$ interface, and the depleted Si atoms in the c-Si(I) layer are replaced by a-Si. This process eventually makes the $NiSi_2$ precipitate migrate consuming a-Si at the leading interface [c-Si(I)/a-Si interface] and forming the needlelike trail of epitaxial c-Si(II).

Acknowledgements

Author details

Dong Nyung Lee[*] and Sung Bo Lee

*Address all correspondence to: dnlee@snu.ac.kr

Department of Materials Science and Engineering, Seoul National University, Seoul, Republic of Korea

References

[1] Matsuyama T, Terada N, Baba T, Sawada T, Tsuge S, Wakisaka K, Tsuda S. High quality polycrystalline thin film prepared by a solid phase crystallization method. Journal of Non-Crystalline Solids 1996;198–200 940–944.

[2] Song I-H, Kim C-H, Nam W-J, Han M-K. A poly-Si thin film transistor fabricated by new excimer laser recrystallization employing floating active structure. Current Applied Physics 2002;2 225–228.

[3] Hultman L, Robertsson A, Hentzell HTG, Engström I, Psaras PA. Crystallization of amorphous silicon during thin-film gold reaction. Journal of Applied Physics 1987;62 3647–3655.

[4] Radnoczi G, Robertsson A, Hentzell HTG, Gong SF, Hasan MA. Al induced crystallization of a-Si. Journal of Applied Physics 1991;69 6394–6399.

[5] Gong SF, Hentzell HTG, Robertsson AE, Hultman L, Hörnström S-E, Radnoczi G. Al-doped and Sb-doped polycrystalline silicon obtained by means of metal induced crystallization. Journal of Applied Physics 1987;62 3726–3732.

[6] Nemanich RJ, Tsai CC, Thompson MJ, Sigmon TW. Interference enhanced Raman scattering study of the interfacial reaction of Pd on a-Si:H. Journal of Vacuum Science & Technology. 1981;19 685–688.

[7] Kawazu Y, Kudo H, Onari S, Arai T. Low-temperature crystallization of hydrogenated amorphous silicon induced by nickel suicide formation. Japanese Journal of Applied Physics 1990 29; 2698–2704.

[8] Lee SB, Choi D-K, Lee DN. Transmission electron microscopy observations of Cu-induced directional crystallization of amorphous silicon Journal of Applied Physics 2005 98;114911–114917.

[9] Song K-S, Park S-H, Jun S-I. Choi D-K. Crystallizaion of the amorphous silicon using field aided lateral crystallization. In: Lee DN. (ed.) Proceedings of the Annual Meeting of the Research Center for Thin Film Fabrication and Crystal Growth of Ad-

vanced Materials (RETCAM), Seoul National University, Seoul, Korea; 1997. pp. 144–150.

[10]   Jang J, Oh JY, Kim SK, Choi YJ, Yoon SY, Kim CO. Electric-field-enhanced crystallization of amorphous silicon. Nature 1998;395 481–483.

[11]   Park S-H, Jun S-I, Song K-S, Kim C-K, Choi D-K. Field Aided Lateral Crystallization of Amorphous Silicon Thin Film. Japanese Journal of Applied Physics 1999;38 L108–L109.

[12]   Lee J-B, Lee C-J, Choi D-K. Influences of various metal elements on field aided lateral crystallization of amorphous silicon films. Japanese Journal of Applied Physics 2001;40 6177–6181.

[13]   Hayzelden C, Batstone JL, Cammarata RC. ln Situ transmission electron microscopy studies of silicide-mediated crystallization of amorphous silicon. Applied Physics Letters 1992;60 225–227.

[14]   Hayzelden C, Batstone JL. Silicide formation and silicide-mediated crystallization of nickel-implanted amorphous silicon thin films. Journal of Applied Physics 1993;73 8279–8289.

[15]   Anderson RM. Microstructural analysis of evaporated and pyrolytic silicon thin films. Journal of Electrochemical Society 1973;120 1540–1546.

[16]   Chao SS, Gonzalez-Hernandez J, Martin D, Tsu R. Effects of substrate temperature on the orientation of ultrahigh vacuum evaporate Si and Ge films. Applied Physics Letters 1985;46 1089–1091.

[17]   Gonzalez-Hernandez J, Martin D, Chao SS, Tsu R. Crystallization temperature of ultrahigh vacuum deposited silicon films. Applied Physics Letters 1980;45 101–103.

[18]   Haji L, Joubert P, Economou NA, Mode of growth and microstrucure of polycrystalline silicon obtained by solid-phase crystallization of an amorphous silicon film, Journal of Applied Physics 1994;75 3944-3952.

[19]   Hwang C-W, Ryu M-K, Kim K-B, Lee S-C, Kim C-S. Solid phase crystallization of amorphous $Si_{1-x}Ge_x$ films deposited on SiO_2 by molecular beam epitaxy. Journal of Applied Physics 1995;77 3042–3047.

[20]   Lee DN. crystallization of amorphous silicon deposits on glass substrates. Advanced Materials Research 2007;26-28 623–628.

[21]   Lee DN. Solid-phase crystallization of amorphous Si films on glass and Si wafer. Journal of Physical Chemistry of Solids 2011;72 1330–1333.

[22]   Timoshenko SP, Goodier JN. Theory of Elasticity, 3rd edition, McGraw-Hill Kogakusha, Ltd., Tokyo, 1970, Section 28.

[23] Aziz MJ, Sabin PC, Lu G-Q. The activation strain tensor: nonhydrostatic stress effects on crystal-growth kinetics. Physical Review B 1991;44 9812–9816.

[24] Witvrouw A, Spaepen F. Viscosity and elastic constants of amorphous Si and Ge. Journal of Applied Physics 1993;74 7154–7161.

[25] Lu GQ, Nygren E, Aziz MJ, Turnbull D, White CW. Pressure enhanced solid phase epitaxy of silicon. Applied Physics Letters 1989;54 2583–2586.

[26] Weast RC (ed.) Handbook of Chemistry and Physics, 49th ed., The Chemical Rubber Co. Cleveland, OH, 1968, p. B-242.

[27] Custer JS, Thompson MO, Jacobson DC, Poate JM, Roorda S, Sinke WC, Spaepen F. Density of amorphous Si. Applied Physics Letters 1994;64 437–439.

[28] Fabian J, Allen PB. Thermal expansion and Grüneisen parameters of amorphous silicon: a realistic model calculation. Physical Review Letters 1997;79 1885–1888.

[29] Jiang X, Goranchev B, Schmidt K, Grünberg P, Reichelt K. Mechanical Properties of a-Si:H films studied by Brillouin scattering nanoindenter. Journal of Applied Physics 1990; 67 6772–6778.

[30] Lee DN. Elastic properties of thin films of cubic system. Thin Solid Films 2003;434 183–189.

[31] Lee DN. Corrigendum to "Elastic properties of thin films of cubic system" [Thin Solid Films 2003;434 183–189]. Thin Solid Films 2012;520 3708.

[32] McSkimin HJ. Measurement of elastic constants at low temperatures by means of ultrasonic waves- Data for silicon and germanium single crystals, and for fused silica. Journal of Applied Physics 1953;24 988–997.

[33] Data from SGTE alloy databases (revised 2004).

[34] Elliman RG, Gibson JM, Jacobson DC, Poate JM, Williams JS. Diffusion and precipitation in amorphous Si. Applied Physics Letters1985;46 478–480.

[35] Choi D-K, Kim H-C, Kim Y-B. Mechanism of field-aided lateral crystallization of amorphous silicon. Applied Physics Letters 2005;87 063108.

[36] Russell SW, Li J, Mayer JW. *In situ* observation of fractal growth during *a*-Si crystallization in a Cu_3Si matrix. Journal of Applied Physics 1991;70 5153–5155.

[37] Haage T, Schmidt UI, Fath H, Hess P, Schröder B, Oechsner H. Density of glow discharge amorphous silicon films determined by spectroscopic ellipsometry. Journal of Applied Physics 1994;76 4894–4896.

[38] Yeh PH, Yu CH, Chen LJ, Wu HH, Liu PT, Chang TC. Low-power memory device with $NiSi_2$ nanocrystals embedded in silicon dioxide layer. Applied Physics Letters 2005;87 193504 3pp.

[39] Lee DN, Han HN. Orientation relationships between precipitates and their parent phases in steels at low transformation temperatures (review). Journal of Solid Mechanics and Materials Engineering 2012; 6 323–338. Doi: 10.1299/jmmp.6.323.

[40] Tung RT, Gibson JM, Jacobson DC, Poate JM. Liquid phase growth of epitaxial Ni and Co silicides. Applied Physics Letters 1983;43 476–478.

[41] Chu WK, Lau SS, Mayer JW, Müller H, Tu KN. Implanted noble gas atoms as diffusion markers in silicide formation. Thin Solid Films 1975;25 393–402.

[42] Scott DM, Nicolet M-A. Implanted oxygen in NiSi formation. Physica Status Solidi A 1981;66 773–778.

[43] d'Heurle F, Petersson S, Stolt L, Strizker B. Diffusion in intermetallic compounds with the CaF2 structure: a marker study of the formation of NiSi2 thin films. Journal of Applied Physics 1982;53 5678–5681.

[44] Malegori G, Miglio L. Elastic properties of $NiSi_2$, $CoSi_2$, and $FeSi_2$ by tight-binding calculations. Physical Review B 1993;48 9223–9230.

[45] Erokhin YN, Grötzschel R, Oktyabrsky SR, Roorda S, Sinke W, Vyatkin AF. Mesotaxy by nickel diffusion into a buried amorphous silicon layer. Materials Science Engineering B 1992;12 103–106.

Imprinting Chirality in Mesoporous Silica Structures

Gila Levi

Additional information is available at the end of the chapter

http://dx.doi.org/10.5772/59620

1. Introduction

Chirality is one of the significant factors in molecular recognition having many uses in chemical and biological systems. Chiral compounds are extremely important in chemistry, biology and medicine. Discovering efficient systems to produce, control and identify enantiomerically pure chiral compounds is essential for improving the development of pharmaceuticals, agrochemicals, and food additives. The synthesis of chiral compounds and their chiral separation are among the greatest challenges in modern chemical processing and play key roles in pharmaceutical industry [1, 2]. Enantioselective synthesis requires the use of chiral media such as chiral catalysts for synthesis, chiral stationary phases for chromatographic separations, chiral solvents, etc...

In recent years, chirality has also been envisaged to play an important role in nanotechnology [3-5]. Many innovations in nanotechnology significantly benefit from molecular chirality. The advance of molecular devices such as chiroptical molecular switches and molecular motors appears very intriguing where chirality can play the determinative function for providing useful work in many applications. Supramolecules and self-assembled structures on nanometer scale [6-10] e.g., chiral nanosurfaces [11-13], sol-gel materials imprinted with different chiral functionalities and chiral nanoparticles [14-18] are other interesting areas which are being explored for a number of applications such as catalysts, bio-recognition and chiral separation processes.

Many chiral applications such as chiral separations and asymmetric synthesis take advantage from chiral porous materials mainly due to their high surface area, high capacity and large mechanical and thermal stabilities.

In this chapter we will review the current development in chiral synthesis and application of mesoporous silica based materials. All together there are two main paths for the fabrication of chiral mesoporous silica (CMS). The first method is based on molecular self-assembly route.

In this approach, mesoporous silica assemblies are directed in the formation of hierarchical chiral constructions transcribed from chiral organic templates. The preparation of chiral mesoporous silica via self-assembly route is beyond the scoop of this chapter and readers who are interested in this topic are referred to the papers of Oda *et al.* [19-21] and other groups [22, 23] and to the review of Huibin Qiu and Shunai Che [24]. An additional technique to obtain chiral porous structures is to apply molecular imprinting methods. The template-based approach to the formation of amorphous porous silica was defined by Brinker *et al.* as "*a central structure about which a network forms in such a way that removal of the template creates a cavity with morphological and/or stereochemical features related to those of the template*" [25]. Hence, chiral porous structures can be formed in this template-based approach. In the work of Alvaro *et al.* [26], chiral binaphthyl and TEOS served as precursors to prepare a porous material with optical activity, linearly rotating polarized light. In another article, chiral trialkoxysilane was grafted through Si atoms to the organic framework to form mesoporous silica leading to diverse chiral catalysts [27].

We will focus on the fabrication of chiral mesoporous silica by chiral templating processes. It is well known that for the preparation of mesoporous materials, two initial materials are needed: a non-organic material used as the precursor and chiral surfactants used as the templating agent. In the preparation of chiral mesoporous silica, various chiral templating agents can be employed such as small chiral molecules, chiral polymers and chiral biological macromolecules.

2. Silica templated by chiral molecules

As mentioned above, the first examples of chiral templating of mesoporous silica were reported by Alvaro *et al.* [26] and Corma *et al.* [27]. However, the first systematic study and the development of a method for chiral imprinting of enantioselective sol-gel thin films were reported by the group of Prof. David Avnir [14, 15, 28-31]. In these articles, the general approach proposed for the preparation of the chiral of mesoporous silica thin films is schematically shown in Figure 1. The idea of molecular imprinting is to imprint the structure during the polymerization. In chiral sol-gel materials, the imprinting is accomplished by mixing the chiral template molecule with alkoxysilane monomers in the polymerization stage. Afterward, the template molecule is removed from the material matrix, resulting in a three-dimensional chiral porous structure. In this way, enantiopure porous materials can be created, since the pores left inside the matrix have a good potential of discriminatation between enantiomers [14].

In few articles, Avnir *et al.* [15, 30, 31] presented that chiral template molecules such as propranolol, 2,2,2-trifluoro-1-(9-anthryl) ethanol, DOPA, or tyrosine, can serve for the chiral imprint sol-gel matrix preparation. For instance, sol-gel films were imprinted with enantiomers of propranolol and fluorescence was used for the evaluation of the enantioselectivity. The results in Figure 2 indicate that a film imprinted for (*S*)-propranolol recognized that enantiomer better than the (*R*)-enantiomer while the other film imprinted for (*R*)-propranolol recognized better the (*R*)-enantiomer [14].
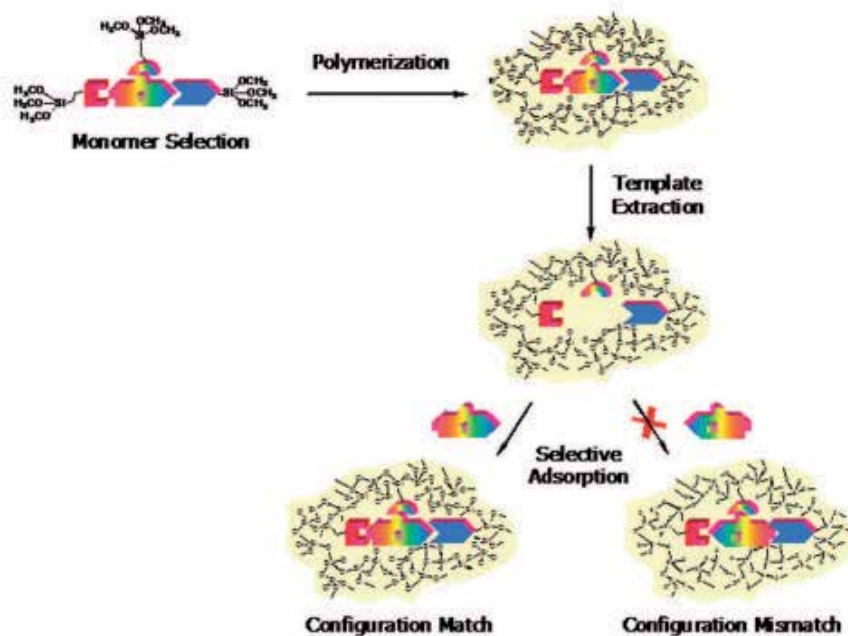
Figure 1. Schematic representation of the strategy of molecular chiral imprinting of a sol-gel matrix using a chiral template and achiral suitable silanes [14].
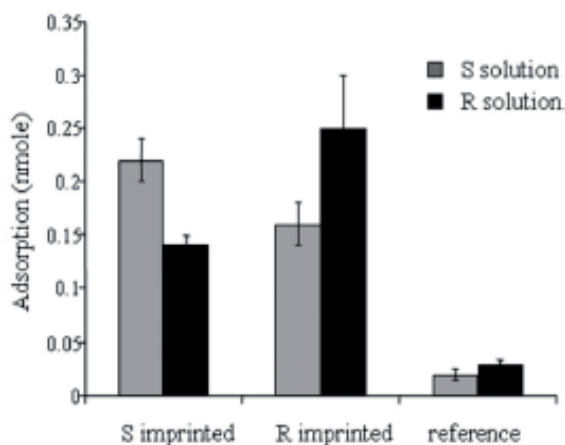

Figure 2. Fluorescent assay of enantioselective binding of the enantiomers of propranolol to sol–gel imprinted with either of the two enantiomers [14].

In another study of Avnir *et al.*, a sol gel thin film was imprinted with the (1R, 2S)-(-)-N-dodecyl-N-methylephedrinium bromide (DMB) cationic chiral surfactant for chiral separations [15]. At a higher concentration than the critical micelle concentration, the surfactant formed areas of

chiral hemimicelles in the material, comparable to other surfactant templated silicas. Then, the surfactant was extracted by a suitable solvent resulting in the formation of an enantioselective material. The selectivity was proved towards enantiomers of small chiral molecules such as propranolol and 2,2,2-trifluoro-1-(9-anthryl)ethanol).

In a similar way, enantioselectivity properties were obtained by chiral carboxylic acids imprinting in TiO_2 thin films [32]. Other imprinting systems for the production of chiral porous materials, including polymers [33] and dendrimers, were investigated.

For example, Yang *et al.* reported the preparation of ordered chiral mesoporous silica including MCM-41 and SBA with various pore sizes and structures using chiral templates of cobalt complex as co-template [34]. The chiral mesoporous silica displayed chiral characteristics due to the presence of the chirally distorted SiO_4 tetrahedra and $Si(OSi)_4$ produced in the synthesis. The synthesized chiral silica materials as drug carriers were demonstrated to control the enantioselective release of an illustrative chiral drug (metoprolol). In the release kinetics study, the release profiles of metoprolol were dependent on the pore structure and diameter of the chiral mesoporous silicas. Compared to the achiral mesoporous silica, R and S-enantiomers of metoprolol displayed different release kinetics on the CMS, which can be explained by the chiral interactions between enantiomers and the local chiral bonding sites of the CMS matrix. The best kinetic resolution was found on CSBA-15 materials having the largest pore diameter. The benefit of the synthesis procedure described in the article is that the enantiopure surfactant is no longer needed in the preparation of CMS since the chirality of the chiral co-template can be relocated to the building blocks of mesoporous silica.

In another study, Yang *et al.* reported the preparation of mesoporous silica materials with molecular chiral entities and the chirality transfer from the chiral organic template to the inorganic building blocks [35]. By tuning the synthesis parameters, chiral MCM-41 with a twisted hexagonal morphology was formed having a left-handed enantiomeric excess. The MCM-41 was obtained due to the interactions among the achiral surfactant CTAB, chiral cotemplate 1,2-cyclohexanediamine: Λ-[Co(+)(chxn)$_3$]I$_3$ and silica. The chirality of chiral MCM-41 was proved by enantioselective adsorption of racemic valine on it. The chiral cobalt complex with a rigid propeller-like configuration and "planar" chirality incorporated into the micelle directed the development of chiral aggregation. Consequently, the chiral aggregation transferred its chirality (distorted SiO_4 tetrahedrons or $Si(OSi)_4$ oligomers) to the building blocks of mesoporous silica via electrostatic interaction. Figure 3 shows SEM images revealing the twisted hexagonal rod-like morphology of the chiral MCM-41 (CMCM-41).

Chiral mesoporous silica has been also successfully synthesized in the presence of basic amino acids. Tatsumi *et al*. [36] reported that the use of basic amino acids with chiral anionic surfactants (as arginine and lysine) is advantageous for the formation of CMS. The handedness of chiral helices in the CMS was essentially governed by the stereoisomerism of the surfactants. It was demonstrated that chiral mesoporous silica are useful for the enantioselective separation of racemic mixtures; the helical CMS with a rod shape led to the asymmetric separation of racemic N-trifluoroacetylalanine ethyl ester. The left handed CMS showed asymmetric favored adsorption of the L isomer and vice versa. This is the first demonstration of the
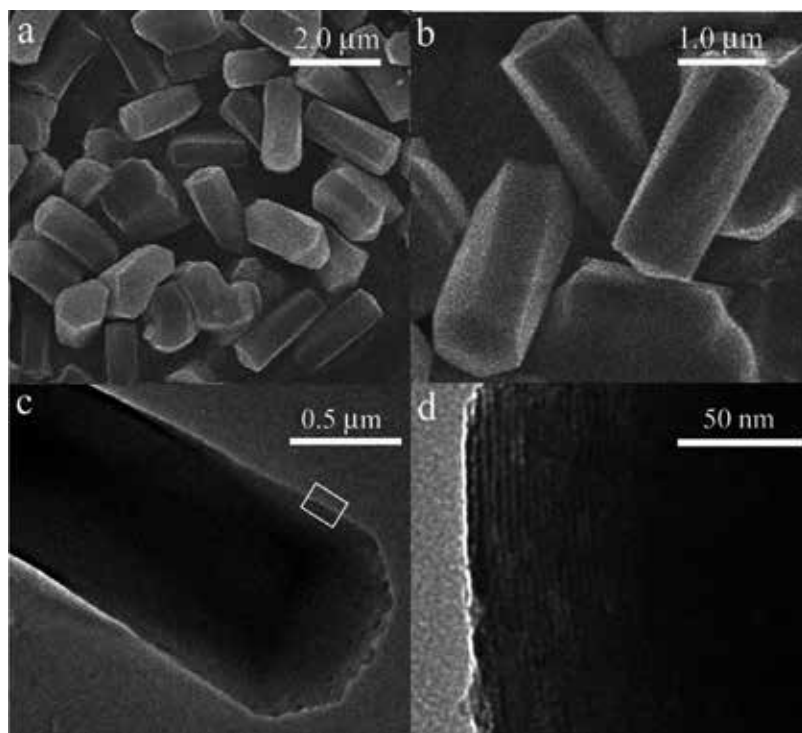
Figure 3. SEM images of CMCM-41 (a) with low magnification and (b) with high magnification. TEM micrographs of CMCM-41 (c) with low magnification and (d) with high magnification [35].

capability of helical mesoporous silica to create optically active substrates with an asymmetric bias.

The use of amino acids for the preparation of chiral mesoporous silica (CMS) was also reported by Casado *et al.* [37]. In their work, chiral ordered mesoporous silica was produced in a basic media by mixing tetraethyl orthosilicate (TEOS) and quaternized aminosilane silica sources (C18-TMS) with various amino acids (arginine, histidine, isoleucine, and proline) [37]. The materials were produced in hexagonal MCM-41-type structure and high specific surface area. Furthermore, they exhibited a good potential for enantiomeric separation explained by the transference of chirality from the amino acid to the silica. Proline-COMS gave rise to the best chiral material in terms of both imprint and racemic resolution of the different racemates studied. Actually, the rigid proline ring, not present in the other three amino acids seems to be the key point in achieving high quality chiral silica. The chiral nature of the proline COMS was demonstrated by the opposite behaviour in induced circular dichroism (ICD) measurements using both enantiomers of proline (Figure 4). The ICD signals for L and D-Pro-COMS are of similar intensity but their value is opposite. Consequently, the chiral handedness of L-Pro-COMS is opposite to that of D-Pro-COMS, as it is predictable for a couple of enantiomers.

In another work, chiral ordered mesoporous silica was formed in the presence of proline using TEOS and quaternized aminosilane silica sources [38]. The organic templates were extracted
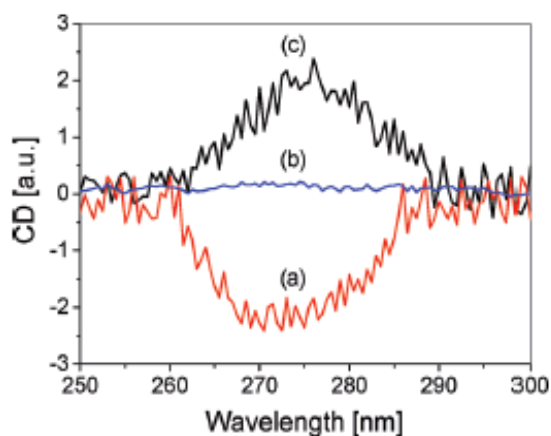
Figure 4. Solid-state ICD spectra of calcined samples after phenol adsorption: (a) L-Pro-COMS, (b) DL-Pro-COMS, and (c) D-Pro-COMS [37].

from the silica matrix by calcination or microwave chemical extraction. The structural and textural features of MCM-41-type silica in COMS were discovered by the powder X-ray diffraction and N_2 adsorption characterization techniques. The chirality of the material was verified by the adsorption of L and D-proline on the COMS prepared with L-proline and D-proline. Figure 5 shows the adsorption comparison of L and D-proline enantiomers on the three possible COMSs. After calcination, the-adsorption capacities of proline enantiomers on L-Pro-COMS were found to be ca. 2.3 mmol/g in L-proline and 0.6 mmol/g, in D-proline. Inversely, in the adsorption test on D-Pro-COMS, D-proline was more adsorbed than L-proline. DL-Pro-COMS did not show preferential adsorption. Both activation routes generated enantioselective silicas able to separate proline racemate. These results confirmed the chiral nature of L and D-Pro-COMS owing to the effective imprinting of the amino acid in the ordered mesoporous silica formation.
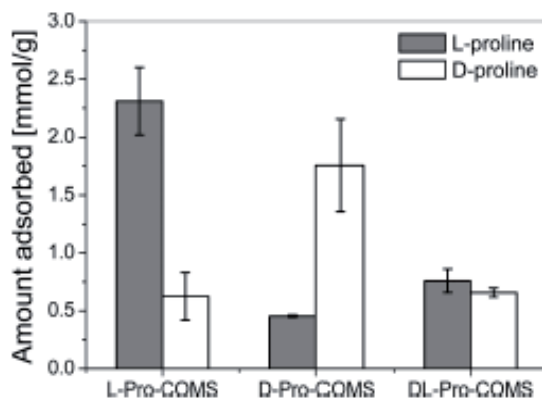
Figure 5. L and D-proline (100 mM) adsorption on the calcined L-Pro-COMS, D-Pro-COMS, and DL-Pro-COMS [38].

Che *et al.* [39] have reviewed the literature on anionic surfactant templated mesoporous silica (AMS) with the help of a co-structure directing agent (CSDA) to induct the interaction between the surfactant head group and the silica species. Templated mesoporous silica based on anionic surfactant can have diverse structures and morphologies since the adjustment in the ionization of the surfactant head group affects its geometric arrangement. Owing to the influence of the co-structure directing agent and the surfactant used together, a regular arrangement of the organic groups is generated, producing tuned materials with a uniform distribution of their organic groups. According to the reactions conditions and to the system parameters, various morphologies such as chiral mesoporous silica, nanoparticles, hollow spheres, nanotubes and ribbons can be synthesized. Chiral mesoporous silicas are applicable in many chiral uses, for example in asymmetric catalysis, chiral separation and recognition. Chiral imprinting in CMS has established new methods for the preparation and application of different new chiral materials.

For example Jin *et al.* [40] reported that chiral mesoporous silicas with ordered helical nano-sized channels were effectively produced using chiral anionic amphiphilic molecules (N-acyl-L-alanine) as templates in a CSDA method. In a typical synthesis, the chiral anionic amphiphilic molecule was neutralized with hydroxide and then partially acidified with mineral acid. TMAPS was chosen as CSDA because of its constant positive charge. The anionic ions in the reaction system have affected the morphology, mesopores and microstructures of the CMSs. Several observations were shown: In different inorganic acids reaction system, chiral meso-porous silica materials were obtained. In addition, the pore size at a range of 2.40-2.95 nm has been shown to be adjusted by varying the types of inorganic acids in the reaction system. Finally, the pitch length as well as the rod diameter preserved a linear relationship, once the acids were varied from HCl, HBr and HNO_3 to H_2SO_4. The HRTEM data of the calcined samples confirmed the rodlike morphology (Figure 6).

Among biomimetic silica formation, the silicateins attracted interest because they act as templates to deposit silica around the surface of the fibrils and form fibrous hybrids composed of axial filaments and silica shell. Recently, Matsukizono *et al.* [41] have developed a new method to form silica using nanocrystalline aggregates from linear polyethyleneimine (sPEI). Since these aggregates are composed of many basic amine groups on the surface, they are used as templates and catalysts to promote the alkoxysilane hydrolysis and to produce silica enclosing the templates. In this way, controlled nanostructured powders or thin films can be obtained. To develop structurally organized chiral silica, the researchers extended the crystalline sPEI methodology to a chiral crystalline complex (C.C.C) by combination of sPEI with tartaric acid and with the presence of the C.C.C as a catalytic template in the chiral silica deposition. As an inspection of chirality, achiral chromophores were introduced onto the calcined chiral silica by chemical modification and physical adsorption, and their circular dichroism spectra were investigated. The chromophore of $PhSiO_3$ chemically bound onto the 600 °C and 900 °C calcined SiO_2@D and SiO_2@L revealed an induced solid-state diffuse reflectance circular dichroism (DRCD) spectra with a mirror pattern within the UV absorbance band (210-280 nm) of the $PhSiO_3$ group (Figure 7 a). Comparable to the chemically bounded chromophore, a porphyrin residue physically adsorbed on the chiral silica showed induced
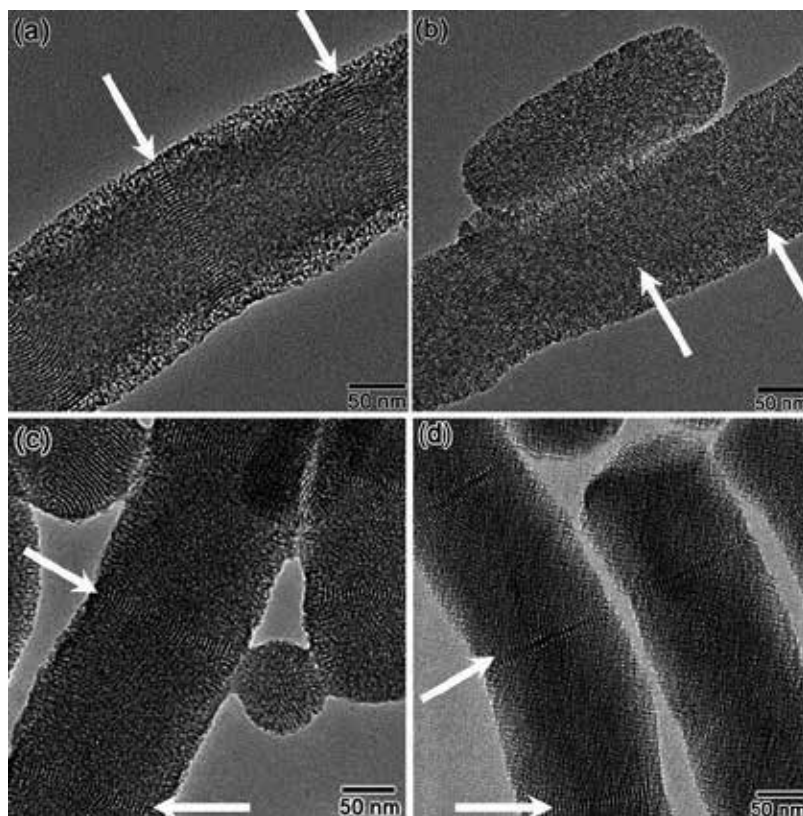
Figure 6. TEM images of calcined mesoporous silicas synthesized with different acids. (a) HCl, (b) HBr, (c) HNO$_3$, and (d) H$_2$SO$_4$ [40].

DRCD spectra with formation of mirror relation at the Soret band (420-450 nm) of the porphyrin (Figure 7 b). These DRCD spectra retained the same signs of ellipticity with the original chiral silica SiO$_2$@L and SiO$_2$@D. Moreover, the encapsulation of gold nanoparticles into the chiral silica was performed by spontaneous in situ reduction of NaAuCl$_3$. For this purpose, both chiral hybrids SiO$_2$/sPEI@D and SiO$_2$/sPEI@L in which the sPEI can reduce the ionic gold were combined together. Crystalline gold nanoparticles formed on SiO$_2$/sPEI@D exposed negative ellipticity whereas SiO$_2$/sPEI@L had positive ellipticity (Figure 7 c) within the wavelength range around 450–700 nm attributed to the nanoscale gold plasmon absorption (Figure 7 d). This is a proof that there are considerable interactions between the gold nanoparticles formed in situ and the chiral silica wall, implying the inductive chirality of the gold nanoparticles.

Recently, I have synthesized chiral mesoporous silica based on collagen as a chiral template in the template-based approach. The chiral synthesized silica was characterized by various techniques such as electron microscopy, and analytical surface methods such as BET that have demonstrated that the templating process procured well-ordered mesoporous silica with uniformly distributed pore size and high surface area, improving the chiral surface accessi-
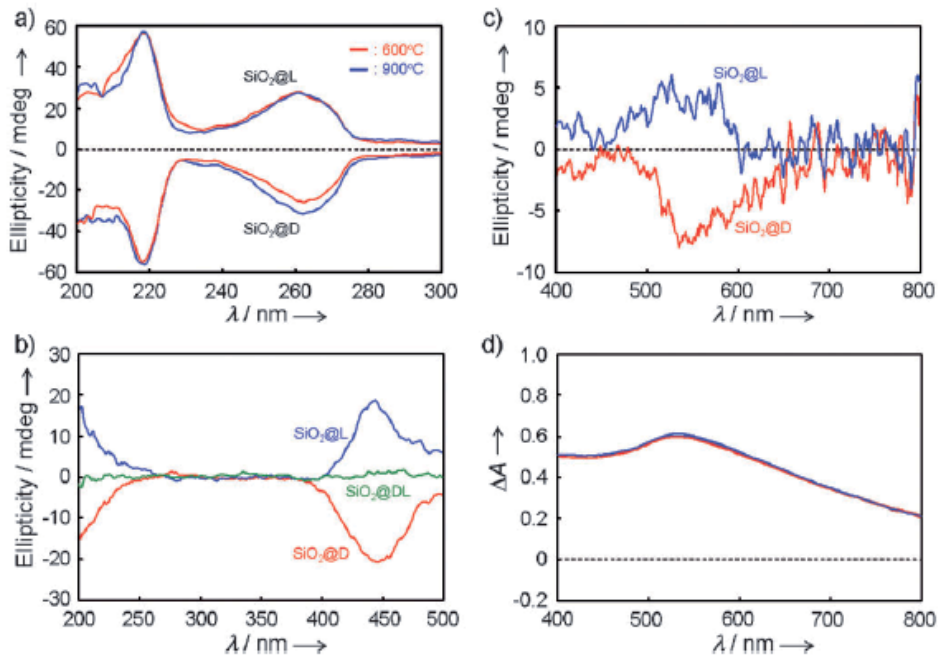
Figure 7. Induced DRCD spectra on the chiral silica. a) After introduction of PhSiO$_3$ residues onto SiO$_2$@D and SiO$_2$@L calcined at 600 °C (red) and 900 °C (blue); b) after adsorption of tetrakis(3,5-hydroxyphenyl) porphyrin onto SiO$_2$@D and SiO$_2$@L and SiO$_2$@DL calcined at 600 °C; c) gold nanoparticles encapsulated by SiO$_2$/sPEI@D and SiO$_2$/sPEI@L; d) diffuse reflectance absorption spectra of gold nanoparticles on SiO$_2$/sPEI@D and SiO$_2$/sPEI@L [41].

bility. Collagen has been shown to be effective as a chiral template for the preparation of mesoporous silica nanoparticles with a high surface area of ca. 140 m^2/g and a pore size of ca. 1.5 nm (Figure 8).
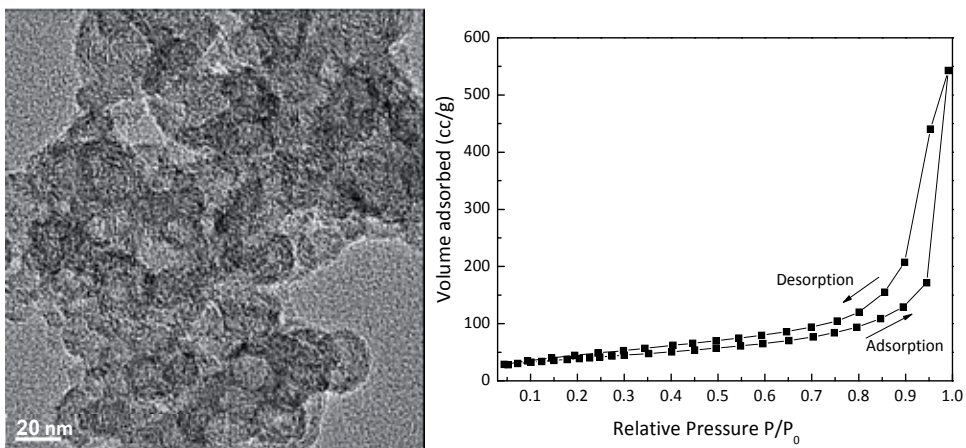
Figure 8. HR-TEM image of silica templated by collagen (left) and N$_2$ isotherms of silica templated by collagen (right).

After the extraction of collagen, the enantioselectivity feature of silica was examined by selective adsorption of enantiomers and racemic solutions of valine using circular dichroism (CD) spectroscopy. Selective chiral adsorption measurements were performed on 5 mM valine solutions added to the chiral-imprinted silica (3 mg/mL) and their optical activities were measured with time, as shown in Figure 9. An enantiomeric excess of 16% D-valine was found in the racemic solution, indicating that L-valine was preferably adsorbed on the mesoporous silica. It is clear that in the near future, a variety of new approaches for chiral resolution based on chiral mesoporous materials will be innovated and my work is a part of the general trend in the development of novel chiral methods.
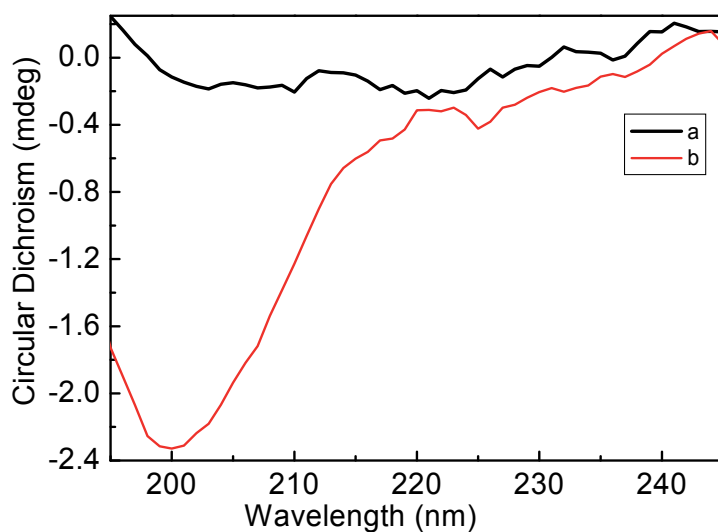
Figure 9. CD spectra of DL-valine: pure solution (a) and 23 h after its adsorption on the CMS (b).

3. Silica templated by chiral polymers

In recent times, Mastai *et al.* have demonstrated a new approach for chiral imprinting onto a solid based on the use of chiral block copolymers [42-45]. In general, the synthesis of the chiral double hydrophilic block copolymers (DHBCs) is based on a ring opening polymerization of protected amino acid *N*-carboxyanhydrides (NCAs). This procedure leads to the development of chiral block copolymers based on PEO_n-*b*-D- or L-amino acids having a helical structure in acidic solution, as checked by CD measurements. The aggregation of chiral DHBCs into well-defined micelles at the reaction conditions was critical to the creation of a well-defined template. Then, the TEOS silica precursor was added to the solution comprising the chiral DHBC in order to accomplish the sol-gel process. As a final step, the chiral template was removed by solvent extraction, producing chiral cavities in the silica. Silica has been templated by DHBCs of a poly (ethylene oxide) block and a chiral block of D-phenylalanine [PEO-*b*-D-

Phe]. The synthesized copolymer was composed of an average of ten amino acid repeating units. At their critical micelle concentration (CMC), the copolymers formed spherical micelles with a 10 nm diameter at pH=2 to give the chiral mesoporous silica after their extraction. Consequently, CMS was achieved with chiral hexagonal pores of 5 nm diameter and high surface area (700 m^2/g), as shown in Figure 10.
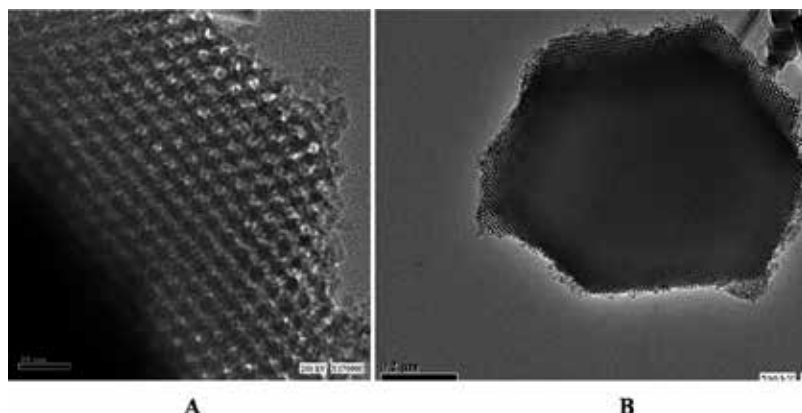
Figure 10. TEM images: (A) high resolution (B) low resolution of chiral silica made from PEO$_{113}$-*b*-D-Phe$_{10}$ after chiral copolymer extraction [44].

The chiral recognition aptitude of the silica was studied by the selective adsorption of enantiomers from racemic solutions of D and L-valine. The mesoporous silica displayed chiral recognition toward D-valine enantiomer, compatible to the chirality imprinted on the silica. The chiral recognition was maximal after 16 hours and a chiral selectivity factor of 2.34 was found.

After the report on chiral imprinting of silica by chiral double hydrophilic block copolymers, Paik *et al.* continued to investigate chiral silica synthesis with chiral DHBCs. In the first paper, the synthesis of chiral mesoporous silica spheres was described [43]. The chiral mesoporous silica particles were obtained using a chiral DHBC template of [PEO$_{113}$-*b*-(GluA)$_{10}$] block. The template left a chiral print on the silica walls after its removing from the matrix. These particles revealed a 2-3 nm pore size with high surface area of 614 m^2/g, and exhibited enantioselectivity towards valine enantiomers equivalent to the chirality imprinted on the silica support (selectivity factor of 5.22), as shown in Figure 11. As a result, these CMS particles could be useful in diverse enantioselective applications.

In an additional paper, Paik *et al.* described the synthesis of CMSs templated with DHBC of [PEO$_{45}$-*b*-(D/L-AspA$_{10}$)] [42]. These particles obtained were exposed to D, L-valine and D, L-alanine solutions, and showed a high affinity toward one enantiomer matching to the chirality imprinted on the silica. The calculated selectivity factor was 7.52, as shown in Figure 12.

Another interesting example for imprinting chirality in silica using chiral biological macromolecules is reported in the paper of Fadeev *et.al.* [46]. In their work, novel ordered chiral
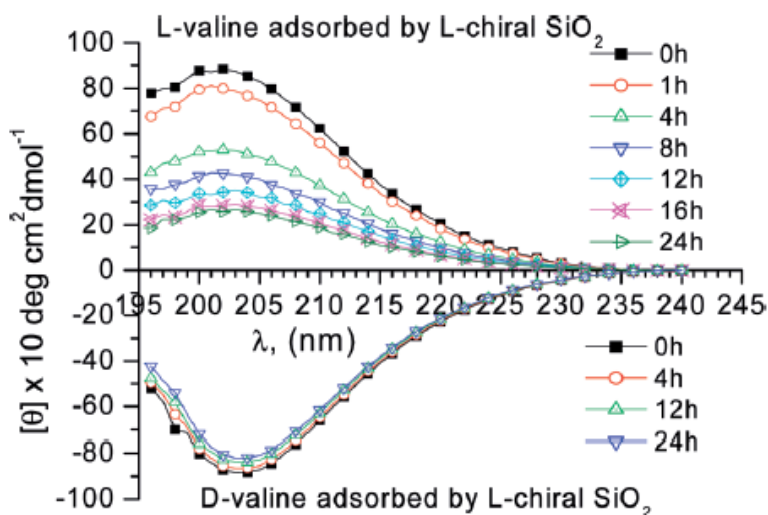
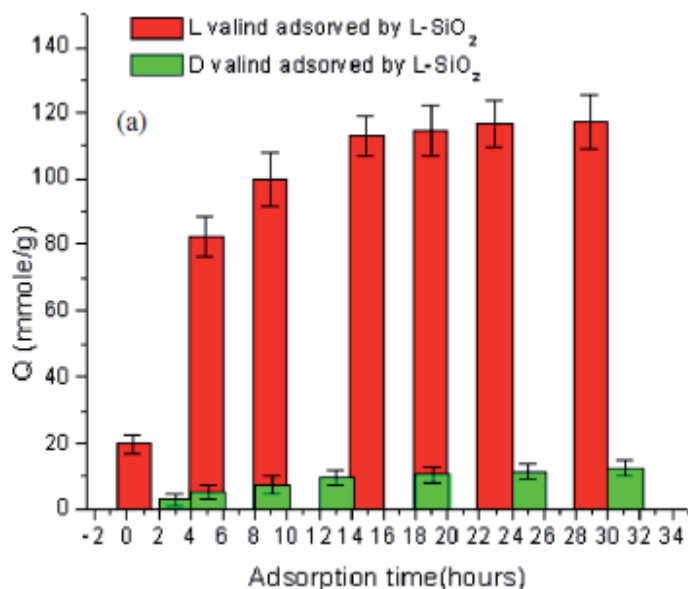**Figure 11.** Circular dichroism spectra of L and D-valine into the L-imprinted mesoporous chiral Ex-SiO$_2$ [43].

Figure 12. Adsorption dynamics from a solution of valine enantiomers into the L-chiral-imprinted silica (Ex-SiO$_2$) [42].

mesoporous silicas (SBA-15) with chemically bonded oligo(saccharides) were achieved through the cocondensation of organosilicon derivatives of the oligo(saccharides) (glucose, maltotriose, and maltoheptaose groups) and the silica precursors in the presence of polymer surfactant template under mild acidic conditions [46]. The pore structure of the silica materials prepared in these conditions was investigated by transmission electron microscopy and

nitrogen adsorption. It was proved that the oligo(saccharide)-grafted SBA-15 stationary phases are effective in the HPLC separations of stereoisomers.

4. Conclusions

In summary, we have reviewed the current approaches based on chiral imprinting processes for the fabrication of chiral mesoporous silica. The basic principles for the chiral imprinting of silica and potentials of these chiral mesoporous silicas were given for specific examples. As we present here, chiral mesoporous silicas are promising materials for controlling chirality and for chiral resolution processes. The investigation of the interactions between chiral molecules and silica surfaces still remains a major challenge to develop effective chiral mesoporous silica for various applications. Thanks to the advanced analytical techniques, the molecular study of chiral interactions in mesoporous silica is currently possible. Such researches can provide new abilities for rationally design of different types of chiral mesoporous silica. We hope that chiral mesoporous silica will play an essential role in the advance of new and effective methods for chiral resolution and other chiral applications.

In general, the research on preparation and use of chiral mesoporous silica is still in its preliminary stages. Further researches to explore the mechanism and factors responsible for imprinting chirality in mesoporous silica are still required. The basic issues of fundamental nature, like chiral interactions with silica, mechanisms for the formation of hierarchical chiral structures in silica and the mechanism of chiral imprinting are still to be addressed. We believe that a deeper understanding of molecular mechanism of chiral imprinting in silica could add knowledge in many other fields of research associated with mesoporous materials. It is obvious that an improved design of chiral mesoporous silica is expected to have high potential for chiral technological applications and this may also open up opportunities in other fields of chemistry like chiral catalysis, analytical chemistry, surface science and nanomaterials.

Acknowledgements

Author details

Gila Levi

Address all correspondence to: gui.bench@gmail.com

Department of Chemistry and the Institute of Nanotechnology Bar-Ilan University, Ramat-Gan, Israel

References

[1] Maher TJ, Johnson DA. Review of chirality and its importance in pharmacology. Drug development research. 1991;24(2):149-56.

[2] Maier NM, Franco P, Lindner W. Separation of enantiomers: needs, challenges, perspectives. Journal of Chromatography A. 2001;906(1):3-33.

[3] Amabilino DB. Chiral nanoscale systems: preparation, structure, properties and function. Chemical Society Reviews. 2009;38(3):669-70.

[4] Bag DS, Shami T, Rao K. Chiral Nanoscience and Nanotechnology. Defence Science Journal. 2008;58(5).

[5] Zhang J, Albelda MT, Liu Y, Canary JW. Chiral nanotechnology. Chirality. 2005;17(7):404-20.

[6] Barlow SM, Raval R. Complex organic molecules at metal surfaces: bonding, organisation and chirality. Surface Science Reports. 2003;50(6):201-341.

[7] Ernst K-H. Supramolecular surface chirality. Supramolecular Chirality: Springer; 2006. p. 209-52.

[8] Ernst K-H. Amplification of chirality in two-dimensional molecular lattices. Current Opinion in Colloid & Interface Science. 2008;13(1):54-9.

[9] Humblot V, Barlow S, Raval R. Two-dimensional organisational chirality through supramolecular assembly of molecules at metal surfaces. Progress in surface science. 2004;76(1):1-19.

[10] Raval R. Chiral expressions at metal surfaces. Current Opinion in Solid State and Materials Science. 2003;7(1):67-74.

[11] Mastai Y. Enantioselective crystallization on nanochiral surfaces. Chemical Society Reviews. 2009;38(3):772-80.

[12] McFadden CF, Cremer PS, Gellman AJ. Adsorption of chiral alcohols on "chiral" metal surfaces. Langmuir. 1996;12(10):2483-7.

[13] Gellman AJ. Chiral surfaces: accomplishments and challenges. ACS nano. 2010;4(1):5-10.

[14] Marx S, Avnir D. The Induction of Chirality in Sol–Gel Materials. Accounts of chemical research. 2007;40(9):768-76.

[15] Fireman-Shoresh S, Popov I, Avnir D, Marx S. Enantioselective, chirally templated sol-gel thin films. Journal of the American Chemical Society. 2005;127(8):2650-5.

[16] Gautier C, Burgi T. Chiral inversion of gold nanoparticles. Journal of the American Chemical Society. 2008;130(22):7077-84.

[17] Ben-Moshe A, Govorov AO, Markovich G. Enantioselective Synthesis of Intrinsically Chiral Mercury Sulfide Nanocrystals. Angewandte Chemie. 2013;125(4):1313-7.

[18] Dolamic I, Knoppe S, Dass A, Bürgi T. First enantioseparation and circular dichroism spectra of Au38 clusters protected by achiral ligands. Nature communications. 2012;3:798.

[19] Oda R, Huc I, Schmutz M, Candau S, MacKintosh F. Tuning bilayer twist using chiral counterions. Nature. 1999;399(6736):566-9.

[20] Sugiyasu K, Tamaru S-i, Takeuchi M, Berthier D, Huc I, Oda R, et al. Double helical silica fibrils by sol–gel transcription of chiral aggregates of gemini surfactants. Chem Commun. 2002 (11):1212-3.

[21] Berthier D, Buffeteau T, Léger J-M, Oda R, Huc I. From chiral counterions to twisted membranes. Journal of the American Chemical Society. 2002;124(45):13486-94.

[22] Che S, Liu Z, Ohsuna T, Sakamoto K, Terasaki O, Tatsumi T. Synthesis and characterization of chiral mesoporous silica. Nature. 2004;429(6989):281-4.

[23] Jung JH, Ono Y, Hanabusa K, Shinkai S. Creation of both right-handed and left-handed silica structures by sol-gel transcription of organogel fibers comprised of chiral diaminocyclohexane derivatives. Journal of the American Chemical Society. 2000;122(20):5008-9.

[24] Qiu H, Che S. Chiral mesoporous silica: Chiral construction and imprinting via cooperative self-assembly of amphiphiles and silica precursors. Chemical Society Reviews. 2011;40(3):1259-68.

[25] Raman NK, Anderson MT, Brinker CJ. Template-based approaches to the preparation of amorphous, nanoporous silicas. Chemistry of Materials. 1996;8(8):1682-701.

[26] Álvaro M, Benitez M, Das D, Ferrer B, García H. Synthesis of chiral periodic mesoporous silicas (ChiMO) of MCM-41 type with binaphthyl and cyclohexadiyl groups incorporated in the framework and direct measurement of their optical activity. Chemistry of materials. 2004;16(11):2222-8.

[27] Baleizão C, Gigante B, Das D, Alvaro M, Garcia H, Corma A. Synthesis and catalytic activity of a chiral periodic mesoporous organosilica (ChiMO). Chemical Communications. 2003 (15):1860-1.

[28] Fireman-Shoresh S, Marx S, Avnir D. Enantioselective sol–gel materials obtained by either doping or imprinting with a chiral surfactant. Advanced Materials. 2007;19(16):2145-50.

[29] Fireman-Shoresh S, Marx S, Avnir D. Induction and detection of chirality in doped sol–gel materials: NMR and circular dichroism studies. Journal of Materials Chemistry. 2007;17(6):536-44.

[30] Fireman-Shoresh S, Turyan I, Mandler D, Avnir D, Marx S. Chiral electrochemical recognition by very thin molecularly imprinted sol-gel films. Langmuir. 2005;21(17): 7842-7.

[31] Fireman-Shoresh S, Avnir D, Marx S. General method for chiral imprinting of sol-gel thin films exhibiting enantioselectivity. Chemistry of materials. 2003;15(19):3607-13.

[32] Lahav M, Kharitonov AB, Willner I. Imprinting of Chiral Molecular Recognition Sites in Thin TiO2 Films Associated with Field-Effect Transistors: Novel Functionalized Devices for Chiroselective and Chirospecific Analyses. Chemistry-A European Journal. 2001;7(18):3992-7.

[33] Palmer CP, McCarney JP. Developments in the use of soluble ionic polymers as pseudo-stationary phases for electrokinetic chromatography and stationary phases for electrochromatography. Journal of Chromatography A. 2004;1044(1):159-76.

[34] Guo Z, Du Y, Liu X, Ng S-C, Chen Y, Yang Y. Enantioselectively controlled release of chiral drug (metoprolol) using chiral mesoporous silica materials. Nanotechnology. 2010;21(16):165103.

[35] Guo Z, Du Y, Chen Y, Ng S-C, Yang Y. Understanding the Mechanism of Chirality Transfer in the Formation of a Chiral MCM-41 Mesoporous Silica. The Journal of Physical Chemistry C. 2010;114(34):14353-61.

[36] Yokoi T, Sato S, Ara Y, Lu D, Kubota Y, Tatsumi T. Synthesis of chiral mesoporous silica and its potential application to asymmetric separation. Adsorption. 2010;16(6): 577-86.

[37] Lacasta S, Sebastián V, Casado C, Mayoral Á, Romero P, Larrea Á, et al. Chiral Imprinting with Amino Acids of Ordered Mesoporous Silica Exhibiting Enantioselectivity after Calcination. Chemistry of Materials. 2011;23(5):1280-7.

[38] Casado C, Castań J, Gracia I, Yus M, Mayoral Al, Sebastián V, et al. L-and D-proline adsorption by chiral ordered mesoporous silica. Langmuir. 2012;28(16):6638-44.

[39] Han L, Che S. Anionic surfactant templated mesoporous silicas (AMSs). Chemical Society Reviews. 2013;42(9):3740-52.

[40] Jin H, Wang L, Bing N. Chiral mesoporous silica synthesized with the presence of different anionic acids. Materials Chemistry and Physics. 2011;127(1):409-12.

[41] Matsukizono H, Jin RH. High-Temperature-Resistant Chiral Silica Generated on Chiral Crystalline Templates at Neutral pH and Ambient Conditions. Angewandte Chemie International Edition. 2012;51(24):5862-5.

[42] Paik P, Gedanken A, Mastai Y. Chiral separation abilities: Aspartic acid block copolymer-imprinted mesoporous silica. Microporous and Mesoporous Materials. 2010;129(1):82-9.

[43] Paik P, Gedanken A, Mastai Y. Enantioselective separation using chiral mesoporous spherical silica prepared by templating of chiral block copolymers. ACS applied materials & interfaces. 2009;1(8):1834-42.

[44] Gabashvili A, Medina DD, Gedanken A, Mastai Y. Templating mesoporous silica with chiral block copolymers and its application for enantioselective separation. The Journal of Physical Chemistry B. 2007;111(38):11105-10.

[45] Paik P, Gedanken A, Mastai Y. Chiral-mesoporous-polypyrrole nanoparticles: Its chiral recognition abilities and use in enantioselective separation. Journal of Materials Chemistry. 2010;20(20):4085-93.

[46] Vega E, Marzabadi C, Kazakevich Y, Fadeev AY. Synthesis of chiral mesoporous silicas with oligo (saccharide) surfaces and their use in separation of stereoisomers. Journal of colloid and interface science. 2011;359(2):542-4.

Advanced Control of Crystallization Processes

Some Features of Growing Single Crystals of Refractory Metals from the Melt

Vadim Glebovsky

Additional information is available at the end of the chapter

http://dx.doi.org/10.5772/59651

1. Introduction

Mostly single crystals of semiconductors, dielectrics, metals, or alloys are produced in the process of crystallization or solidification from the melt. The rates of crystallization can reach tens of millimeters per minute. During crystallization in single crystals, structural defects can be collected, that have a negative effect on the mechanical and other properties of materials. High demands for structural perfection and chemical purity of single crystals caused considerable research efforts aimed at the study and improvement of the main techniques of growing single crystals from the melt (Czochralski, Stepanov, Bridgman, Verneuil, floating zone). Single crystals of refractory *bcc* metals, especially molybdenum and tungsten, are widely used in several areas of modern technology, such as nuclear energy, electronics, lighting fixtures, mainly for the manufacture of parts and devices (anodes, cathodes, *etc*.) working at high temperatures. A scope of single crystals of refractory metals is continuously expanding, and requirements for chemical purity of crystals, their structural quality and geometry are constantly growing. Currently, the most pure single crystals of molybdenum and tungsten, as well of a number of other refractory metals can be produced by electron-beam floating zone melting (EBFZM). However, their crystallographic perfection due to the specific features of the floating zone method with electron-beam heating, often no longer satisfies the developers of new instruments and devices. A characteristic blocky structure and a high density of dislocations make such crystals unsuitable, for example, for research of channeling high-energy particles or posing a number of other subtle physical experiments. Further increase in a degree of purity and crystallographic perfection of single crystals of refractory metals is closely related to a development of theoretical and experimental researches of crystallization processes, the development of new apparatuses and methods for producing single crystals, as well as optimization of known processes. Therefore, to obtain additional information about

the laws of formation of a dislocation structure, an impact on specific parameters of crystal growth in the floating zone method seems to be relevant scientific and technical challenge. The basis of this decision is a study of peculiarities of structural defects in single crystals grown by crystallization, which is one of the fundamental problems of solid state physics, physical chemistry, and theory of phase transitions.

2. Basic physical features of crystallization

2.1. Methods of growing single crystals from the melt

For growing oriented single crystals of semiconductors and dielectrics Czochralski method became widespread [1-3]. The essence of the method consists in pulling of single crystals by seeding at a surface of the melt. Although this method of capillary formation is known by its low stability, at high precision heating control and automation of pulling [4-6] it allows obtaining such semiconductors as silicon and germanium which are widely used in modern technology. Bridgman method, which also refers to the crucible methods similar to Czochralski, is used in a much smaller scale and mostly for growing single crystals of low-temperature melting metals. This is due to the fact that at high temperatures there are significant difficulties in finding materials for crucibles. Another widely used technique is Stepanov method of growing single crystals. Its difference from Czochralski consists in that the shaper is immersed into the melt, providing not only pulling cylindrical rods, but also production of a wide assortment of shaped crystals (tapes, tubes, polyhedrons, and other crystals of a complex shape). Stepanov method has much greater margins of stability during capillary shaping than Czochralski, which accounts for its wide distribution. However, for growing single crystals of refractory metals, especially molybdenum and tungsten, the above-mentioned methods are not suitable, as the high melting temperature and high chemical reactivity of liquid refractory metals do not allow obtaining them by any crucible method. The actual process of the growth is desirable to maintain in a vacuum or in an inert gas. For refractory metals Verneuil method is also used provided with another kind of a heater as plasma. This method yielded the most by large-scale tungsten single crystals of 40 mm in diameter and weighing up to 10 kg [7]. However, those single crystals were of poor structural quality and had high gas content, especially of a plasma gas. The most perfect single crystals of refractory metals can be obtained by electron-beam floating zone melting. The growth of these crystals is characterized by the fact that the method is a crucible-less one and a melt has no any contact with other materials. The melt is supported by forces of surface tension and the process is carried out in UHV. A phase diagram can give information on the type, number and volume fraction of phases at crystal growing from the melt [8]. This is true only in the case when crystallization proceeds at an infinitesimal rate. In practice, a finite rate and solidification conditions are far from thermodynamic equilibrium. Thus, binary alloy solidification occurs with enrichment or depletion of solid with a dissolved component. When impurity accumulation exceeds some critical value and a temperature gradient in liquid is reduced below a critical level, there comes concentration supercooling and the interphase surface changes from cellular to dendritic. This is nonequilibrium solidification and is typical of most alloys. A main feature of such solidifi-

cation is that a primary axis of dendrites is strictly parallel to a heat flow direction and interdendritic spaces are enriched with impurities. This segregation further can be partially eliminated by prolonged high-temperature annealing. In some cases, there may be precipitates of a second phase in interdendritic spaces. When crystal growth conditions are such that a part of a two-phase zone is large and a growth rate is high, so that the factor is a lot less than zero: $G - V(FR)_{eff}(1/D) \ll 0$, where, G the temperature gradient in fluid; V the growth rate; $(FR)_{eff}$ the effective solidification range; D the diffusion coefficient. Thus, there is a porosity which may occur even in growing single crystals of pure refractory metals by EBFZM. It occurs especially after the first liquid zone passage during purifying the initial PM feed and growing a single crystal from. EBFZM provides not only a given orientation of crystal growth, but also due to refining by a zone effect mainly from substitution impurities. Refining of interstitial impurities occurs mainly by vacuum evaporation, the more that the melting points of refractory metals are very high. Impurities in a growing crystal often are undesirable as adversely affecting its structure and properties. In the process of accumulation of impurities before moving crystallization front, the plane crystallization front may become unstable due to so-called phenomenon of concentration supercooling. Impurities will greatly impair the dislocation substructure and unevenly distributed in a radial direction and a length of the crystal along the growth axis.

2.2. Mechanisms of crystallization of metals

Crystallization processes are widely used in modern science and technology: the growth of single crystals, production of pure substances by directional crystallization and zone melting. Crystallization in metallurgy - is one of the stages of producing metals, such as crystallization in molds, continuous casting, and processes in molds during refining. Currently, by theory of crystallization the following molecular mechanisms of the crystal growth are developed: nucleus, spiral, normal, continuous [1,2]. The crystal growth by two-dimensional nucleation leads to an expression for the growth rate:

$$v = C \exp(-U/kT)\exp(-A/kT), \tag{1}$$

where, A the work of two-dimensional nucleation; U the activation energy of the atom addition to the brink of the nuclei; C the kinetic coefficient, which is first analyzed in [9,10]. It should be noted that much more other growth mechanisms implemented. Thus, the crystals containing dislocations cannot be grown by two-dimensional nucleation. A spiral stage formed near an exit of the dislocation on the crystal surface plays a role of non-vanishing two-dimensional nucleation, which facilitates the connection of new particles to the crystal. This theory gives an expression for the crystal growth rate in the following form [2]: $v = DL \, \Delta T / 4\pi r T_0^2$, where, D the diffusion coefficient; ΔT the supercooling; L the heat of crystallization; T_0 the melting point. Two-face growth mechanisms in a tangential direction are implemented in practice. A condition for the growth by these mechanisms is the presence of an atomically smooth surface that holds only for substances with high heat of fusion and areas with low crystallographic indices. Crystals with low heat of fusion, which include almost all metals, have atomically

rough edges; their micro relief varies continuously over time. Micro fluctuations of the atomic structure of the interface lead to active participation of all points on the surface of the crystal, and for all metals L / kT_0 <2. Thus, metals are characterized by a normal growth mechanism. This mechanism is used for all values of supercooling, and specifically in the field of small deviations from equilibrium state of the system it becomes predominant. A normal mechanism is related to thermal fluctuations at the interface and therefore has greater sensitivity to small differences in temperature. According to theory of continuous growth, crystals in the neighborhood of equilibrium can grow exclusively through nucleation at the interface. Disadvantage of this theory is neglecting thermal fluctuations of the equilibrium type on the interphase between solid and liquid phases. This leads to the fact that the growth rate is described by quadratic or exponential functions which is characteristic of classical theories. Considered mechanisms of the crystal growth are characteristic for most typical cases of the free growth, *i.e.*, when nothing prevents the crystal growing in either direction. However, in Czochralski and floating zone one has to deal with cases of the stimulated growth.

2.3. Heat and mass transfer processes in crystal growth from the melt

When moving the crystallization front in the melts a set of complex physical and chemical processes occur: heat transfer and mass transfer in the melt and crystal, oust impurities processes and impurity redistribution at the crystallization front, capillary phenomena, and metal evaporation. Under these conditions, the most important and crucial for the structural quality of the growing crystal is the temperature gradient in the liquid and solid phases ($G = (\partial T / \partial n)_{S,L}$). Temperature gradients (K mm^{-1}) occur at the crystallization front and are defined by intensity of a heat sink, chemical composition of the metal, release of crystallization heat, a heat input to the liquid metal, and convective flows in the melt [11]. In principle, stability of the crystallization process and quality of the single crystals grown are mostly influenced by the temperature field in the thermal zone of the growth set-ups, *i.e.*, the temperature field in the crystal and melt. Of particular importance are temperature conditions at the crystallization front. A heat balance at the interface looks like:

$$\lambda_L \ (\partial T / \partial n)_L \ + L\gamma v = \lambda_S \ (\partial T / \partial n)_S , \qquad (2)$$

where, v the rate of crystallization; L the latent heat of crystallization; γ the melt density, kg m^{-3}; λ_L, λ_S the thermal conductivity of the liquid and solid phases, W cm^{-1} K^{-1}; n the normal to the surface of the interface; $(\partial T / \partial n)_S$ and $(\partial T / \partial n)_L$ the temperature gradients near the crystallization front. In simplified calculations suggest the phase boundary plane and then $(\partial T / \partial n) = (\partial T / \partial z)$, which are the axial temperature gradients. The temperature field in the growing crystal also has a significant impact on its structure. The main cause of dislocations in the crystal is plastic deformation caused by thermal stresses which are typically caused by uneven cooling the crystal in the region of loss of plastic properties of material. The lower $(\partial T / \partial n)_S$ for the growing crystal, the more perfect is its structure; a low value means a lower productivity of the process. Indeed, if we take $(\partial T / \partial n)_L = 0$, we obtain:

$$v_{max} = (\lambda_S / L\gamma)(\partial T / \partial n)_S,\tag{3}$$

Now, if we assume that a heat transfer from the surface of the crystal is carried out mainly by radiation, we obtain:

$$v_{max} = (1 / L\gamma)\sqrt{4\lambda_S \sigma_0 \varepsilon T_0^S / 3d_0}.\tag{4}$$

Where, T_0 the crystallization temperature, K; $\sigma_0 = 5.67 \times 10^{-12}$, W cm^{-2} K^{-4}, the Stefan-Boltzmann constant; ε the emissivity of surface radiation of the crystal; d_0 the crystal diameter, cm. A significant impact on the structure of the growing single crystal has a shape of the interface crystal-melt, which can be considered as the isothermal surface having a temperature of solidification. The most favorable form of the crystallization front is flat or somewhat convex to the melt [12,13]. This reduces the number of defects formed and contributes to their more uniform distribution in the crystal. For example, dislocation-free silicon single crystals are grown under the conditions of the crystallization front of forms close to a plane. The power needed to produce a molten zone of a predetermined shape is studied using a simplified model [14]. It is shown that Laplace's equation can describe the temperature changes along the rod and in the zone with a help of numerical methods. It is also found that the temperature distribution is characterized by several dimensionless Bio numbers, representing the ratio of the thermal conductivities in the liquid and solid phases, ratio between the length of the rod and width of the molten zone along the radius of the crystal, and power. The resulting temperature distribution and forms of the liquid zone for different Biot numbers and coefficients of thermal conductivity obtained as functions of the energy supplied to the zone. A horizontality of isotherms near the solidification front decreases the radial gradient and thus stabilizes the axial gradient $(\partial T / \partial n)$. As for the value of the latter, on this account, there are conflicting opinions. On the one hand, increased $(\partial T / \partial z)_L$ near the phase boundary promotes better ousting impurities, improve stability of the crystallization process, increase the growth rate, reducing a likelihood of spontaneous crystallization due to concentration supercooling. On the other hand, excessive $(\partial T / \partial z)_L$ at the interface causes increasing convective flows; this can lead to uncontrolled temperature fluctuations near the crystallization front. The latter circumstance causes a very common defect in crystals – a streaky micro inhomogeneity of impurities [15]. In addition to the temperature distribution near the crystallization front in the vicinity of the phase boundary, the temperature field is also important in a whole volume of the melt, as a prerequisite exception of spontaneous crystallization is overheating the melt outside the phase boundary. The temperature field in the entire volume of the melt determines existing natural convection flows. It is also important obtaining an axial symmetry of the temperature field. When growing semiconductors, it is necessary to reproduce temperature gradients with accuracy of $\pm 0.5^0$ C cm^{-1} in certain areas of the thermal processing zone. Of particular note is the fact that the temperature field in the crystal and in the melt cannot be considered outside the context of each other. Adjustment of the temperature field in the crystal will cause changes of the temperature field in the melt (opposite is also true). This makes it difficult to control when growing. The technological practice (primarily for growing semicon-

ductor crystals) shows that for high-quality single crystals with desired properties it is necessary to accurately maintain the set of the temperature mode in time. A tough time maintaining the temperature field should be of the high-precision and high-rate automatic control system. The most important is to maintain the constant temperature in time at the crystallization front. The main factors disturbing the thermal regime are oscillations of the power input and fluctuations of the heat loss. The latter means impermanence of the cooling water to elements of a design as well a variable heat removal through the growing crystal. In some cases, to eliminate disturbances associated with a change in internal conditions it is necessary to make corrections in advance by changing the computer programmed temperature. In this case allowable temperature fluctuations in obtaining perfect semiconductor crystals should not exceed 0.1^0 C. Instabilities of the temperature lead to the increased dislocations density, but in some cases of more serious defects (twins, portions of the polycrystalline structure, *etc*.). In addition, the structural quality of single crystals affects by the rate of the zone movement and its fluctuations. With increase in the rate, the dislocation density is greatly increased. This limit for niobium is of 0.5 mm min^{-1}. From perspectives of influence on the structure, the zone movement rate must be stable up to about 1%, and all kinds of vibration should be excluded.

2.4. Influence of convection in the melt on the crystal structure

In recent years, an interest has grown significantly to convective phenomena in the melt during the growth of single crystals. In particular, this is due to the possibility of conducting experiments in space. A large number of studies on convection in the melt during the growth of single crystals were done by various methods. Hydrodynamic phenomena are typical of the floating zone method [13-15]. It should be noted that phenomena of convection are studied by two ways: convective phenomena experimentally investigated by physical modeling of the crystal growth in transparent liquids and by constructing mathematical and computer models. Mathematical models tend to represent a complex system of differential equations. Main assumptions in constructing models are stationary, two-dimensional and axisymmetric of the hydrodynamic problem [13]. Characteristic of models is the extensive use of dimensionless criteria of similarity theory. Particular attention is paid to thermocapillary convection (Marangoni convection) [15]. Results of model experiments and calculations are used to explain some properties of single crystals of molybdenum, so that study is considered in more detail. Convective flows in the melt can have a significant impact on the structure and properties of the growing single crystal. Important parameters such as impurities and the concentration and temperature gradients in the melt are dependent on nature of flows. The shape of the crystal-melt interface appears to depend not only on heat transfer processes, but also on conditions of the melt flows. Consider the most important similarity criteria which give a relation between the convective and diffusive heat and mass transfer. It is accordingly Prandtl $Pr = \theta/\varphi$ and Schmidt $Sc = \theta/D$, where θ the kinematic viscosity of the melt; D the diffusion coefficient; φ the thermal diffusivity. For typical metallic melts $Pr \ll 1$, $Sc \gg 1$, *i.e.*, the heat transfer occurs mainly by conduction, and the impurity transfer occurs by convection which plays a significant role. Therefore, it can be expected that microsegregation in the crystal melt is associated with hydrodynamics of the melt. The experiments were done by EBFZM of molybdenum with

additives of iridium-192 ($K_0 = 0.37$) and tungsten ($K_0 = 50$). X-ray topograms and autoradio-grams of longitudinal cross-sections of samples showed characteristic bands enriched with impurities. If we assume that the melt is the incompressible fluid, the density of which depends on the temperature and impurity content, the forces, that give rise to convective flows in the melt, are the following: gravitational forces (cause natural convection), capillary forces (cause Marangoni convection) and inertial forces (occur when the crystal is rotated). In general, flow patterns in the molten zone are the result of the joint effect of these forces. Before discussing the problem of convection we should consider features of the temperature distribution in the molten zone. The interfacial crystal-melt surface at the crystallization front has a temperature T_0. The maximum temperature $T_0 + \Delta T$ is in the middle of the zone, *i.e.*, there is the positive axial temperature gradient. Furthermore, there is the negative radial gradient directed from the periphery toward the center of the zone. Arising under these conditions vertical density gradients, causing steady natural convection, can be described by Rayleigh numbers $Ra = \alpha g \Delta T h^3 / \vartheta \varphi \sim 10^3$, where, g the acceleration due to gravity; α the coefficient of thermal expansion; h the half a zone length. As for radial temperature gradients, they correspond to Rayleigh numbers, almost equal to zero. Acting on the free surface of the melt the surface tension forces are functions of temperature, $\sigma = f(T)$. If on the free melt surface the temperature gradient exists, resulting in changes in surface energy, then capillary Marangoni forces begin to act. These forces give rise to characteristic convection in the melt. The rate of flows caused by Marangoni forces is greatest at the surface of the melt. With increasing the distance from the surface the rate decreases and then changes its sign. In the case of the zone melting Marangoni forces act on the periphery of the zone from its middle to interphase boundaries. The power of Marangoni forces is characterized by Marangoni numbers $Ma = |\partial \sigma / \partial T| (\Delta T h^2 / \rho v \varphi)$, where, $|\partial \sigma / \partial T|$ is the temperature coefficient of surface tension; ρ the density of the melt. The ratio of Rayleigh number to Marangoni number characterizes the ratio of forces of free convection and Marangoni convection: $Bo = Ra / Ma = g \rho \alpha h^2 / |\partial \sigma / \partial T|$. When $Bo < 1$, Marangoni flow dominates in the melt. It takes place in normal gravity when $h \leq 1$ cm [15]. In the absence of rotation, Marangoni flow in the melt is toroidal axially symmetric. With increasing Bo outer vortices increasingly dominate over the lower ones. This leads to the non-uniform transfer of impurities in the melt and eventually to the radial non-uniformity of impurities. Increase in the dislocation density in the crystal can be explained by the interfacial surface curvature produced by convection. At $Ma > 3.4 \times 10^3$ flows become unstable. There are variations in the temperature within the melt with a frequency $f \sim h^{-1} d^{-1}$, where d is the diameter of the crystal. This leads to such defects in the crystal as impurity bands which is found at the respective longitudinal sections of the X-ray topographs [15]. The width of the bands associated with the zone and the rate of the oscillation frequency f: $a = v / f$, where, v is the growth rate; a is the width of the band. Temperature fluctuations lead to reduction of K_{eff} and further to macrosegregation. The banded heterogeneity may disappear at growth rates below a certain critical value due to fairly good diffusion in the solid phase. We must also mention the detected submicroporosity in molybdenum single crystals grown by EBFZM after the first and second zone runs. These submicropores of diameter 0.3-0.5 micron decorate the interphase boundary and are also associated with temperature oscillation, because arranged by bands and seen on cleaved samples in scanning electron microscope.

2.5. Thermal stresses and dislocation structure of single crystals

For the first time in 1958, Dash [16] has grown dislocation-free silicon single crystals from the melt using the method of a narrow waist or a neck. He believed that dislocations appeared from the seed in the waist region, come to the surface, and stresses, occurring during further growth, cannot generate dislocations, if initially they did not exist in the crystal. Since dislocation defects are non-equilibrium, they may only be a consequence of non-equilibrium growth conditions. According to [1,2,15], for the formation of dislocations are responsible: external stresses of mechanical origin; thermal stresses; local stresses due to concentration gradients; condensation of vacancies; local stresses due to inclusions; errors during growth. Thermal stresses, occurring during the growth of single crystals from the melt, lead to significant increase in the dislocation density. Application of dislocation theory and theory of internal stresses to the problem of the crystal growth has led to significant achievements. It is shown that the main source of stresses causing deformation and dislocation multiplication in the growing crystal is the inhomogeneous temperature field. Thus, in the case of growing the single crystal of the radius R by crystallization from the melt, the following estimate for an absolute value arising from thermal stresses in the crystal: $\tau = k\alpha E R^2 T_z''$, where, α is the coefficient of linear expansion; k is the coefficient; E is the Young's modulus; R is the radius of the crystal; T_z'' is the second derivative of the temperature by a coordinate z. From this it follows that the crystal growth is necessary to strive to ensure that the temperature field in the growing crystal should be as close as possible to the linear one, so T_z'' would be minimal. A number of experiments in growing single crystals of germanium show that in a case of active shielding (heated screens) it was succeeded by significantly reduce of the amount of T_z'' down to values of an order of 0.05 K mm^{-2}. Due to this, the dislocation density has been reduced by almost two orders of magnitude. Admissible a following upper estimate for the density of dislocations arising from thermal stresses: $\rho \geq \alpha\, gradT\, /b$, where, α is the coefficient of thermal expansion; b is the Burgers vector. Note that growing single crystals of metals with the low dislocation density is significantly harder than single crystals of semiconductors or dielectrics. This is due to the fact that elastic constants of metals go to zero much faster as the temperature approaches the melting point [9,10]. The structural perfection of single crystals grown from the melt is influenced not only by the temperature gradients themselves, but the important factor in this respect is the cooling rate which is implemented at the stage of the crystal growth itself, and then under cooling to room temperature [17]. An influence of growth conditions on the dislocation substructure of copper single crystals is investigated in [18]. At a regular control of the dislocation structure, the Cu[111] single crystals are grown from the melt at the rate of 0.2-120 mm min^{-1}. Variation of the growth rate in this range had a little effect on the random growth of the dislocation density inside subgrains which was ~2x10^6 cm^{-2}. With an increase in the growth rate an average size of subgrains is significantly reduced from 5x10^{-2} cm to 0.5x10^{-2} cm, and this decline is roughly proportional to the cooling rate of the crystal rising -0.5 in accordance with the model of the dislocation origin of sub-boundaries. On the basis of these experiments, the conclusion is made that the model of the sub-boundaries formation is valid, and impurities do not play any significant role in the formation of the substructure in copper single crystals of purity less than 99.999%.

3. Experimental

3.1. The set-ups for electron beam floating zone melting

History of the development of EBFZM method to produce refractory metals in the single-crystal form has more than seventy years [19,20]. Over the past thirty years there was a significant progress both in improving experimental techniques used for growing single crystals of refractory metals, and the study of their structure and properties. However, even the well-known and successful designs of the electron gun [19] and EBFZM set-ups did not allowed to conduct a lengthy process of growing and were "not-easy" to operate. Then, the most advanced electron-beam guns are presented in [21-24]. There have been developed and tested the original EBFZM set-ups for growing single crystals of refractory metals. In the design of these set-ups have been successfully resolved the main problems concerning the mechanisms of the movement of the cathode assembly, the electron gun, the power supply and others (Figure 1). Single crystals, bicrystals and tubular crystal of many transition and refractory metals were grown using the electron guns with the protected annular filament-cathode in EBFZM set-ups.
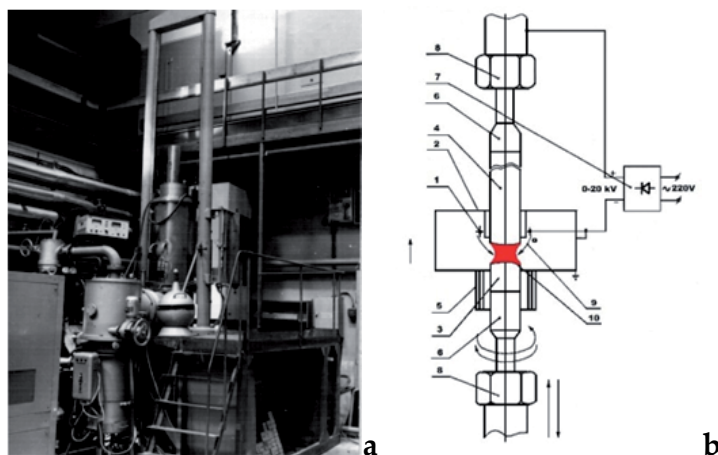
Figure 1. EBFZM set-up (**a**) and scheme of a thermal zone (**b**).

A principle of operation of EBFZM set-ups with annular electron guns, in a certain extent, is similar to a function of the vacuum triode: the tungsten filament (cathode), the feed sample (anode), focusing electrodes (control grid), the melting chamber (housing). The voltage, current and power, which are consumed for melting the feed, refining the liquid metal and growing the single crystal, are determined not only by both the anode voltage and the current of the cathode filament, but also by the residual gas pressure in the cathode-anode gap. In EBFZM set-ups for operation of the electron gun is very important the gas release from the feed during melting. Any sudden rise in pressure due to the gas release, metal evaporation or local vacuum decay even to 10^{-1} Pa in the electron gun lead to avalanche of a low resistance of

the anode-cathode system and even to complete destabilization of the electron gun. From the above there are basic requirements to EBFZM set-ups providing conditions for the stable zone melting: stability of the electron gun; stability of the power supply; perfection of moveable nodes; an impurity homogeneity of the feed, otherwise it can cause unpredictable sharp increase in pressure in the melting chamber. It should be noted that the most sensitive element of EBFZM set-ups is the electron gun, so the focus of this section will be paid to the designs of electron guns, which should create the optimal and stable over time temperature field. Electron guns in many EBFZM set-ups have some disadvantages that prevented widespread of the method and demanded a lot of efforts to correct them. Typically, the designs of all known guns are such that spatters and vapors of metal get to the cathode filament, thereby destabilizing functions of the gun, changing its power due to local decrease in emissivity of the cathode filament. This often leads to burnout of the cathode and to finish the growing process. Another disadvantage of existing electron guns is contamination of the feed and crystal by metal vapors from which the cathode is made (usually tungsten), and the electron gun itself. Such contamination is most likely when the cathode is located in "line of sight" visibility of the feed, which is typical for almost all designs of electron guns. At 2500K the rate of evaporation of tungsten is less than 2×10^{-10} g s^{-1} cm^{-2} and thermionic tungsten cathodes are sufficient to melt all metals. Three-electrode electron guns with a single accelerating electrode allow to stabilize power supplied to the zone and to eliminate variations of the temperature during the growing process. It was also assumed that accelerating electrodes could act as modulators of the anode current, which would maintain without inertia the given heat regime and have significant advantages compared with known control systems. Naturally, electron guns, in which the upper and lower borders of focusing are realized by mechanical devices, do not meet these requirements.

Benefits of both EBFZM set-ups and electron guns [20] compared to previous ones consisted in the fact that metal vapors and spatters cannot reach the cathode and the liquid zone because the cathode filament is outside of a "line of sight". Main criteria for using new guns in EBFZM set-ups are: simplicity of the design, as well as reliability of operation at high temperatures and intensive sputtering. The density of the electron flux from the filament (with the current leads nearby) is for 3-5 times higher as compared with the opposite side of the same filament (without the current leads nearby). Such asymmetry of electron fluxes is observed in all guns in which the ring filament is made of two semi-rings. The asymmetric distribution of the electron density causes an asymmetry of the temperature field in the liquid zone and, as a result, the asymmetry of heating of the growing crystal. By the way, this may be one of reasons for the "snap" growth of single crystals. Apparently, the heterogeneous structure, which is characterized by a layered distribution of both impurities and defects, is a consequence of a mismatch of the thermal axis and the axis of the growing crystal. One of the main practical conclusions is that, despite an apparent lack of difference between one- and two-element cathodes, only a singleton cathode in the form of the loop provides satisfactory symmetry of the electron flux and temperature field. It contributes to the problem of obtaining homogeneous single crystals with the reproducible structure and crystallographic characteristics along the entire length. The basic requirements that determine conditions for the stable operation of the electronic guns and, especially, EBFZM set-ups can be formulated as follows: an absence

of sputter on the filament, *i.e.*, the filament should be in the "shadow", and the system of focusing electrodes should provide the appropriate curvilinear electron beam and focus it on the sample-anode; the design of the electron gun should ensure a prompt removal from the inter-electrode space all gases released from the sample; the gun design must give certain rigidity and total absence of warping after the prolonged exposure to high temperatures, so all the parts of the gun must be performed of a high thermal conductivity material (*e.g.*, copper) and cooled by water; high vacuum EBFZM set-ups should be met by the tightness of the melting chamber, the pumping powerful vacuum system and reduced gas release from samples; the power supply must provide a long-term operation of the annular electron gun at given electric modes; moving both the annular electron gun and sample-anode during growing should be coaxial at the whole length of the sample [20,21]. Figure 1b shows a schematic interior of EBFZM set-up for growing crystals and bicrystals. The liquid zone *10* on the single-crystalline rod *4* is produced by the electron beam *9* emitted from the tungsten filament (cathode) *1*. Focusing is carried out by the electron gun *2*. The power supply provides the accelerating voltage of 25 kV and the anode current up to 1 A. The growth rate of bicrystals is 1÷1.5 mm min^{-1} while rotating the seed *6* at the rate 20 rev min^{-1}. A lack of positive feedbacks between the cathode and the anode in the electron gun allows maintaining the average power of the electron beam, which is almost constant throughout the growing single crystals or bicrystals. Random power fluctuations with a frequency of several hertz do not exceed 0.1% of a nominal value.

3.2. Metallographic examinations

Metallographic examinations of the crystal structure at the macro and micro levels provide extensive qualitative and quantitative information about the structure [22-24]. A possibility exists to measure of various structural elements up to 1 micron. A range of crystallographic planes of the crystal orientation can be determined by etch pits and execute it with an accuracy of ±3÷5°. The dislocation density in the crystal can be evaluated according to the number of etch pits per unit area (in the event that it does not exceed 10^8 cm^{-2}). An interference attachment to a metallographic microscope gives a possibility to evaluate the surface roughness of cross-sections. The polarization console allows detecting inclusions of the second phase in a sample, if the latter is present in significant amounts. To carry out metallographic studies the sample must first be cut off from the corresponding bulk single crystal and then prepared by grinding. Cutting samples of molybdenum and tungsten single crystals of necessary geometry and crystallographic orientations can be produced by the electroerosion device. It is well known that this technique can produce a significant damage of the sample surface - to a depth of about 300 microns. When this happens, the surface contamination and defects lead to increase of dislocations in the surface layer, but also there appear a typical network of cracks extending to a considerable depth. After cutting, all the above defects must be removed by both the mechanical grinding and polishing. Then, the cold-worked layer should be removed by chemical etching and electropolishing at the optimal conditions. However, it is necessary to keep in mind two things. First, all etchants are divided into two large groups. The first group has a pronounced orientation effect, *i.e.*, gives well-cut pits that are useful for determining an orientation of the crystal. In general, the etching figures revealed by these etchants have

nothing with the outgrowth of dislocations. The second group represent etchants to produce etch pits, revealing the outgrowing low-angle boundaries and individual dislocations. But even in this case to speak about one correspondence of etch pits and dislocation is not correct, it requires evidences in each case. With regard to detection of the microstructure of tungsten and molybdenum crystals is, for example, a commonly known Murakami etchant (10 g NaOH, 30 g of $K_3Fe(CN)_6$, 100 g of H_2O) which has a strong orientation effect, although it is also identifies some low-angle boundaries. Electrochemical etching in a 5% aqueous solution H_4OH gives similar results as Murakami etchant. In our view, it is more convenient to identify the substructure of the molybdenum and tungsten single crystals by an electrolytic etching in 25% NH_4OH solution under the following conditions: the current density j = 5÷10 mA cm^{-2}, the voltage U = 2÷3 V and the time τ = 60÷90 s. It turns out that the etchant "works" not only to identify dislocations, but also to reveal dislocations introduced into the crystal as a result of plastic deformation at the surface with a prick of the diamond indenter. Furthermore, this etchant identifies sub-boundaries with small misorientation angles and thus it has been widely used to detect the substructure of molybdenum and tungsten single crystals, grown from the melt by EBFZM. For metallographic studies the optical microscopes and automatic analyzer are used. The latter is widely used for the quantitative metallographic analysis of the linear substructure: the subgrain size distribution along and across the crystal, the dislocation density inside the subgrains averaged at least for 20 fields of view, and by the stereometric metallographic analysis as well. It should be noted that at identification of the subgrain structure of molybdenum and tungsten single crystals by means of the above proposed etchants, the metallographic studies are possible mainly at the planes of low crystallographic indices of the type {001} and {111} planes as well as with higher indices deviate from these planes in opposite directions at angles in the range 10÷15°.

3.3. X-ray studies

It is known that in many cases some low-angle boundaries can be qualitatively compared by misorientation angles. In other words, it is a qualitative determination, where misorientation angles of neighboring subgrains are more and where – less, because aA quantitative determination of misorientation angles by metallographic methods is impossible. To obtain such information on the real structure of the crystal it is necessary to use methods of X-ray diffraction microscopy. Here, to obtain the quantitative information about misorientation angles of the substructure elements of molybdenum and tungsten single crystals we used both the X-ray topograms of angular scanning and X-ray recording by the wide divergent beam. Especially clear for determining misorientation angles is the method of the X-ray wide divergent beam [25]. On the X-ray record of the perfect crystal, free of low-angle boundaries, Kossel lines are solid curves of the second order. In the block crystal, recording through the low-angle boundary between adjacent subgrains, the orientation changes abruptly and Kossel lines contain gaps. Both methods allow defining misorientation angles of substructure elements with a resolution of ~1 arc min, and linear dimensions of subgrains with a resolution of about 3÷5 microns. To determine the orientation of crystals and the fulfillment of their orientation in the desired crystallographic direction with an accuracy of ±1÷2° was used as the standard method of taking Laue epigrams.

3.4. Electron microscopy studies

Of serious interest is the question about what kind of dislocations occurs during growth from the melt? It rises from the standpoint of a study of physical aspects of the crystallization process. Most of disclocations are assembled into grids and walls as a result of poligonization processes and form the characteristic substructure. Such dislocation ensembles consisting of growth dislocations are also of interest. To undertake such a research on the real crystal structure the most suitable method is transmission electron microscopy, which allows determining the type of dislocations, their Burgers vectors and crystallography of low-angle boundaries. However, consider the following fact: as a rule, in molybdenum and tungsten single crystals grown from the melt by zone melting, the dislocation density inside the subgrains is of a value $\rho \geq 10^5$ cm^{-2}. By other words, an average distance between dislocations is $X \approx 0,003$ cm $\simeq 30$ micron with an average size of subgrains $d \simeq 500$ micron. It means that the volume, occupied by actual low-angle boundaries, is negligible. This also means that in the case of preparing foils for electron microscopy of an arbitrary portion of a bulk sample, a single dislocation from a subgrain volume can be observed in one of 5÷10 samples. Observation of low-angle boundaries of such samples would require at least 10 times more samples (taking into account that a really observable surface of a sample has an area of about 5 micron^2). Naturally, to prepare samples having such little hope of success is a real Sisyphean task. Therefore, a method of preparation of foils is used, which provides a hole in a specified area in vicinity of low-angle boundaries. An essence of the method is as follows. On one side of the original sample in a form of the washer of diameter 3 mm and thickness of 0.3-0.4 mm the substructure is detected using metallographic techniques. Then, on this side of the sample a protective film of a clearcoat (in the simplest case – a collodion) is applied to the surface and thoroughly dried. Next by the microhardness recorder PMT-3 using a diamond indenter the protective layer is violated in the right place (or a series of injections or scratches) and by electropolishing a recess of a required depth is received. Optionally, this set of operations might be repeated. It should only be kept in mind that in the process of the electropolishing all of dislocations should be removed from the surface layer of the sample, introduced there by the action of the indenter. Thereafter, the varnish is removed from the sample surface by using an organic solvent (acetone, ether) and the electropolishing is performed from the reverse side of the sample before the formation of holes. With the described method of the sample preparation, a likelihood that low-angle boundaries would be available for observation increases substantially - to 1/5÷1/10 (an experimental evaluation).

3.5. Chemical purity

As mentioned before, the presence of significant amounts of impurities has a significant impact on the structure and properties of the crystals, and for molybdenum and tungsten the greatest impact on the properties is made by interstitial impurities, primarily carbon, which is characterized by very low solubility limits in the solid state at room temperature [26]. Therefore, the analysis of the chemical composition and purity control of single crystals is an important part of the characterization of a material. In this work, an oxygen content is determined by fast neutron activation with a sensitivity of 5x10^{-5}%, carbon is analyzed by deuteron-activation with a sensitivity of 10^{-6}% [27,28]. Additionally, carbon is monitored by the coulometric method on

AN-160 device with a sensitivity of 5x10⁻⁴%. To determine other impurities in single crystals and bicrystals, mass-spectrometry with a sensitivity of 10^{-6}% is used. The content of impurities is shown in Table 1. The purity of metals is also checked by a residual resistivity at liquid-helium temperatures, since at low temperatures the main mechanism of the carriers scattering in metals is scattering on impurities [29]. Here, the ratio of resistivities at room and liquid-helium temperatures is defined by the non-contact and four-contact methods. For the single crystals studied this value is not less than (2÷3)x10⁴.

Metal	Content of impurities, x10⁻⁴%											
	O	C	N	H	Si	Al	K	Ca	Na	P	S	Mn
Mo	<0.5	<0.5	<0.6	<1.0	<0.3	<0.1	<0.1	<0.1	<0.1	<0.03	<0.1	<0.03
W	<0.5	<1.0	<0.6	-	<0.3	<0.1	<0.1	<0.1	<0.3	<0.3	<0.3	<0.3
	Mo	Nb	Re	V	Fe	Ni	Co	Ti	Cr	Cu	Rb	Zr
Mo	-	<1	<0.3	<0.1	<0.1	<0.03	<0.03	<0.03	<0.3	<0.03	<0.03	<0.1
W	<1	-	<0.1	<0.1	<0.3	<0.1	<0.03	<0.06	<0.3	<0.03	<0.05	<0.1

Table 1. Content of impurities in the pure molybdenum and tungsten.

4. Growing bicrystals of refractory metals

4.1. Some features of growing bicrystals

Metals and their alloys in the polycrystalline state represent a set of randomly oriented crystallites, or grains, which separated by high-angle boundaries. Properties of polycrystalline materials that are widely used conventionally in materials science and technology largely depend on the size and crystallographic orientation of the constituent grains and, consequently, on the properties of boundaries between the grains. Therefore it is not accidental that the interfacial properties of a type "solid – solid" attracted the most attention of specialists for many years. In recent years a number of theoretical and experimental studies of the interface boundary structure, the energetic and regularities of the grain boundary diffusion and high-temperature creep, the segregation of impurities and structural defects at the interface, as well as processes of heterogeneous nucleation at the interface during phase transitions, is significantly increased [29]. For an experimental investigation of the above phenomena, it is desirable to have samples with well known or readily determinable geometrical relationships between crystallites. From this point of view, of course, the interfaces in bicrystals with known crystallographic parameters are the most convenient and preferable objects. Growing methods of metal bicrystals can be divided into two main groups. The first one includes methods in which oriented bicrystals can be grown from two oriented seeds using standard methods of Chalmers, Czochralski, Bridgman or zone recrystallization. The second group includes methods in which the interphase boundary is obtained by sintering together two plates of oriented single crystals. It should be noted that both groups of methods allow receiving both twist and tilt boundaries, as well as mixed ones. Consider the specific advantages and disadvantages of both

groups. There is a lot of information on getting oriented bicrystals of various metals and alloys by sintering or diffusion welding [30-48]. Using this method to obtain bicrystals usually leads to the fact that boundaries contain a substantial amount of pores and oxide inclusions. Upgraded versions of the method are used to produce bicrystals of copper, silver, nickel, copper-indium and copper-arsenic alloys. In this case, the boundary turns out fairly flat, and does not contain inclusions of the second phase; although sometimes on the boundary an emergence of a small stray of grains of arbitrary crystallographic orientations have been found. Unfortunately, this is not the only downside: sophisticated UHV equipment is necessary for sintering, and the sintering processes last for 10÷20 hours. Furthermore, disks prepared for sintering should be flat and have a surface roughness of not more than 0.1÷0.3 micron, which could be achieved by using diamond polishing pastes. It is clear that before sintering the electropolished deformed surface layer should be removed, otherwise recrystallization becomes inevitable and qualitative boundaries cannot be obtained. Bicrystals of low-melting-points metals can be grown using the method from other group. The essence is that bicrystals can be grown from the melt with the help of two correctly oriented seeds causes no problems at all. Somewhat more complicated is the situation in this way to grow bicrystals of refractory metals such as molybdenum, tungsten, niobium, tantalum, vanadium, *etc*. There is information on growing niobium bicrystals by arc zone melting method [40]. However, this technique does not permit to obtain the required stability of the molten zone and the symmetry of the temperature gradients in the melt and in the solid phase. This leads both to an increased density of dislocations and low quality of the grown bicrystals. The original method of growing bicrystals of niobium by electron-beam zone melting is described in [38]. The essence of this method consists in the following. The single crystalline seed of a cylindrical shape partially cut along a plane of symmetry parallel to the growth axis [110]. Next by moving apart the halves of the original single-crystal seed typed at the desired misorientation angle of the boundary of the bicrystal to grow. Then the bicrystal can be grown simultaneously from both halves of the seed. Thus, the niobium bicrystals of diameter of 6.3 mm and length of 100 mm are obtained. In our opinion, this technique of growing bicrystals, though captivating by its simplicity, but it is too "capricious", on which, however, suggest the authors themselves. They managed to get good bicrystals in only one case out of four. In our view, the failure of the following causes: a poor quality of the electron gun in heating and a complexity of the adjustment of the Y-shaped seed in the thermal zone. Another method of producing bicrystals of refractory metals is described in [30]. The essence of this simple method is as follows: on single-crystal rods the molten zone is created. Then after rotation of the base bar to the desired angle the zone is "frozen". For all its simplicity and attractiveness of this technique it is also not free from shortcomings. First, a small size of a boundary: no more than a diameter of the rod; secondly, the boundary is wavy, as it turns out not as a result of the joint growth of two neighboring grains, but as a result of the "collapse" of moving towards each other two crystallization fronts whose profile in the process of EBFZM is substantially non-planar. In our opinion, the most suitable melting technique for obtaining bicrystals of refractory metals with *bcc* lattice, which do not undergo phase transitions in the solid state, is only EBFZM. This technique allows obtaining a necessary stability of the molten zone and the axial temperature gradient, as well as the required symmetry of the radial temperature gradients. The latter

condition is largely ensures a stability of the growth process of bicrystalline boundaries when growing simultaneously from two seeds oriented in a predetermined manner [36,39]. Stability of the growth of the grain boundary in bicrystals simultaneously from two seed crystals oriented in the predetermined manner, largely due to the symmetry and uniformity of the temperature field. Based on structural features of EBFZM set-up, we would like to note some highlights that should be considered when growing bicrystals of pure refractory metals: (1) the stability and radial uniformity of the power supplied by the electron gun; (2) the co-axiality of the growing bicrystal and electron gun (coincidence of thermal and geometric axes or centers in the liquid zone); (3) the uniformity of the heat removal from the growing bicrystal through the elements of the seed and bicrystal. An important advantage of this method is the possibility of growing bicrystals of up to 150÷200 mm long and up to 15÷25 mm in diameter, suitable for investigating properties of the bicrystalline boundaries both parallel and perpendicular to the growth axis in a large number of reproducible samples. Experiments are carried out on growing bicrystals without rotation, but it turned out that this may affect even minor violations of the local temperature profile in the liquid zone, resulting in one of the growing crystals in the bicrystal can die out. For the manufacture of seeds of 10÷25 mm in diameter and 15÷20 mm in length, consisting of two halves with different single-crystal orientations, the cylindrical single crystals of certain crystallographic directions are used. A deviation from the certain crystallographic direction does not exceed 1÷2°. At first, to prepare the parts for the seeds the initial single crystal should be cut by the electroerosion into cylinders of 20 mm long (Figure 2). The cylinders are cut by the diametrical plane to segments for the purpose of obtaining the desired misorientation angle.
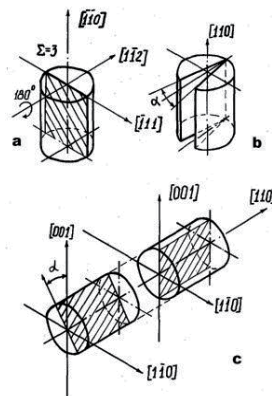
Figure 2. Schemes of preparation of bicrystalline seeds.

The segments of the bicrystalline seed are chemically etched in a mixture of hydrofluoric and nitric acids. Bicrystalline seeds are produced by combining the single-crystalline segments (*e.g.*, 1a+2b or 1b+2a) prepared by the method described above. Another method of preparing the seeds is that one of the segments further cut at an angle equal to the misorientation angle of the bicrystal to grow. This method proved to be a little bit easier, because it does not require

additional operations of the orientation of single crystals. In cases where, besides the misor-ientation angle, the defined crystallographic parameters should also have the bedding plane of the grain boundary, the plane is defined with respect to which the boundary should be symmetrical. Then a cut is made along a plane that is separated from it by an angle equal to half of the misorientation angle of the bicrystal to grow. The resulting combined two single-crystalline segments after rotation of one of them in the cutting plane by 180° around the axis perpendicular to this plane. Later the plane of the contact between two segments of the bicrystalline seed should be the grain boundary of the growing bicrystal. In the process of the zone growing the grain boundary remains strictly specified and parallel to the axis of the bicrystal and to the axes of both single-crystalline halves of the seed. Our experience has shown that these procedures of preparing bicrystalline seeds are the most important and sufficient for the reproducible growth of bicrystals with any misorientation angle. The method allows growing bicrystals of niobium and molybdenum with the misorientation angles from 5 to 55°. Bicrystals are of 30 mm in diameter and of 100-150 mm long (Figure 3). A correct preparation of bicrystalline seeds and a compliance of the optimal temperature distribution allow avoiding pinching one grain by another. The visual and metallographic examinations of bicrystalline samples show that the grain boundaries are macroscopically flat over large areas and do not contain "parasitic" grains or the second phase inclusions. Transverse sections of niobium bicrystals are examined by the optical and scanning electron microscopes, after the mechanical and chemical polishing treatment of the samples in the heated until 50÷70°C solution of a mixture of hydrofluoric and nitric acids. Then, the grain boundaries are detected by etching in the same solution at 20°C.
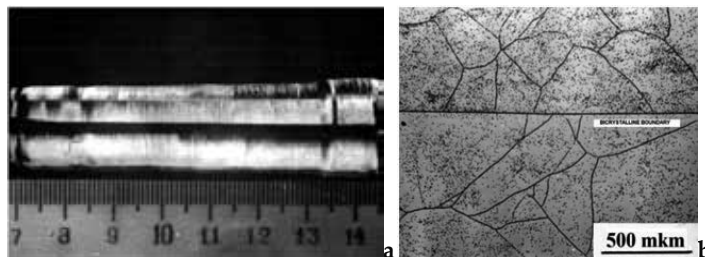
Figure 3. Mo bicrystal of 16 mm in dia (a) and bicrystalline boundary on cross-section (b).

4.2. Studies of strength of high-angle boundaries in molybdenum bicrystals

Tendency of undoped refractory metals of Group 6 (molybdenum, tungsten) to intergranular embrittleness do not only create difficulties in processing, but also significantly reduce the scope of their practical use [32]. Because of complexity of grain boundaries in polycrystalline samples, containing a large and, to some extent, uncontrollable set of grains, studies are carried out on specially prepared bicrystals with well-known crystallographic parameters, because they are the most convenient model objects for the grain boundaries studies. In [30,32,36,49], the dependence of the strength of grain boundaries in molybdenum bicrystals is revealed on
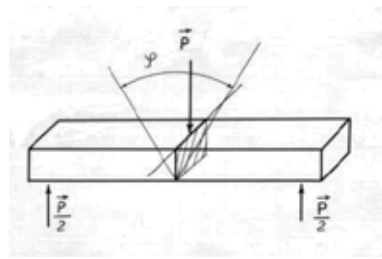
Figure 4. points bend test of bicrystals.

the type of boundaries and the misorientation angle between the grains. By the 3-points bend test (Figure 4) it is established that the high-angle boundaries (over 7÷10°) less strong in comparison to low-angle boundaries, and that the higher strength the closer to the boundary planes (100) or (110). It is proved that the twist boundaries in the molybdenum bicrystals are more brittle compared to the tilt ones [41,42]. True, in both types of boundaries (twist and tilt) the possible influence of the bedding plane of the grain boundaries is not taken into account. It should be noted that in the polycrystalline ingots of molybdenum are usually found all types of boundaries and the misorientation angles in different sections of the ingots vary widely. The main reason for the different behavior of the high- and low-angle grain boundaries is the nature of the interaction of these boundaries with impurity atoms. Low-angle boundaries with misorientation angles up to 7÷10°, as a rule, consist of lattice dislocations. In the boundaries of high-angle (over 10÷15°) the distance between dislocations is so small that their nuclei combine, causing to have different atomic structures. Apparently, impurity atoms by a reaction with the low-angle boundaries are located on their constituent dislocations, whereby the low-angle boundaries occur at areas with a reduced content of impurities. At the high-angle boundaries the impurities segregate more evenly along the boundary, strongly weakening a grip of grains. Therefore, there is an increased susceptibility to intergranular embrittlement. The embrittlement of cast or recrystallized molybdenum largely depends on the interstitial impurities (carbon, oxygen, nitrogen), which, due to the low solubility in the crystal lattice, are allocated along the grain boundaries [41-46]. It was qualitatively shown that at the carbon content of less than 10^{-3}% the strength of bicrystalline boundaries depends on their structure, and above this content - the strength of the bicrystalline boundaries is the same and does not depend on the carbon content. However, it remains unclear why there is the "critical" content, the more that the solubility of carbon and oxygen in molybdenum is by several orders of magnitude lower. Also unclear is the question, what is the relationship between the total content of interstitial impurities in molybdenum and the content of second phase (carbides, oxides) at the grain boundaries. Using the molybdenum bicrystals in studies of grain boundaries usually encounter with serious difficulties in getting bicrystals of given crystallographic parameters, as well in preparing a sufficiently large number of reproducible bicrystalline samples from the same bicrystal.

Apparently, one of the essential crystallographic parameters of the samples is the bedding plane of the grain boundaries, which are still obtained by chance, since the known methods do not allow to grow the molybdenum bicrystals with any desired plane boundary. In the

bicrystalline twist boundaries the axis of twist uniquely determines the plane of the grain boundary. The widest range of the bedding planes of the grain boundaries can be obtained at bicrystals with the tilt boundaries when at one axis in the case of the symmetrical boundaries can exist two bedding planes and in the case of asymmetric boundaries - of any number. In [36,46], the strength of the bicrystalline twist and tilt boundaries in molybdenum bicrystals is studied depending on the misorientation angle between two grains and on the bedding plane of the grain boundary (*i.e.*, the boundaries with a different number of coincident nodes Σ). In [46], the molybdenum bicrystals are grown by the method, the main feature of which is the existence of the optimal temperature distribution in the liquid zone. The samples with twist boundaries are prepared as described in [47,48], but for the growth the better electron gun is used, which allows to create the very narrow liquid zone on the sample and, consequently, more even grain boundaries. In the grown bicrystals the symmetric tilt boundary [100] lies along the plane (120), and the twist boundary - along (100). The bicrystals with the tilt boundaries [100] have misorientation angles and bedding plane other than special boundaries (σ = 36.5°) with a number of matching nodes Σ = 5. The bicrystals with the twist boundaries also differ by the misorientation angle of the special twist boundary (σ = 36.5°) with Σ = 5. Also, the bicrystals with the tilt boundaries [110] are grown, which are intended for similar studies. In particular, bicrystals are prepared with tilt twin boundaries [110] and the misorientation angle of 70° between the grains and the bedding plane of the boundaries (112) and (111); for comparison it is grown the bicrystal with the misorientation angle of 64° and the plane of the grain boundary, deviated from the (111) plane for 3°. The initial single-crystalline rods, from which the bicrystals are then grown, are prepared in two ways. First, the molybdenum bicrystals (Mo-1) are of a standard purity (*see* Table 2). Secondly, for comparison, the molybdenum bicrystals (Mo-II) of highly-pure molybdenum are grown.

Samples	Impurity content, x10^{-3}%					Metallic impurities	Residual resistivity ratio (RRR) R$_{273K}$/R$_{4,2K}$
	O	C	N	H	W		
I	<0.1	<1	<0.4	<0.1	<3	<1	1500
II	<0.1	<0.01	<0.02	<0.1	<0.3	<0.1	30000

Table 2. Impurity contents and residual resistivity of molybdenum (two levels of purity).

Bicrystalline samples are tested for strength by the three-point bend device (the rate of deformation 0.01-0.1 mm.min^{-1}). The distance between supports is 9 mm, the radius of supports and the knife - 1 mm. For testing of each bicrystal, 3÷5 bars of the size 1,5x2x16 mm are prepared. The bending axis in bars lies in the plane of the grain boundary and is perpendicular to the common axis of the bicrystal. Tests are conducted at room temperature, and then the fracture stress is calculated by loading curves. The yield criterion is the stress at which plastic deformation is of 0.2%. The dependence of the fracture stress on the misorientation angle of the special (36.5°) tilt and twist [100] boundaries is shown in Figure 5. Topography of fracture surfaces is examined in the scanning electron microscope JSM-T35 at the accelerating voltage of 25-35 kV. Auger spectra of the surfaces of fractured grain boundaries are recorded on the

Auger spectrometer PHI-551 with the base residual pressure in the chamber, not exceeding 1×10^{-7} Pa. "Fresh" surfaces of the grain boundary fracture are obtained in the pre-chamber of the Auger spectrometer at vacuum of 1×10^{-5} Pa. The spectrum recording time - no more than 1 min, the focal spot diameter - 10^{-5} m. Grain boundaries are revealed by etching in the mixture of nitric and sulfuric acids. For the X-ray diffraction study of the grain boundaries, the bicrystalline samples are mechanically polished and electropolished in a concentrated sulfuric acid. Laue patterns are obtained from individual grains with an accuracy of $1 \div 2°$. The tests have shown that almost all bicrystals have the brittle fracture, although on some of them plots of plastic deformation before fracture are observed (Table 3). The fracture of specimens under the applied load passes strictly along the grain boundary. The study by the optical microscope reveals that all samples have the flat boundary parallel to the axis of the bicrystal. Without plastic deformation, the fracture stress perpendicular to the grain boundary is calculated from the load to fracture, considering the sample as the elastic bar.
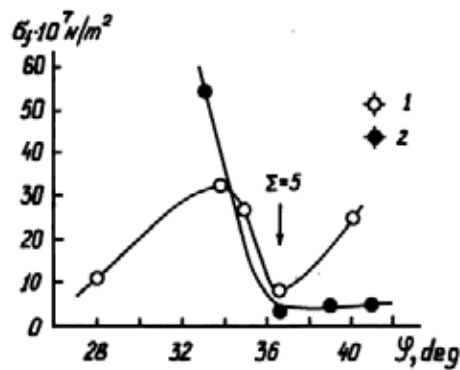
Figure 5. Fracture stress vs. misorientation angle.

Strength does not exceed the fracture stress of the boundaries on the cleavage plane (100) and depends both on the misorientation angle between the grains and on the bedding plane of the grain boundary at the same misorientation angle between grains. The significant stress of the fracture equal 30×10^7 N m^{-2} is observed on the sample Nr 13 with the boundary of a general type; the fracture takes place with appreciable plastic deformation (up to 7%). The fracture stress equal 25×10^7 N m^{-2} is obtained on the sample Nr 11 with the twin tilt boundary lying in the incoherent twinning plane (112). This bicrystal has an elongation approximately 1%. The stress fracture of the sample Nr 12 with the twin boundary and the bedding plane along the coherent twin plane (111) is 11×10^7 N m^{-2}. On the sample Nr 10 with the misorientation angle of 64^0 the fracture stress is equal 15×10^7 N m^{-2}. The molybdenum bicrystals with the special tilt and twist [100] grain boundaries are fractured at low loads and often uncontrollable, although the boundaries other than special, it turns out, tend to be of the much higher strength. The strength of the tilt boundaries [100] with the misorientation angle of 33° reach relatively high values - 55×10^7 N m^{-2}, although at other angles the strength is low (below 10×10^7 N m^{-2}). The twist boundaries [100] at the misorientation angles of $34 \div 35^0$ and 40^0 are quite strong -

$(25 \div 30) \times 10^7$ N m^{-2}, but at 28° the strength decreases to 10×10^7 N m^{-2}. It is seen in Figure 5 that in the special boundary minimum of the strength is observed for twist and tilt boundaries in the region adjacent to the angle of 36.5°. To test the effect of the bedding plane of the grain boundary on its strength the bicrystal is grown. It contains the misorientation angle 33° and the bedding plane deviated by 45° from the plane of the boundary in the bicrystals with the greatest strength, equal 55×10^7 N m^{-2}. The tests have shown that the strength of such boundary is almost five times lower. According to [45], the orientation dependence of the strength of the grain boundaries is of the monotonous character and the strength of the tilt and twist boundaries in the range of angles from 20 to 45°, as a rule, does not exceed $(8 \div 10) \times 10^7$ N m^{-2}. The slight deviation from the monotony is found for the twin tilt boundaries [100]. In [44], extremes are found on the orientation dependence of the tilt boundaries [110] with the misorientation angles of approximately 10^0 and 55°, but absolute values of the fracture stress for the boundaries of both types are too high – up to $(100 \div 150) \times 10^7$ N m^{-2}, *i.e.*, even exceed the tensile strength of the molybdenum single crystals and, apparently, is incorrect. Kinks on the twist boundaries are shown in Figure 6. It is clearly visible chains of the second phase precipitates (presumably, carbides) at the terraced kinks and precipitates like needles at right angles to each other.
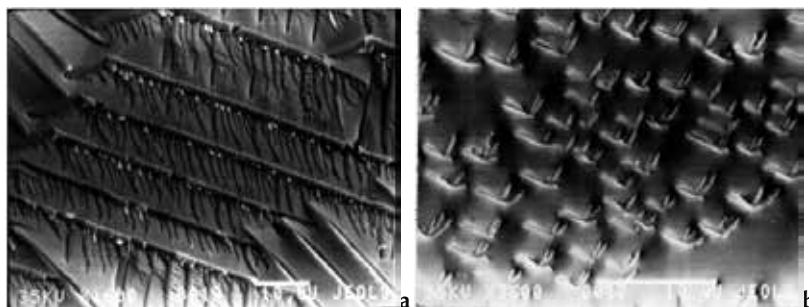
Figure 6. Fractography of the fracture surface of the twist [100] grain boundary (a) and of the tilt twin boundary [110] (b).

It should be noted that on the fractures of the twist bicrystalline boundaries of Mo-II the significantly smaller amount of the second phase is present, in comparison to samples from Mo-I. The molybdenum bicrystals with special twist boundaries, however, are fractured with the uncontrolled stress, although the precipitates at the fractured boundaries are virtually absent. The small precipitates in a form of thin films on fractured surfaces of the special tilt boundaries are observed; however, they disappear when exposed to the electron beam. Analysis of Auger spectra from different areas of the fracture surface of tilt boundaries [110] has shown that the intensity of Auger peaks of carbon, oxygen and nitrogen is varied. Near the outer surface there is the extended zone of a width $0.1 \div 0.2$ mm, in which the oxygen content is 20% higher in comparison with central areas. On peripheral areas there is also the high nitrogen content; however, at central areas at the grain boundary the intensity of Auger lines is close to zero. The intensity of Auger lines of carbon, conversely, is increased from the periphery to the center. These data, of course, are qualitative in nature, as in the pre-chamber

Sample	Boundary	Misorienttion angle, angular degree	Bedding plane of boundary	Σ	$\sigma_f \, x10^7$, H m^{-2}
1	Tilt [110]	17	(551)	-	14
2	Tilt [110]	20	(119)	33	10
3	Tilt [110]	26	(331)	19	17.5
4*	Tilt [110]	26	(331)	19	3.5
5	Tilt [110]	39	(221)	9	12.5
6*	Tilt [110]	39	(114)	9	14
7	Tilt [110]	39	(114)	9	8
8	Tilt [110]	50	(113)	11	9
9*	Tilt [110]	50	(113)	11	3.7
10	Tilt [110]	64	(111) dev.3^0	-	15
11	Tilt [110]	70	(112)	3	25
12	Tilt [110]	70	(111)	3	11
13	Tilt [110]	General type	-	-	30
14	Tilt [100]	33	-	-	55
15	Tilt [100]	36.5	(120)	5	3
16	Tilt [100]	39	-	-	9
17	Tilt [100]	41	-	-	8
18	Twist [100]	28	(100)	-	11
19	Twist [100]	35	(100)	-	31
20	Twist [100]	35	(100)	-	27
21	Twist [100]	36.5	(100)	5	8
22	Twist [100]	40	(100)	-	25

*bicrystals grown from Mo-II.

Table 3. Crystallographic and strength characteristics of samples with the tilt and twist boundaries [110] and [100].

of the Auger spectrometer the residual pressure is such that the number of atoms colliding with the surface for one second corresponds to one atomic layer, while the process of transferring the sample in the chamber of the Auger spectrometer takes about 10 minutes. The Auger spectrum of the fracture surface of the sample Nr 7 shows that it contains lines, except the molybdenum line, of carbon (272 eV) and oxygen (503 eV). The low intensity line (380 eV) is, apparently, due to nitrogen. A peak of oxygen should be partially attributed to the adsorption of oxygen from the residual gas in the pre-chamber. A form of the Auger carbon line reveals that it is partially caused by adsorbed hydrocarbons, and partially - by a presence in the analysis zone of molybdenum carbide, as evidenced by the low-energy characteristic of the comb structure of lines. It is unlikely that in the presence of the significant amount of dissociated oxygen the surface carbide formed immediately after destruction of the sample along the bicrystalline boundary. Most likely, the Auger spectrum has elicited the three-dimensional carbide precipitates that already exist on the grain boundary. After the ion etching of the fracture surface at the grain boundary the contents of elements in the area of the analysis have

been varied somewhat. The intensities of Auger lines during the etching of the sample Nr 7 show that at transition to deeper layers carbon and oxygen decrease as compared with the "fresh" fracture surface.

The shape of the Auger line of carbon during etching also varies considerably and becomes fully "carbide-like". Due to the lower sputter coefficient of carbon compared with the sputter coefficient of molybdenum, the carbon accumulation can occur near the surface. The absolute value of the ratio C/Mo determined from the Auger spectra after the prolonged etching is substantially overstated. To correct the carbon content profile in view of this accumulation is not yet possible; however, given in Table 4, the values of C/Mo permit make a comparison between the samples by the volume content of carbon, so long as at the prolonged etching the enrichment of carbon should be proportional to the volume content of carbon. Oxygen distribution is the same for all bicrystalline samples, although in the course of ion etching the intensity of the Auger line of oxygen falls. The region, rich of oxygen, is no more than 80 Å. The character of distribution with the depth is different for all the samples, but the intensity of the Auger line falls with the depth. On some specimens the marked intensity of the Auger lines persists to a depth of 800÷6000 Å. The maximum intensity of the Auger line of molybdenum is in the range 20÷50 Å. It is because the early etching removes contaminated layers in which the content of molybdenum is relatively lower than in the matrix. In the course of etching the analyzed surface roughness caused by uneven etching of its various portions is enhanced, which leads to additional scattering of the Auger electrons. Because of low solubility of interstitial impurities in molybdenum at cooling rates typical for growing molybdenum bicrystals they are allocated as the second phase. While it is not possible to correctly assess the degree of enrichment of the grain boundaries with the interstitial impurities or precipitates. It can only be based on comparison of the relative content of interstitials on the tilt and twist boundaries. At the "fresh" fracture surface and at the depth of up to 1000 Å from the surface, it is possible to argue that the degrees of "contamination" of the boundaries of both types are identical. Secondly, it can be concluded that most of the carbon on the fracture surface is bound to carbide precipitates.

Grain boundary	Analyzed layer depth, Å	Ratio of analyzed elements			
		C_{tot}/Mo	C_{carb}/Mo	N/Mo	O/Mo
Tilt	0	1.60	0.55	0.01	0.45
Tilt	1000	-	1.40	0	0.08
Twist	0	1.26	0.56	0.13	0.36
Twist	1000	-	1.38	0	0.12

Table 4. Ratio of chemical elements on the surface of the grain boundaries and at the depth of up to 1000 Å from the surface of the tilt and twist grain boundaries [100].

Of particular interest is comparison of bicrystals with the different initial purity. Although the content of interstitials in Mo-II is much lower even in comparison with pure Mo-I, the boundary strength of the tilt bicrystals, grown from Mo-II, differ a little from the strength of the samples of Mo-I. This is all the more surprising that, according to the Auger analysis at

grain boundaries of samples grown from Mo-I, as the carbon content on the fracture surface, and in the depth of grains is substantially higher. The oxygen content is the same at boundaries of all samples. In [43,45], argued that the fracture stress of twist boundaries is inversely to the oxygen content on boundaries, and the role of carbon was reduced mainly to suppress this effect. Experimental results obtained so far are not enough to talk about any influence of oxygen on the strength of grain boundaries. The boundary strength of pure molybdenum, which conducted the present study on, is primarily dependent on high misorientation angles of boundaries, and change of the total content of interstitials in the investigated content range does not lead to any noticeable change in strength.

4.3. Studies of fine structure of low-angle boundaries in tungsten bicrystals

In *bcc* metals is most likely the presence of dislocations with Burgers vectors of $a/2[111]$ and $a[100]$, where, a is the period of a cubic lattice [23,41,48]. However, there is no information about the presence of dislocations with Burgers vector $a[110]$ in the *bcc* metal crystals. Low-angle boundaries and the characteristic dislocation substructure, particularly of tungsten, are formed from these dislocations arising during the crystal growth (probably due to high thermal stresses). There is tendency to form low-angle boundaries of tilt or twist at the relatively low dislocation density in the crystal (~$10^5 \div 10^6$ cm^{-2}) [48]. Such boundaries may consist of one (for tilt boundaries - symmetric), two, three or more families of dislocations. The fine structure of such boundaries has been comprehensively investigated in [22,23] on single crystals of tungsten and molybdenum exposed to the high-temperature creep. An average size of subgrains in such crystals is several microns. Low angle boundaries have the misorientation angle in the area $2 \div 4°$, but consisted mainly of dislocations introduced in the crystal by means of plastic deformation instead of so-called dislocation growth. It should be noted that the dislocation model of low-angle boundaries is well established. Systems of dislocations forming low-angle boundaries are in the metal lattice and tend to have the lowest energy in crystallographic planes being located close to crystallographic planes of low indices. In particular, for the *bcc* lattice symmetrical tilt boundaries consisting of parallel edge dislocations, are most likely in planes {111} and {100}, asymmetric tilt boundaries - in planes of {hko}, and net twist boundaries - in planes of {110}. Thus, if to the system of dislocations, created in the flat layer of the low-angle misorientation, provide the opportunity to move (by glide and climb of), the system of low-angle boundaries should strive for the finite number of planar nets. All of the above indicates that the triple junctions of low-angle boundaries do not necessarily have to be of 120-degree. In some cases, low-angle boundaries are observed on facets on the microscale, what also appear crystallographic structural features of low-angle boundaries. It is known that the crystal grown from the seed inherits its substructure. The seed already contains stable low-angle boundaries which germinate in the growing crystal. If the bedding plane of boundaries is parallel to the crystal growth axis, such low-angle boundaries remain in the crystal and germinate over long distances, for example, in the axis and having the misorientation angle up to $1 \div 2°$. Using the method of stereometric metallography we found that the bedding plane of the sub-boundaries with an accuracy of $1 \div 2^0$ corresponds to crystallographic planes of the type {100} (Figure 7a). Low-angle boundaries are identified by etching on the plane of the single crystal W(010) with the growth axis [001].
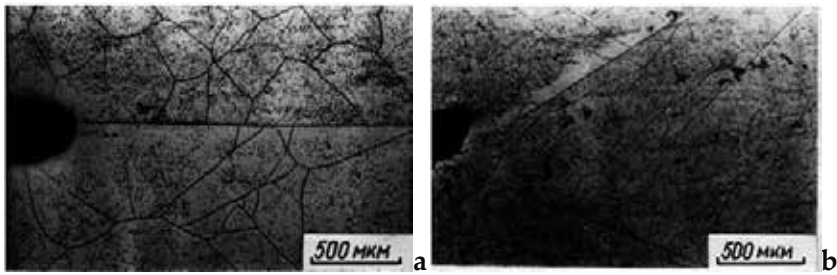
Figure 8. Symmetrical low-angle twist boundary (a), occurs in the {110} plane and grows in the crystal with the growth axis [110] and the low-angle tilt boundary (b) created artificially in the {110} plane, which tapers off the crystal.
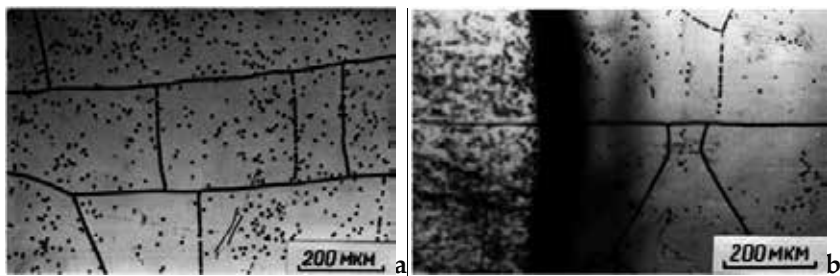
Figure 7. Low-angle boundaries: on (010) plane, growth axis W[001] (a), and on (100) plane along W[100], the stereo-metric metallography (b).

On Figure 7b metallographic cross-sections presented with a plane parallel to the axis of the crystal growth [001] correspond to the plane (010) and contains the step with a height of about 300 microns, which is greater than the depth of the focus of the microscope objective and the top of the stairs because blurred. However, it is seen that the sub-boundary located in the center is in the {100} plane. Earlier, similar results were obtained in [50] by X-ray topography. It would certainly be interesting to investigate the fine structure of such small-angle boundaries, *i.e.*, decipher Burgers vectors of constituent dislocations, but, unfortunately, to prepare suitable electron microscopic samples is not yet possible. In principle, it is possible to create the low-angle twist or tilt misorientation in any crystallographic plane parallel to the crystal growth axis by the preparation of bicrystals. However, if in this plane cannot be obtained the artificially created misorientation by using the known complete lattice of dislocations, such low-angle boundaries cannot exist and should be quickly tapered off the crystal during the growth. Several tungsten bicrystals containing low-angle tilt or twist boundaries are grown. The characteristics of these boundaries and results of their growth are given in Table 5. For example, the pure twist boundary in the plane {110} is possible and it grows into the crystal, but the symmetric tilt boundary – no, and, naturally, it tapers off in the growing process, which shown in Figure 8.

The dislocation structure of low-angle boundaries in the tungsten single crystal is presented in electron micrographs (Figure 9a). On Figure 9b, the corresponding electron diffraction

pattern of the area containing low-angle boundaries is shown. The foil plane corresponds approximately to the {111} plane. Having completed a flat grid of a reciprocal lattice (Figure 9c), it can be shown that the trace of the plane crossing the low-angle boundary and the foil plane is the direction $\vec{l} = [4\bar{5}1]$. Unfortunately, the sample was too thick and the determination of Burgers vector of dislocations forming the sub-boundary, in contrast attenuation condition $\vec{g}\vec{b} = 0$, is failed.
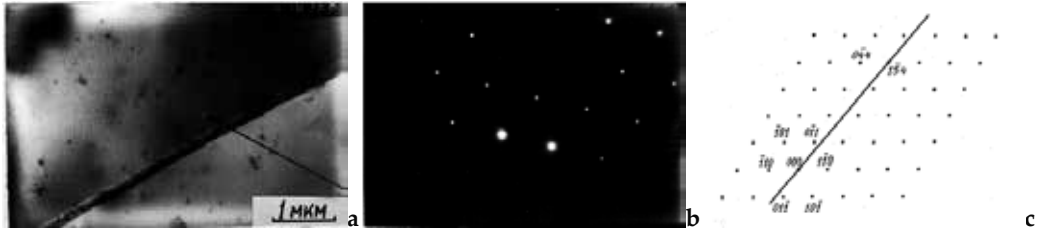
Figure 9. Electron micrograph (a), electron diffraction pattern (b) & flat grid of a reciprocal lattice reconstructed (c) of the small-angle twist boundary in W bicrystal.

Sample	Growth axis	Bedding plane of boundary	Boundary type	Results of the growth
1	[100]	{110}	Tilt	Taper off
2	[100]	{110}	Twist	Grows in crystal
3	[100]	{100}	Tilt	Grows in crystal
4	[100]	{100}	Twist	Grows in crystal
5	[110]	{110}	Tilt	Taper off
6	[110]	{110}	Twist	Grows in crystal
7	[110]	{100}	Tilt	Grows in crystal
8	[110]	{100}	Twist	Taper off
9	[110]	{111}	Tilt	Grows in crystal
10	[110]	{111}	Twist	Grows in crystal
Misorientation angle of low-angle boundaries always in range from 1^0 to 3^0				

Table 5. Crystallographic parameters of the tungsten bicrystals with the low-angle boundaries.

However, the available information, in particular about the angle $\gamma = L\ (\vec{\vartheta}, \vec{l}),$ leads to the conclusion that the presented sub-boundary is the twist low-angle boundary and consists of two families of screw dislocations with Burgers vector $(\vec{b} \mid \mid \vec{\vartheta})\ \vec{b} = a/2[111]$. The low-angle

boundary plane is n = (134), and the corresponding Burgers vectors of screw dislocations are $\vec{b}_1 = a/2\ [1\bar{1}1]$ and $\vec{b}_2 = a/2\ [\bar{1}11]$. The structure of the boundary is different on different sites. It is possible to find a site of the low-angle boundary, in which dislocations of one of the families are placed non-equidistantly, but at intervals 3-4-3-4. Thus, the specific dislocation structure of low-angle boundaries formed by growth dislocations can be very difficult to reveal.

4.4. Studies of molybdenum bicrystals by low-energy ion scattering

Bicrystals, consisting of two differently oriented grains of high structural quality and purity, and grain boundary plane are the excellent models for experimental studies of various physical properties of both the surface and the grain boundary [37,51-55]. Here, the dignity of bicrystals in the studies of surface and bulk processes is shown for segregation, atomic reconstruction and self-diffusion on different crystallographic surfaces. Specifically targeted surfaces of the molybdenum bicrystals presented preselected surfaces of two grains (single crystals) and an interface therebetween. In this case both the grains are grown in exactly the same conditions, and processing of both grain surfaces is carried out in fully identical conditions. The specimens are cut of the massive molybdenum bicrystals normally to their axes, so the bicrystalline boundary is always at the centre of the flat specimens. The specimens are studied by low-energy ion scattering (LEIS). This method has a very high surface sensitivity and allows studying selectively processes taking place in the uppermost atomic layer. The LEIS signal intensity is directly proportional to the density of atoms on the surface and, therefore, must be different for differently oriented surfaces. Until recently, the LEIS technique is used for detailed studies of the surface structure of single crystals and various adsorbents on it by the angular dependence of the LEIS signal. However, the dependence of the scattering intensity of the ions from the atomic density is not obvious, experimental studies of this relationship are still not enough. Unfortunately, almost no studies that compare the LEIS signal intensities for differently oriented surfaces of the same object. The only study was done on silicon many years before where LEIS signals from the Si (111), Si (110) and Si (100) are compared. However, the ion doses used at that early time were so high that they cause severe destruction of the surface. Most likely, the correlation is discovered by accident. Now, we are able to identify and compare atomic densities on the surfaces of different low indexes single crystals and bicrystals of molybdenum and tungsten.

A clearer understanding of the crystallographic dependence of the signals is very important for the quantitative analysis by LEIS. For example, in the case of single-crystalline surfaces and adsorbents, this method allows getting detailed information about the atomic structure. The advantage of LEIS - an opportunity to get a statistically average result, since the scanning ion beam has a permanent, fixed diameter (from about 10 microns to about 1 mm). In the case of non-homogeneous samples scanning is possible perhaps even on an area of 1 cm^2. Problems arising in the study of the crystallographic dependence of the LEIS signal, may partly explain the lack of experimental evidence; however, this relationship can only be measured on clean and well-oriented surfaces. Moreover, for comparison of two different crystallographic planes it is indispensable the preparation of the specimens in absolutely identical conditions. These problems can be successfully solved by using bicrystals. In conducting the present study were
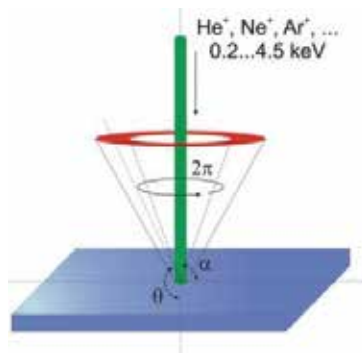
Figure 10. Scheme of the LEIS experiment.

prepared surfaces of molybdenum bicrystals Mo(110) and Mo(100). These planes have been chosen due to differences in the density of atoms on the surface. Thus, Mo(110) is a close-packed surface with the higher density of atoms in *bcc* structure, and Mo(100) - an "open" surface with the lower density of atoms. Both surface planes are the perfect single crystals with crystallographic orientations of Mo[110] and Mo[100]. The bicrystalline boundary separating two single crystals in the center of the sample, held on {100} plane, is macroscopically smooth over the entire sample and does not contain "parasitic" inclusions of other phases. For the LEIS study, the "Mini-Mobis" with a base pressure of 2×10^{-10} mbar is used. The unit is equipped with measuring devices for LEIS, Auger electron spectroscopy (AES) and low-energy electron diffraction (LEED). When measuring by LEIS, the monoenergetic beams of Ne^+ ions and $^4He^+$ ions with energy of 3 keV are used. The beams bombard the sample in direction perpendicular to the surface of the sample. The ions, scattered at an angle of 136^0, are detected by the analyzer of the "cylindrical mirror" type. This analyzer is used also for Auger measurements. To avoid structural defects on the surface of the sample during the experiment the ion doses do not exceed 10^{14} ion cm^{-2}. The diameter of ion beam is about 400 microns, since for some LEIS intensity measurements in the boundary region between two grains (crystals), the diameter of the beam is too large, so a part of experiments are conducted on a similar LEIS set-up in which could be used the ion beam of the diameter up to 25 micron. It is comparable to the thickness of the grain boundaries in the bicrystals under study. Heating of the samples is carried out *in situ* by means of special cathodes consisting of a heating element and a source of electrons. Between the sample and the cathode an accelerating voltage is applied. As a result, electrons bombard the surface of the sample, causing thereby its rapid heating to temperatures of approximately 2500°C. For the present study there are grown two different molybdenum bicrystals by electron-beam floating zone melting. One bicrystal contains two grains (crystals) Mo[110] separated by a tilt boundary with a misorientation angle of 70° between grains (crystals). Another bicrystal contains grains (crystals) Mo[100] and Mo[110] separated by a 45-degree twist boundary. Both molybdenum bicrystals of 15 mm in dia are cut into the plates of 7.5x7.5x1 mm^3. Thereafter, the plates are subjected to the mechanical and electrolytic polishing, followed by annealing in an oxygen atmosphere. The study of bicrystalline samples by LEIS is carried out after the final cleaning the surface *in situ* by the electron gun with a rapid heating

to 2500°C directly in the measuring chamber. To reduce contamination of the samples in the measuring chamber, near-by elements of chamber are made of the massive high-purity molybdenum. Experiments are performed on atomically clean surfaces that are monitored by LEIS, AES and LEED. The residual contents of carbon and oxygen are below the sensitivity of LEIS (<0.1% of the monolayer using $^4He^+$ ions with energy of 3 keV). With LEED could be seen a clear picture of the crystallographic planes (110) and (100), corresponding to two grains (crystals) of the molybdenum bicrystals. After long exposure of the specimens in the measuring chamber even in UHV, an intensity of the LEIS signal dropped, apparently due to adsorption of atoms of the residual gases present in the chamber. After repeating short heating, the sample surface becomes clean again. The quadrupole mass-spectrometer, mounted in the measuring chamber, shows that the main impurity in the annealing chamber during the sample annealing - the elements of masses 2 and 28, which correspond to nitrogen and hydrogen (or carbon monoxide), respectively. At the beginning of the experiment the surface of both grains (crystals) Mo(111) and Mo(100) are at the same level of the sample (by height). However, after "vacuum oxy-polishing" of the molybdenum bicrystal, both grains (crystals) are at different levels depending on their crystallography, and the boundary groove appeared after vacuum etching (Figure 11), the slope of the sides of which also depends on the crystallographic orientation of the grains (crystals) constituting the bicrystal.
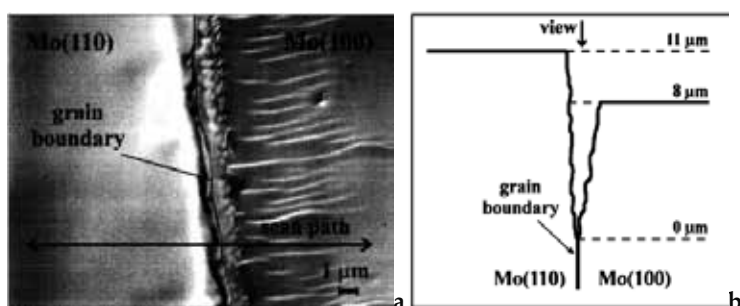
Figure 11. SEM micrograph of a Mo bicrystal, top view (a), and graphic profile (b) of the bicrystal boundary.

Experiments are carried out by scanning the surface of the bicrystal by a narrow beam of Ne^+ ions with the diameter of 25 microns and energy of 3 keV. The measured elastic peak of the molybdenum intensity is a function of the ion beam position on the surface of the bicrystal. The studies of the bicrystal, in which both grains (crystals) are of the similar surface orientation Mo(110) and the tilt boundary, do not reveal any difference in the signal intensity between two grains (crystals). This shows that the crystallographic orientation of the surface plane itself has no effect on the value of the LEIS signal intensity, so the greatest interest is the molybdenum bicrystal with different orientations of the two grains (crystals). Interestingly, the heat treatments result in difference of segregation of carbon at different crystallographic surfaces. After the prolonged anneal of the bicrystalline sample in UHV (1 hour at 1100°C), carbon segregation from the volume on the surface Mo(100) has been detected (Fig. 12a). Naturally, at the initial state the molybdenum bicrystal has the same carbon concentration in both the

grains (crystals). The volume carbon concentration does not depend on the crystallographic orientation of both surfaces of the grains (crystals). In addition, on the surface of the grain Mo(100) the carbon atoms in the initial state are not fixed at all. Carbon occurred as a result of the annealing the surface (100) is then removed by *in situ* annealing in an oxygen atmosphere (~10^{-6} Pa) at about 1500°C. However, after the prolonged anneal at about 1100°C it again appears on the surface Mo(100). In the study of the crystallographic dependence of the LEIS intensity, the signal of molybdenum is normalized to the most densely packed plane (110). It has been established (Figure 12b) that there is a clear dependence of the LEIS signal intensity from the crystallographic orientation of each grain (crystal). The presence of the grain boundary between the different planes is marked by a sharp change of the signal in position 0. The ratio R of the signal from the surface Mo(100) to the signal from the Mo(110) is found to be 0.74 ± 0.02, which is slightly higher than the ratio of the atomic densities for these crystallographic planes (0.707). As shown in [6,8], for the close-packed crystal surfaces of tungsten and rhodium, contributions to the LEIS signal intensity from the second and third atomic layers are negligible. This means that for these surfaces the signal intensity is proportional to the surface density of atoms at the uppermost atomic layer. Since we found almost exact ratio of the signals from the surfaces of Mo(110) and Mo(100), this suggests that even for an "open" plane (100) the contribution from the second and third layers to the elastic peak is negligible. To study the effect of ion bombardment on the LEIS signal, the Mo(110)/Mo(100) bicrystal is subjected to ion sputtering by the defocused ion Ne$^+$ beam with energy of 3 keV at room temperature. The ion dose is in the range from 7×10^{15} ion cm^{-2} to 40×10^{15} ion cm^{-2} at a constant ion current 6×10^{-12} ion cm^{-2} s^{-1}. After ion bombardment, a repeated measurement is done of the same surfaces of the sample as before sputtering (Figure 12b). The measured scan shows that after ion bombardment there is the significantly decreased signal intensity, especially for the molybdenum surface Mo(110), where the signal is decreased by 25%, whereas for molybdenum surface Mo(100) - only by 10% (*see* Table 6).
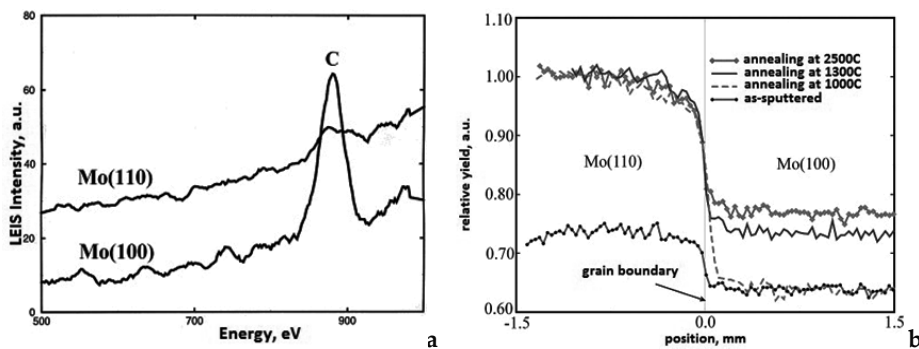
Figure 12. Spectra: C segregation on Mo(110)/(100) faces (a) and recovery of LEIS yield on Mo(110)/(100) faces (b).

Sputtering increases the surface roughness. This effect can be understood if we consider the sputtered atoms from the surface Mo(110). At first glance, in this situation, for the incident ion it is easier to penetrate into the second atomic layer and not to be neutralized in the first atomic

layer. Yet it is unlikely that ions could be reflected in the opposite direction and go back through the top atomic layer, remaining ionized. This situation is indeed confirmed by our experiments, since the ion beam is directed to the sample surface normal and the detector detects only ions scattered at an angle of 136°, so the sputtered atoms of the first atomic layer from the surface Mo(110) leads to decrease in the effective atomic density. However, when a sufficiently large number of atoms will be sputtered, dynamic equilibrium will be established, because accumulation of single vacancies should make the second atomic layer more open. For the Mo(100) surface, which is already quite "open", the possibility of backscattering from the second atomic layer after surface sputtering will be much greater. Thus, it becomes clear why decrease of the LEIS signal intensity after sputtering is more significant for the close-packed Mo(110) surface. Even at high doses of sputtering, the difference between the signal intensities from the different crystallographic surfaces still remains. This is partly due to the conservation of the structure in the bulk crystal, and partly due to the fact that ion etching not only makes the surface amorphized, but also removes a lot of layers. At a dose of 40×10^{15} ion cm^{-2}, almost hundred atomic layers are removed from the surface, which far exceeds the range of thicknesses where Ne$^+$ ions with energy of 3 keV could make the surface amorphized. Apparently, the result of these processes is dynamic equilibrium.

Treatment	Relative LEIS yield		Atomic density (x10^{15} cm^{-2})	
Mo(110)	Mo(100)	Mo(110)	Mo(100)	
As sputtered	0.73	0.64	1.02	0.91
700K, 1 min	0.89	0.64	1.25	0.91
1000K, few seconds	0.97	0.64	1.47	0.91
1300K, 3 minutes	0.99	0.73	1.40	1.03
1600K, flash	1.00	0.76	1.41	1.07
2500K, flash	1.00	0.76	1.41	1.07
Ideal lattice, first atoms, normalized to (110)	1.000	0.707	1,41	1.00

Table 6. The relative LEIS yields and atomic densities of the Mo(110) and Mo(100) after various annealing treatments.

After sputtering, the molybdenum bicrystal is annealed at different temperatures and scanned along the surface by the ion beam of Ne$^+$ with energy 3 keV. In this case, the amplitude of the elastic peak is recorded as a function of the position of the ion beam (Figure 12b). Measurements show that recrystallization of the surface Mo(110) after ion bombardment begins at about 700°C and completed at about 1100°C, and for Mo(100) recrystallization starts at ~1300°C. After high temperature annealing (~2500°C) the signals are the same as in the initial undamaged clean surface. Based on this, it is supposed that the different surface structures have different mobility of atoms, and the difference of the signal intensities can be used as a measure that determines the amount of disorder in the surface. The high mobility of atoms in the upper

atomic layer of Mo(110) is supported by the lower surface energy of the molybdenum "close"-packed structure (110) as compared to "open" Mo(100).

5. Growing tube single crystals of refractory metals

5.1. Main features of growing tungsten tubular single crystals

Shaped tungsten single crystals are used as screens of different shapes, inputs, crucibles, shapers and other products. There is considerable interest to profiled tubular shaped single crystals (primarily, of tungsten) in connection with their use in prospective designs of thermionic converters. The production of tubular tungsten single crystals from bulk cylindrical crystals by traditional machining (drilling, broaching) is extremely labor-intensive, low-tech and uneconomical process. Get such tubes pulling from the melt, for example, by Stepanov method, is impossible even for the reason that there are no available materials for the shaper. The only possibility to obtain single-crystalline tungsten tubes by crystallization from the melt is to use for this purpose EBFZM method. Various materials can be successfully applied in industry to create structures, machine parts and devices only if they can be given in the required shape. Such shaping of crystalline materials may be done of the solid material (rolling, forging, shaping by cutting, *etc*.) and liquid phase (casting, welding). The shaping methods are now widely used to obtain polycrystalline products. Recently, in science and technology becoming more widely used are single crystals in the form of plates, tubes, rods of various sizes. In principle, the single-crystalline tube may be cut out from a bulk single crystal by mechanical or electrical discharge machining. However, using such kinds of processing, the single crystal will inevitably contain multiple structural defects that can alter the properties of the crystal in an unpredictable manner. For example, during the electroerosion cut of tungsten single crystals a network of cracks in the sub-surface layer occurs, and the dislocation density increases. Furthermore, such treatments are inefficient; too much of waste material is usually lost. The low economic efficiency and non-technological methods have led to search of alternative methods of getting profiled single crystals. Among them are plastic deformation, epitaxial growth from the gaseous phase, crystallization from a molten solution, crystallization from the melt. Advantages of the latter forming method consist mainly in the higher productivity and better quality (because of both the structure and properties) of the final product. Crystallization from the melt provides the most perfect structure and high purity of single crystals because of the contact-less melting with no contaminating material at the front of crystallization (*e.g.*, Czochralski method). However, due to the low stability of the capillary shaping this method can allows obtaining only products of the simplest form – the rods. Verneuil method, including plasma heating, allows obtaining single crystals of various materials in the form of tubes. It seems that the most suitable method for obtaining the tubular single crystals by crystallization from the melt is Stepanov method. The method consists in a capillary shaping of the column from the melt using a special shaper and its crystallization proceeds outside the container with the melt. Stepanov method has a significant margin of stability and enables the profiled metal and semiconductor crystals of high quality. A float zone method can also be used for crystallization of single crystal tubes from the melt. An

example of using this method to obtain tubes can be found in the monograph by Pfann [8]. In principle, the float zone methods may use any heating source, but the most suitable method to obtain the tungsten tubular single crystals with thin walls is floating zone method with electron-beam heating [60-62]. Until now, by the method of EBFZM from the melt were grown the most perfect and the purest single crystals of tungsten and other refractory metals. Crystals obtained by this method typically have a cylindrical shape. EBFZM method seems to be the most promising for growing shaped single crystals of tungsten and other refractory metals in the form of tubes. Growing tubular crystals of tungsten was done on the set-up for EBFZM. Tungsten tubular feeds which were produced by CVD had an outer diameter of 16 mm and a wall thickness of 1.5 mm (a diameter of feeds varies from 10 to 22 mm). Seeds for growing single crystals were cut from the tubular cylindrical tungsten single crystals with the growth axis [111] and [001] by electroerosion, followed by removal of the damaged layer. Tubular crystals were grown in a vacuum higher than 10^{-4} Pa and at the rate of 4 mm min^{-1}. A special tubular holder for the tubular feed and single crystal was developed (Figure 13).
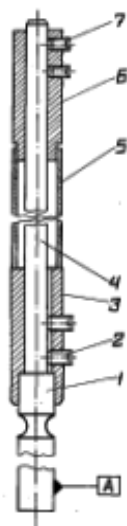
Figure 13. Device for growing tubular crystals.

The holder consists of the base *1*, support shanks *3* and *6*, the support rod *4*, mounting screws *2* and *7*. A small circular groove is performed on the base *1*, through which it is possible quick and accurate align of the tubular feed. Since melting tubular feeds has some specific features, the relationship between the height of the liquid zone stability at EBFZM and the wall thickness is studied. Some prolixity (blurring) of these two areas is possible due to the presence of destabilizing factors leading to local overheating in the zone: defects of cathode filament, oscillations of the impurity content in samples, as well as misalignment of the sample, cathode and focusing elements. A lower limit is due to the fact that an effect of the electron beam cutting is observed with increasing the current density of the electron beam. The obtained experimental dependence allows with sufficient reliability to pick up the electrical parameters of

melting using tubular specimens with the different diameters and wall thickness. In some cases, individual batches of feeds obtained by CVD have a high gas content which forced to resort to an additional step – the high-temperature vacuum annealing at pre-melting temperatures directly in the set-up. It turns out that without this preliminary operation the growth of tubular single crystals is impossible, since the escaping gases can tear off a liquid meniscus. A metallographic picture in Figure 14 shows the cross-section of the original CVD tubular feed after the above-described annealing operation (with partial melting). It shows also a clearly visible residual porosity. The assessment shows that for stable melting tubular feeds with a given wall thickness (from 0.5 to 1.5 mm) the zone height should be, respectively, from 2 to 4 mm. Naturally, these values meet the conditions of the focusing of the electron beam without local inhomogeneities in the density of the electron beam current.
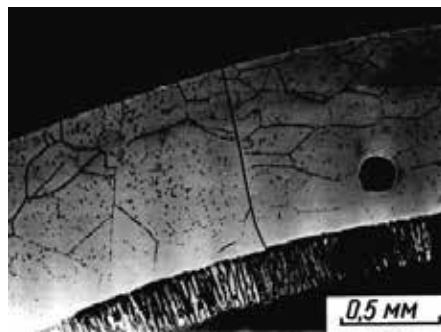
Figure 14. The cross-section of a tubular feed annealed.

The implementation of this condition is associated with great difficulties since it is necessary to supply large power to the tubular sample with a large radiating surface, which in turn affects the degree of superheating of the melt surface and the surface tension of the melt. Thus it is necessary to take into account the dependence of the stable zone height on superheating of the liquid metal, as well as decrease of viscosity of the liquid metal along with growing possibility of electron-beam cutting. Before the actual process of growing the tubular single crystal the radial heating by the filament of the electron gun should be carefully adjusted. The local density of the annular electron beam in either direction along the radius of no more than ±20% from the average current density, as shown in Figure 15.

When growing the tungsten tubular single crystals by seeding on a single crystalline seed of the desired crystallographic orientation, this operation is much more responsible than in the growth massive single crystals of cylindrical shape, since the presence of the slightest gap between the seed and the feed during welding them together can lead to rupture of the liquid meniscus. When growing tubular crystals without seeds, the grains from the base of the original CVD feed grow into the tubular crystal, and the high-angle boundaries tend to occupy the position of minimum energy, *i.e.*, they lie along the growth axis in diametrically opposite planes (Figure 16).
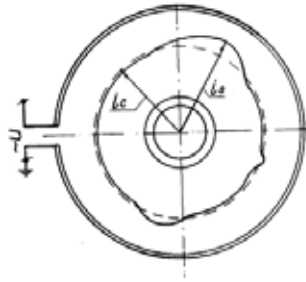
Figure 15. EB gun: optimal radial current density distribution.
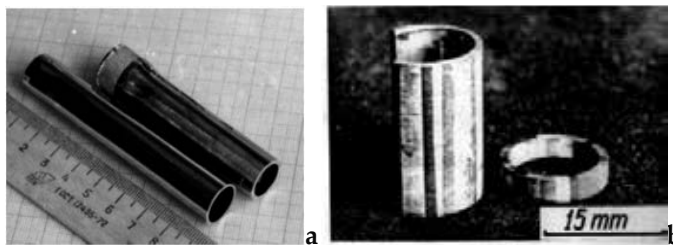
Figure 16. Single-crystalline (a) and polycrystalline (b) W tubes.

Thus obtained the polycrystalline tungsten tubes are very fragile and can be easily destroyed along the grain boundaries even from the weak strikes. When using the specially prepared single-crystal seeds it is possible to grow tubular single crystals of the length up to 180÷200 mm. The investigation of the real structure of the tubular single crystals of pure tungsten with the growth axes [111] and [001] is made by the metallographic and X-ray methods. In Figure 17 in the cross-section of the tubular single crystal, the low-angle boundaries are clearly seen, the majority of which begins and ends on the inner and outer surfaces of the tube.
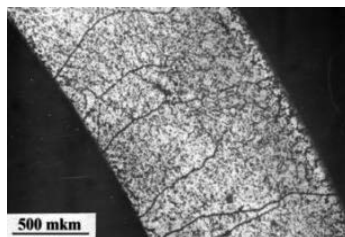
Figure 17. Low-angle boundaries in W tube crystal.

Subgrains originally contained in the seed have grown into a tubular single crystal, and their misorientation angles along the single crystal tend to be somewhat increased. A topogram of

angular scanning of the cross-section of the tubular tungsten single crystal with the growth axis [111] is shown in Figure 18.

Figure 18. Topogram of angular scanning of a cross-section of W tube crystal.

In the cross-section, there are several large subgrains of first order, separated by low-angle boundaries with the misorientation angles less than 1÷2°. Thus, the tungsten tubular single-crystals, obtained by EBFZM, at their crystallographic perfection are not inferior to the cylindrical tungsten single crystals obtained by the crystallization from the melt.

5.2. Features of capillary shaping in growing tubes

When growing single crystal at the initial portion of the tube at distances of about $(1.5÷2)R_1$, where R_1 is the outer radius of an initial feed, there is a portion of unsteady growth. The radius of the growing crystal is continuously changed until a steady-state mode. Figure 19 shows the process of growing the tubular sample on the stationary phase.
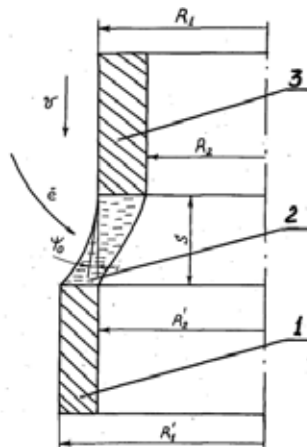
Figure 19. Growing a tubular W sample on the stationary phase: *1*-feed, *2*–meniscus, *3*–tube crystal.

By solving Laplace equation of capillary the connection of the outer and inner radii of the growing tube crystal can be found. Forming the tube crystal would be stable if the capillary

constant a will be higher than the wall thickness [62], $\sigma = 2500$ erg cm^{-2} (the surface tension of the liquid W) and $a = \sqrt{2\sigma/\rho g} = 0.54$ см (the capillary constant) [61]. In our case, the wall thickness of the initial feed is much less, and the fact that the height of the meniscus of the melt does not really exceed 3÷4 mm. So, it allows us, in a first approximation, to neglect by gravitational forces acting on the isothermal liquid meniscus. Using these simple limitations, it is posssible to obtain connection between the initial tubular feed and the growing crystal. In a steady state the growth angle φ_0 = Const and the tube crystal with a constant cross-section can grow. The mathematical profile description of the outer surface of the liquid meniscus is of considerable interest. Since the weight of the melt is neglected, then there is only a thin liquid film stretched between two rings with radii R_1' and R_1, spaced at a distance of S (the height of the meniscus). Now, the profile of the meniscus can be found, if Laplace equation will be written in polar coordinates:

$$\partial^2 H / \partial r^2 + (1/r)(\partial H / \partial r) = 0 \tag{5}$$

with boundary conditions $H(r)\big|_{r=R1} = 0; H(r)\big|_{r=R1'} = S$. Problem is completely analogous to the problem of electrostatics for potential distribution within the cylindrical capacitor, so the solution of the equation after some simple transformations can be written as $H(r) = C\ln(r/R_1)$. Here, $S = C\ln(R_1'/R_1); C = S/\ln(R_1'/R_1)$. As a result, the surface profile to have a liquid meniscus equation:

$$H(r) = S / \ln\left(R_1' / R_1\right) x \ln\left(r / R_1\right) \tag{6}$$

From which for the growth angle the equation can be written

$$\varphi_0 = \pi/2 - \text{arctg}(dH/dr\big|_{r=R1}) \text{ or } \varphi_0 = \pi/2 - \text{arctg}\left[S / \ln\left(\tfrac{R1'}{R1}\right) x \left(1/R_1\right)\right]. \tag{7}$$

The last equation can be written in a more convenient form:

$$S = \text{tg}(\pi/2 - \varphi_0) R_1 \ln R'_1 \tag{8}$$

Since the growth angle φ_0 is a constant of material, the last equation gives an unambiguous link between the outer radius of the feed and the outer radius of the tubular crystal growing at a given height of the liquid meniscus S. The ratio for the tube inner radius R_2 is obtained from the law of mass conservation of (the difference between the density of the feed and the crystal, and evaporation losses are neglected)

$$R_2 = \sqrt{R_1^2 - \left(R_1'\right)^2 + \left(R_2'\right)^2} \tag{9}$$

The results of calculations are shown in Figure 20. It can be seen that the radius of the growing tubular crystal can be controlled by changing the height of the meniscus depending on the change of the electron beam power.
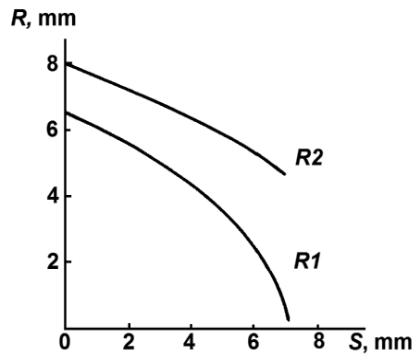
Figure 20. Dependence of radius of tube crystal on meniscus height.

The profile of the outer surface of the liquid meniscus is shown in Figure 21. According to measurements of the crystallized menisci the growth angle φ_0 is evaluated. For tungsten, it is found to be 20±5°, which is used in the calculations. It should be noted that in actual experiments, the height of the liquid meniscus S depends on many parameters: the initial feed geometry, thermal properties of material, power, focusing the electron beam, *etc*. In general, the quantity of S can be obtained by solving the experimental scheme of Stephen, but this is extremely difficult and hardly advisable. It should also be noted that the tungsten tubular single crystal grown by EBFZM have not only the high structural perfection, but also have even surfaces. The maximum height of the profile does not exceed ~100 microns. Shown that by EBFZM method the bicrystals with low-angle tilt and twist boundaries can be grown, and if the sub-boundary located in a plane parallel to the growth axis of the crystal grown, they can travel from the seed on considerable distances in the body of the crystal. Thus, the misorientation usually somewhat increases. This process takes place when low-angle boundaries in the given plane can be established by more or less complete combination of lattice dislocations.

It was shown that EBFZM method implemented at the new set-up, it is possible to grow single single-crystalline tungsten tubes of the high crystallographic and geometric perfection. This is due to the fact that the process of a capillary forming in the case, shown in Figure 19, has a high stability as repeatedly confirmed experimentally. Due to changes in the electron beam power it can be quite widely vary the height of the liquid meniscus S, *i.e.*, actually control of the diameter of the growing crystal. This gives us a hope that the process of growing single crystal tubes of refractory metals by EBFZM in perspective can be automatic that is particularly necessary in the case of the serial production of such products. Currently, the process of growing tubes by an operator control, which actually measures the relevant parameters: the meniscus height S and diameter of the growing tubular crystal $2R_1$ "by eye", which is totally
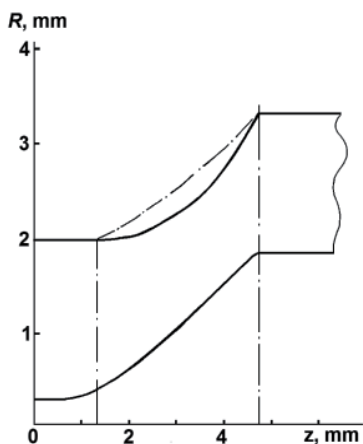
Figure 21. Inner and outer profiles in the feed-melt-crystal system.

inadequate in the sense of obtaining single-crystal tubes of specified geometrical sizes. Furthermore, if the growth process is in a stationary stage, and power of the electron beam with a high accuracy (±0.5% for setting "area") is maintained at a constant preset level, it does not mean that the crystal will grow of a constant cross-section. The shank and the free end of the tubular feed influence on the heat transfer from the liquid meniscus portion. As a result of change of the meniscus height S, and hence change of the diameter of the growing crystal is happened. The latter leads to presence in the tubular single crystal tapers of both signs. This is clearly seen in Figure 22. Obviously, the taper can be eliminated by an automatic control system of the growth process. For example, in growing single crystals of semiconductor materials by Czochralski or Stepanov such automatic systems are already widely used [7]. It should be noted that such a process parameter to measure the height of the meniscus is in any way unlikely. Measuring the diameter of the growing crystal is possible by means of an optical system or a TV monitor. The resulting signal from the sensor of the diameter is then used to synthesize an appropriate control signal to an analog control unit or microcomputer. One of the important parameters of the automatic control system is its speed. Obviously, in the case of growing tubes by EBFZM this value should be much smaller than the thermal time constant of the thermal process zone (the crystal plus the corresponding accessories). Since, as previously shown, the taper in mostly due to change of heat removal by conduction, it is possible to obtain the following estimate for the time constant of the form: $\tau = Q/\chi$, where, χ the thermal diffusivity, $cm^2 s^{-1}$; Q the cross-section of the crystal, cm^2. For the tungsten tubular single crystal with the outer diameter of 16 mm, the wall thickness $\delta = 2$ mm and the registered thermal time constant yields to $\tau = 4$ s. Therefore, the creation of ACS for growing tubes by EBFZM with the rate much less than 4 s do not represent currently any technical difficulties. The system would eliminate defects like geometric tapers and grow single crystalline tubes of refractory metals by EBFZM with a deviation of the inner and outer diameters from the nominal value within ±200 microns, and getting these products on an industrial scale.
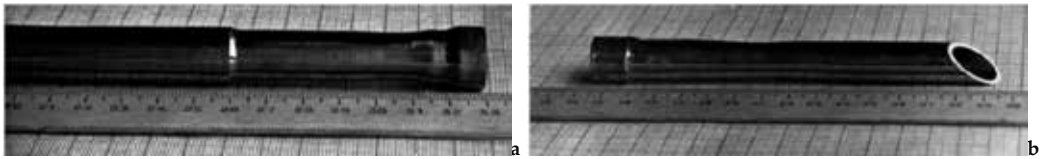
Figure 22. W tubular single crystals with a growth axis [111], comprising one-two runs (a) and a tapering defect in the middle (b).

6. Key findings

1. The method is developed of growing bicrystals of refractory metals up to 150-200 mm in diameter and 15-25 mm with the desired crystallographic parameters - of misorientation angles and both the grain boundaries and bedding planes of boundaries. The method is based on stability and radial uniformity of power supplied to the sample by an electron gun, co-axiality of the growing bicrystal and the electron gun, and the uniformity of heat removal from the growing bicrystal. Proposed and tested three methods of preparing bicrystalline seeds allow to grow bicrystals of niobium, molybdenum and tungsten with crystallographic parameters within 1-2°. Shown that by EBFZM method can be grown the bicrystals with desired low-angle tilt and twist boundaries, and if sub-boundary is located in a plane parallel to the growth axis of the crystal grown, they can travel from the seed on considerable distances in the body of the crystal. Thus the misorientation usually somewhat increases. This process takes place when the small-angle boundary in the given plane can be established by more or less complete combination of lattice dislocations. It is shown that a new set-up meets the most stringent requirements to the electron-beam zone melting set-ups for the radial uniformity of heating, power stability, and production efficiency.

2. The thirty-years experience of growing single crystals, bicrystals, and tubular crystals with desired crystallographic parameters and geometry have shown that the developed EBFZM set-ups together with new electron-beam guns are of the successful design. They give an excellent possibility to grow any of single-crystalline samples of transition metals of diameter from 4 to 30 mm. These opportunities are determined primarily by the original circular electron guns for growing crystals of different diameters. The electron guns themselves have no restrictions in duration of their work and life and are essentially "eternal". Single crystals grown of all studied transition metals satisfy the highest requirements for both the chemical purity and structural perfection. Duration of the circular tungsten cathodes made of tungsten wire with a diameter of 0.8-1 mm is longer than 100 hours. Growing crystals up to 600 mm long is provided by the design of EBFZM set-ups. The main principle of designing the set-ups is the co-axiality of the cathode and anode assemblies throughout the whole length of the growing crystal. In other words, the geometric and thermal centers of the crystal and the melt should be matched, as well as

high precision of moving mechanisms of both the anode and cathode assemblies and offset buckling and vibration as result of thermal effects.

3. Proposed and tested three methods of preparing bicrystalline seeds to grow bicrystals with controlled crystallographic parameters of high accuracy (up to 1-2°). The fracture strength of high-angle tilt and twist boundaries in the pure molybdenum bicrystals is low; special boundaries differ markedly from other boundaries on their strength: twin boundaries are several times stronger and boundaries with small numbers of coincident nodes have the lowest strength. The contents of interstitials at boundaries of high-angle misorientation, according to Auger electron spectroscopy, almost tenfold higher than their content in the grain volume. However, increasing the purity of molybdenum on interstitials does not lead to change in the fracture strength of grain boundaries. Shown that by EBFZM method can be grown bicrystals with low-angle tilt and twist boundaries.

4. Our results have shown that the combination of bicrystalline samples and low-energy ions scattering (LEIS) is very fruitful. The experimental results show that using bicrystals in combination with LEIS opens new possibilities for studying properties of surfaces. Experimentally shown that the LEIS signal intensity from the different crystallographic surfaces of molybdenum bicrystals is defined by both the atomic density of the uppermost atomic layer and its structure. Contributions of second and deeper layers in the LEIS signal are very small (<2%). After bombardment by the Ne^+ ions with energy of 3 keV and different ion doses (from 7×10^{15} to 4×10^{16} ion cm^{-2}) with current of 6×10^{12} ion cm^{-2} c^{-1}, the difference between the LEIS signal intensities for molybdenum planes Mo(110) and Mo(100) remain at 10%, indicating partial damage of the surface. Rather, at such ion fluxes sputtering the surfaces occurs layer-by-layer. Our studies have shown that the processes can also be examined using the self-diffusion method of LEIS as the LEIS signal may be to some extent an indication of damage of the surface. Using this method the study of properties of the surface recrystallization can also be conducted. We have found that recrystallization of molybdenum surface Mo(110) begins at 750°C and of ~Mo (100) - at about 1300°C, indicating the different mobility of atoms in the uppermost atomic layers of different crystallographic orientations surface. Moreover, the LEIS signal intensity of the surface Mo(110) during sputtering drops to 75% of its initial level (for a clean surface free of damage), and of Mo(100) – to 90% only. It follows that the close-packed surface structure is more sensitive to these influences, which may be attributed to its low free energy.

5. The growing technology of tubular tungsten single crystals by EBFZM is developed. It is shown that capillary shaping of the tube crystals is stable. A crystallographic perfection of tungsten tubular single crystals is not inferior to the cylindrical single crystals, obtained by EBFZM. This is due to the fact that capillary forming is of high stability what is confirmed experimentally. Due to changes in power the height of the liquid meniscus can be widely varied what is very important to check the diameter of growing tubular crystals. This gives a hope that growing single crystalline tubes of transition metals by EBFZM can be automatic in perspective.

Acknowledgements

Author details

Vadim Glebovsky[*]

Address all correspondence to: glebovs@issp.ac.ru

Institute of Solid State Physics, the Russian Academy of Sciences, Russia

References

[1] Chernov A.A., Givargizov E.I., Bagdasarov H.S., Kuznetzov V.A., Demyanetz P.N., Lobachev A.N. The Contemporary Crystallography. Moscow: Nauka, 1980.

[2] Laudise, R. A., Parker R.L. The Growth of Single Crystals. Moscow: Mir, 2010.

[3] Parker, R. L. Crystal Growth Mechanisms: Energetics, Kinetics and Transport. New York: Academic, 1970.

[4] Ullhoff M.K. Shape and Stability of Menisci in Czochralski Growth and Comparison with Analytic Approximation. Journal of Crystal Growth 1975;30(1) 9-20. DOI: 10.1016/0022-0248(75)90192-X.

[5] Hurle D.T. Control of Diameter in Czochralski and Related Crystal Growth Techniques. Journal of Crystal Growth 1977;42 473-482. DOI: 10.1016/0022-0248(77)90233-0.

[6] Langer J.S. Instabilities and Pattern Formation in Crystal Growth. Revue of Modern Physics 1980;52(1) 1-28.

[7] Savitsky E.M., Burkhanov G.S. Growth of Single Crystals of High Melting Metal Alloys and Compounds by Plasma Heating. Journal of Crystal Growth 1978; 43(4) 616-624. DOI: 10.1016/0022-0248(78)90343-3.

[8] Pfann W.G. Zone Melting (2nd Edition), New York, 1966.

[9] Tiller W.A. The Science of Crystallization: Macroscopic Phenomena and Defect Generation, Cambridge University Press, 1991. ISBN 978-0-521-38828-3.

[10] Tiller W.A. The Science of Crystallization: Microscopic Interfacial Phenomena, Cambridge University Press; 1991. ISBN 978-0-521-38827-6.

[11] Buckley-Golder J.M., Hurphreys C.J. Theoretical Investigation of Temperature Distribution during Chochralski Crystal Growth. Philosophical Magazine 1979; 39(1) 41-57. DOI:10.1080/01418617908239274.

[12] Kobayashi N. Power Required to Form a Floating Zone and the Zone Shape. Journal of Crystal Growth 1978; 43(4) 417-424. DOI: 10.1016/0022-0248(78)90339-1.

[13] Kobayashi N., Wilcox W.C. Computational Studies of Convection in a Cylindrical Floating Growth. Journal of Crystal Growth 1982; 59(3) 616-624. DOI: 10.1016/0022-0248(82)90385-2.

[14] Wilcox W.R., Fuller L.D. Turbulent Free Convection in Czochralski Crystal Growth. Journal of Applied Physics 1965;36 2201-2205.

[15] Barthel J. Hydrodynamics of the Melt in Zone Floating and its Influence on Single Crystal Perfection. In: ISSCG-4, Moscow, 1980;1: p203-267.

[16] Dash W.C. Silicon Crystals Free of Dislocations. Journal of Applied Physics 1958; 29: 736-737.

[17] Nes E., Most W. Dislocation Densities in Slow Cooled Aluminum Single Crystals. Philosophical Magazine 1966;13(124) 855-859.

[18] Akita H., Sampare D.S., Flore N.F. Substructure Control by Solidification Control in Copper Crystals. Metallurgical Transactions 1973;4 1593-1597.

[19] Cole M., Fisher D.S., Bucklow J.A. Improved Electron Beam Device for Zone Melting. British Journal of Applied Physics 1961;12(10) 577-578.

[20] Glebovsky V. Crystal Growth: Substructure and Recrystallization. In: Recrystallization, Ed. K. Sztwiertnia, Rieka: InTech, 2012. ISBN 978-953-51-0122-2.

[21] Glebovsky V.G., Lomeyko V.V., Semenov V.N. Unit for Electron-beam Zone Melting of Refractory Materials. Journal of Less-Common Metals 1986;117 385-389. DOI: 10.1016/0022-5088(86)90064-0.

[22] Glebovsky V.G., Semenov V.N., Lomeyko V.V. Influence of the Crystallization Conditions on the Structural Perfection of Molybdenum and Tungsten Single Crystals. Journal of Crystal Growth 1988; 87(1) 142-150. DOI:10.1016/0022-0248(88)90353-3.

[23] Glebovsky V.G., Kopetsky C.V., Myshlyaev M.M., Romanov Y.A. Steady-state Creep and Dislocation Structure of Molybdenum. Physics of Metals & Metallography 1976;41(3) 150–158.

[24]   Myshlyaev M.M., Romanov Y.A., Senkov O.N., Khodos I.I., Glebovsky V.G. High Temperature Creep and Dislocation Structure in Tungsten Single Crystals. Problemy Prochnosty 1979;5 26-34.

[25]   Aristov V.V., Shmytko I.M., Shulakov E.V. Application of the X-ray Divergent-beam Technique for the Determination of the Angles between Crystal Blocks. I. Reflexion from the planes parallel to the crystal surface. Journal of Applied Crystallography 1974; 7(4) 409-413. doi:10.1107/S0021889874010028.

[26]   Fromm E., Gebhardt E. Gase und Kohlenstoff in Metallen. Berlin. 1976.

[27]   Glebovsky V.G., Kazantsev A.M., Pronman I.M., Shipilevsky B.M. Investigation of oxygen distribution in Nb single crystals by the method of fast-neutron activation. Physics of Metals & Metallography 1980;49(3) 130-136.

[28]   Glebovsky V.G., Kapchenko I.V., Kireyko V.V., Oblivantsev A.N., Rybasov A.G. The behaviour of Oxygen and Carbon in the Process of Electron Beam Zone Melting of Niobium. Journal of Crystal Growth 1986;74(3) 529-534. DOI: 10.1016/0022-0248(86)90198-3.

[29]   Gantmacher V.F., Petrashev V.T. Scattering of Conduction Electrons on Pure Metals. In: Metals of High Purity. Moscow: Nauka, 1976; 31-35.

[30]   Gust W., Hirtz M.B., Predel B., Roll U. Techniques for the Production of Oriented Bicrystals and Results on Specimens Prepared by these Methods. Acta Metallurgica 1980; 28(9) 1235-1244.

[31]   Yastrebkov A.A., Ivakin Y.P. Influence of the Misorientation Angle on Strength of Intergranular Boundaries of Molybdenum. Physics of Metals & Metallography 1975; 40(3) 594-598.

[32]   Clough S.P., Vonk S.J., Stein D.F. Preparation of Oriented Molybdenum Twist Boundaries by Electron-beam Zone Melting. Journal of Less-Common Metals 1976; 50(1) 161-163.

[33]   Liu J.M., Shen W.-W. Grain Boundary Fracture in Tungsten Bicrystals. Acta Metallurgica 1982; 30(6) 1197-1202.

[34]   Glebovsky V.G., Sursaeva V.G., Semenov V.N. The Strength of Individual Grain Boundaries of High Purity Molybdenum. In: Int. High Purity Materials in Science and Technology, Dresden, 1985, p.337-338.

[35]   Cai B.C., Dasgupta A., Chou Y.T. A New Technique for the Growth of Bicrystals of Refractory Metals. Journal of Less-Common Metals 1982;86 145-151.

[36]   Pande C.S., Lin L.S., Bulter S.R., Chou Y.T. Use of Floating Zone Melting Technique for the Growth of Niobium Bicrystals. Journal of Crystal Growth 1973;19(5) 209-210. DOI: 10.1016/0022-0248(73)90112-7.

[37] Glebovsky V.G., Moskvin S.I., Semenov V.N. Growing Techniques and Structure of Niobium Bicrystals. Journal of Crystal Growth 1982;59 450-454. DOI: 10.1016/0022-0248(82)90366-9.

[38] Brehm W.P., Gregg I.L. Growth of Oriented Nb Bicrystals by Arc-Zone Melting. Journal of Less-Common Metals 1968;14 463- 465. DOI: 10.1016/0022-5088(68)90171-9.

[39] Brosse J.B., Fillit R., Biscondi M. Intrinsic Intergranular Brittleness of Molybdenum. Scripta Metallurgica 1981;15(6) 619-623.

[40] Kobylanski A., Goux C. Sur la Fragilite Intergranulaire du Molybdene Etudiee l'aide de Bicristaux de Flexion Symetrique autmur de Laxe [001]. C.R.Acad.Sc.Paris 1971;272(C) 1937-1940.

[41] Reid C.N. Dislocation Widths in Anisotropic bcc Crystals. Acta Metallurgica 1966;14 13-16.

[42] Kurishita H., Yoshinaga A. The Strength of Grain Boundary in Molybdenum. Japan Materials Science, Japan 1980;17 239-240.

[43] Kumar A., Eyre B.L. Grain Boundary Segregation and Intergranular Fracture in Molybdenum. Progress of Royal Society A, London 1980;370 431-458.

[44] V.G. Sursaeva, V.G. Glebovsky, V.N. Semenov, C.V. Kopetsky, Y.M. Shulga, L.S. Shvindlerman. Strength of Intergranular Tilt and Twist Boundaries in Molybdenum Bicrystals. Physics of Metals & Metallography 1985;59(4) 166-173.

[45] Vinnikov L.Y., Glebovsky V.G., Moskvin S.I. Vortex Pinning in Nb Bicrystals. JETP Letters 1981;33 239-243.

[46] Glebovsky V.G., Lomeyko V.V., Moskvin S.I., Semenov V.N., Vinnikov L.Y. Growth and Structure of Niobium Bicrystals. Physics of Metals & Metallography 1982;54(4) 137-140.

[47] V.G. Sursaeva, V.G. Glebovsky, Y.M. Shulga, L.S. Shvindlerman. Strength of Individual Special Tilt and Twist Boundaries in Molybdenum Bicrystals. Scripta Metallurgica 1985;19 411-414.

[48] Mishlyaev M.M.,Khodos I.I., Senkov O.N., Romanov Y.A. Features of Dislocation Structure of Interblock Boundaries in bcc Single Crystals. Physics of Metals & Metallography 1980; 48(1) 148-157.

[49] Yastrebkov A.A., Ivakin Y.P. Influence of Misorientation Angle on Brittleness of Tungsten Bicrystals. Physics of Metals & Metallography 1973;36 135-139.

[50] Sosnina E.I., Matvienko L.F., Meleshko L.I. Growth anisotropy of misorientations and the symmetry of substructure boundaries in alloyed single crystals of molybdenum and tungsten. Physics of Metals 1981;3(2) 101-110.

[51] Ermolov S.N., Jansen W.P.A., Markin S.N., Glebovsky V.G., Brongersma H.H. Surfaces of Mo Bicrystals Studied by Low Energy Ion Scattering. Surface Science 2002;512 221-228. DOI: 10.1016/S0039-6028(02)01663-1

[52] Ermolov S.N., Glebovsky V.G., Jansen W., Markin S.N., Brongersma H.H. Study of Mo Bicrystals by Low Energy Ion Scattering. Izvestiya RAS, Fizicheskaya Seriya 2002;66(4) 580–585.

[53] Sutton A.P., Baluffi R.W. Interfaces in Crystalline Materials. Oxford: Clarendon Press, 1995.

[54] Cortenraad R., Ermolov S.N., Moest B., A.W. Denier van der Gon, Glebovsky V.G., Brongersma H.H. Crystal Face Dependence of Low Energy Ion Scattering Signals. Nuclear Instruments & Methods in Physics Research B 2001;174(1-2) 173–180. DOI: 10.1016/S0168-583X(00)00452-3.

[55] Cortenraad R., A.W. Denier van der Gon, Brongersma H.H., Ermolov S.N., Glebovsky V.G. On the Quantification of the Surface Composition of Low Work Function Surfaces Using Low Energy Ion Scattering. Surface & Interface Analysis 2001;31 (3) 200–205. DOI: 10.1002/sia.972.

[56] Bergmans R.H. Energy and Angle Resolved Ion Scattering and Recoiling Spectroscopy on Bimetallic Systems. PhD Thesis. Eindhoven University of Technology, Eindhoven, The Netherlands, 1996. ISBN 90-386-0057-7.

[57] Glebovsky V.G., Semenov V.N., Lomeyko V.V. Peculiarities of the Growth and Structure of Pure Tungsten Tubular Polycrystals and Single Crystals. Visokochistie Veschestva (High Purity Materials) 1988;5 37-41.

[58] Glebovsky V.G., Semenov V.N., Lomeyko V.V. The Characteristic Features of Growth and the Real Structure of Tungsten Tube Crystals. J. Crystal Growth 1989;98(2) 487-491. DOI: 10.1016/0022-0248(89)90165-6.

[59] Glebovsky V.G., Semenov V.N., Lomeyko V.V. On the Problem of Growing Tungsten Single-Crystalline Tubes from the Melt. Vacuum 1990;41 2165-2166. DOI: 10.1016/0042-207X(90)94214-B.

[60] Surek T, Cornell S.R., Chalmers B. The Growth of Shaped Crystals from the Melt. Journal of Crystal Growth 1980;50(1) 21-32. DOI: 10.1016/0022-0248(80)90227-4

[61] Fogel A.A. HF Induction Levitation of Liquid Metals. Leningrad: Mashinostroenie. 1989.

[62] Eriss l., Stormont R.W., Surek T., Taylor A.S. The Growth of Silicon Tubes by EFG process. Journal of Crystal Growth 1980;50(1) 200-211. DOI: 10.1016/0022-0248(80)90244-4.

Calcium Ferrit Generation During Iron Ore Sintering — Crystallization Behavior and Influencing Factors

Min Gan, Xiaohui Fan and Xuling Chen

1. Introduction

Iron ore sintering is a heat treatment process for agglomerating fine particles into larger lumps, which then serve as the major burden for blast furnace. The production of high-quality sinter is critical for efficient blast furnace operation [1-3].

Sintering is a complex process involving, as it does, many interrelated physico-chemical phenomena pertaining to flow of gas through the bed of packed granules, heat transfer between gas and solids, chemical reactions between components of the sinter feed and between solid components and gas, etc. Mineralization reaction mainly occurs in preheating layer, combustion layer and initial cooling layer during the sintering process, which is reflected by the ability of solid-phase reactions, the capacity for the generation of liquid phase and the behavior of condensation and crystallization [4,5].

Crystalline condensation is the significant stage of mineralization during iron ore sintering, including the processes that crystalline substance and amorphous substance precipitate from high temperature solution phase, and material is consolidated when melt cooling down. Binder phase of calcium ferrite and part of iron oxides crystallize in this process, which have an important influence on mineral composition and microstructure of sinter, finally determine the sinter strength and metallurgical properties [6-9].

Calcium ferrite has special features such as good intensity, excellent reducibility and low formation temperature, which is suitable for developing low-temperature sintering, improving the qualities of sinter and reducing energy consumption. Crystalline condensation is a key stage to the forming and developing of calcium ferrite, which directly affects its precipitation behavior and crystalline morphology [10-16]. In the paper, the microstructure characteristics of sinter are analyzed, and crystalline condensation mechanism of calcium ferrite binder phase

system based on minerals' precipitation behavior and crystallization condition are studied, also the major factors influencing the generation of calcium ferrite are discussed, which provide theoretical support on improving microstructure of sinter and optimizing its quality.

2. Materials and methods

2.1. Properties of materials

The chemical compositions of raw material for mini-sintering are summarized in Table 1. This mineral, which belongs to oxidized ore, has high iron grade, low gangue content, and the ratio of Total Iron (TFe) to FeO is much higher than 3.5. The chemical, flux (calcium oxide), and the additive (Al_2O_3, SiO_2), is analytic grade reagent.

Raw material	TFe	FeO	CaO	MgO	SiO_2	Al_2O_3	LOI
Iron ore	64.94	0.86	0.03	0.01	3.78	0.77	1.67

Table 1. The chemical compositions of raw material wt/%

2.2. Methods for mini-sintering

Mini-sintering test was used to research the mineralization reactions, such as liquid generation, crystallization behaviour, ect., under high temperature. Horizontal heating furnace whose temperature and atmosphere could be controlled by program was adopted to conduct mini-sintering experiment. The device of mini-sintering was shown in Fig.1.
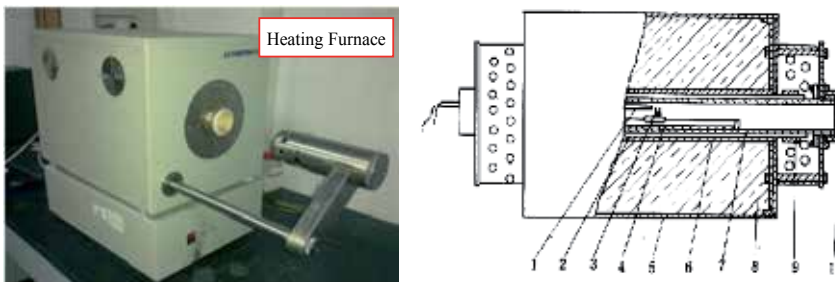
1—thermocouple；2—Silicon tube；3—standard pyrometric cone；4—corundum porcelain boat to load the cone；5—furnace shell；6—outer thimble of corundum；7—inner sleeve of corundum；8—insulating brick of bubble alumina；9—panel piece；10—peep door

Figure 1. The device of mini-sinter test

In order to simulate sintering process exactly, this experiment divided sintering process into preheating belt, reaction belt, melt belt, solidification belt and sintered belt. On the basis of

physicochemical characteristics of each belt and the actual temperature curve of sintering bed, the heating program and atmosphere simulated were shown in Table.2.

	Temperature/℃	Heating up time /min	Atmosphere
Preheating belt	60 → 700	1	N_2
Reaction belt	700 → 1200	1	$CO:O_2:CO_2=1:1:5$
Melt belt	1200 → 1300	With rate the of 10℃/min	$CO:O_2:CO_2=1:1:5$
Solidification belt	1300 → 1000	2	Air
Sintered belt	1000 → 700	1	Air

Table 2. The heating program and atmosphere of mini-sintering
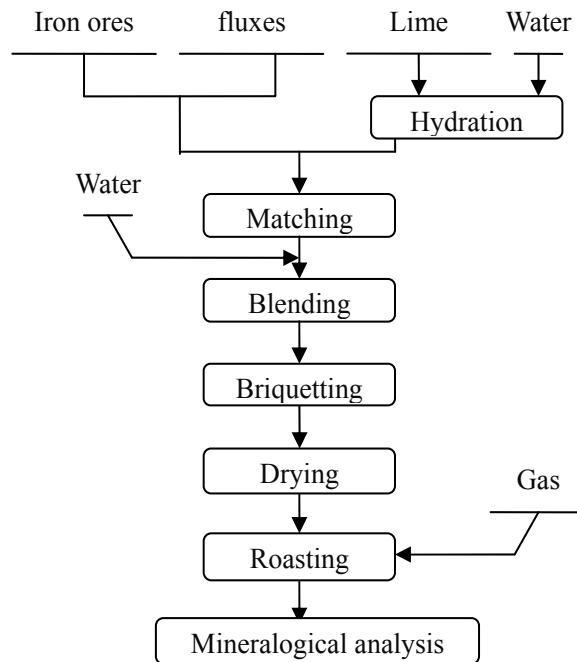
Figure 2. Experimental flow of mini-sintering

The research regarding the formation behavior of SFCA ((Quaternary compound of calcium ferrite containing silicate and alumina) was adopted mini-sinter. The steps of testing mineralization were agglomeration, roasting and mineralogical analysis. The experimental flow is shown in Fig.2.

After ore blended, the mixture was compacted into a cylinder with the size of Φ30×25mm under the pressure of 300kg/cm² for 1 min. Then the cylinders were sintered at 1280~1300℃ according

to the heating programs in Table.1. The sintered sample was used to observe the mineralization of sintering mixture. The agglomerates were mounted with epoxy resin, and then polished to form a section, which the microstructures were observed by optical microscope and SEM, and mineral components were detected by image analysis software.

Columnar&acicular SFCA was defined as the ratio of length-diameter was bigger than 2.5. The graphic processing software could recognize the SFCA and figure out its content. The process consisted of image reading, image filtering, identification and segmentation, length-diameter ratio detection, and statistics of selected area.

2.3. Sinter pot test

A 700 mm deep×Φ 180 mm sinter pot was utilised to simulate sintering process, and its schematic diagram was demonstrated in Fig.3.
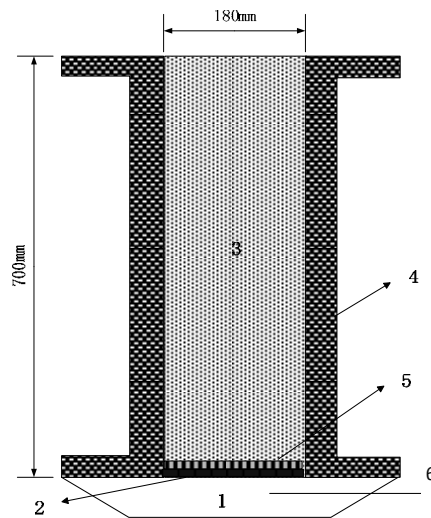
1 vacuum chamber; 2 refracory grate; 3 mixed raw materials;

4 stainless sinter pot; 5 hearth layer;6 thermocouple

Figure 3. Schematic diagram of laboratory sinter pot

Raw materials having been blended and granulated were charged into the sinter pot. Under the mixtures, a hearth layer of approximate 20mm thick was previously prepared to protect the grate from thermal erosion. After charging, the fuel in the surface layer was ignited by an ignition hood initially, and then the combustion front moved downwards with the support of downdraught system, which was mainly a draught fan used to enable sufficient air to be sucked into sinter pot from top.

Apart from that, sintering speed, yield, tumbler index, productivity etc. were detected to evaluate sinter quality. Sintering speed was the ratio of layer height and sintering time, and

yield was the percentage of sinter above 5mm after screening. Productivity reflected the quantity of sinter produced unit area and unit time. Tumbler index, which could reflect sinter strength, was the percentage of sinter above 6.3mm after 7.5kg sinter was tested in a Φ1000×500mm tumbler for 200r.

3. Formation characteristics of calcium ferrite

3.1. Mineralization model for sintering

The mineralization behavior of sintering mixtures in different temperature has been re-searched, as is shown in Fig.4. When the temperature is at 1100-1150℃, solid-phase reaction occurs, but it was not obvious because of the slow reaction speed. Then when the temperature increases to 1200℃, a large number of CF generate by solid-phase reactions. As the temperature reaches to 1225-1250℃, the liquid phase generates obviously and the holes begin to shrink. Liquid content is developed when the temperature increases to 1300℃. At the temperature of 1300℃, the main mineral constituents are CF, secondary magnetite and hematite.

（a）1100℃；（b)1150℃；（c）1200℃；（d）1225℃；（e）1250℃；（f）1300℃
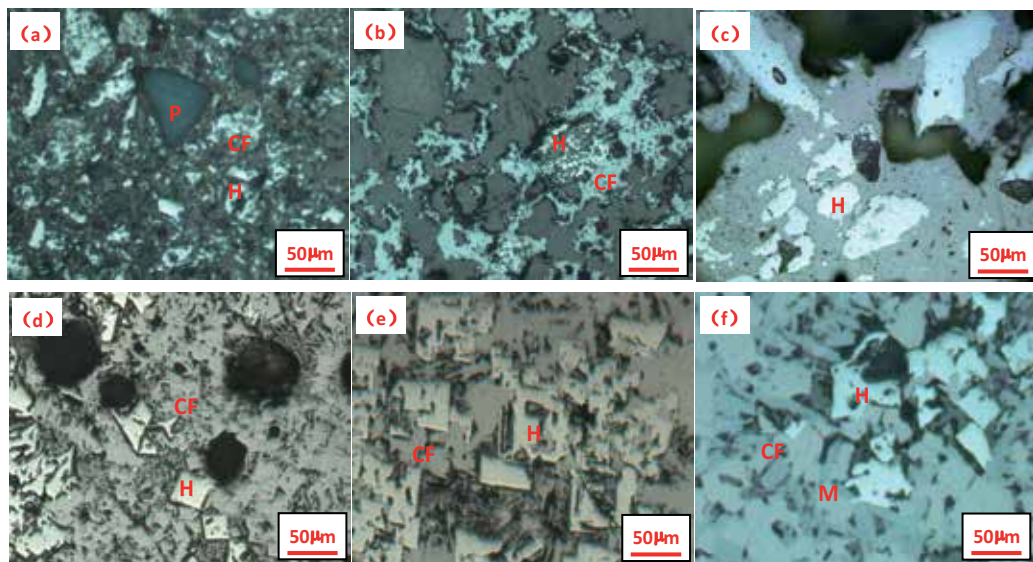
H—hematite，M—magnetite，CF—calcium ferrite，P—pole

Figure 4. Effect of temperature on mineralization of mixture

So, with the increase of the temperature during sintering, reactions occur between fine particles of iron ores and fluxes to form low-melting compounds and then generate liquid phase, but iron ore nuclei almost would not participate in the reaction for its low reacting speed. As the

temperature rises continually, the amount of liquid phase is increased and the fluidity of liquid improved. In the process of temperature-fall, crystals start to form with the condensation of liquid phase. Therefore, the macrostructure model of sinter can be divided into two parts, the melt zone and unfused ores, which is composed of the melt bonding the unfused ores together (as shown in Fig.5).
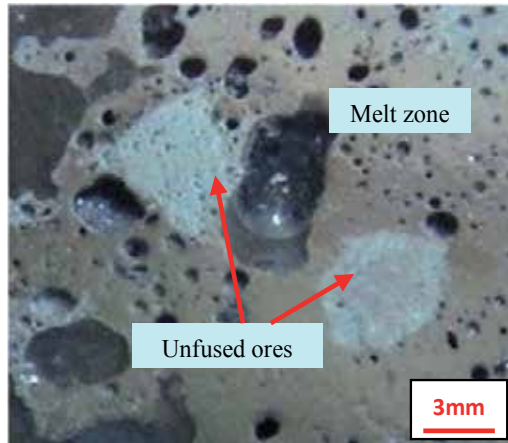
Figure 5. The structure of sinter

3.2. Microstructure of sinter

The microstructures of sinter were studied (Fig.6). The minerals in unfused ores are relatively simple, mainly for iron oxides, and its structure is relatively dense. Melt zone as the product of liquid condensing and crystallization, a variety of substances are precipitated during cooling process, and holes formed due to the shrinkage of liquid phase.
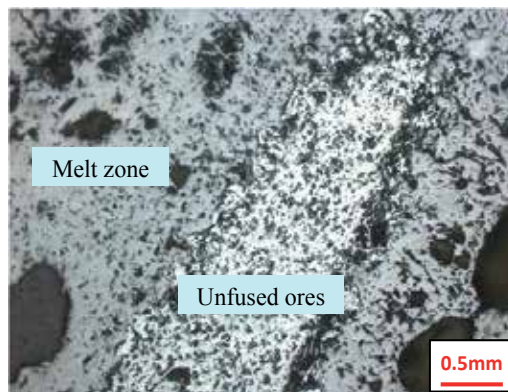
Figure 6. The Microstructure structure of sinter

The microstructures of melt zone are mainly divided into 3 kinds, corrosion structure of magnetite and CF, eutectic structure of CF and silicate, and pilotaxitic texture of hematite and CF, as shown in Fig.7. It's shown that the melt zone of sinter mainly presents as the corrosion structure of magnetite and calcium ferrite, which accounts for 80%-90% in melt zone. And a few partial areas rich in porosity present as mixed structure of hematite and calcium ferrite, or the eutectic structure of calcium ferrite and silicate. So, SFCA is the most important bonding phase in melt zone.
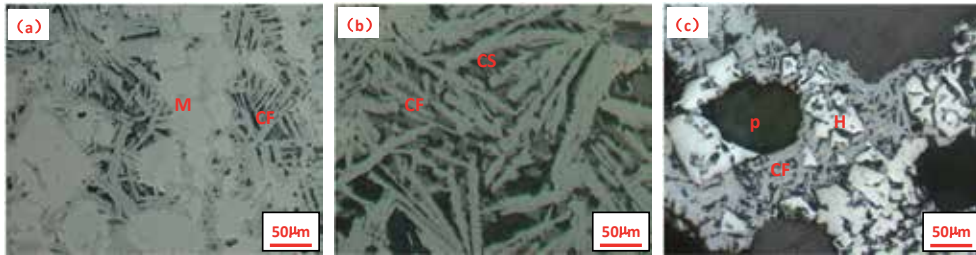
(a) corrosion structure of magnetite and CF, (b) eutectic structure of CF and silicate, (c) pilotaxitic texture of hematite and CF;H—hematite, M—magnetite, CF—calcium ferrite, CS—silicate, P—pole

Figure 7. Microstructures of melt zone

3.3. Morphology characteristics of calcium ferrite

According to the difference in the characteristics of calcium ferrite, they can be divided into four types of morphology, including plate-type, sheet-type, columnar-type, and acicular-type, which are shown in Fig.8. The chemical compositions of four kinds of calcium ferrite were studied, and the fracture toughness of different morphology of calcium ferrite was tested.

The results of energy spectrum analyses and fracture toughness tests for different types of SFCA are shown in Table 3. It can be seen that SFCA of acicular-type and columnar-type have lower Fe_2O_3 content than plate-type and granular-type, but higher contents of Ca and Si. There was no obvious difference in the content of Al_2O_3 among four structures, while SFCA of columnar& acicular-type has lower content of MgO than plate& sheet-type. The components of columnar-SFCA is closed to calcium diferrite ($\omega(CaO) = 14.9$), and acicular-SFCA has a relative component between calcium diferrite and the eutectic chemicals of $CaO \cdot Fe_2O_3$-$CaO \cdot Fe_2O_3$.

Fracture toughness was used to measure the microstrength of various types of SFCA. As shown in Table 3, the order of the strength of four kinds of SFCA is acicular-type>columnar-type>sheet-type>platy-type, while the strength of the sheet-type and plate-type are close, as well as the plate-type and sheet-type. Due to their similar strength, acicular-type and columnar-type are named as columnar&acicular-type, as well as the plate&sheet-type. The corrosion structure of magnetite and the columnar&acicular-type is the best microstructure with the highest strength.
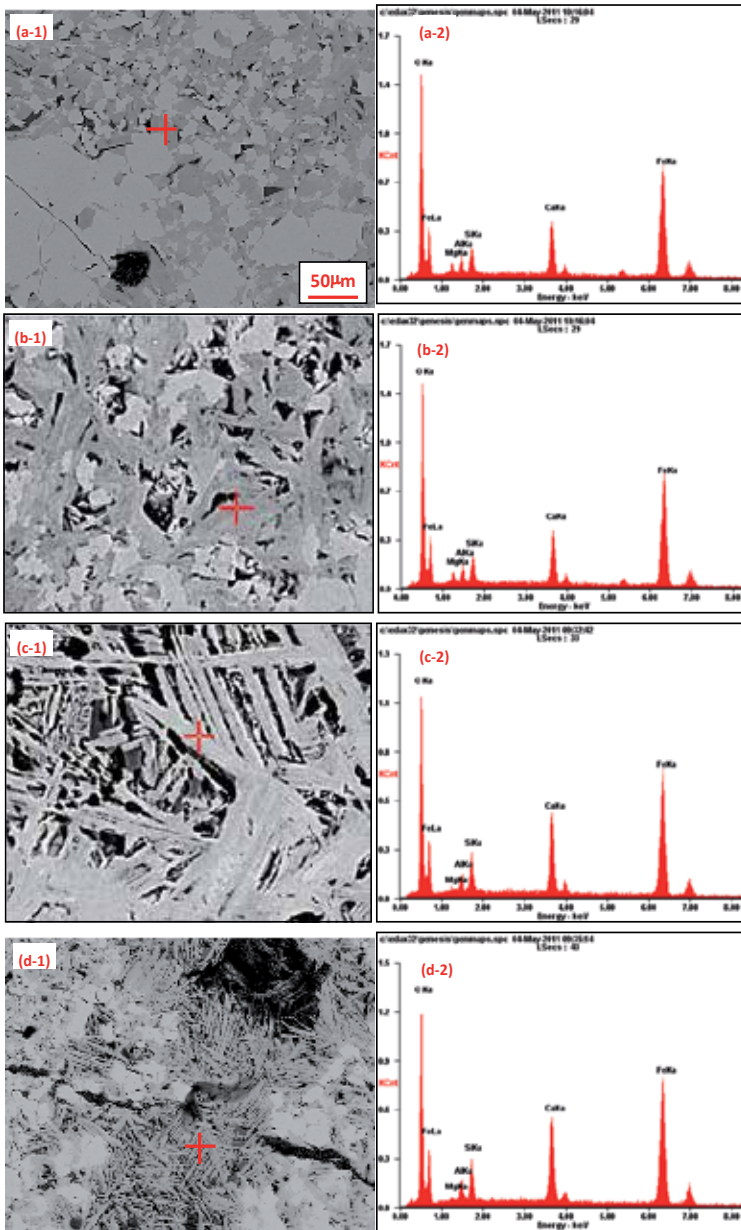
(a-1) Platy SFCA of SEM;(b-1) Sheet SFCA of SEM;(c-1) Columnar SFCA of SEM;(d-1) Acicular SFCA of SEM

(a-2) Platy SFCA of EDS;(b-2) Sheet SFCA of EDS;(c-2) Columnar SFCA of EDS;(d-2) Acicular SFCA of EDS

Figure 8. The structural morphology of SFCA

Consequently, increasing the content of liquid phase in melt zone and developing the bonding phase that is mainly composed by columnar&acicular-type SFCA seem to be effective measures to improve sinter strength.

Structure of SFCA	Fracture toughness / MPa·m^{-2}	Chemical component /%				
		CaO	Fe$_2$O$_3$	SiO$_2$	Al$_2$O$_3$	MgO
Platy-type	0.85	9.07-10.65	82.50-89.00	2.59-4.05	2.83-4.16	0.55-1.92
Sheet-type	0.91	10.75-12.49	71.79-85.66	3.73-6.66	3.03-4.11	0.92-2.28
Columnar-type	1.33	13.27-15.43	68.07-78.86	7.09-9.26	3.39-4.44	0.40-1.43
Acicular-type	1.39	13.99-17.04	70.57-75.37	6.60-9.99	3.20-4.25	0.57-0.80

Table 3. The component and fracture toughness of various SFCA

4. Crystal behavior of calcium ferrite during cooling process

4.1. Crystal behavior of calcium ferrite at different temperature

Calcium oxide (mass fraction 8%) was added into iron ores to ensure the formation of CF melt during sintering. Briquettes were cooled down to 1280℃, 1250℃, 1200℃, 1150℃, and 1050℃ at a cooling rate of 50℃/min respectively, and then quenched by water. Fig.9 shows the micrograph of products at different quenching temperature.

Dominated mineral composition were hematite and CF in each products, and microstructure was corrading, however the crystallization had obvious differences (Table 4).

According to the results, we preliminary deduce that the precipitation temperature of crystal in CF system is close to 1200℃.In order to verify this inference, briquettes were cooled with 50 ℃/min to 1200 ℃, and holding 10 min at this temperature, then quenched by water finally. It was found experimentally that as the holding time prolonged, crystalline morphology became significant needle-like. Although dominated mineral compositions were hematite and CF, precipitation quantity of CF increased.

Quenching temperature	Micrograph	Mineral composition and microstructure
1280℃ 1250℃	Fig. 1a Fig. 1b	No crystalline state were formed. The binder phase, which had no time to crystallize under high temperature quenching, kept the original morphology.
1200℃	Fig. 1c	The rudiment of the crystalline state CF was obtained, and its characteristic of morphology was unidirectional extension.
1150℃ 1050℃	Fig. 1d Fig. 1e	Melt were crystallized gradually, developed more fully, in addition, needle-like CF were precipitated.

Table 4. Mineral composition and microstructure of different quenching temperature

Undercooling is a essential driving force for phase transition. When the temperature is lower than the melting point, undercooling $\triangle T(\triangle T{=}T_m\text{-}T,\ T_m$—melting temperature, T—actual

temperature) is obtained. It was found by spectrum, the component of CF was close to the eutectic point of Fe_2O_3–CaO system. Fig. 10 [5]shows the temperature of melt precipitation nearby eutectic point was just higher than 1200 ℃, and the crystal had undercooling condition at this temperature.It also proved the conclusion that CF,which precipitated at about 1200℃, had good crystallization capacity. The crystal precipitation process was closed to the equilibrium state.
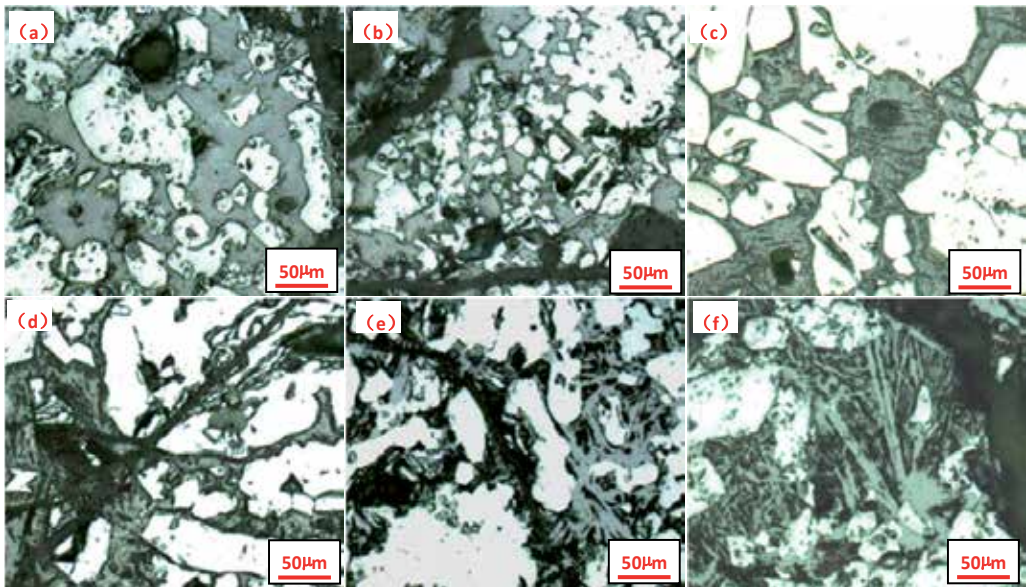
(a) 1280℃；(b) 1250℃；(c) 1200℃；(d) 1150℃
(e) 1050℃；(f) Holding 10 min at 1200℃
White—Hematite，Gray—CF，Black—Void

Figure 9. Micrograph of different quenching temperature

In addition, we can find that the rudiment of CF was excessive and small, and exhibited unidirectional extension, which would become needle-liked when it developed. All of these conform to the morphology features of rapid crystallization, which proved that CF crystal had rapid growth speed, strong crystal ability, and little affection by dynamics and extenal factors.

4.2. Effect of the cooling rate on crystallization of calcium ferrite

Cooling rate determines the time of crystal precipitation, which is one of important factors of crystallization. Using controllable cooling design, cooling rate was controled at 150℃/min, 100℃/min, 50℃/min in high temperature stage (≥1000℃), and 50℃/min in low temperature stage (≤ 1000℃). Natural cooling method was adopted when briquettes was cooled down to 600℃.
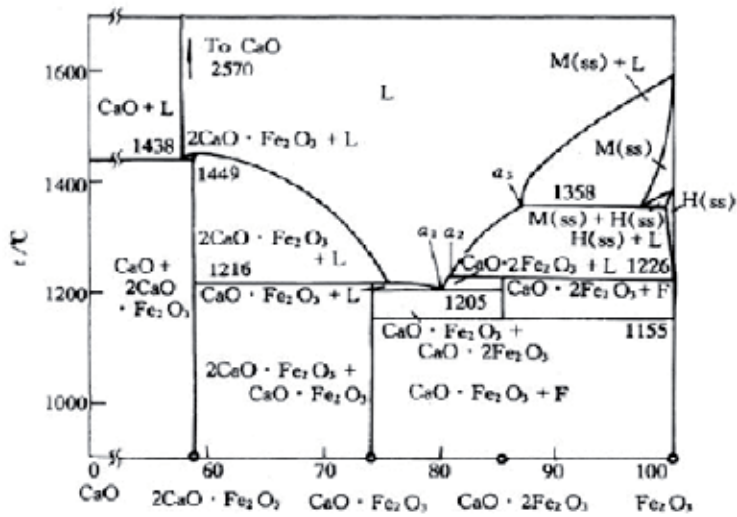
L—Liquid;F—Hematite;M(ss)—Magnetite solid solution;H(ss) —Hematite solid solution

Figure 10. Binary phase diagram of CaO and Fe$_2$O$_3$ [17,18]

Adding 8% of calcium oxide(R=2.3) into raw material as flux. After sintering and cooling, Fig. 11 and Table 5 provides a set of typical microstructure corresponding to the samples prepared from different cooling rate.
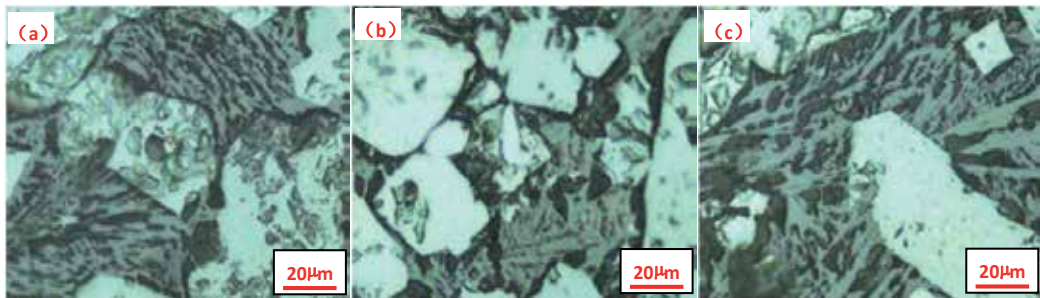
(a) 150℃/min；(b) 100℃/min ；(c) 50℃/min

White—Hematite，Gray—CF，Black—Void

Figure 11. Micrograph of different cooling rate

Based on the experimental results, it was said that CF crystal can precipitate in rapid cooling rate. At the same time, slowing cooling rate was significantly in favour of further development of the crystal.

In the actual production process, cooling rate of the upper and lower material layers are 120~130℃/min and 40~50℃/min respectively [6]. During the production of high-basicity sinter, we can deduce that the cooling process of lower material layer is relative slow, and this can be in favor of the crystallization of needle-like CF and development of melting structure. From the perspective of crystal precipitation behavior, we conclude that the lower material layer is superior to upper one.

Cooling rate	Micrograph	Mineral composition and microstructure
150℃/min	Fig. 3a	Crystal rudiment of CF was found, which further confirmed that CF had strong crystalize abiliity.
100℃/min	Fig. 3b	The crystal precipitation became obvious with decreasing cooling rate, and crystal tended to intensive.
50℃/min	Fig. 3c	Along with melt crystallizing fully, CF developed to needle-like morphology, which formed interlaced and corrasive structrue with hematite.

Table 5. Mineral composition and microstructure of different cooling rate

5. Effect of chemical compositions on crystallization of calcium ferrite

The influences of Ca/Fe, SiO_2, Al_2O_3 and MgO on the generation of calcium ferrite in melt zone were studied. The molar ratio of Ca/Fe and the content of MgO were changed by adding calcium or magnesium fluxes, and the contents of SiO_2 and Al_2O_3 were changed by regulating the types of iron ores used.

5.1. Ca/Fe in melt zone

The influences of Ca/Fe on the generation of columnar&acicular-SFCA in melt zone were studied. The results are shown in Fig.12. As the molar ration of Ca/Fe is low, there is little columnar&acicular-SFCA in melt zone. With the increase of Ca/Fe, the generation of SFCA is improved first, then down when the Ca/Fe exceeds 0.4.

The influence of Ca/Fe on the microstructure of melt zone is shown in Fig.10. The total content of SFCA increases with the improvement of the molar ratio of Ca/Fe, but columnar&acicular-SFCA increases first and then decreases. When Ca/Fe is 0.23, the morphology of SFCA is mainly platy-type(Fig.13(a)). As Ca/Fe reaches to 0.3-0.4, the main form of SFCA exists as columnar&acicular-type, which reaches the maximum amount (Fig.13(c) ~ Fig.13(e)). When Ca/Fe increases to 0.5, the content of columnar&acicular-SFCA decreases instead, and sheet-type SFCA of interconnection mode forms remarkably (Fig.13(f)).
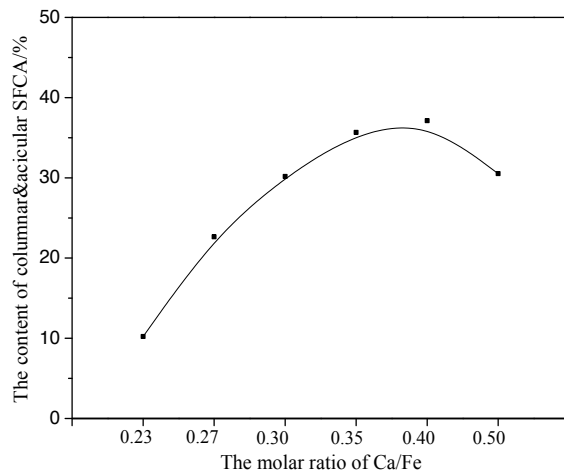
Figure 12. Influence of Ca/Fe on the generation of SFCA in melt zone
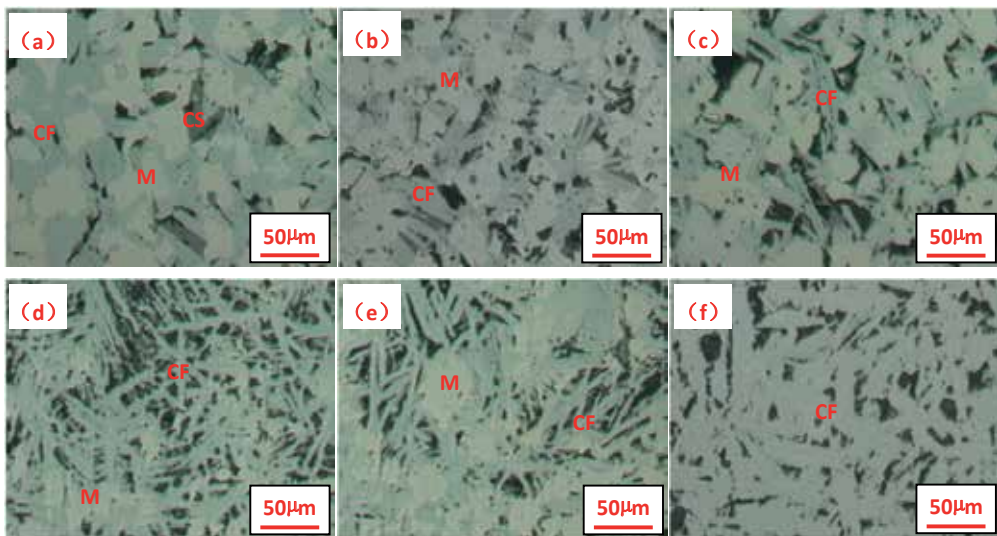
(a) Ca/Fe=0.23；(b) Ca/Fe=0.27；(c) Ca/Fe=0.30

(d) Ca/Fe =0.35；(e) Ca/Fe =0.40；(f) Ca/Fe =0.50

M—Magnetite，SFCA—Calcium ferrite，CS—Silicate

Figure 13. Influence of Ca/Fe on the microstructure of melt zone

5.2. SiO$_2$ content in melt zone

The influences of SiO$_2$ content in melt zone on the generation of columnar&acicular-SFCA and the microstructure were studied. The results are shown in Fig.14 and Fig.15.
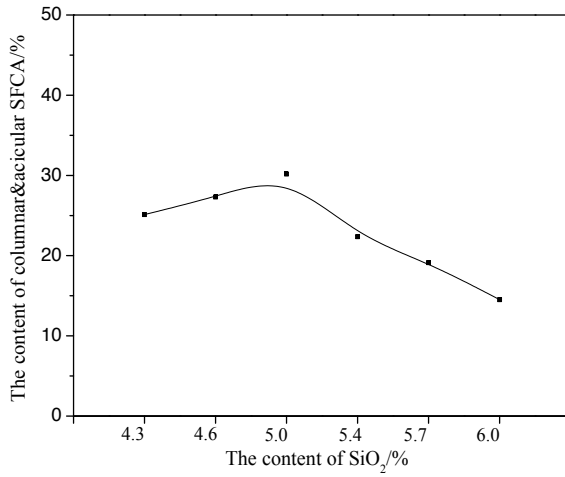
Figure 14. Influence of SiO_2 on the generation of SFCA in melt zone
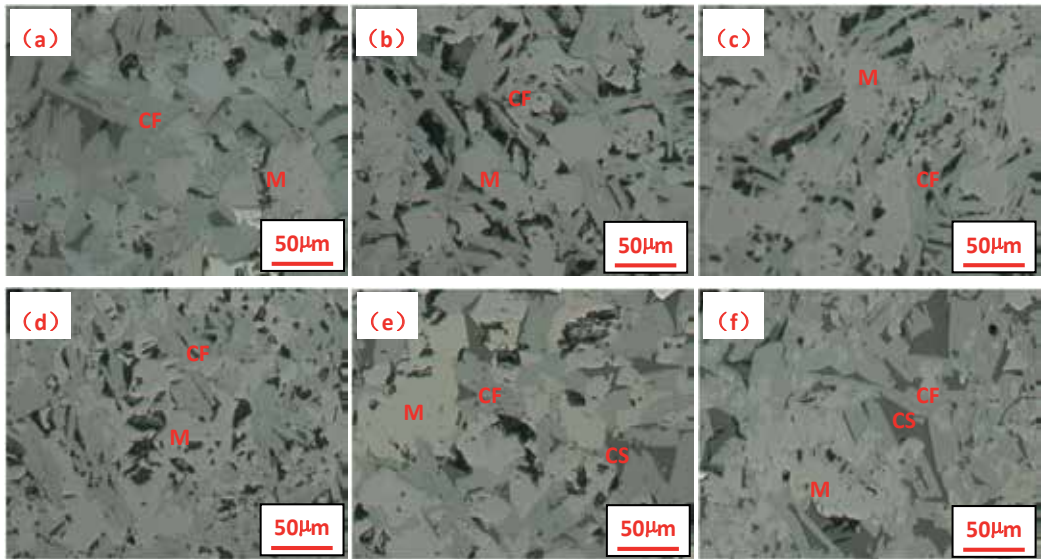
(a) SiO_2 4.3%; (b) SiO_2 4.6%; (c) SiO_2 5.0%; (d) SiO_2 5.4%; (e) SiO_2 5.7%; (f) SiO_2 6.0%

M—Magnetite, SFCA—Calcium ferrite, CS—Silicate

Figure 15. Influence of SiO_2 on the microstructure of melt zone

For the influence of SiO_2, when the content of SiO_2 increases from 4.3% to 5.0%, the content of columnar&acicular-SFCA increases to some extent (Fig.15(a) ~ Fig.15 (c)). SiO_2 content of 5.0% would benefit the generation of columnar&acicular-SFCA because SiO_2 is an important ingredient for SFCA formation. While SiO_2 exceeds 5.0%, the reaction between CaO and SiO_2

 occurs more easily than that between CaO and Fe_2O_3. As a consequence, the amount of SFCA coming from the reaction between CaO and Fe_2O_3 is reduced. And it facilitates producing platy SFCA other than columnar&acicular-type since more silicate is generated (Fig.15(e) and Fig. 15(f)).

5.3. Al_2O_3 content in melt zone

Al_2O_3 is also an influencing factor for SFCA [19]. The effect of Al_2O_3 on the generation of SFCA in melt zone is investigated, and the results are shown in Fig.16. When the content of Al_2O_3 is not more than 1.8%, columnar&acicular-SFCA generates sufficiently. As Al_2O_3 content continues to increase, it's disadvantage for the form of columnar&acicular-SFCA.
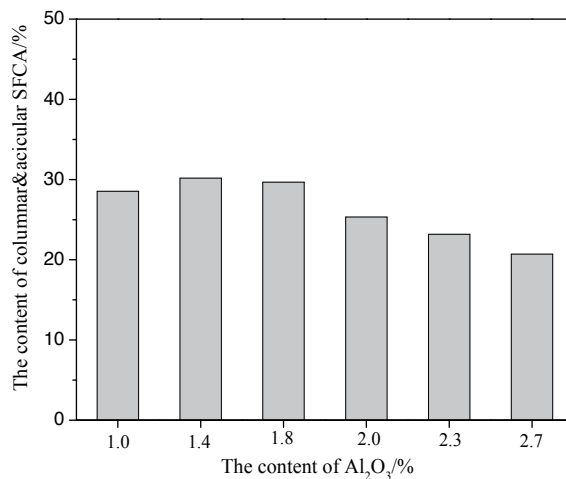
Figure 16. Influence of Al_2O_3 on the generation of SFCA in melt zone

The influence of Al_2O_3 on the microstructure of melt zone is presented in Fig.10. When the content of Al_2O_3 is under 1.8%, melt zone mainly consists of the corrosion structure formed by SFCA and magnetite(Fig.17(a)~ (Fig.17(c)). But the microstructure would change markedly when the content of Al_2O_3 is more than 1.8%. The columnar&acicular-SFCA is suppressed and the platy SFCA gets developed (Fig.17(d)~ (Fig.17(f))). When the content of Al_2O_3 is excessively high, it would not only increase the melting point of sintering mix, but also increase the viscosity of liquid phase. Thus the fluidity of liquid phase is worsened, which makes it difficult for the precipitation of columnar&acicular-SFCA that crystallises along one-way extension, and makes the size and quantity of the pores in the melt zone increase.

5.4. MgO content in melt zone

In the same way, the influence of MgO on the formation of SFCA was researched. With the increase of the content of MgO, the content of SFCA decreases(as shown in Fig.18). And the main reason is that Mg^{2+} entered into the crystal lattice of magnetite, forming magnesiaspinel
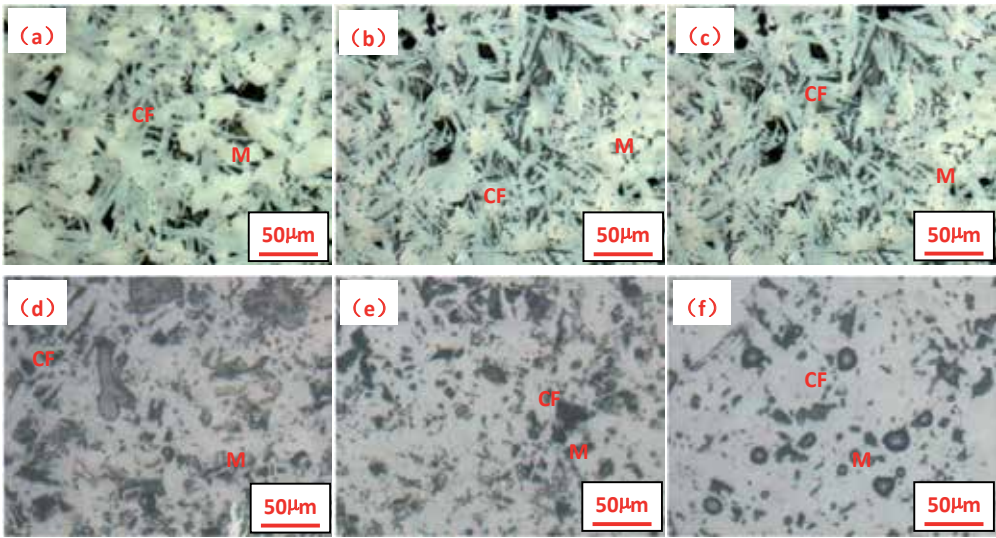
(a) $Al_2O_3$1.0%；(b) $Al_2O_3$1.4%；(c) $Al_2O_3$1.8%
(d) $Al_2O_3$2.0%；(e) $Al_2O_3$2.2%；(f) $Al_2O_3$2.6%

Figure 17. Influence of Al_2O_3 on the microstructure of melt zone

[(Fe,Mg) O Fe_2O_3]. The crystal lattice of magnetite is stabilised by solid solution of Mg^{2+}. As a result, it would suppress the formation of SFCA by preventing the oxidising reaction from magnetite to hematite [20,21]. With the increase of MgO from 1.4% to 6.4%, the content of columnar&acicular-SFCA decreases from 34.67% to 18.17%.
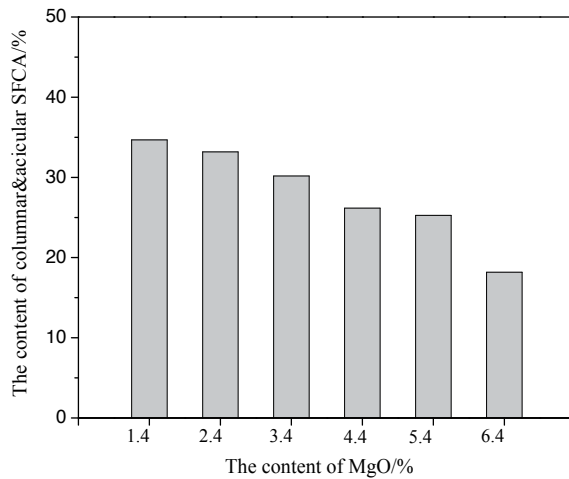
Figure 18. Influence of MgO on the generation of SFCA in melt zone

The influence of MgO on the microstructure of melt zone is shown in Fig.19. When the content of MgO is excessively high, lumpy pieces of recrystallisation magnetite are generated in melt zone, and the content of columnar&acicular-SFCA is decreased significantly.
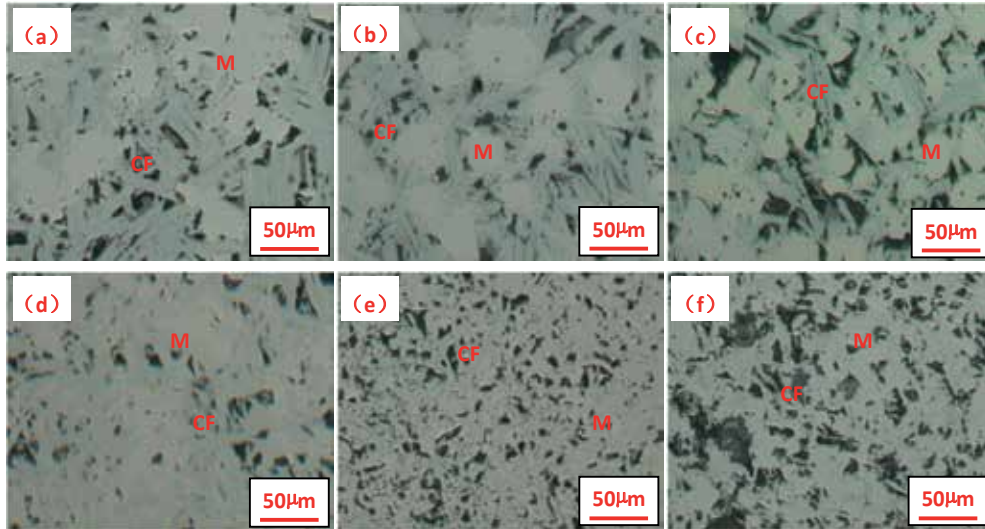
(a) MgO1.4%；(b) MgO2.4%；(c) MgO3.4%

(d) MgO4.4%；(e) MgO5.4%；(f) MgO6.4%

Figure 19. Influence of MgO on the microstructure of melt zone

5.5. Methods of optimising SFCA generation

Therefore, the chemical composition of melt zone plays a considerably important role in liquid phase and the generation of SFCA. The suitable chemical components of melt zone have been proved to be that, the molar ratio of Ca/Fe is 0.3-0.4, the content of SiO_2 is about 5%, the content of Al_2O_3 is less than 1.8%, the content of MgO should be controlled as low as possible under the condition guaranteeing the slag-making of blast furnace. In accordance with the principles introduced above (Table 6), the performance of mixtures on the mineralization can be optimised.

Ca/Fe(molar ratio)	SiO_2 content/%	Al_2O_3 content/%	MgO content/%
0.3-0.4	about 5.0%	≤1.8	Low as possible

Table 6. Suitable ranges of chemical component in melt zone for mineralization

The chemical composition of melt zone can be calculated by Equation 1. On the basis of that, all of the fluxes react with the fine iron ores less than 0.5mm to form the melt zone. According

to the equation, as knowing the composition of raw materials, adhesive fines (-0.5mm) content and the proportions of raw materials, the chemical compositions in melt zone can be figured out.

$$w(Q) = \frac{\sum x_i \cdot x_i^{-0.5} \cdot w_i^Q + \sum x_j \cdot w_j^Q}{(\sum x_i \cdot x_i^{-0.5} + \sum x_j)(1 - \sum x_i \cdot x_i^{-0.5} \cdot w_i^{LOI} - \sum x_j \cdot w_j^{LOI})} \tag{1}$$

Where $w(Q)$ is the content of chemical composition Q in melt zone, %;

x_i is the ratio of iron ore i in the mixture, %;

$x_i^{-0.5}$ is the content of fine grains(-0.5mm) in ore i, %;

w_i^Q is the content of chemical composition Q in adhesive fines(-0.5mm) of ore i, %;

w_i^{LOI} is the loss on ignition of fraction -0.5mm in ore i, %;

x_j is the ratio of flux j in the mixture, %;

w_j^Q is the content of chemical composition Q in flux j, %;

w_j^{LOI} is the loss on ignition of flux j,%.

Take a sintering plant in china as an example. The basic ore blending scheme is the producing plan before optimizing. The chemical composition in melt zone of basic scheme is shown in Table 7. According the suitable ranges of relative components, the molar ratio of Ca/Fe and the contents of SiO_2, Al_2O_3 are all beyond their appropriate values in basic scheme. Columnar&acicular-SFCA are low because the chemical component of melt zone fails to meet the expected match.

Scheme	Chemical component of melt zone				Content of C.&A.-SFCA/%
Molar ratio of Ca/Fe	SiO2 /%	Al_2O_3 /%	MgO /%		
Basic	0.28	5.43	2.03	2.98	23.86
Optimization A	0.32	5.08	1.78	3.08	32.66
Optimization B	0.33	5.16	1.82	3.14	34.27

Table 7. The chemical component of melt zone and the property of mineralisation

In order to optimise the chemical components of melt zone, it is necessary to increase the molar ratio of Ca/Fe and reduce the contents of Al_2O_3 and SiO_2 in the fraction of -0.5mm on the basis of basic scheme. The methods of optimisation are decreasing the content of -0.5mm in blending ores to raise the Ca/Fe, and decreasing the ores of high Al_2O_3 and SiO_2. Two ore blending schemes of optimisation are obtained. The chemical components of melt zone are shown in

Table 7 after optimising the ore blending. It can be seen that the molar ratio of Ca/Fe of Optimisation A and Optimisation B increased to 0.32 and 0.33 respectively, the content of SiO_2 decreased to 5.08% and 5.16%, and Al_2O_3 decreased to 1.78% and 1.82%, all reaching or approaching the suitable range for mineralisation. Compared with the basic scheme.

The influences of mineralisation improvement by optimising the ore blending on sintering are shown in Table 8. When the proportion of coke breeze remained at 5%, sintering speed of two optimising schemes increases from 21.94mm/min to 23.55mm/min, 23.78mm/min, the yield increases from 72.66 to 74.05%, 73.69%, the productivity increases from 1.48t/(m^2 h) to 1.60t/(m^2 h), 1.59t/(m^2 h), and the tumbler strength increases from 65.00% to 66.40%, 66.45%. When the production and quality indexes are comparative, the ratio of coke breeze can be decreased from 5.0% to 4.7%, and the solid fuel consumption reduces by 5.6%.

Scheme	Ratio of coke breeze/%	Sintering speed /mm·min⁻¹	Yield/%	Tumbler index/%	Productivity /t·m⁻²·h⁻¹
Standard	5.0	21.94	72.66	65.00	1.48
Optimization A	5.0	23.55	74.05	66.74	1.60
Optimization A	4.7	22.22	71.88	64.56	1.48
Optimization B	5.0	23.78	73.69	66.45	1.59

Table 8. The influence of the optimisation of mineralisation to the sintering

6. Conclusions

1. The structure of sinter composes of a melt zone and unfused ores. Sinter strength is mainly subjected to the properties of melt zone since unfused ores are wrapped by melt zone is proposed. It facilitates obtaining sinter of high strength with the increase of SFCA in melt zone during melt condensation.

2. Crystalline CF began to precipitate at about 1200℃.The lower cooling temperature, the better crystal growth, and the more content of precipitated needle-like CF. CF crystal has rapid growing speed, strong crystal ability, and little affection by dynamics and external factors. However, slowdowning the cooling rate is obviously favorable to development of crystal.

3. SFCA can be divided into four structural types, including plate-type, sheet-type, colum‐nar-type, and acicular-type. The strength of columnar&acicular-type SFCA is better than that of plate& sheet-type.

4. The suitable chemical components for mineralisation of the melt zone are that, the molar ratio of Ca/Fe is 0.3-0.4, the content of SiO_2 is about 5%, the content of Al_2O_3 is less than 1.8%, and the content of MgO should be controlled as low as possible for guaranteeing the slag-making of blast furnace.

Acknowledgements

Author details

Min Gan, Xiaohui Fan[*] and Xuling Chen

*Address all correspondence to: 156703017@qq.com

Department of Ferrous Metallurgy, Central South University Changsha, Hunan, China

References

[1] M.J.Cumming, and J.A.Thurlby. Developments in the modelling and simulation of iron ore sintering, *Ironmaking & Steelmaking*, 1990, 17 (4), 245-254.

[2] D.F.Ball. Agglomeration of iron ores, 1973, Heinemann Educational.

[3] P.R.Dawson. Recent developments in iron ore sintering, *Ironmaking & Steelmaking*, 1993, 20 (2), 135-143.

[4] M.I.Pownceby and J. M. F.Clout. Importance of Fine Ore Chemical Composition and High Temperature Phase Relations: Applications to Iron Ore Sintering and Pelletising. Mineral Processing and Extractive Metallurgy: Transactions of the Institute of Mining and Metallurgy, Section C, 2003, 112(1), 44-51.

[5] X.H.Fan,J.Meng,X.L.Chen,J.M.Zhuang,Y.Li,and L.S.Yuan. Influence Factors of Calcium Ferrite Formation in Iron Ore Sintering, Journal of Central South University, 2008, 36, (6),1125-1131. (in Chinese)

[6] T.Miyashita, N.Sakamoto, and Hiroshi Fukuyo. Influence of Mineral Structure on Sinter Agglomerate's Propeties, Trans ISIJ, 1982, 22(7), B-199.

[7] Y.Ishikawa. Improvement of Sinter Quality Based on the Mineralogical Propeties of Ores, Ironmaking Proc, 1983,42,17-29.

[8] X.R.Liu,G.Z.Qiu,R.Z.Cai,and S.F.Lin. The Mineralogy Research on the Ferrite of Low-temperature Sintering, Sintering and Pelletizing, 2000, 25 (2),7-10. (in Chinese)

[9]   A.Cores, A.Babich, M.Muniz, S.Ferreira and J.Mochon.The Influence of Different Iron Ores Mixtures Composition on the Quality of Sinter. ISIJ International, 2010, 50(8), 1089-1098.

[10]   L.H. Hsieh and J.A.Whiterman. Sintering conditions for simulating the formation of mineral phases in industrial iron ore sinter, *ISIJ Int.*, 1989, 29 (1), 24-32.

[11]   C.E.Loo, R.P. Williarns and L.T. Mattews. Designing iron ore sinter mixes for optimum raw material utilization, Proceeding of The Six International Iron & Steel Congress, 1990, Nagoya, the Iron and Steel Institute of Japan.

[12]   H.G.Li, J.L.Zhang, Y.D.Pei, Z.X.Zhao and Z.J.Ma. Melting characteristics of iron ore fine during sintering process, *J. Iron Steel Res. Int.*, 2011, 18, (5), 11-15.

[13]   O.Iun, H.Kenichi, H.Yohozoh and K.Shinagawa, Influence of iron ore characteristics on penetrating behavior of melt into layer, *ISIJ Int.*, 2003, 43 (9), 1384-1392.

[14]   X.H.Fan. Principle and technology of iron ore matching for sintering, 2013, 39-42, Beijing, Metallurgical industry press. (in Chinese)

[15]   G. S.Feng, S. L.Wu, H. L.Han, L.W.Ma and W. Z.Jiang. Sintering Characteristics of Fluxes and Their Structure Optimization. International Journal of Minerals Metallurgy and Materials, 2011, 18(03): 270-276.

[16]   M.Gan: Fundamental Research on Iron Ore Sintering with Biomass Energy, Doctor Dissertation, (2012), 85. (in Chinese)

[17]   P.Bert, M.Arnulf. Phase Equilibria in the System CaO-Iron Oxide in Air and at 1 Atm. O_2 Pressure. Journal of The American Ceramic Society, 1958, 41(11), 445-454

[18]   J. W.Jeon, S.M.Jung and Y.Sasaki. Formation of Calcium Ferrites under Controlled Oxygen. ISIJ International, 2010, 50(8), 1064-1070.

[19]   L.Lu, R. J.Holmes and J. R. Manuel, Effects of alumina on Sintering Performance of Hematite Iron Ores. ISIJ International, 2007, 47(3), 349-358.

[20]   H. S.Kim, J. H.Park and Y. C.Cho. Crystal Structure of Calcium and Aluminium Silicoferrite in Iron Ore Sinter. Ironmaking & Steelmaking, 2002, 29(4), 266-270.

[21]   K.Yajima, and S. M.Jung. Data Arrangement and Consideration of Evaluation Standard for Silico-Ferrite of Calcium and Alminum (SFCA) Phase in Sintering Process. ISIJ International, 2012, 52(3), 535-537.

Crystallization of Fe and Mn Oxides-Hydroxides in Saline and Hypersaline Enviro nments and In vitro

Nurit Taitel-Goldman

1. Introduction

Iron oxides crystallize in various enviro nments. This chapter focuses on short-range ordered or well-crystallized iron oxides and Fe - Mn oxides that crystallize in saline and in hypersaline enviro nments or in similar conditions in vitro.

1.1. Geological background

In the actively diverging central part of the Red Sea, a series of submarine Deeps were formed (Figure 1a). Red Sea deep water interacts with hot magmatic rocks, dissolves salt layers and then discharges into the Deeps creating hydrothermal hypersaline brine that feeds the Deeps. A hydrothermal hypersaline brine (68°C, 270‰) [1] discharges into the southwestern basin of Atlantis II Deep located between 21°19N and 21°27N and is 15 km long and 8 km wide (Figure 1b). The water depth reaches 2190 m. [2, 3, 4]. The hydrothermal hypersaline brine forms a stable stratified water column resulting from density differences. Iron concentration increases with depth from 0.01 m g/kg to 75-81 m g/kg in the lower brine. Mn concentration in the lower brine is 82 m g/kg whereas in the Red Sea deep water, it is 0.009 m g/kg [5]. Mixing between the discharging brine and the aerobic Red Sea deep water, which occurs at the depth of 2008-1990m below sea level, leads to iron oxidation and crystallization of iron oxide-hydroxides. Variability in iron oxides or hydroxides results from the conditions in which they crystallized.

The hypersaline and hydrothermal brine that fills the Atlantis II Deep overflows into the close Chain and Discovery Deeps. This leads to elevated temperatures in the lower water layer in the Discovery Deep that reach 48°C. Lately it was suggested that hydrothermal brine also discharges into the Discovery Deep which has lead to a constant temperature over the last 40 years [1] The elevated temperature salinity and iron concentrations lead to crystalliza-

tion of iron and manganese oxides or hydroxides in these Deeps as well. Mn-Fe oxide-hydroxides were crystallized either in the margins of the Deeps or close to the interface between the hydrothermal brines and the overlying aerobic Red Sea deep water. Fe-oxides that crystallize in the oxic-unoxic boundary settle down to the Deep floor whereas Mn oxides-hydroxides dissolve while settling down on the Deep floor but they accumulate on the flanks of the Deeps [6].

Iron oxides were collected from sediments of the Thetis Deep in the Red Sea located between 22°46N and 22°49N with a water depth of 1780m (Figure 1c). Currently, no hydrothermal brine discharges into this Deep, yet it is possible that hydrothermal brine was present in the Thetis Deep during deposition of iron oxides [7]. Cores studied from the Thetis Deep have a higher Fe and Mn oxide-hydroxides than cores sampled outside the Deep. Similarly, V, Cu, Zn, and Pb are enriched in Thetis Deep sediments [8].
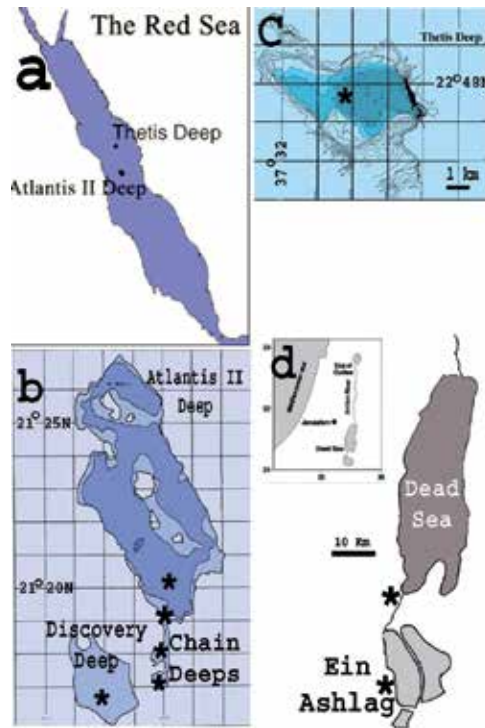
Figure 1. Location maps: a) Red Sea; b) Atlantis II Deep, Chain Deeps and Discovery Deep; c) Thetis Deep; d) Dead Sea area and in the upper part of the map of Israel with the Dead Sea location. Ein-Ashlag seepage is in the southern part of the dead Sea on the eastern flank of the Mount Sedom diapir. (*- sampling area)

Dead Sea samples were collected near saline springs that discharge close to the Dead Sea or from Ein-Ashlag located on the eastern flanks of Mount Sedom diapir (Figure 1d). The springs and Dead Sea water are Ca-Chloride hypersaline brine, initially formed in a Pliocene lagoon. The salinity of the Dead Sea reaches 340 g/l [9]. Ein-Ashlag is a hypersaline seepage that results

from hypersaline brine body that is associated with Mt. Sedom salt diapir. The salinity of the seepage (390 TDS/l) is even higher than Dead Sea water (340gTDS/l). The amount of dissolved Fe^{2+} in the Ein-Ashlag spring is 0.12 g/l [10] Initially formed iron and manganese oxides that crystallize close to the discharging spring are commonly preserved within halite crystals, hence their initial composition remains and recrystallization processes are restrained.

Minerals presented in this chapter are short-range ordered ferrihydrite ($Fe_5HO_8*4H_2O$), singerite ($SiFe_4(OH)_4*H_2O$) and Mn-oxide-hydroxide layers. Well- crystallized phases presented are goethite ((αFeOOH), akaganéite (βFeOOH), lepidocrocite (γFeOOH), feroxyhyte (δFeOOH), hematite (αFe_2O_3), magnetite (Fe_3O_4), todorokite (($Ca, mg)_{1-x}Mn^{4+}O_{12}$ *3-4 H_2O), groutite (αMnOOH) and manganite (γMnOOH). Laboratory imitation of the hydrothermal and hypersaline enviro nments enabled the understanding of the conditions in which each phase precipitated.

2. Methods

Morphology of the phases was observed using high resolution scanning electron microscopy (HRSEM) or high resolution transmission electron microscopy (HRTEM). Using point analyses, a solid solution between two phases or impurities within crystals were detected. In most of the samples studied, the fine fraction was checked with High Resolution Transmission Electron Microscopy using a JEOL FasTEM 2010 electron microscope equipped with a Noran energy dispersive spectrometer (EDS) for microprobe elemental analyses. The results presented are in atomic ratios. Beam width for point analyses was 25 nm. Crystalline phases or short-range ordered phases were identified using selected area electron diffraction (SAED) in the HRTEM. The smallest area for SAED was 100 nm. The data obtained from the HRTEM were processed using fast Fourier transformation with Digital Micrograph (Gatan) software.

3. Short-range ordered phases

3.1. Crystallization of short-range ordered ferrihydrite in the Red Sea and in the Dead Sea area

Nanometer-size phases showing short range periodity are common in the newly formed sediments in the hydrothermal hypersaline enviro nment of the Red Sea and in the Dead Sea area. Ferrihydrite (<10 nm) has euhedral to subhedral morphology and a short-range ordered pattern in the inner part. Crystallization of ferrihydrite occurs as dissolved Fe oxidizes at the presence of dissolve Si that hinders crystal growth so nano-sized crystals are formed with Si impurity with Si/Fe molar ratios varying between 0.17-0.89.

The initial stage of ferrihydrite formation was observed on a plastic bag floating in the Dead Sea water close to a discharging spring with a Si/Fe atomic ratio of 0.26 (Figure 2a). Other ferrihydrite crystals in the Dead Sea were preserved within halite crystals that prevented

recrystallization processes. Point analyses in ferrihydrite crystals yielded Si and Mn impurities with ratios of Si/Fe 0.105 and Mn/Fe 0.013 (Figure 2b).

2-line ferrihydrite clusters of 200 nm were found in samples from the uppermost layer of sediments in the Atlantis II Deep at a water depth of 2165m, [11]. The ferrihydrite presented (Figure 2c) was suspended in the lowermost 10 cm of the hydrothermal brine with a crystal size of 5 nm and point analyses yielded a Si/Fe elevated 0.53 ratio (Figure 2c).

Mn and Fe share similar atomic size (0.645 nm), hence formation of a solid solution between Mn-hydroxides and Fe-hydroxides is feasible. In the Dead Sea, Chain and Discovery Deeps in the Red Sea impurity of Mn in ferrihydrite was observed with an Mn/Fe atomic ratio of 0.013 to 0.244 respectively (Figure 2d).
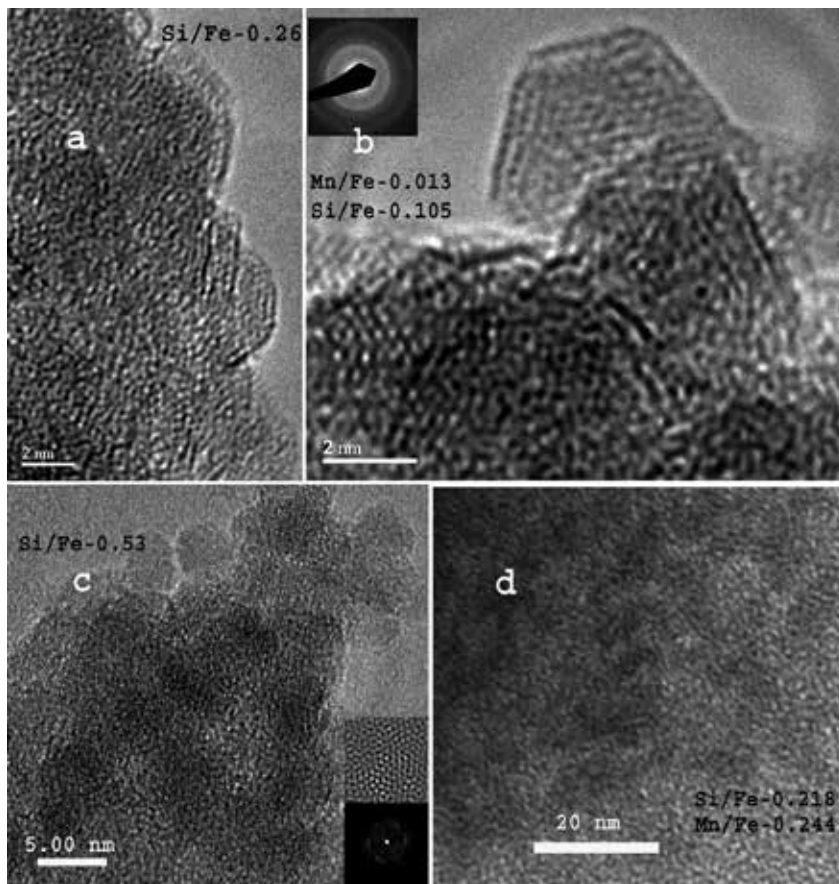
Figure 2. a) 2-line ferrihydrite that crystallized on a floating plastic bag close to a discharging spring into Dead Sea water; b) 2-line ferrihydrite that was preserved within halite crystals. At the upper part of the image, electron diffraction at 0.247 and at 0.1462 nm; c) 2-line ferrihydrite from uppermost centimeter of sediments in the Atlantis II Deep, Red Sea. Electron diffraction yielded 0.25-0.26 and 0.145 nm and Fast Fourier Transformation resulting from the electron diffraction at 0.26 nm; d) ferrihydrite from southern Chain Deep upper 30 cm of the sediments.

3.2. Crystallization of short-range ordered singerite ($SiFe_4O_6(OH)_4*H_2O$)

Singerite appears as rounded platy particles with distinct electron dense, relatively ordered margin and less crystalline inner core. The width of the particles is around 100-200 nm and the dense margins are 5 nm wide [12]. It has a rhombohedral symmetry with unit cell parameters of a=0.504 nm and c=1.08 nm [13]. Singerite was found mainly in the hypersaline hydrothermal brine and the upper sedimental column of the Atlantis II Deep and in the close Chain and Discovery Deeps [14]. Formation in this area results from large amounts of dissolved Si and Fe that lead to formation of short- range ordered phase with elevated atomic Si/Fe ratios (Si/Fe=0.2-0.6). It probably precipitates at the transition zone between the hydrothermal Si-Fe enriched brine and the Red Sea Deep water. Particles of singerite were found in the sediments column down to a depth of few meters with preserved initial morphology.

Synthesis in a brine (40°C, pH7, 2M NaCl) designed to simulate crystallization, singerite was performed successfully with an elevated dissolved initial Si/Fe=1.5 ratio (Figure 3d, e).

3.3. Crystallization of short-range ordered phases Fe-Si-Mn oxides

A short-range ordered Fe-Si-Mn oxide phase made of nano-sized particles forming thin layers that tend to curve and fold was found in the Discovery Deep in the Red Sea. The short-range ordered layers had elevated Si and Mn impurities (Si/Fe of 0.24 and Mn/Fe 0.25) (Figure 3f, g). Association with Si probably hindered crystals growth leading to a short-range ordered phase. The phase resembles in its morphology feroxyhyte but due to elevated Si concentration, it became a short-range ordered phase.

4. Well-crystallized phases

4.1. Crystallization of goethite in the Red Sea Deeps, in the Dead Sea and simulations in vitro

Goethite usually crystallizes from Fe^{2+} at pH 4-9 by fast oxidation/hydrolysis and in the presence of CO_2 [15]. Dissolved Fe^{2+} is supplied by venting hydrothermal hypersaline brines of the Red Sea or in the Dead Sea area. Oxidation of the iron occurred in the Red Sea Deeps as the hydrothermal brine interacts with Red Sea deep water whereas in the Dead Sea area exposure to the atmosphere leads to Fe^{2+} oxidation and goethite precipitation..

Two types of morphologies dominate in most goethite samples of the Red Sea: monodomain, acicular crystals (Figure 4a) and multi-domain crystallites that crystallize from common nuclei and then diverge (Figure 4b, c). Formation of multi-domain crystal of goethite was attributed to the elevated Na concentrations [16] that probably prevail in the hydrothermal brines.

Twinning appears in both morphologies and star-shaped twinning is attributed to formation at elevated temperatures, 60-90°C [17].

Goethite crystals with elevated Si/Fe 0.12 atomic ratios are usually smaller and poorly crystalline, exhibiting numerous crystal defects whereas larger crystals with higher crystal-
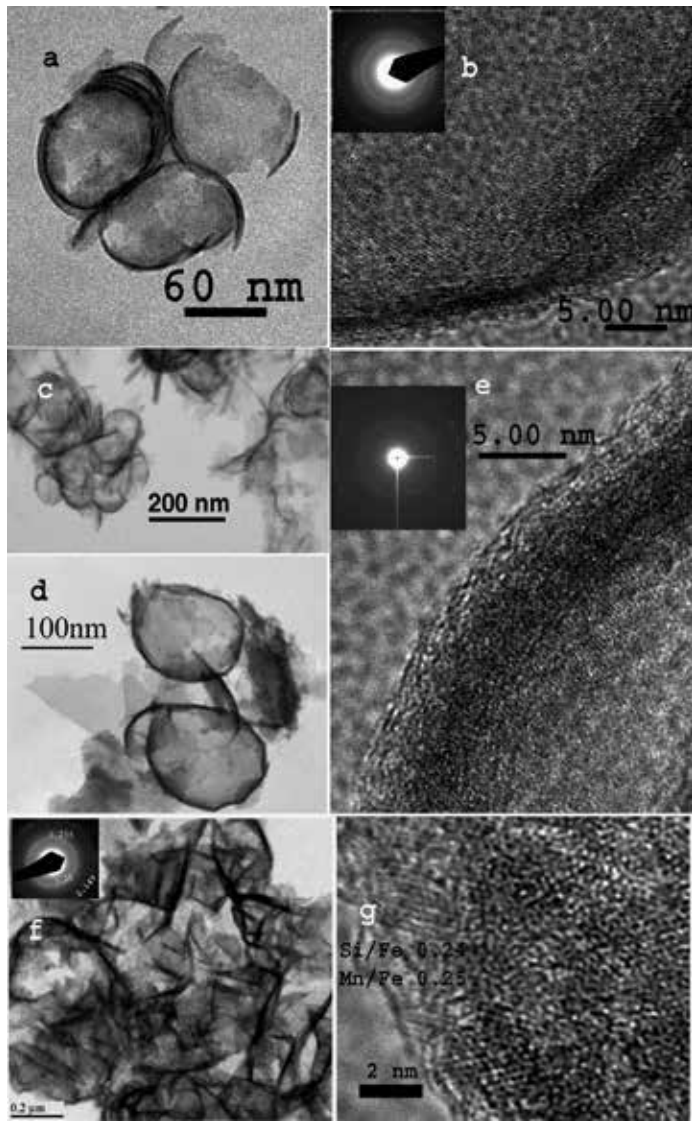
Figure 3. a) Singerite round plates from the Atlantis II Deep, Red Sea; b) High resolution image of the outer rim of the face with short-range ordered inner core. Electron diffraction yielded 0.245 and 0.143 nm; c) Singerite particles from sediments in the Chain Deep; d) Synthetic singerite particles with an outer dense ring; e) High resolution image of synthetic singerite with electron diffraction of 0.25 and 0.27 nm; f) Plates of Fe-Mn-Si oxides from the Discovery Deep; g) High resolution image of the Fe-Si-Mn phase.

linity have a lower Si/Fe elemental ratio. At relatively low Si/Fe ratios, the major effect of Si is to retard growth of the crystallites. Since the amount of soluble Si concentration in the brine was higher in Atlantis II Deep than in Thetis Deep, smaller goethite crystals were formed in the Atlantis II Deep (Figure 4 c, d). Elevated Si concentrations in the brines caused dislocation within the crystals (Figure 4b).

Well-crystallized multi-domain goethite (longer than 500 nm) form mono-layers of iron oxides in the Thetis Deep that were formed at slow oxidation epochs of discharging dissolved Fe^{+2} in a brine with lower Si/Fe values [18].

In the Dead Sea area where Na concentration in the springs or in the brines is high, multi-domain goethite crystallized with a Si/Fe atomic ratio of 0.08 and Mn/Fe 0.04 (Figure 4 e, f)

Star-shaped twinning was observed in a sample from the Atlantis II Deep and in synthesized goethite that crystallized at elevated temperatures (0.8 M NaCl, 60°C) (Figure 4g). At a lower temperature (25°C) synthesized in a 5M NaCl brine, large crystals were formed (Figure 4h) [19].
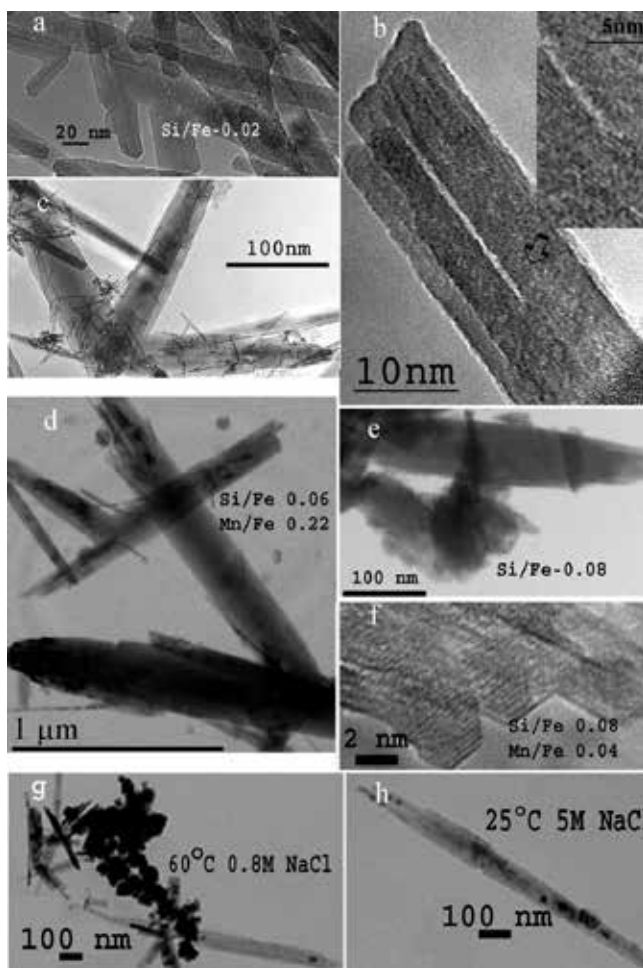
Figure 4. a) Monodomain acicular goethite with twinning from the Atlantis II Deep, Red Sea; b) High resolution image of goethite acicular twins from the Atlantis II Deep, Red Sea; c) Star twinning of multi-domain goethite from Atlantis II Deep, Red Sea; d) Multi-domain goethite from Thetis Deep, Red Sea; e) Multi domain goethite from the Dead Sea area; f) A high resolution image of multi-domain goethite from the Dead Sea; g) Star-shaped multi-domain goethite crystals formed in vitro along with magnetite crystals; h) Multi-domain goethite crystal formed in vitro.

4.2. Crystallization of a solid solution goethite-groutite

Goethite αFeOOH and groutite αMnOOH form a solid solution since both have the structure of Orthorhombic – Dipyramidal H-M Symbol (2/m 2/m 2/m) with space group Pb nm. A solid solution was found in the sediments of the Discovery Deep Mn/Fe 0.33-0.77, Thetis Deep (Mn/Fe 0.10-0.22) in the Red Sea and in sediments that crystallize in the Dead Sea Area (Mn/Fe 0.31) (Figure 5a, b, c).
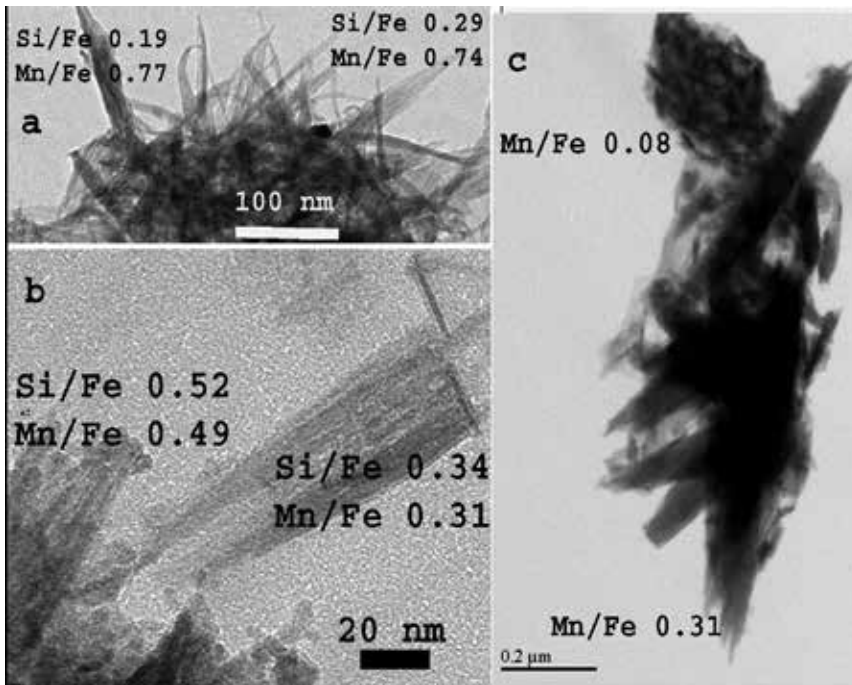
Figure 5. Solid solution of goethite groutite; a, b) Goethite groutite crystals from the Discovery Deep; c) Cluster of goethite-groutite solid solution from the Dead Sea area.

4.3. Crystallization of groutite

Monodomain large crystals of groutite were observed in the southern marginal facies of the Atlantis II Deep of the Red Sea. Impurities of Fe, Si and Ca were found in the crystals. Si retards Mn oxides growth hence lower Si/Mn leads to larger groutite crystals (Figure 6 a, b).

4.4. Crystallization of akaganéite in the Dead Sea area

Akaganeite crystals from the Dead Sea area were crystallized from the hypersaline brine that discharges close to the northern part of the evaporation ponds (Figure 7a). Usually crystallization of akaganéite requires the presence of Cl$^-$ ions for the crystal's stability. In the Dead Sea area, akaganéite were preserved within halite crystals and had acicular or a multi-domain structure (<100 nm) (Figure 7a, b). Incorporation of Si in akaganéite caused twinning [20]
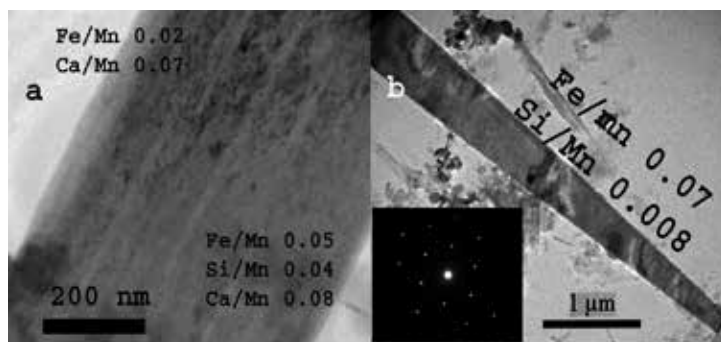
Figure 6. Groutite from the Atlantis II Deep; a) Enlarged image with results of two point analyses; b) Large groutite crystal with electron diffraction.
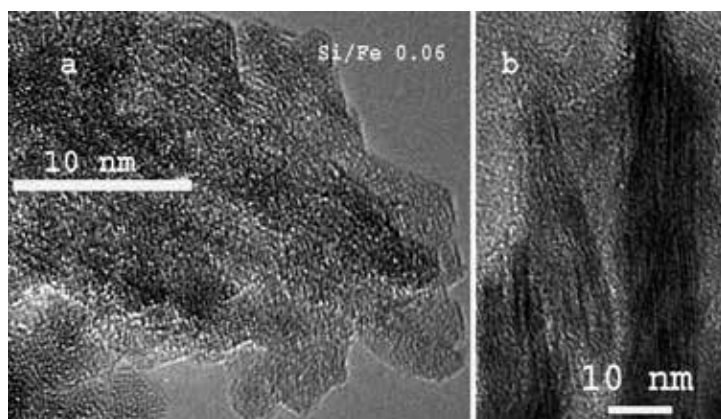
Figure 7. a) Multi-domain akaganéite crystals with Si impurity; b) Acicular crystals of akaganéite with d spacing around 0.7 nm.

4.5. Crystallization of lepidocrocite in the Red Sea Deeps, in the Dead Sea and simulations in vitro

Lepidocrocite usually forms in the presence of chloride at an elevated pH and by slow oxidation relatively to goethite [15]. Three lepidocrocite morphologies were observed in samples from the Atlantis II Deep, Red Sea (Figure 8 a, b): Subhedral plates, rods and multi-domainic crystals, resulting from enhanced crystal growth along the 010 face due to a higher pH [13, 19].

Well-crystallized lepidocrocite of the Thetis Deep in the Red Sea appears as euhedral plates (140-340 nm) or acicular crystals (500-600 nm long and few nm wide) (Figure 8c). In the Discovery Deep, laths-like lepidocrocite were observed (Figure 8d). A high resolution image of platy lepidocrocite from the Thetis Deep had no dislocations and d spacing of 0.62 nm can be observed (Figure 8f).
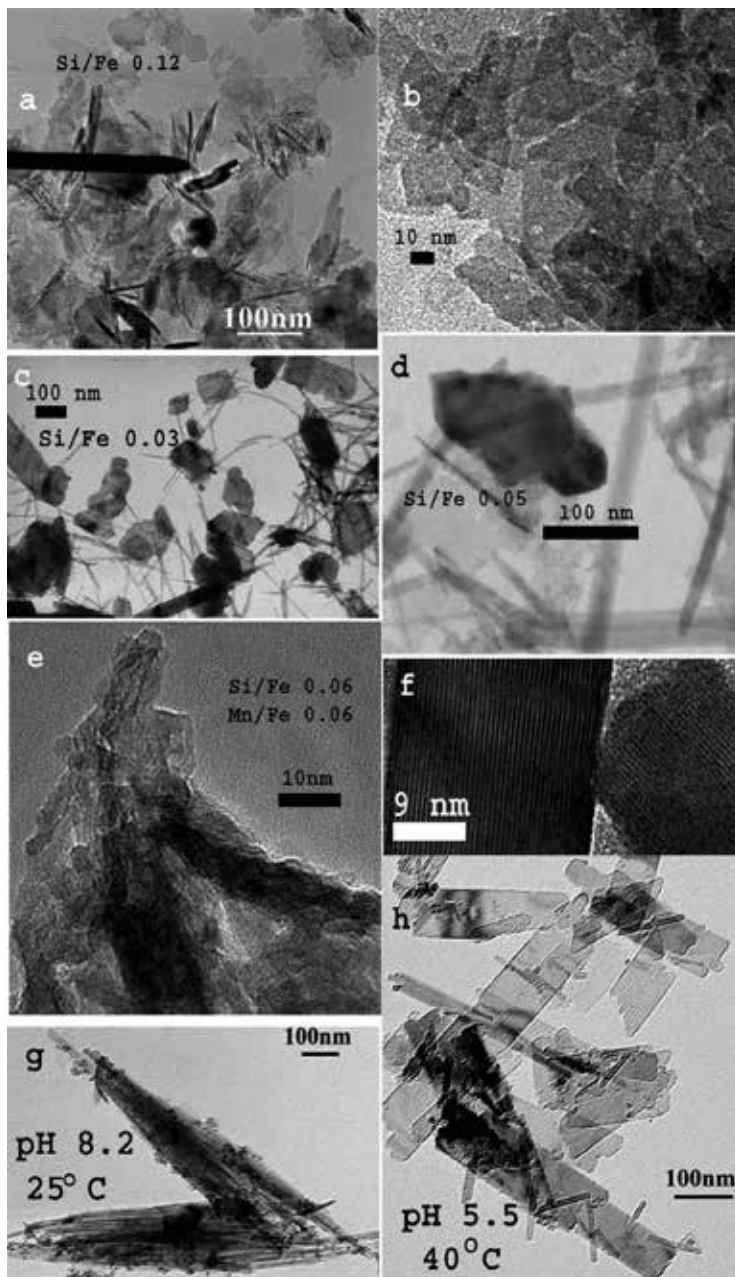
Figure 8. Various morphologies of lepidocrocite: a) Lepidocrocite plates and multi-domain crystals from the Atlantis II Deep, Red Sea; b) Plates of lepidocrocite from the Atlantis II Deep; c) Plates and rods of lepidocrocite from the Thetis Deep, Red Sea; d) Plates of lepidocrocite from Discovery Deep, Red Sea; e) Tiny crystallites of lepidocrocite from the Dead Sea; f) A high resolution image of lepidocrocite crystal from the Thetis Deep Red Sea. (d spacing was 0.62 nm); g) Multi-domain lepidocrocite synthesized at a high pH and low temperature; h) Plates and some rods synthesized at a low pH and elevated temperature.

Platy and rod lepidocrocite from the Thetis and Atlantis II Deeps were probably formed under slightly acidic conditions of the hydrothermal brines. Soluble Si concentration in the brine was higher (Si/Fe 0.11) in the Atlantis II Deep than in the Thetis Deep, leading to larger lepidocrocite crystals in the latter. Lepidocrocite forms mono-layers of iron oxides in Atlantis II and Thetis Deeps due to abrupt oxidation epochs. They were probably formed as down-welling of dense oxidized Red Sea Deep Water formed wide mixing layer which introduced large amounts of dissolved oxygen into the brine leading to abrupt Fe oxidation and lepidocrocite precipitation [21].

Dead Sea lepidocrocite were preserved within halite crystals. In some of the lepidocrocite crystals, impurities of Si and Mn reached the values of Si/Fe 0.06 and Mn/Fe 0.06 (Figure 8e).

Synthesized lepidocrocite morphology changes from plates at pH 5.5 through rods at pH 7 to multi-domainic crystals at pH 8.2, due to enhanced crystal growth along the 010 face (Figure 8g, h). Salinity and temperature have contradictory effects on lepidocrocite crystallinity. Elevated salinity improved lepidocrocite crystallinity while temperature increase had an only partial effect.

4.6. Crystallization of feroxyhyte in the Atlantis II Deep, Red Sea

Feroxyhyte has a morphology of folded layers with Si/Fe=0.3 (Figure 9). Usually feroxyhyte crystallizes over a wide range of pH at high oxidation conditions [15]. Feroxyhyte was found in a sample from the top centimeter of a floppy layer in the Atlantis II Deep [11], indicating that it probably crystallized close to the transition zone between the brine and the Red Sea deep water.
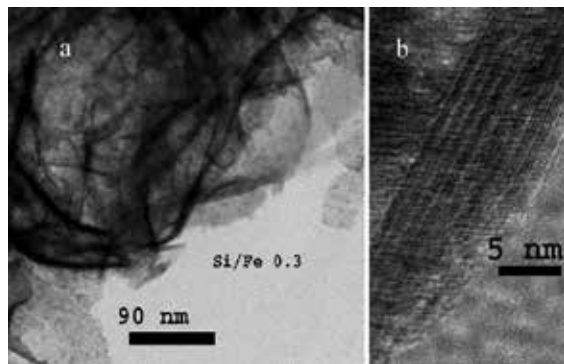
Figure 9. a) Feroxyhyte curved layers from the uppermost layer of sediments in the Atlantis II Deep, Red Sea; b) A high resolution lattice image of feroxyhyte with no dislocations.

4.7. Hematite from the Red Sea

Hematite usually forms by dehydration and rearrangement of ferrihydrite or by thermal transformation from various phases of iron oxides-hydroxides [15]. Hematite usually had platy

morphology (Figure 10a) yet recrystallization of multi-domain iron oxide yielded multi-domain hematite (Si/Fe=0.05) [22].
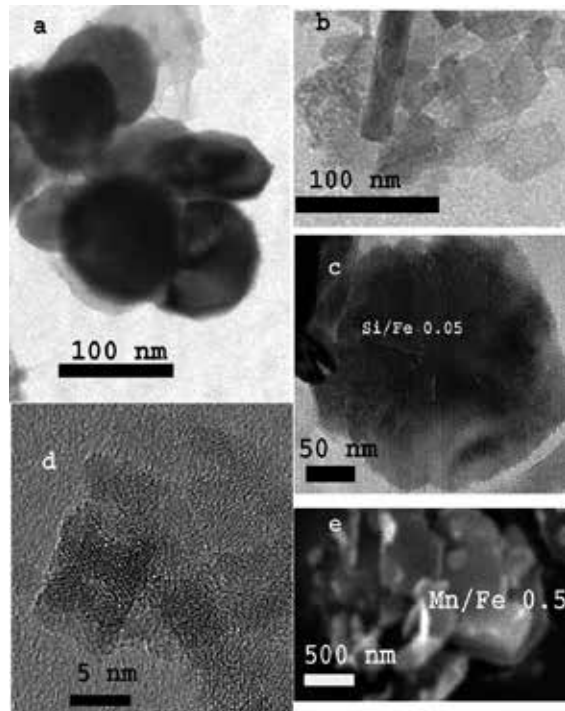
Figure 10. Hematite crystals from the Red Sea Deeps: a) Well-crystallized pure hematite plates from the margins of the Atlantis II Deep; b) Tiny crystallites of hematite from the Discovery Deep and a needle of goethite; c) Large hematite crystal from the lowermost brine in the southwestern part of the Atlantis II Deep; d) A high resolution image of tiny crystallites of hematite from the lowermost brine from the south-western Atlantis II Deep; e) Scanning electron micrograph of hematite plate from the Thetis Deep.

Hematite crystals in the border between the Atlantis II Deep and Chain Deep had a Mn impurity with a Mn/Fe=0.04 ratio. Pure hematite plates were also observed in the Discovery Deep sediments (Figure 10b). Large hematite crystals and nano-sized crystals were found in suspension of the lower hydrothermal brine above the sediments, indicating that they were formed within the brine and not in the sediments (Figure 10c, d).

Hematite crystals from the Thetis Deep had a platy morphology (1-2µm), with an elevated Mn/Fe ratio of 0.5 (Figure 10e). Recrystallization into hematite in the Thetis Deep probably occurred after the hydrothermal discharge ceased and oxygen reached the bottom of the Deep.

4.8. Crystallization of magnetite in the Thetis Deep in the Red Sea and simulations in vitro

Magnetite from the Thetis Deep had octahedral morphology (1-3µm) enriched with small amounts of V, P, and Mn that might have resulted from the leached shales (Figures 11a, b). Similar enrichments in Fe layers were found of the Thetis Deep [23]. It could have precipitated

from a hot (40º-60ºC) and slightly alkaline brine. Incomplete oxidation of dissolved Fe^{2+} led to magnetite crystallization at the lowermost part of the hydrothermal brine. According to the study of rare earth elements, it is possible that hydrothermal saline fluids were temporarily trapped in the Thetis Deep, forming reduced and metal-rich brine bodies [8].
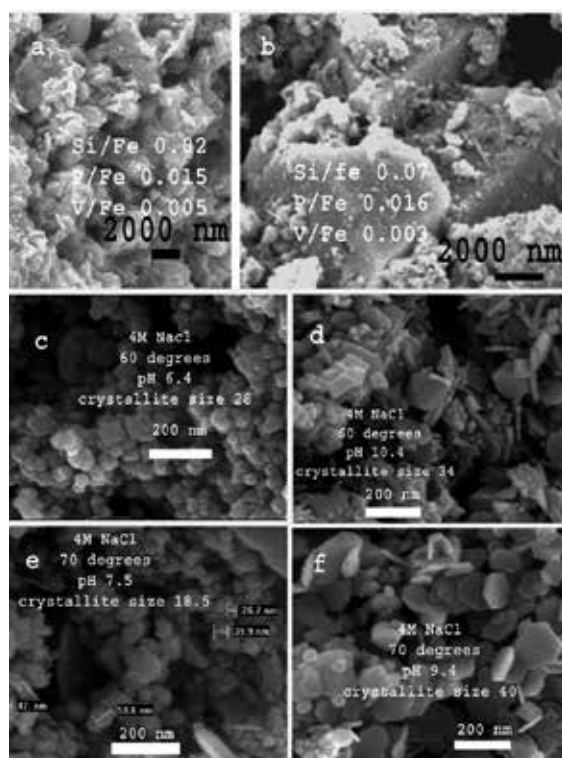
Figure 11. Scanning electron micrographs of magnetite from the Thetis Deep and synthesized in vitro: a) Image of magnetite large crystals from the Thetis Deep partially covered by clay minerals; b) Large crystals of magnetite from the Thetis Deep; c-f) Synthetic magnetite observed by a high resolution scanning electron microscope (HRSEM).

In synthesized magnetite (60°C-80ºC, 0.8, 2, 4, 5 M NaCl and at varying alkalinities pH 6-10.4), crystallite size varied between 18 nm to 45 nm and unit cell parameters varied between 0.8373-0.8396 nm. Morphology varied between euhedral plates or octahedra and unhedral crystals (Figures 11 c-f). The euhedral plates were probably preserving platy green rust or a $Fe(OH)_2$ precursor due to quick crystallization. An increase in pH solution at elevated temperatures (70º and 80ºC) and salinity (4 and 5 M NaCl) yielded magnetite with larger crystallite size and greater unit cell parameters. An opposite trend was observed in magnetite that crystallized at 60ºC, mainly in the 5 M NaCl solution and to a lesser extent in magnetite, crystallized at 4M NaCl solutions.

As observed in previous studies, introducing dissolved silica into the solutions hindered magnetite crystallization and led to decrease in both, crystallite size and unit cell parameters.

4.9. Crystallization of manganite in the Red Sea

Multi-domainic crystals of manganite were observed in sediments from the Chain Deep (200-300 nm), Discovery Deep (>1μm) and from the margins of the Atlantis II Deep. Manganite crystals from the southern Chain Deep had iron impurity Fe/Mn atomic ratios 0.53-0.79 and Si/Mn ratios of 0.14-0.2 (Figure 12a). An elevated Si/Mn ratio probably affected the crystal size of manganite as observed in the crystal size of samples from Chain and Atlantis II Deeps. Manganite crystals from the southern part of the Atlantis II Deep had a Fe/Mn 0.2 ratio and Si/Mn 0.1 ratio (Figure 12c). A high resolution image of manganite crystals from the Atlantis II Deep showed d spacing of 0.48 nm with some dislocations (Figure 12c). Twinning of manganite crystals was observed in the sample from the Discovery Deep (Figure 12d)
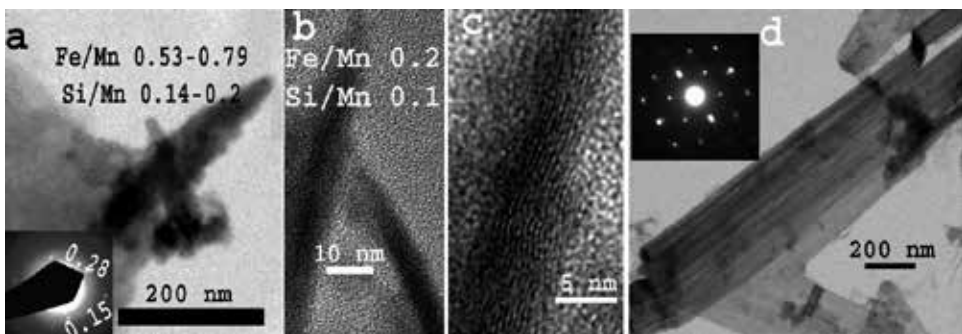
Figure 12. Manganite from the Red Sea: a) Multi-domain manganite from the southern Chain Deep with iron and Si impurities; b) 2 magnetite crystals from the margins of the Atlantis II Deep; c) A high resolution image of manganite from the Atlantis II Deep; d) Twinned manganite crystals from the Discovery Deep with electron diffraction in the upper part.
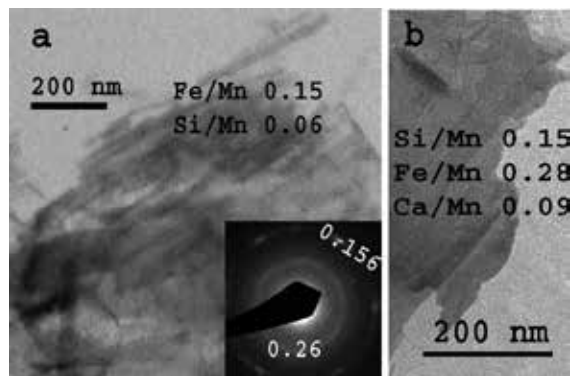
Figure 13. Multi-domain todorokite from the Red Sea Deeps: a) Todorokite from the northern Chain Deep; b) Todorokite from the marginal Atlantis II Deep.

4.10. Crystallization of todorokite in the Red Sea

Plates of todorokite and multi-domain crystals were found in Atlantis II and northern Chain Deeps. Todorokite had Fe and Si impurities with a Fe/Mn atomic ratio of 0.08-0.28 and Si/Mn 0.06-0.15 (Figure 13 a, b). Todorokite crystallized from the hydrothermal brine closer to its origin in the southwestern Atlantis II Deep that overflows into the northern Chain Deep.

5. Conclusions

Crystallization of Fe and Mn oxides - hydroxides occurred in the hypersaline and hydrothermal enviro nment of the Atlantis II, Chain and Discovery Deeps. Iron oxides that were sampled in the Thetis Deep probably crystallized from hydrothermal brine that filled the Deep. Mn oxides - hydroxides were found in the southern part of the Atlantis II and the close Chain and Discovery Deeps in the Red Sea. The minerals studied include short-range ordered ferrihydrite, singerite and Fe-Mn-Si oxides that crystallize at elevated Si concentrations in the brine. Si was found as the main impurity within the phases presented and it hinders crystallization of Fe well-crystallized phases like goethite, lepidocrocite and magnetite or Mn phases like todorokite and manganite. Lower Si concentration in the brine enabled the formation of larger crystals in the Thetis Deep.

Crystallization in hypersaline brine with an elevated Na concentration leads to the formation of multi-domain goethite from the Deeps of the Red Sea and from the Dead Sea. Mn appears as an impurity within iron oxides or forms a solid solution with them. In Mn oxides-hydroxides, Fe appears as an impurity.

Synthesis of the iron oxides hydroxides presented simulated precipitation conditions of the phases.

Author details

Nurit Taitel-Goldman[*]

Address all correspondence to: nuritg@openu.ac.il

The Open University of Israel, Israel

References

[1] Swift, S.A., Bower, S.A. and Schmidt, R.W., 2012, Vertical, horizontal and temporal changes in temperature in the Atlantis II and Discovery pools, Red Sea. *Deep Sea Research*, 1 64, 118-128.

[2]   Schoell, M. and Hartmann, M., 1973, Detailed temperature structure of the hot brines in the Atlantis II Deep area (Red Sea). *Marine geology*, 14, 1-14.

[3]   Hartmann, M., 1985, Atlantis II Deep geothermal brine system, Chemical processes between hydrothermal brines and Red Sea deep water. *Marine Geology*, 64, 157-177.

[4]   Hartmann, M., Scholten, J.C., Stoffers, P. and Wehner, F.,1998, Hydrographic structure of brine filled deeps in the Red Sea – new results from Shaban, Kerbit, Atlantis II, and Discovery Deep. *Marine Geology*, 144, 311-330.

[5]   Shanks, W.C. and Bischoff, J., 1977, Ore transport and deposition in the Red Sea geothermal system: a geochemical model. *Geochimica and Cosmochimica Acta*, 41, 1507-1519.

[6]   Laurila, T.E., Hannington, M.D., Petrson, S. and Garbe-Schönberg, 2014, Early depositional history of metalliferous sediments in the Atlantis II Deep of the Red Sea: Evidence from rare earth element geochemistry. *Geochimica et Cosmochimica acta*, 126, 146-168.

[7]   Scholten, J.C., Stoffers, P., Walters, P., Pflünger, W., 1991, Evidence for episodic hydrothermal activity in the Red Sea from composition and formation of hydrothermal sediments, Thetis Deep. *Tectonophysics*, 190, 109-117.

[8]   Pierret, M.C., Clauer, N. Bosch, D. and Blanc, G., 2010, Formation of Thetis Deep metal rich sediments in the absence of brines, Red Sea, *Journal of Geochemical exploration*, 104, 12-26.

[9]   Katz, A., and Starinsky, A., 2009, Geochemical history of the Dead Sea. *Aquat Geochem.* 15, 159-194.

[10] Kawamura, K. and Nissenbaum A., 1992, High abundance of low molecular weight organic acids in hypersaline spring water associated with salt diapir. *Org. Geoche.* 18, 469-476.

[11] Taitel-Goldman, N. and Singer A., 2001, High-resolution transmission electron microscopy study of newly formed sediments in the Atlantis II Deep Red Sea. *Clays and Clay Minerals*, 49, 174-182.

[12] Taitel-Goldman N., Singer A., Stoffers, P., 1999, A new short-range ordered, Fe-Si phases in the Atlantis II Deep, Red Sea hydrothermal sediments. *Proceedings 11th International Clay Conference, Ottawa, Canada 1997 (KodamaH. Mermut A.R. and Torrance J.K. eds.)*, 697-705.

[13] Taitel-Goldman, N. and Singer, A., 2002a, Metastable Si-Fe phases in hydrothermal sediments of Atlantis II Deep, Red Sea. *Clay Minerals*, 37, 236-248.

[14] Taitel-Goldman, N., Ezersky, V. and Mogilianski, D., 2009, High resolution transmission electron microscopy study of Fe-Mn oxides in the hydrothermal sediments of the Red Sea Deeps system. *Clays and Clay Minerals*, 57, 465-475.

[15] Cornell, R.M. and Schwertmann, U., 2003, The Iron Oxides, Structure, Properties, Re-actions, Occurrences and Uses. *Wiley-VCH Verlag GmbH & Co. KGaA Weinheim* Pp664.

[16] Cornell, R.M. and Giovanoli, R., 1986, Factors that govern the formation of multi-do-main goethites. *Clays and Clay Minerals*, 34, 557-564.

[17] Schwertmann, U., Cambier, P. and Murad, E., 1985, Properties of goethite of varying crystallinity. *Clays and Clay Minerals*, 33, 369-375.

[18] Taitel-Goldman, N., Bender-Koch, C., and Singer, A., 2004, Si associated goethite in hydrothermal sediments of the Atlantis II and Thetis Deeps, Red Sea, *Clays and Clay Minerals*, 52, 115-129.

[19] Taitel-Goldman, N. and Singer, A., 2002b, Synthesis of clay-sized iron oxides under marine hydrothermal conditions. *Clay Minerals*, 37, 719-731.

[20] Cornell, R.M., 1992, Preparation and properties of Si substituted akaganéite (β-FeOOH). *Z. Pflanzenernä*hr. *Bodenk*. 155, 449-453.

[21] Taitel-Goldman, N., Bender-Koch, C., and Singer, A., 2002, lepidocrocite in hydro-thermal sediments of the Atlantis II and Thetis Deeps, Red Sea, *Clays and Clay Miner-als*, 50, 186-197.

[22] Taitel-Goldman, N., 2009, Nanosized iron oxides and clays of the Red Sea Hydro-thermal Deeps. Characterization and formation processes. *VDM Verlg Dr. Müller*, 118Pp

[23] Butuzova, G.Y. and Lyapunov, S.M., 1995, Rare earth elements in hydrothermal sedi-mentary deposits from the Red Sea. Lithology and Mineral resources, 1, 13-26.

Syntheses and X-Ray Crystal Structures of Magnesium-Substituted Polyoxometalates

Chika Nozaki Kato, Nami Ukai, Daisuke Miyamae,
Shunya Arata, Toshifumi Kashiwagi,
Masaru Nagami, Toshiya Mori, Yusuke Kataoka,
Yasutaka Kitagawa and Hidemitsu Uno

Additional information is available at the end of the chapter

1. Introduction

Polyoxometalates have attracted much attention in the fields of catalytic chemistry, surface science, and materials science because their acidity, redox property, and solubility in various media can be controlled at molecular levels [1 – 3]. In particular, coordination of metal ions and organometallics to the vacant site(s) of lacunary polyoxometalates is one of the powerful techniques to construct effective and well-defined metal centers. Among the various metals and their derivatives that can be coordinated to the vacant site(s) of lacunary polyoxometalates, magnesium and magnesium derivatives are intriguing because of their efficient properties as catalysts, reagents for organic syntheses, pharmaceutical compounds, and so on [4, 5]. However, magnesium-coordinated polyoxometalates (characterized by X-ray crystallography) are still one of the least reported compounds: Examples that have been reported include $Mg_8SiW_9O_{37} \cdot 24.5H_2O$ [6], $Mg_8SiW_9O_{37} \cdot 12H_2O$ [6], and $Mg_7(MgW_{12}O_{42})(OH)_4(H_2O)_8$ [7].

In this study, we first report the syntheses and molecular structures of cesium and tetra-n-butylammonium salts of α-Keggin–type mono-magnesium–substituted polyoxotungstate, i.e., $Cs_{5.25}H_{1.75}[\alpha\text{-}PW_{11}MgO_{40}] \cdot 6H_2O$ and $[(n\text{-}C_4H_9)_4N]_{4.25}H_{2.75}[\alpha\text{-}PW_{11}MgO_{40}] \cdot H_2O \cdot CH_3CN$, and potassium and dimethylammonium salts of α-Dawson–type mono-magnesium–substituted polyoxotungstate, i.e., $K_8H_2[\alpha_2\text{-}P_2W_{17}MgO_{62}] \cdot 15H_2O$ and $[(CH_3)_2NH_2]_{7.5}H_{2.5}[\alpha_2\text{-}P_2W_{17}MgO_{62}] \cdot 6H_2O$; these salts were characterized via X-ray crystallography, elemental

analysis, thermogravimetric/differential thermal analysis, Fourier–transform infrared spectroscopy, solution nuclear magnetic resonance spectroscopies, and density-functional-theory (DFT) calculations. The X-ray crystallography results for $Cs_{5.25}H_{1.75}[\alpha\text{-}PW_{11}MgO_{40}]\cdot 6H_2O$, $[(n\text{-}C_4H_9)_4N]_{4.25}H_{2.75}[\alpha\text{-}PW_{11}MgO_{40}]\cdot H_2O$, and $[(CH_3)_2NH_2]_{7.5}H_{2.5}[\alpha_2\text{-}P_2W_{17}MgO_{62}]\cdot 6H_2O$ showed that the mono-magnesium–substituted sites in the α-Keggin and α-Dawson structures could not be identified because of the high symmetry of the compounds, as has been observed for mono-metal–substituted polyoxometalates; however, the bonding modes (i.e., bond lengths and angles) were significantly influenced by the insertion of magnesium ions into the vacant sites. The DFT calculation results also showed that coordination of a hydroxyl group and water molecule to the mono-magnesium–substituted site distorted the molecular structures.

2. Experimental section

2.1. Materials

$K_7[\alpha\text{-}PW_{11}O_{39}]\cdot xH_2O$ (x = 16 and 20) [8] and $K_{10}[\alpha_2\text{-}P_2W_{17}O_{61}]\cdot 14H_2O$ [9] were prepared as described in the literature. The number of solvated water molecules was determined by thermogravimetric/differential thermal analyses. All the reagents and solvents were obtained and used as received from commercial sources.

2.2. Instrumentation/analytical procedures

Elemental analyses were carried out by Mikroanalytisches Labor Pascher (Remagen, Germany). Prior to analysis, the samples were dried overnight at room temperature under pressures of $10^{-3} - 10^{-4}$ Torr. Infrared spectra of the solid samples were recorded on a Perkin Elmer Spectrum100 FT-IR spectrometer in KBr disks at around 25 °C in air. Infrared spectra of the liquid samples were recorded on a Perkin Elmer Frontier FT-IR spectrometer attached to a Universal ATR sampling accessory at around 25 °C in air. Thermogravimetric (TG) and differential thermal analyses (DTA) data were obtained using Rigaku Thermo Plus 2 TG/DTA TG 8120 and Rigaku Thermo Plus EVO2 TG/DTA 81205Z instruments and were performed in air while constantly increasing the temperature from 20 to 500 °C at rates of 1 and 4 °C/min. ^1H (600.17 MHz) and $^{31}P\text{-}\{^1H\}$ (242.95 MHz) nuclear magnetic resonance (NMR) spectra were recorded in tubes (outer diameter: 5 mm) on a JEOL ECA-600 NMR spectrometer (Shizuoka University). ^1H NMR spectra were measured in dimethylsulfoxide-d_6 and referenced to tetramethylsilane (TMS). Chemical shifts were reported as positive for resonances downfield of TMS (δ 0). ^{31}P NMR spectra were referenced to an external standard of 85% H_3PO_4 in a sealed capillary. Negative chemical shifts were reported on the δ scale for resonances upfield of H_3PO_4 (δ 0). ^{183}W NMR (25.00 MHz) spectra were recorded in tubes (outer diameter: 10 mm) on a JEOL ECA-600 NMR spectrometer (Kyushu University). The ^{183}W NMR spectrum measured in 2.0 mM $Mg(NO_3)_2$-D_2O was referenced to an external standard of saturated Na_2WO_4-D_2O solution (substitution method). Chemical shifts were reported as negative for resonances upfield of Na_2WO_4 (δ 0).

2.3. Synthesis of $Cs_{5.25}H_{1.75}[\alpha\text{-}PW_{11}MgO_{40}]\cdot 6H_2O$

Solid $K_7[\alpha\text{-}PW_{11}O_{39}]$ 20H_2O (1.01 g; 0.31 mmol) was added to a solution of $MgBr_2$ 6H_2O (0.18 g; 0.62 mmol) in 10 mL of water. After stirring for 10 min at 75 °C, solid CsCl (1.02 g; 6.06 mmol) was added to the solution, which was then stirred at 25 °C for 15 min. The resultant white precipitate was collected using a membrane filter (JG 0.2 μm). At this stage, 0.927 g of crude product was obtained. For purification, the crude product (0.927 g) was dissolved in 7 mL of a 3.3 mM solution of $MgBr_2$ at 75 °C; the resulting solution was filtered through a folded filter paper (Whatman No. 5). After the product was left standing for a day at 25 °C, colorless crystals formed. The obtained crystals weighed 0.384 g (the yield calculated via [mol of $Cs_{5.25}H_{1.75}[\alpha\text{-}PW_{11}MgO_{40}]\cdot 6H_2O$]/[mol of $K_7[\alpha\text{-}PW_{11}O_{39}]\cdot 20H_2O$] × 100% was 35.7%). The elemental analysis results were as follows: H, ≤ 0.1; Cs, 20.5; Mg, 0.65; P, 0.87; W, 58.9; Br, 0.01%. The calculated values for $Cs_{5.25}H_{1.75}[\alpha\text{-}PW_{11}MgO_{40}] = H_{1.75}Mg_1Cs_{5.25}O_{40}P_1W_{11}$ were as follows: H, 0.05; Cs, 20.42; Mg, 0.71; P, 0.91; W, 59.18; Br, 0%. A weight loss of 3.03% was observed in the product during overnight drying at room temperature at 10^{-3}–10^{-4} Torr before the analysis, which suggested that the complex contained six adsorbed water molecules (3.07%). TG/DTA obtained at a heating rate of 4 °C/min under atmospheric conditions showed a weight loss of 3.0% with an endothermic peak at 242 °C in the temperature range of 25 to 500 °C; our calculations indicated the presence of six water molecules (calcd. 3.07%). The results were as follows: IR spectroscopy (KBr disk): 1081s, 1058s, 961s, 888s, 830m, 808m, 769m, 724m cm^{-1}; IR spectroscopy (in water): 1079m, 1056s, 1017w, 957s, 898m, 823m, 779w, 724w cm^{-1}; ^{31}P NMR (27 °C, D_2O): δ−10.81.

2.4. Synthesis of $[(n\text{-}C_4H_9)_4N]_{4.25}H_{2.75}[\alpha\text{-}PW_{11}MgO_{40}]\cdot H_2O\cdot CH_3CN$

The tetra-n-butylammonium salt of $[\alpha\text{-}PW_{11}MgO_{40}]^{7-}$ was obtained from the reaction of $K_7[\alpha\text{-}PW_{11}O_{39}]\cdot 16H_2O$ (2.00 g; 0.62 mmol) with $MgBr_2\cdot 6H_2O$ (0.19 g, 0.65 mmol) in 250 mL of water at 70 °C. After stirring for 1 h at 70 °C, solid $[(CH_3)_4N]Br$ (4.75 g; 30.8 mmol) was added to the solution, which was then stirred at 25 °C for 4 d. The resultant white precipitate was collected using a membrane filter (JG 0.2 μm). The white precipitate (1.708 g) was dissolved in water (350 mL) at 80 °C, $[(n\text{-}C_4H_9)_4N]Br$ (16.99 g; 52.7 mmol) was added to the colorless clear solution, and the solution was stirred at 80 °C for 1 h. The resultant white precipitate was collected on a glass frit (G4). At this stage, 1.862 g of the crude product was obtained. The crude product (1.862 g) was dissolved in acetonitrile (5.5 mL). After filtration through a folded filter paper (Whatman No. 5), colorless crystals were obtained by vapor diffusion from methanol at ~25 °C for one week. The obtained crystals weighed 0.765 g (the yield calculated from [mol of $[(n\text{-}C_4H_9)_4N]_{4.25}H_{2.75}[\alpha\text{-}PW_{11}MgO_{40}]\cdot H_2O\cdot CH_3CN$]/[mol of $K_7[\alpha\text{-}PW_{11}O_{39}]\cdot 16H_2O$] × 100% was 32.5%). The elemental analysis results were as follows: C, 21.5; H, 4.08; N, 1.72; P, 0.83; Mg, 0.63; W, 54.0; K, <0.03%. The calculated values for $[(n\text{-}C_4H_9)_4N]_{4.25}H_{2.75}[\alpha\text{-}PW_{11}MgO_{40}]\cdot H_2O = C_{68}H_{157.75}Mg_1N_{4.25}O_{41}P_1W_{11}$ were as follows: C, 21.67; H, 4.22; N, 1.58; P, 0.82; Mg, 0.64; W, 53.66; K, 0%. A weight loss of 1.44% from the product was observed during overnight drying at room temperature at 10^{-3}–10^{-4} Torr before the analysis, which suggested the presence of a weakly solvated or adsorbed acetonitrile molecule (1.08%); this was also supported by the presence of a signal at 2.10 ppm in the ^{1}H NMR spectrum (in DMSO-d_6) of the sample after drying overnight, which was due to an acetonitrile molecule. TG/DTA results obtained under

atmospheric conditions at a rate of 4 °C/min showed a weight loss of 27.46% with an endothermic peak at 312.2 °C and an exothermic peak at 412.7 °C in the temperature range of 25 to 500 °C; our calculations indicated the presence of $4.25[(C_4H_9)_4N]^+$ ions, a water molecule, and an acetonitrile molecule (calcd. 28.6%). The results were as follows: IR spectroscopy (KBr disk): 1081m, 1060s, 957s, 891s, 819s, 734s cm^{-1}; IR spectroscopy (in acetonitrile): 1082m, 1059s, 955s, 889s, 811s, 733s cm^{-1}; ^{31}P NMR (20.5 °C, acetonitrile-d_3): δ −10.26.

2.5. Synthesis of $K_8H_2[\alpha_2$-$P_2W_{17}MgO_{62}]\cdot15H_2O$

Solid $K_{10}[\alpha_2$-$P_2W_{17}O_{61}]\cdot14H_2O$ (2.00 g; 0.42 mmol) was added to a solution of $Mg(NO_3)_2\cdot6H_2O$ (0.32 g; 1.25 mmol) in 50 mL of water. After stirring for 2 h at 25 °C, solid KCl (1.57 g; 21.1 mmol) was added to the solution. The resultant white precipitate was collected using a glass frit (G3) and washed with methanol. At this stage, 1.730 g of a crude product was obtained. For purification, the crude product (1.730 g) was dissolved in 17 mL of a 2.0 mM $Mg(NO_3)_2$ aqueous solution; the resulting solution was filtered through a folded filter paper (Whatman No. 5). After standing in a refrigerator overnight, white crystals formed, which were collected using a membrane filter (JG 0.2 μm) and yielded 0.693 g of product. The percent yield calculated using [mol of $K_8H_2[\alpha_2$-$P_2W_{17}MgO_{62}]\cdot15H_2O$]/[mol of $K_{10}[\alpha_2$-$P_2W_{17}O_{61}]\cdot14H_2O$] × 100% was 34.8 %. The elemental analysis results were as follows: H, <0.1; K, 7.17; Mg, 0.52; P, 1.34; W, 68.6; N, <0.1%; the calculated values for $K_8H_2[\alpha_2$-$P_2W_{17}MgO_{62}]\cdot xH_2O$ (x = 1) = $H_4K_8Mg_1O_{63}P_2W_{17}$ were H, 0.09; K, 6.90; Mg, 0.54; P, 1.37; W, 68.89; N, 0%. A weight loss of 5.30% was observed during overnight drying at room temperature at 10^{-3}–10^{-4} Torr before analysis, suggesting the presence of 14 weakly solvated or adsorbed water molecules (5.27%). TG/DTA results obtained at a heating rate of 4 °C/min under atmospheric conditions showed a weight loss of 5.62% below 500 °C with an endothermic point at 101.4 °C; calculations showed that 5.64% corresponded to 15 water molecules. The results were as follows: IR spectroscopy (KBr disk): 1084s, 1063m, 1015m, 945s, 920s, 892sh, 823s, 786s, 736s cm^{-1}; IR spectroscopy (in water): 1086s, 1064m, 1015w, 946s, 914s, 811s, 788s, 724m cm^{-1}; ^{31}P NMR (D_2O, 23.9 °C): δ −7.77, −13.77. ^{183}W NMR (2.0 mM $Mg(NO_3)_2$-D_2O, 40 °C): δ −57.04, −80.87, −131.47, −176.59, −181.67, −201.40, −207.65, −208.63, −230.51.

2.6. Synthesis of $[(CH_3)_2NH_2]_{7.5}H_{2.5}[\alpha_2$-$P_2W_{17}MgO_{62}]\cdot6H_2O$

The dimethylammonium salt of $[\alpha_2$-$P_2W_{17}MgO_{62}]^{10-}$ was obtained via the reaction of $K_{10}[\alpha_2$-$P_2W_{17}O_{61}]\cdot14H_2O$ (2.00 g; 0.42 mmol) with $Mg(NO_3)_2\cdot6H_2O$ (0.11g; 0.43 mmol) in 50 mL of water. After stirring for 1 h at 25 °C, solid $(CH_3)_2NHHCl$ (3.44 g; 42.2mmol) was added to the solution. The resultant white precipitate was collected using a glass frit (G4). At this stage, 1.363 g of the crude product was obtained. For purification, the crude product (1.363 g) was dissolved in 32 mL of water. After filtration through a folded filter paper (Whatman No. 5), colorless crystals were obtained by vapor diffusion from ethanol at 25 °C for 4 d. The obtained crystals weighed 0.740 g (the yield calculated from [mol of $[(CH_3)_2NH_2]_{7.5}H_{2.5}[\alpha_2$-$P_2W_{17}MgO_{62}]\cdot6H_2O$]/[mol of $K_{10}[\alpha_2$-$P_2W_{17}O_{61}]\cdot14H_2O$] × 100% was 38.1%). The elemental analysis results were as follows: C, 3.72; H, 1.42; N, 2.50; Mg, 0.42; P, 1.34; W, 68.0; K, <0.1%; the calculated values for $[(CH_3)_2NH_2]_{7.5}H_{2.5}[\alpha_2$-$P_2W_{17}MgO_{62}]\cdot xH_2O$ (x = 3) = $C_{15}H_{68.5}Mg_1N_{7.5}O_{65}P_2W_{17}$ were C, 3.91; H, 1.50; N, 2.28; Mg,

0.53; P, 1.35; W, 67.86; K, 0%. A weight loss of 1.30% was observed during overnight drying at room temperature at 10^{-3}–10^{-4} Torr before analysis, suggesting the presence of three weakly solvated or adsorbed water molecules (1.16%). TG/DTA results obtained at a rate of 1 °C/min under atmospheric conditions showed weight losses of 2.33% and 7.42% without clear endothermic and exothermic points in the temperature ranges of 25 to 200 °C and 200 to 500 °C, respectively; calculations showed that 2.32% and 7.42% corresponded to six water molecules and 7.5 dimethylammonium ions, respectively. The results were as follows: IR spectroscopy (KBr disk): 1087s, 1065m, 1018m, 948s, 919s, 891s, 805s, 777s, 717s cm^{-1}; IR spectroscopy (in water): 1086s, 1065m, 1020w, 945s, 913s, 808s, 790s, 723m cm^{-1}; ^{31}P NMR (D$_2$O, 21.7 °C): δ −7.73, −13.74.

2.7. X-Ray crystallography

A colorless prism crystal of Cs$_{5.25}$H$_{1.75}$[α-PW$_{11}$MgO$_{40}$]·6H$_2$O (0.090 × 0.070 × 0.060 mm), colorless platelet crystal of [(n-C$_4$H$_9$)$_4$N]$_{4.25}$H$_{2.75}$[α-PW$_{11}$MgO$_{40}$]·H$_2$O CH$_3$CN (0.200 × 0.100 × 0.020 mm), and colorless block crystal of [(CH$_3$)$_2$NH$_2$]$_{7.5}$H$_{2.5}$[α_2-P$_2$W$_{17}$MgO$_{62}$]·6H$_2$O (0.200 × 0.100 × 0.100 mm) were mounted on a loop or MicroMount. The measurements for the cesium and tetra-n-butylammonium salts of α-Keggin mono-magnesium–substituted polyoxotungstate were obtained using a Rigaku VariMax with a Saturn diffractometer using multi-layer mirror-monochromated Mo Kα radiation (λ = 0.71075 Å) at 100±1 K. The measurement for the dimethylammonium salt of α-Dawson mono-magnesium–substituted polyoxotungstate was carried out using a Rigaku VariMax with an XtaLAB P200 diffractometer using multi-layer mirror-monochromated Mo Kα radiation (λ = 0.71075 Å) at 153±1 K. Data were collected and processed using CrystalClear, CrystalClear-SM Expert for Windows, and structural analysis was performed using CrystalStructure for Windows. The structure was solved by SHELXS-97, SHELXS-2013, and SIR-2004 (direct methods) and refined by SHELXL-97 and SHELXL2013 [10, 11]. In these magnesium compounds, a magnesium atom was disordered over ten and twelve tungsten atoms in [α-PW$_{11}$MgO$_{40}$]$^{7-}$, and six tungsten atoms at B-sites (cap units) in [α-PW$_{17}$MgO$_{62}$]$^{10-}$. The occupancies for the magnesium and tungsten atoms were fixed at 1/10 and 9/10, 1/12 and 11/12, and 1/6 and 5/6, respectively. For Cs$_{5.25}$H$_{1.75}$[α-PW$_{11}$MgO$_{40}$]·6H$_2$O, 5.25 cesium ions were disordered at Cs(1) and Cs(2) and the water molecules were disordered. For the structural analysis of [(CH$_3$)$_2$NH$_2$]$_{7.5}$H$_{2.5}$[α_2-P$_2$W$_{17}$MgO$_{62}$]·6H$_2$O, the chemical formula of [(CH$_3$)$_2$NH$_2$]$_{7.5}$H$_{2.5}$[α_2-P$_2$W$_{17}$MgO$_{62}$]·3H$_2$O was used, and the water molecules were also disordered. With regard to [(n-C$_4$H$_9$)$_4$N]$_{4.25}$H$_{2.75}$[α-PW$_{11}$MgO$_{40}$]·H$_2$O·CH$_3$CN, tetra-n-butylammonium ions, water molecules, and acetonitrile molecules could not be modeled because of disorder of the atoms. Accordingly, the residual electron density was removed using the SQUEEZE routine in PLATON [12]. Disordered counter-cations and solvated molecules are common in polyoxometalate chemistry [13 – 16].

2.8. Crystal data for Cs$_{5.25}$H$_{1.75}$[α-PW$_{11}$MgO$_{40}$]·6H$_2$O

H$_{13.75}$Cs$_{5.25}$MgO$_{46}$PW$_{11}$; M = 3525.27, *tetragonal*, space group: $P4_2/ncm$ (#138), a = 20.859(4) Å, c = 10.387(2) Å, V = 4520(2) Å^3, Z = 4, Dc = 5.181 g/cm^3, μ(Mo Kα) = 321.99 cm^{-1}, R_1 = 0.0508 [I > 2σ(I)], wR_2 = 0.1070 (for all data). GOF = 1.248 [52491 total reflections and 2703 unique reflections where I > 2σ(I)]. CCDC No. 1020993

2.9. Crystal data for [(*n*-C$_4$H$_9$)$_4$N]$_{4.25}$H$_{2.75}$[α-PW$_{11}$MgO$_{40}$]·H$_2$O·CH$_3$CN

C$_{70}$H$_{160.75}$MgN$_{5.25}$O$_{41}$PW$_{11}$; M = 3809.93, *cubic*, space group: *Im-3m* (#229), *a* = 17.650(6) Å, *V* = 5498(3) Å^3, Z = 2, D_c = 2.301 g/cm^3, μ(Mo Kα) = 115.627 cm^{-1}, R_1 = 0.0578 [*I* > 2σ(*I*)], wR_2 = 0.1312 (for all data). GOF = 1.181 (44531 total reflections, 653 unique reflections where *I* > 2σ(*I*)). CCDC No. 1020994

2.10. Crystal data for [(CH$_3$)$_2$NH$_2$]$_{7.5}$H$_{2.5}$[α$_2$-P$_2$W$_{17}$MgO$_{62}$]·3H$_2$O

C$_{15}$H$_{68.50}$MgN$_{7.50}$O$_{65}$P$_2$W$_{17}$; M = 4605.92, *orthorhombic*, space group: *Pnma* (#62), *a* = 27.7901(12) Å, *b* = 20.4263(9) Å, *c* = 15.0638(6) Å, V = 8550.9(7) Å^3, Z = 4, D_c = 3.577 g/cm^3, μ(Mo Kα) = 229.323 cm^{-1}, R_1 = 0.0685 [*I* > 2σ(*I*)], wR_2 = 0.1980 (for all data). GOF = 1.096 (95493 total reflections, 12764 unique reflections where *I* > 2σ(*I*)). CCDC No. 1020995

2.11. Computational details

The optimal geometries of [α-PW$_{11}${Mg(OH)}O$_{39}$]$^{6-}$ and [α-PW$_{11}${Mg(OH$_2$)}O$_{39}$]$^{5-}$ were computed using a DFT method. First, we optimized the molecular geometries and then applied single-point calculations with larger basis sets. All calculations were performed using a spin-restricted B3LYP method with the Gaussian09 program package [17]. The solvent effect of acetonitrile was considered using the polarizable continuum model. The basis sets used for geometry optimization were LANL2DZ for the W atoms, 6-31+G* for the P atoms, and 6-31G* for the H, O, and Mg atoms. LANL2DZ and 6-31+G* were used for the W and other atoms, respectively, for the single-point calculations. Geometry optimization was started using the X-ray structure of [α-PW$_{12}$O$_{40}$]$^{3-}$ as the initial geometry, and was performed in acetonitrile. The optimized geometries were confirmed to be true minima by frequency analyses. All atomic charges used in this text were obtained from Mulliken population analysis. Zero-point energy-corrected total energies were used to consider the structural stabilities of [α-PW$_{11}${Mg(OH)}O$_{39}$]$^{6-}$ and [α-PW$_{11}${Mg(OH$_2$)}O$_{39}$]$^{5-}$.

3. Results and discussion

3.1. Syntheses and molecular structures of cesium and tetra-*n*-butylammonium salts of α-Keggin mono-magnesium-substituted polyoxotungstate Cs$_{5.25}$H$_{1.75}$[α-PW$_{11}$MgO$_{40}$]·6H$_2$O and [(*n*-C$_4$H$_9$)$_4$N]$_{4.25}$H$_{2.75}$[α-PW$_{11}$MgO$_{40}$]·H$_2$O·CH$_3$CN

The cesium salt of [α-PW$_{11}$MgO$_{40}$]$^{7-}$ was formed by the direct reaction of magnesium bromide with [α-PW$_{11}$O$_{39}$]$^{7-}$ (at a Mg^{2+}/[α-PW$_{11}$O$_{39}$]$^{7-}$ ratio of ~2.0) in aqueous solution, followed by the addition of excess cesium chloride. The pure cesium salt was not obtained by a stoichiometric reaction of Mg^{2+} with [α-PW$_{11}$O$_{39}$]$^{7-}$ in aqueous solution. Crystallization was performed via slow-evaporation from a 3.3 mM MgBr$_2$ solution at 70 °C. Here, single crystals suitable for X-ray crystallography could not be obtained in water because a mono-lacunary polyoxoanion formed upon the removal of magnesium ions from [α-PW$_{11}$MgO$_{40}$]$^{7-}$ in water at around 70 °C. In contrast, the tetra-*n*-butylammonium salt of [α-PW$_{11}$MgO$_{40}$]$^{7-}$ was formed by a stoichiometric reaction of magnesium bromide with [α-PW$_{11}$O$_{39}$]$^{7-}$ in aqueous solution, followed by the

addition of excess tetra-*n*-butylammonium bromide. Crystallization was performed by vapor diffusion from acetonitrile/methanol at ~25 °C.

Samples for the elemental analyses were dried overnight at room temperature under a vacuum of $10^{-3} - 10^{-4}$ Torr. The elemental analysis results for H, Cs, Mg, P, and W were in good agreement with the calculated values for the formula of $Cs_{5.25}H_{1.75}[\alpha\text{-}PW_{11}MgO_{40}]$. Br analysis revealed no contamination of bromide ions from $MgBr_2$. The weight loss observed during the course of drying before the analysis was 3.03% for $Cs_{5.25}H_{1.75}[\alpha\text{-}PW_{11}MgO_{40}]\cdot6H_2O$; this corresponded to six weakly solvated or adsorbed water molecules. TG/DTA measurements also showed a weight loss of 3.1% in the temperature range of 25 to 500 °C, which corresponded to six water molecules. For the tetra-*n*-butylammonium salt, the elemental analysis results for C, H, N, P, Mg, and W were in good agreement with the calculated values for the formula of $[(n\text{-}C_4H_9)_4N]_{4.25}H_{2.75}[\alpha\text{-}PW_{11}MgO_{40}]\cdot H_2O$. K analysis revealed no contamination of potassium ions from $K_7[\alpha\text{-}PW_{11}O_{39}]$. The weight loss observed during the course of drying before the analysis was 1.44% for $[(n\text{-}C_4H_9)_4N]_{4.25}H_{2.75}[\alpha\text{-}PW_{11}MgO_{40}]\cdot H_2O\cdot CH_3CN$; this corresponded to one weakly solvated or adsorbed acetonitrile molecule. The ^1H NMR spectrum in DMSO-d_6 also showed the presence of an acetonitrile molecule in the sample after drying under vacuum overnight. TG/DTA measurements showed a weight loss of 27.46% in the temperature range of 25 to 500 °C, which corresponded to 4.25 $[(C_4H_9)_4N]^+$ ions, a water molecule, and an acetonitrile molecule.

The molecular structures of cesium and tetra-*n*-butylammonium salts of $[\alpha\text{-}PW_{11}MgO_{40}]^{7-}$ as determined by X-ray crystallography, are shown in Figs. 1 and 2. The lengths of the bonds involving oxygen atoms in the central PO_4 tetrahedron (O_a), bridging oxygen atoms between corner-sharing MO_6 (M = W and Mg) octahedra (O_c), bridging oxygen atoms between edge-sharing MO_6 octahedra (O_e), and terminal oxygen atoms (O_t) are summarized in Table 1. The molecular structures of these magnesium compounds were identical to that of a monomeric, α-Keggin polyoxotungstate $[\alpha\text{-}PW_{12}O_{40}]^{3-}$ [18, 19]. Due to the high-symmetry space groups of the structures, the ten or eleven tungsten(VI) atoms were disordered and the mono-magnesium-substituted site was not identified, as previously reported for $[\alpha\text{-}PW_{11}\{Al(OH_2)\}O_{39}]^{4-}$ [20]. However, it was clear that the average bond lengths of $W(Mg)$-O_a in $Cs_{5.25}H_{1.75}[\alpha\text{-}PW_{11}MgO_{40}]\cdot6H_2O$ (2.478 Å) and $[(n\text{-}C_4H_9)_4N]_{4.25}H_{2.75}[\alpha\text{-}PW_{11}MgO_{40}]\cdot H_2O$ CH_3CN (2.483 Å) were longer than those of $[CH_3NH_3]_3[PW_{12}O_{40}]\cdot2H_2O$ (2.4398 Å), $[(CH_3)_2NH_2]_3[PW_{12}O_{40}]$ (2.4430 Å), and $[(CH_3)_3NH]_3[PW_{12}O_{40}]$ (2.4313 Å) [19] (Table 1); this suggested that the magnesium ion was coordinated to the mono-lacunary Keggin-type polyoxotungstate.

Although a hydroxyl group and/or water molecule should be coordinated to the magnesium site in $[\alpha\text{-}PW_{11}MgO_{40}]^{7-}$, it could not be identified by X-ray crystallography. On the basis of the Cs analysis results, $Cs_{5.25}H_{1.75}[\alpha\text{-}PW_{11}MgO_{40}]\cdot6H_2O$ should contain species with hydroxyl groups in at least 25% of the molecules. To investigate the coordination spheres around the mono-magnesium-substituted sites containing a hydroxyl group and water molecule, optimized geometries of $[\alpha\text{-}PW_{11}\{Mg(OH)\}O_{39}]^{6-}$ and $[\alpha\text{-}PW_{11}\{Mg(OH_2)\}O_{39}]^{5-}$ were computed by means of a DFT method, as shown in Fig. 3. The bond-length ranges, mean bond distances, and Mulliken charges for DFT-optimized $[\alpha\text{-}PW_{11}\{Mg(OH)\}O_{39}]^{6-}$ and $[\alpha\text{-}PW_{11}\{Mg(OH_2)\}O_{39}]^{5-}$ are summarized in Tables 2 and 3. As shown in Fig. 3, the ligands coordinated to the mono-magnesium-substituted site caused remarkable distortion of the α-Keggin molecular structure:

The Mg–P distance of $[\alpha\text{-PW}_{11}\{\text{Mg(OH)}\}\text{O}_{39}]^{6-}$ was 3.652 Å, which was longer than that of $[\alpha\text{-PW}_{11}\{\text{Mg(OH}_2)\}\text{O}_{39}]^{5-}$ (3.330 Å). The charges of all atoms in $[\alpha\text{-PW}_{11}\{\text{Mg(OH)}\}\text{O}_{39}]^{6-}$ and $[\alpha\text{-PW}_{11}\{\text{Mg(OH}_2)\}\text{O}_{39}]^{5-}$ were also influenced by the ligands, as shown in Table 3.
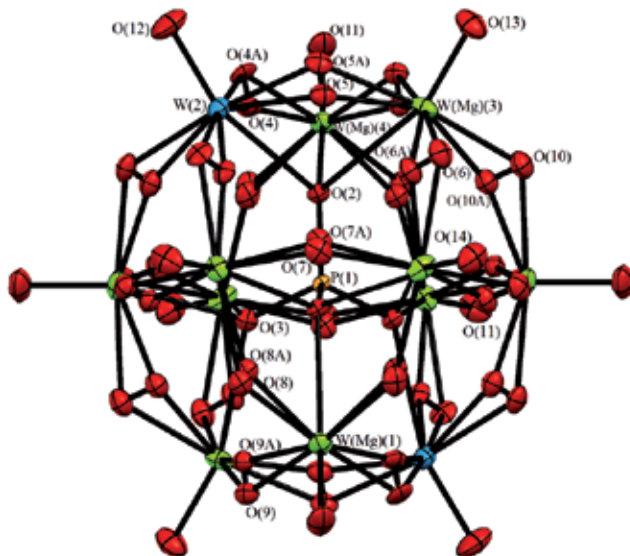

Figure 1. The molecular structure (ORTEP drawing) of $\text{Cs}_{5.25}\text{H}_{1.75}[\alpha\text{-PW}_{11}\text{MgO}_{40}]\cdot6\text{H}_2\text{O}$. The corner- and edge-sharing oxygen atoms in the α-Keggin structure were disordered. W(2) was clearly identified; however, a magnesium atom was disordered over ten tungsten sites in $[\alpha\text{-PW}_{11}\text{MgO}_{40}]^{7-}$, and the occupancies for the magnesium and tungsten sites were fixed at 1/10 and 9/10 throughout the refinement.
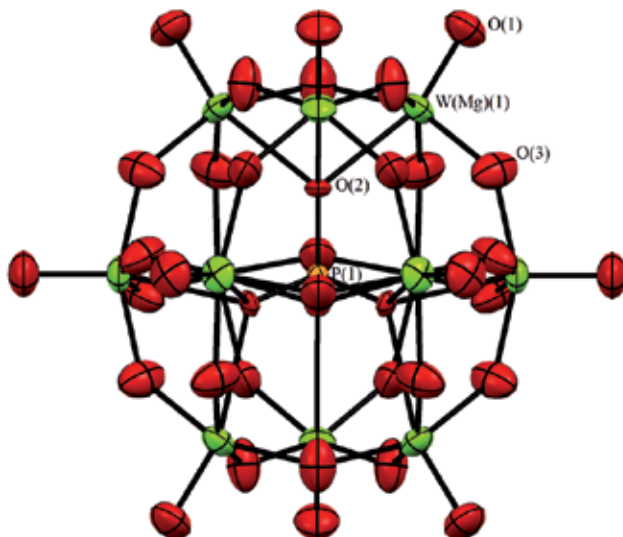
Figure 2. The molecular structure (ORTEP drawing) of $[(n\text{-C}_4\text{H}_9)_4\text{N}]_{4.25}\text{H}_{2.75}[\alpha\text{-PW}_{11}\text{MgO}_{40}]\cdot\text{H}_2\text{O}$. A magnesium atom was disordered over eleven tungsten sites in $[\alpha\text{-PW}_{11}\text{MgO}_{40}]^{7-}$, and the occupancies for the magnesium and tungsten sites were fixed at 1/12 and 11/12 throughout the refinement.

	$Cs_{5.25}H_{1.75}[\alpha\text{-}PW_{11}MgO_{40}]\cdot 6H_2O$
W(Mg)-O_a	2.426 – 2.521 (2.478)
W(Mg)-O_c	1.827 – 2.426 (1.945)
W(Mg)-O_e	1.827 – 2.426 (1.945)
W(Mg)-O_t	1.688 – 1.712 (1.696)
W(2)-O_a	2.423
W(2)-O_c	1.859 – 1.979 (1.927)
W(2)-O_e	1.859 – 1.979 (1.927)
W(2)-O_t	1.726
P-O	1.544 – 1.590 (1.562)
	$[(n\text{-}C_4H_9)_4N]_{4.25}H_{2.75}[\alpha\text{-}PW_{11}MgO_{40}]\cdot H_2O\cdot CH_3CN$
W(Mg)-O_a	2.483 (2.483)
W(Mg)-O_c	1.894 (1.894)
W(Mg)-O_e	1.894 (1.894)
W(Mg)-O_t	1.703 (1.703)
P-O	1.511 (1.511)

Table 1. Ranges and mean bond distances (Å) of $Cs_{5.25}H_{1.75}[\alpha\text{-}PW_{11}MgO_{40}]\cdot 6H_2O$ and $[(n\text{-}C_4H_9)_4N]_{4.25}H_{2.75}[\alpha\text{-}PW_{11}MgO_{40}]\cdot H_2O\cdot CH_3CN$. O_a: oxygen atoms belonging to the central PO_4 tetrahedron; O_c: bridging oxygen atoms between corner-sharing MO_6 (M = Mg and W) octahedra; O_e: bridging oxygen atoms between edge-sharing MO_6 octahedra (M = Mg and W); and O_t: terminal oxygen atoms. The mean values are provided in parentheses.

Here, the sum of the zero-point energy-corrected total energies (Hartree) of ($[\alpha\text{-}PW_{11}\{Mg(OH)\}O_{39}]^{6-}$ + H_3O^+) and ($[\alpha\text{-}PW_{11}\{Mg(OH_2)\}O_{39}]^{5-}$ + H_2O) was –4377.185183 and –4377.287786, respectively; the thermal energy of ($[\alpha\text{-}PW_{11}\{Mg(OH_2)\}O_{39}]^{5-}$ + H_2O) calculated on the basis of zero-point energy was 64.4 kcal/mol lower than that of ($[\alpha\text{-}PW_{11}\{Mg(OH)\}O_{39}]^{6-}$ + H_3O^+). Thus, $[\alpha\text{-}PW_{11}\{Mg(OH_2)\}O_{39}]^{5-}$ was more stable than $[\alpha\text{-}PW_{11}\{Mg(OH)\}O_{39}]^{6-}$. It was noted that the Mg-O_c and Mg-O_e bond lengths of the optimized $[\alpha\text{-}PW_{11}\{Mg(OH)\}O_{39}]^{6-}$ structure were longer than those of $[\alpha\text{-}PW_{11}\{Mg(OH_2)\}O_{39}]^{5-}$, as shown in Table 2. In the X-ray crystal structures of $Cs_{5.25}H_{1.75}[\alpha\text{-}PW_{11}MgO_{40}]\cdot 6H_2O$ and $[(n\text{-}C_4H_9)_4N]_{4.25}H_{2.75}[\alpha\text{-}PW_{11}MgO_{40}]\cdot H_2O\cdot CH_3CN$, the mean W(Mg)-$O_c$ and W(Mg)-O_e bond lengths of the cesium salt were longer than those of the tetra-n-butylammonium salt. The mean P-O bond length of $Cs_{5.25}H_{1.75}[\alpha\text{-}PW_{11}MgO_{40}]\cdot 6H_2O$ (1.562 Å) was also longer than that of $[(n\text{-}C_4H_9)_4N]_{4.25}H_{2.75}[\alpha\text{-}PW_{11}MgO_{40}]\cdot H_2O\cdot CH_3CN$ (1.511 Å); this was consistent with the DFT calculation results. These results suggested that $Cs_{5.25}H_{1.75}[\alpha\text{-}PW_{11}MgO_{40}]\cdot 6H_2O$ contained both $[\alpha\text{-}PW_{11}\{Mg(OH)\}O_{39}]^{6-}$ and $[\alpha\text{-}PW_{11}\{Mg(OH_2)\}O_{39}]^{5-}$; in contrast, the molecular structure of $[(n\text{-}C_4H_9)_4N]_{4.25}H_{2.75}[\alpha\text{-}PW_{11}MgO_{40}]\cdot H_2O\cdot CH_3CN$ was predominantly $[\alpha\text{-}PW_{11}\{Mg(OH_2)\}O_{39}]^{5-}$.

The ^{31}P NMR spectrum in D_2O of $Cs_{5.25}H_{1.75}[\alpha\text{-}PW_{11}MgO_{40}]\cdot 6H_2O$ showed a signal at −10.8 ppm that corresponded to the internal phosphorus atom; this demonstrated the high purity of

$Cs_{5.25}H_{1.75}[\alpha\text{-}PW_{11}MgO_{40}]\cdot 6H_2O$ in water. However, the presence of polyoxoanions possessing Mg–OH and/or Mg–OH$_2$ moieties could not be identified by ^{31}P NMR spectroscopy in water. For the ^{31}P NMR spectrum in acetonitrile-d_3 of $[(n\text{-}C_4H_9)_4N]_{4.25}H_{2.75}[\alpha\text{-}PW_{11}MgO_{40}]\cdot H_2O\cdot CH_3CN$, a signal was also observed at −10.3 ppm. These signals exhibited a shift from the signals of $K_7[\alpha\text{-}PW_{11}O_{39}]$ (δ −10.6) in D_2O and the tetra-n-butylammonium salt of $[\alpha\text{-}PW_{11}O_{39}]^{7-}$ (δ −12.0) in acetonitrile-d_3, respectively. This showed that the magnesium ion was inserted into the vacant site.
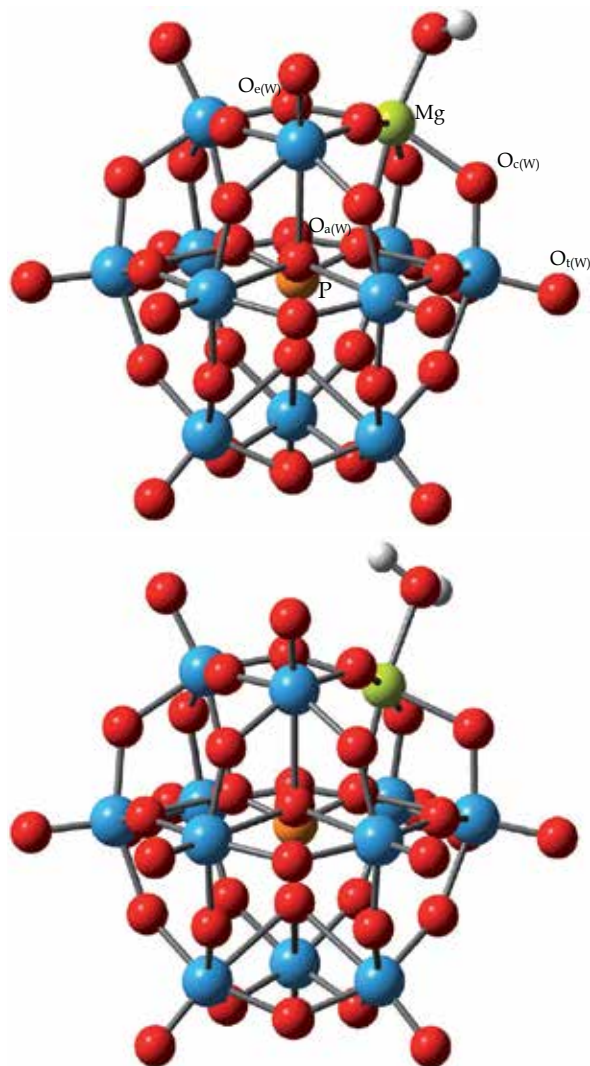

Figure 3. DFT-optimized geometries of $[\alpha\text{-}PW_{11}\{Mg(OH)\}O_{39}]^{6-}$ (top) and $[\alpha\text{-}PW_{11}\{Mg(OH_2)\}O_{39}]^{5-}$ (bottom). The phosphorus, oxygen, magnesium, tungsten, and hydrogen atoms are represented by orange, red, green, blue, and white balls, respectively.

	$[\alpha\text{-PW}_{11}\{\text{Mg(OH)}\}\text{O}_{39}]^{6-}$	$[\alpha\text{-PW}_{11}\{\text{Mg(OH}_2)\}\text{O}_{39}]^{5-}$
W-O$_a$	2.42491 – 2.50502 (2.45747)	2.43078 – 2.49519 (2.46749)
W-O$_c$	1.77745 – 2.06287 (1.92795)	1.78987 – 2.04292 (1.92730)
W-O$_e$	1.77336 – 2.06166 (1.92035)	1.78511 – 2.03477 (1.92000)
W-O$_t$	1.72294 – 1.73069 (1.72654)	1.72076 – 1.72696 (1.72356)
P-O	1.54748 – 1.56478 (1.55930)	1.55541 – 1.55857 (1.55763)
Mg-O$_a$	2.52990 (2.52990)	2.18152 (2.18152)
Mg-O$_c$	2.10554 – 2.11671 (2.11113)	2.04263 – 2.05034 (2.04649)
Mg-O$_e$	2.08702 – 2.09720 (2.09211)	2.06585 – 2.08177 (2.07381)
Mg-OH/OH$_2$	1.93732 (1.93732)	2.12343 (2.12343)

Table 2. Ranges and mean bond distances (Å) of $[\alpha\text{-PW}_{11}\{\text{Mg(OH)}\}\text{O}_{39}]^{6-}$ and $[\alpha\text{-PW}_{11}\{\text{Mg(OH}_2)\}\text{O}_{39}]^{5-}$ optimized by DFT calculations. The mean values are provided in parentheses.

	$[\alpha\text{-PW}_{11}\{\text{Mg(OH)}\}\text{O}_{39}]^{6-}$	$[\alpha\text{-PW}_{11}\{\text{Mg(OH}_2)\}\text{O}_{39}]^{5-}$
O$_{a\,(W)}$	−0.752 – −0.731 (−0.740)	−0.789 – −0.752 (−0.768)
O$_{c\,(W)}$	−1.166 – −0.975 (−1.084)	−1.170 – −1.009 (−1.095)
O$_{e\,(W)}$	−1.359 – −1.143 (-1.300)	−1.366 – −1.194 (−1.314)
O$_{t\,(W)}$	−0.774 – −0.725 (−0.748)	−0.743 – −0.708 (−0.730)
P	6.849	7.192
W	2.105 – 2.474 (2.304)	2.151 – 2.460 (2.313)
O$_{a(Mg)}$	−0.489	−0.481
O$_{c(Mg)}$	−0.694 – −0.680 (−0.687)	−0.749 – −0.690 (−0.720)
O$_{e(Mg)}$	−0.638 – −0.616 (−0.627)	−0.674 – −0.636 (−0.655)
O$_{t(Mg)}$	−0.961	−0.844
Mg	−0.253	−0.274
H	0.428	0.556 – 0.564 (0.560)

Table 3. Mulliken charges computed for $[\alpha\text{-PW}_{11}\{\text{Mg(OH)}\}\text{O}_{39}]^{6-}$ and $[\alpha\text{-PW}_{11}\{\text{Mg(OH}_2)\}\text{O}_{39}]^{5-}$. The mean values are provided in parentheses.

The FT-IR spectra measured as KBr disks of $\text{Cs}_{5.25}\text{H}_{1.75}[\alpha\text{-PW}_{11}\text{MgO}_{40}]\cdot6\text{H}_2\text{O}$ and $[(n\text{-}C_4\text{H}_9)_4\text{N}]_{4.25}\text{H}_{2.75}[\alpha\text{-PW}_{11}\text{MgO}_{40}]\cdot\text{H}_2\text{O}\cdot\text{CH}_3\text{CN}$ are shown in Fig. 4. These spectra showed bands at 1081, 1058, 961, 888, 830, 808, 769, and 724 cm^{-1} and 1081, 1060, 957, 891, 819, and 734 cm^{-1}, respectively; these bands were different from those of $\text{K}_7[\alpha\text{-PW}_{11}\text{O}_{39}]$ (1086, 1043, 953, 903, 862, 810, and 734 cm^{-1}) [21, 22]. This also supported that the magnesium ion was coordinated to the vacant site in the polyoxometalate.

The spectral pattern of solid $Cs_{5.25}H_{1.75}[\alpha\text{-}PW_{11}MgO_{40}]\cdot 6H_2O$ was different from that of solid $[(n\text{-}C_4H_9)_4N]_{4.25}H_{2.75}[\alpha\text{-}PW_{11}MgO_{40}]\cdot H_2O\cdot CH_3CN$ even though the counter-ions affected their spectra [21, 22]. As shown in Fig. 5, the FT-IR spectral pattern of solid $[(n\text{-}PW_{11}MgO_{40}]\cdot H_2O\cdot CH_3CN$ was the same as that of a liquid sample observed in acetonitrile (1082, 1059, 955, 889, 811, and 733 cm^{-1}); this showed that the molecular structure of $[(n\text{-}C_4H_9)_4N]_{4.25}H_{2.75}[\alpha\text{-}PW_{11}MgO_{40}]\cdot H_2O\cdot CH_3CN$ observed in a solid was the same as that in acetonitrile solution. In contrast, the spectral pattern of solid $Cs_{5.25}H_{1.75}[\alpha\text{-}PW_{11}MgO_{40}]\cdot 6H_2O$ was somewhat different from that in water (1079, 1056, 1017, 957, 898, 823, 779, and 724 cm^{-1}). Since a single line was observed in the ^{31}P NMR spectrum of $Cs_{5.25}H_{1.75}[\alpha\text{-}PW_{11}MgO_{40}]\cdot 6H_2O$ in D_2O at around 25 °C, this change was not due to decomposition of the cesium salt in aqueous solution; however, water may have influenced the structure.
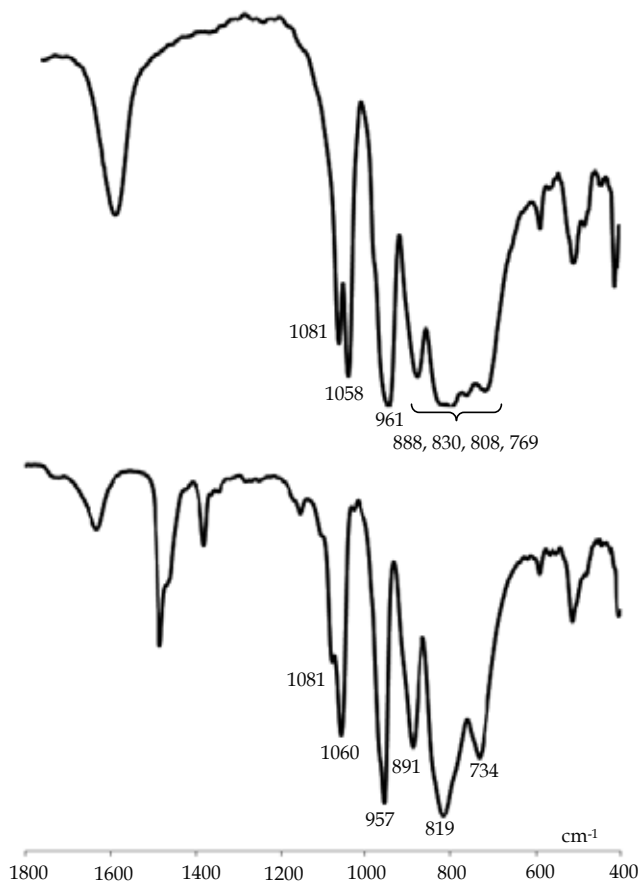

Figure 4. FT-IR spectra (as KBr disks) of $Cs_{5.25}H_{1.75}[\alpha\text{-}PW_{11}MgO_{40}]\cdot 6H_2O$ (top) and $[(n\text{-}C_4H_9)_4N]_{4.25}H_{2.75}[\alpha\text{-}PW_{11}MgO_{40}]\cdot H_2O\cdot CH_3CN$ (bottom) in the range of 1800 – 400 cm^{-1}.
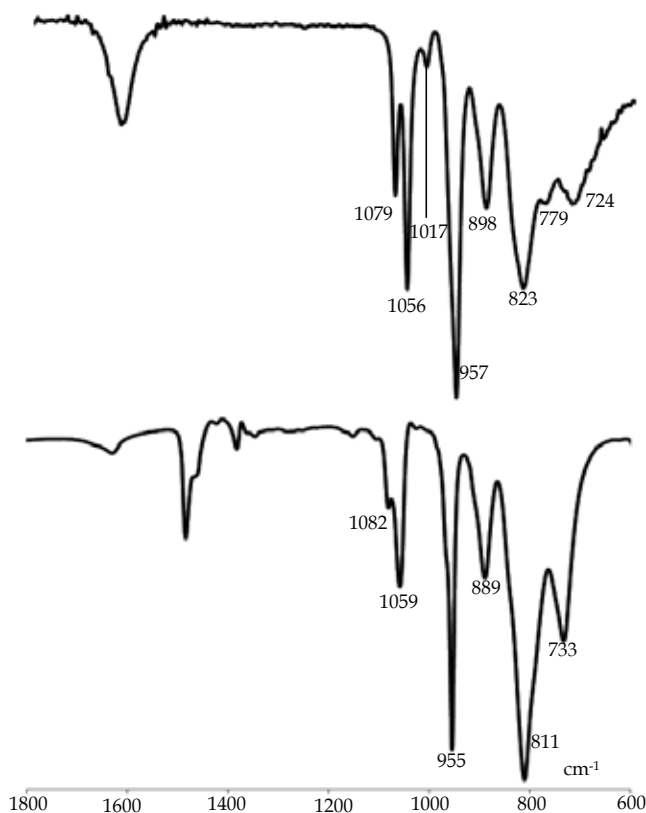
Figure 5. FT-IR spectra of $Cs_{5.25}H_{1.75}[\alpha\text{-}PW_{11}MgO_{40}]\cdot 6H_2O$ observed in water (top) and $[(n\text{-}C_4H_9)_4N]_{4.25}H_{2.75}[\alpha\text{-}PW_{11}MgO_{40}]\cdot H_2O\cdot CH_3CN$ observed in acetonitrile (bottom) in the range of $1800 - 600$ cm^{-1}.

3.2. Syntheses and molecular structures of potassium and dimethylammonium salts of α-Dawson-type mono-magnesium–substituted polyoxotungstate $K_8H_2[\alpha_2\text{-}P_2W_{17}MgO_{62}]\cdot 15H_2O$ and $[(CH_3)_2NH_2]_{7.5}H_{2.5}[\alpha_2\text{-}P_2W_{17}MgO_{62}]\cdot 6H_2O$

The potassium salt of $[\alpha_2\text{-}P_2W_{17}MgO_{62}]^{10-}$ was formed by the direct reaction of magnesium bromide with $[\alpha_2\text{-}P_2W_{17}O_{61}]^{10-}$ (at a $Mg^{2+}/[\alpha_2\text{-}P_2W_{17}O_{61}]^{10-}$ molar ratio of ~3.0) in aqueous solution, followed by the addition of excess potassium chloride. Pure potassium salt was not obtained by the stoichiometric reaction of magnesium ions with $[\alpha_2\text{-}P_2W_{17}O_{61}]^{10-}$ in aqueous solution, as was observed for $Cs_{5.25}H_{1.75}[\alpha\text{-}PW_{11}MgO_{40}]\cdot 6H_2O$. In contrast, the dimethylammonium salt was formed via a stoichiometric reaction of magnesium nitrate with $[\alpha_2\text{-}P_2W_{17}O_{61}]^{10-}$ in aqueous solution, followed by the addition of excess dimethylammonium chloride. Crystallization was performed by vapor diffusion from water/ethanol at around 25 °C.
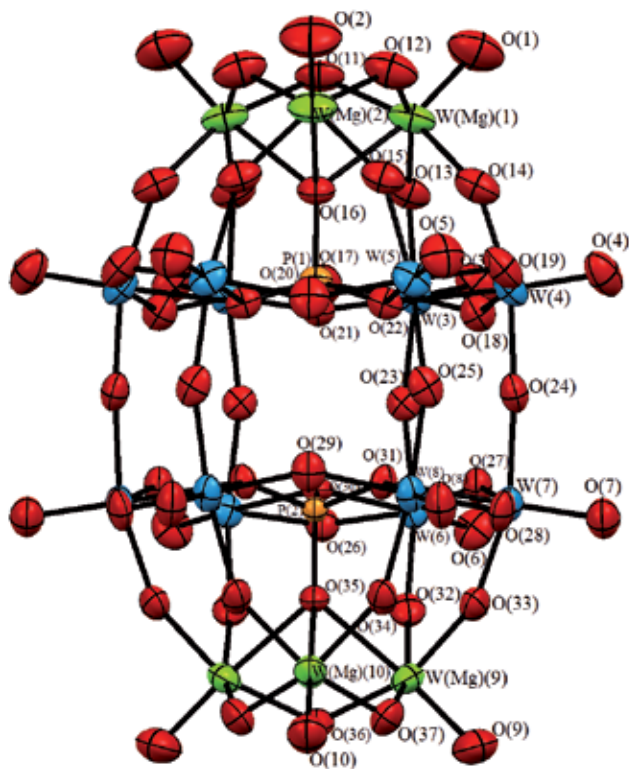
Figure 6. Molecular structure (ORTEP drawing) of $[(CH_3)_2NH_2]_{7.5}H_{2.5}[\alpha_2-P_2W_{17}MgO_{62}]\cdot 6H_2O$. One magnesium atom was disordered over six tungsten atoms at the B-sites (i.e., cap units) in $[\alpha_2-P_2W_{17}MgO_{62}]^{10-}$. The occupancies for the magnesium and tungsten sites were fixed at 1/6 and 5/6 throughout the refinement; however, the populations of these atoms differed.

The elemental analysis results for H, K, Mg, P, and W were in good agreement with the calculated values for $K_8H_2[\alpha_2-P_2W_{17}MgO_{62}]\cdot H_2O$. N analysis revealed no contamination of nitrate ions from $Mg(NO_3)_2$. The weight loss observed during drying before the analysis was 5.30% for $K_8H_2[\alpha_2-P_2W_{17}MgO_{62}]\cdot 15H_2O$; this corresponded to 14 weakly solvated or adsorbed water molecules. TG/DTA data also showed a weight loss of 5.62% in the temperature range of 25 to 500 °C, which corresponded to 15 water molecules. For the dimethylammonium salt, the C, H, N, P, Mg, and W elemental analysis results were in good agreement with the calculated values for $[(CH_3)_2NH_2]_{7.5}H_{2.5}[\alpha_2-P_2W_{17}MgO_{62}]\cdot 3H_2O$. The K analysis revealed no contamination of potassium ions from $K_{10}[\alpha_2-P_2W_{17}O_{61}]\cdot 14H_2O$. The weight loss observed during drying before the analysis was 1.30% for $[(CH_3)_2NH_2]_{7.5}H_{2.5}[\alpha_2-P_2W_{17}MgO_{62}]\cdot 6H_2O$; this corresponded to three weakly solvated molecules. TG/DTA data showed weight losses of 2.33 and 7.42% observed in the temperature ranges of 25 to 200 °C and 200 to 500 °C, respectively; these values corresponded to six water molecules and 7.5 $[(CH_3)_2NH_2]^+$ ions, respectively.

$[(CH_3)_2NH_2]_{7.5}H_{2.5}[\alpha_2-P_2W_{17}MgO_{62}]\cdot 6H_2O$	
belt units (W(3) –W(8))	
W-O_a	2.338 – 2.374 (2.359)
W-O_c	1.874 – 1.962 (1.908)
W-O_e	1.904 – 1.935 (1.924)
W-O_t	1.698 – 1.733 (1.717)
cap units (W(Mg) (1), W(Mg)(2), W(Mg)(9), W(Mg)(10))	
W(Mg)-O_a	2.348 – 2.393 (2.369)
W(Mg)-O_c	1.909 – 1.966 (1.934)
W(Mg)-O_e	1.910 – 1.948 (1.930)
W(Mg)-O_t	1.73 – 1.788 (1.760)
P-O	1.505 – 1.584 (1.538)

Table 4. Ranges and mean bond distances (Å) of $[(CH_3)_2NH_2]_{7.5}H_{2.5}[\alpha_2-P_2W_{17}MgO_{62}]\cdot 6H_2O$. O_a: oxygen atoms belonging to the central PO_4 tetrahedron; O_c: bridging oxygen atoms between corner-sharing MO_6 (M = Mg and W) octahedra; O_e: bridging oxygen atoms between edge-sharing MO_6 octahedra (M = Mg and W); and O_t: terminal oxygen atoms. Mean values are provided in parentheses.

The molecular structure of $[(CH_3)_2NH_2]_{7.5}H_{2.5}[\alpha_2-P_2W_{17}MgO_{62}]\cdot 6H_2O$ determined by X-ray crystallography is shown in Fig. 6. This molecular structure was identical to that of monomeric α-Dawson-type polyoxotungstate $[\alpha-P_2W_{18}O_{62}]^{6-}$ [23], which was constructed from cap (W(Mg) (1, 2, 9, 10)) and belt (W(3 – 8)) units. The bond lengths are summarized in Table 4. Because of the high symmetry of the space group, the six tungsten(VI) atoms at the two cap units were disordered and the partial structure around the magnesium site in $[(CH_3)_2NH_2]_{7.5}H_{2.5}[\alpha_2-P_2W_{17}MgO_{62}]\cdot 6H_2O$ was not identified by X-ray crystallography, as was observed for $Cs_{5.25}H_{1.75}[\alpha-PW_{11}MgO_{40}]\cdot 6H_2O$ and $[(n-C_4H_9)_4N]_{4.25}H_{2.75}[\alpha-PW_{11}MgO_{40}]\cdot H_2O\cdot CH_3CN$; however, the W(Mg)–$O_t$ bond lengths in the cap units (average 1.760 Å) were remarkably longer than those of W–O_t in the belt units (average 1.717 Å) and $[\alpha_2-P_2W_{17}O_{61}]^{10-}$ (~1.7 Å) [24]. Although it was difficult to discuss that the W(Mg)–O_t lengths of $Cs_{5.25}H_{1.75}[\alpha-PW_{11}MgO_{40}]\cdot 6H_2O$ and $[(n-C_4H_9)_4N]_{4.25}H_{2.75}[\alpha-PW_{11}MgO_{40}]\cdot H_2O\cdot CH_3CN$ were longer than those of $[CH_3NH_3]_3[PW_{12}O_{40}]\cdot 2H_2O$ (1.6951 Å), $[(CH_3)_2NH_2]_3[PW_{12}O_{40}]$ (1.7026 Å), and $[(CH_3)_3NH]_3[PW_{12}O_{40}]$ (1.6933 Å) [19], the DFT calculation results for $[\alpha-PW_{11}\{Mg(OH)\}O_{39}]^{6-}$ and $[\alpha-PW_{11}\{Mg(OH_2)\}O_{39}]^{5-}$ showed that the Mg–OH_2 bond distance in $[\alpha-PW_{11}\{Mg(OH_2)\}O_{39}]^{5-}$ (2.12343 Å) was longer than that of Mg–OH in $[\alpha-PW_{11}\{Mg(OH)\}O_{39}]^{6-}$ (1.93732 Å) (Table 2). For the other magnesium compounds, the Mg–OH_2 bond lengths in $[Mg(TDC)(H_2O)_2]$ (TDC = 2,5-thiophenedicarboxylate) (2.080 Å) [25] and Mg(3,5-PDC)(H_2O)_2 (PDC = pyridinedicarboxylate) (2.04 Å) [26] were longer than that of Mg–OH in $[2MgSO_4\cdot Mg(OH)_2]$ (2.025 Å) [27]. These results suggested that a water molecule was coordinated to the mono-magnesium-substituted site in $[(CH_3)_2NH_2]_{7.5}H_{2.5}[\alpha_2-P_2W_{17}MgO_{62}]\cdot 6H_2O$.

The ^{31}P NMR spectrum of $K_8H_2[\alpha_2\text{-}P_2W_{17}MgO_{62}]\cdot15H_2O$ in D_2O showed signals at –7.8 and –13.8 ppm, which were the same as those of $[(CH_3)_2NH_2]_{7.5}H_{2.5}[\alpha_2\text{-}P_2W_{17}MgO_{62}]\cdot6H_2O$ (–7.7 and -13.7 ppm); this was also confirmed by the two-line spectrum observed for a mixture of the potassium and dimethylammonium salts in D_2O. These signals were different from those of $K_{10}[\alpha_2\text{-}P_2W_{17}O_{61}]\cdot14H_2O$ (δ –6.8 and –13.9), suggesting that a magnesium ion was coordinated to the vacant site of $[\alpha_2\text{-}P_2W_{17}O_{61}]^{10-}$. The ^{183}W NMR spectrum of $K_8H_2[\alpha_2\text{-}P_2W_{17}MgO_{62}]\cdot15H_2O$ in 2.0 mM $Mg(NO_3)_2$-D_2O showed nine signals at –57.04, –80.87, –131.47, –176.59, –181.67, –201.40, –207.65, –208.63, and –230.51, as shown in Fig. 7. These signals were also different from those of $K_{10}[\alpha_2\text{-}P_2W_{17}O_{61}]\cdot14H_2O$ (δ –117.1, –140.4, –151.7, –181.0, –183.1, –218.1, –220.5, –224.0, and –242.6) observed in D_2O [28]. These results also supported that a magnesium ion was coordinated to the vacant site of $[\alpha_2\text{-}P_2W_{17}O_{61}]^{10-}$, resulting in an overall C_s symmetry.
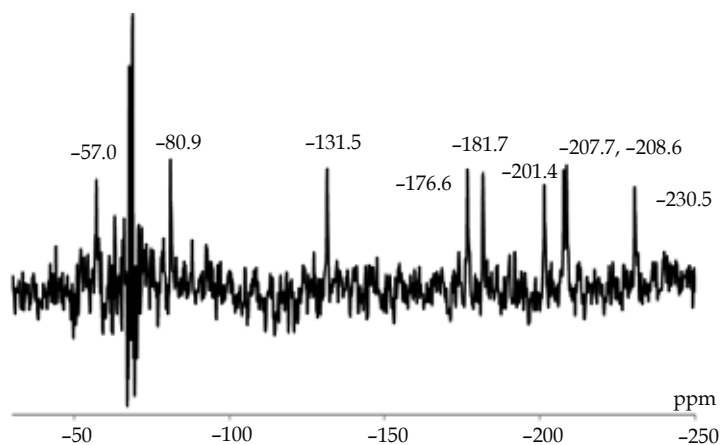

Figure 7. NMR spectrum of $K_8H_2[\alpha_2\text{-}P_2W_{17}MgO_{62}]\cdot15H_2O$ in 2.0 mM $Mg(NO_3)_2$-D_2O.

The FT-IR spectra of $K_8H_2[\alpha_2\text{-}P_2W_{17}MgO_{62}]\cdot15H_2O$ and $[(CH_3)_2NH_2]_{7.5}H_{2.5}[\alpha_2\text{-}P_2W_{17}MgO_{62}]\cdot6H_2O$ measured as KBr disks are shown in Fig. 8. The potassium and dimethylammonium salts showed bands at 1084, 1063, 1015, 945, 920, 892, 823, 786, and 736 cm^{-1} and 1087, 1065, 1018, 948, 919, 891, 805, 777, and 717 cm^{-1}, respectively. These bands were different from those of $K_{10}[\alpha_2\text{-}P_2W_{17}O_{61}]\cdot14H_2O$ (1084, 1051, 1016, 940, 918, 887, 811, 740, and 601 cm^{-1}), which also supported that a magnesium atom was coordinated in the vacant site of $[\alpha_2\text{-}P_2W_{17}O_{61}]^{10-}$. The spectral pattern of solid $[(CH_3)_2NH_2]_{7.5}H_{2.5}[\alpha_2\text{-}P_2W_{17}MgO_{62}]\cdot6H_2O$ was quite similar to that in water (1086, 1065, 1020, 945, 913, 808, 790, and 723 cm^{-1}); this suggested that the molecular structure of $[(CH_3)_2NH_2]_{7.5}H_{2.5}[\alpha_2\text{-}P_2W_{17}MgO_{62}]\cdot6H_2O$ observed in a solid was maintained in an aqueous solution. In addition, the FT-IR spectrum of $[(CH_3)_2NH_2]_{7.5}H_{2.5}[\alpha_2\text{-}P_2W_{17}MgO_{62}]\cdot6H_2O$ observed in water was the same as that of a liquid sample of $K_8H_2[\alpha_2\text{-}P_2W_{17}MgO_{62}]\cdot15H_2O$ (1086, 1064, 1015, 946, 914, 811, 788, and 724 cm^{-1}). These results showed that the molecular structure of potassium salt was the same as that of the dimethylammonium salt, as suggested by the ^{31}P NMR spectra of the salts in D_2O.
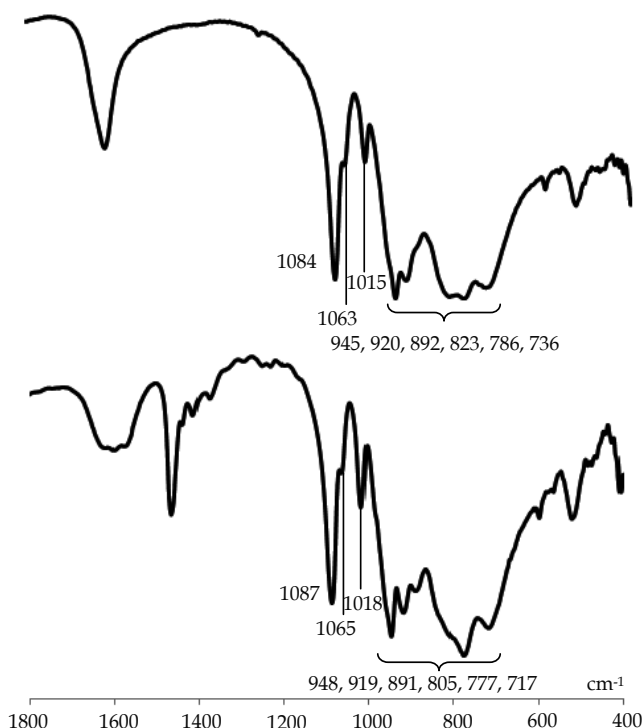
Figure 8. FTIR spectra (as KBr disks) of $K_8H_2[\alpha_2\text{-}P_2W_{17}MgO_{62}]\cdot15H_2O$ (Top) and $[(CH_3)_2NH_2]_{7.5}H_{2.5}[\alpha_2\text{-}P_2W_{17}MgO_{62}]\cdot6H_2O$ (bottom) in the range of 1800 – 400 cm^{-1}.

4. Conclusion

In this study, we synthesized α-Keggin-type mono-magnesium-substituted polyoxotungstate $Cs_{5.25}H_{1.75}[\alpha\text{-}PW_{11}MgO_{40}]\cdot6H_2O$ and $[(n\text{-}C_4H_9)_4N]_{4.25}H_{2.75}[\alpha\text{-}PW_{11}MgO_{40}]\cdot H_2O\cdot CH_3CN$, and α-Dawson-type mono-magnesium-substituted polyoxotungstate $K_8H_2[\alpha_2\text{-}P_2W_{17}MgO_{62}]\cdot15H_2O$ and $[(CH_3)_2NH_2]_{7.5}H_{2.5}[\alpha_2\text{-}P_2W_{17}MgO_{62}]\cdot6H_2O$ by reacting magnesium ions with mono-lacunary α-Keggin and α-Dawson-type phosphotungstates. The compounds were character-ized by X-ray crystallography, elemental analysis, thermogravimetric/differential thermal analysis, Fourier-transform infrared spectra, and solution ^{31}P and [183]W nuclear magnetic resonance spectroscopy. The single-crystal X-ray structure analyses of $Cs_{5.25}H_{1.75}[\alpha\text{-}PW_{11}MgO_{40}]\cdot6H_2O$, $[(n\text{-}C_4H_9)_4N]_{4.25}H_{2.75}[\alpha\text{-}PW_{11}MgO_{40}]\cdot H_2O\cdot CH_3CN$, and $[(CH_3)_2NH_2]_{7.5}H_{2.5}[\alpha_2\text{-}P_2W_{17}MgO_{62}]\cdot6H_2O$ revealed monomeric, α-Keggin, and α-Dawson structures, respectively; the mono-magnesium–substituted sites could not be identified because of the high symmetry of the products. However, the bonding modes (i.e., bond lengths and bond angles) suggested that a hydroxyl group and/or water molecule were coordinated to the mono-magnesium-substituted site in $[\alpha\text{-}PW_{11}MgO_{40}]^{7-}$ and $[\alpha_2\text{-}P_2W_{17}MgO_{62}]^{10-}$. The DFT and zero-point energy calculation results also suggested that the molecular structures of $[\alpha$-

PW$_{11}${Mg(OH)}O$_{39}$]$^{6-}$ and [α-PW$_{11}${Mg(OH$_2$)}O$_{39}$]$^{5-}$ were significantly influenced by coordination of a hydroxyl group and water molecule to the magnesium site, and [α-PW$_{11}${Mg(OH$_2$)}O$_{39}$]$^{5-}$ was more stable than [α-PW$_{11}${Mg(OH)}O$_{39}$]$^{6-}$.

Acknowledgements

Author details

Chika Nozaki Kato[1*], Nami Ukai[1], Daisuke Miyamae[1], Shunya Arata[1], Toshifumi Kashiwagi[1], Masaru Nagami[1], Toshiya Mori[1], Yusuke Kataoka[2], Yasutaka Kitagawa[3] and Hidemitsu Uno[4]

*Address all correspondence to: sckatou@ipc.shizuoka.ac.jp

1 Shizuoka University, Japan

2 Shimane University, Japan

3 Osaka University, Japan

4 Ehime University, Japan

References

[1] Pope MT. Heteropoly and Isopoly Oxometalates. Berlin: Springer-Verlag; 1983.

[2] Pope MT, Müller A. Polyoxometalate Chemistry. An Old Field with New Dimensions in Several Disciplines. Angewandte Chemie International Edition in English 1991; 30 (1) 34–48.

[3] Pope MT, Müller A., editors. Polyoxometalates: From Platonic Solids to Anti-Retroviral Activity. Dordrecht: Kluwer Academic Publishers; 1994.

[4] Cotton, FA, Wilkinson G. Advanced Inorganic Chemistry, Fifth Edition. New York: John Wiley & Sons; 1988.

[5] Ono Y, Hattori H. Solid Base Catalysis. Berlin: Springer-Verlag and Tokyo Institute of Technology Press; 2011.

[6]   Günter JR, Bensch W. Two New Trigonal Magnesium Heteropolytungstates: Crystal Structures, Topotactic Relations, and Thermal Dehydration. Journal of Solid State Chemistry 1987; 69 (2) 202–214.

[7]   Günter JR, Schmalle HW, Dubler E. Crystal Structure and Properties of A New Magnesium Heteropoly-tungstate, $Mg_7(MgW_{12}O_{42})(OH)_4(H_2O)_8$, and The Isostructural Compounds of Manganese, Iron, Cobalt, and Nickel. Solid State Ionics 1990; 43 85–92.

[8]   Contant R. Relation between Tungstophosphates Related to the Phosphorus Tungsten Oxide Anion ($PW_{12}O_{40}{}^{3-}$). Synthesis and Properties of a New Lacunary Potassium Polyoxotungstophosphate ($K_{10}P_2W_{20}O_{70}\cdot 24H_2O$). Canadian Journal of Chemistry 1987; 65 (3) 568–573.

[9]   Lyon DK, Miller WK, Novet T, Domaille PJ, Evitt E, Johnson DC, Finke RG. Highly Oxidation Resistant Inorganic-Porphyrin Analog Polyoxometalate Oxidation Catalysts. 1. The Synthesis and Characterization of Aqueous-Soluble Potassium Salts of α_2-$P_2W_{17}O_{61}(M^{n+}\cdot OH_2)^{(n-10)}$ and Organic Solvent Soluble Tetra-n-butylammonium Salts of α_2-$P_2W_{17}O_{61}(M^{n+}\cdot Br)^{(n-11)}$ (M = Mn^{3+}, Fe^{3+}, Co^{2+}, Ni^{2+}, Cu^{2+}). Journal of the American Chemical Society 1991; 113 (19) 7209–7221.

[10]   Burla MC, Caliandro R, Camalli M, Carrozzini B, Cascarano GL, De Caro L, Giacovazzo C, Polidori G, Spagna R. *SIR2004*: An Improved Tool for Crystal Structure Determination and Refinement. Journal of Applies Crystallography 2005; 38 (2) 381-388.

[11]   Sheldrick GM. A Short History of SHELX. Acta Crystallographica Section A 2008; A64 (1) 112–122.

[12]   Spek, AL. Structure Validation in Chemical Crystallography. Acta Crystallographica Section D 2009; D65 (2) 148–155.

[13]   Nomiya K, Takahashi M, Ohsawa K, Widegren JA. Synthesis and Characterization of Tri-titanium(IV)-1,2,3-substituted α-Keggin Polyoxotungstates with Heteroatoms P and Si. Crystal Structure of the Dimeric, Ti-O-Ti Bridged Anhydride Form $K_{10}H_2[\alpha,\alpha$-$P_2W_{18}Ti_6O_{77}]\cdot 17H_2O$ and Confirmation of Dimeric Forms in Aqueous Solution by Ultracentrifugation Molecular Weight Measurements. Journal of the Chemical Society Dalton Transactions 2001; 19 2872–2878.

[14]   Nomiya K, Takahashi M, Widegren JA, Aizawa T, Sakai Y, Kasuga NC. Synthesis and pH-Variable Ultracentrifugation Molecular Weight Measurements of the Dimeric, Ti-O-Ti Bridged Anhydride Form of a Novel Di-Ti^{IV}-1,2-substituted α-Keggin Polyoxotungstate. Molecular Structure of the $[(\alpha$-1,2-$PW_{10}Ti_2O_{39})_2]^{10-}$ Polyoxoanion. Journal of the Chemical Society Dalton Transactions 2002; 19 3679–3685.

[15]   Weakley TJR, Finke RG. Single-crystal X-Ray Structures of the Polyoxotungstate Salts $K_{8.3}Na_{1.7}[Cu_4(H_2O)_2(PW_9O_{34})_2]\cdot 24H_2O$ and $Na_{14}Cu[Cu_4(H_2O)_2(P_2W_{15}O_{56})_2]\cdot 53H_2O$. Inorganic Chemistry 1990; 29 (6) 1235–1241.

[16] Lin Y, Weakley TJR, Rapko B, Finke RG. Polyoxoanions Derived from Tungstosilicate (A-β-$SiW_9O_{34}^{10-}$): Synthesis, Single-crystal Structural Determination, and Solution Structural Characterization by Tungsten-183 NMR and IR of Titanotungstosilicate (A-β-$Si_2W_{18}Ti_6O_{77}^{14-}$). Inorganic Chemistry 1993; 32 (23) 5095–5101.

[17] Frisch MJ, Trucks GW, Schlegel HB, Scuseria GE, Robb MA, Cheeseman JR, Scalmani G, Barone V, Mennucci B, Petersson GA, Nakatsuji H, Caricato M, Li X, Hratchian HP, Izmaylov AF, Bloino J, Zheng G, Sonnenberg JL, Hada M, Ehara M, Toyota K, Fukuda R, Hasegawa J, Ishida M, Nakajima T, Honda Y, Kitao O, Nakai H, Vreven T, Montgomery JA, Peralta JE, Ogliaro F, Bearpark M, Heyd JJ, Brothers E, Kudin KN, Staroverov VN, Kobayashi R, Normand J, Raghavachari K, Rendell A, Burant JC, Iyengar SS, Tomasi J, Cossi M, Rega N, Millam JM, Klene M, Knox JE, Cross JB, Bakken V, Adamo C, Jaramillo J, Gomperts R, Stratmann RE, Yazyev O, Austin AJ, Cammi R, Pomelli C, Ochterski JW, Martin RL, Morokuma K, Zakrzewski VG, Voth GA, Salvador P, Dannenberg JJ, Dapprich S, Daniels AD, Farkas Ö, Foresman JB, Ortiz JV, Cioslowski J, Fox DJ. Gaussian 09, Revision B, 01, Wallingford CT: Gaussian, Inc.; 2009.

[18] Neiwert WA, Cowan JJ, Hardcastle KI, Hill CL, Weinstock IA. Stability and Structure in α- and β-Keggin Heteropolytungstates, $[X^{n+}W_{12}O_{40}]^{(8-n)-}$, X = p-Block Cation. Inorganic Chemistry 2002; 41 (26) 6950–6952.

[19] Busbongthong S, Ozeki T. Structural Relationships among Methyl-, Dimethyl-, and Trimethylammonium Phosphododecatungstates. Bulletin of Chemical Society in Japan 2009; 82 (11) 1393–1397.

[20] Kato CN, Makino Y, Yamasaki M, Kataoka U, Kitagawa Y, Okumura M. Synthesis and X-Ray Crystal Structure of α-Keggin-type Aluminum-substituted Polyoxotungstate. Advances in Crystallization processes, Rijeka: InTech; 2012.

[21] Rocchiccioli-Deltcheff C, Fournier M, Franck R, Thouvenot R. Vibrational Investigations of Polyoxometalates. 2. Evidence for Anion-Anion Interactions in Molybdenum(VI) and Tungsten(VI) Compounds Related to the Keggin Structure. Inorganic Chemistry 1983; 22 207–216.

[22] Thouvenot R, Fournier M, Franck R, Rocchiccioli-Deltcheff C. Vibrational Investigations of Polyoxometalates. 3. Isomerism in Molybdenum(VI) and Tungsten(VI) Compounds Related to the Keggin Structure. Inorganic Chemistry 1984; 23 (5) 598–605.

[23] Dawson B. The Structure of the 9(18)-Heteropoly Anion in Potassium 9(18)-Tungstophosphate, $K_6(P_2W_{18}O_{62})\cdot 14H_2O$. Acta Crystallographica 1953; 6 113–126.

[24] Sakai Y, Shinohara A, Hayashi K, Nomiya K. Synthesis and Characterization of Two Novel, Mono-lacunary Dawson Polyoxometalate-based, Water-soluble Organometallic Ruthenium(II) Complexes: Molecular Structure of $[\{(C_6H_6)Ru(H_2O)\}(\alpha_2$-$P_2W_{17}O_{61})]^{8-}$. European Journal of Inorganic Chemistry 2006; 163 – 171.

[25] Calderone PJ, Banerjee D, Santulli AC, Wong SS, Parise JB. Synthesis, Characterization, and Luminescence Properties of Magnesium Coordination Networks using a Thiophene-based Linker. Inorganica Chimica Acta 2011; 378 (1) 109–114.

[26] Banerjee D, Finkelstein J, Smirnov A, Forster PM, Borkowski LA, Teat SJ, Parise JB. Synthesis and Structural Characterization of Magnesium Based Coordination Networks in Different Solvents. Crystal Growth & Design 2011; 11 (6) 2572–2579.

[27] Fleet ME, Knipe SW. Structure of Magnesium Hydroxide Sulfate [2MgSO$_4$.Mg(OH)$_2$] and Solid Solution in Magnesium Hydroxide Sulfate Hydrate and Caminite. Acta Crystallographica 1997; B53 (3) 358–363.

[28] Kato CN, Shinohara A, Hayashi K, Nomiya K. Syntheses and X-ray Crystal Structures of Zirconium(IV) and Hafnium(IV) Complexes Containing Monovacant Wells-Dawson and Keggin Polyoxotungstates. Inorganic Chemistry 2006; 45 (20) 8108–8119.

Edited by Yitzhak Mastai

In nearly all process industries, crystallization is used at some stage as a method of production, purification or recovery of solid materials. In recent years, a number of new applications have also come to rely on crystallization processes such as the crystallization of nano and amorphous materials. The articles in this book have been contributed by some of the most respected researchers in this area and cover the frontier areas of research and developments in crystallization processes. Divided into three sections, this book provides the latest research developments in many aspects of crystallization including the crystallization of biological macromolecules and pharmaceutical compounds, the crystallization of nanomaterials and the crystallization of amorphous and glassy materials. This book is of interest to both fundamental research and practicing scientists and will prove invaluable to all chemical engineers and industrial chemists in process industries, as well as crystallization workers and students in industry and academia.

Photo by memoriesarecaptured / iStock

IntechOpen